Resonant Band Gaps from a Narrow Slit at Terahertz Frequencies

Yan Zhang, Kuo Meng, and Yanhua Wang

Beijing Key Lab for Terahertz Spectroscopy and Imaging, Key Laboratory of Terahertz Optoelectronics
Ministry of Education, Department of Physics, Capital Normal University
Beijing 100037, China

Abstract— We report a simple sub-wavelength device for resonant band gaps generation at the terahertz (THz) frequencies. Employing the surface plasmon polaritons, only a single sub wavelength slit can cut out the THz spectrum effectively. The transmission spectrum of thus device is measured using the THz time domain spectroscopy system. With the slit becomes narrower, the transmission peaks move to the high frequency direction and the depth of the forbidden gap increase. Theoretical simulations are also carried out by using the the finite difference time domain method. The simulation results agree with experimental results well. This kind of devices can provide an approach to control the THz photons.

1. INTRODUCTION

Recently, the work by Ebbesen *et al.* shows that two dimensional periodic arrays of subwavelength metallic holes can present remarkable transmission [1]. The transmitted spectral response exhibits much more transmission than predicted by the standard aperture theory. Further researches show that the property of the transmission spectrum can be controlled by the parameters of subwavelength holes arrays. The theoretical works on gratings with narrow slits in metal screens have also been carried out [2, 3] for giving a physical explanation of the extraordinary high transmission. For simplify the structure, a single slit case has also been studied both theoretically and experimentally in the microwave frequencies [4–6]. However, all of these investigations concentrated on the amplitude modulation of the slit on the incident radiation, the phase change which is also quite important has been neglected.

The terahertz (THz) radiation sandwiched between the microwave and the infrared has attached extensive attentions due to its potential applications [7–9]. Since many materials inherently do not respond to the THz radiation, artificially structured materials operating within this range are quite necessary for fabricating different kinds of devices. Comparing with the reports at microwave, near-infrared, and visible frequencies, less work on metamaterial devices has been done in the THz range [10–12]. However, the choice of THz range for investigation of the extraordinary high transmission is particularly expedient for the following advantages. First, the metal in the THz range may be considered as almost perfectly conducting, which can provide simple parameters for theoretical predication. Second, it is easier to fabricate and vary the dimensions of the slit in this range with relative long wavelength. Third, the coherent detection technology is used to detect the THz signal, both the amplitude and phase information of the transmission signal can be achieved which can provide more information on investigation of interaction between the metallic slit with illuminating light.

In this presentation, the THz time domain spectroscopy (THz-TDS) is used to character the transmission spectrum of a single subwavelength metal slit. The results show that only a single narrow slit may act as a resonant transmission filter and generate the band gap in the transmission spectra. The transmission spectra also exhibits the Fabry-P èrot-like behavior. The finite difference time domain simulation is also carried out to confirm the experiment result. It was found that simulation results agree with experimental results well.

2. EXPERIMENT RESULTS

The experiment arrangement is schematically shown in Fig. 1. The metallic slit sample is made from two 200 μm thick and 20 mm long blades. Two blades are bound on two electric stages respectively. The edges of blades form a slit with horn opening. The stages can be separated with position resolution of 0.5 μm, thus the slit with different widthes can be easily achieved. The silt is put on the focus point of the THz beam in a conventional THz time domain spectroscopy. The size of the focus point is 1.1 mm. To avoided the effect of vapor in the air, the THz beam is covered by a pressurized box filling with nitrogen. The time domain waveform of the impulsive THz radiation is recorded, and then the electric field spectral amplitude and phase can be obtained via the Fourier

transform. Normalizing the signals with the reference signal obtained without any object in the THz path, the complex transmission as a function of frequency can be determined. Limited by the emitter and detector crystal, the valid range of our system is 0.2–2.6 THz.

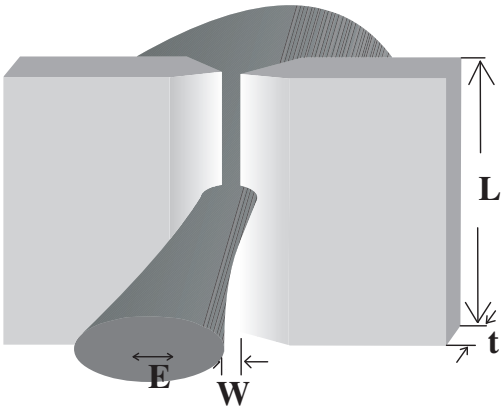

Figure 1: Schematic plan of the setup and sample geometry.

All experiments are performed at normal incidence. The polarization of the THz electric field was perpendicular to the slit gap, *i.e.*, the incident beam is TM polarized. The measured complex transmission spectra are shown in Fig. 2 for different slit widths. The widthes of the slit are 200 μm, 150 μm, 100 μm, 80 μm, 60 μm, 40 μm, and 20 μm, respectively. For the wide slit with 200 μm width, the transmission spectrum exhibits only the cut off feature. There is no obvious oscillation in the transmission spectrum. With the slit becoming narrow, transmission spectra exhibit stronger oscillations. Furthermore, the position of the transmission peaks move to the high frequency direction. For the narrow slit with 20 μm width, the transmission spectrum exhibits the Fabry-Pèrot-like band gaps, the passband transmittances are 9.9%, 11.3%, 10.3%, and 9.0% at frequencies of 0.264 THz, 0.881 THz, 1.63 THz, and 2.51 THz, respectively. The phase information of the transmission spectra have also been presented in Fig. 3(b). The strong oscillations can also be found for narrow slits. With the slit becoming narrower, the oscillations become stronger.

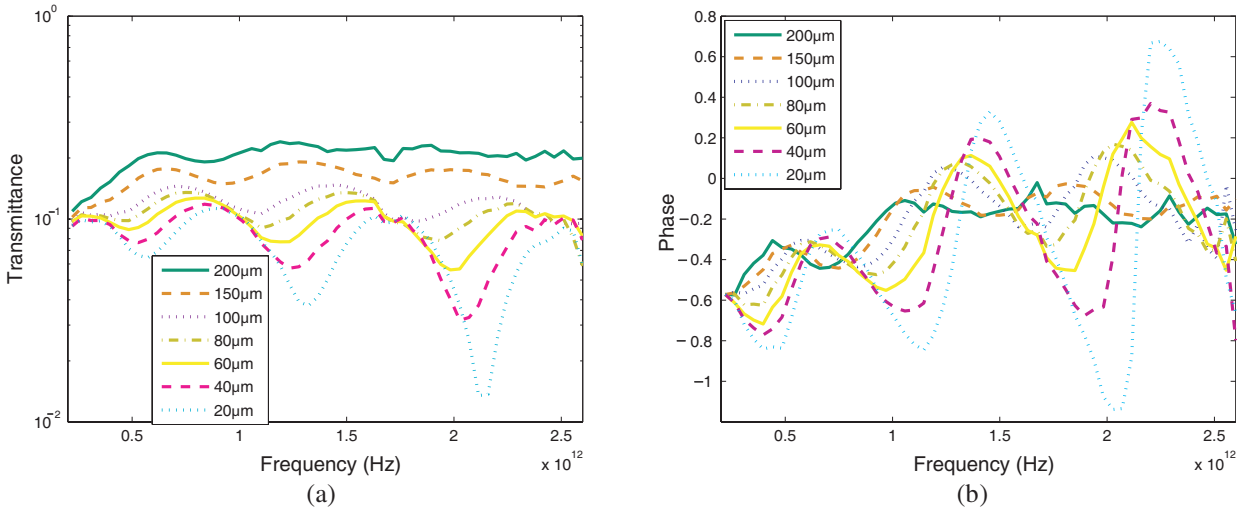

Figure 2: Measured complex transmission spectra for the single metallic slit with different widths. (a) Amplitude and (b) phase distribution.

3. SIMULATION RESULTS

The theoretical simulations have been carried out using the homemade finite difference time domain (FDTD) programm to verify experiment results. Three assumptions are used in the simulations for simplification. First, the used metal is assumed to be the perfect conductor. Second, the slit is

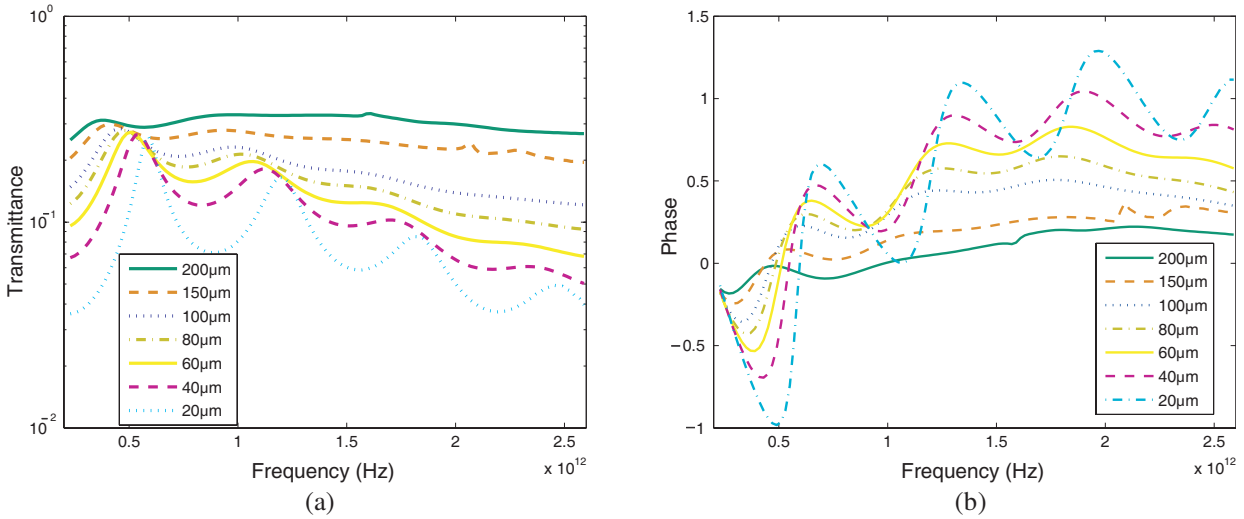

Figure 3: Calculated complex transmission spectra for the single metallic slit with different width. (a) Amplitude and (b) phase distributions.

simplified as a rectangle one, the horn opening is neglected. Third, the slit is illuminated by the plane wave unlike the focused Gaussian beam used in the experiment. Other parameters of the sample are the same with that used in experiment.

The transmission spectra of the single metallic slit with different widths for TM-polarized wave are shown in Fig. 4. For the wider slit, the simulation results correspond to the experiment data well. The transmission spectrum exhibit only a cut o frequency. With the slit become narrow, the spectrum exhibit more and more strong oscillations. The positions of the transmission peaks move to the high frequency direction. All of these characters correspond to the experiment results well. The only difference is the descending of transmission peaks with frequency increasing for narrow slit in the simulation. The reason can be explained as follows: In the experiment, the focused THz beam is used to illuminate the slit. The beam with high frequency can be focused well, thus transmission energy of the high frequency in experiment is enhanced.

4. CONCLUSION

In conclusion, the transmission of the THz TM-polarized radiation through the subwavelength slit have been experimentally investigated in the THz region. When the slit is narrow enough, the Fabry-P*è*rot-like band gap feature in the transmission spectrum has been discover. The FDTD simulations correspond to the experimental results well. These results may provide a potential application of fabrication wavelength scale device to control and manipulate THz wave.

ACKNOWLEDGMENT

This work was supported by the Chinese National Key Basic Research Special Fund under Grant No. 2006CB302901 and the National Natural Science Foundation of China under Grant No. 10674038.

REFERENCES

1. Ebbesen, T. W., J. J. Lezec, H. F. Ghaemi, T. Thio, and P. A. Wolff, "Extraordinary optical transmission through subwavelength hole arrays," *Nature*, Vol. 391, 667–669, 1998.
2. Porto, J. A., F. J. Garcia-Vidal, and J. B. Pendry, "Transmission resonances on metallic gratings with very narrow slits," *Phys. Rev. Lett.*, Vol. 83, 2845–2828, 1999.
3. Hibbins, A. P., J. R. Sambles, C. R. Lawrence, and D. M. Robinson, "Remarkable transmission of microwaves through a wall of long metallic bricks," *Appl. Phys. Lett.*, Vol. 79, 2844–2846, 2001.
4. Takakura, Y., "Optical resonance in a narrow slit in a thick metallic screen," *Phys. Rev. Lett.*, Vol. 86, 5601–5603, 2001.
5. Yang, F. and J. R. Sambles, "Resonant transmission of microwaves through a narrow metallic slit," *Phys. Rev. Lett.*, Vol. 89, 063901, 2002.

6. Suckling, J. R., A. P. Hibbins, M. J. Lockyear, T. W. Preist, and J. R. Sambles, "Finite conductance governs the resonance transmission of thin metal slits at microwave frequencies," *Phys. Rev. Lett.*, Vol. 92, 147401, 2004.
7. Tonouchi, M., "Cutting-edge terahertz technology," *Nature Photonics*, Vol. 1, 97–105, 2007.
8. Liu, H-B, Y. Cheng, G. J. Bastiaans, and X-C. Zhang, "Detection and identification of explosive RDX by THz diffuse reflection spectroscopy," *Opt. Express*, Vol. 14, 415–423, 2006.
9. Kawas, K., Y. Ogawa, Y. Watanabe, and H. Inoue, "Non-destructive terahertz imaging of illicit drugs using spectral fingerprints," *Opt. Express*, Vol. 11, 2549–2554, 2003.
10. Chen, H.-T., W. J. Padilla, J. M. O. Zide, A. C. Gossard, A. J. Taylor, and R. D. Averitt, "Active terahertz metamaterial devices," *Nature*, Vol. 444, 597–600, 2006.
11. Yen, T. J., W. J. Padilla, N. Fang, D. C. Vier, D. R. Smith, J. B. Pendry, D. N. Basov, and X. Zhang, "Terahertz magnetic response from artificial materials," *Science*, Vol. 303, 1494–1496, 2004.
12. Padilla, W. J., A. J. Taylor, C. Highstrete, M. Lee, and R. D. Averitt, "Dynamical electric and magnetic metamaterial response at terahertz frequencies," *Phys. Rev. Lett.*, Vol. 96, 107401, 2006.

Beam Pattern Investigation of Terahertz Quantum Cascade Lasers

S. Fathololoumi[1, 2], **D. Ban**[2], **H. Luo**[1], **P. Grant**[1], **S. R. Laframboise**[1]
Z. Wasilewski[1], **M. Buchanan**[1], **and H. C. Liu**[1]

[1]Institute for Microstructure Sciences, National Research Council, Ottawa, Canada
[2]Department of Electrical and Computer Engineering, University of Waterloo, Waterloo, Canada

Abstract— Far-field beam pattern measurement results of in-house fabricated 1 mm long THz QCLs with ridge widths of 30 µm and 100 µm are presented. Both devices show diffractive-like beam patterns in the elevation direction (perpendicular to semiconductor heterojunction plane). In the in-plane direction (parallel to semiconductor heterojunction plane), the device with a wider ridge width (100 µm) shows a quasi-Gaussian-like beam profile. A radio-frequency (RF) design simulator (HFSS) is deployed to simulate far-field beam pattern of the QCL devices. The simulation results are in good agreement with the experimental results.

1. INTRODUCTION

Terahertz (THz) quantum cascade lasers (QCL) are becoming a major technology for THz compact, coherent and single-frequency radiation sources, after first demonstrated in 2002 [1]. Recently QCLs with maximum operating temperature up to 164 K in pulse mode and 117 K in continuous mode [2] and wavelengths down to 1.2 THz ($\lambda = 250$ µm) have been reported [3]. Such a source has many potential applications, particularly in spectroscopy, imaging, and local oscillators for heterodyne receivers. Almost for all of the THz QCL applications, a well-defined and narrow beam is required. Such a beam pattern also focuses all of the output power onto a small arbitrary surface. However considering the wavelength of THz laser emission (30 µm to 300 µm), the sub-wavelength dimensions of laser ridge facet suggests that output beam pattern is not a Gaussian beam anymore, but rather becomes a diffractive-like pattern. This paper first briefly reviews the THz QCL fabrication process. Then the experimental results of the device output beam pattern will be presented and discussed.

2. PROCESSING

THz QCLs are fabricated by growing multiple periods of GaAs/$Al_{0.15}Ga_{0.85}As$ quantum wells (MQW) using molecular beam epitaxy (MBE) followed by patterning laser ridge using photolithography techniques. Due to the time limitation of MBE growth duration, the active region of a QCL device is typically not thicker than 10 µm. Thicker wafers also exhibit higher level of defect densities in active region, which limits the optical gain required for lasing. The heterostructure design used for MQW is based on resonant longitudinal-optical phonon scattering to depopulate the lower lasing level with three-well active module [4]. The QCL waveguide is fabricated using metal-metal structure by low temperature In-Au wafer bonding and subsequent wafer removal. Various ridge widths of the devices can be defined in subsequent device fabrication processing. An air-bridge structure is used to fabricate the QCL ridge with a 100 µm width (see Figure 1(a)). This structure provides a 250 µm wide contact pad for multiple Au wires bonding. We use bottom of the wafer as ground contact. The carrier substrate is n^+ GaAs, yielding very small contact resistance. The sample is then cleaved into 1 mm long Fabry-Perot resonator laser bars. Figure 1(b) shows the quality of cleaved facets. Laser bar finally is Indium soldered top-side up on a copper package. Facet of lasers is accurately placed as close as possible to the edge of the mount. In the last step, device is wire bonded connecting the top contact of the device to the package pins and placed on a cryostat cold finger for measurements. Figure 2 shows the characterization results of one fabricated QCL, which operates above liquid Nitrogen temperature. The inset of Figure 2 shows the laser spectrum at 10 K. The QCL device lases in single mode with a frequency of 3.39 THz (wavenumber 112.9 cm^{-1}), which corresponds to a free-space wavelength of $\lambda = 88.6$ µm.

3. BEAM PATTERN MEASUREMENT RESULTS AND DISCUSSION

After mounting QCL bars on the package, the devices are placed in a closed cycle liquid Helium cooled cryostat. The laser radiation passes through a polyethylene window, which is around 70% transparent in terahertz frequencies, and is detected by a liquid-He cooled Silicon Bolometer (IR Lab. Inc., Model HDL-5). The space between the cryostat and the detector is purged with dry

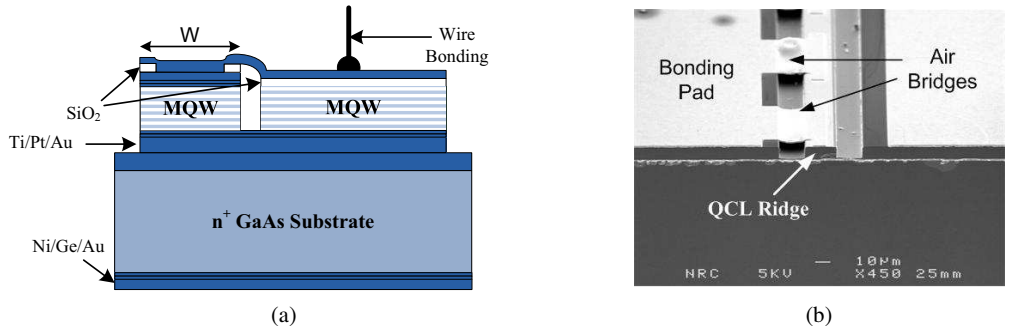

(a) (b)

Figure 1: (a) schematic diagram of the cross-section of an air-bridge structure THz QCL ridge, (b) scanning electron microscopy (SEM) of a fabricated THz QCL with an air-bridge structure.

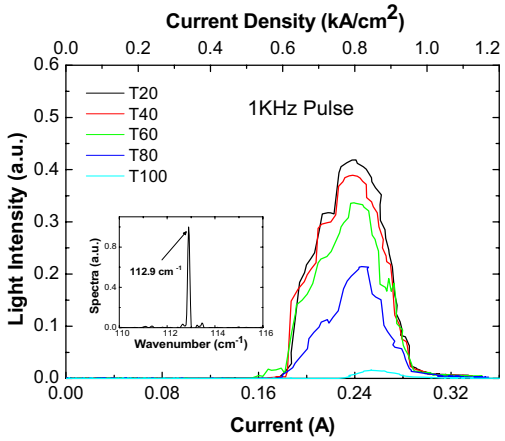

Figure 2: THz light intensity vs. current of a fabricated QCL at different temperatures. The threshold current density is around 0.6 kA/cm^{-2} at temperatures of 20–80 K. The inset shows the lasing spectrum of the device.

nitrogen to minimize moisture absorption. The THz signal, after passing through a polyethylene window of the bolometer, is collected by a Winston cone that is placed inside the bolometer dewar and the beam is focused onto the detector. The electrical signal from the Si bolometer is fed into a lock-in amplifier and acquired using a computer. In order to measure the far field radiation pattern, the Bolometer detector is placed on a rotating stage to move along a circle centered at the QCL device under test with a radius of 10 cm ($> 1000\lambda$). An iris with opening diameter of 2 mm is installed in front of the bolometer window for a sufficient angular resolution. The QCL device is electrically biased using an HP 8114A pulse generator in pulse mode (repetition rate 500 Hz and duty cycle 10%). Figure 3 shows the schematic diagram of the measurement setup.

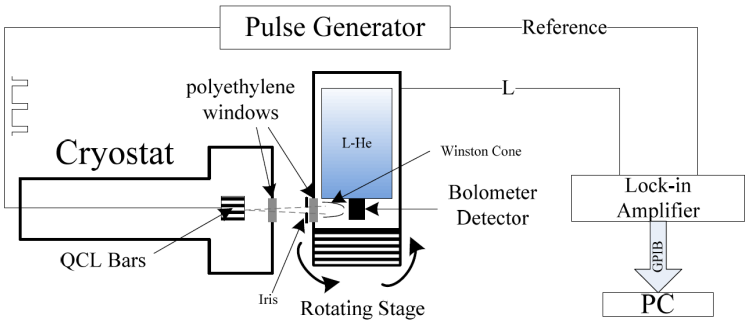

Figure 3: Schematic diagram of the setup for THz QCL beam pattern measurement.

The output beam pattern of a THz QCL is first assumed to be approximated as a Gaussian beam profile, in which the electric field and intensity distribution at each given distance from the

emission source is described by a Gaussian function. Defining the spot size boundary to be where the intensity drops to $1/e^2$ of the value at the beam center, the radius of the spot size at a distance z from the source is given by

$$w(z) = w_0\sqrt{1+\left(\frac{\lambda z}{\pi w_0^2}\right)^2} \cong \frac{\lambda z}{\pi w_0} \tag{1}$$

where w_0 is the beam radius at beam waist and λ is the wavelength of radiation [5]. w_0 is typically equal to the beam radius at the emission facet of the source, that is, the radius of the radiation source. The intensity profile of the beam at a cross-sectional plane is defined by the following Gaussian function as

$$I(r) = I_0 e^{-2r^2/w^2} \tag{2}$$

where I_0 is the intensity of beam at the center, r is the radial distance from the beam center and $w = w(z)$. So the (full width at half maximum) FWHM radius can be calculated by finding the radius at which the exponential factor in (2) drops to one half. The divergence angle (θ) of a beam can be defined as FWHM radius divided by z,

$$\theta = \frac{FWHM/2}{z} = 0.58 \times \frac{\lambda}{\pi w_0}(rad) = 33.7 \times \frac{\lambda}{\pi w_0}\ ^\circ \tag{3}$$

Equation (3) can be used to estimate the beam profile of the THz emission of QCL devices. For example, the QCL device, shown in Figure 2 has a cross-sectional size of $10 \times 100\,\mu m^2$, emitting at $\lambda = 88.6\,\mu m$, the divergence angles are calculated to be 19 (in-plane direction) and 190.1 (elevation direction) degrees (!). The calculated divergence angle in the elevation direction is over 180 degrees, which indicates the beam is so diffractive in the elevation direction and the Gaussian beam model may not be a good approximation any more.

Figure 4 shows the beam pattern measurement results for the 100 µm wide QCL, in both in-plane (theta) and elevation (phi) directions. The beam pattern in the in-plane direction exhibits multiple peaks besides the main peak at zero degree. It shows that the beam pattern can not be approximated by a single-mode Gaussian profile. Nevertheless, the FWHM of the main peak is measured to be 18 degree, agreeing well with the calculated result from Gaussian model approximation. In the elevation direction the beam patterns are much more complicated, which is due to strong beam diffraction. Because of omnidirectional radiation from both front and rear facets of the device, the fringes observed in Figure 4(b) are constructed by interference of coherent radiation from the front and rear facets, and hence spread over a wide angular range.

A radio-frequency (RF) design simulator (HFSS), from Ansoft, was deployed to simulate far-field beam pattern of the QCL devices. A QCL ridge with a metal-metal waveguide, as depicted in Figure 1(a), is simulated using the simulator. In the simulation model, a semi-insulating GaAs layer is used as the active region of the device, which is quite good approximation due to similar electric permittivity of GaAs and $Al_{0.15}Ga_{0.85}As$. The active region is sandwiched between two 1 µm gold layers with the bulk conductivity of 41 MS/m. Due to absence of a gain medium in the simulated structure; the active region is excited by an electromagnetic (EM) wave with a suitable frequency.

The simulation results of the far field pattern of a QCL with a 100 µm wide ridge are shown in the Figure 4 (upper curves). The simulation results shows a central peak with a quasi-Gaussian beam profile that has a FWHM of 16 degree along the in-plane direction, which is in good agreement with both the measured value (18 degree) and the calculated value from Gaussian beam approximation (19 degree). The simulated beam fringes in both in-plane and elevation directions match with measurement results within an angular range of -30 to 30 degree. Beyond this angular range the THz emission beam of the device might be blocked/deflected by the cryostat window, leading to discrepancies between the experimental data and the simulation results. The non-symmetrical shape of the in-plane profile at ± 25 degree (Figure 4(a)) can be attributed to the asymmetrical device configuration — the air-bridges are only on one side of the ridge (Figure 1), which may influence the beam emission on that side. Discrepancy between the experimental and simulation results is also observed for the portion below the laser/package interface plane (negative Phi angles), where some peaks are missing in the measurement results. This could be attributed to the presence of the metallic package underneath of the QCL devices that may strongly alter the radiation patterns at negative angles in the elevation direction. In the positive elevation direction (the portion above

the laser/package interface plane), simulated far-field pattern shows fairly good consistence with the experimental data. The agreement between RF calculations and the measurement results suggests that an EM model based on Maxwell's equations predicts behavior of THz QCL beam more accurately than the simple Gaussian beam approximation approach does.

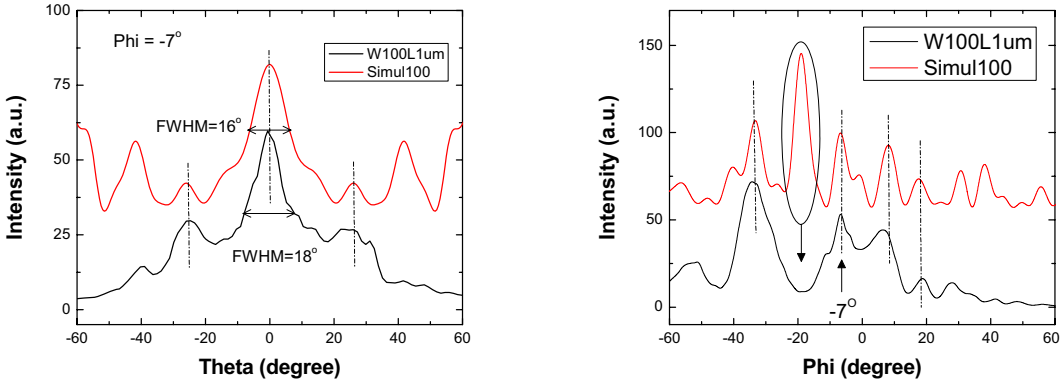

Figure 4: THz QCL beam pattern measurement and simulation results for 100 µm wide and 1 mm long ridge, (a) In-plane angle, Theta; (b) elevation angle, Phi.

4. CONCLUSIONS

The laser beam pattern of the THz QCL devices was investigated experimentally and theoretically. Both the measurement data and the simulation results show strong diffraction-like profiles of the far-field pattern because of the sub-wavelength dimensions of the laser structure. Along the in-plane direction, a central peak with a quasi-Gaussian profile is observed. The diffraction behavior of the beam pattern is more significant in the elevation direction, which could be attributed to the interference of coherent radiation from both facets of the device. The experimental results are in fairly good agreement with simulation results.

ACKNOWLEDGMENT

This work is partially supported by NSERC, NRC and ERA.

REFERENCES

1. Kohler, R., A. Tredicucci, F. Beltram, H. E. Beere, E. H. Linfield, A. G. Davies, D. A. Ritchie, R. C. Iotti, and F. Rossi, "Terahertz semiconductor-heterostructure laser," *Nature*, Vol. 417, 156–159, 2002.
2. Williams, B. S., S. Kumar, Q. Hu, and J. L. Reno, "Operation of terahertz quantum-cascade lasers at 164 K in pulsed mode and at 117 K in continuous-wave mode," *Optics Express*, Vol. 13, 3331–3339, 2005.
3. Walther, C., M. Fischer, G. Scalari, R. Terazzi, N. Hoyler, and J. Faist, "Quantum cascade lasers operating from 1.2 to 1.6 THz," *Appl. Phys. Lett.*, Vol. 91, 131122, 2007.
4. Liu, H. C., M. Wachter, D. Ban, Z. R. Wasilewski, M. Buchanan, G. C. Aers, J. C. Cao, S. L. Feng, B. S. Williams, and Q. Hu, "Effect of doping concentration on the performance of terahertz quantum-cascade lasers," *Appl. Phys. Lett.*, Vol. 87, 141102, 2005.
5. Saleh, B. E. A. and T. M. Carl, "Beam optics," *Fundamentals of Photonics*, Chapter 3, 80–107, John Wiley, New York, 1991.

Fabrication of Terahertz Coupling Structures by Electron Beam Lithography

Grahame Rosolen
Information and Communication Technologies Centre
Commonwealth Scientific and Industrial Research Organisation
Vimiera Road, Marsfield, NSW 2121, Australia

Abstract—In order to design electromagnetic radiation coupling structures such as antennas and photonic crystals the critical dimensions of the structures must be commensurate with the wavelengths of the radiation of interest. In the case of Terahertz radiation the characteristic wavelength is in the range 1 mm to 30 μm. To achieve high quality structures the fabrication technique must have a resolution capability considerably finer than the wavelength. For Terahertz coupling structures this constraint is at the limit of many conventional machining based fabrication capabilities. One technique to overcome this resolution issue is to pattern structures using electron beam lithography (EBL) and then use semiconductor fabrication techniques to produce the final structures. This technique provides a flexible patterning capability for fabricating devices with a wide range of topologies and sizes. The principle advantages of EBL are the ability to pattern features with dimensions in the micron and sub-micron range as well as the ability to directly pattern structures on a substrate without the need for a prefabricated mask. The technique also affords the flexibility to change the pattern topology by altering the lithography data file and it provides the ability to fabricate structures containing elements ranging in size from microns up to millimetres on the same substrate. This enables structures which operate over a wide band of Terahertz frequencies to be patterned. The structures are defined using conventional CAD drafting packages and then converted into lithography data files for exposure. The structures are patterned using a scanning electron microscope which has been modified for direct write EBL. The planar structures are exposed in a layer of electron sensitive resist, which after developing produces an opening in the resist in the shape of the desired structure. This opening is used for the deposition of metal. The resist is then removed leaving the structure on the substrate. In situations where electrical contact is required part of the structure can be patterned to form the contacts for bonding to other components in a system.

1. INTRODUCTION

Terahertz radiation typically covers the frequency band from 300 GHz to 10 THz and has a corresponding wavelength range of 1 mm to 30 μm. The ability to interact with radiation at these frequencies is challenging as neither purely optical or purely electronic approaches are suitable over this wide frequency range [1, 2]. Electronics may be used for the lower end of THz radiation but the difficulty of obtaining electronic devices that operate at these frequencies and also the problems associated with making accurate electronic measurements at these frequencies are severe limitations. Conversely optical techniques work well at the upper range of THz radiation but the difficulty of fabricating conventional optical components at the lower frequencies is a challenge [3]. An analogous situation exists with the fabrication of antenna structures over the THz band. At the lower frequencies conventional machining techniques may be used to produce antennas. However as the frequency rises the machining tolerances required exceed the capabilities of conventional machining based manufacturing techniques. Furthermore the ability to produce wideband structures requires a fabrication capability that can cover a wide dimensional range. Conventional semiconductor processing is an important tool for fabricating planar structures operating at THz frequencies. Such devices include individual antennas [4], focal plane arrays [5], bolometers [6], superconducting tunnel junctions [7] and wideband coupling structures [8]. In order to fabricate these structures a patterning capability is required. Electron beam lithography (EBL) is ideally suited to this role as it offers the submicron resolution required for high frequency structures as well as the ability to pattern areas up to several millimetres to cater for the lower frequency components. A further advantage of electron beam lithography is that the pattern data is stored in a computer file and so no separate mask fabrication is required. This affords flexibility in the device patterning stage in that the device topology and size can be changed by simply changing the lithography data file. It is also an efficient patterning technique as the time and expense of fabricating an optical mask is avoided.

2. ELECTRON BEAM LITHOGRAPHY INSTRUMENTATION

The electron beam lithography instrument comprises a purpose built pattern exposure system interfaced to a modified LEO 440 scanning electron microscope (SEM) [9]. A photograph of the instrument is shown in Figure 1. The SEM has been modified with the addition of beam blanking plates and interface electronics and software to enable external control of the objective lens, beam deflection coils and sample stage of the SEM [10].

Figure 1: Electron beam lithography instrument.

In order to accommodate a variety of substrate materials and sample types a sample holder which can accommodate wafers of 2, 3 or 4 inch diameters and mask plates of 4 inches has been fitted to the sample stage of the SEM.

The entire instrument is controlled from the console which comprises both SEM and lithography computers. The SEM computer is used to configure the electron optics, control the vacuum system and provide interactive imaging functions. The lithography computer is used to prepare the pattern data files, sequence the lithography functions and control the dedicated lithography electronics. The pattern exposure system comprises the dual processor architecture of the lithography computer (PC) and digital signal processor (DSP) system, together with the associated analog and digital electronics [11].

The lithography PC provides the user interface for controlling and sequencing all the high level lithography functions and for controlling the sample stage and focus adjustment during lithography operation. The pattern data is also prepared and converted into data files suitable for exposure using software running on the lithography PC. The lithography pattern data files provide the input to dedicated DSP code which calculates in real time the low level pattern digital data. This digital data is converted into analog signals by a pair of digital to analog converters. The analog signals are then further conditioned by low noise amplifiers before being directly applied to the beam deflection coils on the SEM. The DSP affords full digital control of the beam so that it may be accurately positioned anywhere within the field of view. The rate at which the beam is deflected is under the control of the DSP to ensure that accurate doses may be delivered to the sample during exposure.

To ensure that the beam remains at the optimal focus during pattern exposure a focus plane fitting algorithm has been incorporated into the exposure system. This algorithm uses the focus values obtained at three positions on the sample to determine the equation of the plane which describes the motion of the sample. This plane fitting technique is used to calculate the correct focus value at each position. The focus values are automatically used to directly adjust the SEM objective lens current as the stage is moved so that the correct focus is maintained at all points on the sample.

3. PATTERN PREPARATION

Conventional EBL pattern generators are usually designed for exposing rectangular structures and so are typically configured for patterning horizontal or vertical lines. Some of the more interesting antenna structures require detailed curves or angular structures and may include a large variety of linewidths. This poses an interesting challenge in converting THz structures into pattern data files that may be exposed using the EBL pattern generator. In order to define the structures a number of 2D CAD drawing packages are available. These packages are able to output the design in a variety of file formats. The dxf format was chosen as it is an ASCII file and so can be examined manually. Software was written to convert the dxf file into the EBL lithography files. A number of test structures have been designed using AutoCAD and successfully converted into EBL data files. An additional feature of the software is an exposure ordering tool that sequences the elements of the exposure file to minimise the distance the beam has to move between exposure points. This helps reduce artifacts associated with the beam settling time during the exposure of structures which contain many elements.

4. FABRICATION PROCESS

Once the planar THz structure has been defined and converted into an EBL exposure file it is ready to be patterned. The fabrication sequence involves initially spin coating the substrate with 400 nm thick layer of Polymethylmethacrylate (PMMA) electron sensitive resist. The patterns are exposed with a beam energy of 30 kV with the sample at a working distance of 15 mm. After exposure the sample is developed in a solution of 1 Methyl Isobutyl Ketone (MIBK) : 3 Isopropyl Alcohol (IPA) for 5 minutes. After development the openings in the resist appear where the beam has exposed. These resist openings provide the mask for the evaporation of 20 nm of titanium and then 200 nm of gold. The resist layer is removed in acetone leaving the THz coupling structure on the substrate. An example of a double spiral pattern antenna structure fabricated using this technique is shown in Figure 2.

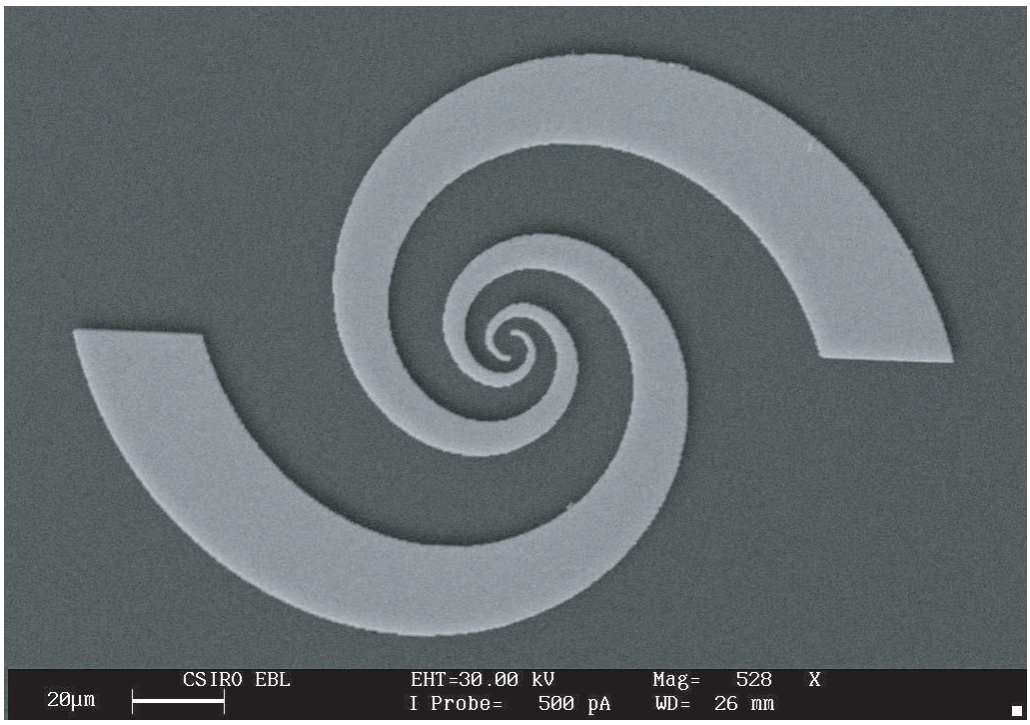

Figure 2: Double spiral antenna structure patterned by electron beam lithography.

5. CONCLUSIONS

Electron beam lithography is a valuable tool for patterning structures designed to interact with electromagnetic radiation in the THz range. It has the principle advantages of a resolution capability which is suitable for the highest THz frequencies and also the ability to pattern structures

with a wide range of dimensions. Furthermore as the patterns are defined as files on a computer it affords the possibility to create and experiment with a wide range of designs without the need for fabricating a separate exposure mask. As a consequence structures with a variety of topologies suitable for coupling THz radiation over a wide range of frequencies may be fabricated.

REFERENCES

1. Siegel, P. H., "Terahertz technology," *IEEE Transactions on Microwave Theory and Techniques*, Vol. 50, No. 3, 910–928, 2002.
2. Hu, B. B. and M. C. Nuss, "Imaging with terahertz waves," *Optics Letters*, Vol. 20, No. 16, 1995.
3. Seibert, K. J., H. Quast, R. Leonhardt, T. Loffer, M. Thomson, T. Bauer, H. G. Roskos, and S. Czash, "Continuous-wave all-optoelectronic terahertz imaging," *Appl. Phys. Lett.*, Vol. 80, 3003–3005, 2002.
4. Hesler, J. L., H. Kai, R. K. Dahlstrom, R. M. Weikle, T. W. Crowe, C. M. Mann, and H. B. Wallace, "Analysis of an octagonal micromachined horn antenna for submillimeter-wave applications," *IEEE Transactions on Antennas and Propagation*, Vol. 49, No. 6, 2001.
5. Wei, A., M. Lee, and Q. Hu, "Real-time, continuous-wave terahertz imaging by use of a microbolometer focal plane array," *Optics Letters*, Vol. 30, No. 19, 2005.
6. Burns, M. J., A. W. Kleinsasser, K. A. Delin, R. P. Vasquez, B. S. Karasik, W. R. McGrath, and M. Gaidis, "Fabrication of high-Tc hot-electron bolometric mixers for terahertz applications," *IEEE Transactions on Applied Superconductivity*, Vol. 7, 3564–3567, 1997.
7. Ariyoshi, S., C. Otani, A. Dobroiu, H. Sato, K. Kawase, H. M. Shimizu, T. Taino, and H. Matsuo, "Terahertz imaging with a direct detector based on superconducting tunnel junctions," *Appl. Phys. Lett.*, Vol. 88, 203503, 2006.
8. Van der Weide, D. W., "Planar antennas for all-electronic terahertz systems," *J. Opt. Soc. Am. B*, Vol. 11, No. 12, 1994.
9. Rosolen, G. C., "Optically variable devices fabricated by electron beam lithography," *Proc. SPIE*, Vol. 5276, 318–323, 2003.
10. Rosolen, G. C., "Combined optical and electron beam lithography for integrated circuit fabrication," *Lithography for Semiconductor Manufacturing, Proc. SPIE*, Vol. 4404, 238–244, 2001.
11. Rosolen, G. C., "Automatically aligned electron beam lithography on the nanometre scale," *Applied Surface Science*, Vol. 144–145, 467–471, 1999.

Terahertz Sensing for Ensuring the Safety and Security

Y. Ogawa[1], **S. Hayashi**[1,2], **C. Otani**[2], **and K. Kawase**[1,2,3]

[1]Tohoku University, Japan
[2]RIKEN, Japan
[3]Nagoya University, Japan

Abstract— We are studying some novel steps toward real-life applications of terahertz wave. In this paper, we introduce two THz sensing methods for ensuring the safety and security of the lives of people, such as, i) Nondestructive detection of illicit drugs using spectral fingerprints, ii) Label-free detections of protein-protein interactions for allergy test.

1. INTRODUCTION

Terahertz (THz) waves, at the gap between microwaves and the far infrared, have long been unexplored field, mainly because of the lack of sources and detectors. However, recent remarkable developments in THz technology allow THz radiation to be applied in solving real-world problems, such as in material science, atmospheric research, biology, solid state physics, chemistry and gas tracing [1, 2]. Among the most prominent advantages that the THz radiation offers we mention its ability to penetrate a wide range of materials which are opaque to visible and near infrared light or produce only low-constant X-ray images. As the THz photon energy is roughly six orders of magnitude smaller than that of an X-ray photon, its interaction with matter, particularly with biological tissues, is considered to cause no detectable damage, at least not by ionization processes. A comparison with the other side of the electromagnetic spectrum, the microwave range, highlights again the advantage of THz waves: With their shorter wavelength they provide a considerably better imaging resolution that is sufficient in many applications. The existence of chemically-specific absorption spectra in the THz range, reflecting molecular transitions and intermolecular bonds, facilitates fingerprinting and brings about a whole area of spectroscopic detection, testing, and analysis techniques. On the other hand, the technologies for ensuring the safety and security have been becoming the important in an increasingly internationalized world. The THz technology has been expected to solve such problems. We have been studying a few THz sensing methods for ensuring the safety and security of the lives of people, such as, i) Nondestructive detection of illicit drugs using spectral fingerprints, ii) Label-free detections of protein-protein interactions for allergy test.

The absence of non-destructive inspection technique for illicit drugs hidden in mail envelopes has resulted in such drugs being not only smuggled across international borders but also transported from one jurisdiction to another within a country with surprising ease. The situation must also be attributed to the inconvenience of having to obtain a search warrant to examine the contents every time the need arises. A majority of the legal systems in the world prohibit private letters, whether they are suspected or otherwise, from being examined without a search warrant. There exist several inspection techniques such as passing the mail through an X-ray scanner, having it sniffed by a trained dog, or swiping its outside with a trace detection system. However, the ability of X-ray scanners is limited to identifying the shape of a vinyl plastic bag or a tablet, and not the type of the drug, providing insufficient grounds for opening the envelope for examination. Trace detection and canine detection, on the other hand, can only be effective if there are detectable signs outside the envelope, such as a scent or trace amounts of the concealed drug. In contrast, the THz-wave is suitable for drug detection purposes, being able to screen the contents of envelopes and our measurement results having proven the existence of fingerprint spectra peculiar to illicit drugs in the THz region. In this paper, we will report a demonstration to detect illicit drugs in envelope using a THz spectroscopic imaging system.

In recent years, Japanese consumers have become increasingly aware of food safety issues (e.g., residual agricultural chemicals in food, mislabeled beef and tampered food). In particular, a detection of an allergic substance in food materials is very important, because a substance that triggers allergies causes serious allergic reaction. We think the label-free biosensing is a good way to detect them. However, it is necessary to detect a very small amount of allergen in food. To obtain high sensitivity, we demonstrated a sensing application using thin metallic mesh — a two-dimensional array of sub-wavelength holes.

2. NONDESTRUCTIVE DETECTION OF ILLICIT DRUGS USING SPECTRAL FINGERPRINTS [3]

We have developed a basic technology for terahertz imaging, which allows detection and identification of drugs concealed in envelopes, by introducing the component spatial pattern analysis [4]. As samples we chose for this experiment three drugs that were: methamphetamine (*d*-methamphetamine hydrochloride, more than 98% purity), currently the most widely consumed drug of abuse in Japan, MDMA (*dl*-3, 4-methylenedioxymethamphetamine hydrochloride, 67% purity), another drug of abuse becoming widespread on a global scale, and aspirin (100% purity) as a reference. As shown in Fig. 1, ∼20 mg of each substance were placed in a small 10 × 10 mm polyethylene bag. The three bags were then placed inside a usual airmail-type envelope. THz images of the rectangular area indicated by the white line in Fig. 1 were captured.

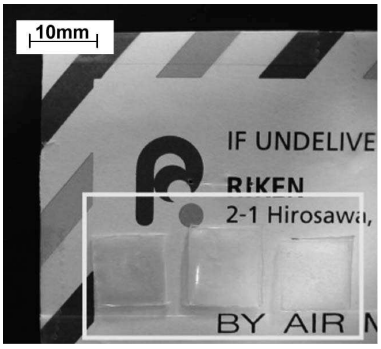

Figure 1: View of the samples. The small polyethylene bags contain from left to right: MDMA, aspirin, and methamphetamine. The bags were placed inside the envelope during imaging. The area indicated by the white line represents the imaging target, 20 × 38 mm in size. Since methamphetamine and aspirin are similar in appearance, we used a slightly longer bag for the latter to avoid confusion.

The THz spectroscopic imaging system [5] consists of a Q-switched Nd:YAG laser, a TPO (THz-wave parametric oscillator) [6], imaging optics, an xy scanning stage, a detector, a lock-in amplifier, and a personal computer . By changing the frequency emitted by the TPO within the 1.3 to 2.0 THz range, we obtained seven multispectral images as shown in Fig. 2. In Fig. 2, the scale of the image $-\ln(I_t/I_0)$ is the logarithm of the transmitted THz-wave intensity I_t divided by the intensity of the THz-wave that was only transmitted through the envelope I_0. This means that the greater the absorption, the brighter the shades.

The absorption spectra of the three drugs were measured with the same TPO system as shown in Fig. 3. The corresponding absorption intensity values at the seven frequencies were extracted to obtain the information of spectra. Although the spectra of methamphetamine and MDMA are

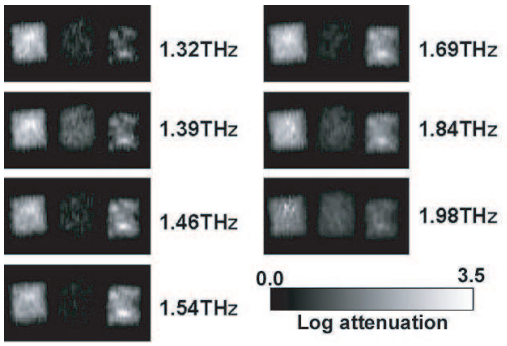

Figure 2: Seven multispectral images.

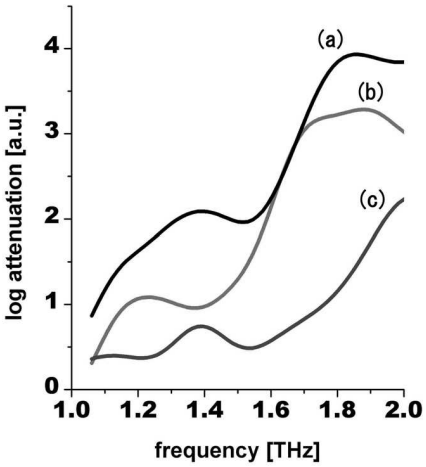

Figure 3: Absorption spectra of MDMA (a), methamphetamine (b), and aspirin (c).

similar, the difference between them enabled us to distinguish between the two using the component pattern analysis method.

By using the seven recorded images and the information of spectra, the spatial pattern was calculated. Fig. 4 shows the result of extracting the three components, with each image corresponding to each of the sample drugs. As it is evident from these images, the three drugs have been clearly distinguished and the corresponding spatial patterns obtained. A ROI (region of interest) was set in each area of the component patterns in Fig. 4 and then we took the average of tone in each ROI. The ROI was a square with 20×20 pixels, which is similar to the size of a plastic bag. The averages of MDMA, aspirin, and methamphetamine were 122, 119 and 138, respectively. The errors were less than $\pm 10\%$, which is sufficient for the drug detection purposes.

3. LABEL-FREE DETECTION OF PROTEIN-PROTEIN INTERACTIONS FOR ALLERGY TEST

We have been developing a novel sensing method which uses the highsensitivity phenomenon of a thin conductive metal mesh. The transmission characteristics of thin metallic meshes, investigated since the 1960s [7, 8], are those of a band-pass filter in the far-infrared region. The transmission properties of a thin metallic mesh are determined mainly by its geometric parameters, but, when a material is placed near the mesh openings, are also affected by the refractive index of that material, in the sense that a shift of the resonant transmission frequency occurs [9]. Our sensing method is based on the change of the transmittance of THz radiation through a thin metallic mesh accompanied by the resonant frequency shift when a sample substance is applied on the mesh openings. The transmittance of the thin metallic mesh does not change due to the absorption, but dominantly due to the variation of the refractive index of the sample substances near the openings [10].

In our experiment, we measured the transmission spectra of a thin metallic mesh using a Fourier Transform Infrared (FT-IR) spectrometer, in which the THz beam was focused into an area of about 7 mm in diameter on the thin metallic mesh. The transmission dip frequency shows the incident angle dependence [11]. We observed the shift of this transmission dip frequency. The thin metallic mesh was made from electroformed nickel, allowing the fabrication of a smooth surface and precise periodicity of the grating. The two dimensional square metallic mesh was 6 μm thick with a grating period of 76.3 μm and a metallic line width of 18.3 μm, in both dimensions. This metallic mesh behaves as a high-pass filter and the transmission at the dip frequency is approximately 70% at 2.94 THz (Fig. 5).

We demonstrate the experiment of a label-free detection of casein/anti-casein reaction which causes allergy to milk. We used alpha-casein from bobime milk and rabbit IgG anti alpha-casein. For quantitative blotting the antigen protein (alpha-casein) to a polyvinylidene difluoride (PVDF)

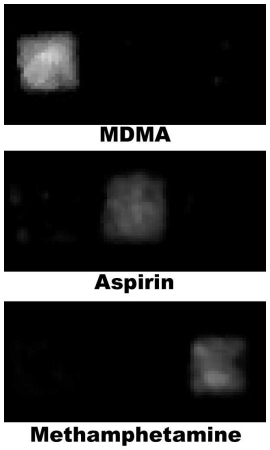

Figure 4: Extracted spatial patterns of MDMA, aspirin and methamphetamine, using the component spatial pattern analysis. The three drugs are clearly distinguished and corresponding spatial patterns obtained.

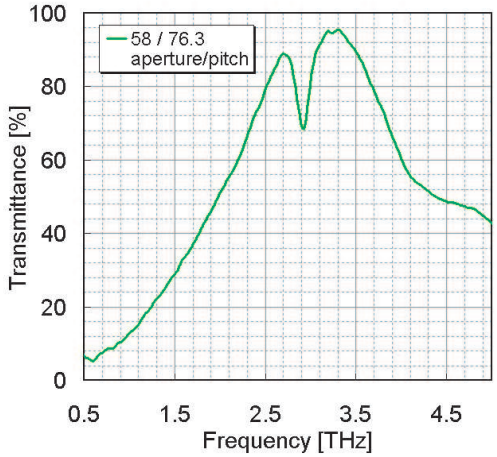

Figure 5: A measured transmission spectrum of the thin metal mesh. This metal mesh behaves as a high-pass filter and the peak transmission is approximately 95% at 3.37 THz. The transmittance of dip is observed at 2.94 THz.

membrane, we used a printing device (KONICA MINOLTA IJ co., Japan). The amount of the sample was controlled using an image processing software. For viscosity control, alpha-casein was dissolved in solution of glycerine (40%) and isopropyl alcohol (5%) in distilled water. In our case, the solution concentration is 1.0 mg/ml. In order to make the PVDF membrane hydrophilic it was soaked in methanol 100% for 20 seconds, then washed with distilled water for 2×5 minutes and rinsed in Tris-buffered saline (TBS) (20 mM Tris, 500 mM NaCl, pH 7.5). Alpha-casein solution was applied by the printing device on the membrane. The blotted membrane was immersed in the blocking with the BSA solution (0.1% BSA in TTBS (20 mM Tris, 500 mM NaCl, 0.05% Tween-20, pH 7.5)) for 2 hours at room temperature. After the washing with the TTBS solution, it was Incubated with 20 µl monoclonal rabbit IgG anti alpha-casein (1.0 mg/ml) over night at room temperature.

We measured samples using our FT-IR at three steps PVDF membrane which were (a) untreated, (b) applied alpha-casein solution and blocked with the BSA solution, and (c) incubated with rabbit IgG anti alpha-casein. The PVDF membrane shows transmittance more than 70% under 3 THz. Each PVDF membrane was attached to the input surface of the thin metallic mesh. We present the transmission spectra only in the frequency range around the transmission dip observed in Fig. 6. The transmission dip frequency, which is estimated from the fitting of the measured spectrum with a Lorentz function, is plotted in the inset of Fig. 6 as a function of each step. The transmission spectrum of the applied-casein solution and blocked with the BSA solution on PVDF membrane (b) was found to shift towards lower frequencies relative to the untreated PVDF membrane (a). And the transmission spectrum of the incubated with rabbit IgG anti alpha-casein on PVDF membrane (c) was also found to shift towards lower frequencies relative to the non-incubated PVDF membrane (b). In this case, the amount of rabbit IgG anti alpha-casein on PVDF membrane is estimated 8.7×10^{-7} M. This shift is believed to be caused by the different refractive index of antigen-antibody combination in the vicinity of metallic mash. Such a small variation of the transmittance makes it difficult to detect the sample substances by monitoring the transmission intensity at a single frequency. However, owing to the shift of the dip frequency depending on the refractive index in the vicinity of the metallic openings, a sensitive detection of the sample substances becomes possible with the single frequency source in the THz regime.

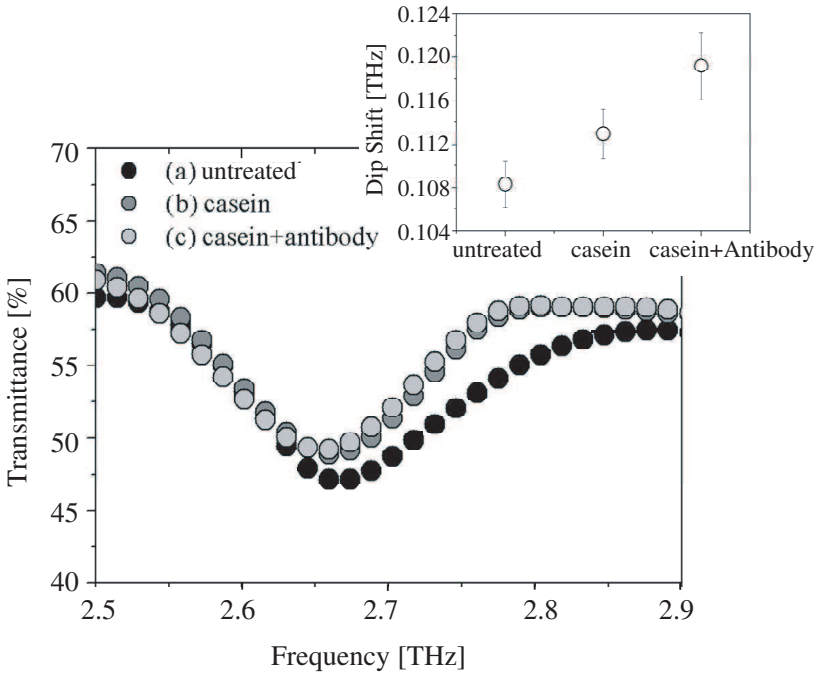

Figure 6: Measured transmission spectra of a thin metallic mesh with various conditions of PVDF membrane. At the inset figure shows the sift of transmission dip frequency as a function of the each conditions of PVDF membrane.

ACKNOWLEDGMENT

This work was supported in part by a Grant-in-Aid for Young Scientists from The Ministry of Health, Labour and Welfare of Japan.

REFERENCES

1. Tonouchi, M., "Cutting-edge terahertz technology," *Nature Photonics*, Vol. 1, 97–105, 2007.
2. Ferguson, B. and X.-C. Zhang, "Materials for terahertz science and technology," *Nature Materials*, Vol. 1, 26–33, 2002.
3. Kawase, K., Y. Ogawa, Y. Watanabe, and H. Inoue, "Non-destructive terahertz imaging of illicit drugs using spectral fingerprints," *Opt. Express*, Vol. 11, 2549–2554, 2003.
4. Kawata, S., K. Sasaki, and S. Minami, "Component analysis of spatial and spectral patterns in multispectral images. I. Basis.," *J. Opt. Soc. Am. A*, Vol. 4, 2101–2106, 1987.
5. Watanabe, Y., K. Kawase, T. Ikari, H. Ito, Y. Ishikawa, and H. Minamide, "Component spatial pattern analysis of chemicals using terahertz spectroscopic imaging," *Appl. Phys. Lett.*, Vol. 83, 800–802, 2003.
6. Kawase, K., J. Shikata, and H. Ito, "Terahertz wave parametric source," *J. Phys. D: Appl. Phys.*, Vol. 35, R1–R14, 2002.
7. Ulrich, R., "Far-infrared properties of metallic mesh and its complimentary structure," *Infrared Phys.*, Vol. 7, 37–55, 1967.
8. Sakai, K., T. Fukui, Y. Tsunawaki, and H. Yoshinaga, "Metallic mesh bandpass filters and fabry-perot interferometer for the far infrared," *Jpn. J. Appl. Phys.*, Vol. 8, 1046–1055, 1969.
9. Miyamaru, F. and M. Hangyo, "Finite size effect of transmission property for metal hole arrays in subterahertz region," *Appl. Phys. Lett.*, Vol. 84, 2742–2744, 2004.
10. Miyamaru, F., S. Hayashi, C. Otani, K. Kawase, Y. Ogawa, H. Yoshida, and E. Kato, "Terahertz surface-wave resonant sensor with a metal hole array," *Opt. Lett.*, Vol. 31, 1118–1120, 2006.
11. Lamarre, J. M., N. Coron, R. Courtin, G. Dambier, and M. Charra, "Metallic mesh properties and design of submillimeter filters," *Int. J. of Infrared and Millimeter Waves*, Vol. 2, 273–292, 1981.

Live Electro-optic Imaging (LEI) for Real-time Analyses of Electric Near-fields over Microwave Circuits

Kiyotaka Sasagawa, **Atsushi Kanno**, **and Masahiro Tsuchiya**
National Institute of Information and Communications Technology, Japan

Abstract— Live electro-optic imaging (LEI) system is described in this paper, which enables the real-time imaging functionality of electrical signals on up to 10 GHz-class circuits in realtime on a screen at video frame rates as high as 30 frames per second. In the system, photonics provides important features of the system: its 100×100-channel parallel detection and the low invasiveness of electrooptic crystal. With the LEI system, novel diagnostic methods are provided through instantaneous and intuitive analyses of RF signal distribution changes. As an example, LEI observation results for a coplanar waveguide with a moving metal plate are presented.

1. INTRODUCTION

In this paper, we report instantaneous and continuous imaging of microwave electric near-fields, which is named live electro-optic imaging (LEI). The concept of LEI is shown in Figure 1. By the LEI system, electric near-field distibuions over a microwave curcuit can be visualized as a motion picture.

Wireless communications systems with higher performance and functionality will be essential in the highly networked information societies of the future. In development and production of such systems, a lot of prototypes are designed, built and tested in order to achieve desired specifications. If the performance of prototype is not enough, it is important to determine the cause of trouble promptly. It is expected that LEI is an innovative technology for this purpose. In the vicinitiy of microwave circuit, electric near-field distribution image beyond its diffraction limit can be obtained. Because there is a correlation between microwave electric near-fields and the status of each circuit, observation of electro near-fields will be important to deal with them.

We have developed a LEI system on the basis of photonics technology. Figure 2 shows a photograph of the LEI system. In our LEI system, parallel detection [1, 2] and real-time image processing [3] of electric fields are realized. Its resolution is 100×100 pixels and its frame rate is 30 frames per second. Electric field imaging with such a high resolution and high speed have not been achieved before, and motion pictures of electric near-field distribution were successfully acquired for the first time. In this paper, we describe the operation principle of the LEI system and some of the advanced microwave electric field measurements that can be done with it.

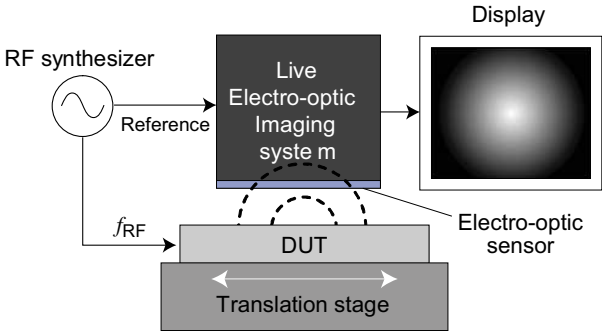

Figure 1: Concept of the LEI system.

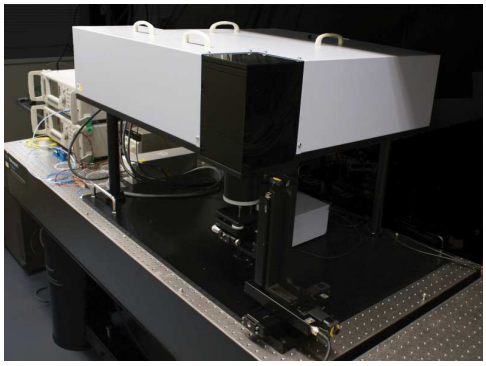

Figure 2: Photograph of the LEI system.

2. LEI SYSTEM

Figure 3 shows a schemetic diagram of LEI system. In the LEI system, an ZnTe crystal plate with dimensions of 25 mm × 25 mm × 1 mm is used as a electro-optic sensor. Refractive indices of the electro-optical crystal are changed by applying an electric field via the Pockels effect and measured by an optical beam. The polarization of optical beam is modulated as it passes through

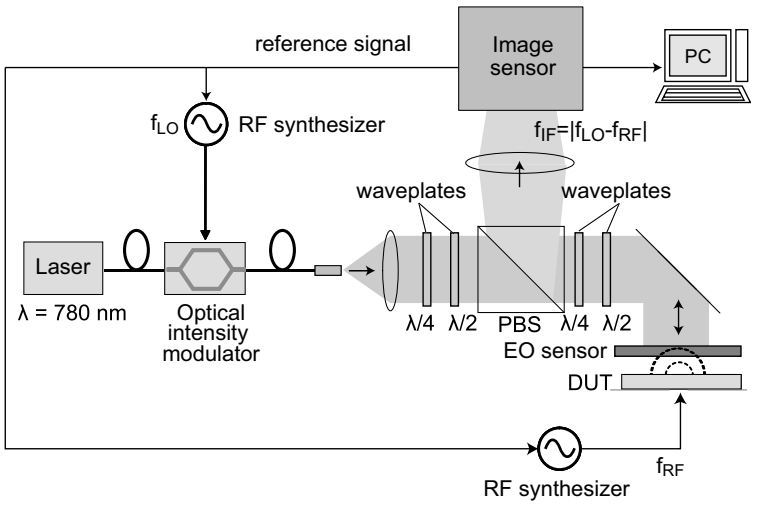

Figure 3: Experimental setup of LEI. PBS: polarization beam splitter, DUT: device under test.

the sensor plate. The amplitude of polarization modulation corresponds to that of electric field. By passing through a polarization beam splitter or an optical analyzer, the polarization modulation is converted to intensity modulation.

The electric field measurement technique based on the electro-optic effect was reported for the first time by Valdmanis et al. [4]. One of the problems of the electro-optic measurement is its long image acquisition time. To improve it, Sasaki et al. proposed high speed scanning technique [5]. On the other hand, in the LEI system, electric field signals are measured in parallel with an electrooptic crystal plate and an optical image sensor as a photodiode array. As a result, acquisition time for an electric field images is much shorter than the scanning systems. Low invasiveness to electric fields, optical parallel signal processing, and high resolution are satisfied simultaneously by photonics technology.

The resolution of the image sensor used in the is 100×100 pixels, and the frame rate is 10 kHz. The frequency of measured microwave signal f_{RF} is several GHz, which is much higher than the frame rate of the image sensor, and it is impossible to detect the microwave signal directly. In the LEI system, this problem is solved by parallel optical heterodyne. The intensity of input light is modulated at a frequency of f_{LO} by an optical modulator. This optical signal is modulated again by the electro-optic sensor. As a result, the intermediate frequency $f_{\mathrm{IF}}(= |f_{\mathrm{RF}} - f_{\mathrm{LO}}|)$ is generated. By setting f_{IF} sufficiently low, the microwave electric fields are downconverted and detected by the image sensor.

3. REAL-TIME ELECTRO-OPTIC IMAGE PROCESSING

The output data from the image sensor is too large to send the computer in real-time. Therefore, to eliminate the bottleneck, we separated the signal processing procedure into two parts: "pre-processing" and "image rendering". These signal processing substitutes for the lock-in amplifier used in a conventional single channel system. In other words, the signal received from the image sensor is mixed with a reference signal and filtered by a low pass filter. The amplitude and phase of the original microwave signal are numerically deduced from the output signal. Equivalently, the "pre-processing" procedure corresponds to a mixer (a) and a low pass filter (b): (a) the received signal is multiplied with reference signals with a phase difference of $\pi/2$, and (b) high frequency components are filtered out via accumulation of all the frames. As a result, the amount of data is reduced by a factor of

$$R = 2\frac{f_{\mathrm{IS}}}{f_{\mathrm{LEI}}}, \tag{1}$$

where f_{IS} and f_{LEI} are the frame rates of the high-speed image sensor and LEI, respectively. In the "image rendering" procedure, the amplitude and phase of the electric field are numerically deduced from the pre-processed data. In addition, the sensitivity of each pixel is equalized according to the Gaussian profile of the expanded light. Finally, these patterns are displayed on the computers screen.

The "pre-processing" is carried out in a digital signal processor (DSP) before the data is transferred to the computer as shown in Figure 4. Consequently, the data to be transferred is reduced by a factor of R, which is approximately one thousand at maximum. On the computer, the "image rendering" takes place so that the intensity and phase patterns of the electric field are constructed two-dimensionally. All processes mentioned above are performed in real-time. The details of the data processing will be reported elsewhere.

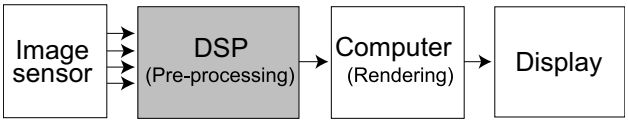

Figure 4: Block diagram of the signal processing unit of the LEI system. DSP: digital signal processor.

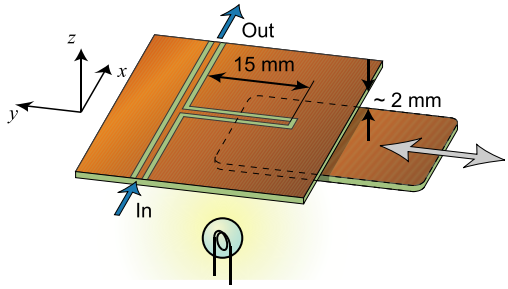

Figure 5: Configuration of the CPW stub resonator and the metal plate. The metal plate is placed on a translation stage. The stub resonator is illuminated from the backside.

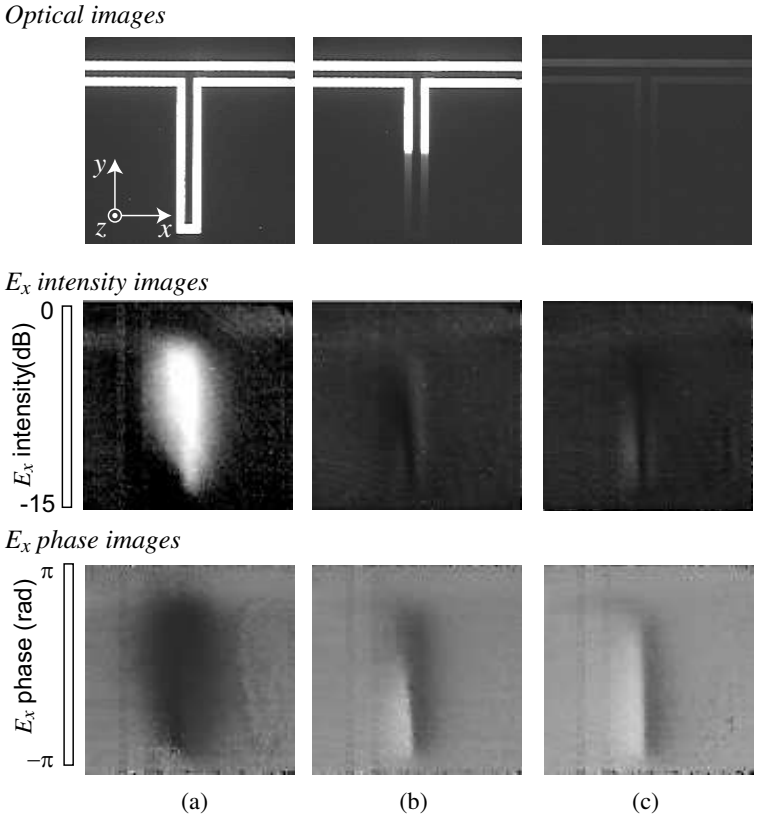

Figure 6: Sequential optical images and intensity and phase images of the E_x component over the CPW stub resonator as the metal plate is being inserted. Input RF signal frequency and intensity are 2.7 GHz and 23 dBm, respectively. Acquisition time for each image is 0.41 seconds, (a) $t = 0$ s, (b) $t = 6$ s, (c) $t = 12$ s.

4. LEI DEMONSTRATION

Amplitude and phase images of electric fields are measured in real-time by the LEI system. In other words, variation of electric field is displayed as a motion picture. This feature realizes observation with (a) environmental variation, (b) phase rotation, (c) frequency sweep, and (d) imaging area scan. Especially, observation with environmental variation is impossible for the conventional single channel systems because of their long acquisition time.

Figure 5 Here, as an extreme example, consider the coplanar waveguide (CPW) stub resonator fabricated on an FR4 substrate with a moving metal (copper) plate shown in Figure 5 as a DUT. The distance between the CPW and the metal was 2 mm. A (110) ZnTe plate, which is an electro-optic sensor sensitive to the x component of the electric field, was placed 0.3 mm above the CPW.

Figures 6 show frame shots of optical, E_x intensity, and phase pattern images taken as the metal plate moved. The frequency of the input signal was 2.7 GHz, which is the resonant frequency of the DUT without the metal plate. The metal plate was gradually inserted until it covered the CPW resonator (within 12 seconds). The DUT was illuminated from the back, and the position of the metal plate can be determined from its shadow in the optical images. The electric field pattern changed rapidly as the plate was inserted. Where the stub overlaps the metal plate, the intensity and phase images change significantly. These results suggest the electric field is coupled with the metal plate and the propagation mode changes. As shown in this demonstration, the LEI system can visualize the electric field variations over RF circuits under varying environmental conditions. This feature is useful to diagnose the influence of objects near the DUT.

5. CONCLUSION

We developed a live electro-optic imgaing (LEI) system, which visualizes microwave electric nearfields as 100×100-pixel images with a frame rate of 30 frames per second. Real-time observation of electric field variation over microwave cirtuits has been demonstrated for the first time. Through the LEI demonstrations, we showed that the agile imaging feature significantly improves the capability of electric field imaging.

ACKNOWLEDGMENT

This work was supported by the NICT presidential fund. The authors would like to thank Dr. Tetsuya Kawanishi for his support.

REFERENCES

1. Sasagawa, K. and M. Tsuchiya, "Real-time monitoring system of RF near-field distribution images on the basis of 64-channel parallel electro-optic data acquisition" *IEICE Electron. Express*, Vol. 2, No. 24, 600–606, Dec. 2005.
2. Sasagawa, K., T. Kawanishi, and M. Tsuchiya, "10,000 parallel heterodyne system for instantaneous photonics- based acquisition of near-fields images over microwave devices/circuits," *Dig. Asia-Pacific Microwave Conf. 2006*, FR2C-5, 1587–1590, Dec. 2006.
3. Sasagawa, K., A. Kanno, T. Kawanishi, and M. Tsuchiya, "Live electro-optic imaging of microwave neawr-fields via ultra-parallel photonic heterodyne," *Dig. Int. Microwave Symp. 2007*, WE1F-05, 401–404, June 2007.
4. Vandmanis, J. A., G. Mourou, and C. W. Gabel, "Picosecond electro-optic sampling system," *Appl. Phys. Lett.*, Vol. 41, No. 3, 211–212,Aug. 2003.
5. Sasaki, A. and T. Nagatsuma, "Electric-field scanning system using electro-optic sensor," *IEICE Trans. Electron.*, Vol. E86-C, No. 7, 1345–1351, July 2003.

Latest Trends in Millimeter-wave Imaging Technology

S. Oka, **H. Togo**, **N. Kukutsu**, **and T. Nagatsuma**
NTT Microsystem Integration Laboratories
3-1, Morinosato Wakamiya Atsugi-shi, Kanagawa 243-1908, Japan

Abstract— This paper overviews the latest trends of millimeter-wave (MMW) imaging technologies, focusing mainly on applications of and technical parameter variations for security surveillance and nondestructive inspections (NDI). We introduce a smart NDI tool using active W-band imaging, which is capable of detecting hidden surface cracks in concrete structures.

1. INTRODUCTION

The history of MMW technologies started in the 1890s [1], and in recent years, various applications have been developed as a result of the rapid progress in monolithic MMW integrated circuit (MMIC) technology. One of the mainstream applications is imaging for security surveillance, and products currently available on the market include active and passive security gates [2, 3], the handheld passive scanners [4], and passive video-rate cameras [5]. Furthermore, researchers are actively exploring other application fields of MMW imaging with much higher sensitivity and resolution.

MMWs penetrate dielectric materials, such as plastic or cloth, and are strongly reflected by metalic materials. These characteristics are very favorable for security surveillance, especially for the detection of weapons concealed under people's clothing and in baggage at airports [6–8]. Figure 1 shows a scissors that was detected hidden in a business card holder [9]. As other examples, life detection in wreckage [10] and a collision avoidance system [11] have been studied.

Nondestructive inspection is also a promising application field of MMW imaging. Figure 2 shows a MMW image of cookies in a box, which shows that the left one is split down the middle. Mizuno et al. performed experiments in which MMW imaging was used to check the maturity of fruit and white-ant-damaged in timber [12]. In this paper, we discuss practical issues of MMW imaging and describe the technical key parameters.

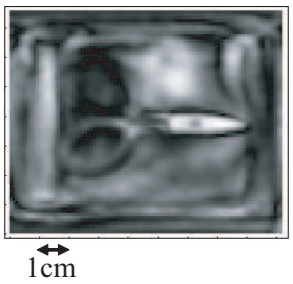

Figure 1: Detection of a scissors hidden in a business card holder (100 GHz).

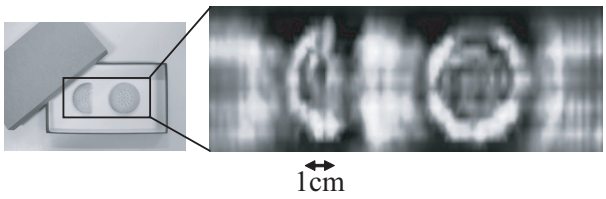

Figure 2: Inspection of cookies in a paper box (94 GHz). The left cookie is split down.

2. PRACTIAL ISSUES OF MMW IMAGING

In any applications of MMW imaging, appropriate integration of key parameters shown in table 1 is important.

Table 1: Key parameters of MMW imaging

Choice of frequency	30 to 110 GHz
Illumination method	Active or passive
Target distance	Far distance; close distance; near-field
Types of detector	Single detector with X-Y stage control; 1D/2D arrayed detectors
Image processing	Deblurring with holography; deblurring with blind-deconvolution

(1) Choice of Frequency

A MMW is an electromagnetic wave with a wavelength from 10 mm to 1 mm (i.e., 30 to 300 GHz). In this region, the transmission of MMW is attenuated by atmospheric absorption caused by water vapor and oxygen [13]. However, there are some regions of low attenuation called "atmospheric windows" around 35, 94, 140, and 220 GHz. At present, 140 and 220 GHz are not normally used, because MMIC products that can work at frequencies higher than the W-band (75–110 GHz) frequency have not matured yet. Therefore, the choice of frequency is basically decided by a simple rule; use a lower frequency for deeper penetration of the dielectric materials; use a higher frequency for higher resolution. In addition, waves at lower frequencies need a wider aperture antenna for illumination and detection.

(2) Illumination Method

When a target does not emit detectable MMW signals, we have to use active illumination. A Gunn diode oscillator is commonly used for coherent active illumination. When using active illumination, the interference and multi-path problem must be carefully considered. Mizuno et al. attempted to use a household fluorescent light as an incoherent illumination [12]. On the other hand, when a target scene includes a thermal source, such as a black-body object, passive sensing is commonly used. The natural emission of MMWs from the human body has been captured by using a high-sensitivity Schottky diode detector with a low-noise amplifier [14].

(3) Target Distance From the early stage, MMW imaging has been used at far distances (> 10 wavelength) for security surveillance. Because the 10 wavelength is about 30 mm at 94 GHz, it is obvious that the normal distance of security camera (1–5 m to a target) reaches the far distance region. Serious problems in long-distance imaging are the degradation of resolution and diffusive attenuation. A focal dielectric lens is often applied to improve them. Such lenses are made of Teflon and weigh several kilograms, which makes the system large and heavy.

On the other hand, new practical applications at close distance (< 10 wavelength) have been explored in recent years. Sheen et al. demonstrated the detection of concealed items in a gypsum wall with a sophisticated image reconstruction algorithm in near-field region [6], Nozokido et al. observed the evolution of photo-excited free-career distribution using a metal slit probe [15], and we has developed a concrete crack detection scanner, which is described in next section.

(4) Types of Detector

In experimental studies in laboratories, the basic approach for image capturing is to sweep a single detector with an X-Y motor-controlled stage. For practical use, arrayed detectors are preferable in order to shorten the scanning time. Brijot Inc. has achieved fast video-rate capturing (0.5 seconds per frame) for the security surveillance cameras. They used a 1D array of 16 detectors and a mirror reflector that periodically moves to sweep a whole area in a scene. The integration of a fixed 1D/2D array of detectors and a movable mirror reflector is common for video-rate MMW cameras [14, 16, 17]. Another approach of image capturing is to use a leaky wave antenna as 1D array detector, which can capture the MMW reflections arriving from 60 directions simultaneously (20 seconds per frame) [18].

(5) Image Processing

In imaging systems, the diffusive scattering and the speckle of electromagnetic waves makes an observed image blurry. To improve resolution, several image-processing techniques have been proposed [19, 20]. Sheen et al. employed a holographic approach using both magnitude and phase information at 10–30 GHz, and performed image reconstruction with sub-wavelength resolution using a 2D/3D Fourier transform algorithm [6, 7]. Another deblurring technique is blind deconvolution, which works when phase information is not available. A demonstration of this technique used for deblurring an evanescent microwave image has been reported [21].

3. AN APPLICATION TO CIVIL STRUCTURES AND MATERIALS

In this section, we introduce a new our application of MMW imaging, which aims at a nondestructive inspection of civil structures [22].

Alarm to the hazards of old decrepit concrete structures is spreading, and the possibility of unscrupulous developers falsifying construction data, as seen in the recent faked earthquake-proof certification scandal in Japan, is becoming a serious social concern [23]. The integrity of concrete structures is commonly evaluated through crack inspection. However, cracks are often hidden by wallpaper, paint, and tile. To solve this problem, we developed an NDI MMW-imaging tool called "Crack Scan", which is used as shown in Figure 3.

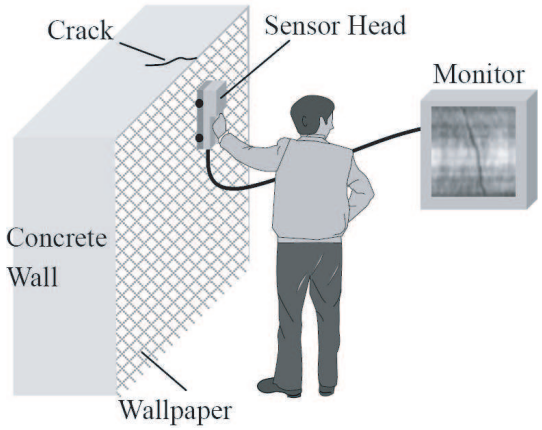

Figure 3: Practical scene of Crack Scan.

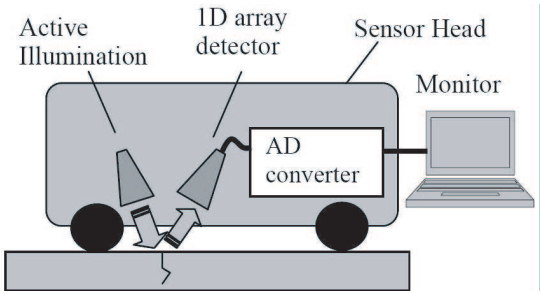

Figure 4: System layout of Crack Scan.

The target in this case does not include black-body radiation. Therefore, we chose a Gunn oscillator with W-band frequency (75–110 GHz) for active illumination. In addition, considering the need for portability and working efficiency, the tool must be compact, about the size of a handhold imager. To meet this requirement, we chose close-distance sensing without a focal lens, but with a 1D detector array. Figure 4 shows the system layout. Scanning this device over a wall surface makes it possible to display hidden surface cracks as 2D images on a monitor. The MMWs pass through wallpaper and lining paint but are scattered on impact with fine cracks.

Figure 5 shows a photograph of Crack Scan and an experimental result of crack detection under wallpaper. Generally, the spatial resolution of imaging in the far-distance region is limited to the radiowave wavelength. However, by detecting the dispersion of MMWs scattered by cracks in at close distance, crack-inspection accuracy covering sub-millimeter widths (specified in civil engineering standards) is obtained.

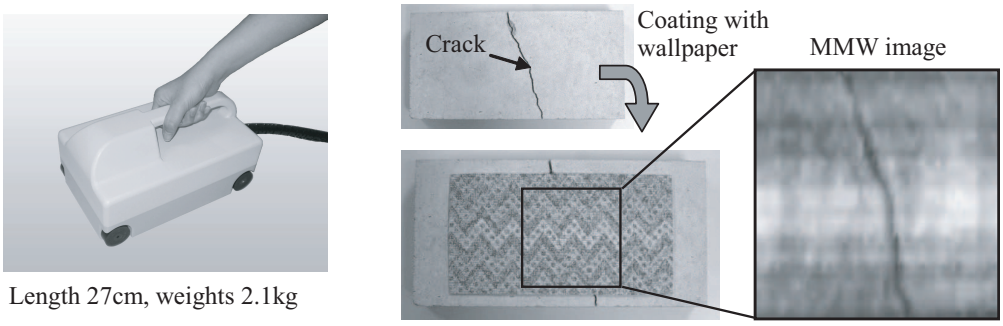

Figure 5: Photograph of Crack Scan and a result of crack detection under wallpaper.

We are aiming to deploy the Crack Scan technology in the repair and maintenance departments of facilities as a non-destructive inspection method for concrete structures. Moreover, we are pushing ahead with research and development on applications of Crack Scan in areas other than concrete-structure inspection, such as security surveillance and food inspection.

4. CONCLUSION

To achieve a MMW imaging system, we have to carefully select targets on the basis of the transmission and reflection principals in this frequency region, and consider the best integration of frequency, illumination, distance, detector type, and image processing. As major price decline of MMIC products, the millimeter-wave imaging will prevail among our daily life in the near future.

ACKNOWLEDGMENT

The development of Crack Scan was supported by AIREC Engineering Corporation.

REFERENCES

1. Wiltse, J. C., "History of millimeter and submillimeter waves," *IEEE Trans. on Microwave Theo. and Tech.*, Vol. 32, No. 9, 1118–1127, 1984.
2. http://www.safeviewinc.com/frontend/index.aspx
3. http://www.millivision.com/
4. http://www.sagosystems.com/
5. http://www.brijot.com/
6. Sheen, D. M., D. L. McMakin, and T. E. Hall, "Near field imaging at microwave and millimeter wave frequencies," *Proc. of IEEE IMS*, 1693–696, Honolulu, Hawaii, USA, June 2007.
7. Sheen, D. M., D. L. McMakin, and T. E. Hall, "Three-dimensional millimeter-wave imaging for concealed weapon detection," *IEEE Trans. on Microwave Theo. and Tech.*, Vol. 49, No. 9, 1581–1592, 2001.
8. Clark, S. E., J. A. Lovberg, C. A. Martin, and V. Kolinko, "Passive millimeter-wave imaging for airborne and security applications," *Proc. of SPIE*, Vol. 5077, 16–21, August 2003.
9. Sasaki, A. and T. Nagatsuma, "Millimeter-wave imaging using an electrooptic detector as a harmonic mixer," *IEEE J. of Selected Topics in Quan. Elec.*, Vol. 6, No. 5, 735–740, 2000.
10. Lubecke, V. M., O. Boric-Lubecke, A. Host-Madsen, and A. E. Fathy, "Through-the-wall radar life detection and monitoring," *Proc. of IEEE IMS*, 769–772, Honolulu, USA, June 2007.
11. Salmon, N. A., "A w-band real-time passive millimeter-wave imager for helicopter collision avoidance," *Proc. of SPIE on Passive Milli.-Wave Imaging Tech. III*, Vol. 3703, 28–32, Orlando, Florida, USA, April 1999.
12. Mizuno, K., H. Matono, Y. Wagatsuma, H. Warashina, H. Sato, S. Miyanaga, and Y. Yamanaka, "New applications of millimeter-wave incoherent imaging," *Proc. of IEEE IMS2005*, Long Beach, California, USA, June 2005.
13. Appleby, R., "Passive millimetre-wave imaging and how it differs from terahertz imaging," *Phil. Trans. of T. L. Soc.*, Lond. A, Vol. 362, No. 8, 379–394, 2003.
14. Lovberg, J. A., C. Martin, and V. Kolinko, "Video-rate passive millimeter-wave imaging using phased arrays," *Proc. of IEEE IMS*, 1689–1692, Honolulu, USA, June 2007.
15. Nozokido, T., J. Bae, and K. Mizuno, "Scanning near-field millimeter-wave microscopy using a metal slit as a scanning probe," *IEEE Trans. on Microwave Theo. and Tech.*, Vol. 49, No. 3, 491–499, 2001.
16. Appleby, R. and R. N. Anderton, "Millimeter-wave and submillimeter-wave imaging for security and surveillance," *Proc. of IEEE*, Vol. 95, No. 8, 1683–1690, 2007.
17. Appleby, R., R. N. Anderton, S. Price, N. A. Salmon, G. N. Sinclair, J. R. Borrill, P. R. Coward, P. Papakosta, and A. H. Lettington, "Compact real-time (video rate) passive millimeter-wave imager," *Proc. of SPIE on Passive Milli.-Wave Imaging Tech. III*, Vol. 3703, 13–19, Orlando, Florida, USA, April 1999.
18. http://www.nhk.or.jp/strl/
19. Pirogov, Y. A., M. F. Attia, I. M. Blankson, A. I. Dubina, V. V. Gladun, C. D. Papanicolopoulos, E. N. Terentiev, and O. A. Tarasova, "Problem of radiovision system resolution improvement in millimeter-wave range," *Proc. of SPIE on Passive Milli.-Wave Imaging Tech. III*, Vol. 3703, 175–180, Orlando, Florida, USA, April 1999.
20. Terentiev, E. N., Y. A. Pirogov, V. V. Gladun, B. A. Rozanov, A. S. Pavlov, and O. A. Tarasova, "Problem of the sun radiovision system super-resolution in 3 mm wavelength range," *Proc. of SPIE on Passive Milli.-Wave Imaging Tech. III*, Vol. 3703, 181–189, Orlando, Florida, USA, April 1999.
21. Oka, S. and S. LeClair, "Image mining of evanescent microwave data for nondestructive material inspection," *Proc. of IPMM*, Sendai, Japan, May 2003.
22. Bolomey, J. C. and F. E. Gardiol, *Engineering Applications of the Modulated Scatterer Technique*, Artech House Publishers, Boston, London, 2001.
23. Nadakuduti, J., G. Chen, and R. Zoughi, "Semiempirical electromagnetic modeling of crack detection and sizing in cement-based materials using near-field microwave mothods," *IEEE Trans. on Inst. and Meas.*, Vol. 55, No. 2, 588–597, 2006.

Trends in Next Generation Optical Access Networks and a Proposed Hybrid Optical/Wireless Wide-area Access Network

Junichi Kani

NTT Access Network Service Systems Laboratories, NTT Corporation, Japan

Abstract— This paper first reviews trends toward the next-generation optical access networks; one of the key points is how to utilize wavelength-division multiplexing. It also overviews the technique of fiber-wireless access as a candidate to provide wireless connection in the last one step of the future access network. In the latter half, a novel hybrid optical/wireless access network is proposed; the importance of microwave photonics technologies is emphasized. The proposed network provides next-generation optical access and high radio frequency wireless access on the same platform.

1. INTRODUCTION

In the last few years, the optical access service based on Fiber-to-the-Home (FTTH) has been proven to be the most promising fixed Internet access service; the number of customers in Japan exceeded that of ADSL in early 2007. The typical Gigabit-capable passive optical network (PON) system shares 1 Gbit/s total bandwidth among 16 to 32 subscribers. A complementary technology to support broadband access is the wireless network using the microwave band; it forms the last one step of the access network, e.g., inside stations/floors. In these networks, average bandwidth per user is assumed to be around several tens of Mbit/s.

This paper first reviews technologies and standardization trends toward the next-generation optical access networks (NG-OAN), whose target can be assumed to be providing new services with the average bandwidth of several hundreds of Mbit/s to several Gbit/s. One of the key points is how to utilize optical multiplexing technologies including wavelength-division multiplexing (WDM) in the NG-OAN [1]. It next overviews the technique of fiber-wireless access to provide the last one step of the future access network. Last, a novel hybrid dense-WDM and fiber-wireless access system is proposed for constructing the next-generation wide-area access network. In the network, microwave photonics play a key role in terms of multi-wavelength generation, as we reported before [2], as well as fiber-wireless transmission. The proposed system utilizes DWDM wavelengths divided to several wavelength groups, and each of the wavelength groups can provide high speed optical connection services (e.g., 10 Gbit/s) via full-fiber access and/or next-generation wireless services (e.g., 100 Mbit/s) via fiber-wireless access depending on the situation.

2. NEXT-GENERATION ACCESS NETWORK

2.1. Next-generation Optical Access

Gigabit-capable PON systems such as GE-PON (IEEE standard 802.3ah) and G-PON (ITU-T Recommendation G.984 series) are now being deployed to support broadband optical access services. These PONs use time-division multiple access (TDMA) to realize the point-to-multipoint connection between an optical line terminal (OLT) located in an operator's building and the optical network units (ONUs) in the users' homes. Each connection provides 1 Gbit/s (to 2.5 Gbit/s) total bandwidth that is shared among 16 to 32 subscribers; Figure 1(a) shows the typical schematic of the TDMA-based PON. The dynamic Bandwidth Allocation (DBA) algorithm is one of the keys to maximizing TDMA-PON performance while keeping fairness among subscribers. Gigabit capable PONs provide enough bandwidth for end users and they occupy the current sweet spot of opto-electronic components, i.e., maximum performance and minimum cost. However, considering the continuous evolution of communication services such as bidirectional video communication and three-dimensional image transmission, long-term efforts on the next generation system are important.

As a candidate technology for NG-OAN, one attempt being extensively pursued is the WDM-PON, where a dedicated bandwidth is provided by assigning a wavelength to each user. This scheme of assigning wavelengths instead of time slots (TDMA) is called wavelength-division multiple access (WDMA). Figure 1(b) shows a typical schematic of a WDM-PON with WDMA. A simple implementation of WDM-PON is to put a differently colored laser (i.e., a laser with a different

wavelength) in each ONU, but then operators have to control who uses which wavelength as well as maintain stocks of devices for all wavelengths. To resolve such issues, technologies to realize "colorless ONUs" are being widely pursued [1]. One example is to employ wavelength-tunable lasers in ONUs and another is to remotely lock the wavelength of ONU lasers by sending the seed wavelength from the OLT side.

A combination of TDMA and WDMA is also possible to increase the maximum bandwidth by WDM while retaining gradual bandwidth allocation made possible by TDMA. Dynamic Wavelength Allocation (DWA) algorithm has been researched for such networks [3].

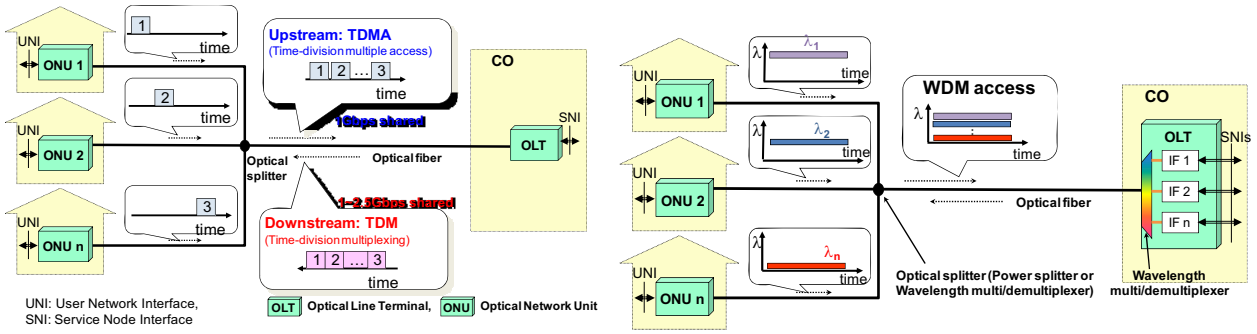

(a) (b)

Figure 1: Typical schematics of TDMA-PON and WDM-PON, (a) TDMA-PON, (b) WDM-PON.

Another possible approach to NG-OAN is to extend the reach so as to realize consolidation with metro networks [2, 4]. The motivation of these works is to reduce operational expenditure (OPEX) by reducing or eliminating elements that raise the cost of the operation, administration and maintenance functions in the operator's buildings nearest to the end users. Extending PON reach and splitting ratio by the use of optical amplifiers has been extensively researched [4, 5]. The use of WDM is also important to increase the transmission capacity in the trunk line between two operator's buildings [2].

As for the standardization trends of NG-OANs, IEEE has started discussion on 10GE-PON [6]. The 10GE-PON simply increases the speed of time-division multiplexing (TDM) to ten times the GE-PON level, where the issues are to realize opto-electronics that can work at 10-Giga speed as well as lower cost. The FSAN (full service access network) forum, which submitted B-PON and G-PON proposals to ITU-T, is also studying the next-generation access (NGA), where WDM functionality, reach extension, and evolution scenarios are under study in addition to increasing the speed of TDM [7].

2.2. Fiber-wireless Access

Wireless access technologies are evolving to use multi-input/multi-output (MIMO) channels and/or higher radio frequencies for carrying the next generation services at over 100 Mbit/s. Among them, an interesting approach is the radio-on-fiber technology, which simplifies the system architecture by directly delivering high radio frequency broadband signals through optical fibers.

One interesting approach is to heterodyne two optical frequencies whose difference corresponds to the radio frequency (RF), e.g., 60 GHz [8]. By modulating one of these two optical frequencies before fiber transmission, the RF signal can be extracted by heterodyne detection after fiber transmission. This approach can eliminate not only the local RF generator in each base station (BS), the boundary between the fiber link and the wireless link, but also provide better fiber-transmission performance than direct optical carrier modulation with a high RF signal. However, the optical phases of the two optical frequencies must be synchronized to generate a stable RF signal after detection. Multi-wavelength light sources that can inherently provide such phase synchronization between any two wavelengths are an attractive candidate for this purpose as well as for multiplexing many different RF signals.

DWDM (dense wavelength division multiplexing) extension of these radio-on-fiber access systems has been demonstrated; it multiplexes many sets of RF signals onto one feeder fiber to connect to the central station (CS); a supercontinuum-type multi-wavelength light source has been used [9].

3. A PROPOSED HYBRID OPTICAL/WIRELESS WIDE-AREA ACCESS NETWORK

As described in the above section, the trends in next-generation optical access networks include reach extension for a wide-area access network that realizes consolidated operation to reduce OPEX while fiber-wireless access is interesting for simplifying the architecture of next-generation high speed wireless access. In this section, we propose a hybrid optical/wireless wide-area access network based on DWDM group multi/demultiplexing; Figure 2 illustrates its configuration. OLTs and an optical carrier supply module (OCSM) are located in the center node; the OCSM is a multi-wavelength light source (described later) that supplies multi-wavelength carriers to several OLTs. The OLT has interfaces for radio-on-fiber access (RoF IFs) as well as those for high speed optical access such as 10 Gigabit Ethernet (10GE IFs). This network uses DWDM wavelength channels (e.g., 64 channels) and the group multi/demultiplexer (G-MUX) in each remote node divides/combines the DWDM channels into/from several groups of wavelengths (e.g., 8 wavelengths $\times$8 groups). Each wavelength group is dedicated to a building/apartment, where a wavelength pair can provide either optical access via an ONU or RoF access with a BS (e.g., 1 $\times$ 10GE-ONU and 3$\times$RoF BSs in each building/apartment).

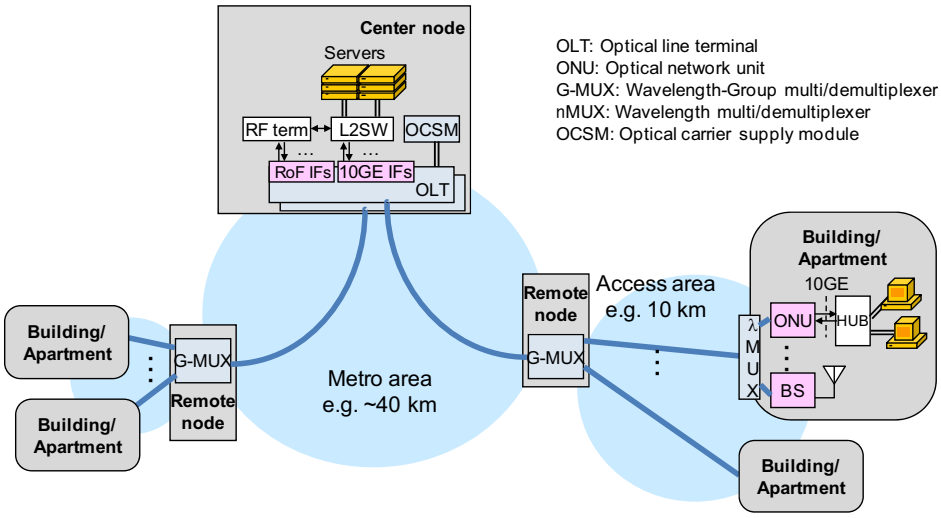

Figure 2: Proposed hybrid optical/wireless access network.

Figures 3(a) and (b) show the configuration and optical spectrum of the OCSM that we reported previously [2]. By modulating seed laser diodes (LDs $\lambda 1$ to λn in the figure) with a phase modulator (PM) and an intensity modulator (IM) using 25-GHz radio frequencies with appropriate amplitudes, we can obtain multi-wavelength optical carriers as the modulation sideband as shown in Figure 3(b); the spectrum consists of four wavelength groups where each group consists of eight wavelengths with 25-GHz spacing. Typically, low-cost optical filters for group multi/demultiplexing require an adequate guard-band between neighboring groups. As you can see in the spectrum, this OCSM is very suitable for such a group multi/demultiplexing because one can easily adjust the spacing between neighboring wavelength groups by adjusting the seed wavelengths.

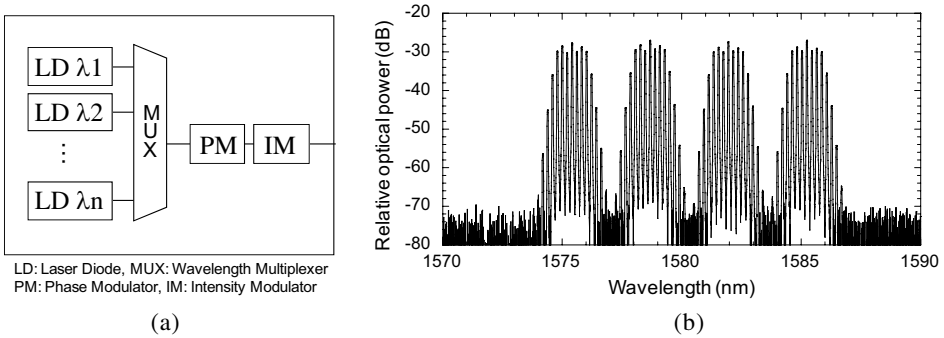

Figure 3: OCSM, (a) configuration, (b) output optical spectrum.

Figure 4 shows a detailed configuration of the proposed network system. Wavelength pairs to be used for an ONU or a BS are $\lambda_{k1}/\lambda_{k3}$, $\lambda_{k2}/\lambda_{k4}$, $\lambda_{k5}/\lambda_{k7}$, $\lambda_{k6}/\lambda_{k8}$ where k is the group number (runs from 1 to n). In the case of the OCSM shown in Figure 3, n is 4; we can increase n by adding seed wavelengths to OCSM. The center node consists of n sets of modulation arrays (Mod array), n sets of receiver arrays (Rec array) and group multi/demultiplexers (G-MUX/G-DMX). Each Mod array multi/demultiplexes the eight wavelengths in each group by using arrayed-waveguide gratings (AWGs), and λ_{k1}, λ_{k2}, λ_{k5}, λ_{k6} are modulated by 10 Gbit/s binary NRZ data (for optical access) or 10 GHz-band IF data (for RoF access). In the remote node, the G-MUX/DMX divides/combines signals by wavelength groups. In the building, AWGs multi/demultiplex the eight wavelengths. BS receives the RoF signal by heterodyning the wavelength pair (e.g., $\lambda_{k1}/\lambda_{k3}$) to generate a wireless signal with 60-GHz RF as well as transmitting the RoF signal by remotely modulating and transmitting one of the wavelength pairs (e.g., λ_{k3}) upstream [9]. ONU simply receives one modulated wavelength pair (e.g., λ_{k2}) as well as modulating/demodulating another wavelength pair (e.g., λ_{k4}). By using this system configuration, we can realize a wide-area access network that provides both high-speed optical access and fiber-wireless access flexibly depending on need. As described, microwave photonics technologies play a key role in terms of multi-wavelength generation as well as fiber-wireless transmission in the proposed network.

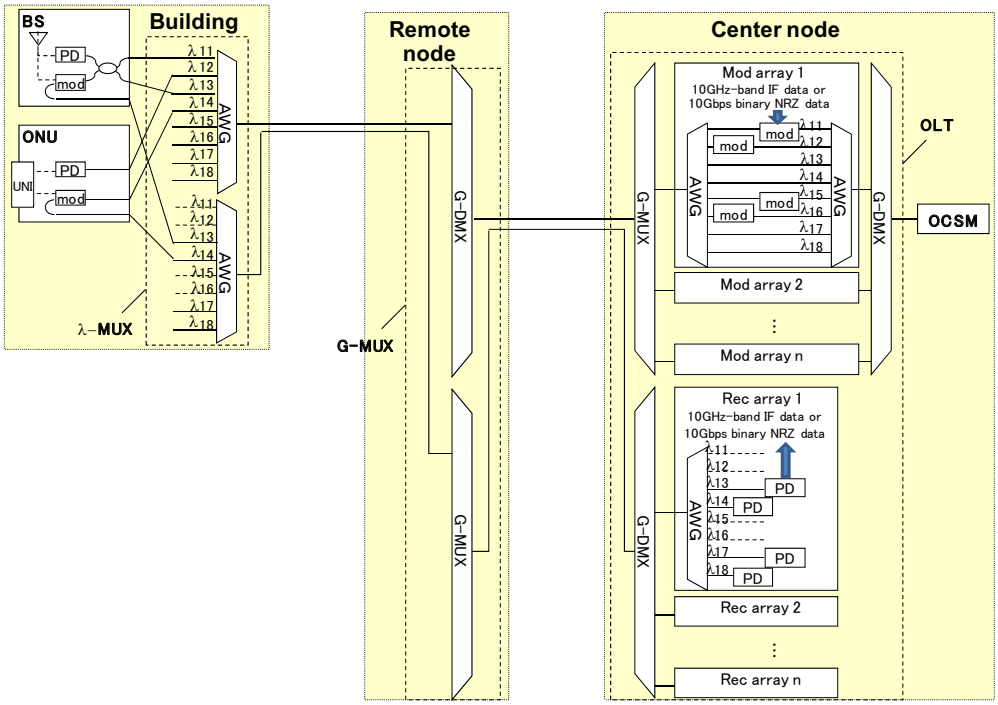

Figure 4: System configuration.

4. CONCLUSIONS

This paper first reviewed trends in the next-generation optical access networks; possible directions included how to utilize WDM technologies in the NG-OAN as well as reach extension to realize wide-area access networks. Next, fiber-wireless technologies were described as an interesting candidate with which to deliver high radio frequency broadband signals through optical fibers directly. Last, a hybrid optical/wireless wide-area network was proposed for providing next-generation high-speed optical access and next-generation high radio frequency wireless access on the same platform.

REFERENCES

1. Kani, J., K. Iwatsuki, and T. Imai, "Optical multiplexing technologies for access-area applications," *IEEE Journal of Selected Topics in Quantum Electronics*, Vol. 12, Issue 4, 661–668, July–Aug. 2006.
2. Kani, J., M. Teshima, K. Akimoto, N. Takachio, H. Suzuki, K. Iwatsuki, and M. Ishii, "A

WDM-based optical access network for wide-area gigabit access services," *IEEE Communication Magazine*, Vol. 41, Issue 2, S43–S48, February 2003.
3. An, F.-T., et al., "SUCCESS-HPON: A next-generation optical access architecture for smooth migration from TDM-PON to WDM-PON," *IEEE Communications Magazine*, Vol. 43, Issue 11, S40–S47, November 2005.
4. Van de Voorde, I., et al., "The superPON demonstrator: An exploration of possible evolution paths for optical access networks," *IEEE Communications Magazine*, 74–82, February 2000.
5. Suzuki, K. I., et al., "Amplified gigabit PON systems," *IEEE J. Optical Networking*, Vol. 6, 422–433, 2007.
6. http://www.ieee802.org/3/av/.
7. http://www.fsanweb.org/nga.asp.
8. Taniguchi, T., et al., "Loop-back optical heterodyne technique for 1.0-Gb/s data transmission over 60-GHz radio-on-fiber uplink," *IEEE J. Lightwave Technol.*, Vol. 25, 1484–1494, 2007.
9. Sono, T., et al., "Full-duplex 25-GHz spacing DWDM MM-wave-band radio-on-fiber system using a supercontinuum light source and arrayed-waveguide-grating filters," *Tech. Dig. of International Topical Meeting on Microwave Photonics (MWP)*, 2006.

Development of Radio on Free Space Optics System for Ubiquitous Wireless

Katsutoshi Tsukamoto[1], **Takeshi Higashino**[1], **Takuya Nakamura**[1], **Koichi Takahashi**[1]
Yuji Aburakawa[1], **Shozo Komaki**[1], **Kazuhiko Wakamori**[2], **Toshiji Suzuki**[2]
Kamugisya Kazaura[2], **Alam Mohammad Shah**[2], **Kazunori Omae**[2], **and Mitsuji Matsumoto**[2]

[1]Graduate School of Engineering, Osaka University, Japan
[2]GITI, Waseda University, Japan

Abstract— Radio on Fiber (RoF) with layer 1 routing capability can realize a cost effective universal platform for future ubiquitous wireless services. The layer 1 routing concept can be realize by not only RoF but also RoFSO (Radio on Free Space Optics) or RoR (Radio on Radio) networks, which provide a free space for heterogeneous wireless services in Free Space Optics or millimeter wave radio. Development of a new advanced RoFSO system has been started. This paper describes its concept and features, and furthermore, discusses about its role in future ubiquitous wireless.

1. INTRODUCTION

In ubiquitous network society, users want an environment to access any communication services at any time, any place, and any situations. In order to realize the ubiquitous networks, a combination of IP network and broadband heterogeneous wireless access services will play an important role. In current wireless networks, however, various operators independently overlaid their own radio base stations and networks. This leads redundant equipments and investments on infrastructures, and prevents the quick start of a new wireless service and employing microcellular architecture. These problems are revealed especially in in-building, underground at urban areas, and rural areas where broadband fiber-infrastructures have not yet been constructed due to their high cost and a low population.

Radio on Fiber (RoF) technologies can realize a cost effective universal platforms for future ubiquitous wireless services. Furthermore, RoF networks can be extended to Virtual Radio Free Space Network with layer 1 routing realized by not only RoF but also RoFSO (Radio on Free Space Optics) or RoR (Radio on Radio) networks, which can provide a free space for heterogeneous wireless services in Free Space Optics or millimeter wave radio. This paper describes the concept and features of a new advanced RoFSO system development, and furthermore, discusses software definable radio networks [1, 2] from a viewpoint of its role in future ubiquitous wireless.

2. LAYER 1 ROUTING WITH RADIO ON FIBER, RADIO, AND FREE SPACE OPTICS

Radio on Fiber (RoF) links shown in Fig. 1 have a function of transmitting radio signals to remote stations with keeping their radio formats. Consequently, RoF link becomes a hopeful candidate of a common platform for various wireless access networks. When RoF equips photonic routing functions, any radio signal can be forwarded to its destination control station. We call such RoF networks "Virtual Radio Free Space Network (VRFSN)" [3]. By using RoF, architecture for radio access zones easily employs micro or pico cellular systems. A RBS receiving or transmitting radio signals in each radio zone, equips only O/E and O/E converters. The RBS requires neither the modulation functions nor demodulation functions of radio signals. The radio signals converted into optical signals are transmitted via a RoF link with the benefit of its low transmission loss and broadband. Therefore, RoF links can be independent of radio signal formats and can provide universality for various types of radio access methods. This means that VRFSNs are very flexible to the modification of radio signal formats, the opening of new radio services, or the accommodation of different types of radio signal formats.

VRFSNs with layer 1 routing are required for ubiquitous wireless especially in radio dead zones at private or public spaces such as in-house, in-building, and underground at urban areas, and at rural areas where broadband fiber-infrastructures have not yet been constructed due to their high cost and a low population. The layer 1 routing concept shown in Fig. 2 can be also extended to RoFSO (Radio on Free Space Optics) or RoR (Radio on Radio) networks, which can provide a free space for heterogeneous wireless services in Free Space Optics or millimeter wave radio. Therefore,

RoF links can be replaced with RoFSO or RoR links. In each network, radio signals are converted into FSO or MMW signals with wideband frequency conversion. The Layer 1 routing would be important for the transparency not only for various protocols on Layer 2 and upper, but also for various types of air interfaces.

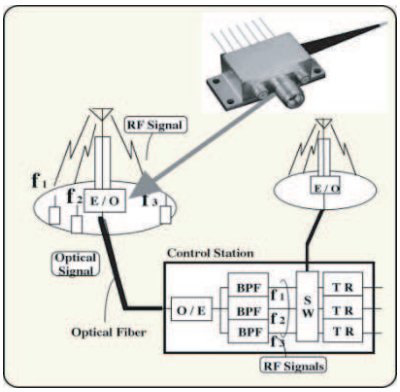

Figure 1: Radio on Fiber (RoF) links.

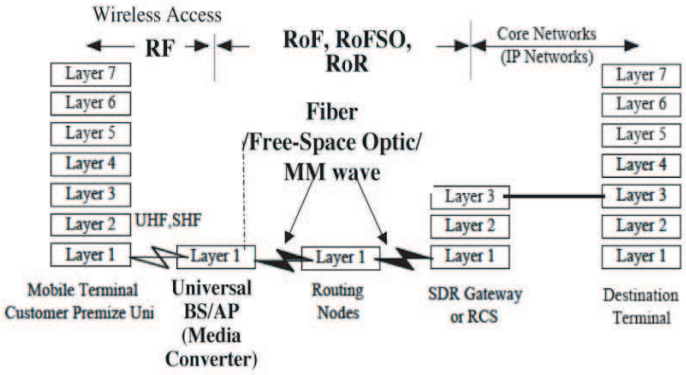

Figure 2: Layer 1 routing and Radio on Free Space concept.

3. DEVELOPMENT OF ROFSO SYSTEM

3.1. Concept and Object

The development of DWDM RoFSO link system has been started to realize an effective and quick provide of heterogeneous wireless services for not only urban area but rural area, that has a little or no infrastructure for broadband services [4]. Fig. 3 illustrates the concept of advanced DWDM RoFSO link system. An object of the development is to realize an advanced RoFSO link system, which can transparently transfer cellular phone, wireless LAN, terrestrial digital broadcasting, and future coming new wireless services by using DWDM optical wireless channels.

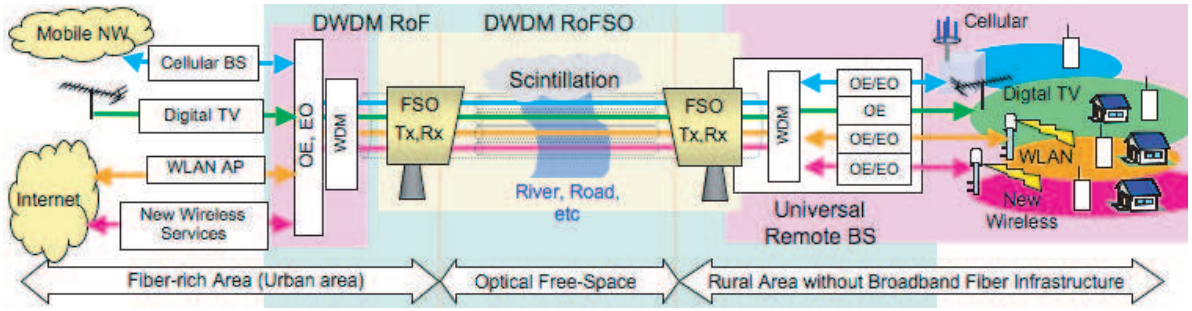

Figure 3: Concept of advanced DWDM RoFSO link system.

3.2. Feaures of RoFSO System

Figure 4 illustrates features of RoFSO link system. Conventional FSO system has been prepared for each of digital data transmissions with different data rates such as Ethernet, cellular entrance, digital CATV, and so on. Recently, next generation FSO system [5] has successfully realized a stable 10 Gbps WDM FSO transmission. Therefore, a protocol-free digital FSO link with an equivalent performance as an optical fiber has been realized. On the other hand, the object of our development is to realize RoFSO link that has an equivalent capacity for heterogeneous wireless services as RoF. We will employ the direct optical amplification and emission of RoF signal into free space, and direct focusing of the received optical beam into the core of SMF, that technologies have been developed in the next generation FSO system [5]. Since RoF and RoFSO are essentially analog transmission links, higher stability and reliability will be required. One object of the development is to improve accuracy of the optical beam tracking system. The target is more than 1 km link distance, DWDM with more than 4 wavelengths, transmission of more than 4 different wireless services including terrestrial digital TV broadcasting.

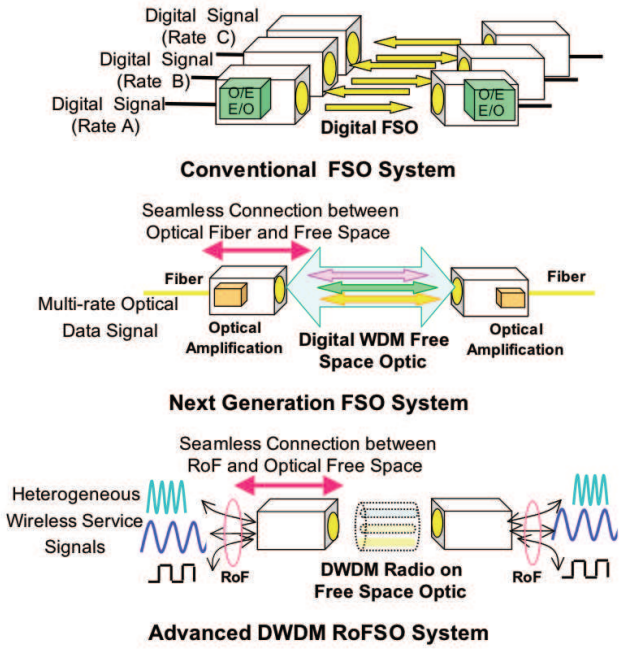

Figure 4: Advanced DWDM RoFSO link.

3.3. Development of Advanced DWDM RoFSO Link System

Figure 5 illustrates the developed RoFSO Transmitter / Receiver with Fine Beam Tracking Optic System [6] to emit DWDM RoF signals directly from SMF into free space and focus a received optical beam directly into a core of SMF. Objective design parameters are followings: Optical Transmitting Power: 20 dBm/wave, Geometric Loss: 2.6 dB at 1 km (Beam angle width: 47.3 μrad at 1.55 μm), Equipment Loss: < 10 dB (Tx & Rx total).

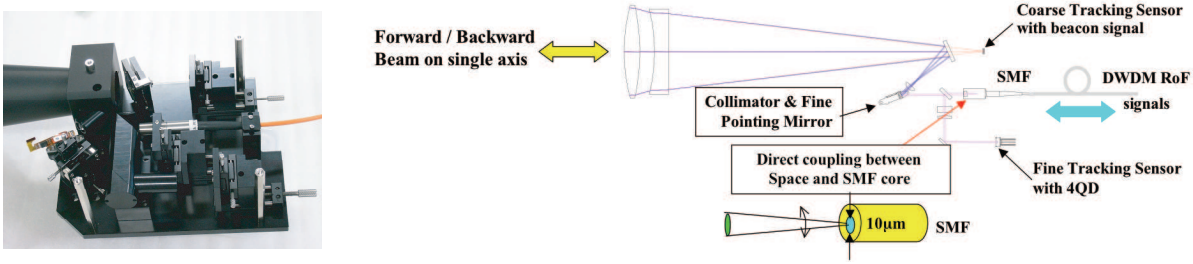

Figure 5: Developed RoFSO Transmitter / Receiver with fine beam tracking optic system which emits DWDM RoF signals directly from SMF into free space and focuses a received optical beam directly into a core of SMF.

3.4. Development of Seamless Connecting Equipments between RoF and RoFSO

To design RoFSO link, we have to examine a total performance through RoF, RoFSO and wireless access links. Since different wireless services have different data-rate, modulation formats, and sensitivity, we have to investigate the influence of distortion or disturbances suffered on RoF and RoFSO links for each wireless services. Fig. 6 shows indoor short-range experiment setup to confirm FSO loss compensation effect with optical amplifier. A RoF signal with 1.55 μm wavelength modulated by WLAN signals at 2.4 GHz is amplified at EDFA, transmitted directly from SMF into FSO channel, directly focused into a core of SMA, amplified at post EDFA up to 0 dBm and then received at PD. Fig. 6 shows experimental results of RF output power versus RF input power of RoFSO link when the optical loss between Tx and Rx was 50 dB, and received optical power, $P_{opt\,R}$ was -3.75 dBm. In this figure, experimental results for RoF when $P_{opt\,R} = -3.3$ dBm are also shown for comparison. It is seen from the figure that booster and post EDFA can compensate the loss of RoFSO link without any IMD3 increase, and realize RoFSO link equivalent to RoF link.

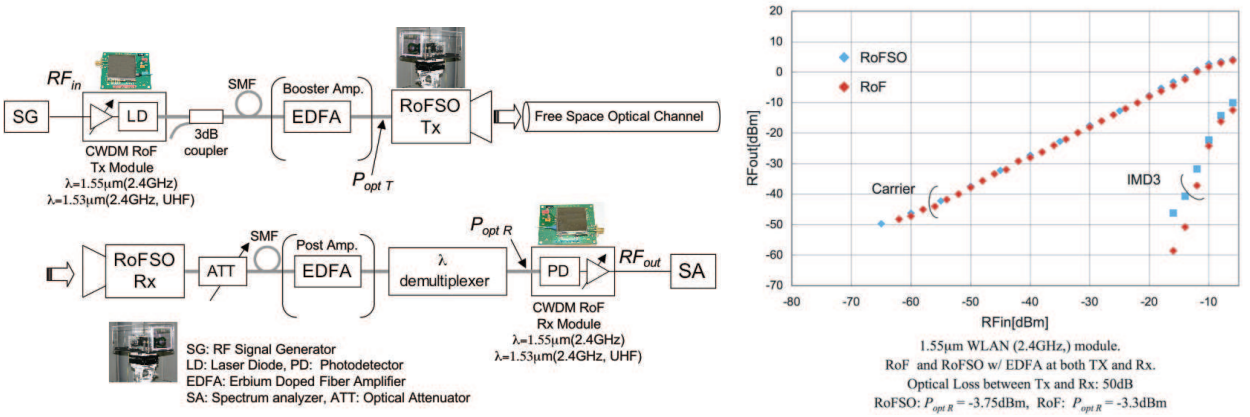

Figure 6: Indoor short range experiment setup of RoFSO link for 2.4 GHz and UHF band radio signals and experimental results of RF output power versus input power.

3.5. Long-term Demonstrative Measurements of RoFSO Link

In outdoor environments, an atmospheric turbulence has a significant impact on the quality of the free-space optical beam. Optical intensity fading due to beam broadening, angle-of-arrival fluctuations, and scintillation will reduce the received optical beam power, and causes burst errors in transmitted RF signals. We have started constructing a statistical model of scintillation and performed some simulations. Also, a long-term measurement of scintillation has been started using a measurement setup with conventional 800 nm FSO system. Fig. 7 shows the experiment setup at Waseda University, Tokyo, and some examples of measurement results of scintillation variance versus time in a day in May or September. It is found that a large variation in temperature causes a large variation in scintillation variance. After long-term measurement of scintillation, and evaluation of its influences on four types of RF signals transmitted on RoFSO link, then we will conduct a long-term and pragmatic demonstration of the developed RoFSO link.

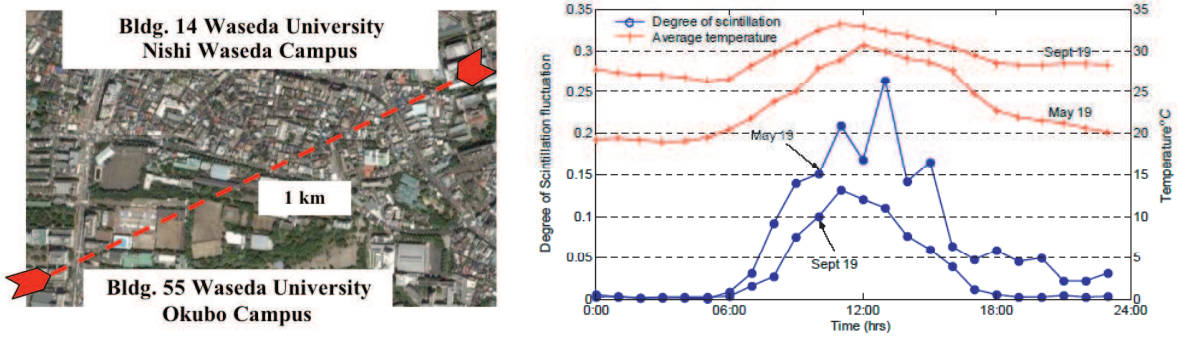

Figure 7: Experiment field at Waseda Univ., Tokyo and measurement setup with conventional 800 nm FSO system and example of measurement results of scintillation variance versus time in a day in May or September.

4. SOFTWARE DEFINABLE RADIO NETWORKS

Figure 8 illustrates the concept of extended VRFSN, called Software Definable Radio Network (SDRN) [1, 2]. The SDRN is composed with Radio on Free Space (RoFSx) networks such as RoF, RoFSO and RoR, universal RBS and software definable control server (SDRCS) in IP network for various types of wireless services, and SDRGW (Software Definable Radio Gateway), which provides a seamless connectivity between local RoF networks and IP network. RoFSx (Fiber, Optics, Radio, LCX etc) networks can transparently connects multi-dimensional radio spaces with Photonic Intensity (1 dimension). In the SDRN, any radio signals in a RoFSx network with routing functions are transmitted to their desirable SDRGW. At SDRGW, air-interface conversion or IP packeterization of wireless data and control signals are executed. The later function is that the datagram in any radio signal are converted to IP packet, which are transferred to its SDRCS altogether with the control channel signal (Wireless service over IP [7]). This can realize a cross layer platform on the

IP network for heterogeneous wireless services networks. RoFSx networks with several distributed universal BS can also achieve SDMA to improve frequency efficiency (Heterogeneous Radio Smart Space Construction [8]).

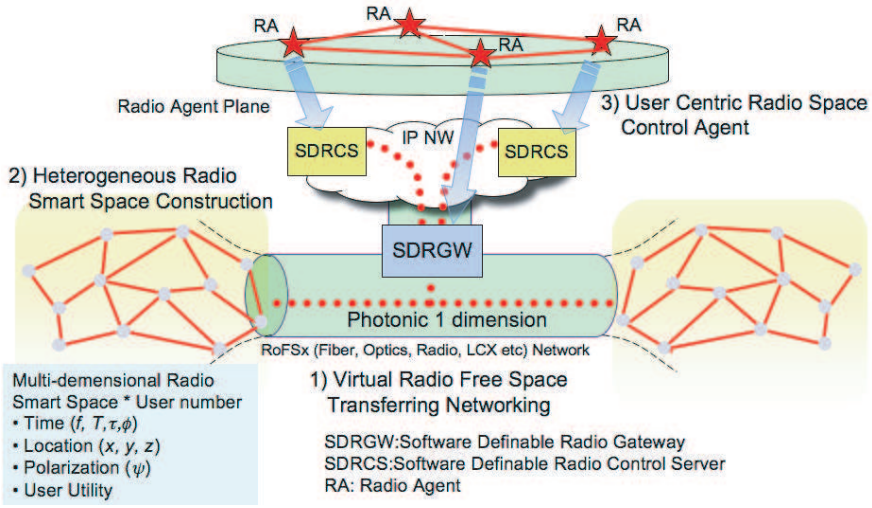

Figure 8: Software Definable Radios.

5. CONCLUSIONS

We have described the concept and object of advanced DWDM RoFSO system development. We are developing RoFSO link equipments transferring more than 4 different wireless services with DWDM techniques, and we will conduct a long-term demonstrative measurement in the next phase. Furthermore, we have described the concept of SDRN and its availability for ubiquitous wireless.

ACKNOWLEDGMENT

This work is supported by a grant from the National Institute of Information and Communications Technology (NICT) of Japan.

REFERENCES

1. Komaki, S., "Microwave technologies for software radio networks," *Proceedings of APMC2003*, Vol. 3, No. FC7-1, 1780–1785, November 2003.
2. Tsukamoto, K., "Software definable radio networks for the ubiquitous networks," *XXXIIIth GA of URSI*, Vol. 1, 205, October 2005.
3. Komaki, S., et al., "Proposal of radio high-way networks for future multimedia-personal wireless communications," *IEEE ICPWC'94*, Vol. 1, No. 1, 204–208, August 1994.
4. Tsukamoto, K., K. Nakaduka, M. Kamei, T. Higashino, S. Komaki, K. Wakamori, Y. Aburakawa, T. Nakamura, K. Takahashi, T. Suzuki, K. Kazaura, K. Ohmae, M. Matsumoto, S. Kuwano, and H. Watanabe, "Development of DWDM radio on free space optic link system for ubiquitous wireless," *Technical Digest of AP-MWP 2007*, Vol. 1, No. 1, 1, April 2007.
5. Kazaura, K., et al., "Experimental performance evaluation of next generation FSO communication system," *AP-MWP 2006*, Vol. 1, 289–292, April 2006.
6. Takahashi, K., et al., "Development of radio on free space optics system for ubiquitous wireless services — (2) Basic design of optical system —," *Proc. of 2007 IEICE General Conf.*, C-14–6, 257, Japanese, March 2007.
7. Tajima, K., et al., "A consideration on handover delay for wireless service over IP networks using wireless LAN," *IEICE Tech. Report*, Vol. 105, No. 80, 7–12, Japanese, May 2005.
8. Hai, L. H., et al., "Performance improvement of radio-on-fiber ubiquitous antenna system using sub-carrier resource management," *Proc. of SPIE — Broadband Access Commun. Technols*, Vol. 6390, B1–B11, Oct. 2006.

Photonic Millimeter-wave Generation and Distribution System Applicable to the ALMA Radio Telescopes

H. Kiuchi[1], **T. Kawanishi**[2], **M. Yamada**[1], **T. Sakamoto**[2]
M. Tsuchiya[2], **J. Amagai**[2], **and M. Izutsu**[2]

[1]National Astronomical Observatory of Japan, Japan
[2]National Institute of Information and Communications Technology, Japan

Abstract— This paper discusses the possibility of applying the high extinction ratio optical modulator to a high stability and high frequency (over 100 GHz) optical reference signal generator. High-frequency reference signals are generated by a highly stable optical two-tone generator. ALMA (Atacama Large Millimeter/sub-millimeter Array) is a high-frequency radio interferometer array currently under development, and each of the ALMA antennas has a 10-band receiver, and its highest receiving frequency reaches 950 GHz. To receive such high frequencies, higher reference frequency is required for the 1st local (as much as over 100 GHz), and stability to maintain the signal coherence is also required. To address these issues, we have developed a new method to generate and transmit a reference signal in the form of frequency difference between two coherent light waves. One method to generate two optical signals is producing them from a pair of laser sources using optical phase lock loop for feed back control, however, optical phase lock loop has a stability problem in its operation. A good alternative method to the optical phase lock scheme is the $LiNbO_3$ Mach-Zehnder optical intensity modulator which is capable of generating two highly stable optical signals (upper sideband and lower sideband components) by applying a sinusoidal microwave signal to an input laser signal. The two optical signals require phase stability better than 10^{-13} in the Allan standard deviation, vibration robustness and polarization maintaining capability. The signal coherence loss estimated from the phase stability of the two optical signals generated by the Mach-Zehnder modulator shows that the modulator has the ability to generate highly stable optical signals.

1. INTRODUCTION

This paper discusses the possibility of applying the high extinction ratio Mach-Zehnder $LiNbO_3$ optical modulator to a high stability and high frequency (over 100 GHz) optical reference signal generator for Astronomical Radio Interferometer: ALMA (Atacama Large Millimeter/sub-millimeter Array). Current optical two-tone generators of the ALMA baseline plan are based on an optical phase lock schemes. In the high-extinction ratio lithium niobate ($LiNbO_3$) Mach-Zehnder intensity modulator, the optical frequency difference between two optical signals is exactly twice (or four times) the modulation frequency. Compared to the optical phase lock scheme, the Mach-Zehnder modulator has significant advantages in terms of robustness to mechanical vibration and acoustic noise, stability (free from the influence of the input laser line-width), and capability of maintaining polarization state of the input laser.

2. TWO OPERATION MODES OF THE MACH-ZEHNDER MODULATOR

In the Mach-Zehnder structure, the output spectrum depends on the DC bias voltage applied to the electrodes (Fig. 1). The Mach-Zehnder modulator has two operation modes: null-bias point operation mode and full-bias point operation mode.

When the bias of the Mach-Zehnder modulator is set to a minimum transmission point (null-bias point), the first-order upper side band (USB) and lower side band (LSB) components are strengthened, and the carrier is suppressed (Fig. 2). The frequency difference between the two spectral components is twice the modulation sinusoidal signal frequency. However, as the modulation frequency is limited by the frequency response of the modulator, the frequency upper limit of the two optical signals can not be higher than 100 GHz in the null-bias point operation mode.

On the other hand, when the bias is set to a maximum transmission point (full-bias point), the optical frequency of even-order (zero- and second-order) components is remained (Fig. 3 left side). The frequency difference between the zero-order and second-order components is $2fm$ (fm is the modulation frequency of the RF signal applied to the modulator). When $4fm > 50$ GHz, the frequency difference is large enough, and thus the zero-order component can be eliminated with a conventional optical filter (Fig. 3 right side). Eliminating the zero-order component (carrier), the

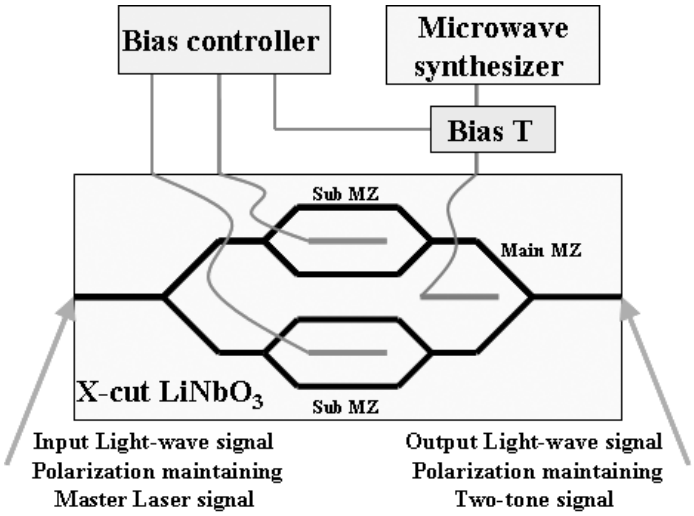

Figure 1: Simplified structure of an optical modulator with two arms and electrodes. Optical phase of each arm is controlled by applying DC bias to the electrodes. Amplitude imbalance due to fabrication error is compensated with sub-Mach-Zehnder trimmers. When two lightwaves are in phase, the output optical signals are strengthened each other. On the other hand, when the phases of the input lightwaves are shifted, the phase-shifted lightwaves are radiated away as higher-order waves, and do not reach the optical waveguide. This is the main feature of the Mach-Zehnder modulator.

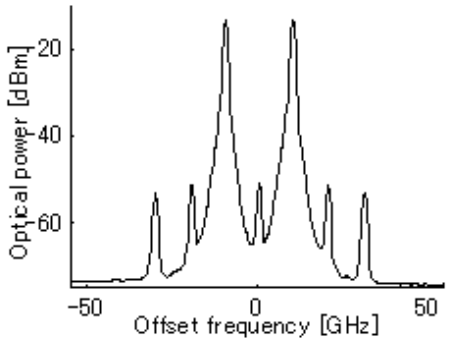

Figure 2: Null-bias point operation.

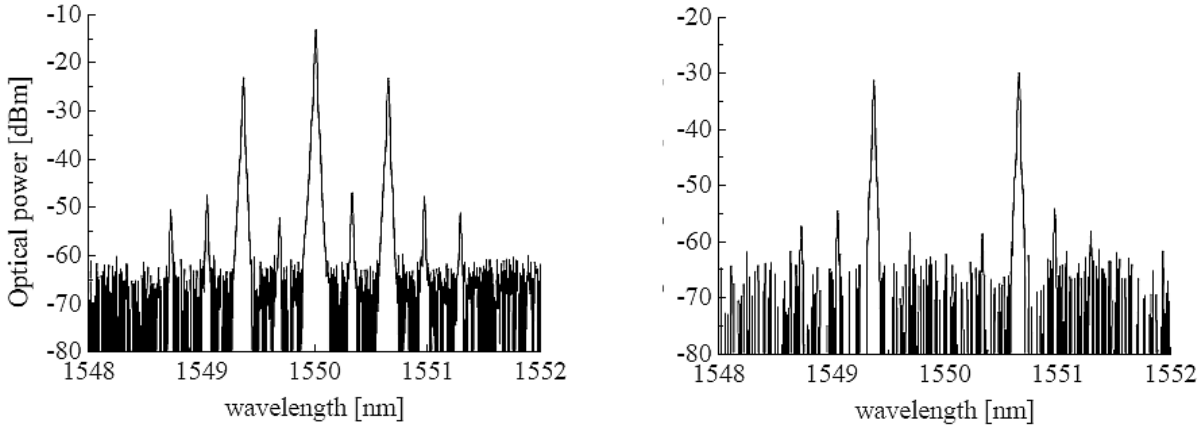

Figure 3: Full-bias point operation. Even-order components is remained (left chart). Eliminating the zero-order component (right chart).

remaining is a two-tone optical spectrum whose frequency is four times the modulation frequency. The optical signal filtered by the optical filter is amplified by an optical amplifier.

3. PHASE NOISE

The behavior of phase noise can be analyzed by the Allan standard deviation. Fig. 4 shows the phase stability of the Mach-Zehnder modulator measured using the Allan standard deviation. The stability is independent of the input laser line-width. Input lasers applied in this experiment are a DFB-laser (10 MHz line-width) and a fiber-laser (1 kHz line-width).

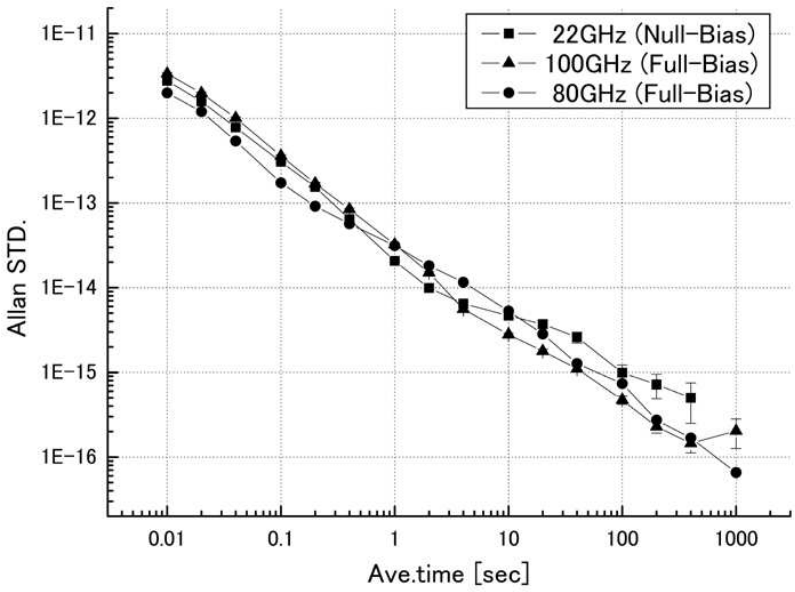

Figure 4: Measured phase stabilities of the Mach-Zehnder modulator, the first-order 22 GHz signal and the second-order 100 GHz signal.

Table 1: Estimated coherence loss.

ALMA receivers	Highest Local freq. in GHz	Mult. numb.	White PM Time independent coherence loss in %	Operation Mode
Band 1	33	1	0.00	Null-Bias
Band 2	94	1	0.01	
Band 3	108	1	0.01	
Band 4	151	2	0.03	
Band 5	199	2	0.05	
Band 6	263	3	0.12	Full-Bias
Band 7	365	3	0.24	
Band 8	488	5	0.71	
Band 9	708	6	1.78	
Band 10	938	9	4.69	

4. ASTRONOMICAL APPLICATION

The region from 27 GHz to 122 GHz is used for operational frequency for 10-band receivers. The two-tone generator requires polarization maintaining capability as well as mechanical vibration and acoustic noise robustness to avert the impact of the polarization effect on the photo-mixer and that of the polarization mode dispersion (PMD) on the transmission fiber. According to the requirements of ALMA, the short time stability of white phase modulation noise is $\sigma_y(\tau = 1) = 9.2 \times 10^{-14}$ with $\sigma_y(\tau = 1) = 1.56 \times 10^{-16}$ (flicker phase modulation noise) in the long-time period.

The measured stability of the null-bias point operation mode is 2.4×10^{-14} (white phase modulation noise) with 1.3×10^{-14} (white frequency modulation noise) at $\tau = 1$ sec, while the stability of the full-bias point operation mode is 3×10^{-14} (white phase modulation noise). The coherence loss is shown in Table 1.

5. CONCLUSION

Based on our experiment results, we propose a new high carrier suppression optical double-sideband intensity modulation technique using the integrated $LiNbO_3$ Mach-Zehnder modulator which is capable of compensating the imbalance of the Mach-Zehnder arms with a pair of active trimmers (null-bias operation mode). The full-bias point operation mode introduced in this paper is also a novel modulation technique for the second-order harmonic generation. The Mach-Zehnder modulator can generate two coherent light waves with frequency difference equivalent to four times the modulation frequency. Photonic local signals of 120 GHz can also be generated using this technique. The phase stability over 100 GHz could not be measured due to the reduction of the multiplier power, however, estimated phase stability and coherence loss indicate that this method is applicable to the ALMA and VLBI (very long baseline interferometer) experiments.

The two spectral components of the two optical signals generated with this technique are phase-locked without using any complicated feedback control. All of the measurements were carried out on a table (without vibration isolation) in a normally air-conditioned room without acoustic noise isolation. In short, all of the measurements were performed under normal environment. Temperature change and mechanical vibrations may have affected the output lightwaves to some degree, however there was no chaotic phenomenon such as mode hopping or mode competition during the experiments. Based on these results, we concluded that the proposed techniques will be useful to construct a robust, low-cost and simple setup for the photonic local signals.

ACKNOWLEDGMENT

The authors appreciate the help received from the Sumitomo-Osaka Cement Inc. and the NGK Insulators Inc. in establishing this modulator system.

REFERENCES

1. Kawanishi, T., T. Sakamoto, and M. Izutsu, "High-speed control of lightwave amplitude, phase, and frequency by use of electrooptic effect," *IEEE Journal of Selected Topics in Quantum Electronics*, Vol. 13, No. 1, 2007.
2. Kiuchi, H., T. Kawanishi, M. Yamada, T. Sakamoto, M. Tsuchiya, J. Amagai, and M. Izutsu, "High extinction ratio Mach-Zehnder modulator applied to a highly stable optical signal generator," *IEEE Trans. Microwave Theory and Techniques*, Vol. 55, No. 9, 1964–1972, 2007.

Microwave Dielectric Spectroscopy of Moist Soils in the Problem of Radar and Radiometric Remote Sensing of the Land

V. L. Mironov
Kirensky Institute of Physics SB RAS, Russia

Abstract— There was carried out analysis of dielectric spectroscopic models regarding moist soils, with the soil water dielectric relaxation parameters being employed as a function of soil mineralogy and temperature. Some efficient applications of those models to the problems of radar and radio thermal remote sensing of land surface were discussed as well.

1. INTRODUCTION

In aerospace radar and radiometric remote sensing of soils and vegetation cover, a dielectric model of moist soils is considered to be a most important block of data processing algorithms. For the radio sounding of soil moisture, biomass, thawed or frozen state of the land, and classification of soils by mineral and granulometric contents, the relationships between these geophysical characteristics and the moist soil dielectric constant represent a critical basis of physical origin [1, 2]. Such dielectric models must include the dependence on temperature, mineral contents parameters, volumetric or gravimetric moisture, and frequency.

For developing the data processing algorithms in radio sounding from space, the semiempirical mixing dielectric model (SMDM) proposed in [3] is most widely employed, so that it has become a kind of classical model. In this model, there are used dielectric spectra and spectral parameters of the Debye origin, which concern the water out of soil. While the dielectric spectrum of soil water, which is bound on the surface of solid soil particles, mineral or organic is ignored. Hence, the parameters of a bound water spectrum can not be involved in predicting the dielectric spectra of moist soils. Instead, in the SMDM, the impact of the mineral and granulometric composition of soil, which completely determines the dielectric spectrum of bound soil moisture, is taken into account only empirically, through modifying the dependence of dielectric constant on the content of moisture. In particular, for this reason, the SMDM can not be applied to frozen moist soils, as their dielectric frequency dispersion is completely induced by the bound (unfrozen) soil moisture.

2. DIELECTRIC SPECTROSCOPY OF MOIST SOILS

Spectroscopy of moist soils in the microwave frequency band underwent further development in the works of the author and his coauthors [4–18]. In works [4, 5], there were created the methodical basis for dielectric spectroscopy of moist soils, in which the Debye spectroscopic parameters were employed for both the bound and unbound soil water, and techniques for deriving these physical quantities from dielectric measurements were proposed [4, 7]. The model suggested in [4, 5] was named the generalized refractive mixing dielectric mode (GRMDM).

In this presentation, an analytical review is given as to the results obtained in this area. Specifically, there was considered the dependence of dielectric spectroscopic parameters pertaining to moist soils on the granulometric composition of solid fraction and the fraction of organic matter in soil [7–11]. The study was conducted on the basis of data set measured for a conglomerate of soils collected in the chernozem area in the European part of Russia, in some steppe, forest, and forest-tundra territories in Siberia, as well as in Kansas and Mississippi states (USA). As a result of that study, a dielectric model was developed, in which the temperature, clay and humus content, volumetric moisture, and electromagnetic field frequency are the only input parameters allowing to make predictions for dielectric spectra of moist soils in the microwave frequency band [12–14]. This model, named the mineralogy based soil dielectric model (MBSDM), was shown to be as simple in usage as the SMDM is, ensuring dielectric predictions with less error, then classical dielectric model of [3], over the significantly extended range of granulometric and mineralogical parameters.

In the frame of the GRMDM, the temperature dependences of spectroscopic parameters were studied on the basis of the bentonite clay [15] and some types of arctic soils in Alaska [16]. In addition, there was created a physically appropriate model of dielectric frequency dispersion in the moist frozen soils, accounting for the contribution of both bound soil water and transitional bound water in soil. Moreover, for the first time, the processes of converting liquid soil water into

bound soil water of transitional type was observed, and the dependences of dielectric spectroscopic parameters with regard to transitional bound water were studied, describing gradual transition of its phase state to that of the ice.

Using the GRMDM for the soils including water solution, there was carried out analysis to study how spectroscopic parameters of bound water containing ions depend on the temperature, with frozen soils being spanned. A technique was also proposed to make estimations of dielectric spectra for salt solution in the unbound soil water, which ensured dielectric predictions in the case of saline moist soils [17, 18].

3. DIELECTRIC SPECTROSCOPIC MODEL APPLICATIONS

With the use of the GRMDM, the impact of soil humus on the retrieved values of soil moisture was distinctly taken into account when processing the radiometric remote sensing data [19]. There was also noticeably decreased the error of prediction for the diurnal cycle of bare soil radiobrightness [20]. This spectroscopic model was found to be an effective mean to make prediction of the radiobrightness, radar backscatter and its polarization pattern, as well as to develop a physical basis for subsurface radar sounding, in the condition of freezing or thawing of the active permafrost layer [21–25].

4. CONCLUSIONS

Henceforth, the methodology suggested for microwave dielectric spectroscopy will ensure dielectric databases to be developed for the moist top-soil cover. A principle difference of such databases is that they will be using spectroscopic parameters as a primary element, which ensure taking into account the mineral and organic composition of soils, as well as the seasonal weather variations for a concrete physiographic territory. With the use of such dielectric databases, the reliability of data processing algorithms is expected to be substantially increased in regard with the aerospace radar and radiometric remote sensing of the Earth.

ACKNOWLEDGMENT

The work was supported by the Siberian Branch of the Russian Academy of Sciences, Project 70, and by the RFBR grant No. 05-02-97712-r-yenisei-a.

REFERENCES

1. Ulaby, F. T., R. K. Moor, and A. K. Fung, *Microwave Remote Sensing, Active and Passive*, Vol. 3, Artech House, Dedham, MA, 1986.
2. Komarov, S. A. and V. L. Mironov, *Microwave Remote Sensing of Soils*, Nauka, Novosibirsk, 2000 (in Russian).
3. Dobson, M. C., F. T. Ulaby, M. T. Hallikainen, and M. A. El-Rayes, "Microwave dielectric behavior of wet soil-part II: Dielectric mixing models," *IEEE Trans. Geosci. Remote Sensing*, Vol. 23, No. 1, 35–46, 1985.
4. Mironov, V. L., M. C. Dobson, V. H. Kaupp, S. A. Komarov, and V. N. Kleshchenko, "Generalized refractive mixing dielectric model for moist soils," *Proc. IGARSS*, Vol. 6, 35563558, Toronto, Canada, 2002.
5. Mironov, V. L., M. C. Dobson, V. H. Kaupp, S. A. Komarov, and V. N. Kleshchenko, "Generalized refractive mixing dielectric model for moist soils," *IEEE Trans. Geosci. Remote Sensing*, Vol. 42, No. 4, 773–785, 2004.
6. Mironov, V. L., P. P. Bobrov, L. G. Kosolapova, V. N. Mandrygina, and S. V. Fomin, "Data processing technique for deriving soil water spectroscopic parameters in microwave," *Proc. IGARSS*, Vol. 6, 2957–2961, Denver, USA, 2006.
7. Mironov, V. L., L. G. Kosolapova, and S. V. Fomin, "A method for developing a moist-soil dielectric database in the microwave band," *Radiophysics and Quantum Electronics*, Vol. 50, No. 4, 339–349, USA, 2007.
8. Mironov, V. L. and P. P. Bobrov, "Soil dielectric spectroscopic parameters dependence on humus content," *Proc. IGARSS'03*, Vol. 2, 1106–1108, Toulouse, France, 2003.
9. Mironov, V. L., P. P. Bobrov, and V. N. Mandrygina, "Bound water spectroscopy for the soils with varying mineralogy," *Proc. IGARSS*, Vol. 5, 3478–3480, Anchorage, USA, 2004.
10. Mironov, V. L., "Spectral dielectric properties of moist soils in the microwave band," *Proc. IGARSS'04*, Vol. 5, 3474–3477, Anchorage, USA, 2004.

11. Mironov, V. L., P. P. Bobrov, A. P. Bobrov, V. N. Mandrygina, and V. D. Stasuk, "Microwave dielectric spectroscopy of moist soils for a forest-tundra region," *Proc. IGARSS'05*, Vol. 7, 4485–4488, Seoul, Korea, 2005.
12. Mironov, V. L., L. G. Kosolapova, and S. V. Fomin, "Validation of the soil dielectric spectroscopic models with input parameters based on soil composition," *Proc. IGARSS'07*, Barcelona, Spane, July 22–27, 2007.
13. Mironov, V. L., L. G. Kosolapova, and S. V. Fomin, "Physically and mineralogically based spectroscopic dielectric model for moist soils," *IEEE Trans. Geosci. Remote Sensing*, (submitted paper), 2007.
14. Bobrov, P. P., V. L. Mironov, O. A. Ivchenko, and V. N. Krasnoukhova, "Microwave spectroscopic dielectric model of moist soils using physical and hydrological characteristics as input parameters," *Proc. IGARSS'07*, Barcelona, Spane, July 22–27, 2007.
15. Mironov, V. L., V. H. Kaupp, S. A. Komarov, and V. N. Kleshchenko, "Frozen Soil dielectric model using unfrozen water spectroscopic parameters," *Proc. IGARSS*, Vol. 7, 4172–4174, Toulouse, France, 2003.
16. Mironov, V. L., R. D. Roo, and I. V. Savin, "Dielectric spectroscopic model for tussock and shrub tundra soils," *Proc. IGARSS'07*, Barcelona, Spain, July 22–27, 2007.
17. Mironov, V. L., S. A. Komarov, and V. N. Kleshchenko, "Microwave dielectric spectroscopy for bound water in saline soil," *Proc. IGARSS*, Vol. 5, 3196–3199, Seoul, Korea, 2005.
18. Mironov, V. L., S. A. Komarov, and V. N. Kleshchenko, "Dielectric model for saline moist soils in the microwave band," *Proc. of the All Russian Conference on Physics of Radio Waves*, Vol. 3, 17–20, Tomsk, 2002 (in Russian).
19. Mironov, V. L., P. P. Bobrov, O. A. Ivchenko, S. V. Krivaltsevitsh, and A. S. Jaschenko, "Dynamic radiobrightness for drying soils as a function of humus content," *Proc. IGARSS'05*, Vol. 2, 1127–1130, Seoul, Korea, 2005.
20. Mironov, V. L., V. V. Scherbinin, A. S. Komarov, and A. A. Bogdanov, "Measurement and simulation of diurnal radiobrightness variations for a bare unfrozen soil," *Proc. IGARSS'07*, Barcelona, Spane, July 22–27, 2007.
21. Mironov, V. L., P. P. Bobrov, P. V. Zhirov, S. V. Krivaltsevitsh, A. S. Jaschenko, and R. D. de Roo, "Radiobrightness dinamics of freezing/thawing processes for different soil," *Proc. IGARSS'06*, Vol. 6, 3015–3018, Denver, USA, 2006.
22. Komarov, A., V. L. Mironov, and S. Li, "SAR polarimetry for permafrost active layer freeze/thaw processes," *Proc. IGARSS'02*, Vol. 5, 2654–2656, Toronto, Canada, 2002.
23. Mironov, V. L., S. A. Komarov, S. Li, V. E. Romanovsky, T. V. Baikalova, and V. V. Skoroglyadov, "Freeze-thaw processes radar remote sensing: Modeling and image processing," *Proc. IGARSS'05*, Vol. 1, 608–611, Seoul, Korea, 2005.
24. Mironov, V. L., S. A. Komarov, T. V. Baikalova, and V. V. Skoroglyadov, "Influence of snow and plant covers on the seasonal radar remote sensing signal variations," *Proc. of IGARSS*, Vol. 6, 2705–2707, Denver, USA, 2006.
25. Komarov, S. A., V. L. Mironov, and K. V. Muzalevsky, "GPR signal simulations in the course of freeze/thaw process for a permafrost area," *Proc. IGARSS'05*, Vol. 7, 4600–4603, Seoul, Korea, 2005.

Estimation of Relative Permittivity of Shallow Soils by Using the Ground Penetrating Radar Response from Different Buried Targets

L. Capineri[1], **D. J. Daniels**[2], **P. Falorni**[1], **O. L. Lopera**[3], **and C. G. Windsor**[4]

[1]Dipartimento Elettronica e Telecomunicazioni, Università di Firenze, Italy
[2]ERA Technology, United Kingdom
[3]Royal Military School, Belgium
[4]116 East Hagbourne, OX11 9LD, United Kingdom

Abstract— Combined ground penetrating radar and metal detector equipment are now available (e.g., MINEHOUND, ERA Technology-Vallon GmbH) for landmine detection. The performance of the radar detector is influenced by the electromagnetic characteristics of the soil. In this paper we present an experimental procedure that uses the same equipment for the detection and calibration by means of signal processing procedures for the estimation of the relative permittivity of the soil. The experimental uncertainties of this method are also reported.

1. INTRODUCTION

Ground penetrating radar (GPR) for landmine detection has reached the stage where portable equipment for field operations is commercially available. Dual sensor systems in which high performance metal detectors (MD) are combined with GPR have been extensively trialled [1–6].

The operating conditions for the GPR depend on the electromagnetic characteristics (magnetic susceptibility μ_R, conductivity σ and relative permittivity ε_R) of the soil. It has been shown that the relative permittivity changes in space and also in time [7, 8]. These variations are the main reasons why the GPR systems need either manual or auto-calibration before their use as a mine detector. Where systems provide an indication of burial depth of the target it is important that the propagation velocity is known for the soil under investigation and this paper addresses this issue.

The paper describes an assessment of methods that can be used by supervisory operators in the field for the estimation of ε_R of soil at shallow depth. This aim is also currently under discussion by the CEN WS7 [9]. The estimation of ε_R is obtained indirectly by the propagation velocity $v = c/\sqrt{\varepsilon_R}$, where c is the speed of light in vacuum.

Experiments were carried out at the test site of ERA Technology using the MINEHOUND$^{(TM)}$ dual sensor system jointly developed with Vallon GmbH for the MD unit. Different metal targets were buried at different depths in a soil defined as ballast.

2. EXPERIMENTAL MEASUREMENTS

2.1. Test Site

The test site at ERA Technology in Leatherhead comprises area 5 metres by 10 metres of depth 1 m of a mixture of pea gravel and sand to form a ballast soil. The nominal value of ε_R of this soil was estimated to be 5. All experiments were conducted in two consecutive days. During the second daythe soil moisture was higher due to a rainfall in the night.

2.2. MINEHOUND Radar System Parameters

ITEM	VALUE		ITEM	VALUE
Internal pulse duration	240 ps at −6 dB, unipolar		Receiver time range	19.2 ns
Internal pulse amplitude	15 V peak		Receiver sampling interval	37.5 ps
Pulse repetition frequencies	1 MHz		Output scan rate	61 Hz
Bandwidth of operation	from 250 MHz to 2.5 GHz		Sweep speed	$<1.5\,\mathrm{ms}^{-1}$
EIRP[1]	< -41 dBm/MHz		Output	Audio/Visual
Radar sampling	512 samples per scan		**Temperature**	**from −32°C to 65°C**

[1]Equivalent Isotropically Radiated Power

2.3. Targets

A variety of targets can be used to enable the measurement of relative dielectric constant and these can be either metallic or dielectric. The following metallic targets were selected:

- A metal pipe 80 cm long, external diameter of 20 mm acquired during first day.
- A metal sphere, 70 mm diameter acquired during second day.

All these targets are low cost and are readily available in most countries, particularly for those in the Third World. Metal spheres can be found also as toy balls.

2.4. Radar Target Response

Material for all metal targets should be highly conductive metal (e.g., copper, iron, and chromium plated steel). Hollow pipes or spheres with metal thickness of at least 1 mm are also acceptable. The radar response depends on the target geometry, antenna configuration, frequency and soil properties. To compare the different targets response we report their Radar Cross Sections (RCS) expressions [10]. The calculations of the RCS for $\varepsilon_R = 1$ (air) and $\varepsilon_R = 5$ (soil) according to the dimensions of our targets at radar central frequency $f_C = 1\,\mathrm{GHz}$ are reported in Table 1. The calculated RCSs are valid in the far field and diffraction effects from edges are neglected.

Table 1: Radar Cross-Section values of used targets.

Target	**RCS** ($\varepsilon_R = 1$, $\lambda = c/f_C = 0.3\,\mathbf{m}$)	**RCS** ($\varepsilon_R = 5$, $\lambda = c/f_C = 0.13\,\mathbf{m}$)	**Parameters**
1	0.1340	0.3	a radius = 0.01 m L length = 0.8 m ϑ angle broadside = 0°
2	0.0038	0.0038	a radius = 0.035 m
3	0.0707	0.3534	A plate area = 0.0225 m^2

The pipe target, with the dimensions specified above, has the highest RCS with respect to the other targets. The flat plate has a high RCS but it strongly depends on λ and its radar response is very dependent on the actual incident angle of the transmitted beam: this is why we chose not to use it. When using linearly polarized dipole antennas, metallic pipes and low impedance dielectric pipes are best detected with the long axis of the dipole antennas oriented parallel to the long axis of the pipes and this should be specified in the measurement procedure. A sphere response is less dependent from radar antenna polarization and view angle.

For the aim of testing, it should be noted that the electrical properties of the soil will be changed by excavation and care is needed to replace and compact the soil when emplacing targets. A soil of the type used readily compacts after excavation and is thus ideal because its electrical characteristics soon revert to normal.

2.5. Measurement Technique

The targets were buried with the following depths of cover; 2 cm, 5 cm, 10 cm and 15 cm. In practice an uncertainty of few millimetres will be encountered at these nominal depths. To help the operator, the scanning was carried out with the radar sweeping in contact with the surface of a rectangular thin plastic layer (2 mm thick and $\varepsilon_R = 3$) placed over the soil, covering the area where the target was buried. This layer is thin enough so as to cause minimal effect on the measurements.

Longitudinal and transversal single scan were repeated along the plastic layer's orthogonal axis for both directions (left to right and right to left).

3. ELECTROMAGNETIC MODEL OF THE EXPERIMENT

The estimation of time of flight (TOF) has been done according to an electromagnetic model of the experiment. In a first approximation we can assume the radar operates in a monostatic mode at height h from the surface of the soil and the target as a point-like reflector. The ray path descriptions for the time-of flight calculations are shown in Figure 1. As the soil relative permittivity is unknown, the point y_B at the boundary between air and soil has to be estimated. In order to have an explicit solution for y_B we can consider that the limit position of the incident

point is Y_1 when $\varepsilon_R = 1$ (soil=air) and is given by:

$$Y_1 = Y_S * Z_0/(Z_0 + h) \tag{1}$$

According to Snell law the approximate value of y_B assuming for a soil ε_R greater or equal to 1 is given by:

$$y_B = Y_1/\sqrt{\varepsilon_R} \tag{2}$$

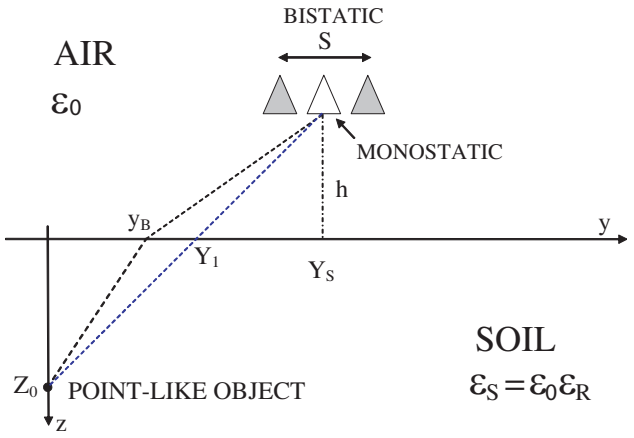

Figure 1: Snell approximation for incident beam at the interface between air-soil layers for the monostatic case.

Assuming that the previous approximations are valid, we can derive the explicit expression of minimum time-of-flight for the case of bistatic antennae, where S is the separation distance (see Figure 1). The minimum TOF is obtained when the radar is centered over the target ($Y_S = 0$).

$$TOF_{1\,\min} = \frac{2}{c}\sqrt{\left(\frac{S}{2} - \frac{S}{2}\frac{Z_0}{Z_0+h}\frac{1}{\sqrt{\varepsilon_R}}\right)^2 + h^2} + \frac{2}{c}\sqrt{\varepsilon_R}\sqrt{\left(\frac{S}{2}\frac{Z_0}{Z_0+h}\frac{1}{\sqrt{\varepsilon_R}}\right)^2 + Z_0^2} \tag{3}$$

The time-of-flight corresponding to the air-soil interface is:

$$TOF_2 = \frac{2}{c}\sqrt{\left(\frac{S}{2}\right)^2 + h^2} \tag{4}$$

The difference between $TOF_{1\,\min}$ and TOF_2 can be experimentally measured and it corresponds to a non-linear expression of the relative permittivity (the unknown parameter). The parameter h is not constant in real experiments besides an operator can be trained to minimize its variability. Moreover in real operating conditions the values of S, Z_0 and h are comparable and simplification of the expression is impossible. In Table 2 we calculated the time difference $\Delta T(h) = TOF_2 - TOF_{1\,\min}$ for $h = 2\,\text{cm}$ and $h = 10\,\text{cm}$ by using Equations (3) and (4). The difference $\Delta T(2\,\text{cm}) - \Delta T(10\,\text{cm})$ is evaluated and shown for two different values of ε_R. For this analysis we assumed the target depths used for the experiments.

Table 2: Variation of time-of-flight difference $\Delta T(2\,\text{cm}) - \Delta T(10\,\text{cm})$.

Soil relative permittivity ε_R	Target depth			
	$Z_0 = 2\,\text{cm}$	$Z_0 = 5\,\text{cm}$	$Z_0 = 10\,\text{cm}$	$Z_0 = 15\,\text{cm}$
5	20 ps	41 ps	50 ps	62 ps
3	26 ps	53 ps	70 ps	72 ps

The results of this analysis shows that the time of flight difference is always less than 100 ps and for some cases (see cells with grey background) is less than 50 ps. Therefore the influence of the antenna height cannot be neglected in the general case.

4. ESTIMATION OF SOIL RELATIVE PERMITTIVITY

The evaluation of the soil relative permittivity ε_R has been done by measuring the difference between $TOF_{1\,\min}$ and TOF_2 with the data for the metal pipe and for the metal sphere. For both we considered minimum $h = 2\,\text{cm}$ and maximum $h = 10\,\text{cm}$.

The minimum of the time difference was calculated by searching the maximum detection trace among the data set. Without an explicit solution for ε_R, we have applied a numerical estimation by using Matlab routines.

The target detector is based on the hypothesis that the signal reflected by the target is similar to the signal reflected by the air-ground interface. The similarity check is made by using the linearity property of the cross correlation operator, like in (5), where s_{BG} is the signal reflected by the air-ground interface, s_T the signal reflected by the target and s the signal under investigation.

$$s_{BG} \cdot s_T = s_{BG} \cdot [s - s_{BG}] = s \cdot s_{BG} - s_{BG} \cdot s_{BG} \tag{5}$$

The amplitude of the expression in formula (5) can be evaluated by using its envelope (Hilbert transform). The maximum value of the amplitude of the function in formula (5) is upper limited by the maximum value of the autocorrelation (energy) of the signal s_{BG}; this is because in GPR experiments the energy carried by the target is always smaller than the energy carried by the air-ground interface. Therefore, the detector operates normalising the cross correlation in formula (5) to the maximum value of the auto correlation of the signal s_{BG} to get a relative estimate, like in formula (6).

$$\frac{|hilbert\,(s \cdot s_{BG} - s_{BG} \cdot s_{BG})|}{\max\{s_{BG} \cdot s_{BG}\}} \tag{6}$$

A good estimator of $\Delta T(h)$ is the lag of the maximum value of the amplitude of the cross correlation between the air-ground reflection signal and the target reflection signal is given by:

$$\Delta T(h) = \arg\max\{|hilbert\,(s \cdot s_{BG} - s_{BG} \cdot s_{BG})|\} \tag{7}$$

5. RESULTS

The evaluation of the mean soil ε_R according to the propagation model for a bistatic antenna is within the standard deviation to the expected value of relative dielectric constant for the ballast of 5.

Table 3: Measured results.

Target	**Depth = 2 cm**		**Depth = 10 cm**	
	Measured value	**Standard Deviation**	**Measured value**	**Standard Deviation**
Pipe	4.81	1.7	4.34	0.4
Sphere	4.35	1.56	3.92	0.25

The larger standard deviation of the pipe was due to one corrupted measurement that is relative to the smaller depth (2 cm). Avoiding this value we calculated a Mean(ε_R) of 3.98 and standard deviation of 0.48.

6. CONCLUSIONS

There is a trend that suggests that the measurements of relative dielectric constant report higher values for shallower targets. Although these results are satisfactory, the authors are investigating other methods and targets as a means of improving the accuracy of the measurement procedure. We are also considering additional signal processing to the remove the direct coupling between the two antennas.

The main source of error in the method is given by the usage of the cross correlation operator that worsten the resolution of the inspected signals.

ACKNOWLEDGMENT

The authors wish to acknowledge Dr Yann Yvnec of Royal Military School for preparing the test bed and collecting experimental data.

REFERENCES

1. *Soil Properties & GPR Detection of Landmines. A Basis for Forecasting & Evaluation of GPR Performance*, Publication DRES CR2000-091, October 1, 1999.
2. Cross, G., D. Benson, J. D. Redman, A. P. Annan, and Y. Das, "GPR for anti-personnel landmine detection: results of experimental and theoretical studies," *SPIE: Detection and Remediation Technologies for Mines and Minelike Targets VIII (OR48)*, 21–25, Orlando, Florida, April, 2003.
3. Druyts, P., A. Merz, M. Peichl, and G. Triltzsch, "HOPE: raising the reliability of mine detection through an innovative a hand-held multi-sensor (MD, GPR, MWR) mine detector prototype with imaging capabilities," *Proceedings of PIERS 2003*, Singapore, January, 2003.
4. Ishikawa, J., M. Kiyota, and K. Furuta, "Evaluation of test results of GPR-based anti-personnel landmine detection systems mounted on robotic vehicles," *Proc. of the IARP International Workshop on Robotics and Mechanical Assistance in Humanitarian Demining (HUDEM2005)*, 39–44, 2005.
5. Rhebergen, J. B. and J. M. Ralston, "Test and evaluation protocols for GPR-based mine-detection systems: A proposal," *Detection and Remediation Technologies for Mines and Minelike Targets X, Proceedings of the SPIE*, Vol. 5794, 941–952, 2005.
6. Schoolderman, A. J. and J. H. J. Roosenboom, "Detection performance assessment of hand-held mine detection systems in a procurement process: test set-up for MDs and MD/GPRs," *Proceedings of SPIE*, Vol. 5794, 2005.
7. Francisca, F. M. and V. A. Rinaldi, "Complex dielectric permittivity of soil-organic mixtures 20 MHz–1.3 GHz," *Journal of Environmental Engineering*, ©ASCE, 347–357, April, 2003.
8. Hendrickx, J. M. H., B. Borchers, J. Woolslayer, L. W. Dekker, C. Ritsema, and S. Paton, "Spatial variability of dielectric properties in field soils," *Detection and Remediation Technologies for Mines and Minelike Targets VI, Proceedings of the SPIE*, Vol. 4394, 398–408, 2001.
9. "Final business plan for a CEN workshop on humanitarian mine action — test and evaluation — metal detectors — Part 2: soil characterisation for metal detector and ground penetrating radar performance," 2006.
10. Daniels, D. J., *Surface-penetrating Radar*, Institution of Electrical Engineers Radar Series, ERA Technology, ISBN 0-85296-862, No. 6, London, 1996.

An Example of Holographic Radar Using at Restoration Works of Historical Building

V. V. Razevig, S. I. Ivashov, A. P. Sheyko, I. A. Vasilyev, and A. V. Zhuravlev
Remote Sensing Laboratory, Bauman Moscow State Technical University
5, 2nd Baumanskaya str., Moscow 105005, Russia

Abstract— The former Senate building, Saint-Petersburg, Russia is being refitted for using it by the Constitutional court of Russian Federation. The team of Remote Sensing Laboratory was invited to participate in this work. The case is that the underfloor water heating system had been installed in the Senate building. The arrangement of pipes hasn't been precisely documented. Besides, there are power and communications cables as well as metal mesh under the concrete floor of the building. Workers were afraid of damaging pipes and cables during laying the parquet floor. Main purpose was to investigate the building floor and to define exact position of pipes and cables with the help of subsurface holographic radars developed by Remote Sensing Laboratory.

1. INTRODUCTION

The paper covers a possible use of holographic subsurface radars different from traditional impulse radars [1]. They are distinguished by the type of frequency spectrum. The impulse radar has continuous frequency spectrum while the holographic radar has discrete one. Impulse radars have larger penetration depths because they have variable amplification in the stroboscopic receiver. The signal reflected from deeper objects is amplified more than the signal from shallow objects. This is the main advantage of impulse radars. The holographic radar has the same amplification for all objects. In this case, the penetration depth depends on medium attenuation and its homogeneity at shallow depths. Shallow heterogeneities would shade deeper objects in recorded images.

At shallow depths, the holographic radar has a distinct advantage in resolution over the impulse radar because the radar frequency range can be easily adapted to the demands of a particular task. Another extremely important advantage of this holographic radar technology is the possibility to image, without reverberation, dielectric materials that lie above a metal surface [2]. Such materials cannot be effectively inspected with traditional time-domain impulse radar technology. Reverberation of pulses between the radar antenna and shallow metal objects obscures the actual location and shape of these objects which are seen as multiple reflections (often called ghosts or phantoms) of the transmitted impulse signal on a relatively uniform background [3].

Holographic radars could be easily adapted to the US Federal Communications Commission regulations and demands as the radar can use free frequency bands that don't interfere with other devices. Also, they are cheaper than impulse radars.

2. EXPERIMENTS

The former Senate building, Saint-Petersburg, Russia is being refitted for using it by the Constitutional court of Russian Federation. The building was built by the outstanding architect K. I. Rossi in 1829–1834 and has great value for Russian culture.

The team of Remote Sensing Laboratory was invited to participate in this work. The case is that the underfloor water heating system had been installed in the Senate building. In this system, warm water is circulated through pipes that are laid into the floor. The arrangement of pipes hasn't been precisely documented. Besides, there are electricity and communications cables as well as metal mesh under the concrete floor of the building. Workers were afraid of damaging pipes and cables during laying parquet. The main purpose was to investigate the building floor and to define the exact position of pipes and cables with the help of subsurface holographic radars developed by Remote Sensing Laboratory.

The following technology of installation of underfloor heating system is usually used. At first the metal mesh is laid on the subfloor. The spacing of mesh bars is 150 mm. Then the pipes are fastened to the mesh by the plastic clips. Various types of pipes are used including cross-linked polyethylene (PEX), multi-layer (a composite of PEX, aluminum and PEX) and polybutylene (PB): copper pipes aren't used now. The spacing of pipes is 300 mm. The pipes are being covered by the cement screed. The depth of the screed above the pipes is about 3 cm.

There was apprehension that the plastic pipes could be invisible on the background of metal mesh because of plastic has lower reflectivity towards environment (cement screed) then metal. It is worth noticing that an object contrast on holographic radar image depends of its reflectivity and phase shift that is a function of the distance to the object. For extended objects radiation polarization has also great influence on resulting contrast.

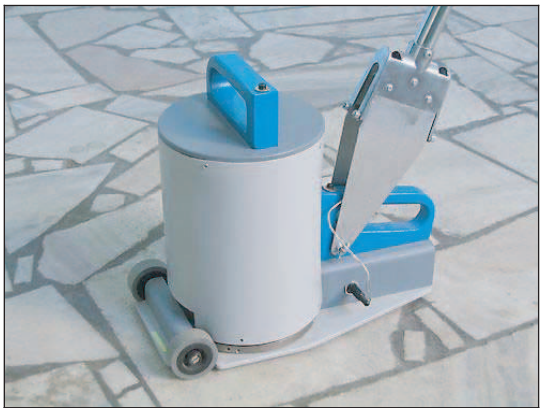

Figure 1: RASCAN-4/2000 radar head.

The work of floor inspection was carried out with the aid of the RASCAN-4/2000 holographic subsurface radar. The total area of the scanned surface was 16.7 sq. m. Overall time of work (disregarding the time for equipment installation) was about 5 hours. More than half of that time was consumed by scanning while the rest was spent in plotting the layout of pipes and cables on the floor.

While inspecting the floor a tangle of power and communications cables was found. This badly complicated the interpretation of the radar images.

The surveyed area was divided into fragments with the size of 1.7 m × 2.0 m. After recording a radar image of each fragment, the operator analyzed the image and drew the results by chalk on the floor. The position of heater tubes was presented by blue chalk, and red chalk was used for cables (Figure 2).

Figure 2: Position of heater tubes was marked by blue chalk, and red chalk was used for cables.

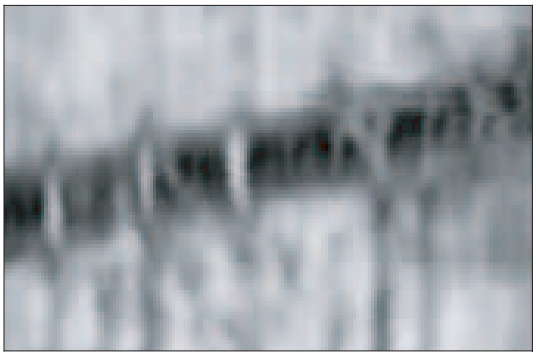

Figure 3: Part of radar image (the image dimensions are 1.70 m × 0.97 m).

As it was assumed before investigation, there was no possibility to distinguish plastic pipes and metal mesh in the parallel polarization radar images. At this polarization background reflections from metal bars suppress signals from plastic pipes that were tied to the bars and parallel to them. In the cross polarization radar images the plastic pipes were clearly visible. An interesting part of the radar image is shown on Figure 3. One can see how heater pipes bent over the cable. Figure 4 presents: a) cross polarization radar image at frequency 2.0 GHz; b) image "a" after numerical filtration (described below); c) plan of tubes (black lines) and communications (section lines). The observable horizontal lines in image "a" are the mesh grid (cross polarization channel). Vertical elements of the grid can be clearly seen in the parallel polarization channel (not shown). The overall dimensions of the radar image are 1.70 m × 8.04 m (170 × 804 pixels).

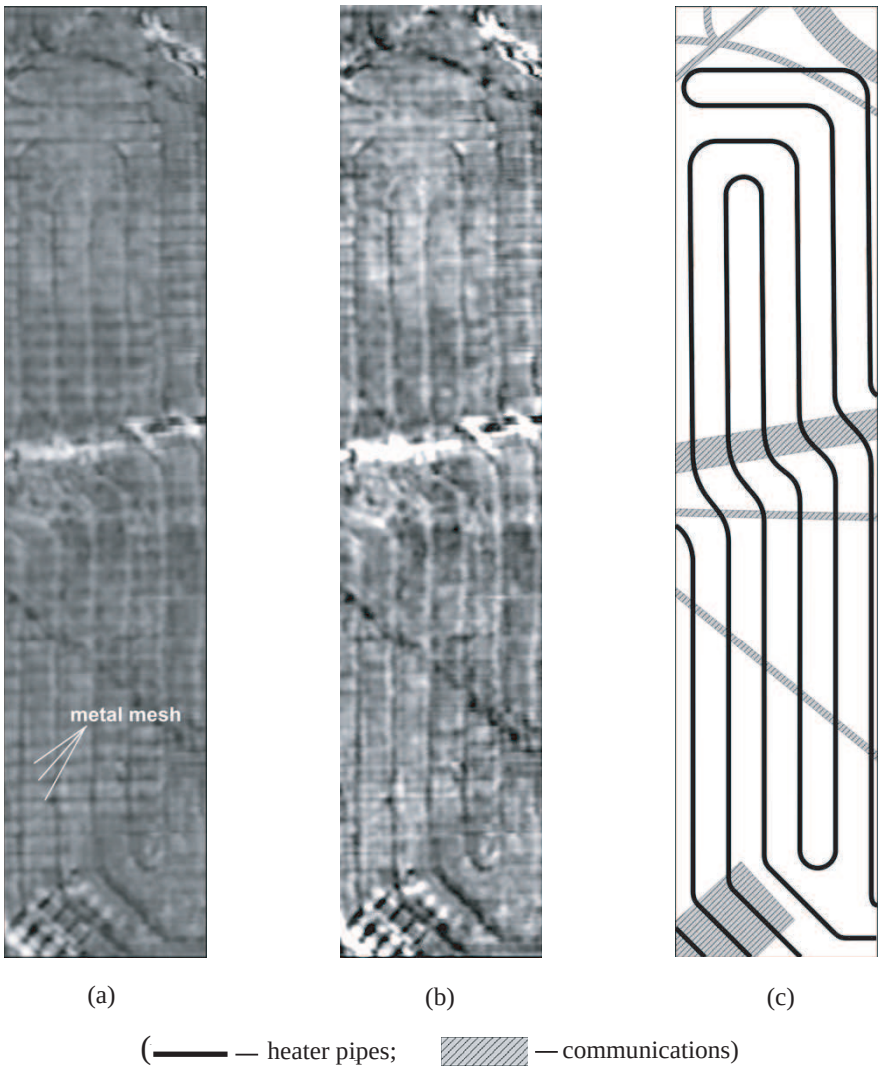

Figure 4: Interpretation of the radar image. (a) Raw radar image at frequency of 2.0 GHz (cross polarization); (b) Image "a" after numerical filtration; (c) Layout of pipes and communications. The overall dimensions of the radar image are 1.70 m × 8.04 m

3. NUMERICAL FILTRATION

To improve quality of radar images by suppressing of background reflections a numerical algorithm was suggested. The horizontal bars visible in Figure 4(a) could be suppressed by filtering in the frequency domain.

Let $f(x, y)$ be an input image, where $x = 0, 1, 2, \ldots, M-1$ and $y = 0, 1, 2, \ldots, N-1$ (in our case $M = 170$, $N = 804$). The 2-D discrete Fourier transform (DFT) $F(u, v)$ of this image is presented by the expression

$$F(u, v) = \sum_{x=0}^{M-1} \sum_{y=0}^{N-1} f(x, y) e^{-j2\pi(ux/M+vy/N)} \tag{1}$$

where $u = 0, 1, 2, \ldots, M-1$ and $v = 0, 1, 2, \ldots, N-1$.

The basic idea of filtering:

1) Apply the Fourier transform to the initial image.
2) Manipulate the spectrum by suppressing periodical mesh of 15 cm.
3) Take the inverse Fourier transform to obtain a "better" image with decreased reflections from metal mesh.

More in details [4]:

1) Multiply the image by $(-1)^{x+y}$ to prepare for a centered FT.
2) Compute $F(u, v)$, the DFT of (step 1).
3) Multiply $F(u, v)$ by a filter function $H(u, v)$.
4) Compute the inverse DFT of (step 3).
5) Obtain the real part of (step 4).
6) Multiply (step 5) by $(-1)^{x+y}$.

The bar spacing in the metal mesh is 15 cm. The radar image resulting from horizontal bars reflections can be approximated as

$$r(x, y) = \sin^4(\pi x/15 + \triangle s) \tag{2}$$

where $\triangle s$ is vertical distance from first bar to image border;
$x = 0, 1, 2, \ldots, 170 - 1$; $y = 0, 1, 2, \ldots, 804 - 1$.

The absolute value of centered DFT of $r(x, y)$ gets the largest extremum in the points with coordinates $(86, 349)$ and $(86, 457)$. So, a filter function should suppress the spectrum of input image at these points. Considering approximation of $r(x, y)$, a filter function has to go to zero not only at these points, but also in some intervals d stretched along axis v. A filter function can be expressed by

$$H(u, v) = \begin{cases} 0 - \text{at} \quad u = 86 \quad \text{and} \quad (v \in (349 - d, 349 + d) \quad \text{or} \quad v \in (457 - d, 457 + d)) \\ 1 - \text{at} \quad u \neq 86 \quad \text{or} \quad v \notin (349 - d, 349 + d) \quad \text{or} \quad v \notin (457 - d, 457 + d) \end{cases} \tag{3}$$

where $d = 10$ (found by fitting).

The result of filtering was obtained as follows: the inverse discrete Fourier transform of $F(u, v) \cdot H(u, v)$ was calculated, the obtained result was contrast enhanced and is shown in Figure 4(b).

4. CONCLUSIONS

The experiments have shown that the choice of correct polarization of antenna allows increasing contrast of objects under investigation in relation to background reflections that are in current case plastic pipes and metal mesh accordingly.

Comparison of the RASCAN-4/2000 radar with RASCAN-4/4000 that has approximately twofold operational frequency indicates that former radar has better efficiency and records higher quality microwave images at concrete floor investigation. The choice of radar operational frequency range has to take into account the property of surveying medium and frequency-dependent attenuation.

Among possible applications of holographic subsurface radars is the inspection of shallow buried objects in flat construction details. In this field, holographic radars have advantage over impulse radars in terms of resolution and quality of recorded images.

ACKNOWLEDGMENT

Support for this work was provided by the International Science and Technology Center, ISTC Project # 2541.

REFERENCES

1. Daniels, D. J., *Surface Penetrating Radar*, pub. by IEE, London, 1996.
2. Ivashov, S. I., I. A. Vasiliev, T. D. Bechtel, and C. Snapp, "Comparison between impulse and holographic subsurface radar for NDT of space vehicle structural materials," *PIERS Online*, Vol. 3, No. 5, 658–661, 2007.
3. Chapursky, V. V., S. I. Ivashov, V. V. Razevig, A. P. Sheyko, I. A. Vasilyev, V. V. Pomozov, N. P. Semeikin, and D. J. Desmond, *Proceedings of the 2002 IEEE Conference on Ultra Wideband Systems and Technologies, UWBST'2002*, 181–186, Baltimore, Maryland USA, May 2002.
4. Gonsales, R. C., R. E. Woods, and S. L. Eddins, *Digital Image Processing Using MATLAB*, Pearson Education Inc, publishing as Prentice Hall, 2004.

Device Fatigue-fracture Caused by High Current Density

Jianhua Xiao
Henan Polytechnic University, Jiaozuo 454000, Henan, China

Abstract— The electrons-migration under high current density can cause the distortion of molecules. The molecules deformation has two possible stable configurations when the electrons-migration is not symmetric in space. Geometrically, the non-symmetric electrons-migration behaves as a local rotation. When the electrons-migration is incompressible flow feature, the conductor may suffer fatigue effects, this is the normal case. However, when the electrons-migration is highly non-symmetric, only one stable configuration is possible, the conductor will produce fracture. The condition of fracture is described by an intrinsic parameter of critical local rotation angular, which is related with the yield stress of conductor material. This research gives the current density condition for the fatigue-fracture deformation. It shows that to increase the ability to against the fatigue-fracture deformation, one can increase the critical angular of material (that is to say, increase the yield stress of material while at the same time reduce the elastic modulus). For fractured conductors, the current density will accelerate the fatigue-fracture process in the fractured position of conductor as it forms a high charge density there when the reference charge density is determined by initial or boundary condition.

1. INTRODUCTION

For VLSI devices, the high current density may produce fatigue-fracture although the current density is well among the limit of device-design. For electrical current induced fatigue-fracture problem, most researches put their attention on the mechanical aspects of material or thermo-mechanical features [1]. However, fracture mechanics predictions made using macroscopic material properties and a fatigue crack threshold of zero are not inconsistent with experiments [2]. Even for medium voltage motors, the experiments showed that mechanical stress or deformation is not enough to produce motor fatigue [3]. Therefore, the problem of fatigue-fracture caused by high current density get some attention recently. When the VLSI devices are largely used in electronic products, this problem should be given enough attention.

Usually speaking, the electrons-migration caused by high current density is uniform and is in parallel with the direction of current. However, when the boundary condition of conductors is put into consideration, this may not be so simple. Generally, even the distribution of conductor wires are symmetric, the instant current density may not be symmetric for high frequency current. So, the non-symmetric motion of electrons-migration should be studied.

The paper will firstly show that the non-symmetric electrons-migration behaves as a local rotation. Secondly, it goes to discuss under what geometrical condition the fatigue-fracture will appear. This leads to detailed discussion about the non-symmetric electrons-migration. After that, the related current density equation to describe such a kind of fatigue-fracture is introduced. Based on this formulation, the paper finally discusses how to evaluate the critical condition for the development of fatigue-fracture in electronic device.

2. GEOMETRIC MECHANICS OF ELECTRONS-MIGRATION

In molecule scale, the position of protons center can be taken to establish a local geometry of molecule. As the current produced by free electrons flows over the molecule, the electrons confined by the molecule structure will produce migration relative to the protons. Such a kind of electrons-migration will produce the distortion of molecules. This distortion, named as molecule deformation (hear after), can be formulated by a geometric field.

For the normal molecule when the current is zero, its position is coordinated by a standard rectangular system (x^1, x^2, x^3). According to the structure theory of molecule, the confined electrons have their own quantum motion orbit. For a stable quantum state, the confined electrons form an electron cloud moving around the center of protons. Taking the position of molecule center $\vec{r}$ as reference, the position representation of electron cloud can be expressed as $\vec{\psi}_0(x)$, thus it behaves as a deterministic orbit round a fixed position:

$$\vec{\psi}_0(x,t) = \vec{r} + \exp\left(\tilde{i}\frac{E}{\hbar}t\right)\cdot \vec{g}_i^{\,0} dx^i \tag{1}$$

where, its quantum state function is $\sqrt{\det(g^0_{ij})} \cdot \exp(\tilde{i}\theta)$, $\tilde{i}$ is imaginary sign, meets Schrödinger Equation [4], E is the energy of electron cloud corresponding to a special orbit, θ is a phase item. $\vec{\psi}_0$ is the position of electron, dx^i is the coordinator variants for the electron relative to the center of molecule, $\vec{g}^0_i$ are the initial base vectors in molecule scale. For a molecule, once it is defined on initial state, the coordinator will be fixed. By this way, the coordinator is rest on the center of molecule. Such a coordinator is named as co-moving dragging coordinator system. The initial size of molecule is given gauge field:

$$g^0_{ij} = \vec{g}^0_i \cdot \vec{g}^0_j \tag{2}$$

when free electrons pass through the molecule, the confined electrons are pushed to migrate a little. Hence, the molecule will deforms. That is described by the variation of the position representation of electron cloud.

$$\vec{\psi}(x,t) = \vec{r} + \exp\left(\tilde{i}\frac{\tilde{E}}{\hbar}t\right) \cdot \vec{g}_i(x)dx^i \tag{3}$$

Now the current base vectors are $\vec{g}_i(x)$, the determine the current size of molecule. Its current gauge field is:

$$g_{ij} = \vec{g}_i \cdot \vec{g}_j \tag{4}$$

Its quantum state function $\sqrt{\det(g_{ij})} \cdot \exp(\tilde{i}\tilde{\theta})$ meets Schrödinger Equation [4].

Geometrically, such a kind of molecule deformation can be expressed by transformation tensor F^i_j defined as:

$$\vec{g}_i(x) = F^j_i(x)\vec{g}^0_j \tag{5}$$

As the position representation of electron cloud is continuous on the measure of probability, covariant differentiation can be introduced. Under this understanding, the molecule deformation can be expressed as the finite deformation of continuum.

By Equations (2), (4) and (5), it is found that:

$$g_{ij} = F^k_i F^l_j g^0_{kl} \tag{6}$$

For continuum, the deformation tensor F is related with macro displacement (distance variation) field U^i. For an idea unit material element, without the lose of generality, supposing the number of molecules in the unit material element is N, and the molecules are homogeneously distributed, then one will have:

$$\sum_N g^N_{ij} = \sum_N F^k_i F^l_j {g^0_{kl}}^N = F^k_i F^l_j \sum_N {g^0_{kl}}^N \tag{7}$$

where, upper index N represents the sequence number of molecules. For simplicity, the initial material is supposed as isotropic, and hence one has:

$$\sum_N {g^0_{kl}}^N = \delta_{ij} \tag{8}$$

Therefore, the current material will have a macro gauge field as:

$$G_{ij} = \sum_N {g_{ij}}^N = F^k_i F^l_j \sum_N {g^0_{kl}}^N = F^l_i F^l_j \tag{9}$$

For continuum, for a given displacement field U^i, the deformation tensor is defined as:

$$F^i_j = \frac{\partial U^i}{\partial x^j} + \delta^i_j \tag{10}$$

For idea simple elastic material, the corresponding stress field is:

$$\sigma^i_j = \lambda(F^l_l - 3)\delta^i_j + 2\mu(F^i_j - \delta^i_j) \tag{11}$$

Therefore, the molecule deformation is related with the macro deformation of material.

3. FEATURE OF DEFORMATION TENSOR

In geometrical field theory, for a continuous displacement field, the deformation tensor can de decomposes as the addition of a symmetric tensor and a orthogonal rotation tensor [5]:

$$F_j^i = S_j^i + \frac{1}{\cos\Theta} R_j^i \tag{12}$$

where,

$$S_j^i = \frac{1}{2}\left(U^i\big|_j + U^i\big|_j^T\right) - \left(\frac{1}{\cos\Theta} - 1\right)(L_k^i L_j^k + \delta_j^i) \tag{13}$$

$$\frac{1}{\cos\Theta} R_j^i = \delta_j^i + L_j^i \frac{\sin\Theta}{\cos\Theta} + \left(\frac{1}{\cos\Theta} - 1\right)(L_k^i L_j^k + \delta_j^i) \tag{14}$$

$$L_j^i = \frac{\cos\Theta}{2\sin\Theta}\left(U^i\big|_j - U^i\big|_j^T\right) \tag{15}$$

$$\begin{aligned}\cos^{-2}\Theta = {} & 1 + \frac{1}{4}\Big[(U^1\big|_2 - U^2\big|_1)^2 \\ & + \left(U^2\big|_3 - U^3\big|_2\right)^2 + \left(U^3\big|_1 - U^1\big|_3\right)^2\Big]\end{aligned} \tag{16}$$

Θ represents the local rotation angular, L_j^i represents the unit vector along the rotation axis, R_j^i is an unit orthogonal rotation tensor, Upper index T represents transpose. Note that when there is no displacement gradient, $F_j^i = \delta_j^i$.

Consider the mass conservation requirement of motion:

$$\frac{\partial m}{\partial t} + \nabla m \cdot \vec{V} + m\nabla \cdot \vec{V} = 0 \tag{17}$$

here, m represents the mass density, $\vec{V}$ is the velocity of electrons migration.

Geometrically, there is a relation equation between the initial and current configurations:

$$m\sqrt{g} = m_0\sqrt{g^0} \tag{18}$$

where, $g = \det(g_{ij})$, $g^0 = \det(g_{ij}^0)$. Hence, one has:

$$\frac{\partial}{\partial t}\left(\frac{1}{\sqrt{g}}\right) + \nabla\left(\frac{1}{\sqrt{g}}\right)\cdot\vec{V} + \left(\frac{1}{\sqrt{g}}\right)\nabla\cdot\vec{V} = 0 \tag{19}$$

It has two typical solutions. One solution is:

$$g_{ij} = \delta_{ij}, \qquad \nabla\cdot\vec{V} = 0 \tag{20}$$

It corresponds to the incompressible fluid model of electrons migration. It usually leads to thermal mechanics interpretation.

Another solution is:

$$g_{ij} = \frac{1}{\cos^2\Theta}\delta_{ij} \tag{21}$$

For such a kind of deformation, one has: $S_j^i = 0$ and:

$$F_j^i = \frac{1}{\cos\Theta} R_j^i \tag{22}$$

Therefore, the molecule has volume variation:

$$\delta = \frac{1}{\cos\Theta} - 1 \tag{23}$$

That means the fatigue-fracture has been appeared in material.

For the former solution $g_{\tilde{i}\tilde{j}} = \delta_{\tilde{i}\tilde{j}}$, $\nabla \cdot \vec{V} = 0$, it is possible only when the following condition is met:

$$1 > \frac{1}{4}\left[\left(U^1\big|_2 - U^2\big|_1\right)^2 + \left(U^2\big|_3 - U^3\big|_2\right)^2 + \left(U^3\big|_1 - U^1\big|_3\right)^2\right] \tag{24}$$

In this case, there is another decomposition of deformation [6]:

$$F_j^i = \tilde{S}_j^i + \tilde{R}_j^i \tag{25}$$

where,

$$\tilde{S}_j^i = \frac{1}{2}\left(U^i\big|_j + U^i\big|_j^T\right) - (1-\cos\tilde{\Theta})\tilde{L}_k^i\tilde{L}_j^k \tag{26}$$

$$\tilde{R}_j^i = \delta_j^i + \sin\tilde{\Theta}\cdot\tilde{L}_j^i + (1-\cos\tilde{\Theta})\tilde{L}_k^i\tilde{L}_j^k \tag{27}$$

$$\tilde{L}_j^i = \frac{1}{2\sin\tilde{\Theta}}\left(U^i\big|_j - U^i\big|_j^T\right) \tag{28}$$

$$\sin^2\tilde{\Theta} = \frac{1}{4}\Big[\left(U^1\big|_2 - U^2\big|_1\right)^2 + \left(U^2\big|_3 - U^3\big|_2\right)^2 + \left(U^3\big|_1 - U^1\big|_3\right)^2\Big] \tag{29}$$

The solution is:

$$\tilde{S}_j^i = 0 \qquad F_j^i = \tilde{R}_j^i \tag{30}$$

For such a kind of deformation, no fatigue-fracture is produced. The deformation is pure elastic.

Based on classical mechanics, the strain for fatigue-fracture deformation is:

$$\varepsilon_j^i = \left(\frac{1}{\cos\Theta} - 1\right)(L_k^i L_j^k + \delta_j^i) \tag{31}$$

as comparing the strain for pure elastic deformation is:

$$\tilde{\varepsilon}_j^i = (1-\cos\tilde{\Theta})\tilde{L}_k^i\tilde{L}_j^k \tag{32}$$

For fatigue-fracture rotation along x^3 axis, $L_2^1 = -L_1^2 = 1$, other $L_j^i = 0$:

$$\varepsilon_3^3 = \frac{1}{\cos\Theta} - 1, \quad \text{others are zero} \tag{33}$$

Therefore, the molecule has elongation along the rotation axis. For such a kind of deformation, excepting the isotropic stress $\lambda\left(\frac{1}{\cos\Theta} - 1\right)\delta_j^i$, there are an additional stress component along the rotation axis $\sigma_{33} = 2\mu\left(\frac{1}{\cos\Theta} - 1\right)$. Therefore, the maximum stress is along the rotation axis direction.

For pure elastic rotation along x^3 axis, $\tilde{L}_2^1 = -\tilde{L}_1^2 = 1$, other $\tilde{L}_j^i = 0$:

$$\tilde{\varepsilon}_1^1 = \tilde{\varepsilon}_2^2 = 1 - \cos\tilde{\Theta}, \quad \text{others are zero} \tag{34}$$

It is a pure rigid rotation. For such a kind of deformation, excepting the isotropic stress $\lambda(1-\cos\tilde{\Theta})\delta_j^i$, there are additional plane stress on the rotation plane $\sigma_{11} = \sigma_{22} = 2\mu(1-\cos\tilde{\Theta})\delta_j^i$. Therefore, the minimum stress is along the rotation axis direction.

Generally speaking, for a given material, there exists an intrinsic parameter of material Θ_c, when:

$$\Theta \geq \Theta_c \tag{35}$$

only fatigue-fracture deformation solution can exist. This topic is well known in plasticity theory for the yield condition. The yield stress and the critical rotation angular for simple elastic material has relation equation: $\sigma_S = (\lambda+2\mu)(1-\cos\tilde{\Theta}_c)$, $(\cos\Theta_c)^{-2} = 1 + \sin^2\tilde{\Theta}_c$. The detailed discussion is out the range of this paper, hence is omitted here.

4. CRITICAL CURRENT DENSITY FOR FATIGUE-FRACTURE DEFORMATION

For fatigue-fracture deformation, as the deformation meets Equations (19) and (22), after simple algebra operation, one has:

$$\frac{\partial}{\partial t}\cos\Theta + \nabla\cos\Theta\cdot\vec{V} + \cos\Theta\cdot\nabla\cdot\vec{V} = 0 \tag{36}$$

Ignoring the space variation of local rotation, it can be approximated as:

$$\frac{\partial}{\partial t}\cos\Theta + \cos\Theta\cdot\nabla\cdot\vec{V} = 0 \tag{37}$$

For a given Θ harmonic motion with intrinsic frequency $\tilde{\omega}$, (which is determined by the quantum state function of molecules, it is an intrinsic parameter of material structure), its form is:

$$\nabla\cdot\vec{V} = \tilde{\omega}\cdot\tan\Theta \tag{38}$$

Based on discussion in last section, when the local rotation angular is bigger than the material critical value, that is when: Equation (35) $\Theta \geq \Theta_c$ is met. The only possible deformation is fatigue-fracture type. This condition can be expressed as:

$$\nabla\cdot\vec{V} \geq \tilde{\omega}\cdot\tan\Theta_c \tag{39}$$

It gives the upper limit for the current density as: $\vec{J} = \rho\vec{V}$, for a constant charge density, one has:

$$\nabla\cdot\vec{J} \geq \rho\tilde{\omega}\cdot\tan\Theta_c \tag{40}$$

This equation gives the current density condition for the fatigue-fracture deformation. It shows that to increase the ability to against the fatigue-fracture deformation, one can increase the critical angular Θ_c of material (that is to say, increase the yield stress of material while at the same time reduce the elastic modulus), or increase the intrinsic frequency of molecules $\tilde{\omega}$, or increase charge density ρ. Theoretically, one has $\tilde{\omega} = \dfrac{\tilde{E} - E}{\hbar}$, if both Schrödinger equations for initial state and current state are met. This parameter usually is discussed by statistical method to relate with temperature. So, here it can be understood as a thermal parameter.

5. CURRENT DENSITY IN FRACTURED CONDUCTOR

Once the fatigue-fracture deformation is produced in conductors, it does not mean that the device will break down at once. So, it is meaningful to discuss the current density in fractured conductors.

Using $\vec{V}_P$ to represent the charge velocity of conductor, then for the fractured conductor, one has:

$$\nabla\cdot\vec{V}_P = \frac{1}{\cos\Theta} - 1 \tag{41}$$

The charge conservation equation gives:

$$\frac{\partial\tilde{\rho}}{\partial t} + \nabla\tilde{\rho}\cdot\vec{V}_P + \tilde{\rho}\nabla\cdot\vec{V}_P = 0 \tag{42}$$

where, $\tilde{\rho}$ is charge density. Putting Equation (41) into (42), letting $\dfrac{\partial\tilde{\rho}}{\partial t} = \omega\cdot a(t)\cdot\tilde{\rho}$, one gets:

$$\nabla\tilde{\rho}\cdot\vec{V}_P = -\left[\left(\frac{1}{\cos\Theta} - 1\right) + \omega\cdot a(t)\right]\tilde{\rho} \tag{43}$$

Its solution in form is:

$$\tilde{\rho} = \tilde{\rho}_P\cdot\exp\{[-A(\Theta,\,\omega,\,t)/V_P]\cdot\vec{k}\cdot d\vec{r}\} \tag{44}$$

where, $\vec{k}$ is a unit vector along the velocity direction, that in fact is the local rotation axis direction, and the parameter is:

$$A(\Theta,\,\omega,\,t) = \left(\frac{1}{\cos\Theta} - 1\right) + \omega\cdot a(t) \tag{45}$$

For the fracture produced by local rotation along x^3 direction, taking the center position of conductor as reference point for charge density, the current density is:

$$J_P = \tilde{\rho}_P \cdot \exp\{[-A(\Theta, \omega, t)/V_P] \cdot x^3\} \cdot V_P \tag{46}$$

Hence, the current density will accelerate the fatigue-fracture process in the fractured position of conductor as it forms a high charge density there when the reference charge density $\tilde{\rho}_P$ is determined by initial or boundary condition. It is very interesting to notice that once the fracture is produced in conductor, the higher frequency will accelerate the further development of fracture, and therefore accelerates the breakdown of device.

Generally, highly non-symmetric electrons-migration appears only when there is a body force. Such a kind of body force may be produced by: the magnetic field produced by high frequency current which may be related with bad layout of wires, the non-symmetric stress acting on the conductor which may be related with bad geometry of device packing, and the anisotropic thermal expansion related with the cooling system. The research shows the geometric feature of fatigue-fracture. For a suitable design, the damage caused by the fracture effects can be reduced theoretically.

REFERENCES

1. Basaran, C., et al., "A thermodynamic model for electrical current induced damage," *2004 Electronic Components and Technology Conference, IEEE/ECTC*, 1738–1745, 2004.
2. Harris, D. O., et al., "Fracture mechanics life prediction for microscale components — with application to wire bonding," *IEEE/IRPS*, 35–43, 1991.
3. Cabanas, M. F., et al., "Analysis of the fatigue causes on the rotor bars of squirrel cage asynchronous motors: experimental analysis and modelling of medium voltage motors," *Symposium on Diagnostics for Electric Machines, Power Electronics and Devices*, 247–252, SDEMPED2003, Atlanta, 2003.
4. Zheng, J., *Quantum Mechanics*, Vol. 1, 59–72, (3ed), Science Press, Beijing, (in Chinese), 2004.
5. Xiao, J., "Decomposition of displacement gradient and strain definition[A]," Y. Lou and Q. Rao ed., *Advance in Rheology and its Application*[C], 864–868, Science Press USA Inc., New York, 2005.
6. Chen, Z., *Rational Mechanics*, 308, China University of Mining and Technology Press, Xizhou, 1987.

Numerical Analysis of Polarization Splitter Based on Vertically Coupled Microring Resonator

Xinlun Cai[1, 2], **Siyuan Yu**[1], **and Dexiu Huang**[2]

[1]Department of Electrical & Electronic Engineering, University of Bristol, UK
[2]Wuhan National Laboratory for Optotelectronics, China

Abstract— A novel polarization splitter which exploits the strong polarization dependence of vertical coupled microring resonator is presented. Based on a combination of a three dimensional, full vectorial film mode matching method (FMM) with a three dimensional full vectorial coupled mode theory (CMT), the device performance of vertically coupled microring resonator is rigorously investigated. Three steps are taken to model the structure: First, the propagation constants and the eigenmodes of straight and bent waveguides are computed using FMM; second, the scattering matrix describing the behavior of coupling region is obtained by means of CMT; and finally the spectral responses of microring resonator for TE and TM mode are calculated. By this method, one obtains a complete three dimensional vectorial microring resonator description without any freee parameters, which permits a convenient investigation of the influence of geometrical parameters on the spectral response. The calculated result shows that the response of microring resonator is indeed strongly polarization dependent and the resonance wavelengths are different for the two polarizations. The resonance wavelengths of the two orthogonal polarization states are different because of the difference in modal index and scattering matrix for different polarizations, hence the different polarized light can be transferred to different output port at specific wavelength. Such property allows for the design of integrated polarization splitter. The investigation of the influence of geometrical parameters on splitting ratio demonstrated that a splitting ratio greater than 20 dB at 1.55 μm can be achieved in this device.

1. INTRODUCTION

Polarization splitters, which can separate the two orthogonal polarization states, are essential components in photonics. Integrated polarization splitters offer the possibility of integration with other optical elements as well as the advantages of compactness [1]. Various types of integrated polarization splitters have been reported in literature [2–4].

Currently integrated photonic devices based on microring resonators have been widely studied because of their compact size and attractive spectral properties suitable for VLSI photonic circuits [5]. The ideal of microring resonator type polarization splitter was first proposed by Klunder [6]. The working principles can be explained in terms of polarization dependent resonance wavelength (PDW): due to the difference in modal index and coupling coefficients for TE and TM mode, the responses of microring resonators show strong polarization dependence and the resonance wavelengths may be different for TE and TM mode. Thus, microring resonators can drop one polarized light to the drop port and transfer the other to the through port at specific wavelength.

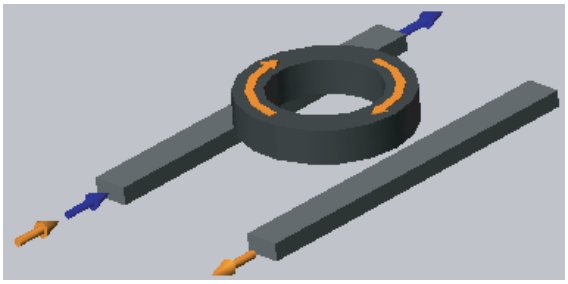

Figure 1: Vertically coupled microring resonator, a 3-D configuration where a ring resonator is placed on top of two parallel bus waveguides. The blue and orange arrows represent two orthogonal polarization states, and they are transferred to different output ports.

In this work, we rigorously analyze a wavelength sensitive polarization splitter based on vertically coupled microring resonator as sketched in Fig. 1. The structure is to be modeled by a combination

of 3-D full vectorial film mode matching method (FMM) [8–10] and 3-D vectorial coupled mode theory (CMT) [11]. We utilize FMM to calculate the eigenmodes and propagation constants of uncoupled straight and bent waveguides. FMM is a rigorous and efficient method to model a real waveguide structure. If the geometries of dielectric waveguides are not too complicated, FMM is always superior to other numerical methods such as finite-difference method and finite-element method, because FMM tackles the problem semi-analytically and avoids unnecessary discretization. CMT has been applied extensively in integrated photonics as an intuitive mathematical tool for the analysis of interaction of modes in different waveguides which are brought into close proximity [12]. Using the eigenmodes of uncoupled waveguides as basis modes, we can obtain the scattering matrix which relates the amplitudes in the beginning and at the end of coupling region by means of CMT. Then the spectral response of the entire structure can be evaluated straightforwardly. The result indicates that the pronounced polarization dependence of the resonance wavelength allows for the design of wavelength sensitive polarization splitters.

2. THEORY AND NUMERICAL RESULTS

Figure 2(a) sketches the basic geometry of the vertically coupled microring resonator under investigation. The ring resonator is symmetrically coupled to two identical straight waveguides. The straight waveguides with width $v = 1.0\,\mu\text{m}$, thickness $s = 0.5\,\mu\text{m}$, and refractive index $n_s = 1.98$ is embedded in a substrate with index $n_g = 1.45$. The bent waveguide of width $w = 1.0\,\mu\text{m}$, thickness $t = 0.5\,\mu\text{m}$ and radius $R = 45\,\mu\text{m}$ with refractive index $n_b = 2.0$ is placed on top of the substrate surface, covered by a material with refractive index $n_a = 1.4017$. The relative position of the straight waveguide is defined by the horizontal gap d and the vertical distance b between them. In our case, $d = 0.5\,\mu\text{m}$ and $b = 0.9\,\mu\text{m}$.

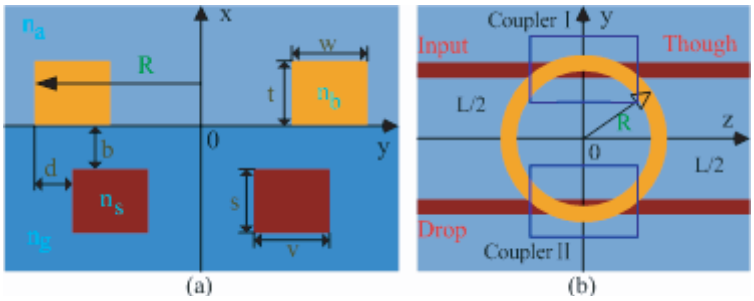

Figure 2: Cross section view and top view of the microresonator structure.

Adhering to the standard resonator model [13], we assume that the interaction between straight and bent waveguide is confined in two "coupling regions" which are enclosed by the blue lines in Fig. 2(b) and individual modes propagate independently in their respective waveguides outside the regions. Thus, the structure can be divided into two couplers (coupler I and II) which are connected by two bends with length of $L/2$. In order to predict the spectral response of the resonator, we need a description of the wave propagation along the bends, the analysis of the behavior of the coupling region, and finally a framework to combine these individual modules.

We take three steps to model the structure: First, the propagation constants and the eigenmodes of straight and bent waveguides are computed using FMM; second, the scattering matrix describing the behavior of coupling region is obtained by means of CMT; and finally the spectral responses of microring resonator for TE and TM mode are calculated.

2.1. Calculation of Eigenmodes of Straight and Bent Waveguides Using FMM

In the mode-solving arithmetic based on FMM, waveguide cross section is divided into vertical slices. In each slice, the mode of entire structure is expressed as a superposition of the slice eigenmodes, and sufficient local guided and radiation modes, with corresponding propagation constants, have to be computed in order to achieve sufficient accuracy. Matching the fields of these slices at the vertical interfaces, we can determine the modes of the entire structure [8].

We calculated the eigenmodes of the individual waveguides described in Fig. 2. Both the two waveguides support only fundamental TE and TM mode. Fig. 3 and Fig. 4 show the cross section of the two waveguides as well as the corresponding modal profiles. Since an electromagnetic field propagating through a bend loses energy due to radiation, γ_b is complex valued, denote $\gamma_b =$

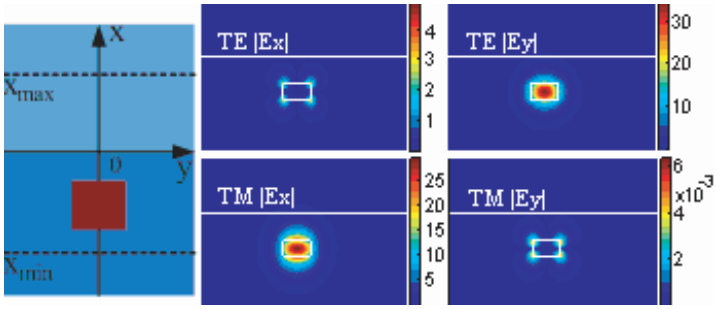

Figure 3: The cross section of uncoupled straight waveguide and corresponding field distributions of the transverse components of the electric intensity of the fundamental TE- and TM-mode.

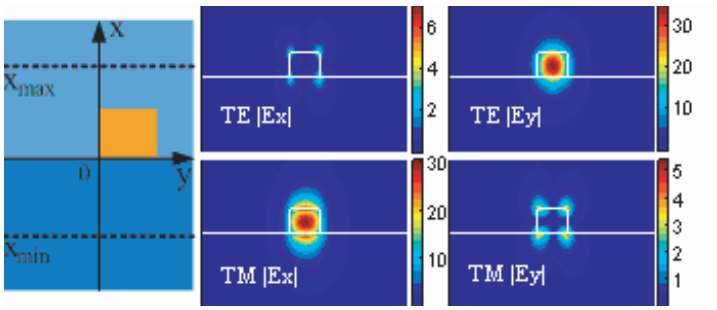

Figure 4: The cross section of uncoupled bent waveguide and corresponding field distributions of the transverse components of the electric intensity of the fundamental TE- and TM-mode.

$(\beta + i\alpha)R$, where β and α is phase constant and attenuation constant. The bending loss is pretty small because of the relatively large refractive index contrast and bending radius.

2.2. Vertical Coupling between Straight Waveguide and Bent Waveguide

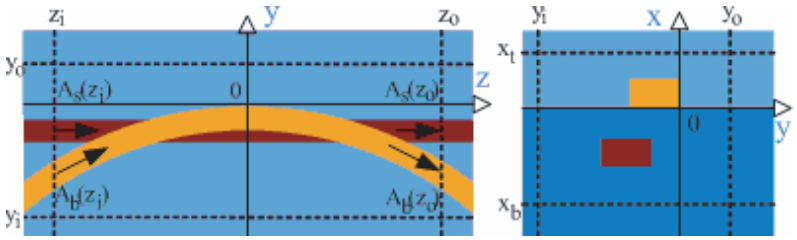

Figure 5: Top view and cross section through the symmetry plane of coupling region. The dashed lines indicate the boundary of computational region $[x_b, x_t] \times [y_i, y_o] \times [z_i, z_o]$.

The coupled mode theory is established on the assumption that the field of the coupling region can be represented as a linear superposition of the modes of uncoupled waveguides. Consider the configuration of coupling region shown in Fig. 5. We assume that the interaction of the modes is restricted in the rectangular computational region $[x_b, x_t] \times [y_i, y_o] \times [z_i, z_o]$. The field in the coupling region can be written as:

$$(E, H) = A_b(z)(E_b, H_b) + A_s(z)(E_s, H_s) \tag{1}$$

(E_b, H_b) and (E_s, H_s) are the fields of the bent and straight waveguides and A_b and A_s are unknown amplitudes. Using Lorentz reciprocity theorem, we can deduce the coupled mode equation [13]:

$$\frac{\mathrm{d}}{\mathrm{d}z}\begin{bmatrix} A_b(z) \\ A_s(z) \end{bmatrix} = iC^{-1}K\begin{bmatrix} A_b(z) \\ A_s(z) \end{bmatrix} \tag{2}$$

C^{-1} and K are two 2×2-matices, and their elements are based on overlap integrals of different fields [10]. Solving the couple mode Equation (2), we can obtain the scattering matrix S which

relates $(A_s(z_o),\ A_s(z_o))$ to $(A_s(z_i),\ A_s(z_i))$ (see Fig. 5) [10, 12]:

$$\begin{bmatrix} A_b(z_o) \\ A_s(z_o) \end{bmatrix} = S \begin{bmatrix} A_b(z_i) \\ A_s(z_i) \end{bmatrix} \begin{bmatrix} S_{bb} & S_{bs} \\ S_{sb} & S_{ss} \end{bmatrix} \begin{bmatrix} A_b(z_i) \\ A_s(z_i) \end{bmatrix} \tag{3}$$

The performance of the coupling region is completely described by scattering matrix. The elements $S_{oi}(o,\ i = b,\ s)$ is a measure of interaction between input mode i and output mode o, and $|S_{oi}|^2$ can be interpreted as relative power transferred to mode o. In order to demonstrate the interaction between the two waveguides, we consider the evolution $S(z)$ as obtained by applying the calculation procedure to a series of computational windows with fixed lower boundary z_i and varying upper boundary at $z \in [z_i,\ z_o]$. In Fig. 6, the evolution of the elements of scattering matrix is presented as functions of z.

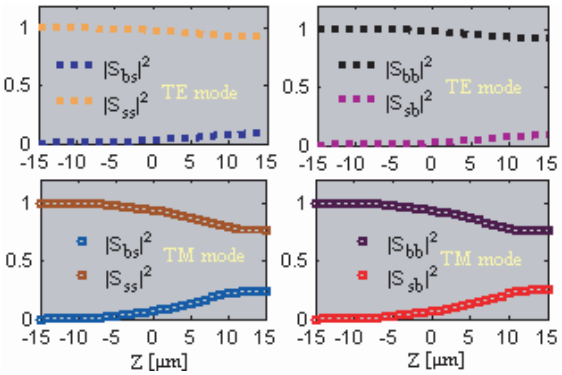

Figure 6: The evolution of the elements of scattering matrix for TE- and TM-polarized light as a function of output plan position z_o of coupling region.

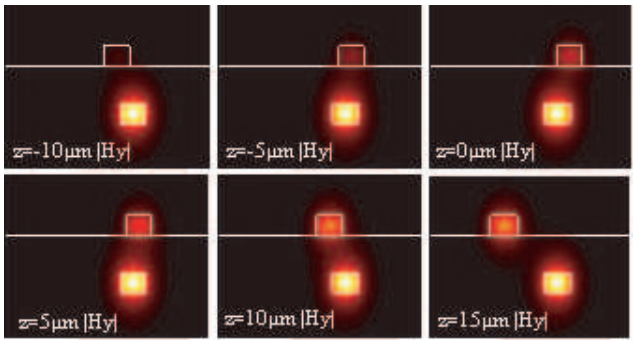

Figure 7: The cross section of both straight and bent waveguides with field distribution of the horizontal component of the magnetic intensity vector for a sequence of longitudinal distance. Coupling between the fundamental TM modes of the two waveguides is shown.

The simulation results in Fig. 6 can be considered as power evolutions in the coupling region. Take Fig. 6(c) for an example, assuming a unit power of TM polarized light is launched into the straight waveguide, $|S_{ss}|^2$ and $|S_{bs}|^2$ describe the local power in the straight and bent waveguide respectively. Initially most of the power is confined in straight waveguide. After a certain propagation distance, the bend mode gets excited and the interaction of the two waveguides becomes significant. Finally, modes in two waveguides become stationary again at the end of the coupling region. In Fig. 7, we show some snapshots of the process described above. Table 1 gives the elements of power scattering matrix calculated by CMT.

Table 1: Power of elements of scattering matrix of the coupling region.

	$\lvert S_{bb}\rvert^2$	$\lvert S_{sb}\rvert^2$	$\lvert S_{bs}\rvert^2$	$\lvert S_{ss}\rvert^2$
TE_0	0.9210	0.0793	0.0786	0.9210
TM_0	0.7563	0.2467	0.2407	0.7563

2.3. Spectrum of the Entire Structure for Different Polarizations

Let $S_{bb} = |S_{bb}| \exp(i\varphi)$ and $S_{ss} - S_{bs}S_{sb}/S_{bb} = d \exp(i\varphi)$. The dropped and through power is given by the equations below [15].

$$P_{drop} = P_{in} \frac{|S_{bs}|^2 |S_{sb}|^2 \exp(-\alpha L)}{1 + |S_{ss}|^4 \exp(-2\alpha L) - 2|S_{ss}|^2 \exp(-\alpha L) \cos(\beta L - 2\varphi)} \tag{4}$$

$$P_{through} = P_{in} \frac{|S_{bb}|^2 \left(1 + |S_{bs}|^2 d^2 \exp(-\alpha L) - 2|S_{bs}| d \exp(-\alpha L) \cos(\beta L - 2\varphi - \phi)\right)}{1 + |S_{ss}|^4 \exp(-2\alpha L) - 2|S_{ss}|^2 \exp(-\alpha L) \cos(\beta L - 2\varphi)} \tag{5}$$

In principle, the spectral response of the device can be obtained by repeating the entire procedure for different wavelengths. However, if only a narrow wavelength range is of interest, one can expect that the scattering matrices are constant and the calculation can be greatly simplified.

In Fig. 8 the spectral responses of the vertically coupled microring resonator for TE and TM mode are shown. As can be easily seen, 1.55 µm is in the center of pass band of TM mode and out of the pass band of TE mode. If TE and TM polarized light at 1.55 µm is launched into the input port simultaneously, the resonator will drop TM polarized light to the drop port and transmit TE polarized light to the though port. In this way, two orthogonal polarization states are split and transferred to different output ports. The device achieves polarization splitting ratios of $SR_1 = 10\log_{10}(P^{\mathrm{TM}}_{drop}/P^{\mathrm{TE}}_{drop}) = 22.99\,\mathrm{dB}$ and $SR_2 = 10\log_{10}(P^{\mathrm{TE}}_{through}/P^{\mathrm{TM}}_{through}) = 22.86\,\mathrm{dB}$.

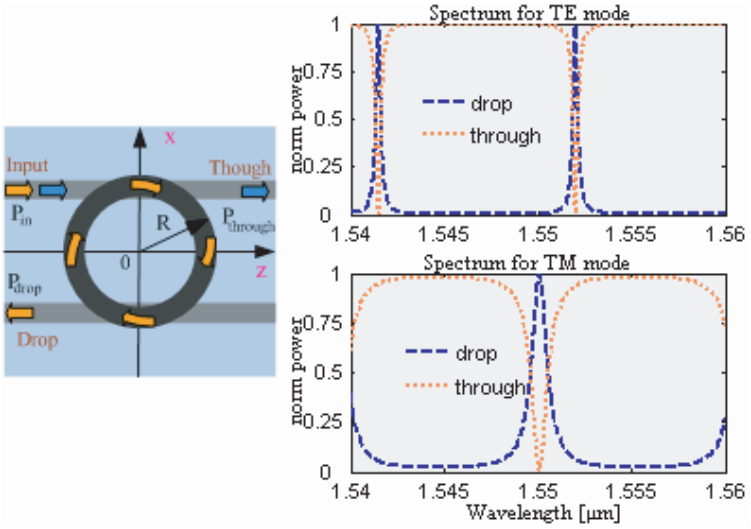

Figure 8: Spectral response of the entire structure for both TE- and TM-mode.

3. CONCLUSION

In this work, a 3D frequency domain model of vertically coupled microring resonator based on full vectorial FMM and 3D CMT has been employed to obtain the eigenmodes of uncoupled waveguides, the scattering matrix of coupling region and, finally, the spectral responses for TE and TM mode. It turns out that the resonance wavelengths of the two orthogonal polarization states are different because of the difference in modal index and scattering matrix for different polarizations, hence the different polarized light can be transfer to different output port at specific wavelength. The structure demonstrate here has a splitting ratio better than 20 dB at 1.55 µm.

REFERENCES

1. Tervonen, A., "Integrated optical polarization splitters," *IEE Colloquium on Polarisation Effects in Optical Switching and Routing Systems*, 1–3, Institution of Electrical Engineers, London, 1990.
2. Hayakawa, T., S. Asakawa, and Y. Kokubun, "ARROW-B type polarization splitter with asymmetric Y-branch fabricated by a self-alignment process," *J. Lightwave Technol.*, Vol. 15, 1165–1170, 1997.
3. Simova, E. and I. Golub, "Polarization splitter/combiner in high index contrast Bragg reflector waveguides," *Opt. Express*, Vol. 11, 3425–3430, 2003. http://www.opticsinfobase.org/abstract.cfm?id=78197.
4. Little, B. E., S. T. Chu, H. A. Haus, J. Foresi, and J.-P. Laine, "Microring resonator channel dropping filters," *J. Lightwave Technol*, Vol. 15, 998–1005, 1997.
5. Klunder, D. J. W., C. G. H. Roeloffzen, and A. Driessen, "A novel polarization-independent wavelength-division-multiplexing filter based on cylindrical microresonators," *IEEE J. Select. Topics Quantum Electron.*, Vol. 8, 1294–1299, 2002.
6. Chilwell, J. and I. Hodgkinson, "Thin-film field-transfer matrix theory of planar multilayer waveguides and reflection from prism-loaded waveguides," *J. Opt. Soc. Am.*, Vol. 1, 742–753, 1984.

7. Prkna, L., M. Hubalek, and J. Ctyroky, "Field modeling of circular microresonators by film mode matching," *IEEE J. Select. Topics Quantum Electron.*, Vol. 11, 217–223, 2005.
8. Prkna, L., M. Hubalek, and J. Ctyroky, "Vectorial eigenmode solver for bent waveguides based on mode matching," *IEEE Photon. Technol. Lett.*, Vol. 15, 1249–1251, 2003.
9. Sudbo, A. S., "Film mode matching: a versatile numerical method for vector mode field calculations in dielectric waveguides," *Pure and Applied Optics*, Vol. 2, 211–233, 1993.
10. Stoffer, R., K. R. Hiremath, M. Hammer, L. Prkna, and J. Ctyroky, "Cylindrical integrated optical microresonators: modeling by 3-D vectorial coupled mode theory," *Opt. Comm.*, Vol. 256, 46–67, 2005.
11. Huang, W. P., "Coupled mode theory for optical waveguides: An overview," *J. Opt. Soc. Am. A*, Vol. 11, 963–983, 1994.
12. Hammer, M., "Standard ringresonator model," NAIS project, Internal document, http://www.math.utwente.nl/aamp/Projects/Nais/Documents/rrrel.pdf.
13. Vassallo, C., *Optical Waveguide Concepts*, Elsevier, Amsterdam, 1991.

Performance of Multigrid in the Context of Beam Dynamics Simulations

G. Pöplau and U. van Rienen
Rostock University, Germany

Abstract— Precise and fast 3D space charge calculations for bunches or clouds of charged particles are of growing importance in design studies for future linear accelerators and light sources. One of the possible approaches is the computation of the potential of the bunch in the rest frame by means of Poisson's equation. The software package MOEVE has been developed for space charge calculations on non-equidistant grids. It consists of several iterative Poisson solvers (MOEVE Poisson solvers), among them the state-of-the-art multigrid Poisson solver. Furthermore, the MOEVE Poisson solvers have been implemented in the tracking code Astra and GPT. In this paper the algorithms of the software package MOEVE will be described and the performance will be tested for very large linear systems of equations. The numerical results will show that the conditions for the Poisson solvers have to be chosen carefully in order to achieve optimal results for real life applications.

1. INTRODUCTION

The design of future light sources and colliders requires increasingly precise 3D beam dynamics simulations. In so-called tracking simulations the particle trajectory is determined which is described by the relativistic equation of motion. The equation of motion is solved by means of an appropriate time integration scheme. In regimes of rather low energy, this implies that the space charge fields have to be taken into account in each time step of the numerical integration. Recently, the efficient calculation of 3D space charge fields gained particular importance in the context of electron cloud studies for the ILC (International Linear Collider) damping rings.

Based on the geometric multigrid technique fast Poisson solvers have been developed and successfully applied for 3D space charge simulations. In theory, these multigrid Poisson solvers have optimal performance, i.e., the numerical effort depends linearly on the number of mesh points. Unfortunately, this optimal convergence rate can sometimes not be achieved in simulations of real life problems. In this paper the performance of the geometric multigrid technique is investigated in the context of space charge calculations, in particular, for huge numbers of mesh points, i.e., up to 4 million. Another problem is the behavior of the multigrid Poisson solver within the particle tracking procedure. Since space charge fields have to be computed in each time step of the numerical integration, the calculated fields of the previous time step can be used as initial guess for the iterative Poisson solver. With this approach the effort for the new space charge calculation can be reduced. The question under investigation is how multigrid can compete with other iterative algorithms for real life tracking simulations.

The iterative Poisson solvers are available as software package MOEVE 2.0 (MOEVE: **M**ultigrid for n**o**n-**e**quidistant grids to sol**v**e Poisson's **e**quation) [8]. Furthermore, these Poisson solvers are implemented in the tracking code Astra (DESY, Hamburg, Germany) [3] and the tracking code GPT (Pulsar Physics, Eindhoven, The Netherlands) [13].

2. MATHEMATICAL MODEL

Space charge calculations for beam dynamics studies are performed within a tracking procedure. The tracking is a method to determine the trajectories of the particles which are described by the relativistic equations of motion [1]. The equations of motion are solved by means of an appropriate time integration scheme. The space charge fields have to be taken into account in each time step of the numerical integration. The space charge calculations are performed in the rest frame of the bunch by means of Poisson's equation given by

$$\begin{aligned} -\Delta\varphi &= \frac{\varrho}{\varepsilon_0} \quad \text{in} \quad \Omega \subset \mathbb{R}^3, \\ \varphi &= 0 \quad \text{on} \quad \partial\Omega_1, \\ \frac{\partial\varphi}{\partial n} + \frac{1}{r}\varphi &= 0 \quad \text{on} \quad \partial\Omega_2, \end{aligned} \tag{1}$$

where φ denotes the potential, ϱ the space charge distribution, ε_0 the dielectric constant and r the distance between the center of the bunch and the boundary. Usually, the domain Ω is a rectangular box constructed around the bunch. On the surface $\partial\Omega = \partial\Omega_1 \cup \partial\Omega_2$ ($\partial\Omega_1 \cap \partial\Omega_2 = \emptyset$) perfectly conducting boundaries ($\partial\Omega_1$) or open boundaries ($\partial\Omega_2$) can be applied. For space charge calculations within a beam pipe the domain Ω is assumed to be a cylinder with elliptical cross section. A detailed description of the 3D space charge model can be found in [11] and the model with elliptical shaped beam pipe in [7], respectively.

The discretization of Equation (1) with second order finite differences leads to a linear system of equations

$$A_h u_h = f_h, \tag{2}$$

where u_h denotes the vector of the unknown values of the potential and f_h the vector of the given space charge density at the grid points. The step size h indicates a certain discretization and the matrix A_h is the discretization of the Laplacian.

3. THE MOEVE POISSON SOLVERS

In the software package MOEVE, different iterative Poisson solvers are implemented for the solution of (2): multigrid (MG) and multigrid pre-conditioned conjugate gradients (MG-PCG); a pre-conditioned conjugate gradient method (PCG) with Jacobi pre-conditioner; (mainly for comparison reasons) the successive over relaxation (SOR); and biconjugated gradients (BiCG) and BiCGSTAB as a stabilized version of BiCG.

The implementation of the methods PCG, SOR, BiCG and BiCGSTAB is simple but these algorithms suffer from the drawback that the number of iterations grows with $\mathcal{O}(N^2)$. Here, N denotes the number of mesh lines in each coordinate direction. Descriptions of these methods can be found elsewhere, e.g., in [4].

As already mentioned above, multigrid has optimal performance. Consequently, it is applied as the state-of-the-art Poisson solver, but the implementation is very complex. We give here only a rough idea of our specific multigrid scheme. For more details see [2, 5].

The multigrid algorithm operates on a certain number of grids starting with the mesh given by the discretization of Poisson's equation which is related to Equation (2). This mesh is referred to as the fine grid or the fine level. Then a sequence of coarser grids is generated by cutting mesh lines. On an equidistant mesh where the number of mesh lines equals $N = 2^t + 1$, every second mesh line can be removed. For space charge calculations, a special coarsening strategy for non-equidistant grids has been developed [12]. Here, the removal of mesh lines follows the rule: two neighboring steps h_1 and h_2 remain in the next coarser grid as long as either $h_1 \geq sh_{\min}$ or $h_2 \geq sh_{\min}$, where $h_{\min}$ denotes the overall minimal step size of the corresponding fine level. The factor s is chosen as $s = 1.6$ or $s = 1.7$ in order to obtain a decreasing aspect ratio of the mesh spacing.

Now the system of Equations (2) is solved iteratively in the following way: first a raw approximation of the solution of the system of equations is obtained by the application of a few steps of a relaxation scheme (e.g., Gauss-Seidel) which is called pre-smoothing. This approximation is then improved by a correction vector obtained on the coarser grids (the so-called coarse grid correction), where restriction and interpolation work as grid transfer operators. After applying interpolation another few steps of relaxation are necessary, these are the post-smoothing steps. For the space charge calculations a multigrid V-cycle is realized. This scheme goes strictly down from the fine to the coarsest grid and then up again to the fine level. The V-cycle is performed with the following components: 2 pre- and 2 post-smoothing steps with red-black Gauss-Seidel relaxation, full-weighting restriction and trilinear interpolation.

Furthermore, multigrid can be applied as a preconditioner for the conjugate gradient algorithm (MG-PCG). This method leads to a better convergence at least in cases where a plain multigrid scheme converges too slowly [6].

Detailed convergence studies for MG, MG-PCG, PCG and SOR in the context of space charge calculations can be found in [11, 12]. In the next section we investigate MG, MG-PCG and PCG for Dirichlet and open boundaries, in particular, for very large linear systems of equations.

4. PERFORMANCE OF THE MULTIGRID POISSON SOLVERS

The objective of this section is to investigate the performance of the multigrid algorithms of MOEVE for a huge number of grid points up to more than 4 millions. The algorithms MG, MG-PCG and PCG were performed for the Poisson Equation (1) on $\Omega = [-0.5, 0.5]^3$ with Dirichlet and

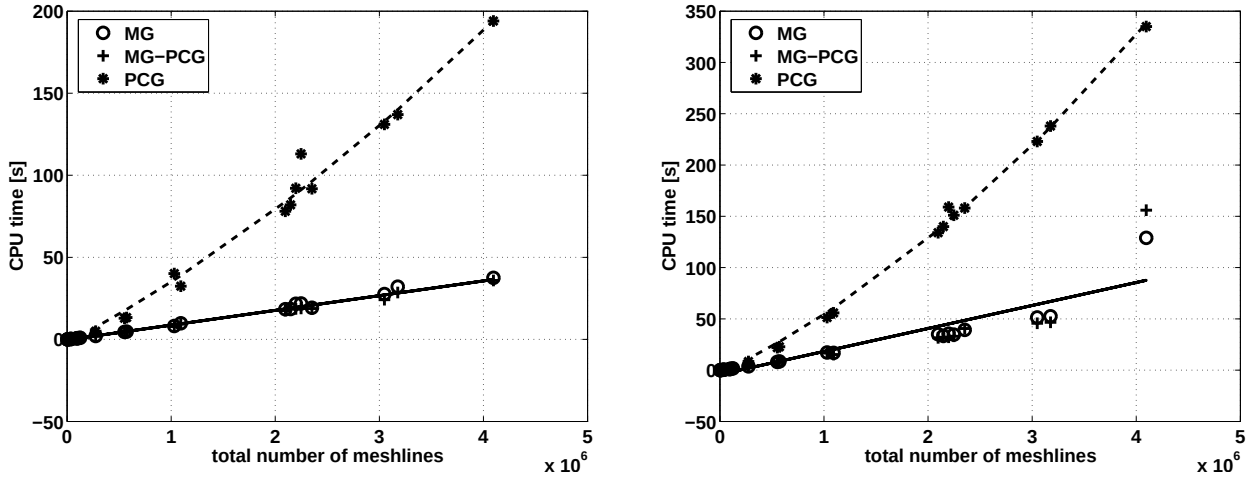

Figure 1: The performance of MG, MG-PCG and PCG for Poisson's equation with Dirichlet boundary conditions on equidistant grids (left) and on non-equidistant grids (right).

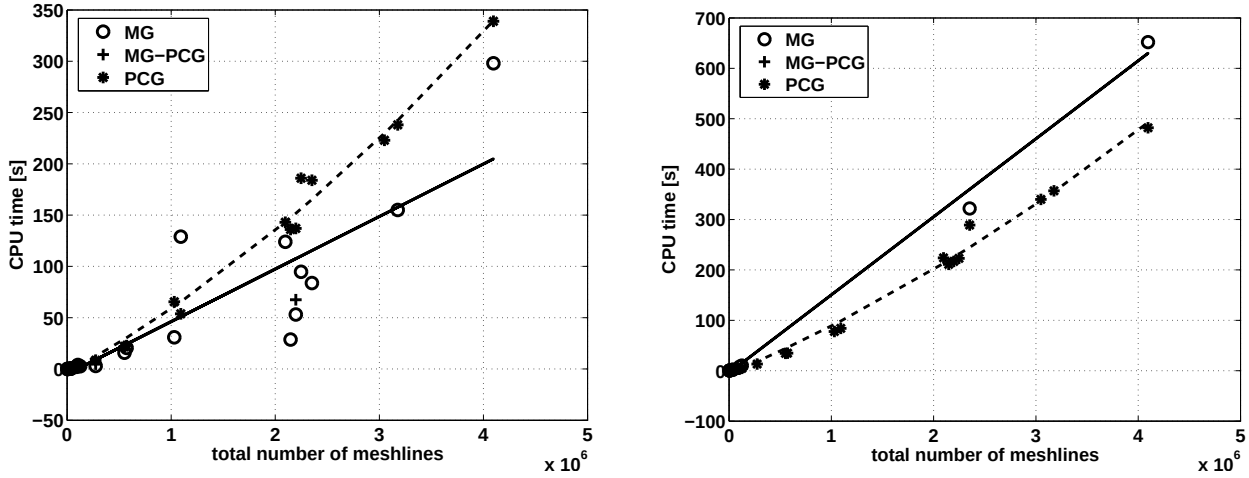

Figure 2: The performance of MG, MG-PCG and PCG for Poisson's equation with open boundary conditions on equidistant grids (left) and on non-equidistant grids (right).

open boundary conditions, respectively. The discretization was chosen equidistant as well as non-equidistant. The non-equidistant distribution of the mesh lines x_i in x-direction was given by the function

$$x_i = \frac{\sinh(6(-0.5 + i/N_x))}{2\sinh(3)}, \quad \text{for } i = 0, \ldots, N_x,$$

where N_x denotes the number of mesh lines in x-direction. The mesh lines in y- and z-direction are distributed in the same way.

A bunch of ellipsoidal shape was chosen as the model's problem, because numerical simulations of so-called pancake shaped bunches have gained in importance in recent years [10, 14]. For the numerical test the ellipsoidal bunch has the extensions $a = 0.2\,\text{mm}$, $b = 0.2\,\text{mm}$, $c = 0.1\,\text{mm}$, where a, b and c denote the length of the half axes in x-, y- and z-direction, respectively. The ellipsoid has a uniformly distributed charge of $Q = -1\,\text{nC}$.

The algorithms where performed until the maximum norm of the relative residual had reached a value less than 10^{-9}. In Figure 1 the results for Dirichlet boundary conditions are presented. MG and MG-PCG achieve optimal convergence on the equidistant grid (Figure 1, left), i.e., the convergence does not depend on the total number of mesh points N_p. The value of the maximum norm of the relative residual was after 9-10 V-cycles less than 10^{-9}. On the non-equidistant grid the optimal performance is not achieved for 4 million grid points (Figure 1, right), here the algorithms MG and MG-PCG require 25 and 24 V-cycles, respectively. The number of V-cycles for $N_p < 4 \cdot 10^6$ was between 10 and 14. Compared to that the numerical effort of the PCG algorithm

grows quadratically with the number of mesh points.

Open boundary conditions pose a problem because the matrix A_h in (2) becomes singular with increasing number of mesh points (see [7] for the structure of the matrix A_h). Figure 2 (left) shows that the behavior of the multigrid algorithms on equidistant meshes becomes unpredictable, if $N_p > 10^6$. The MG-PCG method does not converge, if $N_p > 2.5 \cdot 10^6$, i.e., the norm of the relative residual had not achieved a value of less than 10^{-9}. The performance of multigrid becomes worse on non-equidistant grids. Figure 2 (right) shows that PCG has the better performance compared to multigrid. MG and MG-PCG converge only for a certain number of mesh points, MG-PCG only, if $N_p < 50,000$. Here, further investigations are necessary.

The problem with open boundary conditions has not yet occurred for space charge calculations for several reasons: the algorithms are only performed until the maximum norm of the relative residual is less than 10^{-2}, Dirichlet boundary conditions are applied for meshes with large aspect ratio, the total number of mesh points was less than 1 million. The performance of the multigrid algorithms in a typical tracking simulation will be demonstrated in the next section.

5. MULTIGRID POISSON SOLVERS WITHIN A TRACKING PROCEDURE

The MOEVE Poisson solvers have been implemented in the tracking code Astra (**a** **s**pace **c**harge **tr**acking **a**lgorithm) [3]. The program package Astra has been successfully used in the design of linac and rf photoinjector systems. The Astra suite tracks macro particles through user-defined external fields including the space charge field of the particle cloud.

As a tracking simulation a bunch of 30,000 macro particles representing electrons was chosen. The initial particle distribution is Gaussian with $\sigma_x = \sigma_y = 1.0\,\text{mm}$ and $\sigma_z = 0.5\,\text{mm}$. Further the bunch has a total charge of $-1\,\text{nC}$ and an average energy of 1 MeV. It is tracked over a distance of 2.0 m. Additionally a quadrupole (length 0.2 m, gradient 0.1 T/m) is placed at $z = 1.2\,\text{m}$. The quadrupole stretches the bunch into the transversal y-direction. This behavior requires full 3D space charge calculations.

For the space charge calculations the MG and MG-PCG algorithm was chosen from the MOEVE Poisson solvers. For comparison reasons the same calculations were done additionally using the PCG method. All algorithms were performed until the maximum norm of the relative residual had reached a value of less than 10^{-2}. This value seems to be rather low, but further iterations would not improve the numerical error, because the source term ϱ is discontinues in general.

In Table 1 the performance times are given for the equidistant discretization as well as for a non-equidistant discretization. The non-equidistant mesh is constructed as follows: around the bunch the mesh is equidistant, then the mesh is expanded with double step size. Furthermore, the iterative Poisson solvers have the possibility to set their initial guess, in Table 1 denoted by $u_{h,0}$, as the solution of the space charge calculation of the previous time integration step, i.e., $u_{h,0} \neq 0$. This strategy saves iteration steps and consequently CPU time. In particular, the PCG algorithm profits from this strategy so much that it can be nearly as fast as the MG routine (case $N_p = 24,389$). But this behavior depends of course on the problem and cannot be generalized. In the present simulation MG and MG-PCG needed half of the iteration steps with $u_{h,0} \neq 0$ (for instance 1 or 2 steps instead of 3 or 4 with $u_{h,0} = 0$) while PCG could save up to 3/4 or more of the iteration steps (i.e., it had to perform for example only 10 iterations instead of 40).

Table 1: CPU times for a tracking simulation with different Poisson solvers, 988 space charge calculations were performed.

	Total number of grid points	
Poisson solver	24,389	68,921
MG, non-equidistant, $u_{h,0} = 0$	754 s	902 s
MG, non-equidistant, $u_{h,0} \neq 0$	738 s	828 s
MG-PCG, non-equidistant, $u_{h,0} = 0$	790 s	995 s
MG-PCG, non-equidistant, $u_{h,0} \neq 0$	759 s	873 s
PCG, non-equidistant, $u_{h,0} = 0$	806 s	1239 s
PCG, non-equidistant, $u_{h,0} \neq 0$	739 s	881 s

During the whole tracking simulation, space charge was calculated 988 times. Table 1 shows that in general the tracking times together with the MG method are the fastest. Furthermore it

turns out that performance speed of PCG is also very good as long as the number of unknowns is relatively low. Nevertheless comparing the cases $N_p = 24,389$ and $N_p = 68,921$ the computational time rises more for the PCG routine than for the MG algorithm considering $u_{h,0} = 0$.

6. CONCLUSION

The objective of this paper was to test the performance of iterative Poisson solvers, in particular, for large linear systems of equations. It turned out that the multigrid methods MG and MG-PCG achieve the optimal convergence behavior for the Poisson problem with Dirichlet boundary conditions on equidistant and non-equidistant grids, respectively. The solution of Poisson's equation with open boundary conditions pose a problem to the multigrid solvers. Here, further investigations are necessary. Consequently, boundary conditions and solvers have to be chosen carefully in real life applications. Such, it is recommended to avoid open boundary conditions for very large linear systems of equations. For instance, space charge calculations performed on a larger computational domain with Dirichlet boundary conditions provide sufficiently exact results. Another consequence from the numerical results of this paper is a careful choice of the resolution of the problem. A better alternative to a high resolution is an adaptive meshing. First investigations for space charge calculations on adaptive meshes were done in [9]. The presented tracking simulation takes all this considerations into account. It demonstrates the efficiency and robustness of the MOEVE Poisson solvers.

ACKNOWLEDGMENT

This work was supported by DESY, Hamburg, Germany.

REFERENCES

1. Birdsall, C. K. and A. B. Langdon, *Plasma Physics via Computer Simulation*, The Adam Hilger Series on Plasma Physics, New York, 1991.
2. Briggs, W. L., Van E. Henson, and S. McCormick, *A Multigrid Tutorial (2nd Edition)*, Philadelphia, 2000.
3. Flöttmann, K., *Astra*, DESY, Hamburg, www.desy.de/mpyflo, 2000.
4. Greenbaum, A., *Iterative Methods for Solving Linear Systems of Frontiers in Applied Mathematics*, Vol. 17, Philadelphia, 1997.
5. Hackbusch, W., *Multi-grid Methods and Applications*, Springer-Verlag, Berlin, 1985.
6. Jung, M. and U. Langer, "Applications of multilevel methods to practical problems," *Surv. Math. Ind.*, Vol. 1, 217–257, 1991.
7. Markoviḱ, A., "Numerical computation of space-charge fields of electron bunches in a beam pipe of elliptical shape," TESLA Report 2005-21, DESY, Hamburg, (tesla.desy.de/new_pages/TESLA/TTFnot05.html), 2005.
8. Pöplau, G., "MOEVE 2.0: multigrid Poisson solver for non-equidistant tensor product meshes," Universität Rostock, 2006.
9. Pöplau, G. and U. van Rienen, "A self-adaptive multigrid technique for 3D space charge calculations," *IEEE Transactions on Magnetics*, 2008.
10. Pöplau, G., U. van Rienen, and K. Flöttmann, "3D space charge calculations for bunches in the tracking code Astra," *Proceedings of EPAC 2006 (10th European Particle Accelerator Conference)*, 2203–2205, Edinburgh, Great Britain, 2006.
11. Pöplau, G., U. van Rienen, S. B. van der Geer, and M. J. de Loos, "Fast calculation of space charge in beam line tracking by multigrid techniques," *Scientific Computing in Electrical Engineering*, W. H. A. Schilders, E. J. W. ter Marten, and S. H. M. Houben, editors, No. 4 in Mathematics in Industry, 329–336, Springer-Verlag, Berlin, 2004.
12. Pöplau, G., U. van Rienen, S. B. van der Geer, and M. J. de Loos, "Multigrid algorithms for the fast calculation of space-charge effects in accelerator design," *IEEE Transactions on Magnetics*, Vol. 40, No. 2, 714–717, 2004.
13. Pulsar Physics, Burghstraat 47, 5614 BC Eindhoven, The Netherlands, www.pulsar.nl/gpt. *General Particle Tracer (GPT)*, release 2.70, 2004.
14. Qiang, J., S. Lidia, R. D. Ryne, and C. Limborg-Deprey, "Three-dimensional quasistatic model for high brightness beam dynamics simulation," *Phys. Rev. ST Accel. Beams*, Vol. 9, No. 4, Apr. 2006.

Incorporation of the Continuous Spectrum in Closed Form Expressions for Layered Media Green's Functions

R. R. Boix[1], **F. Mesa**[2], **and F. Medina**[1]

[1]Department of Electronics and Electromagnetism, College of Physics, University of Seville
Av. Reina Mercedes, s/n, Seville 41012, Spain
[2]Department of Applied Physics 1, School of Computer Engineering, University of Seville
Av. Reina Mercedes, s/n, Seville 41012, Spain

Abstract— The rational function fitting method has proved to be useful in the derivation of closed-form expressions of spatial domain Green's functions for multilayered media. However, former implementations of the rational function fitting method lead to Green's functions expressions that are not accurate in the far field when this far field is dominated by the continuous spectrum instead of being dominated by surface waves (as it happens in the case of lossy multilayered media). In this paper the authors introduce a novel implementation of the rational function fitting method which leads to Green's functions expressions that are accurate in the far field when this is dominated either by the continuous spectrum or by surface waves. In the new approach the far field contribution of the continuous spectrum to the Green's functions is obtained in closed form, and it is explicitly added to the total least squares approximations of the Green's functions.

1. INTRODUCTION

The application of the method of moments (MoM) to the solution of mixed potential integral equations (MPIE) has proven to be an efficient numerical tool for the analysis of planar circuits and antennas [1]. In order to solve the MPIE arising from the analysis of planar structures, it is necessary to calculate the spatial domain Green's functions (GF) for the scalar and vector potentials in multilayered media. These GF can be determined via numerical computation of infinite integrals that are commonly known as Sommerfeld integrals (SI). However, the highly-oscillatory nature of the integrands involved makes the numerical computation of SI cumbersome and time consuming [1]. Among the many different methods that have been proposed for speeding up the evaluation of Sommerfeld integrals, the most efficient ones are the discrete complex image method (DCIM) [2] and the rational function fitting method (RFFM) [3, 4]. These two methods lead to closed-form expressions of the GF that either primarily consist of spherical waves (DCIM) or primarily consist of cylindrical waves (RFFM).

Whereas the DCIM usually fails to reproduce the far field behavior of the GF of a multilayered substrate [5], the RFFM seems to be especially suitable for that purpose as demonstrated in [3] and [4]. This is based on the fact that the far field behavior of the GF is frequently dominated by cylindrical surface waves whose amplitudes and propagation constants are well predicted by the RFFM (see [3, Table I] and [4, Table I]). Unfortunately, the far field behavior of the spatial domain GF is not only contributed by the surface waves but is also contributed by the so-called continuous spectrum (the surface waves are related to poles of the spectral domain GF located on the proper Riemann sheet, and the continuous spectrum is related to the branch point singularities of the spectral domain GF [6, 7]). In lossless multilayered media, the surface waves contribution usually dominates over the continuous spectrum contribution in the far field [7] (there are exceptions to this rule, as it happens in the case of GF without TM spectral proper poles at frequencies where TE surface waves are not excited [1, eqn. (104)]) and when this occurs, the RFFM described in [3] and [4] tends to provide accurate results in the far field. However, in lossy multilayered media, the cylindrical surface waves attenuate and, after a certain distance between source and observation points, the continuous spectrum dominates the far field [7]. As a consequence of this, in this case the RFFM of [3] and [4] fails to provide accurate results in the far field.

In this paper we present a novel implementation of the RFFM approach of [4], which leads to accurate values of the GF in the far field when the far field is dominated by surface waves as well as by the continuous spectrum. In the novel approach, the far field contribution of the continuous spectrum to the GF is first derived in closed form both in the spatial domain and in the spectral domain (in fact, although the far field behavior of the continuous spectrum when all the poles are far from the branch points is known to be different from that observed when some of

the poles are very close to the branch points [7, 8], these two different situations are conveniently handled by the expression of the far field contribution of the continuous spectrum that has been derived in the paper). Once the contribution of the continuous spectrum is available, its spectral version is explicitly extracted from the spectral domain GF functions and the method of total least squares is subsequently applied to the resulting expressions [4]. This procedure leads to closed-form expressions of the spatial domain GF that explicitly contain information about the far field contributions of both the surface waves and the continuous spectrum.

2. THEORY

Figure 1 shows a multilayered medium consisting of lossy layers of complex permittivity $\varepsilon_i = \varepsilon_0\varepsilon_{ri}(1 - j\tan\delta_i)$ and thickness $h_i (i = 1, \ldots, N_{\text{la}})$. The multilayered medium is assumed to be limited by free-space at the upper end, and by a perfect electric conductor (PEC) at the lower end. Let (x', y', z') be the coordinates of an infinitesimal dipole source arbitrarily placed either in the multilayered medium or in free space, and let (x, y, z) be the coordinates of an observation point placed in the same environment. If we restrict ourselves to formulation C of Michalski and Zheng for MPIE [9], the GF for the scalar potential as well as the elements of the dyadic GF for the vector potential can all be obtained by means of SI of the type

$$G_n\left(\rho, z, z'\right) = S_n\left\{\widetilde{G}_n\left(k_\rho, z, z'\right)\right\} = \frac{1}{4\pi}\int_{-\infty(\text{SIP})}^{\infty} \widetilde{G}_n\left(k_\rho, z, z'\right) H_n^{(2)}\left(k_\rho\rho\right) k_\rho^{n+1} k_\rho \quad (n = 0, 1) \quad (1)$$

where $\rho = \sqrt{(x - x')^2 + (y - y')^2}$, $H_n^{(2)}(\cdot)$ is the Hankel function of order n and second kind, $\widetilde{G}_n\left(k_\rho, z, z'\right)$ stands for the spectral domain GF (Hankel transform of $G_n\left(\rho, z, z'\right)$), and SIP is an integration path placed in the first and third quadrants of the complex k_ρ plane that detours around the poles and branch cut of $\widetilde{G}_n\left(k_\rho, z, z'\right)$ as shown in Fig. 2 [1]. For an arbitrary multilayered medium, the functions $\widetilde{G}_n\left(k_\rho, z, z'\right)$ can be obtained by means of the algorithms shown in the Appendix II of [9].

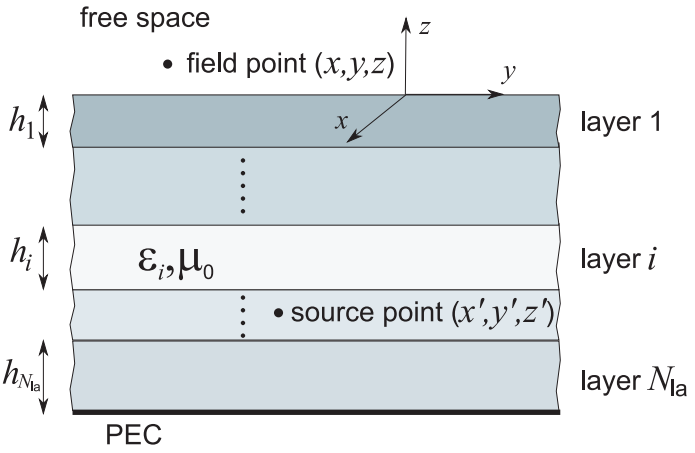

Figure 1: Multilayered lossy medium terminated by a PEC at the bottom.

By invoking Cauchy's theorem, the original Sommerfeld integration path (SIP) of eqn. (1) can be deformed in the proper Riemann sheet of the complex k_ρ plane into a set of paths $C_{SW,i} (i = 1, \ldots, N_{sw})$ that surround the surface-wave poles of $\widetilde{G}_n(k_\rho, z, z')$ plus an additional path C_b that surrounds the branch cut of $\widetilde{G}_n(k_\rho, z, z')$ at $k_\rho = k_0 = \omega\sqrt{\epsilon_0\mu_0}$ (see Fig. 2 for more details). After contour deformation, the SI of eqn. (1) can be expressed as the sum of two contributions

$$G_n\left(\rho, z, z'\right) = G_n^{\text{DS}}\left(\rho, z, z'\right) + G_n^{\text{CS}}\left(\rho, z, z'\right) \quad (n = 0, 1) \quad (2)$$

where $G_n^{\text{DS}}\left(\rho, z, z'\right)$ is the discrete spectrum that accounts for the contribution of the surface-wave poles, and $G_n^{\text{CS}}\left(\rho, z, z'\right)$ is the continuous spectrum that accounts for the contribution of the branch point [6].

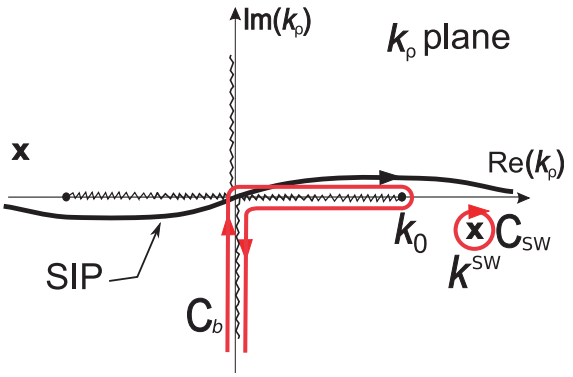

Figure 2: Original and deformed integration paths employed in the determination of the Sommerfeld integrals. Only one surface-wave pole, k^{sw}, is assumed to be located on the proper Riemann sheet.

In particular, the discrete spectrum can be written as

$$G_n^{\mathrm{DS}}\left(\rho,z,z'\right)=-\frac{j}{2}\sum_{i=1}^{N_{SW}}R_{n,i}(z,z')H_n^{(2)}\left(k_i^{SW}\rho\right)\left(k_i^{SW}\right)^{(n+1)}\quad(n=0,1)\tag{3}$$

where $k_i^{sw}(i=1,\ldots,N_{sw})$ are the poles of $\widetilde{G}_n(k_\rho,z,z')$ that are placed in the proper Riemann sheet of the complex k_ρ plane (these poles are equal to the wavenumbers of the surface-wave modes of the multilayered substrate that are above cutoff) and $R_{n,i}(z,z')$ are the residues of $\widetilde{G}_n(k_\rho,z,z')$ at these poles. The continuous spectrum is given by

$$G_n^{\mathrm{CS}}\left(\rho,z,z'\right)=\frac{1}{4\pi}\int_{C_b}\widetilde{G}_n\left(k_\rho,z,z'\right)H_n^{(2)}\left(k_\rho\rho\right)k_\rho^{n+1}\mathrm{d}k_\rho\quad(n=0,1)\tag{4}$$

where the integral has to be computed along the path C_b in Fig. 2 that surrounds the Sommerfeld branch cut.

When the asymptotic expansion of the Hankel function $H_n^{(2)}$ for large argument [10] is used in eqn. (3), it is possible to show that the far field behavior of the discrete spectrum for large ρ is given by

$$G_n^{\mathrm{DS}}\left(\rho,z,z'\right)|_{\rho\gg}\propto\frac{e^{j\frac{n\pi}{2}}}{\sqrt{\rho}}\sum_{i=1}^{N_{SW}}R_{n,i}\left(z,z'\right)e^{-jk_i^{SW}\rho}\left(k_i^{SW}\right)^{n+1}\quad(n=0,1)\tag{5}$$

Also, if we carry out an asymptotic expansion of the integral shown in eqn. (4) for large ρ [6, 8, 11, 12], it is possible to show that the far field behavior of the continuous spectrum for large ρ is given by

$$G_n^{\mathrm{CS}}\left(\rho,z,z'\right)|_{\rho\gg}\propto\begin{cases}\dfrac{e^{-jk_0\rho}}{\rho^2} & \text{all poles are far from the branch point}\\ \dfrac{e^{-jk_0\rho}}{\rho} & \text{one pole is very close to the branch point}\end{cases}\tag{6}$$

The far field behaviors of $G_n^{\mathrm{DS}}\left(\rho,z,z'\right)$ and $G_n^{\mathrm{CS}}\left(\rho,z,z'\right)$ for large ρ appear simultaneously. In the lossless case $G_n^{\mathrm{DS}}\left(\rho,z,z'\right)$ usually dominates the far field since it decays like $\rho^{-1/2}$ for large ρ, and $G_n^{\mathrm{CS}}\left(\rho,z,z'\right)$ shows a faster decay for large ρ. However, there are two important situations where $G_n^{\mathrm{CS}}\left(\rho,z,z'\right)$ dominates the far field:

1. *Lossless multilayered medium when the spectral domain GF does not have proper poles* ($N_{sw}=0$). This occurs to the spectral domain GF $\widetilde{K}_{xx}^A(k_\rho,z,z')$ (xx component of the vector potential GF) at low frequencies. It turns out that $\widetilde{K}_{xx}^A(k_\rho,z,z')$ only has poles associated with TE surface waves of the multilayered substrate [1], and since all these surface waves have nonzero cutoff frequency, $\widetilde{K}_{xx}^A(k_\rho,z,z')$ does not have proper poles below the cutoff frequency of the dominant TE surface wave. Thus, in the range of frequencies where all TE modes are below cutoff, the discrete spectrum of $K_{xx}^A(\rho,z,z')$ does not exist, and the far field behavior of $K_{xx}^A(\rho,z,z')$ is that of the continuous spectrum [1, Sect. 7.2.2].

2. *Multilayered medium with non-negligible losses.* In this case the propagation constants of the surface waves propagating along the multilayered substrate are complex $k_i^{SW} = \beta_i^{SW} - j\alpha_i^{SW}$ where β_i^{SW} and α_i^{SW} are real positive numbers ($i = 1, \ldots, N_{sw}$)), and this leads to the presence of exponential attenuation factors (of the type $e^{-\alpha_i^{SW}\rho}$ in the terms under the summation symbol of (5). As a consequence of this, the far field behavior of the GF for large ρ is dominated by $G_n^{\mathrm{CS}}(\rho, z, z')|_{\rho\gg}$ since the exponential factor in eqn. (6) does not suffer from attenuation [7].

In a recent paper [4] we presented an original implementation of the RFFM focused on the determination of closed-form expressions of spatial domain multilayered GF that are valid both in the near field and in the far field. In this approach the spatial domain GF were expressed in terms of a singular near-field term plus a short series of cylindrical waves whose complex amplitudes and propagation constants were computed by means of the method of total least squares. This method works adequately when the far field behavior of the GF for large ρ is of the type shown in eqn. (5) since the decay of the type $\rho^{-1/2}$ is well accounted for by the cylindrical waves [4]. Unfortunately, the method of [4] cannot provide the far field of the GF when this is dominated by the continuous spectrum since the cylindrical waves cannot reproduce the behavior shown in eqn. (6). In this paper we introduce a modified version of the method of [4] that makes it possible to obtain accurate values for the far field of the GF, not only when the far field is dominated by the discrete spectrum but also when it is dominated by the continuous spectrum. In order to reach this goal, we carry out an asymptotic analysis similar to that of [12] in order to obtain a closed-form expression $G_n^{\mathrm{CS,ff}}(\rho, z, z')$ for the far field behavior of the continuous spectrum, i.e.,

$$G_n^{\mathrm{CS}}\left(\rho, z, z'\right)|_{\rho\gg} \propto G_n^{\mathrm{CS,ff}}\left(\rho, z, z'\right) \quad (n = 0, 1) \tag{7}$$

The expression of $G_n^{\mathrm{CS,ff}}\left(\rho, z, z'\right)$ contains information about the pole $k_\rho = k_p$ of $\widetilde{G}_n(k_\rho, z, z')$ which is closest to the branch point $k_\rho = k_0$ since $G_n^{\mathrm{CS,ff}}\left(\rho, z, z'\right)$ must reproduce the far field of $G_n^{\mathrm{CS}}\left(\rho, z, z'\right)$ both when k_p is far from the branch point and when k_p is very close to the branch point (see eqn. (6)). The pole k_p and its residue $R_p(z, z')$ are determined by carrying out a truncated Laurent expansion of $\widetilde{G}_n(k_\rho, z, z')$ in the neighborhood of $k_\rho = k_0$, and by fitting the Laurent expansion to the exact values of $\widetilde{G}_n(k_\rho, z, z')$ in that neighborhood. It should be also pointed out that the asymptotic expression of $G_n^{\mathrm{CS,ff}}\left(\rho, z, z'\right)$ is conveniently chosen in such a way that it not only reproduces the far field of $G_n^{\mathrm{CS}}\left(\rho, z, z'\right)$ but it also has closed-form Hankel transform $G_n^{\mathrm{CS,ff}}\left(k_\rho, z, z'\right)$ (i.e., its spectral domain version can be obtained in closed-form).

For fixed values of z and z', once we know the values of k_p and $R_p(z, z')$ and we know the expression of $G_n^{\mathrm{CS,ff}}\left(\rho, z, z'\right)$, we propose to approximate the spectral domain GF $\widetilde{G}_n(k_\rho, z, z')$ by means of the following expression

$$\widetilde{G}_n(k_\rho, z, z') \approx \widetilde{G}_n^{as}(k_\rho, z, z') + \widetilde{G}_n^{\mathrm{CS,ff}}\left(k_\rho, z, z'\right) + \frac{2R_p(z, z')k_p}{k_\rho^2 - k_p^2} + \sum_{i=1}^{M} \frac{a_{n,i}(z, z')}{k_\rho^2 - \left[p_{n,i}(z, z')\right]^2} \quad (n = 0, 1) \tag{8}$$

where $\widetilde{G}_n^{as}(k_\rho, z, z')$ (asymptotic behavior of $\widetilde{G}_n(k_\rho, z, z')$ for large k_ρ) has been defined in [4], and the coefficients $a_{n,i}(z, z')$ and $p_{n,i}(z, z')$ must be obtained via the method of total least squares as explained in [4]. Note that whereas the contribution of the pole k_p to $\widetilde{G}_n(k_\rho, z, z')$ is explicitly accounted for in the approximation eqn. (8), the contribution of the rest of the poles is assumed to be accounted for by the method of total least squares [4]. This is due to the fact that the pole k_p may be so close to the branch point $k_\rho = k_0$ that it may affect the behavior of the continuous spectrum [7], and to a certain extent, we cannot consider this pole as a separate part of the continuous spectrum.

The spatial counterpart of eqn. (8) leads to the following closed-form expressions for the GF of the multilayered medium of Fig. 1

$$\begin{aligned} G_n(\rho, z, z') \;=\; & G_n^{as}(\rho, z, z') + G_n^{\mathrm{CS,ff}}\left(\rho, z, z'\right) - \frac{j}{2} R_p(z, z') k_p^{n+1} H_n^{(2)}\left(k_p\rho\right) \\ & - \frac{j}{4} \sum_{i=1}^{M} a_{n,i}(z, z') \left[p_{n,i}(z, z')\right]^n H_n^{(2)}\left[p_{n,i}(z, z')\rho\right] \quad (n = 0, 1) \end{aligned} \tag{9}$$

In eqn. (9) the Hankel functions account for the far field behavior of the discrete spectrum of $G_n(\rho, z, z')$ and the term $G_n^{\mathrm{CS,ff}}(\rho, z, z')$ accounts for the far field behavior of the continuous spectrum of $G_n(\rho, z, z')$. Therefore, the far field behavior of $G_n(\rho, z, z')$ for large is always accurately reproduced by eqn. (9) despite of the component of $G_n(\rho, z, z')$ (see eqn. (2)) dominating the far field.

The numerical results obtained for $G_n(\rho, z, z')$ via eqn. (9) have been compared with numerical results obtained via the approach of [4] and with numerical results obtained via brute-force numerical integration of Sommerfeld integrals. These comparisons have shown that whereas the approach of [4] fails to provide accurate far field results in the cases where the far field is dominated by the continuous spectrum, the approach presented in this paper (eqn. (9)) provides accurate far field results both when the far field is dominated by surface waves and when the far field is dominated by the continuous spectrum. All the comparisons between different sets of results will be presented at the Symposium.

ACKNOWLEDGMENT

This work has been supported by the Spanish Ministerio de Educación y Ciencia and European Union FEDER funds (project TEC2004-03214), and by Junta de Andalucía (project TIC–53).

REFERENCES

1. Mosig, J. R., "Integral equation technique," *Numerical Techniques for Microwave and Millimeter-Wave Passive Structures*, edited by T. Itoh, 133–213, Wiley, New York, 1989.
2. Aksun, M. I., "A robust approach for the derivation of closed-form Green's functions," *IEEE Trans. Microwave Theory Tech.*, Vol. 44, 651–658, May 1996.
3. Kourkoulos, V. N. and A. C. Cangellaris, "Accurate approximation of Green's functions in planar stratified media in terms of a finite sum of spherical and cylindrical waves," *IEEE Trans. Antennas Propagat.*, Vol. 54, 1568–1576, May 2006.
4. Boix, R. R., F. Mesa, and F. Medina, "Application of total least squares to the derivation of closedCform Green's functions for planar layered media," *IEEE Trans. Microwave Theory Tech.*, Vol. 55, 268–280, Feb. 2007.
5. Shuley, N. V., R. R. Boix, F. Medina, and M. Horno, "On the fast approximation of Green's functions in MPIE formulations for planar-layered media," *IEEE Trans. Microwave Theory Tech.*, Vol. 50, 2185–2192, Sept. 2002.
6. Felsen, L. B. and N. Marcuvitz, *Radiation and Scattering of Waves*, Prentice Hall, New York, 1973.
7. Mosig, J. R. and A. A. Álvarez-Melcón, "Green's functions in lossy layered media: integration along the imaginary axis and asymptotic behavior," *IEEE Trans. Antennas Propagat.*, Vol. 51, 3200–3208, Dec. 2003.
8. Demuynck, F. J., G. A. E. Vandenbosch, and A. R. van de Capelle, "The expansion wave concept — Part I: Efficient calculation of spatial Greens functions in a stratified dielectric medium," *IEEE Trans. Antennas Propagat.*, Vol. 46, 397–406, March 1998.
9. Michalski, K. A. and D. Zheng, "Electromagnetic scattering and radiation by surfaces of arbitrary shape in layered media, part I: theory," *IEEE Trans. Antennas Propagat.*, Vol. 38, 335–344, Mar. 1990.
10. Abramowitz, M. and I. Stegun, *Handbook of Mathematical Functions*, Dover Publications, 9th Edition, New York, 1970.
11. Marin, M., S. Barkeshli, and P. H. Pathak, "Efficient analysis of planar microstrip geometries using a closed-form asymptotic representation of the grounded dielectric slab Green's function," *IEEE Trans. Microwave Theory Tech.*, Vol. 37, 669–679, Apr. 1989.
12. Baccarelli, P., P. Burghignoli, F. Frezza, A. Galli, G. Lovat, and D. R. Jackson, "Approximate analytical evaluation of the continuous spectrum in a substrate-superstrate dielectric waveguide," *IEEE Trans. Microwave Theory Tech.*, Vol. 50, 2690–2701, Dec. 2002.

Energy-efficient Data Aggregation Protocol Based on Static Clustering for Wireless Sensor Networks

S.-G. Deng[1, 2], **L.-F. Shen**[1], **and X.-R. Zhu**[1]

[1]National Mobile Communications Research Laboratory, Southeast University, China
[2]Hunan City University, China

Abstract— Using clustering and aggregation enables better resource allocation and helps improve power control in wireless sensor networks (WSNs). Nevertheless, repeated clustering would increase the overhead and reduce network lifetime. An energy-efficient data aggregation protocol based on static clustering (EDASC) is proposed to acquire good network performance. Simulation results show that this approach makes network lifetimes much longer and remarkably reduces control overhead.

1. INTRODUCTION

Wireless sensor networks (WSNs) are typically comprised of a large number of sensors which are randomly deployed for detecting and monitoring tasks [1]. In this network, a typical application is the gathering of sensed data to a distant base station (BS). The main constraint of sensor nodes is their very low finite battery energy, while limiting the lifetime and quality of the network. For that reason, the protocol running on sensor networks must efficiently reduce the node energy consumed in order to achieve a longer network lifetime. Using clustering and aggregation enables better resource allocation and helps improve power control in wireless sensor networks [2–4]. Recently, some data aggregation protocols based on dynamic clustering, such as LEACH [2], HEED [4] and something else, have been proposed for WSNs. In these protocols, the process of clustering is divided into many cycles. This repeated clustering brings about substantive overheads and consumes much sensor energy as a result. The static clustering method [2], that clusters and CHs remain fixed throughout the lifetime of the network, is the effective policy for dealing with these problems. Nevertheless, fixed CH makes energy consumption of each CH very fast. In this paper, we first design a new static clustering policy by utilizing Hausdorff distance. And then, an energy-efficient data aggregation protocol based on static clustering (EDASC) is proposed. This approach can significantly increase the network lifetime and reduce the control overhead.

2. STATIC CLUSTERING METHOD

The static clustering method in our proposed protocol is based on Hausdorff distance. According to [5], we assume that sensor nodes are partitioned into M cluster $\{G_1, G_2, \ldots, G_M\}$. The Euclidean distance $d(v_m, v_n)$ between node m and node n is given by

$$d(v_m, v_n) = \sqrt{(x_m - x_n)^2 + (y_m - y_n)^2} \tag{1}$$

The smallest distance $d^*(v_m, G_k)$ from node m of a cluster to another cluster G_k is given by

$$d^*(v_m, G_k) = \min\{d(v_m, v_n) : v_n \in G_k\} \tag{2}$$

And the directed Hausdorff distance $h(G_j, G_k)$ from cluster G_j to G_k is given by

$$h(G_j, G_k) = \max\left(d^*(v_m, G_k) : v_m \in G_j\right) \tag{3}$$

Then, the Hausdorff distance $H(G_j, G_k)$ between cluster G_j and G_k is given by

$$H(G_j, G_k) = \max\left(h\left(G_j, G_k\right), h\left(G_k, G_j\right)\right) \tag{4}$$

That is to say, if the Hausdorff distance is d, and then every node in G_j must be within a distance d from some nodes in G_k and vice versa.

Let each node have the choice of two transmission power levels just like the Berkeley Motes [4]. The low transmission power level, with a range r, is used to cover the intra-cluster transmission. And the high power level, with a range R, is for reaching neighboring CHs. To guarantee communication efficiency and network connectivity, we must research network coverage requirement before

static clustering. Assume two neighboring clusters j and k as shown in Fig. 1. Then, the worst coverage instance that the distance between the closest two nodes (i.e., A and B nodes) of these two clusters is $2r$. If both C and D nodes are respectively CHs of cluster i and j, which are reachable from each other, then their minimum transmission range R should be $4r$ as shown. Therefore, we define inter-cluster distance as $4r$, and intra-cluster distance as r in this case.

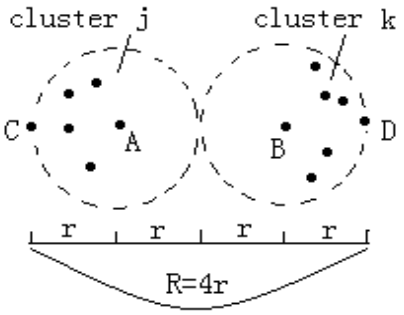

Figure 1: Distributing of two neighboring clusters.

In this paper we assume that each node knows all its neighbors through broadcasting a topology discovery message. Through the above discussing, we can construct a new distributed clustering algorithm based on static clustering approach. The details are as follows: In the beginning, the BS appoints an initiator for starting the clustering operation. Then, the initiator broadcasts a clustering message and awaits join-requests from neighboring nodes. And it then admits cluster members according to the clustering conditions. The two conditions must be satisfied if a node wants to join a cluster: (a) The Hausdorff distance between the node and the cluster must be smaller than r. (b) If the node is admitted, the Hausdorff distance between two neighboring clusters must be no larger than $3r$ to guarantee inter-cluster communication.

Upon receiving the confirmation message, the initiator updates its membership list and informs its neighboring clusters. If more than one cluster accords with the two conditions, the candidate node joins the cluster with the smallest Hausdorff distance. If all the formative clusters cannot satisfy the two conditions, the candidate node will form a new cluster of itself.

3. EDASC PROTOCOL DETAILS

Data aggregation minimizes the number of transmissions and saves energy. Static clustering based on Hausdorff distance can largely reduce control overhead and maintain network connectivity. Alternating the role of CH can balance energy among these clusters members and efficiently prolong network lifetime. In order to get good network performance, we combine all policies above, and propose EDASC protocol by constructing data aggregation (DA) tree. The operation of EDASC is divided into rounds. Each round begins with a CHs selection phase when the clusters are formed. Followed by a set-up phase when the DA tree is constructed. And followed again a data transmission phase when data are transferred from the nodes to the CH and on to BS.

Once a distributed static clustering is formed, CH needs to be scheduled, and the node with the largest residual energy is selected as the CH for each cluster. CH schedule is calculated by comparing residual energy for each cluster. In the same way, the BS broadcasts them to correlative nodes. According to this method, CHs are ascertained for all clusters all the time.

We choose the node energy model proposed in [2]. In this radio model, energy is consumed only when a CH is transmitting data, receiving data or performing data aggregation. The energy used in a CH during a single frame is

$$E_{\mathrm{CH}} = LE_{elec}(N-1) + LE_{elec}n + LE_{DA}(N+n) + LE_{elec} + I\varepsilon_{MP}d^4 \tag{5}$$

Where I is the number of bits in each data message, and N is the number of nodes in a cluster, n is the number of messages that the CH receives from other CHs and d is the distance between CHs. We assume perfect data aggregation.

If the distance between two CHs is far away, the cost of sending data between each other becomes very large and the CHs will die quickly. In order to maximize the network lifetime, we establish a DA tree among these CHs by computing link costs. What link costs is the cost of transmission between two adjacent CHs. The routing information is computed by using approximate Prim's

minimum spanning tree algorithm where the CH of the closest BS is the root. The algorithm works as follows: Initially, we put a CH in the tree which is the closest BS in our case. After that, in each iteration course we select the minimum weighted edge from a vertex in the tree to a vertex not in the tree, and add that edge to the tree. In our case this means that the vertex just included in the tree will send its data through that edge. We will repeat this procedure until all CHs are added to the tree. The running time complexity of the algorithm is $O(n^2)$ assuming there are n CHs in the network.

After the DA tree is constructed, the data are sent from the nodes to their own CHs respectively. Intra-cluster communication protocol is CSMA/CA during the transmission. Once the CH receives all the data, it performs data aggregation to enhance the common signal and sends their data to BS by our DA tree. If CHs topology changes during the network lifetime, the BS reconstructs DA tree and broadcasts them to all nodes. CH schedule for each cluster is recalculated after a period.

4. SIMULATION RESULTS

In order to evaluate the performance of our algorithms, we simulated four different protocols: LEACH, HEED, S-C (traditional static clustering), and EDASC. The last one is our protocol. Note that for these simulations, the different numbers of sensor nodes ranging from 100 to 500 were randomly throughout the 100 m × 100 m area. For ease of comparison, the simulation parameters are chosen to be the same as those in [4], repeated here for ease of reference. Each data point shown is the average of 8 experiments.

The metrics of interest are: network lifetime, which is the time elapsed until the first node in the network depletes its energy, and average control overhead, which is the average total control bytes transmitted for each round.

Figure 2 shows that the lifetime of the network between LEACH, HEED, S-C, and EDASC protocols vary with the number of nodes from 100 to 500. It is obvious that EDASC is uniformly better independent of node density. Well, this may due to the following reasons. First, static clustering makes cluster reformulation eliminated and energy of each node economized in EDASC. Second, alternating the role of CH can balance energy consumption among these clusters member. Third, our DA tree based on approximate Prim's minimum spanning tree algorithm is effective in prolonging the lifetime of CHs.

We can see from Fig. 3 that EDASC has fewer average control overheads than other protocols. The main reason is that EDASC selects static clustering policy and possesses the longest network lifetime. Due to using clustering only once, static clustering possesses fewer control overheads than dynamic clustering. As the number of node increases, the number of information packets increases, more control messages are transmitted, and the total control bytes increase.

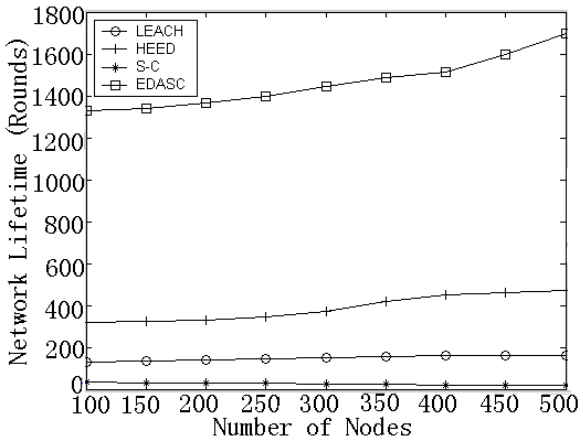

Figure 2: Network lifetime as a function of number of nodes.

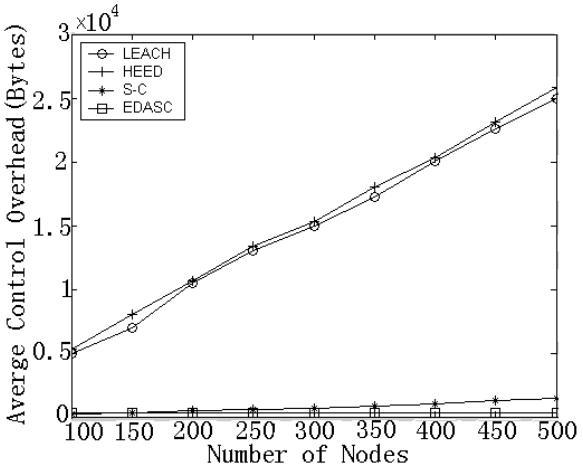

Figure 3: Average control overhead as a function of number of node.

5. CONCLUSION

Although traditional static clustering can reduce control overhead, network connectivity is destroyed due to the alternation of CHs. The static clustering based on Hausdorff distance effectively resolves

this problem. According to this clustering policy, a new protocol, which combines balance energy and approximates minimum spanning tree algorithm, is proposed for wireless sensor networks. Simulation results show that EDASC can remarkably extend the network lifetime and reduce control overhead.

ACKNOWLEDGMENT

This work was supported in part by the National Natural Science Foundation of China (No. 60472053).

REFERENCES

1. Akyildiz, I. F., W. Su, Y. Sankarasubramaniam, and E. Cayirci, "Wireless sensor networks: A survey," *Computer Networks*, Vol. 38, No. 4, 393–422, 2002.
2. Heinzelman, W., A. Chandrakasan, and H. Balakrishnan, "An application-specific protocol architecture for wireless microsensor networks," *IEEE Trans. Wireless Comm.*, Vol. 1, No. 4, 660–670, Oct. 2002.
3. Yu, Y., B. Krishnamachari, and V. K. Prasanna, "Energy-latency tradeoffs for data gathering in wireless sensor networks," *Proc. IEEE INFOCOM*, Apr. 2004.
4. Ossama, Y. and F. Sonia, "HEED: A hybrid, energy-efficient, distributed clustering approach for Ad hoc sensor networks," *IEEE Trans. Mobile Computing*, Vol. 3, No. 4, 366–379, 2004.
5. Huttenlocher, D. P., G. A. Klanderman, and W. J. Rucklidge, "Comparing images using the hausdorff distance," *IEEE Trans. Pattern Analysis and Machine Intelligence*, Vol. 15, No. 9, Sep. 1993.

An Inverse-scattering Iterative Algorithm for EM and Seismic Imaging

Jing Ba[1], **Huizhu Yang**[1], **Jianhua Li**[2], **and Mengqiu Guo**[3]

[1]Tsinghua University, China
[2]GL Geophysical Laboratory, USA
[3]Geological and Geophysical Institute, China

Abstract— Based on the inverse-scattering series (ISS) theory, we presented an iterative algorithm which can numerically solve a higher order ISS term with all lower order ISS terms determined. This work differs from the leading order inverse scattering (LOIS) algorithm [5, 9] and the higher order scattering (HOIS) algorithm that non ISS terms are ignored in the multi-dimensional imaging. Born and WKBJ approximations are used to solve the first order term in ISS series, while the higher order terms are calculated through a band-limited discrete Fourier transform. In the iterative method, we used seismic and electromagnetic differential integral equations to reduce the costs. Our method can be used to solve seismic and electromagnetic inverse problem in geophysics and environmental engineering etc. applications.

1. INTRODUCTION

Inverse-scattering methods are introduced by Weglein et al. (2000) to migrate seismic reflection data to the correct depth in Seismic imaging problem. Comparing with some common imaging methods, inverse-scattering methods have the advantage to image the singularity interface between sublayers with a reference background velocity near the earth surface, and do not need more sublayer knowledge, for example, ISS imaging method do not need the P wave velocity in each layer's material, which is extremely needed in migration imaging method. Following this work, Weglein et al. (2001, 2002) extract task-specific subseries from the inverse scattering series and prove them to be responsible for locating reflectors at the correct spatial location. Shaw et al. [5, 6] isolate a leading order inverse-scattering series (LOISS) and study the leading order terms cooperation algorithm and the convergence properties for 1-D imaging problems. Liu et al. [3] extend the 1D non-linear imaging algorithms to 2D environment. A 2-D depth-only imaging prototype algorithm is designed and tested on synthetic salt-model data.

In this work, considering the case of earth surface seismic observation, we will derive the 3D analytical expressions for high order ISS terms based on Born and WKBJ approximations. Then, the ISS expressions will be degenerated to 1D and 2D cases so as to solve the 1D and 2D imaging problems. In numerical solution, the ISS terms are calculated with the discrete Fourier transform to process the band-limited seismic records. At last, the algorithm is tested with one 1D models and two 2D models.

Recent, we use AGILD and GL seismic and electromagnetic modeling and inversion method by Xie and Li in [8–14] to make seismic and electromagnetic imaging. We find that the AGILD and GL joint inversion will improve the resolution of the imaging.

2. INVERSE-SCATTERING SERIES

The acoustic wave equation in the frequency domain is

$$(\nabla^2 + \frac{\omega^2}{c^2(\vec{x}')})\psi(\vec{x}';\omega) = 0 \tag{1}$$

where c is the velocity. ω is the angular frequency. $\psi(\vec{x}';\omega)$ is the displacement wavefield.

Apply Green's Theorem to Equation (1) so that we get [5]

$$\psi = \psi_0 + \psi_1 + \psi_2 + \cdots = \sum_{n=0}^{\infty} \psi_n \tag{2}$$

where

$$\psi_1(\vec{x}|\vec{x}_s;\omega) = \iiint_{-\infty}^{+\infty} G_0(\vec{x}|\vec{x}';\omega)V(\vec{x}';\omega)\psi_0(\vec{x}'|\vec{x}_s;\omega)d\vec{x}' \tag{3}$$

$$\psi_2(\vec{x}|\vec{x}_s;\omega) = \iiint_{-\infty}^{+\infty} G_0(\vec{x}|\vec{x}';\omega)V(\vec{x}';\omega) \times \iiint_{-\infty}^{+\infty} G_0(\vec{x}'|\vec{x}'';\omega)V(\vec{x}'';\omega)\psi_0(\vec{x}''|\vec{x}_s;\omega)d\vec{x}''d\vec{x}' \tag{4}$$

$$\vdots$$

Let $\psi_0 = G_0$, Equation (2) can be written as

$$\psi = G_0 + G_0VG_0 + G_0VG_0 + G_0VG_0VG_0 + \cdots \tag{5}$$

The inverse series can be derived as ([2, 4]; Weglein et al., 2000)

$$V = V_1 + V_2 + V_3 + \cdots = \sum_{n=1}^{\infty} V_n \tag{6}$$

where V_n is defined as the portion of V that is nth order in the measured values of the scattering field [5].

$$(G_0V_1\psi_0)_m = (\psi_s)_m \tag{7}$$

$$(G_0V_2\psi_0)_m = -(G_0V_1G_0V_1\psi_0)_m \tag{8}$$

$$(G_0V_3\psi_0)_m = -(G_0V_1G_0V_1G_0V_1\psi_0)_m - (G_0V_2G_0V_1\psi_0)_m - (G_0V_1G_0V_2\psi_0)_m \tag{9}$$

$$\vdots$$

Considering Equation (7∼9), if V_1 has been solved from Equation (7), V_2 can be solved from Equation (8), and with V_1 and V_2 determined, V_3 can be solved in Equation (9). Therefore, Any higher order ISS term can be determined with all the lower order terms determined.

Introduce the velocity perturbation $\alpha_n = \frac{1}{k_0^2}V_n$, the infinite ISS can be determined by

$$(\psi_s)_m = k_0^2(G_0\alpha_1\psi_0)_m \tag{10a}$$

$$(G_0\alpha_{n+1}\psi_0)_m = -k_0^2(G_0\alpha_nG_0\alpha_1\psi_0)_m \tag{10b}$$

$$n = 1, 2, 3, 4, 5, \cdots$$

First, to analytically solve α_1 from the Equation (10a). Here ψ_0 is the reference wavefield observed in a homogenous media with the same reference velocity in whole area. It can be the first arrival P waves in seismic records if there are no scattering objects between source and receiver. ψ_s is the scattering displacement wavefield, which is the displacement increment caused by the media heterogeneity.

3. 1D ISS SEISMIC IMAGING

If we only consider the case of 1D problem, the seismic waves will only propagate in one direction. The Equation (29) and Equation (37) will come to

$$\alpha_1(z) = -\int_{-\infty}^{+\infty} \frac{1}{\tilde{S}(\omega)}\tilde{\psi}_s(\omega)e^{i(l_3z)}dl_3, \quad l_3 = 2k_0 \tag{11}$$

$$\alpha_n(z) = -k_0^2\alpha_{n-1}(z)F^{-1}\frac{\tilde{\alpha}_1(k_{z_p})}{k_0^2 - (k_{z_p} + k_0)^2} \tag{12}$$

The model in Figure 2(a) is a 1D acoustic medium model with a free surface and 5 sublayers, and Figure 2(b) is the corresponding velocity perturbation model. In forward modeling, we locate the source and the seismic receiver at the same point on earth surface. The imaging results with the first order term α_1 and ISS series to the order of 10 have been shown in Figure 3(a) and

Figure 3(b) respectively. Comparing Figure 3(b) with Figure 3(a), the high order terms seem to correct the deep interface locations which are wrong imaged with the first order term. The most obvious correction in this example is the interface between the fourth and the fifth layer, at the depth of 400 m. The imaging results with α_1 is nearly 20 meters deeper than the true value, and the ISS imaging results is no more than 5 meters.

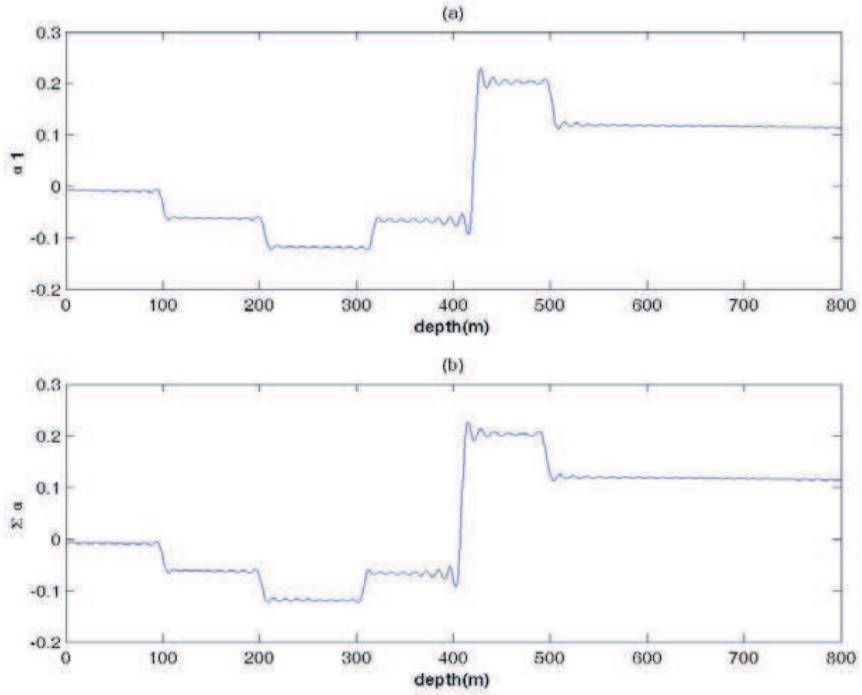

Figure 1: ISS imaging results for 1D seismic waves.

4. 2D ISS SEISMIC IMAGING

In the case of 2D seismic imaging, Equation (29) and Equation (37) will come to

$$\alpha_1(x,z) = -\iint_{-\infty}^{+\infty} \frac{4q_g q_s}{\tilde{S}(\omega)k_0^2}\tilde{\psi}_s(k_g,k_s,\omega)e^{i(l_1x+l_3z)}dl_1dl_3 \tag{13}$$

$$\alpha_n(x,z) = -k_0^2\alpha_{n-1}(x,z)F^{-1}\left(\frac{\tilde{\alpha}_1(k_{x_p},k_{z_p})}{k_0^2-(k_{x_P}+k_s)^2-(k_{z_p}+q_s)^2}\right) \tag{14}$$

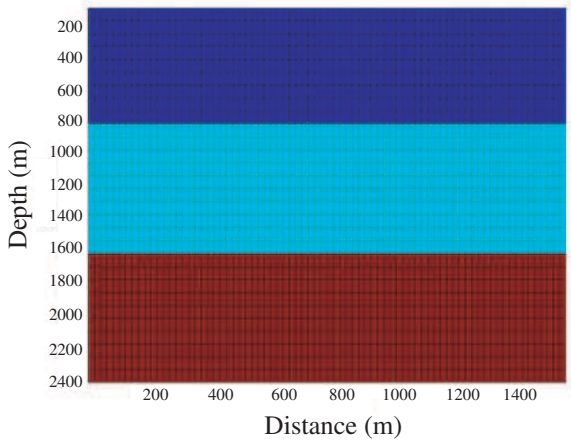

Figure 2: A 2D three-layer acoustic medium with two interfaces.

As to Equation (40), l_1 and l_3 are superdetermined by k_g, k_s, and ω, which means even though we do not consider the relation ships between velocity and frequency in forward modeling, the source's propagation frequency will still affect the velocity perturbation and the wave scattering on sublayer's interface. Therefore, to ignore the source frequency's influence on wave propagation scattering, an approximation should be made with $k_s \equiv 0$.

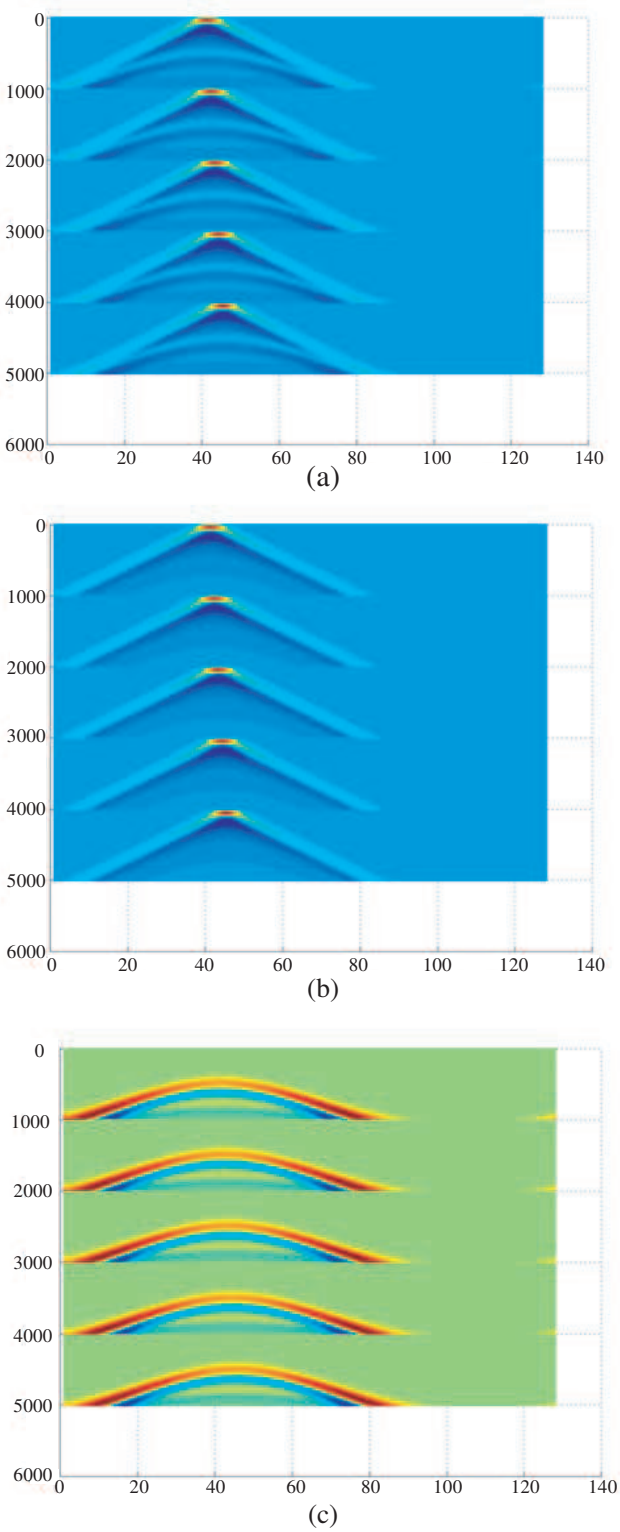

Figure 3: The synthesized seismic records. (a) The shot gather sections observed on earth surface of the three layer model, (b) The first arrival wavefields, (c) The scattering wavefields ψ_s.

For 2D ISS imaging, five processing steps should be followed as below.

1) Remove the first arrivals in the observed seismic records to obtain the scattering wavefields ψ_s.
2) Carry out three dimension Fourier transform on ψ_s over k_g, k_s, and ω.
3) Discretize l_1 and l_3 as the function of k_g, k_s, and ω. Keeping $k_s = 0$, calculate k_g value and ω value.
4) Draw out the two dimension matrix $\tilde{\psi}'_s(l_1, l_3)$ from $\tilde{\psi}_s(k_g, k_s, \omega)$.
5) Carry out inverse Fourier transform on $\tilde{\psi}'_s(l_1, l_3)$ and choose the real part as the first order velocity perturbation $\alpha_1(x, z)$.

The model in Figure 4 is a 2D three-layer acoustic medium with two interfaces. Here we locate the source and the seismic receiver on earth surface. In forward modeling, a pseudo-spectral method is used to simulate the wave propagation and the source center frequency is set at 50 Hz.The synthesized shot gather sections are shown in Figure 5(a), and the first arrival wavefields are shown in Figure 5(b). The scattering wavefields are calculated as Figure 5(c).

The ISS imaging results have been shown in Figure 6. It is obvious that the interfaces can be precisely located with the iterative imaging method.

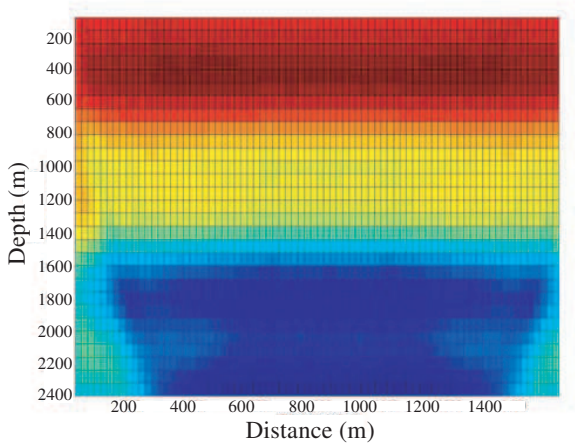

Figure 4: The three layer model imaging results.

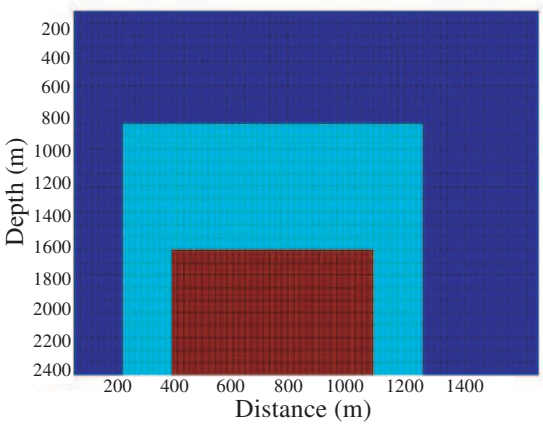

Figure 5: A 2D three-layer acoustic medium with vertical interfaces.

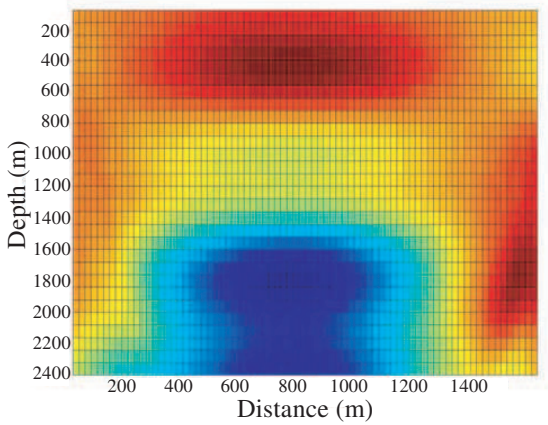

Figure 6: Imaging results of vertical interfaces.

For seismic observation is carried out on earth surface, the inadequate view angle make it much more difficult to locate a vertical sublayer interface than a horizontal interface. To investigate the imaging ability of the iterative ISS method, a velocity model with four vertical interfaces has been

tested with this method. The velocity model is shown in Figure 7, and the imaging results are shown in Figure 8.

It can be seen from Figure 8 that the imaging vertical interfaces are ambiguous and are contorted by the discrete Fourier transform base on the band-limited seismic data.

5. CONCLUSION

An iterative algorithm is presented in the paper based on the ISS theory and the discrete Four transform. The algorithm can be used for 3D seismic imaging of the sublayer interfaces with the surface-observed seismic data. The electromagnetic inversion and resistivity and dielectric imaging will be shown in next paper, because the page limitation. Any high order term in ISS can be calculated through this method as two approximations are made: 1) Propagating in the acoustic media, P wave will nearly keep an invariable velocity as frequency is changed in the seismic band; 2) the high order ISS terms will be independent of source wavenumber. The 1D and 2D examples are tested with the iterative method, and results show that the high order ISS terms can correct the deep interface locations which are wrong imaged with the first order term. Using surface-observed data, the horizontal interfaces can be precisely located with the iterative method, while the imaged vertical interfaces are much more ambiguous. The AGILD and GL are complete new and high resolution seismic and electromagnetic modeling and inversion methods by Xie and Li in [8–14]. We use AGILD method to make seismic and electromagnetic imaging. We will present the AGILD and GL joint inversion imaging in next paper in which resolution is improved.

ACKNOWLEDGMENT

This research is supported by the national basic research program of China (973 program, 2007CB209505). Additional support is provided by the China Petroleum & Chemical Corporation (wx2006-38), the National Science Fundation of China (10572072, 40674061).

REFERENCES

1. Clayton, R. W. and R. H. Stolt, "A Born-WKBJ inversion method for acoustic reflection data," *Geophysics*, Vol. 46, 1559–1567, 1981.
2. Jost, R. and W. Kohn, "Construction of a potential from a phase shift," *Phys. Rev.*, Vol. 87, 977–992, 1952.
3. Liu, F., A. B. Weglein, etc., "Multi-dimensional seismic imaging using the inverse scattering series," *SEG Annual Meeting*, New Orleans, 2006.
4. Moses, H., "Calculation of scattering potential from reflection coefficients," *Phys. Rev.*, Vol. 102, 559–567, 1956.
5. Shaw, S. A., "An inverse scattering series algorithm for depth imaging of reaction data from a layered acoustic medium," PhD Thesis, University of Houston, 2005.
6. Shaw, S. A., A. B. Weglein, etc., "Isolation of a leading order depth imaging series and analysis of its convergence properties for a 1D acoustic medium," *Journal of Seismic Exploration*, Vol. 13, 99–120, 2004.
7. Stolt, R. H., "Migration by Fourier transform," *Geophysics*, Vol. 43, 23–48, 1978.
8. Weglein, A. B., F. A. Gasparotto, etc., "An inverse-scattering series method for attenuating multiples in seismic reflection data," *Geophysics*, Vol. 62, 1975–1989, 1997.
9. Weglein, A. B., D. J. Foster, etc., "Predicting the correct spatial location of reflectors without knowing or determining the precise medium and wave velocity: initial concept, algorithm and analytic and numerical example," *Journal of Seismic Exploration*, Vol. 10, 367–382, 2002.
10. Xie, G., J. Li, M. Majer, D. Zuo, and M. Oristaglio, "3D electromagnetic modeling and nonlinear inversion," *Geophysics*, Vol. 65, No. 3, 804–822, 2000.
11. Xie, G. and J. Li, "New parallel stochastic global integral and local differential equation modeling and inversion," *Physics D*, Vol. 133, 477–487.
12. Xie, G., F. Xie, L. Xie, and J. Li, "GL method and its advantages for resolving historical difficulties," *Progress in Electromagnetics Research*, PIER 63, 141–152, 2006.
13. Xie, G. and J. Li, "Nonlinear integral equation of coefficient inversion of acoustic wave equation and TCCR iteration," *Science in China*, Vol. 32, No. 5, 513–523, 1989.
14. Xie, G., "A new iterative method for solving the coefficient inverse problem of wave equation," *Communication on Pure and Applied Math.*, Vol. 39, 307–322, 1986.

AGILD WMT Ray-tracing Tomography and Its Application

Jianhua Li[1,2], **Chien-Chang Lin**[1], **Ganquan Xie**[2], **and Michael Oristaglio**[3]

[1]Department of Mechanical and Automation Engineering, Da-Yeh University, Taiwan
[2]GL Geophysical Laboratory, USA
[3]Schlumberger Doll Research, USA

Abstract— To implement and develop a new ray-tracing method that provides a useful tool to analyze optical measurement sits and geophysical surface-to-surface, surface-to-borehole, and crosshole data. To develop next-generation wave propagation algorithm and codes for computational geophysics, computational mechanics, biomedical sciences, and interactive 3D wavelength matching topography. In this paper, A new wavelength matching topology method is developed to generate AGILD finite element mesh. The rays are accurately traced using the known velocity expression in the current element instead of in-layered or stratified medium. The wavelength matching topology and the curve ray tracing are combined to construct the AGILD FEM Ray Tracing tomography forward modeling and inversion algorithm.

1. INTRODUCTION

Ray tracing is a general technique from geometrical optics of modeling the path taken by light by following rays of light as they interact with material surfaces and earth surface and other stuctures' surface. It is used in the design of optical systems, such as camera lenses, microscopes, telescopes, binoculars, and geophysical instrument. The instrument design and measurement technology are developing progress. However, the measurement are mostly by observing, recording, and simple calculation using the experimental formula. The measurement data technology and the high resolution and accurate inpterpretion analysis is not match.

In this paper, we propose a new AGILD curve ray-tracing method. Our method is based on mechnical wave ray, eleastic/plastic wave ray and electromagnetic wave propagation in materials and interaction with the materials. The AGILD mechanical ans EM modeling are used to simulate the elastic/plastic and electromagnetic full wave propagation in the air, material, soil, and Earth subsurface etc macro and micro domain. From the simulation, we pick up the key ray and reflection and refraction parameters for our accurate curve ray tracing.

Our AGILD ray-tracying algorithm can be used to cooperate with the optical instrument for material mechanical and engineering geophysical measurement and intepretion.

2. AGILD WMT TOMOGRAPHY APPROACH

An AGILD wavelength matching topology method is developed to generate a finite element mesh that not only eliminates the complications posed by complex, unstructured computational grids, but also enhances the efficiency of the ray-tracing method. The rays are accurately traced using the known velocity expression in the current element instead of in-layered or stratified medium. Critical conditions for total refraction and total internal reflection have been developed and applied instead of older tracing. Therefore, we obtain not only the first arrival ray, but also the last arrival ray. Obviously, the last arrival ray brings us more information about the deeper subsurface. These calculations are ideally suited to take advantage of developments in parallel computing. The method has been implemented for three-dimensional case, in which the wavelength matching topology automatic mesh method has been combined with 3D cubic-hole element [1]. The wavelength matching topology and the curve ray tracing are combined to construct the Finite Element Ray Tracing tomography forward modeling and inversion algorithm.

2.1. The Acoustic Wave Equation

The acoustic equation characterizes the all wave's properties and wave ray properties, and comparing with elastic/plastic and electromagnetic wave equations, it is a simple equation. Therefore, we describe our method through the acoustic wave equation:

$$\nabla(k(r)\nabla u(r,t)) - \frac{\partial^2 u(r,t)}{\partial t^2} = S(r,t) \tag{1}$$

where, t is time, $r = (x, y, z)$, $S(r, t)$ is source, $u(r, t)$ is wave function, $k(r)$ is wave propagation coefficient, $\sqrt{k(r)}$ is the wave velocity, and ∇ is grad operation.

Let the wave front curve surface, $t = \phi(r)$, satisfies the Eckonal equation

$$k(r)|\nabla\phi|^2 = 1 \tag{2}$$

The Equations (1) and (2) are translated into Fermat's minimum travel time principle

$$\int\limits_{ray\,\text{path}} \frac{1}{\sqrt{k(r)}} dr = \min \tag{3}$$

where

$$dr = \sqrt{dx^2 + dy^2 + dz^2}, \tag{4}$$

2.2. New Wavelength Matching Curve Ray Tracing Method

The relationships between frequency, wavelength, and velocity are described by following equations:

$$v(r) = \lambda(r) f \tag{5}$$

and

$$\lambda(r) = \frac{v(r)}{f} = \frac{\sqrt{k(r)}}{f} \tag{6}$$

where, f is frequency, λ is wavelength, and v is wave velocity.

Using the wavelength matching topology, we develop an automatically moving finite element mesh to match the wavelength, which is determined by the local wave velocity and frequency. On the physical wave moving FEM mesh, according to the wave equation, Eckonal equation, and Fermat's minimum travel time principle, we develop a wavelength matching topology ray tracing algorithm.

2.3. New Ray Tomography Inversion

The Fermat's minimum travel time principle (3) can be used to forward curve ray tracing modeling with unknown tracing location curve $r(t)$. Also, according to the Fermat's principle, the Equations (4–6) can be used to construct a new ray tomography inversion, by the following regularizing slowness minimum travel time optimization.

$$\left| \int\limits_{ray\,\text{path}} S(r) dr \right|^2 + \alpha |S(r) - \bar{S}| = \min \tag{7}$$

It is subject to a compact regularizing site, $\bar{S}$ is the average slowness, α is the regularizing parameter.

2.4. Computing the Singular Behavior

Computing the singular behavior of solutions of Cauchy singular integral equations with variable coefficients is a main difficulty in ray-tracing on a complex model. We use the method developed on the paper [2] to handle the singular behavior of solutions.

2.5. Parallel AGILD Method

Our new 3D advanced parallel global integral and local differential (AGILD) [11–13] equation modeling and inversion has been used to develop our wavelength matching ray-tracing tomography [3–6]. The method is naturally parallel. Therefore, the ray-tracing method is feasible and fast for large and complicated three dimesional problem.

3. APPLICATIONS

The new ray-tracing method provides a useful tool to analyze surface-to-surface, surface-to-borehole, and crosshole data [7]. It can be used for developing next-generation wave propagation forward modeling codes for computational mechanics, elastic/plastic dynamic mechanics, computational materials, computational geophysics, biomedical science, and interactive 3D tomography.

3.1. Geophysical Subsurface Tomography

The seismic wave ray tracing tomography inversion developed in this paper is useful for geophysical subsurface tomography imaging. The Figure 1 shows the high resolution subsurface imaging. The deep curve structure is displaying very clear and curve ray tracing search every subsurface target. The seismic ray tracing tomography has wide application in the geophysical engineering, the foundation of civil engineering, underground and under ocean engineering, Earthquake exploration, ungerground water and environment sciences and engineering. These applications are necessary in Taiwan.

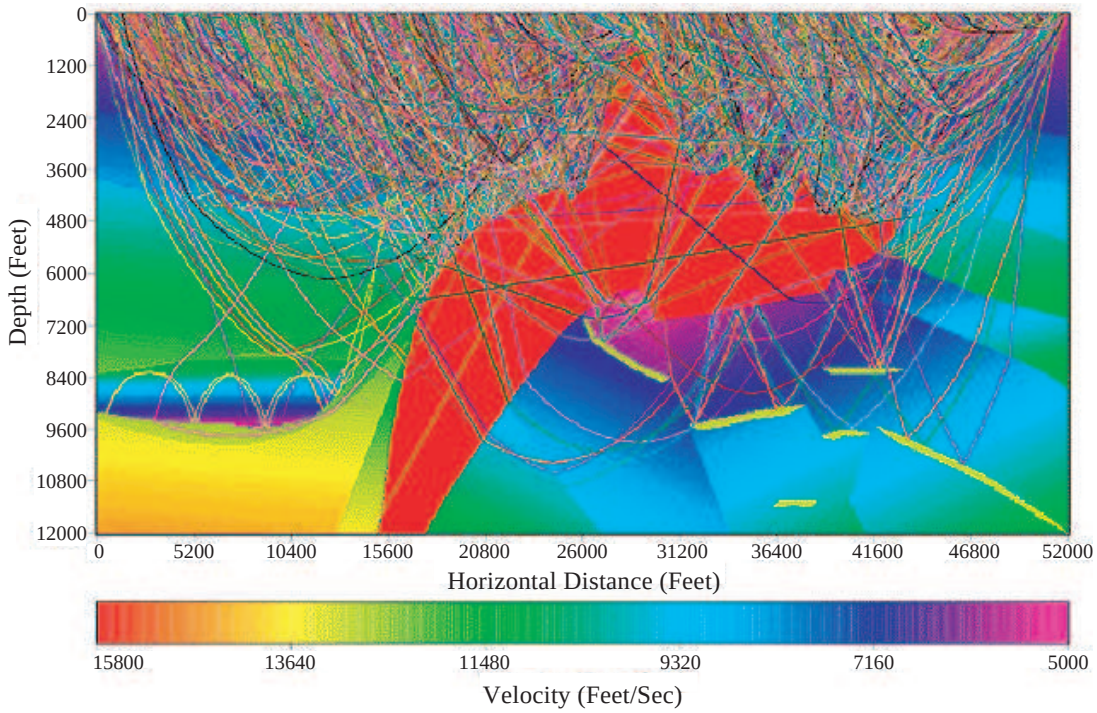

Figure 1: Wavelength matching finite-element ray-tracing tomography.

3.2. Nondestructive Testing for Structure Health

Our acoustic curve ray tracing tomography can be used to nondestructive testing for the machine structure health.

3.3. Micro Fracture Detection

The electromagnetic high frequency curve ray tomography is very useful to investigate the micro and nanometer material. Our electromagnetic-mechanical curve ray tracing will be useful for the micro thin plastic plate's bending deformation and detect its micro fracture, and optical measurement interpreting of the solid, liquid and gas materials [8], [9], [13].

3.4. Biomedical Science

The parallel AGILD [11–13] ray-tracing method can be used to perform radiation exposure investigation.

3.5. Interactive 3D Tomography

Our parallel AGILD [11, 12] ray-tracing method can perform real time speed ray tracing for interactive 3D tomography applications such as demoscene productions, computer and video games, and image rendering.

4. ACCOMPLISHMENTS

We have tested the ray-tracing method using the SEG/EAGE salt model. The numerical experiment was conducted for the velocity distribution in 2.5 D dimensions, in which ray tracings with 109 sources and 22 initial angles for each source were used. In the figure, we plotted only the farthest rays that returned to the surface, with the highest velocity representing the salt dome [10, 13].

The difficulties in ray tracing come from both the geometry and the velocity distribution of the model. The interfaces are complex; some parts are linear, some parts are curved, and some parts are fuzzy; and there are many corners that could result in a singularity when a ray passes them. Velocity distribution is complex with a large contrast (3.16 times), while some parts change continuously. Our AGILD FEM curve ray tomography obtained the high resolution tomography imaging.

5. CONCLUSION

The method has considering of computing the singular behavior of solutions of Cauchy singular integral equations with variable coefficients. We use the method developed on the paper [1] to handle the singular behavior of solutions. It is applicable regardless of how heterogeneous the medium is, as long as the geological parameters (shape and size) and physical parameters (velocity of propagation and gravity) are known analytically or numerically. The method has been implemented for three-dimensional case, in which the wavelength matching topology automatic mesh method has been combined with 3D cubic-hole element. Using the parallel AGILD method, the wavelength matching finite-element ray-tracing tomography successfully overcame the serious disadvantage of traditional ray-tracing performance. Our method is fast and accurate. Many simulation tests and field and laboratory data have been interpreted by using our AGILD FEM curve ray tracing tomography inversion code. That shows our curve ray tracing tomography is accurate, fast and high resolution. The AGILD wavelength matching Ray tracing tomography software has been developed by GLGEO sinced 2004. The software all right is reserved by GLGEO in USA.

ACKNOWLEDGMENT

This research was partially supported by the National Science Council in Taiwan through Grant NSC 95-2221-E-212-052 and GL Geophysical Laboratory. The simulation software is provided by GLGEO.

REFERENCES

1. Li, J. and G. Xie, "A new 3D cubic-hole element and its applications in the resistivity imaging," *Three Dimensional Electromagnetics*, 415–421, 2000.
2. Li, J. and R. P. Srivastav, "Computing the singular behavior of solutions of cauchy singular integral equations with variable coefficients," *Appl. Math. Lett.*, Vol. 10, No. 3, 57–62, 1997.
3. Xie, G. and J. Li, "New 3D parallel GILD EM modeling and inversion," *Annual Report Basic Energy Sciences*, 1988.
4. Xie, G. and J. Li, "New parallel stochastic global integral and local differencial equation modeling and inversion," *Physica D 133*, 477–487, 1999.
5. Xie, G., J. Li, and C.-C. Lin, "New SGILD EM modeling and inversion in geophysics and nano-physics," *Three Dimensional Electromagnetics*, Vol. 2, 193–213, (SCI), 2002.
6. Xie, G., C.-C. Lin, and J. Li, "GILD EM modeling in geophysics and nanometer materials using a magnetic field integral equation," *Three Dimensional Elctromagnetics III*, Vol. 3, 11–12, 2003.
7. Li, J., K. H. Lee, I. Javandel, and G. Xie, "Nonlinear three-dimensional inverse imaging for direct current data," *SEG 65th Annual International Meeting and Exposition, Expanded Abstracts*, 250–253, 1995.
8. Lin, C.-C., G. Xie, J. Li, and B.-J. Lin, "Deformation analysis for materials using GILD mechanical modeling," (Invited paper), *The Chinese Journal of Mechanics-Series A*, (A special issue dedicated to Prof. T. C. T. Ting in celebration of his seventieth birthday), vol. 19, No. l, 207–221 (SCI&EI), 2003.
9. Xie, G., C.-C. Lin, and J. Li, "New 3D GILD mechanical modeling and inversion," *Mathematica Applicata*, Vol. 16, No. 2, 149–156. 2003.
10. Li, J. and G. Xie, "Finite-element ray-tracing tomography," *Annual Report Basic Energy Sciences*, 1988.
11. Xie, G., J. Li, and F. Xie, "Advanced GILD EM modeling and inversion," *PIERS Online*, Vol. 1, No. 1, 105–109, 2005.
12. Xie, G., J. Li, and F. Xie, "2.5D AGLID EM modeling and inversion," *PIERS Online*, Vol. 2, No. 4, 390–394, 2006.
13. Li, J. and G. Xie, "AGILD wavelength matching finite-element ray-tracing tomography," *GL Geophysical Laboratory Technology Report*, GL2004-1, 2004.

Improved Isoparameter FEM for Plastic and EM Modeling

Chien-Chang Lin[1], **Jianhua Li**[1,2], **Ganquan Xie**[2], **and Michael Oristaglio**[3]

[1]Department of Mechanical and Automation Engineering, Da-Yeh University, Taiwan
[2]GL Geophysical Laboratory, USA
[3]Schlumberger Doll Research, USA

Abstract— In this paper, we present an improved isoparameter finite element method to calculate the electromagnetic (EM) field and the stress and deformation of the very thin multiple layered plastic hectograph or heliotype plate. The isoparameter element has high accurate to simulate the multiple layered thin plastic plate deformation and EM modeling. The thin multiple layered plastic plate has more advantages than the glass plate in the new LCD screen etc displayer and other industrial engineering applications.

1. INTRODUCTION

The laptop and new TV are developed very fast. The LCD is an important screen tool in the laptop and new TV. In the LCD design and application, the traditional glass plate has been used. However the glass plate has fragile and heavier etc. shortcomings. The thin multiple layered plastic plate has more advantages in the new LCD screen etc displayer and other industrial engineering. The advantages of the plastic hectograph plate is its plastic, thin, light, and multiple layered material rigid strength. In the new LCD thin plastic hectograph design, the deformation and stress calculation is necessary. Exact and high resolution of simulation of the above thin multiple layered plastic hectograph plate is challenge in the scientific computation. The FEM is used for this product design. The long and wide of the plastic LCD is 20 cm around, but its thick is only 0.1 µm. If we use the trilinear cubic element scaled by thickness, the 20000^2 nodes are needed for simulation. Therefore, the FEM method needs very large computational cost and inaccurate boundary reflection will degrade the computational accurate of the displacement and stress. In this paper, we present an isoparameter FEM method for the plastic thin plate deformation and EM modeling. As early as in 1972, Xie and Li proposed 3D isoparameter curve element with 20 nodes [1]. In paper [1], the author use a novel method to construct the 20 nodes curve isoparameter element and develop 3D elastic FEM and its software first in China, also author used the 3D isoparameter FEM software to calculate all dams and underground structures displacement and stress of China. In particular, Xie and Li discovered superconvergence of the isoparameter element first of the world that discover has been recognized by Brandts, J. and M. Krizek's paper "History and Future of Superconvergence in Three Dimensional Finite Element Methods" [2] and Michael Krizek's paper "Superconvergence Phenomena on Three Dimensional Meshes" [3]. The isoparameter element can be compressed and bended to a singular element automatically. We used these advantages of the isoparameter element for the plastic thin plate deformation and EM modeling simulation.

The description plan of this paper is as follows. The introduction is described in Section 1. In Section 2, we present elastic and plastic and EM modeling and its variation. The improved isoparameter element and its properties are presented in Section 3. In Section 4, we describe applications of the improved 3D and 2D isoparameter element. Accomplishment is described in Section 5. The paper will be concluded in Section 6.

2. ELASTIC AND PLASTIC AND EM MODELING

2.1. The Elastic Plastic Variational Principle

The elastic and plastic field variation equation is as follows [1, 6–12],

$$\int_{\Omega} \varepsilon^{T^*}(u) D(\lambda, \mu, \varepsilon(u)) \varepsilon(u) dr - \int_{\Omega} f u dr = \min, \tag{1}$$

where ε is the strain, D is the elastic-plastic matrix, λ and μ is Lame coefficient which depends on displacement u and strain ε in the plastic materials.

$$\varepsilon(u) = \left(\frac{\partial u}{\partial x}, \frac{\partial u}{\partial y}, \frac{\partial u}{\partial z}, \frac{\partial u}{\partial y} + \frac{\partial v}{\partial x}, \frac{\partial u}{\partial z} + \frac{\partial w}{\partial x}, \frac{\partial u}{\partial y} + \frac{\partial v}{\partial x} \right), \tag{2}$$

$$D = D(\lambda(\varepsilon(u)), \mu(\varepsilon(u))), \tag{3}$$

We use an improved isoparameter element to discrete the Garlekin Equation (1) [1].

2.2. The Magnetic Field Variational Modeling

We describe the magnetic field Garlekin Equation [7, 12] as follows

$$\int_{\Omega} \left(\frac{1}{\sigma + i\omega\varepsilon} \nabla \times H \cdot \nabla \times (\phi I) + i\omega\mu H \cdot (\phi I) \right) dr' = \int_{\Omega} Q_s(\phi I) dr, \tag{4}$$

where σ is the electric conductivity, ε is the dielectric parameter, μ is the permeability, H is the magnetic field, ϕ is the base test function in functional space, ω is the frequency, Q_s is the electromagnetic (EM) source, I is 3×3 unit matrix, I is the complex number unit. We use the improved isparameter element to discrete the magnetic Garlekin Equation (4) for EM modeling [7, 12].

3. IMPROVED ISOPARAMETER ELEMENT

In this section, we proposed various improved isoparameter elements. First we construct the isoparameter by the novel method [1, 4].

3.1. 3D Cubic 20 Nodes Element

We construct 3D cubic element with 20 nodes in this section.

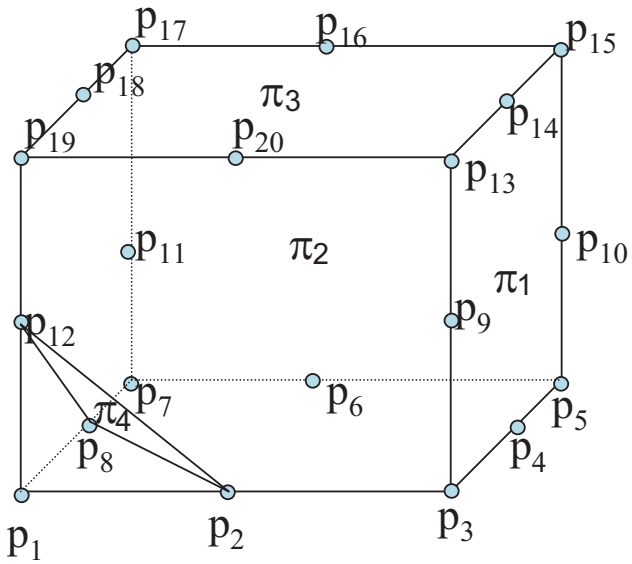

Figure 1: The 3D 20 nodes cubic element.

We use the novel method [1] to construct the 3D 20 nodes cubic element as follows. In the Figure 1, the P_1, P_2, ..., P_{20}, denote the 20 nodes, π_1 denotes the plane on which the nodes P_3, P_4, P_5, P_{10}, P_{15}, P_{14}, P_{13}, P_9 are located. π_2 is the plan on which the nodes P_7, P_6, P_5, P_{10}, P_{15}, P_{16}, P_{17}, P_{11} are located. π_3 is the plan on which the nodes P_{19}, P_{20}, P_{13}, P_{14}, P_{15}, P_{16}, P_{17}, P_{18} are located. π_4 is the plane on which the nodes P_2, P_8, P_{12}, are located. Let (ξ, η, ζ) be local coordinate of the 3D cubic element. The coordinate of the P_1 is (0, 0, 0), P_2's coordinate is (0.5, 0, 0), P_3's coordinate is (1.0, 0, 0), ..., the coordinate of the P_{20} is (0.5, 0, 1.0).

According to the analytical geometry, the coordinate equations of planes π_1, π_2, π_3, and π_4 are described as the following equations, respectively

$$\begin{aligned} \pi_1(\xi, \eta, \zeta) &= \xi - 1 = 0, \\ \pi_2(\xi, \eta, \zeta) &= \eta - 1 = 0, \\ \pi_3(\xi, \eta, \zeta) &= \zeta - 1 = 0, \\ \pi_4(\xi, \eta, \zeta) &= \xi + \eta + \zeta - 0.5 = 0. \end{aligned} \tag{5}$$

We construct base sample function $Q_1(\xi,\eta,\zeta)$, such that $Q_1(P_1)$ =1.0, and $Q_1(P_j)$=0.0 if $j \neq 1$. The novel sample function is as follows:

$$\begin{aligned} Q_1(\xi,\eta,\zeta) &= \frac{\pi_1(\xi,\eta,\zeta)\cdot\pi_2(\xi,\eta,\zeta)\cdot\pi_3(\xi,\eta,\zeta)\cdot\pi_4(\xi,\eta,\zeta)}{\pi_1(P_1)\cdot\pi_2(P_1)\cdot\pi_3(P_1)\cdot\pi_4(P_1)} \\ &= \frac{(\xi-1)\cdot(\eta-1)\cdot(\zeta-1)\cdot(\xi+\eta+\zeta-0.5)}{(0-1)\cdot(0-1)\cdot(0-1)\cdot(0+0+0-0.5)} \\ &= 2(\xi-1)\cdot(\eta-1)\cdot(\zeta-1)\cdot(\xi+\eta+\zeta-0.5), \end{aligned} \tag{6}$$

Similar, we can simply construct the base sample function $Q_2(\xi,\eta,\zeta)$, ..., $Q_{20}(\xi,\eta,\zeta)$. In the past 38 years of FEM history, almost all books and papers describe 3D isoparamter element by incomplete bi second order polynomial with 20 unknown coefficients, then by solving 20×20 matrix equation to determine the coefficient. The paper [1] is unique earliest paper which presents the novel method to use analytical geometry and plane cutting method to construct the base sample function directly and simply. Moreover, polynomial with 20 terms is not complete and no unique. What term should be needed in the polynomial? The polynomial method has no critical role. The geometry plan cutting method guarantees the continuous and constant strain principle. By the geometry plan cutting method we can generate curve element and singularity element etc improved isoparameter elements.

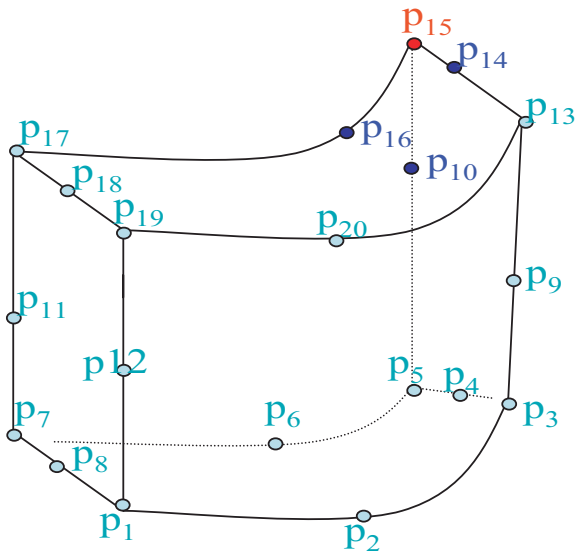

Figure 2: 3D 20 nodes curve element.

3.2. 3D 20 Nodes Isoparameter Element

The 3D 20 nodes curve element is shown in the Figure 2. In the Figure 2, the real nodes P_1, P_2, ..., P_{20} in the 3D curve element are corresponding to the virtual nodes P_1, P_2, ..., P_{20} in the standard model 3D cubic element in Figure 1, respectively. The real coordinate of P_1 is $(x_1,y_1,z_1),\ldots,P_j$'s coordinate is (x_j,y_j,z_j), ..., P_{20}'s coordinate is (x_{20},y_{20},z_{20}). We make the following topological mapping

$$\begin{aligned} x(\xi,\eta,\zeta) &= \sum_j^{20} Q_j(\xi,\eta,\zeta)x_j, \\ y(\xi,\eta,\zeta) &= \sum_j^{20} Q_j(\xi,\eta,\zeta)y_j, \\ z(\xi,\eta,\zeta) &= \sum_j^{20} Q_j(\xi,\eta,\zeta)z_j \end{aligned} \tag{7}$$

to map the standard model 3D 20 nodes cubic element in Figure 1 into the real 3D curve 20 nodes curve element in Figure 2. Suppose that the elastic/plastic displacement u has values u_j in the nodes $p_j = (x_j, y_j, z_j)$, we make bi second order interpolation

$$\begin{aligned} u(\xi,\eta,\zeta) &= \sum_{j}^{20} Q_j(\xi,\eta,\zeta)u_j, \\ v(\xi,\eta,\zeta) &= \sum_{j}^{20} Q_j(\xi,\eta,\zeta)v_j, \\ w(\xi,\eta,\zeta) &= \sum_{j}^{20} Q_j(\xi,\eta,\zeta)w_j \end{aligned} \tag{8}$$

From (8) and $Q_i(p_i) = 1$, $Q_i(p_j) = 0$, $j \neq i$, we have $u(p_i) = u_i$, Because (7) maps node p_i in real 3D curve element into the virtual node $\mathrm{P_i}$ in the cubic 3D element, from (7) we have $u(p_i) = u_i$, so, we have $u(p_i) = u_i$. The mapping (7) and (8) is isoparameter transformation. The real 3D 20 nodes curve element and its corresponding 3D node cubic model element and their isoparmeter mapping (7) and (8) are constructed the 3D 20 nodes curve isoparameter element.

3.3. Improved 3D Isoparameter Element

3.3.1. Middle Points Are Moving in 3D Curve Element

In the 3D standard cubic element in Figure 1, the nodes $\mathrm{P_1}$, $\mathrm{P_3}$, $\mathrm{P_5}$, $\mathrm{P_7}$, $\mathrm{P_{13}}$, $\mathrm{P_{15}}$, $\mathrm{P_{17}}$, and $\mathrm{P_{19}}$ are vertical nodes of the cubic element. the nodes $\mathrm{P_2}$, $\mathrm{P_4}$, $\mathrm{P_6}$, $\mathrm{P_8}$, $\mathrm{P_9}$, $\mathrm{P_{10}}$, $\mathrm{P_{11}}$, $\mathrm{P_{12}}$, $\mathrm{P_{14}}$, $\mathrm{P_{16}}$, $\mathrm{P_{18}}$, and $\mathrm{P_{20}}$ are middle points of the edges. In the 3D 20 nodes curve element in Figure 2, the real nodes $\mathrm{P_1}$, $\mathrm{P_3}$, $\mathrm{P_5}$, $\mathrm{P_7}$, $\mathrm{P_{13}}$, $\mathrm{P_{15}}$, $\mathrm{P_{17}}$, and $\mathrm{P_{19}}$ are vertical nodes of the real 3D curve element. It is very interesting that the node points $\mathrm{P_2}$, $\mathrm{P_4}$, $\mathrm{P_6}$, $\mathrm{P_8}$, $\mathrm{P_9}$, $\mathrm{P_{10}}$, $\mathrm{P_{11}}$, $\mathrm{P_{12}}$, $\mathrm{P_{14}}$, $\mathrm{P_{16}}$, $\mathrm{P_{18}}$, and $\mathrm{P_{20}}$ can be moved from their middle locations to generate some singularity element to present special physical property. In the Figure 2, we see that the blue nodes $\mathrm{P_{10}}$, $\mathrm{P_{14}}$, $\mathrm{P_{16}}$ are moving to red vertical node $\mathrm{P_{15}}$. The blue nodes $\mathrm{P_{10}}$, $\mathrm{P_{14}}$, $\mathrm{P_{16}}$ stop and stay in the locations 0.25 distance of edge from the vertical red node $\mathrm{P_{15}}$. The isoparameter (7) and (8) automatically generate singularity in the vertical node $\mathrm{P_{15}}$. Such the stress and strain have $\frac{1}{r^{\alpha}}$ singularity in the node $\mathrm{P_{15}}$. The 20 node curve element is improved as singularity element with singularity in the node $\mathrm{P_{15}}$.

3.3.2. A Surface Can Be Compressed Together as Edge in Improved Convex Isoparameter Element

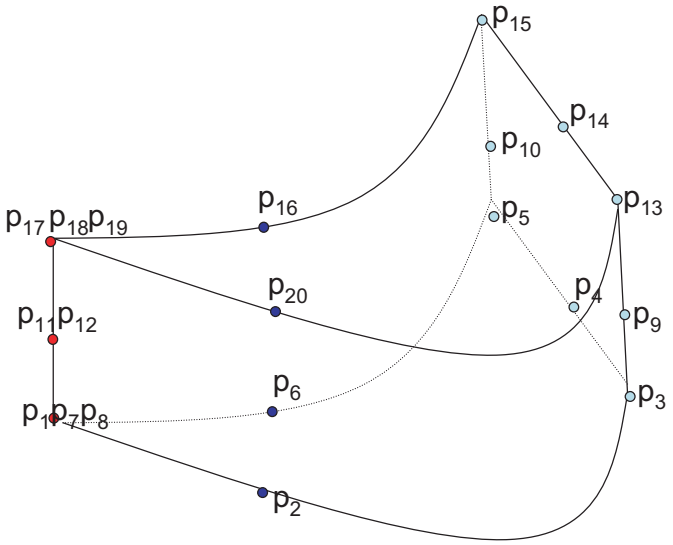

Figure 3: The surface $\Re$ [$\mathrm{P_1}$, $\mathrm{P_7}$, $\mathrm{P_8}$, $\mathrm{P_{11}}$, $\mathrm{P_{17}}$, $\mathrm{P_{18}}$, $\mathrm{P_{19}}$] is compressed together as a curve or straight line edge.

A surface of the 3D 20 nodes curve isoparameter element can be compressed as edge to generate an improved isoparamete 20 node curve element. The Figure 3 shows the improved isoparamter

curve element. In the Figure 3, the surface $\Re$ [P_1, P_7, P_8, P_{11}, P_{17}, P_{18}, P_{19}] is compressed together into a curve or straight line edge. The nodes P_1, P_7, and P_8 are compressed as same node point with same coordinate; The nodes P_{11}, P_{12} are compressed as same point with same coordinate.

The nodes P_{17}, P_{18}, and P_{19} are compressed as same node point with same coordinate. By the isoparameter mapping (7) and (8), the compressed edge $\wp$ [P_1, P_7, P_8, P_{11}, P_{17}, P_{18}, P_{19}] becomes as a singular edge. The 3D 20 nodes isoparameter element generate an improved isoparameter curve element with the singularity edge.

3.3.3. The Isoparameter Element Can Be Bended as a Concave Improved Isoparameter Element and Its Surface Can Be Compress Together as a Edge in the Concave Isoparameter Element

In the last section, we described some surface of the isoparameter can be compress together as a edge with singularity on the edge. The isoparameter element becomes the improve convex isoparamter element. Other important improve isoparameter element is described in this section. The new improved concave isoparameter element is shown in the Figure 4. In the 3D concave improve isoparameter element in Figure 4, the surface $\Re$ [P_1, P_7, P_8, P_{11}, P_{17}, P_{18}, P_{19}] is compressed together into a curve or straight line edge. The nodes P_1, P_7, and P_8 are compressed as same node point with same coordinate; The nodes P_{11}, P_{12} are compressed as same point with same coordinate; The nodes P_{17}, P_{18}, and P_{19} are compressed as same node point with same coordinate. The element is bended along the line through nodes P_2 and P_{20} and line through nodes P_6 and P_{16}. By the isoparameter mapping (7) and (8), we obtained the improved 3D concave isoparameter element and the singular edge in the concave tip.

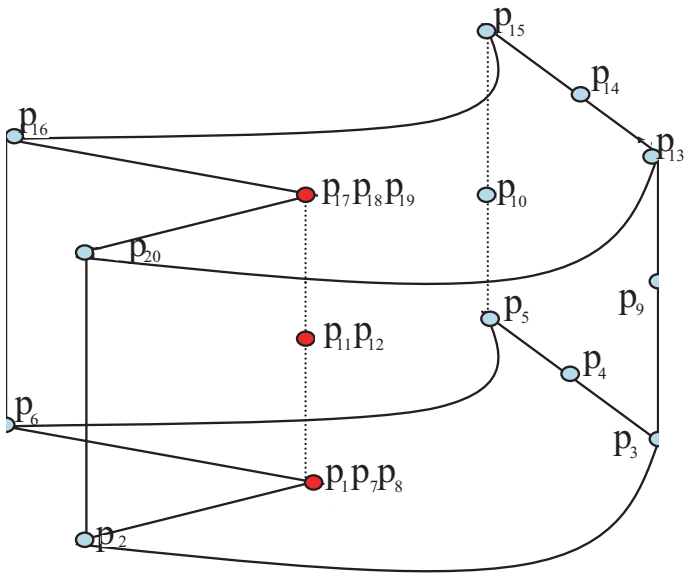

Figure 4: The surface $\Re$ [P_1, P_7, P_8, P_{11}, P_{17}, P_{18}, P_{19}] is compressed together as a curve or straight line edge. The element is bended to the improved 3D concave isoparameter element with singular edge.

4. APPLICATIONS

The improved 3D and 2D isoparameter element has wide applications for the mechanics and electromagnetic modeling in the material sciences and Geophysical exploration.

4.1. Micro Fracture Detection

The improved 3D and 2D improved isoparameter element can automatically generate the singular corner, singular edge element that is very useful for multiple thin elastic/plastic deformation and electromagnetic field. In particular, the improved isoparameter element can be use to calculate the stress and strain singularity [5] in the fracture. The elastic/plastic and electromagnetic improved isoparameter FEM modeling and high frequency curve ray joint tomography is very useful to investigate the micro and nanometer material. Our electromagnetic and mechanical improve isoparameter FEM and WMT reflection and diffraction curve ray tracing tomography will be useful for the micro thin plastic plate's bending deformation and detect its micro fracture and the

optical measurement interpretation of the macro and micro deformation and destruction testing of the solid mechanics [12, 13].

4.2. Geophysical Subsurface Imaging

The improve isoparameter element can be used in the static and dynamic mechanics modeling simulation. It and the seismic wave ray tracing tomography inversion developed in paper [13] joint together is useful for geophysical subsurface tomography imaging. In particular, the improved isparameter can be used to calculate rock's stress singularity and rock deformation singularity propagation. The 3D and 2D improved isoparameter element and our seismic ray tracing tomography have wide application in the geophysical engineering, the foundation inspection of civil engineering, underground and under ocean engineering, Earthquake exploration, underground water and environment sciences and engineering. These applications are necessary in continuance development.

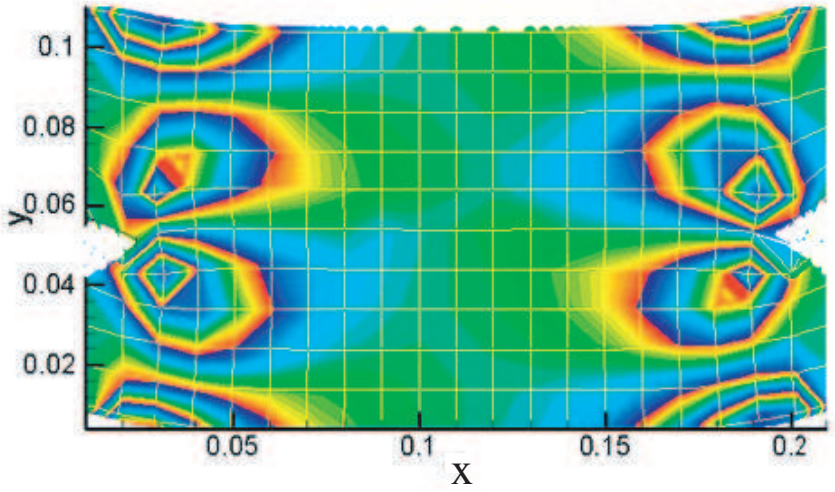

Figure 5: The 2D improved isoparameter concave.

4.3. Nondestructive Testing for Structure Health

Our 3D and 2D improved isoparameter element and acoustic curve ray tracing tomography can be used to nondestructive testing for the machine structure health.

4.4. Biomedical Science

The improved isoparameter element and the parallel AGILD ray tracing can be used to perform radiation exposure investigation [12, 13].

4.5. Interactive 3D Tomography

The parallel AGILD ray tracing [12] and the 3D and 2D improved isoparameter element can perform real time speed ray tracing for interactive 3D tomography applications such as demoscene productions, computer and video games, and image rendering. The improved isoparameter can be interactive automatically.

5. ACCOMPLISHMENTS

We use our 2D improved isoparamter element to simulate the 2D multiple thin elastic and plastic deformation. The computation result is shown in the Figure 5. The isoparameter singularity element is used to simulate the thin elastic plastic deformation. We can clearly see the stress singularity in the isopameter element's concave tip.

6. CONCLUSION

The several simulation tests show that the improved isoparameter element is accurate. It can be conveniently used to simulate the stress and strain singularity and destruction of the large bending deformation. The 3D and 2D improved isoparameter element software has been developed by GLGEO since 2004. The software all right is reserved by GLGEO in USA.

ACKNOWLEDGMENT

This research was partially supported by the National Science Council in Taiwan through Grant NSC 95-2221-E-212-052 and GL Geophysical Laboratory. The simulation software is borrowed from GLGEO.

REFERENCES

1. Xie, G., "Three dimensional finite element method in the elastic problem," *Mathematical Practice and Knowledge*, (Chinese), Vol. 1, 28–41, 1975.
2. Brandts, J. and M. Krizek, "History and future of superconvergence in three dimensional finite element methods," *Mathematical Sciences and Applications*, Vol. 15, 24–35, 2001.
3. Krizek, M., "Superconvergence phenomena on three dimenional meshes," *International Journal of Numerical Analysis and Modeling*, Vol. 2, No. 1, 43–56, 2005.
4. Li, J. and G. Xie, "A new 3D cubic-hole element and its applications in the resistivity imaging," *Three Dimensional Electromagnetics*, 415–421, 2000.
5. Li, J. and R. P. Srivastav, "Computing the singular behavior of solutions of cauchy singular integral equations with variable coefficients," *Appl. Math. Lett.*, Vol. 10, No. 3, 57–62, 1997.
6. Xie, G. and J. Li, "New parallel stochastic global integral and local differencial equation modeling and inversion," *Physica D* 133, 477–487, 1999.
7. Xie, G., J. Li, C.-C. Lin, "New SGILD EM modeling and inversion in geophysics and nanophysics," *Three Dimensional Electromagnetics*, Vol. 2, 193–213, (SCI), 2002.
8. Xie, G., C.-C. Lin, and J. Li, "GILD EM modeling in geophysics and nanometer materials using a magnetic field integral equation," *Three Dimensional Elctromagnetics III*, Vol. 3, 11–12, 2003.
9. Li, J., K. H. Lee, I. Javandel, and G. Xie, "Nonlinear three-dimensional inverse imaging for direct current data," *SEG 65th Annual International Meeting and Exposition*, Expanded Abstracts, 250–253, 1995.
10. Lin, C.-C., G. Xie, J. Li, and B.-J. Lin, "Deformation analysis for materials using GILD mechanical modeling," (Invited paper), *The Chinese Journal of Mechanics-Series A*, (A special issue dedicated to Prof. T. C. T. Ting in celebration of his seventieth birthday), Vol. 19, No. l, 207–221, (SCI&EI), 2003.
11. Xie, G., C.-C. Lin, and J. Li, "New 3D GILD mechanical modeling and inversion," *Mathematica Applicata*, Vol. 16, No. 2, 149–156, 2000.
12. Xie, G., J. Li, and F. Xie, "Advanced GILD EM modeling and inversion," *PIERS Online*, Vol. 1, No. 1, 105–109, 2005.
13. Li, J. and G. Xie, "AGILD wavelength matching finite-element ray-tracing tomography," *GL Geophysical Laboratory Technology Report*, GL2004-1, 2004.

AGILD Seismic Modeling For Double-porosity Media

Jing Ba[1], **Huizhu Yang**[1], **and Ganquan Xie**[2]
[1]Tsinghua University, China
[2]GL Geophysical Laboratory, USA

Abstract— In this paper, we present the seismic field modeling for double-porosity media using AGILD method. The seismic differential integral equations are discretized in the boundary strip zone by collocation FEM method. The seismic Galerkin equations are discretized by FEM method in internal domain. Both integral discretization on the strip zone and Galerkin FEM in the internal domain are used to construct AGILD seismic wave field modeling. The three phases' wavefields are simulated through AGILD method in double-porosity media.

1. INTRODUCTION

Studies on wave propagation in porous media have been carried out for decades. Recently, the major cause of fluid-induced porous rocks is analyzed in three different scales: macroscopic, mesoscopic, and microscopic [22–24].

White [25] was the first to introduce the mesoscopic-loss mechanism based on the framework of Biot's theory. A patch saturation model was presented to describe the wave propagation characteristics in porous rocks partially saturated with water and gas. Carcione [8] numerically modeled the wavefield in a porous media with mesoscopic gas pockets, and predicted higher attenuation than White's model due to multiple scattering and wave conversing. Carcione [9] investigated the White model and modeled different mesoscopic-scale heterogeneities and concluded that the loss because of fluid-modulus and porosity variations was the most important. Pride [24] used a unified theoretical treatment to describe three P wave attenuation models, which included a double-porosity model with a single fluid saturating, a patch-saturation model with two immiscible fluid and a microscopic squirt flow model. Either of the two mesoscopic models produced attenuation in seismic band that was comparable to what was measured in the field.

In this work, we investigate the double-porosity rocks [2, 22–24] with a AGILD method calculating the MFF pressure relaxation. Firstly, we simplify the double-porosity model with the same solid skeleton coupling with the two pore phases, and derive the displacement wave equations. Secondly, we analyze the mesoscopic fluid flow theory presented by Pride [22, 23], derive the integral discretization to numerically solve the divergency increments caused by MFF. Finally, wavefields are simulated.

2. WAVE EQUATIONS OF THE DOUBLE-POROSITY MEDIA

2.1. Double-porosity Local Governing Equations

Pride [22–24] has written the isotropic double-porosity governing equations in frequency domain as below

$$\nabla \cdot \bar{\boldsymbol{\tau}}^D - \nabla \bar{p}_c = -i\omega(\rho \mathbf{v} + \rho_f \mathbf{q}_1 + \rho_f \mathbf{q}_2) - \rho \mathbf{g}, \tag{1a}$$

$$\begin{bmatrix} \mathbf{q_1} \\ \mathbf{q_2} \end{bmatrix} = -\frac{1}{\eta} \begin{bmatrix} \kappa_{11} & \kappa_{12} \\ \kappa_{12} & \kappa_{22} \end{bmatrix} \begin{bmatrix} \nabla \bar{p}_{f1} - \rho_f(i\omega \mathbf{v} + \mathbf{g}) \\ \nabla \bar{p}_{f2} - \rho_f(i\omega \mathbf{v} + \mathbf{g}) \end{bmatrix}, \tag{1b}$$

$$\frac{1}{i\omega} \begin{bmatrix} \nabla \cdot \mathbf{v} \\ \nabla \cdot \mathbf{q_1} \\ \nabla \cdot \mathbf{q_2} \end{bmatrix} = \begin{bmatrix} a_{11} & a_{12} & a_{13} \\ a_{12} & a_{22} & a_{23} \\ a_{13} & a_{23} & a_{33} \end{bmatrix} \begin{bmatrix} \bar{p}_c \\ \bar{p}_{f1} \\ \bar{p}_{f2} \end{bmatrix} + \begin{bmatrix} 0 \\ \zeta_{\text{int}} \\ -\zeta_{\text{int}} \end{bmatrix}, \tag{1c}$$

$$-i\omega\zeta_{\text{int}} = \gamma(\omega)(\bar{p}_{f1} - \bar{p}_{f2}), \tag{1d}$$

$$-i\omega\bar{\boldsymbol{\tau}}^D = [G - i\omega F] \left[\nabla \mathbf{v} + (\nabla \mathbf{v})^T - \frac{2}{3} \nabla \cdot \mathbf{v} \mathbf{I} \right], \tag{1e}$$

where $\mathbf{v}$, $\mathbf{q}_1$ and $\mathbf{q}_2$ represent the average velocity of solid framework, the fluid velocity of phase 1 and the fluid velociy of phase 2. $\bar{p}_c$, $\bar{p}_{f1}$ and $\bar{p}_{f2}$ is the pressure of solid framework, fluid phase 1 and fluid phase 2. $\bar{\boldsymbol{\tau}}^D$ is the deviatoric stress tensor. The dimensionless increment ζ_{int} represents the "mesoscopic flow".

2.2. Double-porosity Displacement Wave Equations in Time Domain

To investigate the propagation features of the double-porosity media with a viscoelastic mesoscopic fluid flow, Equation (1) can not be used directly, and we should derive the time domain form of the double-poroviscoelastic wave equations.

The poroelastic equations of motion with a Biot's diffusive power can be written as

$$\frac{\partial \sigma_{ij}}{\partial x_j} = \frac{\partial^2}{\partial t^2}(\rho_{11}u_i + \rho_{12}U_i) + b(\dot{u}_i - \dot{U}_i), \tag{2a}$$

$$\frac{\partial S_{ij}}{\partial x_j} = \frac{\partial^2}{\partial t^2}(\rho_{12}u_i + \rho_{22}U_i) - b(\dot{u}_i - \dot{U}_i), \tag{2b}$$

where i, $j = 1, 2, 3$ denote the three directions, and u_i and U_i represent the displacement of solid particles and fluid particles in i direction. σ_{ij} and S_{ij} are the stresses of solid particles and fluid particles. b is the Biot's diffusion parameter, which can be determined as

$$b = \frac{\eta\phi^2}{k}, \tag{3}$$

where η is the fluid viscosity, ϕ is porosity, and k is the permeability.

As to Equation (2a) and Equation (2b), if there are two kinds of pores distributed in the reservoir rocks. Motion equations of a double-porosity media will be written as

$$\frac{\partial \sigma_{ij}}{\partial x_j} = \frac{\partial^2}{\partial t^2}(\rho_{11}u_i + \rho_{12}U_i^1 + \rho_{13}U_i^2) + b_1(\dot{u}_i - \dot{U}_i^1) + b_2(\dot{u}_i - \dot{U}_i^2), \tag{4a}$$

$$\frac{\partial S_{ij}^1}{\partial x_j} = \frac{\partial^2}{\partial t^2}(\rho_{12}u_i + \rho_{22}U_i^1) - b_1(\dot{u}_i - \dot{U}_i^1), \tag{4b}$$

$$\frac{\partial S_{ij}^2}{\partial x_j} = \frac{\partial^2}{\partial t^2}(\rho_{13}u_i + \rho_{33}U_i^2) - b_2(\dot{u}_i - \dot{U}_i^2), \tag{4c}$$

where S_{ij}^1 and S_{ij}^2 are the stresses of fluid phase 1 and fluid phase 2. U_{ij}^1 and U_{ij}^2 are the displacements of fluid phase 1 and fluid phase 2. b_1 and b_2 are the Biot's diffusive parameters of the two pore types, which can be determined by

$$b_l = \frac{\eta\phi_l^2}{k}, \quad l = 1, 2, \tag{5}$$

The constitutive equations for an isotropic double-poroelastic media are give by Equations (1c) $\sim$ (1e). Here we write the constitutive equations in another form.

$$\sigma_{ij} = Pe\delta_{ij} + 2N\varepsilon_{ij} + Q_1(\xi_1 - \zeta)\delta_{ij} + Q_2(\xi_2 + \zeta')\delta_{ij}, \tag{6a}$$

$$S_{ij}^1 = Q_1 e\delta_{ij} + R_1(\xi_1 - \zeta)\delta_{ij}, \tag{6b}$$

$$S_{ij}^2 = Q_2 e\delta_{ij} + R_2(\xi_2 + \zeta')\delta_{ij}, \tag{6c}$$

with

$$\begin{aligned} e &= e_{11} + e_{22} + e_{33} \\ \xi_1 &= \xi_{1,11} + \xi_{1,22} + \xi_{1,33} \\ \xi_2 &= \xi_{2,11} + \xi_{2,22} + \xi_{2,33} \\ \zeta &= \zeta_{11} + \zeta_{22} + \zeta_{33} \\ \zeta' &= \zeta'_{11} + \zeta'_{22} + \zeta'_{33} \end{aligned}$$

where ζ and ζ' represent the volume strain increments caused by the mesoscopic fluid flow. The substitution of constitutive Equations (6) into the Biot's motion Equations (4) yields nine displacement wave equations.

$$\begin{aligned} &N\nabla^2\mathbf{u} + (P+N)\nabla e + Q_1\nabla(\xi_1 - \zeta) + Q_2\nabla(\xi_2 + \zeta) \\ &= \rho_{11}\ddot{\mathbf{u}} + \rho_{12}\ddot{\mathbf{U}}^{\mathbf{1}} + \rho_{13}\ddot{\mathbf{U}}^{\mathbf{2}} + b_1(\dot{\mathbf{u}} - \dot{\mathbf{U}}^{\mathbf{1}}) + b_2(\dot{\mathbf{u}} - \dot{\mathbf{U}}^{\mathbf{2}}) \end{aligned} \tag{7a}$$

$$Q_1\nabla e + R_1\nabla(\xi_1 - \zeta) = \rho_{12}\ddot{\mathbf{u}} + \rho_{22}\ddot{\mathbf{U}}^{\mathbf{1}} - b_1(\dot{\mathbf{u}} - \dot{\mathbf{U}}^{\mathbf{1}}) \tag{7b}$$

$$Q_2\nabla e + R_2\nabla(\xi_2 + \zeta) = \rho_{13}\ddot{\mathbf{u}} + \rho_{33}\ddot{\mathbf{U}}^2 - b_2(\dot{\mathbf{u}} - \dot{\mathbf{U}}^2) \tag{7c}$$

where $\mathbf{u}$, $\mathbf{U^1}$ and $\mathbf{U^2}$ are displacement vectors of solid, fluid phase 1 and fluid phase 2. The determination of constants P, N, Q_1, R_1, Q_2, R_2, ρ_{11}, ρ_{12}, ρ_{13}, ρ_{22}, ρ_{33} will be discussed in the next part of the paper.

3. COEFFICIENTS OF THE DOUBLE-POROSITY WAVE EQUATIONS

3.1. Gedanken Experiments for Double-porosity Media

As to a single-porosity media, the constitutive functions can be written as [4, 5]

$$\sigma_{ij} = Pe\delta_{ij} + 2N\varepsilon_{ij} + Q\xi\delta_{ij}, \tag{8a}$$
$$S_{ij} = Qe\delta_{ij} + R\xi\delta_{ij}, \tag{8b}$$

P, N, Q, and R are Biot parameters. They are given in an awkward form by Biot and Willis [33]. Johnson [16] carried out Gedanken experiments with a single-porosity rock being compressed under three different conditions, and write the equations as below

$$P = \frac{(1-\phi)(1-\phi-k_b/k_s)k_s + \phi(k_s/k_f)k_b}{1-\phi-k_b/k_s+\phi k_s/k_f} + \frac{4}{3}N, \tag{9a}$$
$$Q = \frac{(1-\phi-k_b/k_s)\phi k_s}{1-\phi-k_b/k_s+\phi k_s/k_f}, \tag{9b}$$
$$R = \frac{\phi^2 k_s}{1-\phi-k_b/k_s+\phi k_s/k_f}, \tag{9c}$$

N is the shear modulus of the skeleton frame. k_s, k_b, and k_f are the bulk modulus of the solid phase, the bulk modulus of the porous skeleton, and the bulk modulus of the pore fluid. If there exists two types of pores and one single fluid in a rock sample, three similar gedanken experiments can be designed [16, 17].

First, if we make an approximation that there is none fluid viscosity effect on the shear stress (for example: water & gas), therefore the fluid contributes nothing in the shear stress/strain relationships, and it is obvious that N is the shear modulus of the solid skeleton and have nothing to do with the pore fluid.

Second, if the rock sample is surrounded by a flexible rubber jacket, subjected to a hydrostatic pressure, and if the fluid is allowed to flow out. The equation of $\nabla \cdot \mathbf{u} = -p_s/k_b$ still exist and only the skeleton affects the rock's strain. Therefore, an equation about elastic modulus of the double-porosity rocks can be written as

$$1 = \frac{P}{k_b} - \frac{Q_1^2}{k_b R_1} - \frac{Q_2^2}{k_b R_2}, \tag{10}$$

Third, if the sample is subjected to a uniform hydrostatic pressure p_f. Therefore, $\nabla\cdot\mathbf{u} = -p_f/k_s$, $\nabla\cdot\mathbf{U}_1 = \nabla\cdot\mathbf{U_2} = -p_f/k_f$, $\sigma_{ij} = -(1-\phi_1-\phi_2)p_f\delta_{ij}$, $S^1_{ij} = -\phi_1 p_f\delta_{ij}$ and $S^2_{ij} = -\phi_2 p_f\delta_{ij}$. Substitute these results into Equation (6) and ignore the mesoscopic fluid flow on static compression occasion, three equations can be written as

$$1-\phi_1-\phi_2 = \frac{P}{k_s} + \frac{Q_1+Q_2}{k_f}, \tag{11a}$$
$$\phi_1 = \frac{Q_1}{k_s} + \frac{R_1}{k_f}, \tag{11b}$$
$$\phi_2 = \frac{Q_2}{k_s} + \frac{R_2}{k_f}, \tag{11c}$$

As to Equations (10) $\sim$ (11), there are 4 equations and 5 coefficients to be determined, and one more equation is needed to solve these equations. We analyze the second gedanken experiment and find that if a double-porosity rock is surrounded by a jacket, the fluid in the two types of pores will hold the same divergency so that a mesoscopic fluid flow will not occur under the static compressed condition. Therefore, we get the last equation.

$$\frac{Q_1}{R_1} = \frac{Q_2}{R_2}, \tag{12}$$

The coefficients can be determined by solving the equations.

$$P = \frac{k_b k_s/k_f(\phi_1+\phi_2)+(1-\phi_1-\phi_2)(1-\phi_1-\phi_2-k_b/k_s)k_s}{1-\phi_1-\phi_2-k_b/k_s+k_s/k_f(\phi_1+\phi_2)}, \tag{13a}$$

$$Q_1 = \frac{(1-\phi_1-\phi_2-k_b/k_s)\phi_1 k_s}{1-\phi_1-\phi_2-k_b/k_s+k_s/k_f(\phi_1+\phi_2)}, \tag{13b}$$

$$Q_2 = \frac{(1-\phi_1-\phi_2-k_b/k_s)\phi_2 k_s}{1-\phi_1-\phi_2-k_b/k_s+k_s/k_f(\phi_1+\phi_2)}, \tag{13c}$$

$$R_1 = \frac{(\phi_1+\phi_2)\phi_1 k_s}{1-\phi_1-\phi_2-k_b/k_s+k_s/k_f(\phi_1+\phi_2)}, \tag{13d}$$

$$R_2 = \frac{(\phi_1+\phi_2)\phi_2 k_s}{1-\phi_1-\phi_2-k_b/k_s+k_s/k_f(\phi_1+\phi_2)}, \tag{13e}$$

As to the Equations (13a) ∼ (13e), Q_1, R_1, Q_2 and R_2 represent the compressive nature of a double-porosity rock, which contain two types of pores, the same fluid and the same solid skeleton. Equations (13a) ∼ (13e) are constructed based on two assumptions. First, the two types of pores in rock sample differ only in the way of porosity, which means the two pore phases should have different volumes rate per rock unit, and two pore phases should have close geometry shapes, or else the euqations will be much more complicate. Second, both the solid skeleton and pore fluids are assumed to be elastic isotropic, and the pore shapes are nearly spheric, so that we need not consider the porous rocks' anisotropic features.

3.2. The Determination of Density Coefficients

For single-porosity media, Biot [4, 5] got the relations between the single-porosity density coefficients and components' density by deriving from the kinetic energy Lagrange's equations. He earned two expressions as

$$(1-\phi)\rho_s = \rho_{11}+\rho_{12}, \tag{14a}$$

$$\phi\rho_f = \rho_{12}+\rho_{22}, \tag{14b}$$

Here in the same way, we can write the kinetic energy for elastic waves in a double-porosity media.

$$2T = \rho_{11}\dot{\mathbf{u}}\cdot\dot{\mathbf{u}}+2\rho_{12}\dot{\mathbf{u}}\cdot\dot{\mathbf{U}}^{\mathbf{1}}+2\rho_{13}\dot{\mathbf{u}}\cdot\dot{\mathbf{U}}^{2}+\rho_{22}\dot{\mathbf{U}}^{\mathbf{1}}\cdot\dot{\mathbf{U}}^{\mathbf{1}}+\rho_{33}\dot{\mathbf{U}}^{2}\cdot\dot{\mathbf{U}}^{2}, \tag{15}$$

Let us assume that there is no relative motion between solid and fluid, and three equations can be derived by substituting Equation (15) into a Lagrange's equations.

$$(1-\phi_1-\phi_2)\rho_s = \rho_{11}+\rho_{12}+\rho_{13}, \tag{16a}$$

$$\phi_1\rho_f = \rho_{12}+\rho_{22}, \tag{16b}$$

$$\phi_2\rho_f = \rho_{13}+\rho_{33}, \tag{16c}$$

In Equations (16a) ∼ (16c), a mesoscopic fluid flow will occur if there is a fluid pressure gradient, which will affect the velocity of the three phases. Nevertheless, no attenuation terms can be seen in this kinetic energy expression. It is because of that here we have not introduced a Biot's diffusive power which sharply attenuate slow waves. As has been discussed by Carcione [9], a mesoscopic fluid flow will transfer the fast waves' energy to slow waves, but it is the Biot's diffusive power who cause attenuation finally.

Berryman [34] has considered the case of isolated spherical solid particles in the fluid to derive the density coefficients. Based on this approximation, equations (16a) (16c) can be solved.

$$\rho_{11} = (1-\phi_1-\phi_2)\rho_s+\frac{1}{2}(2-\phi_1-\phi_2)\rho_f, \tag{17a}$$

$$\rho_{12} = \frac{1}{2}(\phi_1-1)\rho_f, \tag{17b}$$

$$\rho_{13} = \frac{1}{2}(\phi_2-1)\rho_f, \tag{17c}$$

$$\rho_{22} = \frac{1}{2}(\phi_1+1)\rho_f, \tag{17d}$$

$$\rho_{33} = \frac{1}{2}(\phi_2+1)\rho_f, \tag{17e}$$

4. NUMERICAL SIMULATION FOR MFF

AGILD method is used for wavefield simulation in the double-porosity media with MFF, and the skeleton and the fluid parameters are set as Table 1.

The presence of the Biot's diffusive mode will make the differential equations stiff. If a normal pseudo-spectral method is used directly to solve Equations (7a) $\sim$ (7c), a high value of b_1 and b_2 will make the simulation divergent. Carcione and Quirigo-Goode [7] designed a time-splitting integration algorithm to numerically solve the Biot's differential equations with stiff parts. The same technique is also used to solve the poroviscoelastic equations by Arntsen and Carcione [1]. Here we

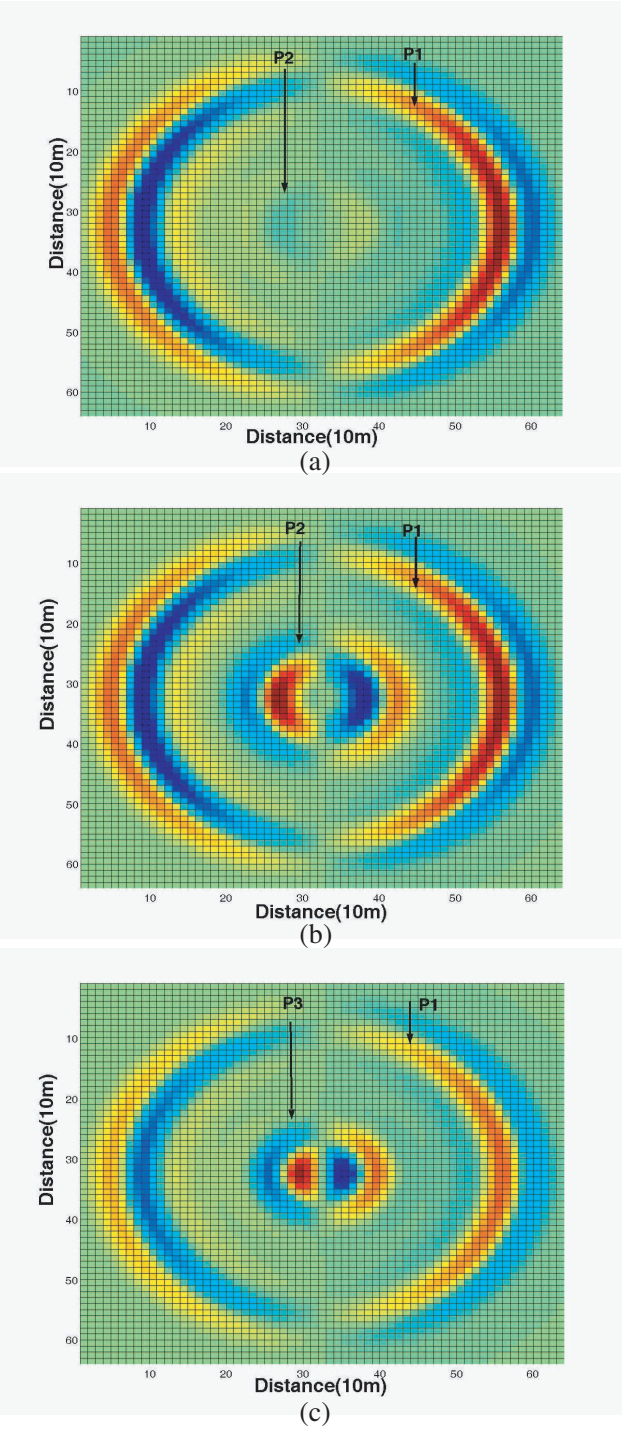

Figure 1: The 80 ms X-direction displacement snapshots of model 1. (a) solid phase snapshot of model 1, (b) pore phase 1 snapshot of model 1, (c) pore phase 2 snapshot of model 1.

introduce the time splitting algorithm to numerically solve the double-porosity wave equations.

Table 1: Parameters for a double-porosity media.

$k_s(\mathrm{N/m^2})$	$k_b(\mathrm{N/m^2})$	$k_f(\mathrm{N/m^2})$	$\mu_f(\mathrm{N/m^2})$	$\rho_s(\mathrm{kg/m^3})$	$\rho_f(\mathrm{kg/m^3})$	ϕ_1	ϕ_1
5.2E9	2.2E9	2.5E9	1E-3	2250	1040	0.20	0.05

Three models are simulated with a source center frequency at 50 Hz, the grid spacing equal to 10 m, and the exact source location at ($x = 320\,\mathrm{m}$, $z = 320\,\mathrm{m}$). In the first model, non Biot diffusion and non MFF is considered to examine the non-attenuation fast P wave and slow P waves' characteristics in the three phases. In the second model, only MFF is considered to examine the local fluid flow effect on the wavefield energy transmission in the three phases. In the third model, we both consider the Biot diffusion and MFF to demonstrate the major attenuation mechanism of the double-porosity media.

5. CONCLUSION

In this paper, we simplify the double-porosity model with the same solid skeleton coupling with the two pore phases, and derive the displacement wave equations in time domain. All the aspects of the wave equations are discussed to determine the modulus coefficients and density coefficients. The three phases' wavefields are simulated through a pseudo-spectral mentod in double-porosity media.

ACKNOWLEDGMENT

This research is supported by the national basic research program of China (973 program, 2007CB20 9505). Additional support is provided by the China Petroleum & Chemical Corporation (wx2006-38), and the National Science Fundation of China (10572072, 40674061).

REFERENCES

1. Arntsen, B. and J. M. Carcione, "Numerical simulation of the Biot slow wave in watersaturated Nivelsteiner sandstone," *Geophysics*, Vol. 66, 890–896, 2001.
2. Berryman, J. G. and H. F. Wang, "The elastic coefficients of double-porosity models for fluid transport in jointed rock," *J. Geophys. Res.*, Vol. 100, 24611–24627, 1995.
3. Berryman, J. G. and H. F. Wang, "Elastic wave propagation and attenuation in a double-porosity dual-permeability medium," *Int. J. Rock. Mech. Min. Sci.*, Vol. 37, 63–68, 2000.
4. Biot, M. A., "Theory of propagation of elastic waves in a saturated porous solid, I. Low-frequency range," *J. Acoust. Soc. Am.*, Vol. 28, 168–178, 1956.
5. Biot, M. A., "Theory of propagation of elastic waves in a saturated porous solid, II. High-frequency range," *J. Acoust. Soc. Am.*, Vol. 28, 179–191, 1956.
6. Biot, M. A., "Mechanics of deformation and acoustic propagation in porous media," *Journal of Applied Physics*, Vol. 33, 1482–1498, 1962.
7. Carcione, J. M. and G. Quiroga-Goode, "Some aspects of the physics and numerical modeling of Biot compressional waves," *J. Comp. Acoust.*, Vol. 3, 261–280, 1996.
8. Carcione, J. M., H. B. Helle, and N. H. Pham, "White's model for wave propagation in partially saturated rocks: Comparison with poroelastic numerical experiments," *Geophysics*, Vol. 68, 1389–1398, 2003.
9. Carcione, J. M. and S. Picotti, "P-wave seismic attenuation by slow-wave diffusion: Effects of inhomogeneous rock properties," *Geophysics*, Vol. 71, O1–O8, 2006.
10. Dai, N., A. Vafidis, and E. R. Kanasewich, "Wave propagation in heterogeneous, porous media: A velocity-stress, finite-difference method," *Geophysics*, Vol. 60, 327–340, 1995.
11. Diallo, M. S. and E. Appel, "Acoustic waves attenuation and velocity dispersion in fluid-filled porous media: Theoretical and experimental investigations," PhD Thesis, Eberhard Karls University, Tübingen, 2000.
12. Diallo, M. S. and E. Appel, "Acoustic wave propagation in saturated porous media: Reformulation of the Biot/Squirt (BISQ) flow theory," *J. Appl. Geophys.*, Vol. 44, 313–325, 2000.

13. Diallo, M. S., M. Prasad, and E. Appel, "Comparison between experimental results and theoretical predictions for P-wave velocity and attenuation at ultrasonic frequency," *Wave Motion*, Vol. 37, 1–16, 2003.
14. Dvorkin, J. and A. Nur, "Dynamic poroelasticity: A unified model with the squirt flow and the Biot mechanism," *Geophysics*, Vol. 58, 524–533, 1993.
15. Dvorkin, J., G. Mavko, and A. Nur, "Squirt flow in fully saturated rocks," *Geophysics*, Vol. 60, 97–107, 1995.
16. Johnson, D. L., "Recent developments in the acoustic properties of porous media," *Frontiers in Physical Acoustics XCIII*, North Holland Elsevier, New York, 255–290, 1986.
17. Johnson, D. L., "Theory of frequency dependent acoustics in patchy-saturated porous media," *J. Acoust. Soc. Am.*, Vol. 110, 682–694, 2001.
18. Li, J., G. Xie, M. Oristaglio, L. Xie, and F. Xie, "3D-2D AGILD EM modeling and inversion," *PIERS Online*, Vol. 3, No. 4, 423–429, 2007.
19. Li, J. and G. Xie, "A cubic-hole finite element for 3D resistivity modeling," *Three-dimensional Electromagnetics*, No. 7, 591–599, edited by Michael Oristaglio, Geophysical Developments, 1995.
20. Li, J., G. Xie, and F. Xie, "New stochastic AGLID EM modeling and inversion," *PIERS Online*, Vol. 2, No. 5, 490–494, 2006.
21. Li, J., G. Xie, and J. Li, "3D and 2.5D AGLID EMS stirring modeling in the cylindrical coordinate system," *PIERS Online*, Vol. 2, No. 5, 505–509, 2006.
22. Pride, S. R. and J. G. Berryman, "Linear dynamics of double-porosity and dualpermeability materials, I. Governing equations and acoustic attenuation," *Phys. Rev. E*, Vol. 68, 036603, 2003.
23. Pride, S. R. and J. G. Berryman, "Linear dynamics of double-porosity and dualpermeability materials, II. Fluid transport equations," *Phys. Rev. E*, Vol. 68, 036604, 2003.
24. Pride, S. R., J. G. Berryman, and J. M. Harris, "Seismic attenuation due to wave-induced flow," *Journal of Geophysical Research*, Vol. 109, B01201 doi: 10.1029/2003JB002639, 2004.
25. White, J. E., "Computed seismic speeds and attenuation in rocks with partial gas saturation," *Geophysics*, Vol. 40, 224–232, 1975.
26. Xie, G., J. Li, M. Majer, D. Zuo, and M. Oristaglio, "3D electromagnetic modeling and nonlinear inversion," *Geophysics*, Vol. 65, No. 3, 804–822, 2000.
27. Xie, G. and J. Li, "New parallel stochastic global integral and local differential equation modeling and inversion," *Physics D*, Vol. 133, 477–487, 1999.
28. Xie, G., J. Li, and F. Xie, "Advanced GILD EM modeling and inversion," *PIERS Online*, Vol. 1, No. 1, 105–109, 2005.
29. Xie, G., J. Li, and F. Xie, "2.5D AGLID EM modeling and inversion," *PIERS Online*, Vol. 2, No. 4, 390–394, 2006.
30. Xie, G., F. Xie, L. Xie, and J. Li, "GL method and its advantages for resolving historical difficulties," *Progress In Electromagnetics Research*, PIER 63, 141–152, 2006.
31. Xie, G., J. Li, and J. Li, "New AGILD EMS electromagnetic field modeling," *PIERS Online*, Vol. 1, No. 2, 168–172, 2005.
32. Xie, G., F. Xie, and J. Li, "New GL and GILD superconductor electromagnetic modeling," *PIERS Online*, Vol. 1, No. 2, 173–177, 2005.
33. Biot, M. A., and D. G. Willis, "The elastic coefficients of the theory of consolidation," *Applied Mechanics Division Summer Conference*, Berkeley, Calif., The American Society of Mechanical Engineers, 1957.
34. Berryman, J. G., "Confirm of Biots theory," *Appl. Phys. Lett,* Vol. 37, No. 4, 382–384, 1980.

Electrical Field and Plasticity for Polar Materials

Jianhua Xiao
Henan Polytechnic University, Jiaozuo, Henan 454000, China

Abstract— For polar materials, the polar molecular will rotate locally when electrical field is applied. When the electrical field is big enough, the fractures will appear in material. In this paper, the material composed by rigid polar molecular is studied. The elastoplastic deformation under electrical field is theoretically formulated to explain the relation between micro geometry and macro geometry. The macro geometry is defined by the traditional strain. The micro geometry is described the base vector transformation of material coordinators. The research shows that there are the two basic plastic configurations of macro geometry. They are named as type-I and type-II elastoplasticity. The type-I elastoplasticity is characterized with plastic contraction on the normal plane of electrical field. The type-II elastoplasticity is characterized with plastic expansion on the electrical field direction. The critical field strength is expressed by the material yield-stress. When the electrical field is bigger than the critical value, the volume ratio of voids or cracks is expressed by the filed strength.

1. INTRODUCTION

For the plasticity of polar materials under electrical field, the micro scale local rotation of polar material plays the essential role to understand plasticity. The plasticity is related with the sliding of grain structure, the local rotation of grain, and the volume distortion of grain structure. Therefore, the micro geometrical deformation and macro geometrical deformation is not identical in general sense [1–4]. To treat polar material problem, the Lagranian coordinators are introduced to identify the material under discussion. This treatment introduces the concept of material point representation [5]. To treat plasticity related with large electrical field, the plastic spin concept is introduced to explain the orientation aspect of micro geometrical deformation [6–9].

2. PLASTIC TYPE-I AND PLASTIC TYPE-II DEFORMATION

For continuum, each material point (element) can be parameterized with continuous coordinators x^i, $i = 1, 2, 3$. When the coordinators are fixed for each material point no matter what motion or deformation happens, the covariant gauge field g_{ij} at time t will define the material element configuration in that time [10–11]. The continuous coordinators endowed with the gauge field tensor define a co-moving dragging coordinator system [3–4]. The length variation is described by the covariant base vector transformation:

$$\vec{g}_i = F_i^j \vec{g}_j^0 \tag{1}$$

The F_j^i is viewed as macro geometry, as it is defined by displacement field. For small shear deformation [1–4], the Chen Form-one deformation can be used.

$$F_j^i = S_j^i + R_j^i \tag{2}$$

The zero intrinsic stretching condition can be written as:

$$S_j^i = \frac{1}{2}\left(u^i|_j + u^i|_j^T\right) - (1-\cos\Theta)L_k^i J_j^k = 0 \tag{3}$$

where,

$$R_j^i = \delta_j^i + \sin\Theta \cdot L_j^i + (1-\cos\Theta)L_k^i L_j^k \tag{4}$$

$$L_j^i = \frac{1}{2\sin\Theta}\left(u^i|_j - u^i|_j^T\right) \tag{5}$$

$$\sin\Theta = \frac{1}{2}\left[\left(u^1|_2 - u^2|_1\right)^2 + \left(u^2|_3 - u^3|_2\right)^2 + \left(u^3|_1 - u^1|_3\right)^2\right]^{\frac{1}{2}} \tag{6}$$

In above expressions, the upper T represents transpose of a tensor, the parameter Θ is called local average rotation angel (from continuity consideration we can set $|\Theta| < \pi/2$) and tensor L_j^k

defines the local average rotation axis direction, it is an anti-symmetric tensor. The R^i_j is an unit orthogonal tensor. The classical strain is defined as:

$$\varepsilon_{ij} = \frac{1}{2}\left(u^i|_j + u^i|^T_j\right) \tag{7}$$

By Equations (3), (2) and (6), letting the L_i is the rotation direction unit vector component, the following equations will be obtained:

$$L^i_k L^k_j + \delta^i_j = L_i L_j \tag{8}$$

By these equations, the classical strain can be rewritten as:

$$\varepsilon_{ij} = (1-\cos\Theta)L^i_k L^k_j = (1-\cos\Theta)(L_i L_j - \delta_{ij}) \tag{9}$$

2.1. Plastic Type-I Deformation

The Type-I plastic deformation is defined as the deformation with material length gauge field as invariant. Hence, no visible micro geometrical variation is observed. However, the macro geometrical deformation has happened. There are many researches on this plastic type [12–15]. The plastic Type-I deformation is defined by the plastic strain:

$$\varepsilon_{ij} = (1-\cos\Theta)(\delta_{ij} - L_i L_j) \tag{10}$$

Therefore, for the displacement field u^i, the Type-I plastic strain is completely determined by the local average rotation. As the incremental deformation is small compared with the reference configuration, the plastic variation can be expressed as:

$$\Delta\widetilde{g}_{ij} = (1-\cos\Theta)(\delta_{ij} - L_i L_j) \tag{11}$$

Without losing generality, for the rotation along the x^3 direction, $L_3 = 1$, $L_1 = L_2 = 0$. The plastic strain is:

$$\varepsilon_{11} = \varepsilon_{22} = (1-\cos\Theta),\ \varepsilon_{33} = 0 \tag{12}$$

It represents the expansion on the normal plane of local rotation. It should be named as rotation-plane-expansion. Therefore, the plastic Type-I deformation is defined by intrinsic (micro) material rigid rotation. Its macro geometry is plane isotropic expansion on the rotation plane.

2.2. Plastic Type-II Deformation

The plastic Type-II deformation is the micro rigid rotation combined with a micro contraction along the rotation axe direction. The macro plastic geometrical configuration has no observable volume changes. For example, the volume invariant soft crystal grains or irregular material grain rotate along one direction (the grain has shape variation) will not change the macro volume of the plastic configuration. Such a kind of plastic deformation is widely used in metal forming industry. In many applications, the device is packaged in a fixed box. So, it is necessary to introduce an additional plastic deformation defined by:

$${}^P F^i_j = \begin{bmatrix} 1 & 0 & 0 \\ 0 & 1 & 0 \\ 0 & 0 & 1-2(1-\cos\Theta) \end{bmatrix} \tag{13}$$

It represents the contraction along the rotation axe direction. The complete deformation will be represented as:

$$F^i_j = \begin{bmatrix} \cos\Theta & \sin\Theta & 0 \\ -\sin\Theta & \cos\Theta & 0 \\ 0 & 0 & 1 \end{bmatrix} \cdot \begin{bmatrix} 1 & 0 & 0 \\ 0 & 1 & 0 \\ 0 & 0 & 1-2(1-\cos\Theta) \end{bmatrix} \tag{14}$$

Therefore, the plastic Type-II deformation is defined by the deformation:

$$\varepsilon_{ij} = (1-\cos\Theta)(\delta_{ij} - L_i L_j) + [1-2(1-\cos\Theta)]L_i L_j \tag{15}$$

3. ELECTRICAL FIELD AND LOCAL ROTATION

For polar materials, when the geometrical boundary is free, the Type-I plasticity will be produced. When the geometrical boundary is fixed, the material has no macro volume variation. Then the Type-II plasticity will be produced. For Type-II plasticity, the additional plastic deformation is achieved by the boundary action. For a given electrical field E on (x^1, x^2) plane at x^1 direction, the positive charge center will move along the electrical field direction and the negative charge center will move in the reverse direction. It forms the rigid rotation on x^3 direction about its original center position. For unit volume polar element, if the charge density is q, the length between the positive charge center and negative charge center is $2a$, the electrical permeability is ε, then the micro asymmetrical stress is:

$$ {}^a\sigma_2^1 = \varepsilon aqE, \quad {}^a\sigma_1^2 = -\varepsilon aqE \tag{16}$$

This asymmetrical stress is can be expressed by the intrinsic deformation stress:

$$ {}^a\sigma_2^1 = 2\mu \sin\Theta, \quad {}^a\sigma_1^2 = -2\mu \sin\Theta \tag{17}$$

So, the intrinsic local rotation angular is determined by:

$$ \Theta = \arcsin\left(\frac{\varepsilon aqE}{2\mu}\right) \tag{18}$$

3.1. Electrical Field Strength and Material Strength for Type-I Plasticity

For Type-I plasticity, the plastic strain is:

$$ \varepsilon_{11} = \varepsilon_{22} = 1 - \cos\Theta = 1 - \sqrt{1 - \left(\frac{\varepsilon aqE}{2\mu}\right)^2}, \quad \varepsilon_{33} = 0 \tag{19}$$

It shows that the stronger is the electrical field, the larger is the plane expansion. As the micro volume of polar material grain is invariant, this means that the distance between the grain centers is increased. This will produce voids or cracks in the materials. The volume ratio $\alpha_{void} = 2(1-\cos\Theta)$ of voids and cracks can be expressed as:

$$ \alpha_{void} = 2\left[1 - \sqrt{1 - \left(\frac{\varepsilon aqE}{2\mu}\right)^2}\right] \tag{20}$$

If the material stress-strength is σ_c, then the maximum electrical strength is:

$$ E_{\max} = \frac{2\mu}{\varepsilon aq}\sqrt{1 - \left(1 - \sqrt{\frac{3}{2}}\frac{\sigma_c}{\lambda + 2\mu}\right)^2} \tag{21}$$

It can be expressed by the material allowable strain-strength as:

$$ E_{\max} = \frac{2\mu}{\varepsilon aq}\sqrt{1 - (1-\varepsilon_c)^2} = \frac{2\mu}{\varepsilon aq}\sqrt{2\varepsilon_c}\cdot\sqrt{1 - \frac{\varepsilon_c}{2}} \tag{22}$$

It shows that the material allowable strain-strength ε_c must be less than 50%. In fact, the maximum electrical strength can be used to define the allowable strain-strength $\widetilde{\varepsilon}_c$.

$$ \widetilde{\varepsilon}_c = \frac{2\mu}{\varepsilon aq} \tag{23}$$

For the materials with allowable strain-strength $\varepsilon_c \le \widetilde{\varepsilon}_c$, increasing the allowable strain-strength will increase the maximum electrical strength. However, for the materials with allowable strain-strength $\varepsilon_c > \widetilde{\varepsilon}_c$, increasing the allowable strain-strength will reduce the maximum electrical strength. Therefore, for Type-I plasticity polar materials, the maximum theoretic electrical field strength is:

$$ \mathrm{Max}(E_{\max}) = \frac{2\mu}{\varepsilon aq}\sqrt{1 - \left(1 - \frac{2\mu}{\varepsilon aq}\right)^2} \tag{24}$$

To achieve such a maximum electrical field strength, the minimum theoretic material stress-strength $\widetilde{\sigma}_c$ is:

$$\mathrm{Min}(\widetilde{\sigma}_c) = \sqrt{\frac{2}{3}}\frac{2\mu}{\varepsilon aq}(\lambda + 2\mu) \tag{25}$$

The equations can be used to the design of electrical field driven smart materials. It shows that, if the maximum electrical field strength is given, the material stress-strength (strain-strength) must be larger than σ_c ($\widetilde{\varepsilon}_c$). Note that the shear parameter μ and polar parameters determine the maximum electrical field strength for Type-I plasticity.

3.2. Electrical Field Strength and Material Strength for Type-II Plasticity

For Type-II plasticity, the plastic strain is:

$$\varepsilon_{11} = \varepsilon_{22} = 1 - \sqrt{1 - \left(\frac{\varepsilon aqE}{2\mu}\right)^2}, \quad \varepsilon_{33} = -2\left(1 - \sqrt{1 - \left(\frac{\varepsilon aqE}{2\mu}\right)^2}\right) \tag{26}$$

As the macro volume is invariant, it will not produce voids or cracks. But, it will produce interface sliding or crystalline sliding. If the material stress-strength is σ_c, then the maximum electrical strength equation is:

$$E_{\max} = \frac{2\mu}{\varepsilon aq}\sqrt{1 - \left(1 - \frac{\sigma_c}{\sqrt{6}(\lambda + 2\mu)}\right)^2} \tag{27}$$

From geometrical limits consideration, the maximum electrical strength as:

$$\widetilde{E}_{\max} = \sqrt{\frac{3}{2}}\frac{2\mu}{\varepsilon aq} \tag{28}$$

To achieve such a maximum electrical field strength, the minimum theoretic material stress-strength $\widetilde{\sigma}_c$ is:

$$\mathrm{Min}(\widetilde{\sigma}_c) = \sqrt{6} \cdot \frac{2\mu}{\varepsilon aq}(\lambda + 2\mu) \tag{29}$$

This value is three times of the value for Type-I plasticity. It shows that for the same maximum electrical field strength, the material stress-strength required for Type-II plasticity is three time higher than the requirement for Type-I plasticity. The shear parameter μ and polar parameters determine the maximum electrical field strength for Type-II plasticity.

4. CONCLUSION

For polar materials, the elastoplastic deformation under electrical field is theoretically formulated to explain the relation between micro geometry and macro geometry. The critical field strength is expressed by the material yield-stress. When the electrical field is bigger than the critical value, the volume ratio of voids or cracks is expressed by the filed strength.

REFERENCES

1. Chen, Z., "Geometric theory of finite deformation mechanics for continuum," *Mechanica Sinica*, No. 2, 107–117, Chinese, 1979.
2. Chen, Z., "Limit rotation expression in non-linear field theory of continuum," *Applied Mathematics and Mechanics*, Vol. 1996, No. 7, 959–968, Chinese, 1986.
3. Chen, Z., *Rational Mechanics-non-linear Mechanics of Continuum*, China University of Mining & Technology Publication, Xizhou, Chinese, 1987.
4. Chen, Z., *Rational Mechanics.*, Chongqin Publication, Chongqin, Chinese, 2000.
5. Lodge, A. S., *Body Tensor Fields in Continuum Mechanics*, Academic Press, New York, 1974.
6. Casey, J. and P. M. Naghdi, "A remark on the use of the decomposition $F=F_eF_p$ in plasticity," *Journal of Applied Mechanics*, Vol. 47, 672–675, 1980.
7. Dafalias, Y. F., "Plastic spin: necessity or redundancy?" *International Journal of Plasticity*, Vol. 14, No. 9, 909–931, 1998.
8. Steinmann, P., "A micropolar theory of finite deformation and finite rotation multiplicative elastoplastigity," *Intern. J. Non-linear Mechanics*, Vol. 32, 103–119, 1994.

9. Grammenoudis, P. and C. Tsakmakis, "Hardening rules for finite deformation micropolar plasticity: Restrictions imposed by the second law of thermodynamics and the postulate of Ii'iushin," *Continuum Mech. Thermodyn.*, Vol. 13, 325–363, 2001.
10. Brillouin, L., *Tensors in Mechanics and Elasticity*, Academic Press, New York, 1964.
11. Dubrovin, B. A., A. T. Fomenko, and S. P. Novikov, *Modern Geometry-methods and Application, Part I: The Geometry of Surfaces, Transformation Groups and Fields*, Springer-Verlag, New York, 1984.
12. Kuroda, M., "Roles of plastic spin in shear banding," *Int. J. Plasticity*, Vol. 12, 671–693, 1996.
13. Kuroda, M., "Interpretation of the behavior of metals under large plastic shear deformations: a microscopic approach," *Int. J. Plasticity*, Vol. 13, 359–383, 1997.
14. Paulun, J. E. and R. B. Pecherski, "On the application of the plastic spin concept for the description of anisotropic hardening in finite deformation plasticity," *Int. J. Plasticity*, Vol. 3, 303–314, 1987.
15. Zbib, H. M. and E. C. Aifantis, "On the concept of relative and plastic spins and its implications to large deformation theories, Part II: Anisotropic hardening plasticity," *Acta Mechanica*, Vol. 75, 35–56, 1988.

Study on Initial Stage of Gas Discharge by Numerical Method

Yun Zhang, Rong Zeng, Xiaochuan Wang, Bo Zhang, and Jinliang He
Department of Electrical Engineering, Tsinghua University, Beijing 100084, China

Abstract— The progress and characteristics of initial stage of gas discharge is studied in this paper by numerical simulation. A program based on the FE-FCT method in its full two-dimension form is developed and employed for the solution of transport equations of charged species under the effect of space-charge electric field. The initial stage of gas discharge between parallel plate electrodes, including the development of avalanche and progression of Townsend or streamer discharge are presented. The influences of length of gap and applied electric field on the mechanism and process of breakdown are analyzed and the breakdown voltage and formative time of discharge are predicted by the numerical method, and is well agree with the experimental result. The actions of cathode secondary emission on discharge are investigated, and photoemission is found to be more efficient than ion-electron emission.

1. INTRODUCTION

Since Townsend discovered the laws governing ionization and the gaseous discharge in a uniform electric field, a considerable amount of theoretical, numerical and experimental effort has been devoted to understand the development of electron avalanche, its transition into streamers and the propagation of streamer fronts.

Numerical method has been increasingly utilized in recent years with the advent of more powerful computers and the development of faster and more accurate algorithms using finite elements (FE) coupled to the FCT (Flux corrected transport) [1]. Georghiou and Kulikovsky [2–4] have utilized these algorithms to simulate the streamer discharge, including the transition from avalanche to streamer and streamer propagation. Some important characteristic such as distributions of electrons, ions and electric field which almost can not be obtained by theoretical or experimental method were acquired. The results have made great contributions in understanding streamer discharge. But the initial stage of the gas discharge including the development of avalanches and the formation of Townsend or streamer discharge was not studied carefully in their simulations. In fact, the initial stage is a very important part in gas discharge, especially in short air gap. It determines whether the discharge mechanism is Townsend or streamer, the break down electric field and the formative time delay of the discharge [5, 6]. Therefore, it is very essential to study the initial stage of gas discharge by numerical method carefully for understanding the characteristics and pushing forward the study of gas discharge.

Accordingly, the goal in this work is mainly focus on the initial stage of gas discharge. The program based on a fully two-dimensional FE and FCT algorithm was developed for numerical simulation of gas discharge. Then the method is utilized to simulate the development of avalanche and the formation of Townsend or streamer discharge. The distribution of electrons, ions and electric field, current evolution, criterion of breakdown and streamer velocity are acquired. The influences of gap length and applied electric voltage on the mechanism of discharge are analyzed. The criterions of formation of these two kinds of discharge mechanisms are investigated. The actions of secondary cathode emission including the photoemission and ion-electron emission are investigated. And finally, the external characteristic of discharge including breakdown voltage of different gaps and formative time under different electric field are predicted by numerical method, and in good agreement with experiment result.

2. NUMERICAL ALGORITHM

The hydrodynamic fluid model is adopted in this paper. It consists of the continuity equations for electrons, positive ions and negative ions (to account for the development of the space-charge) and Poisson's equation (to account for the modification of the electric field due to space-charge). The

continuity equations in their multidimensional form are:

$$\begin{aligned}
\frac{\partial N_e}{\partial t} &= S + N_e\alpha|\boldsymbol{W}_e| - N_e\eta|\boldsymbol{W}_e| - N_eN_p\beta_{ep} - \nabla\cdot(N_e\boldsymbol{W}_e - D\nabla N_e) \\
\frac{\partial N_p}{\partial t} &= S + N_e\alpha|\boldsymbol{W}_e| - N_eN_p\beta_{ep} - N_nN_p\beta_{np} - \nabla\cdot N_p\boldsymbol{W}_p \\
\frac{\partial N_n}{\partial t} &= N_e\eta|\boldsymbol{W}_e| - N_nN_p\beta_{np} - \nabla\cdot(N_n\boldsymbol{W}_n)
\end{aligned} \tag{1}$$

where t is the time, N_e, N_p and N_n are the charge densities for electrons, positive ions and negative ions. $\boldsymbol{W}_e$, $\boldsymbol{W}_p$ and $\boldsymbol{W}_n$ are the drift velocities for electrons, positive ions and negative ions, respectively and D is the electron diffusion coefficient which are all functions of reduced electric field $\boldsymbol{E}/n$, n is the neutral gas number density. The symbols α, η, β_{ep} and β_{np} denote the ionization, attachment, electron-positive ion recombination and negative-positive ion recombination coefficients, respectively. All these transport parameters are found from the kinetic model or from experimental results, in this paper the data of Morrow and Lowke [7] obtained through the solution of the stationary Boltzmann equation are used. The term S is the source term due to photoionization and cathode secondary emission. In our model, both photoionization and cathode emission are considered [8, 9].

Poisson's equation is given by

$$\nabla\cdot(\varepsilon_r\nabla\phi) + \frac{e}{\varepsilon_0}(N_p - N_n - N_e) = 0 \tag{2}$$

where ε_0 is the dielectric constant of free space, ε_r the relative permittivity, e the electron charge and ϕ the electric potential.

The electric field E is computed using

$$\boldsymbol{E} = -\nabla\phi$$

The finite element-flux corrected transport (FE-FCT) algorithm is adopted for the continuity equations. Poisson's equation is solved using standard Taylor-Galerkin method. In the calculation, the adaptive meshing and parallel computing methods were also adopted to improve the computing efficiency.

3. SIMULATION RESULT

Using the method above, the initial stage of gas discharge is simulated first to study the details of development of avalanche and the formation of Townsend or streamer discharge. The current evolution, distribution of electrons and electric field, influences of electric field and gap length on discharge mechanisms, effect of secondary emission, criterion of breakdown and streamer velocity are acquired. Then the breakdown electric field of different gaps and formative time delay under different electric field are calculated by numerical methods.

The results presented were obtained from the following conditions, pressure is 760 torr, gas temperature is 300 K, and gas density is $2.45 \times 10^{19}\,\mathrm{cm}^{-3}$.

3.1. Process of Initial Stage of Discharge

As the electric field in the gap has great influence on the discharge mechanism, different voltages are applied on a 1 cm parallel plane gap to produce different discharge mechanisms, Townsend and streamer discharge. First, 32 kV which is a little higher than breakdown voltage is selected for studying the Townsend discharge. Then 38 kV is selected for studying formation and development of the streamer just after the first avalanche. At last 34 kV which produces streamer after two avalanches is selected just for analyzing influence of voltage on gas discharge.

First, 32 kV is applied on the gap for studying the avalanche and Townsend discharge. The development of the first avalanche is shown in Figure 1. The x-coordinate is the radial distance from the center of the plane while the y-coordinate is axial distance from cathode. The seed electrons produced by the ionization in natural air with the density of 1000 per cm^3 [5] is set near the cathode to observe the avalanche clearly. Under the force of intensive electric field E, these electrons collide with gas molecules knocking off new electrons, which in turn accelerate and create what is known as an electron avalanche. The initial 1000 electrons travel the whole gap

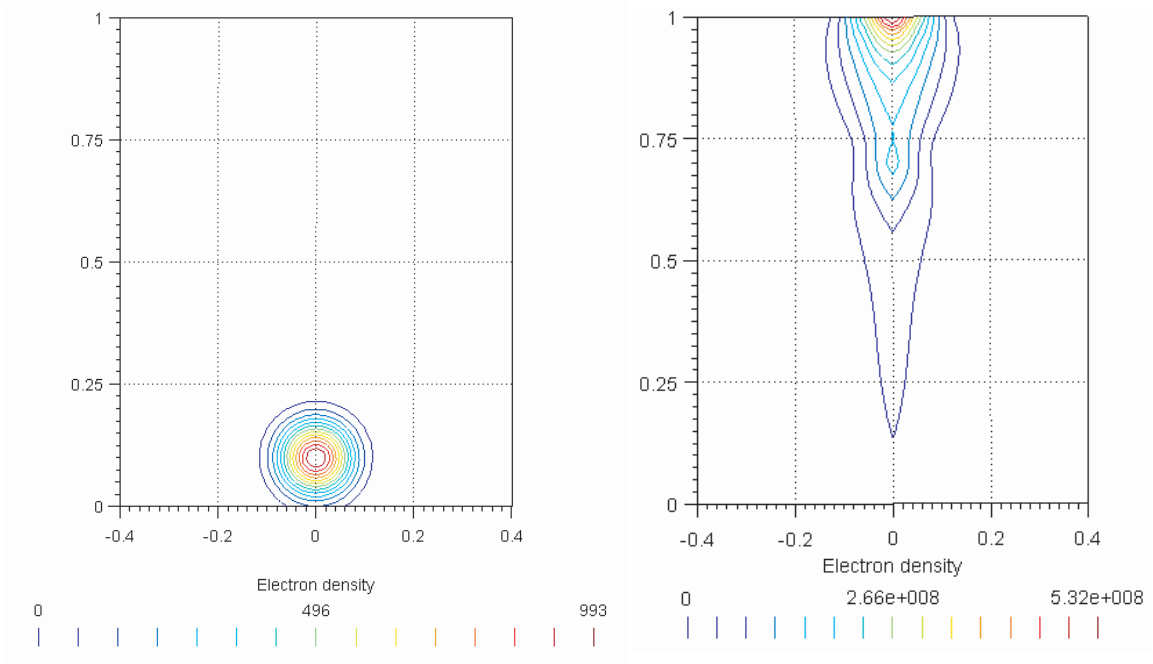

(a) (b)

Figure 1: Avalanche. (a) $t = 0$, (b) $t = 70\,\text{ns}$.

in 70 nanoseconds, and the density increase to be $10^8\,\text{cm}^{-3}$, which is in good agreement with the experiment [6].

Figure 2 illustrates the current evolution of Townsend discharge when different cathode emission mechanisms are considered. When photoemission is considered, the current increases slowly because of a large number of secondary avalanches initialed by photoemission until the Townsend discharge happens at last. But the current decays to low value after the initial avalanche is absorbed into the anode when the ion-electron emission is considered only. So photoemission is more efficient than ion-electron emission.

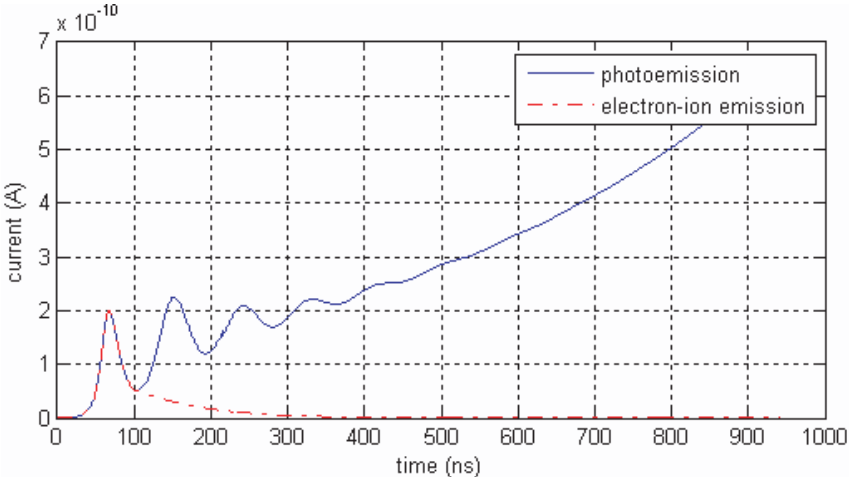

Figure 2: Current evolutions with photoemission and ion-electron emission.

When 38 kV voltage applied, the discharge appears as streamer discharge, as shown in Figure 3, the x and y coordinates are the same as Figure 1. The electron density of first avalanche increases to be $10^{13}\,\text{cm}^{-3}$ when it reaches the anode, the space charges sharply intensify the electric field below the avalanche head to about 80 kV/cm (Figure 3(a)). Under such a high electric field, the collision ionization is intensified, more electron-ion pairs are produced fleetly, so high field region moves quickly towards the cathode, streamer breakdown forms (Figure 3(b)). In the simulation, it can

be found that the electric field and velocity increase as the streamer develops. When the streamer initials, the electric field of streamer head is about 80 kV/cm and the velocity of streamer is about 30 cm/μs, when it reaches the cathode, the electric field increases to 200 kV/cm and velocity to 70 cm/μs, which is in agreement with experiment too [6]. This is because as the cathode direction streamer develops, more secondary avalanches are absorbed into the streamer head, the density of positive ions accumulated increases, which lead to higher electric field, so the streamer velocity also increases.

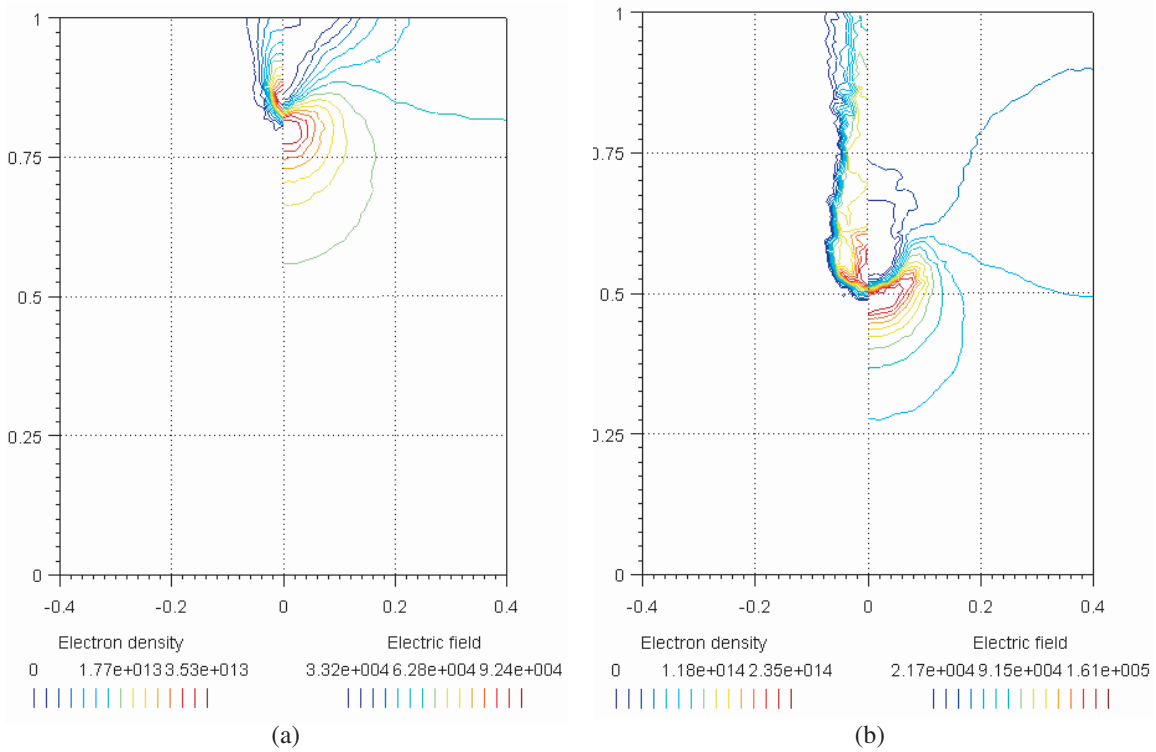

Figure 3: Streamer propagation, the left is the contours of electron density (cm^{-3}), the right electric field (V/cm). (a) $t = 54$ ns, (b) $t = 62$ ns.

Figure 4 shows the current evolution of streamer breakdown under different voltage. Under 38 kV voltage, after 50 ns delay, which is the formative time of the first avalanche, the current increases sharply which means the streamer forms. Under 34 kV voltage, there exists an oscillation before streamer, because of the first avalanche is not intensive enough, and need some secondary avalanches to trigger the streamer. By our simulation, it also can be found that the current increase more quickly under higher voltage. This is because under higher voltage, on one hand the streamer travels more quickly, on the other hand the density of charge in the streamer increase higher.

The influence of gap length on discharge mechanism is also investigated. When the gap length increases, each avalanche travels longer distance in electric field, so its density can increases to the criterion of formation of streamer under lower voltage. When the gap length increases to 3 cm, streamer is observed under 30 kV/cm electric field in our simulation.

3.2. The Breakdown Voltage

Figure 5 shows the breakdown voltage of different gaps. The average breakdown electric field decreases as the distance of the gap increase. In Townsend discharge, the criterion of breakdown is that the electrons produced by secondary emission are more than the initial electrons. The secondary emission lies on the electron density of the former avalanche, so the criterion equals to that the electron density of avalanche reaches a certain value. For streamer discharge, the breakdown criterion is the density of avalanche reach the level of 10^{13} cm^{-3}, so that it can intensify the electric field in the avalanche head. For both Townsend discharge and streamer discharge, the avalanche in longer gaps has more time to multiply, so the electric field required to produce enough electrons is lower.

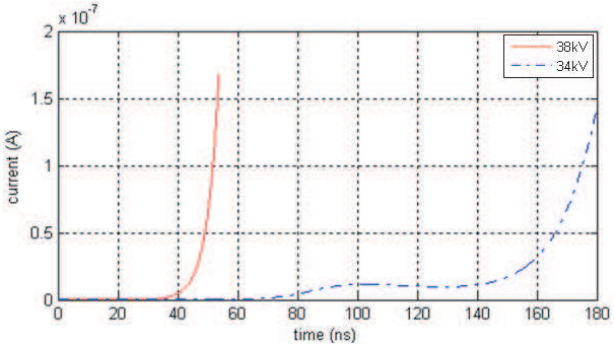

Figure 4: Current evolution of streamer.

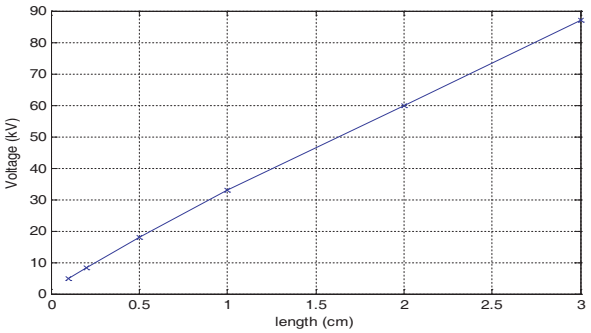

Figure 5: Breakdown voltage versus gap length.

3.3. The Formative Time of Discharge

In this section, the formative time delays of 0.1 cm parallel plane gap discharge under different electric field are calculated by numerical method. The results are illustrated in Table 1. The retardation time decrease under higher electric field. This is because the retardation time of discharge is the formative time of a series avalanches, under higher electric field, on one hand, the drift velocity of electrons is higher, on the other hand, the number of avalanches needed to trigger breakdown is less. When the electric field increases to 65 kV/cm, the first avalanche can produce the streamer, so the retardation time is only 3 ns which is the formative time of first avalanche.

Table 1: Retardation time versus electric field.

Electric field (kV)	50	55	60	65	70
Formative time	5 µs	0.7 µs	8 ns	3 ns	2.6 ns

4. CONCLUSION

A 2-D numerical simulation of initial stage of discharge in atmospheric pressure air between parallel plane electrodes has been performed. The process of avalanche and Townsend or streamer discharge is investigated. Some essential characteristics which can not be obtained by theoretical and experimental method were acquired. The results are as follows:

(1) The initial stage of gas discharge determines the breakdown mechanism, breakdown voltage and the formative time, so it should be considered carefully in study of the gas discharge.
(2) The length of gaps and applied electric field have great influence on discharge mechanism. In longer gaps or higher electric field, the avalanche can grow denser, the streamer forms easier.
(3) The secondary emission plays important role in the gas discharge. And the photoemission is more efficient than ion-electron in atmospheric pressure gas.
(4) The electric field of the streamer head and velocity of streamer increase as the streamer develops.
(5) Under higher electric field, the formative time of the discharge reduces.

REFERENCES

1. Lohner, R., K. Morgan, J. Peraire, and M. Vahdati, "Finite element flux-corrected transport for the Euler and Navier-Stokes equation," *Int. J. Numer. Methods Fluids*, Vol. 7, 1093–102, 1987.
2. Georghiou, G. E., R. Morrow, and A. C. Metaxas, "Two-dimensional simulation of streamers using the FE-FCT algorithm," *J. Phys. D: Appl. Phys.*, Vol. 33, L27–L32, 2000.
3. Georghiou, G. E., R. Morrow and A. C. Metaxas, "A two-dimensional finite element-flux corrected transport algorithm for the solution of gas discharge problems," *J. Phys. D: Appl. Phys.*, Vol. 33, 2453–6, 2000.
4. Kulikovsky, A. A., "Two-dimensional simulation of the positive streamer in N_2 between parallel-plate electrodes," *J. Phys. D: Appl. Phys.*, Vol. 28, 2483–93, 1995.

5. Yang, J., *Gas Discharge*, Science Publishing Company, 1983.
6. Raizer, Y. P., *Gas Discharge Physics*, Springer Verlag, Brelin, Heidelberg, 1991.
7. Morrow, R. and J. J. Lowke, "Streamer propagation in air," *J. Phys. D: Appl. Phys.*, Vol. 30, 614–27, 1997.
8. Zheleznyak, M. B., A. K. Mnatsakanian, and S. V. Sizykh, "Photoionization of nitrogen and oxygen mixtures by radiation from gas discharge," *High Temp.*, Vol. 20, 357–62, 1982.
9. Georghiou, G. E., R. Morrow, and A. C. Metaxas, "The effect of photoemission on the streamer development and propagation in short uniform gaps," *J. Phys. D: Appl. Phys.*, Vol. 34, 200–208, 2001.

Genetic Algorithms for Automated Design of the Multilayer Absorbers in the X-Band and Incident Angle Range

N. Lassouaoui, H. Hafdallah Ouslimani, and A. Priou
University Paris X, Nanterre, Pole Scientifique and Technique, Ville d'Avray
Applied Electromagnetism Group (GEA) 50
rue de Sèvre 92410, Ville d'Avray, France

Abstract— This paper dealt with the research of the optimal geometrical and physical properties of a multilayer absorbing structure that can minimize the reflection coefficient on a wide frequency band and for a wide incidence angle. In this multidimensional research, we construct an electromagnetic analysis and the synthesis genetic methods.

The electromagnetic analysis concerns the calculation of the reflection coefficient of the multiflat layers. Several methods allow an exact computation of this parameter, we use the method based on a concept of impedance transformation. The synthesis is accomplished by a developed genetic algorithm. The genetic parameters are calculated according to the diversity of the populations to ensure an optimal exploration of research space and an automatic processing. Numerical results are presented which demonstrate the efficiency of the method.

1. INTRODUCTION

The use of evolutionary programming techniques to automate the design of antennas has recently much attention [1–4]. Here in, we are interested by the design of multilayer absorbers using genetic algorithms (GAs). The structure is composed by a stack of flat layers materials of different loss and thickness. Since the performances of absorber are defined by the thickness and material composition (properties) of each layer, we propose to find the best configuration and the best properties of the layers in order to minimize the return loss for a wide incidence angle and broad band frequency range. Here, we are interested by the X-band frequency (8.2 to 12.4 GHz). For this study, we developed an electromagnetic analysis method to compute of the reflection parameter and a synthesis by GAs method. The GAs are not the unique method in optimization problem but has the advantage to overcome many problems associated with local optimization procedures. Here in, we give how the genetic parameters are computed and how to estimate them according the diversity of the population and the variability of the chromosomes from generation to another. The method ensures a best exploration of research space and an automatic genetic processing.

In what follows, we present the synthesis with GAs in Section 2 and how we compute the reflection parameter in Section 3. In Section 4, the numerical results of the study are presented. The conclusion and perspectives of this work are presented in Section 5.

2. SYNTHESIS METHOD

An optimization is often a problem of maximization or minimization of a function with one or more independent variables. They encode the problem in a merit function, which gives information about the quality of a solution candidate in the problem. The best solution will have the highest or lowest merit function. There exist mainly the global and local optimization methods.

The local optimizers take advantage of the decrease in value of the function near a minimum to converge to a solution. Two types of local optimizers:

- Those that find the direction in which the value of the function is decreasing by blind searching. However, it is easy to obtain stability with local minima.
- Those that use information about the gradient of the function to find a minimum. These methods are not very useful when the derivative is difficult to calculate or does not exist. Indeed, they do not handle discrete variables, discontinuities in solutions.

The global procedures are able to handle these difficulties because they are less sensitive to the initial values. They begin with a random initialization and converge to a solution through a sequence of structured changes in the parameters. The randomness in movements and in initial population allows global research.

With GAs, we hope to minimize the reflectivity over a wide frequency band and a wide incidence angles, for that, after a generation of initial random population, we follow two steps:

1. Optimization according to the frequencies for a fixed incidence angle.
   For each candidate and each frequency, we point out the worst case corresponding to the poor reflectivity (maximum in dB) which can measure the minimal performance that it can be ensured.
2. Optimization according the incidence angles.
   For various incidence angles θ_i (from 0 to $\pm 90^\circ$) and for a fixed frequency f, the optimization deals with the final population of the last step where the computed reflectivity is minimum (the best).
   Here are the various steps of the genetic process and the choice of the parameters.

2.1. Genetic Processus

Initial population: The parameters of layers are generated randomly. To define the research space, it is necessary to delimit an upper and a lower limits for each variable. Additional constraint concerning the energy conservation law [5] must be satisfied: the imaginary part of the dielectric permittivity and magnetic permeability must be positive ($\mathrm{Im}(\varepsilon) \geq 0$, $\mathrm{Im}(\mu) \geq 0$). Knowing that each layer is characterised by five genes (its thickness T_i, real and imaginary parts of the dielectric $\varepsilon_j = \varepsilon_j^{'} + i\varepsilon_j^{''}$ and real and imaginary parts of the magnetic constants ($\mu_j = \mu_j^{'} + i\mu_j^{''}$); For N layers, we concatenate N vectors of five real values variables which avoid the decoding step and allow an improved gain in the computing times.

Fitness Function: The evolution is based on the value of the merit function. The fitness contains the parameter to be optimized, here, the reflectivity in dB.

Reproduction: We follow two steps:

- Firstly an extinction step is applied for eliminating a full of the population where the candidates have fitness lower than average (a selection by *population decimation*).
- Secondly, the genetic operators are applied for creating new candidates from the survival.

The crossover: It can occur in use of asexual and sexual ways of reproductions (Fig. 1). From sexual crossovers, two chromosomes are created, one of them is chose randomly and it is propagated to the next generation.

Mitosis: It creates a same copy of individual (Fig. 1(a)).

Mitosis with Chain Reversal: A new chromosome is formed by creating a same copy of the parent, and by positioning a part of genes in opposite direction (Fig. 1(b)).

N-Point Crossover: Two parents are chosen randomly, two children could be created by exchanging portions of parents (Fig. 1(c)).

Channeled Crossing Over: It operates as N-point crossover, with the genes of the parts which will be exchanged are positioned in opposite direction in the new chromosomes (Fig. 1(d)).

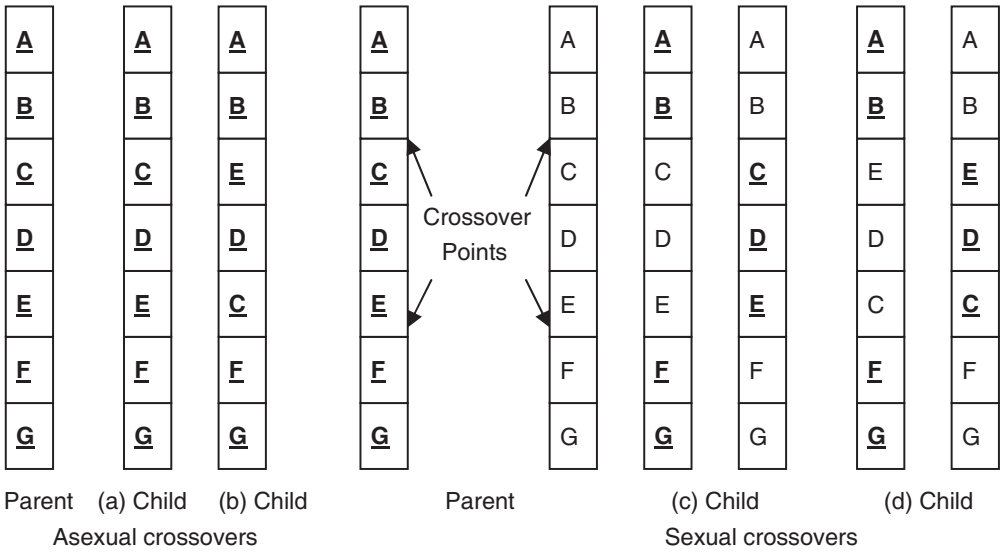

Figure 1: Crossover operators.

The Mutation: It is applied only on the children obtained by crossover. The mutation is applied by checking gene-by-gene basis to see whether or not each gene will be mutated. If a gene is selected for mutation, then its numerical value is randomly changed. Traditional real-based mutation operators usually take the form $gene = [gene + \delta]$ [6, 7]. J.M Hall [4] proposes other manners to apply the mutation, a *multiplicative* operator is proposed which has the form $gene = (gene^{*}\delta)$ where δ is a random multiplier determined from the normal probability distribution having a mean of 1.0, and σ determined by:

$$\sigma = 1 - (Current\ Best\ Fitness/Target\ Fitness) \tag{1}$$

The parameter σ begins as unity ($\sigma = 1$) at the first generation and then will decrease linearly, approaching zero as the "current best fitness" approaches the desired target fitness.

We check the genes in the new chromosomes, if a gene is outside specified constraints; the mutation is ignored and the processes act like as it never happened.

Stopping criteria: The evolution of the cycle (Evaluation by fitness function-Extinction- Reproduction) is repeated until no progress is observed in the population for several generations. Here in, we give how we compute and choose the genetic parameters.

2.2. Genetic Parameters

- **Crossover probability**: In practice, the performances vary generally little according to the type of the crossover operator [6]. Then, from generation to generation, with equal probability, we select one operator from sexual and asexual crossovers.
- **Mutation probability**: The research becomes random when the probability rate is high and there is a risk of stagnation if it is low (population less diversified). Contrary to several works with GA where the mutation probability Pm is a fixed parameter, here in, we propose to decrease its rate along the generations. So, we take an exponentially decrease [8].
- **Size of the population**: if the population is large enough, it allows finding the global extreme and not gets stuck in a local extreme. However, it became time intensive. If the population is too small, the best solution is often missed since the research space is not sampled enough [6, 7].

  Here in, we propose to fix the size of the population N, and to ensure a best sampling of research space, we test the diversity of the population. If from a number of generations, a new best candidate is not found, then the half of the population least adapted to the problem since their fitness is eliminated, and it is replaced by others candidates randomly generated. With this way, we ensure the diversity by testing more the solution candidates and thus, we explore better the research space without increasing the size of the population N.
- **Replacement percentage**: It defines the fraction of the current population that will be replaced at each generation, here in; we replace 50% of the population.

  In what follows, we present how we compute the reflectivity which is used as fitness of candidates.

3. ANALYSIS METHOD: COMPUTATION OF THE REFLECTIVITY PARAMETER

Let us consider a stacking of thin blades resting on a plane substrate. There are several methods to compute the reflectivity of the stack, by using Parratt's recursion formula in terms of the Fresnel coefficients, or by the compute of the layer and propagating matrices [5]. Here in, we use the concept of impedance transformation [9]. We must take into account two different polarizations of light as determined by the direction of the electric (E) field. Perpendicular polarization (TE): In this case, the incident electric field is normal to the plane incidence. Parallel polarization (TM): The electric field is parallel to the plane of incidence. The reflection coefficients are given [9]:

$$r_{TE} = \frac{Z_2 \cos\theta_i - Z_1 \cos\theta_t}{Z_2 \cos\theta_i + Z_1 \cos\theta_t} \qquad r_{TM} = \frac{Z_1 \cos\theta_i - Z_2 \cos\theta_t}{Z_1 \cos\theta_i + Z_2 \cos\theta_t} \tag{2}$$

With Z_1 and Z_2 are respectively the impedance of vacuum (μ_1, ε_1) and media layer (μ_2, ε_2), θ_i is incident angle and θ_t is refraction angle, which is defined according the Snell'law [9].

For multiple layers, the concept of impedance transformation is used to analysis this problem.

TE polarization: The reflection coefficient at the interface between Layer 1 and 2 is obtained as:

$$r_{TE} = \frac{Z_{inTE21} \cos\theta_i - Z_1 \cos\theta_2}{Z_{inTE21} \cos\theta_i + Z_1 \cos\theta_2} \quad \text{with} \quad Z_{inTE21} = Z_2 \frac{Z_{inTE32} \cos\theta_2 + Z_2 \cos\theta_3 \tanh(\gamma_2 d_2 \cos\theta_2)}{Z_2 \cos\theta_3 + Z_{inTE32} \cos\theta_2 \tanh(\gamma_2 d_2 \cos\theta_2)} \tag{3}$$

where Z_{inTE21} denotes the input impedance for TE mode between these two layers, it is obtained by the concept of impedance transformation of successive layers [9], γ_2 is the constant of propagation. Obviously this concept can be generalized to any number of layers, for with expression (3) may be obtained by recursion.

TM polarization: The corresponding expressions for the reflection coefficient and the input impedance for parallel polarization at the interface between layers 1 and 2 may be derived as:

$$r_{TM} = \frac{Z_1 \cos\theta_i - Z_{inTM21} \cos\theta_2}{Z_1 \cos\theta_i + Z_{inTM21} \cos\theta_2} \quad \text{with} \quad Z_{inTM21} = Z_2 \frac{Z_{inTM32} \cos\theta_3 + Z_2 \cos\theta_2 \tanh(\gamma_2 d_2 \cos\theta_2)}{Z_2 \cos\theta_2 + Z_{inTM32} \cos\theta_3 \tanh(\gamma_2 d_2 \cos\theta_2)} \tag{4}$$

We take to reflectivity in decibels, then:

$$R_{TE} = 10^* \log_{10}\left(\left|r_{TE}^2\right|\right) \quad \text{and} \quad R_{TM} = 10^* \log_{10}\left(\left|r_{TM}^2\right|\right) \tag{5}$$

In following section, we give application results for optimization of flat multilayer structures.

4. APPLICATION AND RESULTS

We hope to find the characteristics of the various layers which ensuring the minimal reflection over the X-band frequency (8.2 to 12.4 GHz) and incidence angle (from normal to grazing incidence). During all the evolutionary simulation, the dielectric and magnetic constants values are specified falling between 0 and 4, the thicknesses between [0.6–10] mm. We search the configurations with the real parts of the dielectric and magnetic constants positive, to simplify the realisation of the absorbers with available materials. The studied structure has three layers and 15 variables to optimize. The obtained results are shown (Figs. 2 and 3).

For the TE mode, the Figs. 2(a, d) give the obtained results with optimization over the frequency band for the normal angle (0°). Figs. 2(b, e, f) give those obtained with optimization over the angle band for 8.5 GHz. Fig. 2(f) gives the obtained characteristics.

By Figs. 2(a) and 2(b), we can easily check that the performances of the fittest chromosome is improved according the generations. Figs. 2(e, f) shows a good performance at 8.5 GHz for incidence angle less than 20° and the performance decreases as we approach 30° and more (grazing incidence angle), which is physically correct.

For the TM mode, we present the results in Fig. 3. We obtained similar performances than the TE mode. The optimization over angles is doing in 9 GHz.

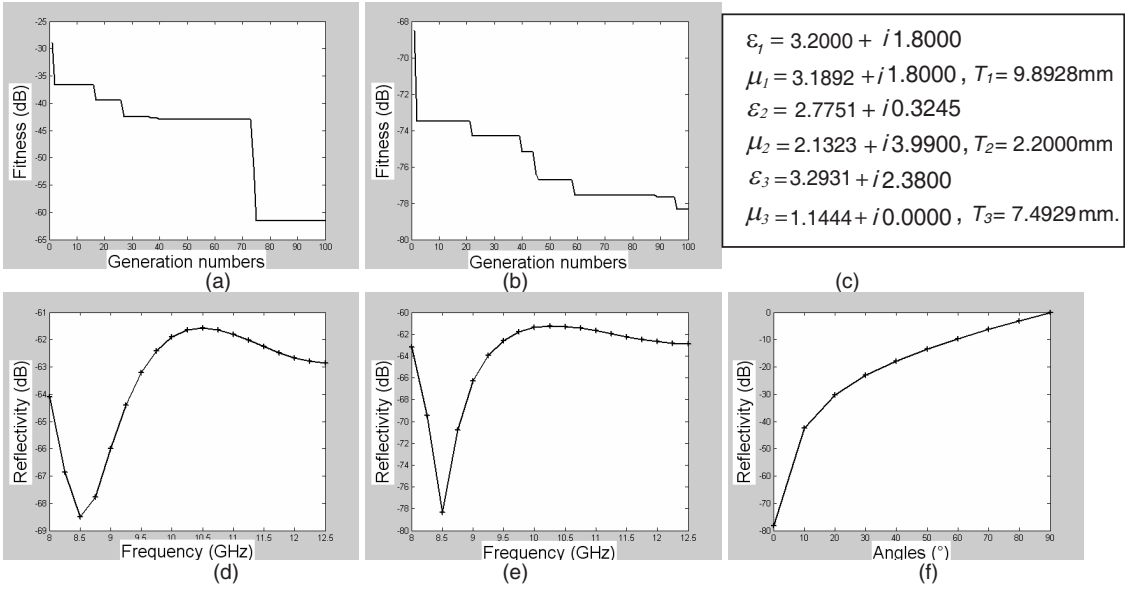

Figure 2: TE Mode: Optimization according frequencies for $\theta_1 = 0°$ (a) and (d). Optimization according to the incidence angle for $f = 8.5$ GHz (b, c, e and f).

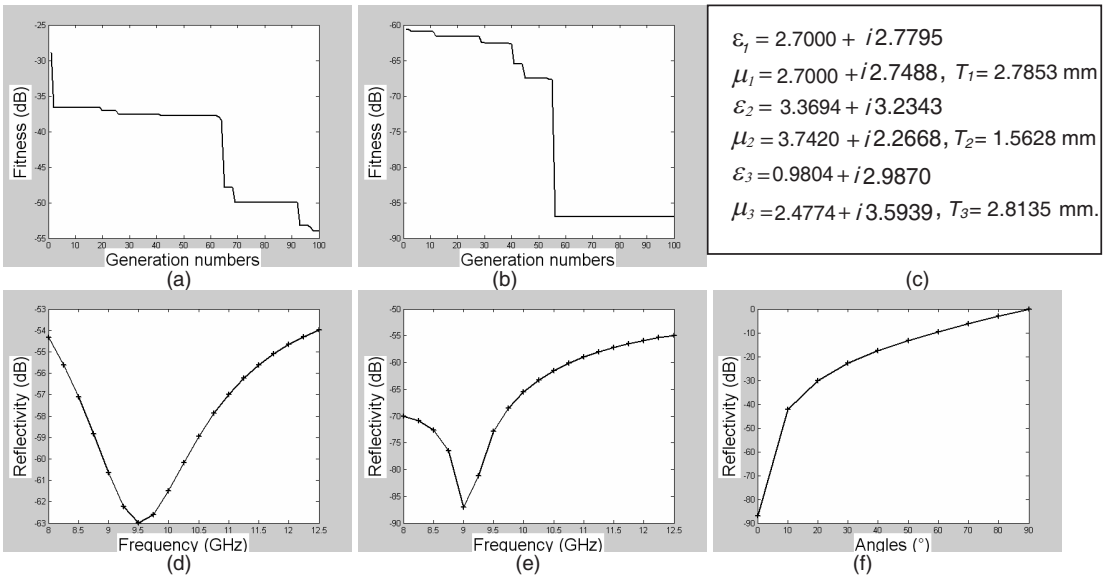

Figure 3: TE Mode: Optimization according frequencies for $\theta_1 = 0°$ (a and d). Optimization according to the incidence angle for $f = 9\,\mathrm{GHz}$ (b, c, e and f).

5. CONCLUSION

In this paper, we have showed how to construct the multilayer absorbers that can minimize the reflection on a wide frequency band (X-band) and a wide incidence angle band (from normal to grazing). Since the reflection is strongly dependent on the characteristics of layers, we have proposed the use of genetic algorithms GAs to find the thicknesses, the electric and magnetic constants of the blades.

We have chosen the GAs because they are especially powerful for problems: Of high dimensions; handle discrete and discontinuities parameters; and that we have no idea where the solution will be.

We have used the reflection parameter as fitness function to direct the genetic research to the configuration which minimizes the reflection.

We give how we compute the genetic parameters in each generation that allows a better exploration of the research space and an automatic genetic research. In future works, the synthesis by GAs method will be applied for study others types of absorbers.

REFERENCES

1. Cui, S., D. S. Weile., and J. L. Volakis, "Novel planar absorber designs using genetic algorithms," *Antennas and Propagation Society International Symposium*, Vol. 2B, 271–274, July 2005.
2. Cui, S. and D. S. Weile, "Robust design of absorbers using genetic algorithms and the finite element-boundary integral method," *IEEE Transactions on Antennas and Propagation*, Vol. 51, No. 12, 3249–3258, December 2003.
3. Donelli, M., S. Caorsi, F. De Natale, M. Pastorino, and A. Massa, "Linear antenna synthesis with a hybrid genetic algorithm," *Progress In Electromagnetics Research*, PIER 49, 1–22, 2004.
4. Hall, J. M., "A novel, real-valued genetic algorithm for optimizing radar absorbing materials," NASA/CR-2004-212669, March 2004.
5. Petit, R., *Electromagnetic Waves in Radio Electricity and Optics*, Masson Edition, 1992.
6. Goldberg, D. E., *Genetic Algorithms in Search, Optimization and Machine Learning*, Addison-Wesley, 1989.
7. Mitchell, M., *Introduction to Genetic Algorithms*, MIT press, 1996.
8. Lutton, E. and P. Martinez, "A genetic algorithm for the detection of 2D geometric primitives in images," *Computer Vision and Image Processing*, Vol. 1, 526–528, 1994.
9. Vinoy, K. J. and R. M. JHA, *Radar Absorbing Materials*, Kluwer Academic Publishers, 1996.

A Novel Analysis for Circular-groove Guide

Yinqin Cheng
Northwest University for Nationalities, China

Abstract— Using method of moment, the circular-groove guide has been studied. The characteristic equation of circular-groove guide has been gotten with this method. The transmission characteristics of the dominant mode have been obtained and discussed.

1. INTRODUCTION

The method of moment (MOM) [1] is one of the classical numerical computation methods for electromagnetic field. It has widely mainly been applied to analyze the electromagnetic radiation and scattering. As one of the millimeter waves transmission lines, the transmission characteristic of circular-groove guide has been studied in previous papers [2–4]. In this paper, it's the first time that eigenvalue equation of the circular-groove guide is obtained by using the method of moment and its cut-off characteristic is gotten and discussed.

2. THEORY ANALYSIS

The cross section of open circular-groove guide and its geometrical dimensions are shown in Fig. 1. Whole guide can be divided into three parts, central groove region I and two parallel plane regions II. According to the geometrical shape, rectangular coordinates in regions II and cylindrical coordinates in region I are adopted. They are of the same z direction. Suppose electromagnetic wave transmits along the z direction, the transverse wave function $\psi_i(x, y)$ satisfies two-dimensional Helmholtz equation in the cross section of groove guide as follows:

$$\nabla_{\mathrm{T}}^2\psi_i(x,y) + k_{\mathrm{c}}^2\psi_i(x,y) = 0 \quad (i = 1, 2). \tag{1}$$

where ∇_{T}^2 is transverse Laplacian operator. Wave function $\psi_i(x, y)$ is E_Z for TM modes or H_Z for TE modes. $k_{\mathrm{c}}^2 = k^2 - \beta^2$, here k_{c} is called longitude cut-off wavenumber of waveguide, k is wavenumber in the free space and β is phase-shift constant. Where $i = 1$ and $i = 2$ represents central groove region I and parallel plane regions II respectively.

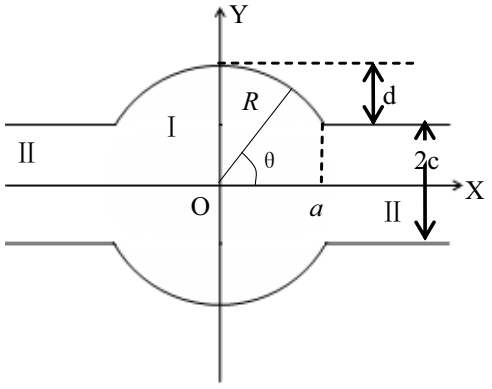

Figure 1: The cross-section of circular-groove guide.

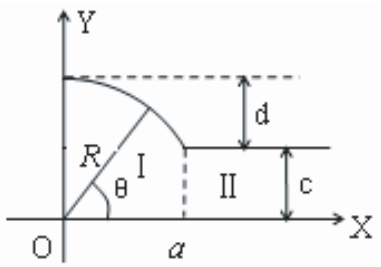

Figure 2: 1/4 analytic model of circular-groove guide.

On the boundary of the cross-section of the waveguide, Equation (1) satisfies Dirichlet boundary condition for the TM modes or the Neumann boundary condition for the TE modes as follows:

$$\begin{cases} \psi = 0 \\ \dfrac{\partial\psi}{\partial n} = 0 \end{cases} \tag{2}$$

Considering symmetry of electromagnetic field structures and simplifying calculation complexity, 1/4 analytic model shown in Fig. 2 is adopted in this paper. According to the electromagnetic

structures, for the main mode TE_{11}, planes at $x = 0$ and $y = 0$ can be respectively regarded as electric wall and magnetic wall.

Let $L = -\nabla_{\mathrm{T}}^2 = -\dfrac{\partial^2}{\partial x^2} - \dfrac{\partial^2}{\partial y^2}$, $\xi = k_{\mathrm{c}}^2$, Equation (1) can be written as:

$$L\psi_i = \xi\psi_i \tag{3}$$

The above problem is just the eigenvalue problem of the MOM. Base functions $\{f_n(x,y)\}$, $\{g_n(x,y)\}$ and corresponding weight functions $w_m(x,y)$, $v_m(x,y)$ are chosen in region I and regions II respectively. And then the transverse wave function $\psi_i(x,y)$ can be expanded as follows:

$$\psi_1(x,y) = \sum_{n=1}^{N} a_n f_n(x,y) \tag{4}$$

$$\psi_2(x,y) = \sum_{n=1}^{N} b_n g_n(x,y) \tag{5}$$

According to Galerkin method described in the MOM, the matrix eigenvalue equation of circle-groove for region I and regions II can be obtained, i.e.,

$$[\mathrm{L}_{mn}][\mathrm{a}_n] = \xi[\mathrm{M}_{mn}][\mathrm{a}_n] \tag{6}$$

$$[\mathrm{P}_{mn}][\mathrm{b}_n] = \xi[\mathrm{Q}_{mn}][\mathrm{b}_n]. \tag{7}$$

where,

$$[\mathrm{L}_{mn}] = \begin{bmatrix} < w_1, Lf_1 > & < w_1, Lf_2 > & \cdots & < w_1, Lf_n > \\ < w_2, Lf_1 > & < w_2, Lf_2 > & \cdots & < w_2, Lf_n > \\ \cdots\cdots\cdots & \cdots\cdots\cdots & \cdots\cdots\cdots & \cdots\cdots \end{bmatrix},$$

$$[\mathrm{M}_{mn}] = \begin{bmatrix} < w_1, f_1 > & < w_1, f_2 > & \cdots & < w_1, f_n > \\ < w_2, f_1 > & < w_2, f_2 > & \cdots & < w_2, f_n > \\ \cdots\cdots\cdots & \cdots\cdots\cdots & \cdots\cdots\cdots & \cdots\cdots \end{bmatrix}$$

$$[\mathrm{P}_{mn}] = \begin{bmatrix} < v_1, Lg_1 > & < v_1, Lg_2 > & \cdots & < v_1, Lg_n > \\ < v_2, Lg_1 > & < v_2, Lg_2 > & \cdots & < v_2, Lg_n > \\ \cdots\cdots\cdots & \cdots\cdots\cdots & \cdots\cdots\cdots & \cdots\cdots \end{bmatrix},$$

$$[\mathrm{Q}_{mn}] = \begin{bmatrix} < v_1, g_1 > & < v_1, g_2 > & \cdots & < v_1, g_n > \\ < v_2, g_1 > & < v_2, g_2 > & \cdots & < v_2, g_n > \\ \cdots\cdots\cdots & \cdots\cdots\cdots & \cdots\cdots\cdots & \cdots\cdots \end{bmatrix}$$

$$[\mathrm{a}_n] = [a_1\, a_2\, \ldots\, a_n]^{\mathrm{t}}$$

$$[\mathrm{b}_n] = [b_1\, b_2\, \ldots\, b_n]^{\mathrm{t}}.$$

According to the matching condition of two regions on the plane $x = a$, i.e.,

$$\begin{cases} \psi_1 = \psi_2 \text{ for } |\mathrm{y}| \le c \\ \dfrac{\partial\psi_1}{\partial x} = \dfrac{\partial\psi_2}{\partial x} \text{ for } |\mathrm{y}| \le c \end{cases} \tag{8}$$

following equation can be gotten.

$$\sum_{n=1}^{N} a_n f_n(a, y_i) = \sum_{n=1}^{N} b_n g_n(a, y_i) \tag{9}$$

Here,

$$y_i = \frac{ic}{N+1} \in [0, c],\ i = 1,\, 2,\, \ldots,\, N.$$

The matrix equation corresponding to (9) is

$$[\mathrm{C}_{mn}][\mathrm{a}_n] = [\mathrm{D}_{mn}][\mathrm{b}_n]. \tag{10}$$

where,

$$[\mathrm{C}_{mn}] = \begin{bmatrix} f_1(a,y_1) & f_2(a,y_1) & \dots & f_N(a,y_1) \\ f_1(a,y_2) & f_2(a,y_2) & \dots & f_N(a,y_2) \\ \dots & \dots & \dots & \dots \\ f_1(a,y_N) & f_2(a,y_N) & \dots & f_N(a,y_N) \end{bmatrix},$$

$$[\mathrm{D}_{mn}] = \begin{bmatrix} g_1(a,y_1) & g_2(a,y_1) & \dots & g_N(a,y_1) \\ g_1(a,y_2) & g_2(a,y_2) & \dots & g_N(a,y_2) \\ \dots & \dots & \dots & \dots \\ g_1(a,y_N) & g_2(a,y_N) & \dots & g_N(a,y_N) \end{bmatrix}$$

Based on (10), relationship of $[\mathrm{b}_n]$ and $[\mathrm{a}_n]$ can be obtained, i.e.,

$$[\mathrm{b}_n] = [\mathrm{D}_{mn}]^{-1}[\mathrm{C}_{mn}][\mathrm{a}_n] = \mathrm{K}_{mn}[\mathrm{a}_n]$$

Plus (6) and (7), the following equation can be obtained

$$[\mathrm{A}_{mn}][\mathrm{a}_n] = \xi[\mathrm{B}_{mn}][\mathrm{a}_n] \tag{11}$$

where,

$$[\mathrm{A}_{mn}] = [\mathrm{L}_{mn}] + [\mathrm{P}_{mn}]\mathrm{K}_{mn}, \quad [\mathrm{B}_{mn}] = [\mathrm{M}_{mn}] + [\mathrm{Q}_{mn}]\mathrm{K}_{mn}$$

Equation (11) is exactly eigenvalue equation of the circular-groove guide. So the cut-off wavenumber k_c can be got by solving it's eigenvalue $\xi = k_c^2$. After the characteristic vectors $[\mathrm{a}_n]$ and $[\mathrm{b}_n]$, namely expansion coefficients $\{a_n\}$ and $\{b_n\}$, are solved from the above equations, the wave function $\psi_i(x, y)$, i.e., the approximate solutions of electromagnetic field in the groove region and parallel plane regions, will be determined.

3. NUMERICAL RESULTS AND DISCUSSIONS

Power function is used as the base function in central groove region I and exponential function, which attenuates along x direction, is used as the base function in parallel plane regions II. They satisfy the electromagnetic boundary condition. Based on the above theory analysis, the cut-off characteristic curves for main mode TE_{11} of circular-groove guide can be gotten and shown in Fig. 3–Fig. 5.

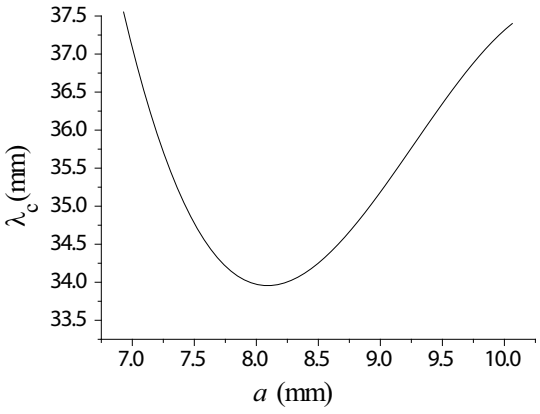

Figure 3: The cut-off characteristic of circular-groove guide with a.

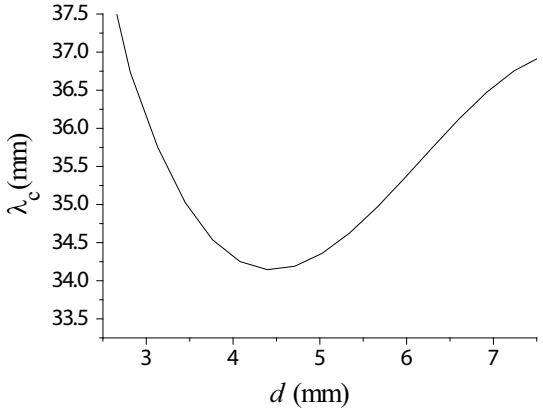

Figure 4: The cut-off characteristic of circular-groove guide with d.

It can be seen from Fig. 3–Fig. 5 that cut-off property of circular-groove guide is better than that of circular guide.

Moreover, the varying tendency of cut-off wavelength of circular-groove guide with groove width a, groove depth d and plane width c is nonlinear. This is in agreement with before.

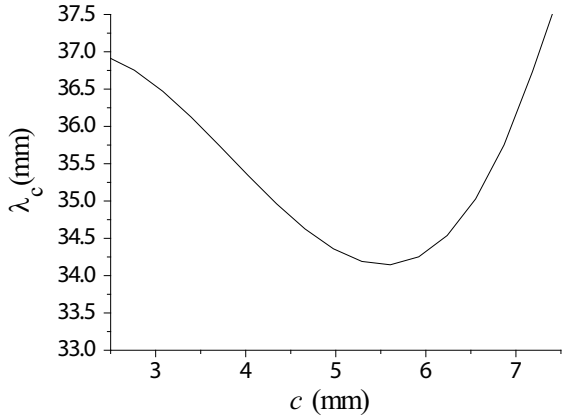

Figure 5: The cut-off characteristic of circular-groove guide with c.

4. CONCLUSION

Using the method of moment, the eigenvalue equation of circular-groove guide is obtained. And the transmission characteristics of the main mode is gotten and discussed. The numerical results concluded in this paper are in agreement with before. So the efficiency of this method is verified. To make the analysis simple, 1/4 analytical model is adopted. The obtained results are of important application values in analyzing and computing the groove guides performances in practical engineering problems.

REFERENCES

1. Harrington, R. F., translated by Wang Erjie, *Field Computation by Moment Methods*, 144–191, National Defence Industry Press, Beijing, 1981.
2. Yang, H., J. Ma, and Z. Lu, "The characteristic eauation and solution of circular-groove guide," *International Journal of Infrared and Millimeter Waves*, Vol. 12, No. 5, 535–541, 1991.
3. Xu, Z., H. Yang, and Z. Lu, "The novel boundary integral equation method for solving arbitrary cross-section waveguides," *International Journal of Infrared and Millimeter Waves*, Vol. 16, No. 7, 1239–1247, 1995.
4. Yan, H. and H. Yang, "A new circular groove guide analysis," *International Journal of Infrared and Millimeter Waves*, Vol. 20, No. 1, 149–154, 1999.

PIC Simulation of Surface Charging in the Wake Zone

J. Wang, J. W. Qiu, and X. G. Qin
National Key Lab. of Vacuum & Cryogenics Technology and Physics
Lanzhou Institute of Physics, Lanzhou 730000, China

Abstract— Space charging process in the wake zone is reviewed and calculated with 3-D particle-in-cell (PIC) simulation soft SPIS under the interactions of two-box and plasma in low earth and auroral orbits (LEO/PEO). A model of two-box immersing in the macro ion and electron flows is built in the paper to numerically simulate the interaction of two-body with space plasma. These macro particles move in manner of electrostatic PIC algorithm, which solves Poisson equation with leap-frog format. In the two-box model, a large conductor denotes spacecraft and a small insulator denotes free flyer all keeping relative stationary in LEO/PEO while macro particles spreads with resultant velocity of thermal and drift components. The secondary electron emission both from the surface of two bodies is treated as an inner boundary condition. The simulation provides a quantitative estimation of electric potential of the existence of the wake zone as well as charging voltage of the free body in the wake zone. It also validates that the same severe charging conditions as literatures described are indispensable to achieve high voltage between the small body and large body in the wake zone while insulators involved.

1. INTRODUCTION

Spacecraft-plasma interaction and its charging problem has been an active field of research from 1970s [1, 2]. Generally, Spacecraft charging at low altitudes is regarded as an inessential problem because typical ambient electron has a temperature of 0.1 eV so that the charging potential of a spacecraft in the ionosphere is at about the same order of the temperature. However, high-voltage charging of large spacecraft under the condition of low or polar orbit plasma had been first predicted by Parks and Katz in 1981 and first observed by Gussenhoven in 1985 [3, 4]. High negative voltage of surface charging in wake zone is important in connection with solar array of complex space station, spacecraft docking, extravehicular activity of astronauts, and so on [5]. The different charging process of Multibody Interaction in Plasma (MIP) [6] or Multibody-Plasma Interactions (MPI) [7] on the wake-side of the spacecrafts has been widely investigated as the man-in-the wake problem for Space Transfer System (STS) and International Space Station (ISS) [8] application. A hybrid Particle-In-Cell (PIC) method or like is used to tackle this surface charging problem [9]. In 2001, J. Forest et al. released the first generation full 3-D PIC spacecraft plasma simulation software, PicUp/SPIS [10]. In 2004, Engwall used the software PicUp3D to carry out numerical simulations of a flowing plasma interaction with a spacecraft [11]. In 2007, the second generation of PicUp3D named SPIS 3.6 is released by SPINE community.

In the paper, the surface charging problem of space body in the wake zone of low polar orbit is reviewed and calculated with 3D PIC Software, SPIS, to validate its feasibility and implementation. In Section 2, a detailed simulation scheme of wake charging is developed with PIC algorithm. In Section 3, the simulation model and numerical results are presented. Section 4 contains some concluding remarks.

2. MODEL OF SPACECRAFT-PLASMA INTERACTION

Spacecraft charging problem at low polar orbit is commonly represented as a moving body immersing dense and cool ionosphere plasma as well as hot auroral electron. Multi bodies keep fixed positions and the plasma moves with drift Maxwell distribution, which means the particle velocity is replaced by resultant velocity based on spacecraft speed and thermal speed. In order to simply the problem, geomagnetic field and anisotropic velocity distribution factors of charging in low attitude are not considered.

The computational model of two bodies charging in the plasma is shown in Fig. 1.

While much computational time of PIC method, it is all of simulation space in Fig. 1 that should

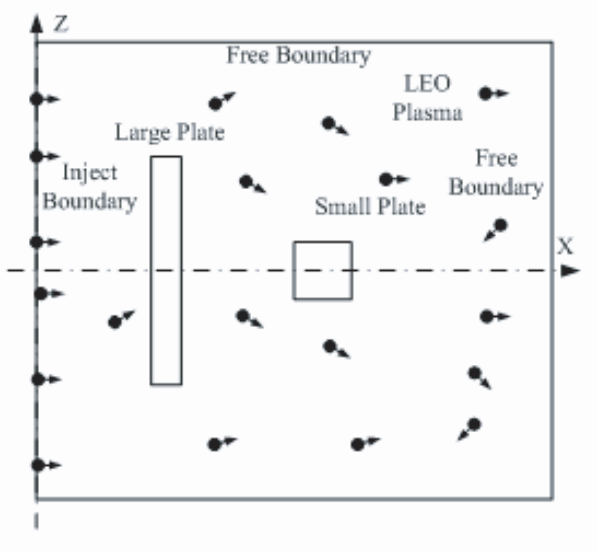

Figure 1: Computational model of two bodies charging in the plasma.

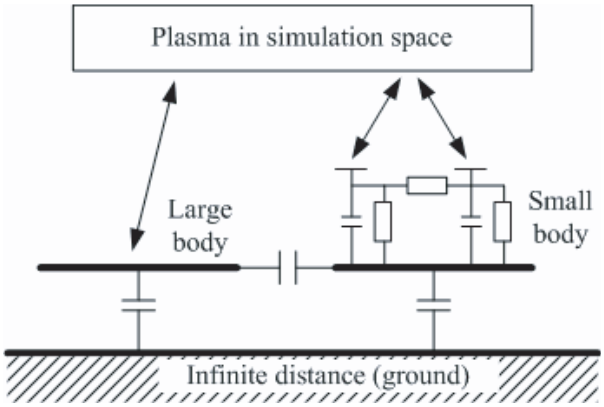

Figure 2: Spacecraft circuit model of two-body charging.

be considered in SPIS. The electrostatic equations of PIC algorithm is as follows:

$$\frac{\partial^2\varphi}{\partial x^2}+\frac{\partial^2\varphi}{\partial y^2}+\frac{\partial^2\varphi}{\partial z^2}=-\frac{\rho}{\varepsilon} \tag{1}$$

$$E=-\nabla\varphi \tag{2}$$

$$m\frac{\mathrm{d}v}{\mathrm{d}t}=qE \tag{3}$$

where v is velocity, q charge, m mass of macro particle, φ space potential, ρ space charge density, ε dielectric constant, and E electric field. The electrostatic field described by Poisson Equation (2) can be solved by in Finite Element Method (FEM) with Dirichlet boundary and Neuman boundary conditions. The treatment of dielectric charge is similar with particles in cells but cumulative charge and ejecting secondary electrons.

The internal boxs are considered as part of simulation domain to be convenient for grid numbering. Different from common Dirichlet boundary condition, potentials of conductor and dielectric regions are not known and should be considered specially. Currently, there are two kinds of methods to tackle the potentials in the simulation space. One is Lumped Element Model (LEM) or spacecraft circuit model, by which the spacecraft charging behavior is equivalent as some electrical components in series or parallel connection, used in SPIS (Spacecraft Plasma Interactions System) of ESA. The other method is to add special conditions in Poisson equation [12]. Here the spacecraft circuit model is taking into consideration in SPIS, shown in Fig. 2.

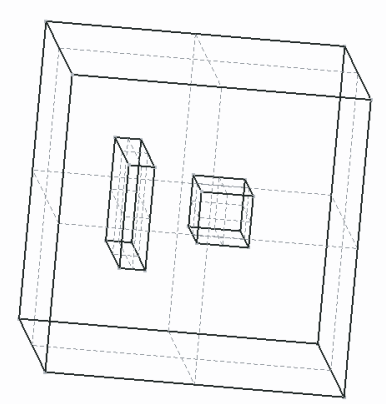

Figure 3: 3-D scheme of two-body charging with GMSH.

3. NUMERICAL SIMULATION AND RESULT

Generally, it is accepted that on the one side, high-voltage charging will only occur under the conditions of a large ratio ambient electron, shade and auroral conditions. On the other side, the wake zone is also accepted as a serious charging zone. As mentioned above, sun shadow, auroral electron and secondary emission are regarded as three main necessary conditions for high-voltage charging in LEO/PEO environment.

For typical LEO/PEO environment at 350 km, the following plasma parameters in the simulation are used: plasma density $10^6\,\mathrm{cm}^{-3}$, electron temperature 0.1 eV, O+ ion temperature 0.05 eV, auroral electron temperature 1 keV, auroral electron density $1\,\mathrm{cm}^{-3}$, Spacecraft or ion drift speed 7700 m/s. Thus the surface potential can be charged to several kilo voltages if the total flux of ions in the aurora zone is lower than electron flux according to literature [3]. Here the magnetic field is neglected to simplify the calculation. The Debye length for cool e- and auroral e- are respectively 2.4 mm and 525.6 m, thus the dimensions of the computational box is $X = Z = 550.0$ m, which should be much larger than Debye length of all three particles. The integration time step is set so that all macro particles should not move through one cell in a time step. The capacity of large aluminum box is roughly set to 5.0e-9F and the mutual capacity between small KAPTON box and large aluminum box is 1.0e-10F.

The 3-D model of two-body is shown in Fig. 3. The potential profile is depicted with Fig. 3 under LEO environment, that is, hot electron is taken out. The large box is charged to 3.6 V and small box 5.5 V. The surface of small KAPTON box is charged to 2560 V.

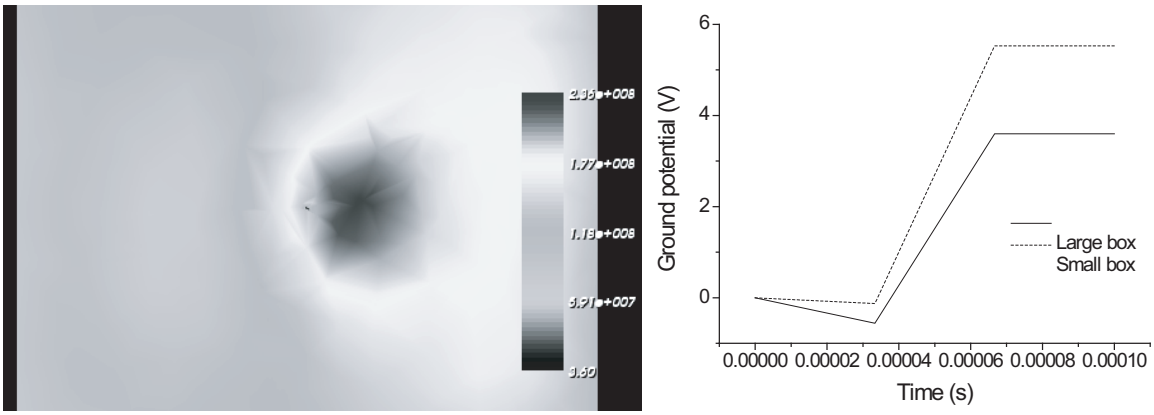

(a) (b)

Figure 4: Potential distribution of computational space of LEO, (a) Volume, (b) Bodies.

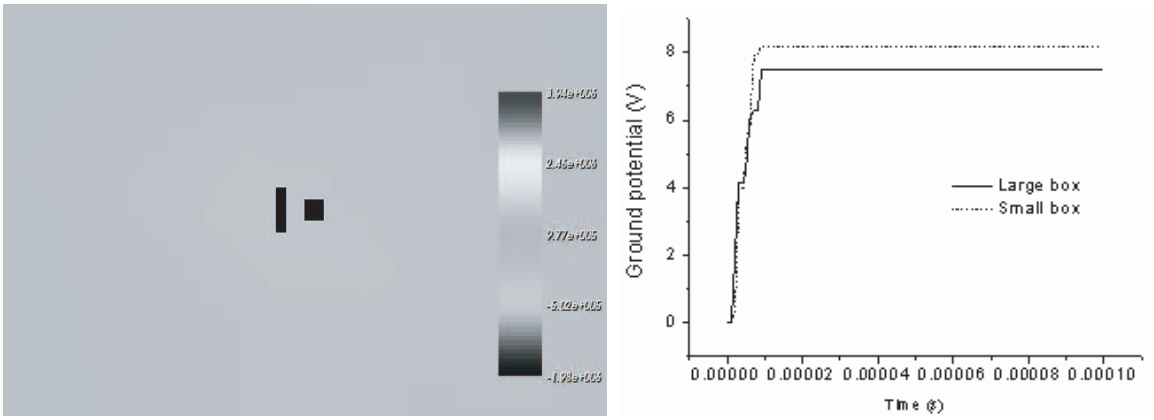

(a) (b)

Figure 5: Potential distribution of computational space of PEO, (a) Volume, (b) Bodies.

Different from LEO environment, the flux of aurora electron is added to simulate PEO environment and the charging results are shown in Fig. 5. The large box is charged to 7.5 V and small box 8.2 V.The surface of small box is charged to 3580 V.

Compared with that in LEO condition, the ground potential of two closing bodies in PEO condition also keep very low voltage, which is different from pervious literatures. However, the surface potential of KAPTON in PEO is charge to near 1.5 times than that in LEO and all keep several kilovolts, which should be seriously considered in docking or extravehicular operations while insulators involved.

4. CONCLUSIONS

Numerical simulation of two-body surface charging in LEO/PEO environment would produce a great deal of usable data for spacecraft docking or extravehicular activity of astronauts. The paper calculates the charging potential of two-body model interaction with plasma in LEO/PEO zone. The simulation results validate that the density ratio of electron and ion is a definitively reason that the potential of bodies in the wake zone increases, especially if the insulators is used, the surface potentials will charge to several kilo voltages. In the development of the paper we consider complex 3D multi-body charging process under true size in aurora zone and involve complicated physical processes rather than simply capacities of bodies.

ACKNOWLEDGMENT

The author would like to express their sincere thanks to Dr. Julien Forest of Artenum Science & Groupware for the SPINE community for advice on the usage of SPIS 3.6 software.

REFERENCES

1. Garrett, H. B. and A. C. Whittlesey, "Spacecraft charging, an update," *IEEE Trans. on Plasma Phys.*, Vol. 28, No. 6, 2017–2028, 2000.
2. Garrett, H. B., "The charging of spacecraft surfaces," *Reviews of Geophysics and Space Physics*, Vol. 19, No. 4, 577–616, 1981.
3. Laframboise, J. G., J. Luo, and L. W. Parker, "High-voltage charging of spacecraft in low polar orbit: A study of physical effects involved," AD-A213 809, Air Force Geophysics Laboratory, Massachusetts, 1986.
4. Gussenhoven, M. S., D. A. Hardy, F. Rich, J. Wang, and H. C. Yeh, "High-level spacecraft charging in the low-attitude polar auroral environment," *Journal of Geophysics Research*, Vol. 90, 11009–11023, 1985.
5. Anderson, P. C., "Spacecraft charging hazards in low earth orbit," *Proceedings of the 7th Spacecraft Charging Technology Conference*, ESA SP-476, 331–336, 2001.
6. Davis, V. A. and L. W. Duncan, "Spacecraft surface charging handbook," AD-A262778, Maxwell Laboratory, California, 1992.
7. Wang, J., P. Leung, H. Garrett, and P. Murphy, "Multibody-plasma interactions: Charging in the wake," *Journal of Spacecraft*, Vol. 31, No. 5, 889–894, 1994.
8. Carolyn, K. P. and S. B. David, "Auroral interactions with ISSA," *NASA Technical Memorandum*, 106794, 1994.
9. Cooke, D. L., "Simulation of an auroral charging anomaly on the DMSP satellite," AIAA-98-0385, *36th Aerospace Science Meeting and Exhibit*, Reno, 1998.
10. Forest, J., L. Eliasson, and A. Hilgers, "A new spacecraft plasma simulation software, PicUp3D/SPIS," *Proc. 7th Spacecraft Charging Technology Conference*, ESTEC, Noordwijk, The Netherlands, April 23–27, 2001.
11. Engwall, E.," Numerical studies of spacecraft-plasma interaction: Simulations of wake effects on the cluster electric field instrument EFW," Swedish Institute of Space Physics, Kiruna, 2004.
12. Wang, J. F., M. L. Qu, S. B. Qu, and B. K. Wang, "A two-dimensional PIC algorithm for numerical solutions of potential in plasma region with undecided conductor boundary conditions (in Chinese)," *Journal of Air Force Engineering University (Natural Science Edition)*, Vol. 7, No. 5, 60–62, 2006.

Physics Based Time Domain Simulation of Magnetic Recording Signal and Noise

Xiaobin Wang[1], **Zhen Jin**[2], **Xuebing Feng**[1], **and Dimitar Dimitrov**[1]

[1]Seagate Technology, Bloomington, USA
[2]Hitachi Global Storage Technology, San Jose, USA

Abstract— Progresses of a fast time domain simulator for magnetic recording signal and noise waveforms are reported. The simulator is a combination of recording physics calculation, micro-magnetic simulation and experimental data information extraction. The simulator takes head media physics parameters as inputs and calibrates to measurements at current area density and scales to recording system at higher area density. It can generate millions of bits in short times, suitable for equalized signal to noise and channel bit error rate simulation. Key topics discussed in this paper to illustrate our techniques include: newly developed transition noise formula and its validation to micro-magnetic simulation, synthesizing time domain position-dependent transition jittering noise and colored electronic noise from measurement data, effects of non-saturation DC noise and head jittering on signal and noise waveforms.

1. INTRODUCTION

Accurately simulating signal and noise waveforms from basic recording head/media physics parameters is a challenge task. This paper reports the progress of a fast time domain simulator for magnetic recording signal and noise waveforms. In order to generate millions of bits for equalized Signal to noise ratio (SNR) and channel bit error rate simulation at short computational times, the simulator combines recording physics calculation, micro-magnetic simulations and experimental data information extraction. The simulator takes head/media physics parameters as inputs, calibrates to measurements at current area density and scales to recording system at higher area density.

After a brief introduction to the simulator procedure in Section 2, progresses in key features of the simulator are discussed. Section 3 discusses analysis and synthesis transition noise based upon newly developed physics formula and demonstrates the validation to micro-magnetic simulation. Section 4 explains our procedure of synthesizing and scaling colored electronic noise waveform in time domain from measurement noise in frequency domain. Effects of non-saturation DC noise and head jittering on signal and noise waveforms are studied in Section 5.

2. SIMULATING PROCEDURE

Random bits waveforms generated by simulator include read-back signal, noise and nonlinear distortion [1]. Key parameters for signal are pulse width and amplitude. Averaged read-back signal width (TW65) mainly depends upon written transition width on media, reader geometry and head media spacing. For high area density recording, signal amplitude quality is strongly affected by written pattern saturation level on the media. In the simulator, parameters of read-back signal are obtained from regression on micro-magnetic simulation. Micro-magnetic read-back simulation is performed to provide pulse width dependence upon given media transition width, reader geometry and head media spacing. Media saturation level in the simulator is determined by writing head field magnitude and regression equation on media magnetization vs external field (MH loop). Media saturation level determines read-back amplitude through regression on micro-magnetic read-back. Noise sources in the simulator include transition noise, electronic noise, DC saturation noise and additional head jittering noise. Detailed noise analysis, synthesizing and scaling will be discussed through Section 3 to Section 5. This paper mainly focuses on signal and noise treatment, particularly on recording noise generation. A novel lookup table technique is used to generate leading and higher orders of nonlinear distortion in the simulator. However, due to paper length constrain, the detailed discussion of nonlinear distortion is deferred to other publications.

3. TRANSITION NOISE ANALYSIZING AND SYNTHESIZING

Media noise is the dominant noise source for current magnetic recording system. Media noise is composed of transition jittering noise and DC saturation noise. Here we will discuss transition noise

analysis and synthesis. In transition noise model [2], Media jittering is determined by transition parameter and cross track correlation length. Analytical formulas have been obtained before for transition parameter and cross track correlation length for high area density recording [3, 4]. Compared to traditional analytical approach such as William-Comstock model, the main contributions of these formulas are the capability of linking media noise parameters to detailed media microphysics parameters (such as grain size, inter-granular exchange etc). When these formulas are validated to micro-magnetic simulation for current recording system, they are further developed. It should be pointed out here that micro-magnetic simulation is still the best approach that can be used to validate media transition noise formulas. The difficulty of directly validating transition noise model to experimental measurement is largely due to reader resolution effects on media noise as described in [5]. The newly development in transition noise formula include media clustering effects, head field angular effects and generalization of cross track correlation length formula. Media clustering formula follows [6] where the cluster size is determined by media mean grain size, grain size distribution, exchange and exchange distribution. Head field angular effect on transition parameter is modeled through dependence of media coercivity on head field angle. The dependence of media coercivity on field angle is obtained from regression equation on micromagnetic simulation of media MH loop. The cross track correlation length formula in [4] is further generalized to include whole M-H loop shape, instead just the slope. An iteration procedure is used to eliminate the limitation of Taylor expansions in the original paper.

Figure 1 shows the validation of transition noise formula to micro-magnetic simulation. There are two ways to extract transition parameter and cross track correlation length from micro-magnetic simulation. In first approach, the transition parameter is obtained by fitting to the mean magnetization transition shape. The cross track correlation length is determined by integration of cross track correlation function of media magnetization. In second approach, transition parameter and cross track correlation length are obtained from normal modes analysis of micro-magnetic simulated media noise waveform. A good reference for media noise normal modes analysis is in [7]. Compared to first approach, second approach is more time consuming because it requires micro-magnetic ensemble simulation to obtain media noise statistics. In our validation, both approaches are used to extract consistent noise parameters from micro-magnetic simulation.

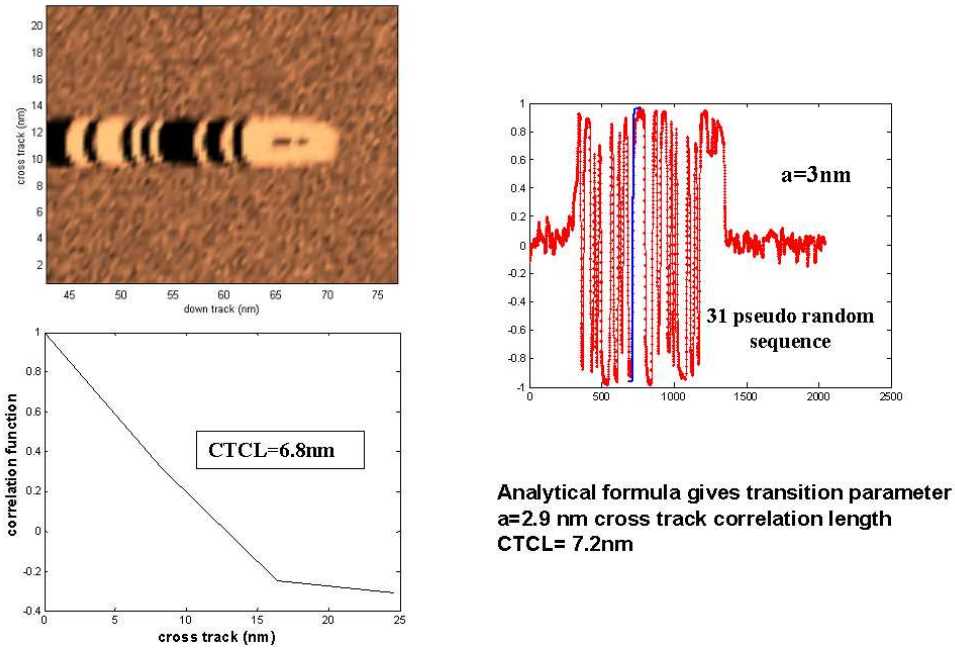

Figure 1: Validation transition parameter and cross track correlation length formulas to micro-magnetic simulation.

Once intrinsic media transition noise parameter and cross track correlation length are obtained, the transition noise waveform can be synthesized based upon normal modes expansion as in [5, 7].

4. ELECTRONIC NOISE SYNTHESIZING AND SCALING

Electronic noise is the noise measured as reader away from media. For high area density recording system, it is of great importance to obtain the electronic signal to noise ratio as head, media and head media spacing scales down. Electronic signal to noise here is simulated as a combination of micro-magnetic simulation for read-back signal and electronic noise formula analysis. The signal is obtained from regression on micro-magnetic simulation as described in Section 1. The electronic noise analysis includes thermal magnetization noise [8, 9], $1/f$ noise and Johnson/shot noise. In our study, these noise formulas are used to fit measured reader electronic noise spectral at current density and head media dimension. An example fitting is shown in Figure 2. The key physics parameters are determined through fitting to measurement and knowledge of current head media dimensions. Then these physics parameters are scaled down to future area density as head dimension, media dimensions and head media spacing shrink. Through this approach, electronic SNR at future area density with decreased head media dimensions and head media spacing can be simulated, as an example in Figure 3. The electronic noise formulas fitted to current noise measurements are in frequency domain. Inverse FFT is used with the assumption of Gaussian or Poisson statistics to generate time domain waveforms. Figure 4 shows an example of generated signal and noise waveform for 128 pseudo-random sequences (both signal, media noise and electronic noise).

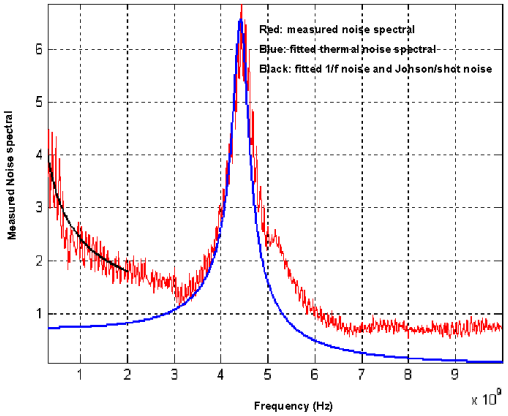

Figure 2: Fitting experimental measured reader noise spectral by thermal noise, $1/f$ noise and shot/Johnson noise.

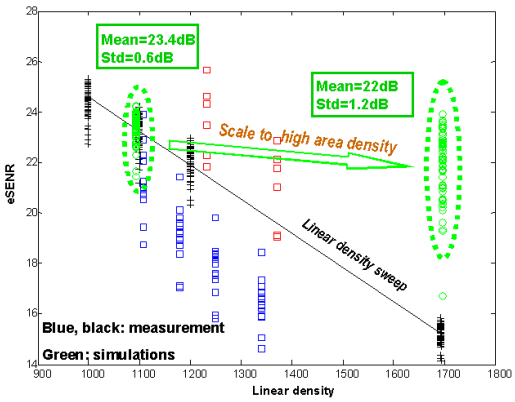

Figure 3: Calibrate electronic SNR calculation to measurement at current linear density and scale to higher linear density through system modeling.

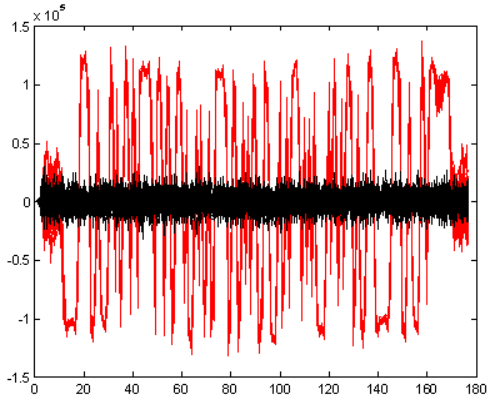

Figure 4: An example of generated signal and noise waveform for 128 pseudo-random sequences: red: signal and media noise, black: colored electronic noise.

5. DC SATURATION AND HEAD JITTERING NOISE

For high area density perpendicular recording, insufficient head writability could cause nonsaturation in media DC region. This will affect both read-back signal and noise. Figure 5 shows the effect of non-saturation on media and read-back signal. Signal could be degraded through amplitude loss and pulse broadening, if writer field is not strong enough to fully saturate media. In our simulator, this effect on signal degradation is modeled through head field magnitude and regression equation on micromagnetic simulation of media magnetization vs external field (MH loop). The media noise in DC region is called DC noise and is modeled by approach in [8]. Besides the major noise sources as discussed above, there are additional noise sources in recording system such as head jittering. The head jittering effects on media noise largely depends upon media damping parameter. This noise source, and other possible neglected noise sources could be injected to noise waveform for simulator data calibration.

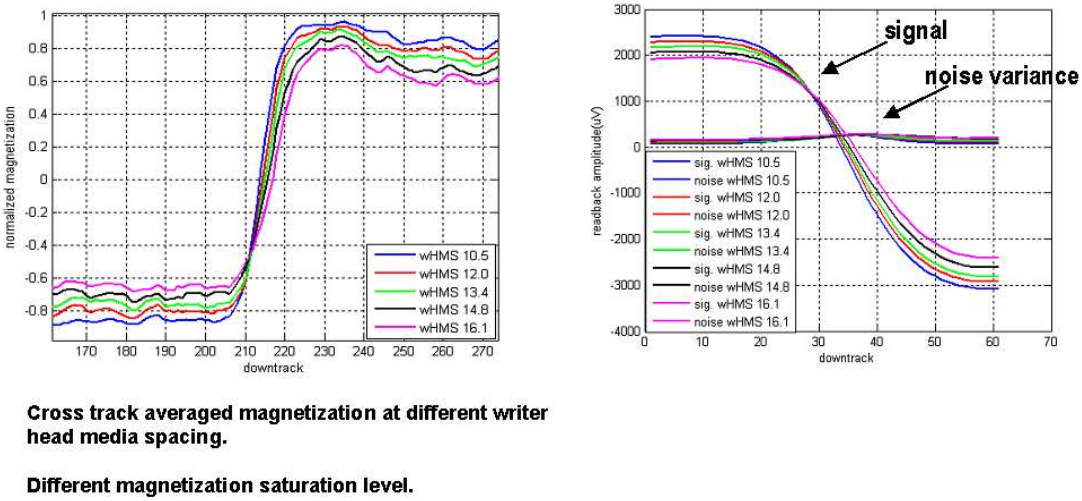

Figure 5: DC nonsaturation effects on signal quality.

6. CONCLUSIONS

Procedure and examples of signal and various noise waveforms simulation in magnetic recording system are shown. The simulator combines newly developed recording physics formulas; micromagnetic simulations and experimental data information extraction to generate random bits waveforms in short time, and thus provides valuable information for data calibration and future system scaling.

REFERENCES

1. Bertram, N. H., *Theory of Magnetic Recording*, Cambridge, 1994.
2. Slutsky, B. and N. H. Bertram, "Transition noise analysis of thin film recording media," *IEEE Transactions on Magnetics*, Vol. 30, No. 5, 2808–2817, 1994.
3. Wang, X. and N. H. Bertram, "Simple transition parameter expression including grain size and intergranular exchange," *J. Appl. Phys.*, Vol. 93, No. 10, 7005–7007, 2003.
4. Jin, Z., X. Wang, and N. H. Bertram, "An analytical model for the cross-track correlation length including inter-granular interactions," *IEEE Transactions on Magnetics*, Vol. 39, No. 5, 2603–2605, 2003.
5. Wang, X., X. Feng, Z. Jin, and J. Fernandez-de-Castro, " Effects of reader response on medium noise modes," *Journal of Applied Physics*, Vol. 99, No. 8, p08k502, 2006.
6. Richter, H. J., E. C. Champion, and Q. Peng, "Theoretical analysis of longitudinal and perpendicular recording potential," *IEEE Transactions on Magnetics*, Vol. 39, No. 2, 697–703, 2003.
7. Xin. X. and N. H. Bertram, "Analysis of transition noise in thin film media," *IEEE Transactions on Magnetics*, Vol. 33, No. 5, 2959–2961, 1997.
8. Smith, N. and P. Arnett, " Thermal magnetization noise in spin valve," *IEEE Transactions on Magnetics*, Vol. 38, No. 1, 32–37, 2002.

9. Bertram, H. N., Z. Jin, and V. L. Safonov, *IEEE Transactions on Magnetics*, Vol. 38, No. 1, 38, 2002.

The Study of PDF Control Technology for a Levitated Globe with Hybrid-excited Magnets

Z. Y. Lu, D. S. Li, L. Z. Ye, W. Wang, and Q. H. Guo
School of Mechanical Engineering and Applied Electronics Technology
Beijing University of Technology, China

Abstract— In order to realize the levitation control of the globe with the hybrid-excited magnets, the authors study the working principle and the mathematical model of the system by the methods of the mechanics analysis and theoretical calculation and obtain parameters based on experiments. According to the data the author deduce the transfer functions of the controlled globe and system. The authors utilize a PDF (Pseudo-Derivative-Feedback) control arithmetic to design the PDF controller. The authors also analyses the systemic stability, robustness and the control precision. The study shows the PDF control method is predominant in the engineering application to the nonlinear and instable system. The method posses the characteristics of robustness and high control precision.

1. INTRODUCTION

A permanent magnet has the advantages of economic energy, working dependably, simple construction and high efficiency, but the disadvantage is the difficulty of magnetic field control when it is used. The electromagnet has the advantage the magnetic field can be controlled easily, but it consumes much energy. In order to utilize the advantage and overcome the above disadvantage, the authors authors uses hybrid-excited magnets to suspend a globe authors. The authors use a standard world globe, where there are seven continents, four oceans.

There are many control methods, such as PDF (Pseudo-Derivative-Feedback) control, self- adjusting control, robust control and artificial neural networks control. All these methods have good effects to solve some certain problem [1]. Among the above methods the PDF control only sets one integral operation in the front channels of the controller [2]. The feedback signal goes a shortcut to directly reach the entrance of the final control element without carrying out a traditional operation. So the derivative feedback signal needn't carry out the operation of actual derivative, but only does the operation of low-order derivative, which brings great convenience for engineering application and makes the system not sensitive to the control parameters. This kind of controller possesses characteristics of high control precision.

2. THE MATHEMATICAL MODEL

2.1. The Working Principle

The working principle diagram for the globe model is shown in Fig. 1, which consists of a sensitive sensor, a globe, a permanent magnet, a electromagnet, a mechanical equipment and a controller. When the globe is in a balance position, the current in the loop is I_0 and the suction F brought by it is equal to the gravity G, then we define the position is a referenced one. If the globe deviates from the referenced position along the down direction, the sensitive sensor can detect and send a signal to the controller. The controller transforms the signal into a control signal and transfers to the amplifier, where the signal is transformed into a control current $I_0 + i$, which takes the place of the original current I_0. Then the electromagnetic suction coming from the electromagnet increases with the control current, so it pulls back the globe to the referenced position. When the globe deviates from the referenced position along the up direction, the control current will drop from I_0 to $I_0 - i$. The electromagnetic suction also drops and the globe drops back by gravity.

2.2. Parameters Based on Experiments

In the referenced position the dynamic equation of the system is Equation (1):

$$mg = F_{\text{elec}} = G_i \left(\frac{i}{y}\right)^2 \tag{1}$$

where m is the globe mass, g is the gravity acceleration, G_i is the magnetic parameter, i is the loop current, y is the levitated gap between the electromagnet and the top of the globe and F_{elec} is the electromagnetic force [3].

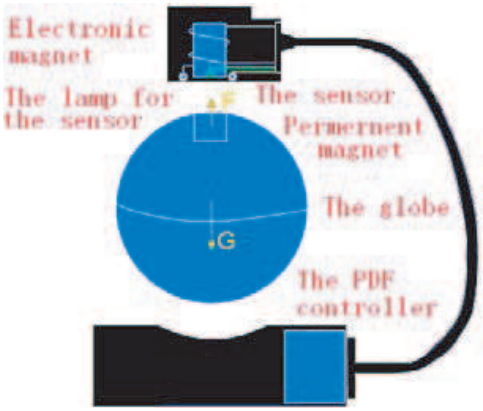

Figure 1: The working principle diagram for the globe model.

Figure 2: The experimental equipment.

The experimental device is shown in Fig. 2, which is a photograph. Where there is a mechanical equipment with hybrid-excited magnets, a globe and some measure equipment. The experimental process is the following. First, we install a mechanical equipment to fix the electromagnet; second, we place the globe in a certain position; then we change the current value to adopt the electromagnetic suction value. When the current value is equal to the gravity G, the first experiment is finished and then we records the first group data including the levitated gap value and the current value. Then we change the levitated distance in the second position to make the second experiment in the method above. After we make the fourteenth experiment in the method above we can obtain the fourteen group original data that are shown in Table 1.

Table 1: The experimental data.

y (mm)	U_1 (v)	U_1 (v)	G_i ($\mathrm{N \cdot m^2/A^2}$)
15.0	3.40	3.68	0.009487
15.5	3.45	4.46	0.008118
16.0	4.47	4.82	0.006270
16.5	5.66	5.85	0.004344
17.0	6.85	6.93	0.003217
17.5	7.99	8.24	0.002380
18.0	9.19	9.20	0.002025

where y is the gap between the electromagnet and the top of the globe, U_1 and U_2 are the voltage value of the electromagnet, G_i is the electromagnet coefficient.

After the data U_1, U_2 are dealt with we obtain the average value $\overline{U}$ and the average electromagnet coefficient value $\overline{G_i} \approx 0.00512\,(\mathrm{N \cdot m^2/A^2})$. According to the data in Table 1, we set the steady levitated value $y = 16\,\mathrm{mm}$. In the end, we put $\overline{G_i}$ into Equation (1) to get the referenced current value $i_0 \approx 0.3894\,\mathrm{A}$.

3. THE TRANSFER FUNCTION FOR THE CONTROLLED OBJECT

According to the second Newton's law we obtain the dynamic equation:

$$my'' = mg - G_i \left(\frac{i}{y}\right)^2 + F_d \tag{2}$$

where F_d is the disturbing force coming from the environment disturbing. Equation (2) can be transformed in the style: $y'' - g - \frac{F_d}{m} + \frac{G_i}{m}(\frac{i}{y})^2 = 0$. Then the authors define a function: $f(y'', i, y) = y'' - g - \frac{F_d}{m} + \frac{G_i}{m}(\frac{i}{y})^2$. After the equation is linearized in the referenced position, we get the equation: $\Delta f(y'', i, y) = \frac{\partial f(y'', i, y)}{\partial y''}\Delta y'' + \frac{\partial f(y'', i, y)}{\partial i}\Delta i + \frac{\partial f(y'', i, y)}{\partial y}\Delta y = 0$.

Defining the following parameters $a_1 = \frac{\partial f(y'',i,y)}{\partial y''} = 1$, $a_2 = \frac{\partial f(y'',i,y)}{\partial i} = 2 \cdot \frac{G_i}{m} \cdot \frac{i}{y^2}$, $a_3 = \frac{\partial f(y'',i,y)}{\partial y} = -2 \cdot \frac{G_i}{m} \cdot \frac{i^2}{y^3}$. Then we get (3) by using these parameters above:

$$a_1 \cdot \Delta y'' + a_2 \cdot \Delta i + a_3 \cdot \Delta y = 0 \tag{3}$$

After Equation (3) is dealt with according to the Laplace transforming rule we get:

$$\frac{\Delta Y(s)}{\Delta I(s)} = \frac{-a_2}{s^2 + a_3} \tag{4}$$

Putting the parameters into (4), we get the transfer function equation for the controlled object:

$$G_P(s) = \frac{\Delta Y(s)}{\Delta I(s)} = \frac{-50.41}{s^2 - 1226.80} \tag{5}$$

Based on (6) we can know the globe system is not steady. It's extremity value is distributed near the value ± 35.0257.

4. THE PDF CONTROLLER

The PDF control system is shown in the Fig. 3, where P, I and D is respectively the proportion, the derivative and the integral parameter. The equation $\frac{K_i/m}{s^2 - K_w/m}$ is the transfer function for the controlled object. The control system mainly utilizes the closed-loop controller to deal with a error signal and sends a control signal to adjust the electromagnetic suction value. Then it can make the controlled object get back the referenced position. As is shown in the Fig. 3, we put the derivative signal $P + D \cdot s$ into the interior feedback channels. The signal is relatively steady so it can avoid the phenomenon of the derivative mutation. Then we put the integral signal $\frac{I}{s}$ into the obverse channels to avoid the static error. We also add a saturated non-linear signal in the channels to avoid the phenomenon of the startup circle and prevent the deferent value of the controller is more than the referenced value. Such controller is prior to the traditional controller [4]. Based on the Fig. 3 we obtain the systemic transforming function:

$$G(s) = \frac{Y(s)}{R(s)} = \frac{\frac{I}{s} \cdot \frac{K_i/m}{s^2 - K_w/m}}{1 + \frac{I}{s} \cdot \frac{K_i/m}{s^2 - K_w/m} + (P + D \cdot s) \cdot \frac{K_i/m}{s^2 - K_w/m}}.$$

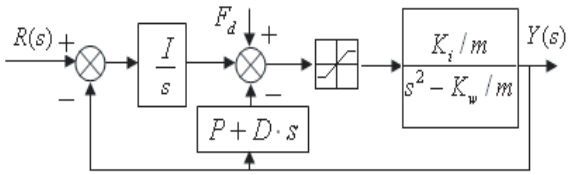

Figure 3: The PDF block diagram for globe model.

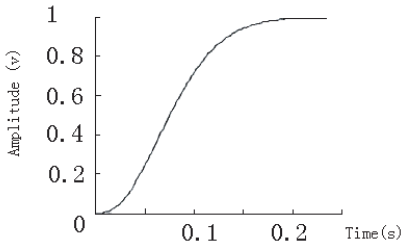

Figure 4: The step response of the closed-loop control system.

Putting the equation $\frac{K_i/m}{s^2 - K_w/m} = \frac{50.41}{s^2 - 1226.80}$ into $G(s)$, we obtain (6):

$$\frac{50.41 \cdot K_i}{s^3 + 50.41D \cdot s^2 + (50.41P - 1226.80) \cdot s + 50.41I} \tag{6}$$

It's closed-loop latent equation is (7)

$$\Delta(s) = s^3 + 50.41D \cdot s^2 + (50.41P - 1226.80) \cdot s + 50.41I \tag{7}$$

The functional index referenced in the design process is the following: the adjusting time $t_s \leq 0.4\,\mathrm{s}$; the ascending time $t_r \leq 0.2\,\mathrm{s}$; the over quantity $M_P \leq 20\%$.

According to these indexes, we get some basic parameters: $\sigma \geq 11.5$, $\omega_n \geq 18$, $\zeta \geq 0.45$, where σ is the real part of the extremity point, ω_n is the natural frequency without damp and ζ is the damp proportion.

Based on the functional index above and the structural theory of Chen Method for the latent root, we select the expected extremity value that the closed-loop system needs: $s_1 = s_2 = -20$, $s_3 = -200$. Here the system posseses the characters of robustness, fast response and no over quantity. Then we obtain the expected latent Equation (8) the system needs:

$$\Delta_1(s) = s^3 + 240s^2 + 8400s + 80000 \tag{8}$$

Comparing (7) and (8), we get the following parameters:

$$P = 190.97,\ I = 1586.99,\ D = 4.76 \tag{9}$$

These parameters include the pluses of the sensor and other units. The plus for the sensor is $K = 250$ and the other pluses are ignored. So we obtain three main parameters of the controlled system: $P^{'}$, $I^{'}$ and $D^{'}$: $P^{'} = \frac{P}{250} = 0.76388,\ I^{'} = \frac{K_i}{250} = 6.34796,\ D^{'} = \frac{D}{250} = 0.01904$.

Putting (9) into (6) we get the transforming function Equation (10) of the PDF controlled system:

$$G(s) = \frac{80000}{s^3 + 240 \cdot s^2 + 8400 \cdot s + 80000} \tag{10}$$

The choice of the latent root for the system above is more than one group and the position of the latent root can affect evidently the parameters in (9). But it have little effect to the system response result, which is also one of the advantages of the PDF control. The reason to choose the group of parameters is that the coefficients in (10) are smaller under the premise condition of satisfying system's request. So in the succedent circuit design proceeding we are convenient to assign coefficients and can make amplifier not saturated.

Figure 4 is the step response of the control system, which is to checkout whether the controller design can meet the need. From it we can know the system response has no over quantity and is satisfied. It can satisfy the need of system response index.

5. CONCLUSION

We can gain some conclusion from the analysis and discussion:

(1) The PDF controller can avoid the phenomenon of the startup circle, and even cancel the derivative abruptly mutative phenomenon of the derivative.
(2) The PDF control method has no high qualification to the mathematical model. Even if it is not accurate the definite error won't bring great functional impact.
(3) The PDF controller possesses the characteristics of fast response velocity, high controllable capability, high control precision, no over quantity, good anti-jamming capability and strong robustness.
(4) The control technology study based on PDF is significant thing. It can be also applied in the control system study of the magnet levitated bearing and so on.

REFERENCES

1. Yang, Z.-J., "Robust position control of a magnetic levitation system via dynamic surface control technique, [J]" *IEEE Transaction on Industrial Electronics*, 26–34, Vol. 51, No. 1, 2004.
2. Panayiotis, S., "Magnetic levitation hardware-in-the-loop and matlab-based experiments for reinforcement of neural network control concepts, [J]" *IEEE Transaction on Education*, Vol. 47, No. 1, 79–87, 2004.
3. Chao, X.-Y. and B.-X. Tang, "The changing construction control in magnetic levitated ball system, [J]" *Automatic Technology and Application*, Vol. 24, No. 4, 4–6, 2005.
4. Gong, M., "The PDF control study in electromagnetic levitated system, [D]", the College of Mechanical Engineering and Applied Electronics Technology in Southwest Jiaotong University, Chendu, June 2000.

Study on a Novel Permanent Magnet Retarder for Vehicles

L. Z. Ye, D. S. Li, Z. Y. Lu, and Q. H. Guo
School of Mechanical Engineering and Applied Electronics Technology
Beijing University of Technology, China

Abstract— This paper proposes a novel permanent magnet retarder (PMR) whose stator subassembly is a magnetic equipment having independent work system. We focus on designing and analyzing its structural parameters. It is simple and feasible that optimize the structural parameters of the magnetic equipment by using magnetic circuit design method, but the precision of the result is not enough. We can get the relative curve between the structural parameters and its magnetic force by using the finite element method (FEM). According to the optimal parameters, we design four kinds of magnetic equipment of PMR. Compared with the analytical and experimental results, it is confirmed that FEM is suitable for optimizing the structural parameters of magnetic equipment.

1. INTRODUCTION

The vehicle retarder is a kind of supplementary brake equipment, which consumes mostly driving kinetic energy before using the friction brake. It not only brings comfort and safe to driver, but also extends brake life greatly. PMR (permanent magnet retarder) is one of the vehicle retarder. Because of the advantages, such as energy saving, small volume, light weight and so on, the research and development of PMR have been a focus in the field of supplementary brake equipment [1].

The mechanical structures of the existing PMR mainly derive from a light automobile permanent magnet retarder which Japan ISUZU Company manufactured. These structures have a common characteristic that the magnetic circuit of retarder is from one permanent magnet to another. There are some disadvantages in those structures: 1) compared with the eddy currents retarder, the brake torque is obviously small, and some structures have the flux leakage torque (the torque exists when don't need brake); 2) their mechanical structures and installation are quite complex, so the cost is high; 3) they can't change the level of brake torque while the road situation or the vehicle's speed changes. Aimed at the disadvantages of the existing PMR, we propose a novel PMR (Fig. 1) that every permanent magnet can work independently. This novel structure has high brake efficiency and easy control method.

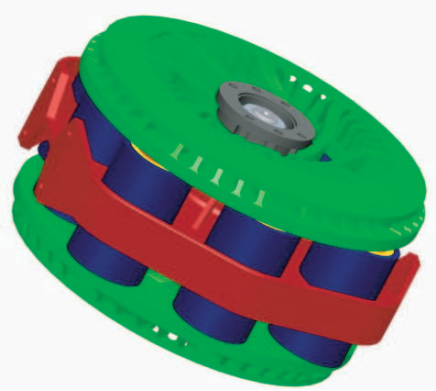

Figure 1: Disk type PMR structure.

Firstly, we introduce the mechanical structure and working principle of the novel PMR, build the mathematic modeling. Then we analyse the electromagnetic field and brake torque by the magnetic circuit design method and the finite element method. At last, we compare the analytic results with the experimental results.

2. STRUCTURAL DESIGN AND WORKING PRINCIPLE

How to design the magnetic equipment is the most important problem. We think PMR must meet three rules when the volume of PMR is limited. Firstly, the brake torque must be large enough when

PMR is working state. Secondly, flux leakage torque (it can't be avoided) must be small enough when non-working state. Finally, the working state should be able to be controlled. According to the rules, we proposed a novel permanent magnet retarder, whose brake torque efficiency can reach the twice of the existing PMR. Fig. 2 is an experimental magnetic equipment and Fig. 3 is the principle structure and magnetic lines of flux. In Fig. 3, the number 1 refers to the rotor, 2 the magnetic yoke, 3 the permanent magnet, 4 the short-circuit ring, 5 shell and 6 the stator.

Figure 2: Experimental magnetic equipment.

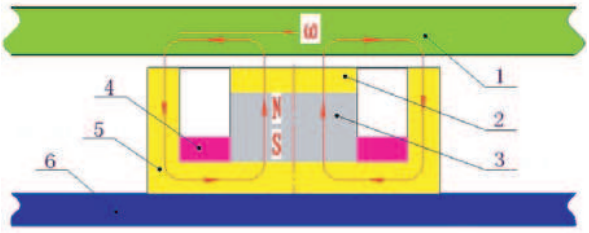

Figure 3: Principle structure of magnetic equipment.

The control of the magnetic circuit is the key to the normal operation of permanent magnet retarder; the shift of permanent magnetic parts between the state of possessing external magnetic property and the state of showing magnetic shield is controlled by the movement of the short-circuit ring. When the short-circuit ring is against the magnetic yoke in the top position of the shell, the permanent magnet is enclosed by the shell, the short-circuit ring and the magnetic yoke, the permanent magnet entering the state of magnetic shield and the system in the non-working state. When the short-circuit ring reaches the bottom of the shell and becomes divided from the magnetic yoke, the position as show in Fig. 3, the permanent magnet gain the external magnetic property and the system enters the working state. The movement of the short-circuit ring is driven by pneumatic control.

3. CALCULATION AND DESIGN OF THE MAGNEITC CIRCUIT

To the torque calculation formula of the retarder, many scholars have done much deep research. Especially the electromagnetic retarder have been given the formula [3]:

$$T = \frac{N_p S_p^2 \Delta_h B^2 \omega}{\pi \rho} \tag{1}$$

In this formula, T is the brake torque; N_p is the pairs of the magnet pole; S_p is the area of the magnetic yoke; Δ_h is the eddy currents penetration depth of the rotor; B is the magnetic induction intensity of the air-gap; ω is the angular velocity of the magnetic change; ρ is the electrical conductivity of the rotor.

From the formula (1), we can know all the influencing factors of the brake torque. Brake power and eddy currents analytic method of the proposed PMR is the same as that of the electromagnetic retarder. The obvious characteristic is magnetic circiut which the novel magnetic equipment is independent. The magnetic circiut is from one magnetic pole N to itself magnetic pole S. Because of this, we can say the pole number N_p of the novel magnetic equipment is twice more than that of the electromagnetic retarder. So its brake efficiency is twice too.

To optimize the structural parameters of the magnetic equipment, we can calculate the Maxwell suction force between the magnetic equipment and the rotor by supposing the rotor is resting. To the uniform magnetic field with a rather small working air-gap, Maxwell suction force formula is:

$$F = \frac{B^2 S}{2\mu_0} \tag{2}$$

The suction between the magnetic equipment and the rotor is linear direct proportion as the square

of the magnetic induction intensity of the air-gap B. If we solve the maximal suction force, we will gain the optimum structural parameters.

When the PMR works, the magnetic equipment and the rotor compose an integrated magnetic system. This magnetic system can be expressed by a simplified magnetic circuit diagram. Fig. 4(a) shows the simplified structure of PMR, and Fig. 4(b) shows the equivalent magnetic circuit diagram. Permanent magnet (PM) can be equaled to a constant magnetic potential, and according to the equivalent magnetic circuit, each magnetic flux of the circuit can be calculated with their respective magnetic resistance R_j.

$$(IW)_m = H_c^{'} l = \phi_m (R_\delta^{'} + R_m) \tag{3}$$

In the formula (3), $H_c^{'}$ is the dummy coercive; $R_\delta^{'}$ is the equivalent magnetic resistance considering $R_{\sigma j}$, R_j, $R_{\sigma g}$.

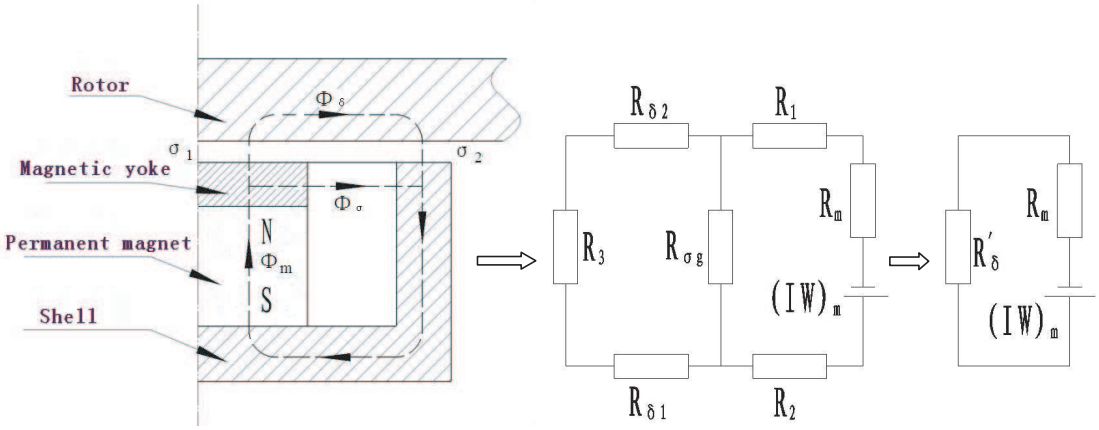

Figure 4: Magnetic circuit diagram. (a) Simplified structure of magnetic equipment, (b) Equivalent magnetic circuit diagram.

From the formula (3), according to magnetic circuit law, we can gain the flux ϕ_m in the permanent magnet, and calculate the magnetic induction intensity of the air-gap B. By the Maxwell suction force formula, the suction force can be gained under the limited volume of PMR. Obviously, the suction force is a formula contains all structural parameters of the magnetic equipment. We can optimize the parameters by solving the equation.

4. FEM AND STRUCTUAL DESIGN

Although it is feasible to solve the problem using the magnetic circuit law, we can't analyze accurately electromagnetic field and gain optimum solution because of much premise. We draw easily the curve between the structural parameters and the suction force F, and avoid much mathematic derivation using the FEM. Taking account of the structural characteristic and computational cost; it is beneficial that the two-dimensional finite element simulation is adopted.

By building model and generating mesh (Fig. 5), we can get the magnetic lines of flux distribution after solution (Fig. 6). We get the curve between the structural parameters and force, assuming only one of the parameters is variable.

According to the magnetic equipment size of the eddy currents retarder DHB20 A (High 140 mm and Diameter 140 mm) which produced by CAMA (Luoyang) Electromechanic Equipment Co., Ltd, we design the novel magnetic equipment of PMR. Taking advantage of the simulation to optimize all structural parameters, we will get the relative curves between all structural parameters and the Maxwell suction force.

Two of the curves are given. Fig. 7 is the relative curve between the length of the magnet l and the force F. There is an optimum length about $l = 20$ mm from the curve taking account of the limited space and economic factors. Fig. 8 is the relative curve between the force F and the distance L, which is between the yoke and the shell. There is also an optimum distance about $L = 10$ mm. If less than 10 mm, the magnetic leakage is high; if more than 10 mm, the space is waste.

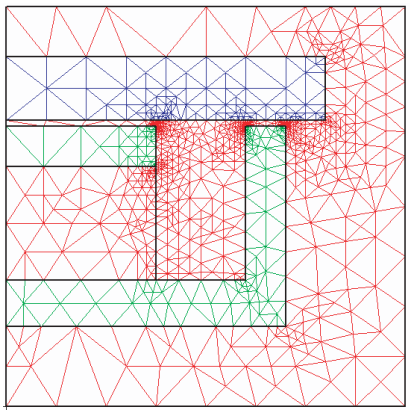

Figure 5: Mesh of the two-dimensional finite model.

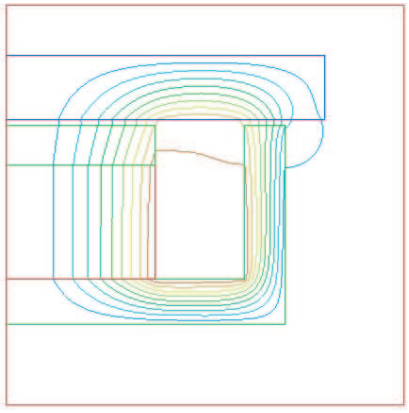

Figure 6: Distribution of the magnetic lines of flux.

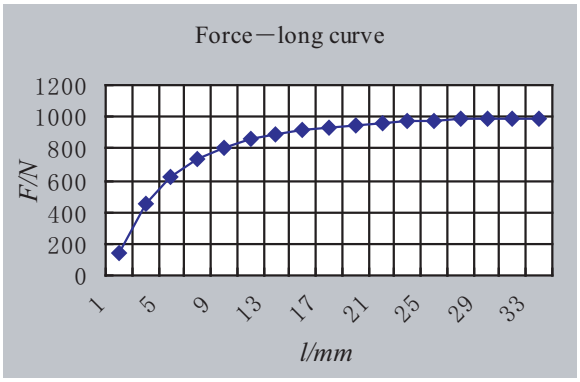

Figure 7: The length of magnet curve.

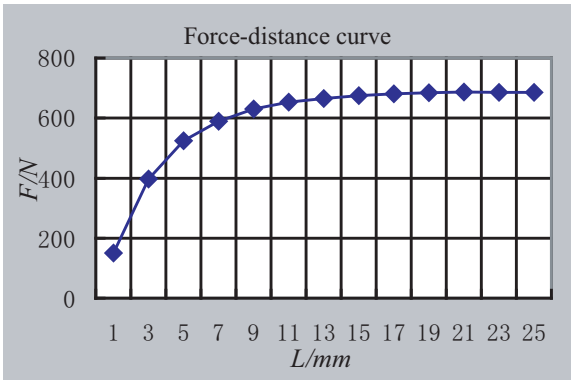

Figure 8: The distance curve.

5. FINITE ELEMENT ANALYSIS AND BENCH TEST

Any magnetic equipment can do the bench test because of the independent magnetic circuit system. The torque of the retarder equals to signal torque of the magnetic equipment multiplying the number of it without considering the temperature effect of the rotor. To validate finite element analysis results, we produce four kinds of magnetic equipment to do the bench test and gain their brake torque data when the rotor revolves at 2000 r/min. Table 1 compares the analysis results with the test results on four kinds of magnetic equipment.

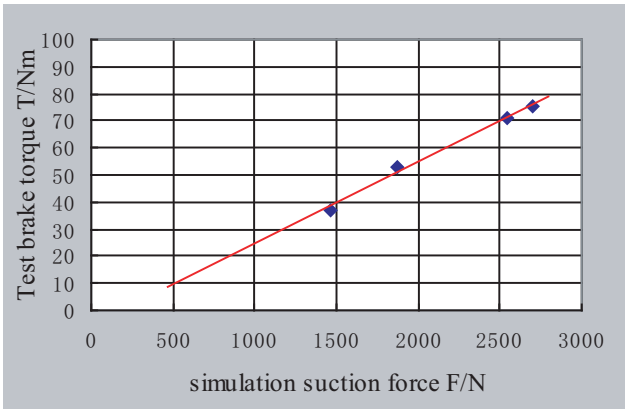

Figure 9: Fitting curve that simulation suction force and test brake torque.

We can draw the fitting curve that simulation suction force F and test brake torque T. From the Fig. 9, they are basically linear relation and the error is small. So it is confirmed that FEM is suitable for optimizing the structural parameters of magnetic equipment.

Table 1: Simulation and test data.

Magnetic equipment	1	2	3	4
Simulation suction force F/N	1463	1868	2700	2541
Test brake torque T/Nm	37	53.2	75.4	70.8

6. CONCLUSIN

We can gain some conclusion from the analysis and discussion:

(1) The novel PMR have these characteristics: high brake efficiency, easy control and little magnetic leakage. There is well application prospect for it.

(2) The magnetic equipment of the novel PMR is an independent work system. It is not only in favor of simplifying the calculation that optimizing the structural parameters, but also gives much convenience to the prophase research.

(3) It is confirmed that FEM is suitable for optimizing the structural parameters of the magnetic equipment.

REFERENCES

1. Hu, Q. X. and R. He, "Working principle and usage of vehicle-used permanent-magnet type retarder design," *Computation Research*, Vol. 3, 22–25, 2005.
2. Zhu, N. and Y. H. Wang, "Light type permanent magnet retarder for vehicle," *Bus Technology and Research*, Vol. 24, No. 4, 19–20, 2002.
3. He, R., *Auxiliary Braking Equipment for Vehicle*, Chemical Industry Press, Beijing, 2005.
4. Wang, B. L., *Electromagnetism and Electro-instrument Design Base*, National Defense Industry Press, Beijing, 1989.

Research on a Maglev Ball Control System Based on DSP2812

Q. H. Guo, **D. S. Li**, **Z. Y. Lu**, **W. Wang**, **and L. Z. Ye**
College of Mechanical Engineering and Applied Electronics Technology
Beijing University of Technology, Beijing 100022, China

Abstract— As the basis of maglev technology, a single-freedom suspension ball control system with hybrid electromagnets is introduced in this paper. According to the physical model of the system we designed, the linear model and control strategy were established and analyzed. A fixed-point digital signal processor TMS320F2812 is chosen as the controller of the system for its high speed and high efficiency of calculation and control. A/D module and the EventManager(EV) module are used in the system. PID algorithm that is applied frequently in industry is adopted and DSP's output signal—PWM signal is used to control the driver. Both the simulation by MATLAB and actual control results show the magnet suspension system works well.

1. INTRODUCTION

The analysis and research of single Maglev(Magnetic Levitation) control system is the basis of analyzing and controlling of the maglev systems such as maglev train, maglev bearing, etc.

The suspension systems can use passive, semi-active or active [1]. However, the passive suspension systems can not assure the desired performance from a modern suspension system and the active systems are complex and expensive and are relatively high energy consumption. In this paper, it proposes an hybrid suspension system which can realize the function and overcome the defects of passive and active suspension systems.

As for the choice of controller, there are many methods [2] such as analog control system, the singlechip controller, DSP control system, etc. Considering the analog controller has a disadvantage that the hardware can not be easily changed and the parameter can't be adjusted and the processing speed of single chip controller often does not meet the needs of system, this paper introduces a method which uses DSP instead of the traditional analog controller and singlechip to realize digital control.

2. SUSPENSION SYSTEMS DESCRIPTION

The maglev ball control system is the platform of the research of maglev system. It contains maglev ball, permanent magnet, electromagnet, electric eddy current displacement sensor, controller and drive circuit, as Figure 1 shows. It uses DSP2812 as the controller and feedback regulation to maintain the ball at a fixed distance from the electromagnet. To be specific, according to the offset the sensor detected, the controller adjusts the duty-cycle of PWM output signal and further the current in the electromagnet. When the ball gets too close to the electromagnet, the current in the electromagnet will decrease, allowing the object to begin to fall away due to gravity. When the objects get too far away from the electromagnet, the current in the electromagnet will increase, pulling the object closer to the electromagnet. Basically, it will do whatever is needed with the current in the electromagnet in order to keep the object at a fixed distance below the electromagnet.

3. SUSPENSION MODEL

The system model is built on the ball's motion equation and the electrical characteristics of electromagnet. The ball's motion equation is

$$m\frac{d^2x(t)}{dt^2} = mg - F(i,x) \tag{1}$$

Suppose x is the distance between the electromagnet and the upside of the ball, $F(i,x)$ is the electromagnet force. According to Kirchhoff's law of magnetic circuit and law of conservation of energy, we got

$$F(i,x) = -\frac{\mu_0 AN^2}{2}\left(\frac{i}{x}\right)^2 \tag{2}$$

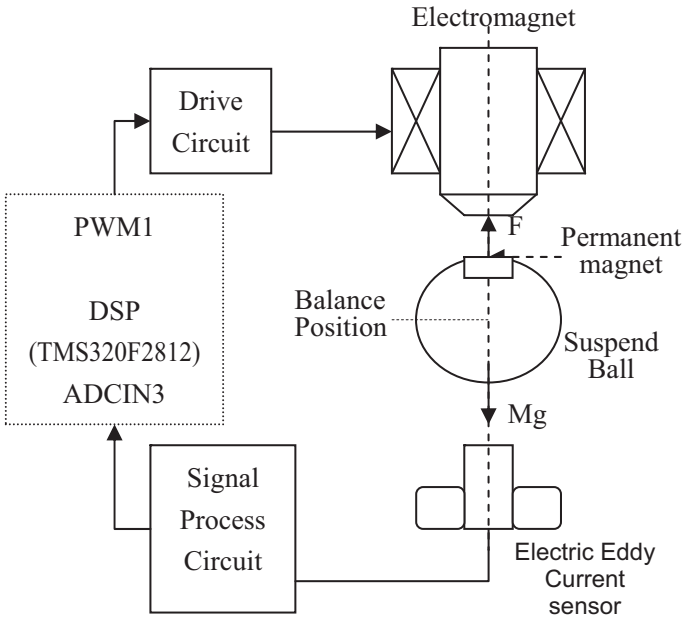

Figure 1: Maglev ball control system.

By Kirchhoff's voltage law, the circuit relationship of the coil is

$$U(t) = Ri(t) + L\frac{di(t)}{dt} \tag{3}$$

As the ball's gravity is equal to the electromagnet force to it at the balance place, we got

$$mg = F(i_0, x_0) = -\frac{\mu_0 AN^2}{2}\left(\frac{i_0}{x_0}\right)^2 \tag{4}$$

Then we got the transfer function of the system according to Equations 1 to 4 above which is

$$G(s) = \frac{k_2/k_1}{s^3 - k_3 s^2 - k_1 s + k_1 k_3} \tag{5}$$

Here, $k = -\frac{\mu_0 AN^2}{2}$, $k_1 = \frac{2ki_0^2}{mx_0^3}$, $k_2 = -\frac{2ki_0}{mx_0^2}$, $k_3 = -\frac{R}{L}$.

As it shows above, there is a root on the right plane, so it is an instable system that we should design a controller to make the system stable. We should take care that this motion equation can not describe the motion exactly if the coefficient or the balance position of the system changes.

4. HARDWARE DESIGN OF THE DIGITAL CONTROLLER

An open loop control system is not stable. We need the ability to control quickly the current of the electromagnet depending upon the position of the ball to the electromagnet. Thus we need a sensor to monitor the position of the ball which is then processed by DSP controller to get a feedback control value to regulate current in the electromagnet, and then control the current in the electromagnet to keep the system dynamic stable.

Figure 2 shows the hardware structure of the digital control system. It is composed by sensor, signal-processing circuit, AD converting circuit, DSP part, driving circuit and so on. We choose TMS320F2812 [3] as the processor. TMS320F2812 is the newest member of the DSP platform. The 32 × 32-bit MAC capabilities of the F2812 and its 32-bit processing capabilities, enable the F2812 to handle efficiently higher numerical resolution problems that would otherwise demand a more expensive advance floating-point processor solution. TMS320F2812 is the best choice to the unsteady maglev system as its fast real time calculation speed.

The project uses F2812's own 12-bit ADC module that makes the system simple and can intensify anti-interference ability. We should attention that the input electrical level must be in a range 0∼3 V

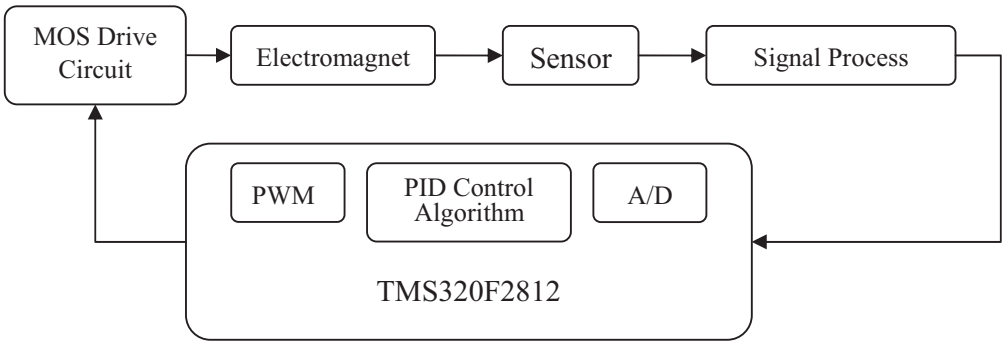

Figure 2: Maglev ball control system hardware block diagram.

that the ADC module of DSP can accept. Thus we realize it by signal regulation circuit in which the resistance voltage divider translates the sensor output to a suitable voltage.

The signal the sensor detected is filtered by DSP controller is calculated in PID control algorithm, and output to drive circuit as a PWM wave [4] in different duty-cycle corresponded to the input signal. PWM wave controls the MOSFET's gate in power amplifier circuit and further controls the current of electromagnet. IRF730 is adopted as the switching element in this amplifier circuit.

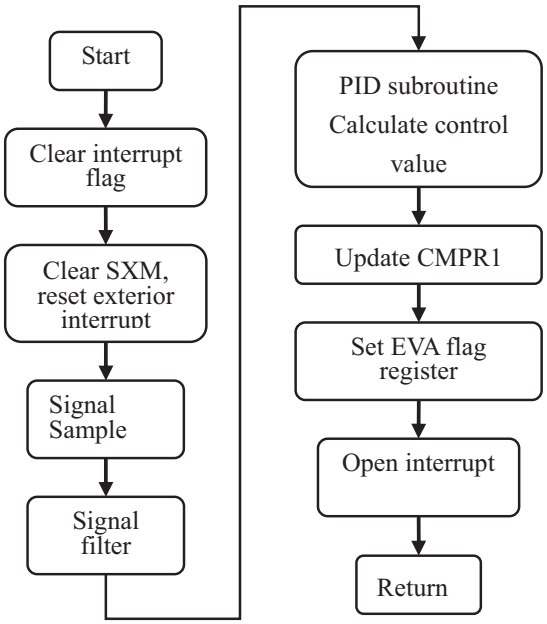

Figure 3: Interruption sub-program.

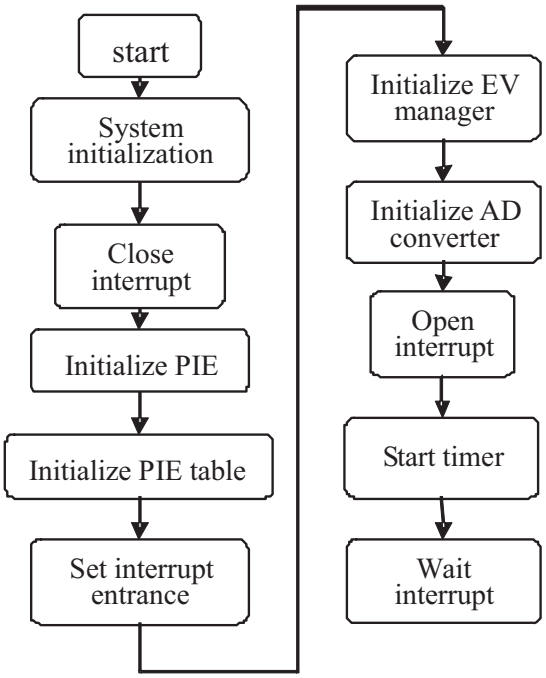

Figure 4: Main program.

5. SOFTWARE DESIGN OF THE DIGITAL CONTROLLER

In the program, we use timer interruption to trigger signal acquisition, to be specific, in every timer period, the program collects signal in the channel, completes algorithm computing and controlling at the same time, then jump to waiting subprogram the rest time until the next timer interruption. Every timer period accomplishes one control that changed the duty-cycle of PWM wave that drives the power tube to regulate the current. The frequency of carrier wave is decided by the value in timer 1 period register, whereas duty-cycle is determined by the value in compare register 1 of full compare unit 1. In the paper, the frequency of carrier wave is set to 1 kHz, and the sample time is set to 1 ms. As Timer 1 period interruption is time-fixed, the current regulation frequency is also fixed.

The software contains initialization program, AD conversion program, digital filter, control algorithm program and EVA's PWM output code. Every function can be realized by corresponding

program module. Figure 3 and Figure 4 shows the main program flowchart and interruption subprogram flowchart.

6. CONTROL ALGORITHM

PID control strategy is one of the most mature method and widely applied in most industry production, and has successfully applied in some domestic and foreign maglev control systems. Its principle is simple, easily to realize since the control parameters are relatively independent. The traditional PID control method [5] is classified to position-model and increment-model. PID incremental control method is adopted in this paper as position-type tends to produce integral saturation in calculation process. After analyzing and reasoning, the difference equation is

$$u(kT) = u(kT-T)+Kp[e(kT)-e(kT-T)]+Ki^*e(kT)+Kd[e(kT)-2e(kT-T)+e(kT-2T)] \quad (6)$$

The option of the three parameters' values such as proportion parameter Kp, integral time Ti and differential time Td are keys of control system. In the actual experiment, we tried many times to determine them according to the influencing tendency of three parameters to the control process and the regulation sequence: first proportion, then integral, and then differential. The final values are $Kp = 2.3$, $Ki = 6$, $Kd = 10$.

7. CONCLUSIONS

To sum up, the hybrid suspension system based on DSP controller can regulates the force between the electromagnet and the ball to make the ball stable, but the overshoot of the system is not small enough and the robust ability is not well enough. All of these show that the model of the system is not perfect and the control algorithm should be improved in future. Above all, the system meets the needs in simulation and actual test. Further developments will increasingly see the improvement. In addition, the technology will be applied to a four freedoms suspension system.

REFERENCES

1. Zhang, S. Y., "The digital control research of hybrid maglev system," *Journal of Northwest University (Natural Science Edition)*, Vol. 33, No. 5, 613–615, 2003.
2. Liu, D. S., L. M. Yin, and L. J. She, "Modeling method and design principle of maglev ball system based on DSP," *Electronic Engineer*, Vol. 27, No. 11, 58–60, 2001.
3. *Texas Instrument, TMS320F28xx Digital Signal Processors Data Manual[Z].*, DSP.ti.com, 2003.
4. Xu, Y. H., "The application of DSP in current control of switching reluctance motor," *Electromechanical Technology*, Vol. 31, No. 4, 42–43, 2002.
5. Zhang, J., G. H. Chen, etc, "Research on hybrid suspension system based on TMS3202812," *Power Electronics*, Vol. 40, No. 4, 14–16, 2006.

Key Technologies for Lidar Detecting Stealth Targets

Bin Zhu[1], **Jing Zhang**[2], **Yan Chen**[2], **Ke Deng**[2]
Dagang Jiang[2], **Peng Zhang**[2], **Zoushi Yao**[2], **and Wei Hu**[2]

[1]Chengdu University, Chengdu 610106, China
[2]University of Electronic Science and Technology of China, Chengdu 610054, China

Abstract— Detecting and tracking stealth targets have drawn more and more attention. With the advantages of high resolution and anti-jamming to mature radar technologies, the lidar has become a new and unique radar mechanism. Key technologies of lidar detecting stealth target have been proposed based on two methods called multi-band and multi-static anti-stealth. The combination of the visible, infrared and laser technologies can improve the detection probability of stealth targets.

1. INTRODUCTION

Stealth technology means that the launchers reduce their own detectable signals so that it is difficult to detect them. It is a kind of disguising technique, and draws more and more attention. Stealth targets will be very important in future high technology war and great threat in air-defense system. Penetration abilities of aircrafts can be greatly improved by using stealth technologies. Meanwhile, anti-stealth technologies is also promoted, which is mainly focusing on centimeter wave radars and developing towards the whole-band detection. Lidars can be used in detecting stealth targets for its higher angular resolution, strong ability of anti-jamming, good concealment, and small size and light weight [1].

Traditional radars use microwave and centimeter wave as carriers, while the lidar uses laser, which has much shorter wavelengths. The lidar uses amplitude, phase, frequency and polarization carries information and does not have essential difference with traditional radars [1]. Several key technologies need to be taken into consideration in detecting stealth targets by lidars.

2. MULTI-BAND ANTI-STEALTH

As the development of photoelectric detections, it has become an important method of obtaining information in battlefields. If we combine photoelectric detection with traditional detection methods to detect stealth targets, the ability of anti-stealth can be improved further.

The target designation radar needs not only discovering stealth targets but also tracking and aiming so as to antagonize them. Extending radar wavelength is necessary. Laser radar can detect stealth targets effectively because it has short wavelength, high beam quality, strong directionality, high measuring accuracy and it has functions of target identifying, posture displaying and orbit recording [2]. The normal operational wavelengths of laser radar include 0.532 μm, 1.064 μm, 10.6 μm, etc. Target and background optical properties on different wavelengths and atmospheric effects of different wavelength need to be considered in lidar detection.

2.1. Target and Background Optical Properties

Targets act as a series of combined reflecting surfaces to lidars, and these reflection surfaces decide the electric levels of echo signals. Both relative movement effects caused by targets movement and vector speed of targets can lead to the variation in reflected signals of lidars. Observed echo signals are called lidar characteristic signals which used to obtain target information. Reflection of several typical targets on 1.064 μm laser is shown in Table 1 [3]. We can draw the conclusion from Table 1 that different target materials correspond to different reflection in the same wavelength.

The main background noise sources are sun light, moon light, atmospheric dispersion and its own radiation, which cause background illegibility in the FOV (Field of View) of receiver. This can be widely used in aircraft photoelectric stealth [4]. In order to improve abilities of anti-jamming and stealth target detection, further research on target and background optical characteristic is necessary.

2.2. Atmospheric Effects

There are three main atmospheric effects on lidar signal transmission. The first one is attenuation caused by atmosphere molecular absorption. H_2O, CO_2 and O_3 are the primary absorbing

Table 1: Reflections of several typical targets on 1.064 μm laser.

Materials	Reflection (%)
Aluminum (weathered)	55
building cement	50
titanium alloy (new)	47
titanium alloy (weathered)	48
paint (saturated olive green)	8

sources. Another kind of attenuation arises from Mie scattering by floating particles. Atmospheric turbulence leads to the random changes of refractive index of atmosphere and causes wave-front aberration. Assuming that the original power of a lidar signal is $P(\lambda)$, the power after transmission of x can be calculated by

$$P(\lambda, x) = P(\lambda, 0) \exp[-k(\lambda)x] \tag{1}$$

where $k(\lambda)$ denotes the attenuation coefficient which contains absorption and diffraction. It can be seen from formula (1) that atmospheric attenuation depends strongly on operational wavelengths of lidars. So it is important to choose lasers with low atmospheric attenuation as the operational wavelength, such as 10.6 μm and 1.064 μm.

Figure 1 shows the relationship between propagation range and atmospheric transmission on the operational wavelength of 1.064 μm. It shows atmospheric transmission under conditions of fine (with visibility of 25 km), clear (with visibility of 15 km), haze (with visibility of 5 km), mist (with visibility of 1 km), light fog (with visibility of 0.7 km) respectively.

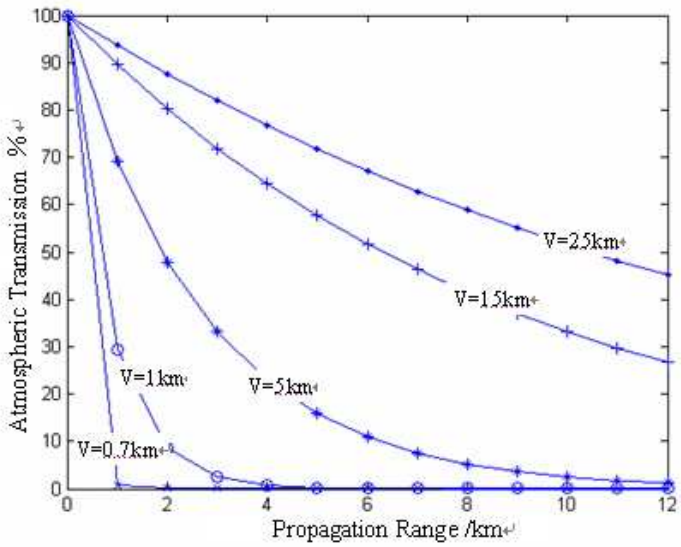

Figure 1: Relationship between propagation range and atmospheric transmission under different weather conditions.

The atmospheric turbulence refers to the density fluctuations arising from atmospheric temperature fluctuations. It leads to the random changes of refractive index of atmosphere. Atmospheric turbulence affects propagations of laser beams in different ways namely scintillation, beam wandering, beam broadening and fluctuations of the arriving angle [5]. Since turbulence effects depend strongly on the operational wavelength, it is important to choose a proper operational wavelength and to fully understand weather conditions of the working area so as to reduce turbulence effects.

As mentioned above, atmospheric attenuations relate strongly to wavelength, and different targets have different reflectivity under the same wavelength. We need to choose operational wavelength according to absorbing and reflective characteristics of different targets. At present, the most familiar bands are 0.532 μm, 10.6 μm and 1.064 μm at present.

3. MULTI-STATIC LIDAR ANTI-STEALTH

Stealth targets degrade the performance of radars by reducing their RCS. The following will introduce the RCS and multi-static radar detections of lidar systems.

3.1. Laser Radar Cross Section — LRCS

The LRCS of target is the symbol of laser scattering ability of target. It refers to the ratio of incident power in unit area to total scattering power when targets are isotropic scattering. This ratio has a dimension of area, and it denotes how much power stealth targets have got from the incident power. The LRCS is a complex function of targets' dynamic and static features, propagation media features and incident wave features. The LRCS can be calculated approximately by the method of RCS in radar [6].

$$\sigma = \frac{4\pi\rho A_R}{\Omega_R} \tag{2}$$

where ρ denotes the reflectivity of target surface, A_R denotes the projection area of target, Ω_R denotes the solid angle of scattering beam. Reflecting signal of diffusive reflection targets will be scattered in a wide area, and the distribution of reflecting signals submit to the rule of Bidirectional Reflecting Distribution Function (BRDF).

The detected power of lidars can be derived from lidar operating range formula [7].

$$P_R = \left(\frac{P_T}{R^2\Omega_T}\right)(\rho A_R)\left(\frac{A_C}{R^2\Omega_R}\right)\tau^2 \tag{3}$$

where P_R denotes the receiving power, P_T denotes the transmitting power, R denotes the operating range, Ω_T denotes the solid angle of transmitting beam, A_C denotes the effective receiving area, and τ denotes the transmission of unidirectional transmission.

The relationship between the LRCS and operating range can be derived from formula (2) and (3) [6].

$$R = \left[\left(\frac{P_T}{P_R\Omega_T}\right)\left(\frac{\sigma A_C}{4\pi}\right)\tau^2\right]^{\frac{1}{4}} \tag{4}$$

When R is the maximum operating range, σ_M is called the Critical LRCS, and the target is stealthy if inequality $\sigma < \sigma_M$ is tenable. At this point, it is necessary to build a complex geometrical model and take account of the surface optical characters or material scattering characters to calculate LRCS of a stealth target with complicated shape. The graphic EM calculating model of a RF system can be used for reference of calculating the LRCS. In calculating RCS, the graphic EM calculating model is the most efficient way [8].

3.2. Multi-static Lidars

Stealth planes are generally designed to restrain the backward scattering so as to reduce the echo signals of radars reflected by the planes, and it is effective to the single-base radar. Stealth planes do not have the same performance in every direction. They mainly restrain the backward scattering of the angle range of $\pm 45^\circ$ in horizontal and $\pm 30^\circ$ in azimuth around the front of the plane and they have obviously larger RCS on other directions [2]. Multi-static lidars detect the lateral or forward scattering signals to detect stealth planes.

Theory and practice proved that the RCS of the targets increase obviously when the scattering angle is larger than 130° [2]. LRCS will increase with the angles between bases, so the targets will be easier to be detected.

Multi-static radar means that transmitters and receivers are placed on two or more stations which are far from each other. Radar netting, selection of station and optimization of the detection probability should be considered in multi-static radar detection. Stations can be on the ground, air-platform or space-based platform (e.g., satellite). Transmitters are located in safe places which are far away from battlefields [9]. According to experiments, the RCS obviously increases when the targets are between the transmitter and the receiver and the received signals are forward or lateral scattering waves. Therefore, the detection probability for targets with small RCS can be considerably improved while the radar is installed on the aircraft or satellite. In addition, multi-static radar net composed by a transmitter on the satellite and several receivers on the ground is a potential means for the stealth targets detection [9].

3.3. Radar Net and Data Fusion

At present, stealth ability can not cover all the working bands. It is not omni-directionally stealthy even at the stealthy band [10]. Setting up radar network by combining the predominance of detection systems based on multi-band and multi-static can improve the anti-stealth ability at frequency and spatial domains. Data fusing is necessary to radar netting. Target association and tracking of general targets are relevant to PDA (Probabilistic Data Association) and JPDA (Joint Probabilistic Data Association). Data fuzziness and discontinuous can not be effectively dealt with when the RCS is small [11].

4. CONCLUSIONS

The lidar possesses higher resolution and anti-jamming ability due to its coherence property and extremely high frequency [12]. This attribute indicates that lidar has huge potential in targets detection, tracking and range. Further more, some transmitter/receiver components and digital signal process technologies have become mature that in turn accelerates the development of the lidar. Theory research proves that lidars can be very useful in stealth aircrafts detection with proper coverage region when the range reaches 20–30 km, and the angle precision exceeds 0.3mrad [12]. This paper also proposes a multi-band and multi-static detection method which combines the visible, infrared and lidar to improve the detection probability of stealth targets. It still needs more efforts to carry out a solution to the system complexity problem.

REFERENCES

1. Dai, Y., *The Principle of Radar*, National Defense Industry Press, Beijing, 2002.
2. Zhou, X., "Anti-stealth radar techniques and electronic countermeasures," *Ship Electronic Engineering*, Vol. 24, 124–131, 2004.
3. Sun, P., W. Gao, and Y. Wang, "Research on calculation and application of LRCS," *Infrared and Laser Engineering*, Vol. 35, No. 5, 597–600, 2006.
4. Fu, W., "Electro-optic stealthy technology of aircraft," *Electronics Optics & Control*, Vol. 9, 7–10, 2002.
5. Zhang, Y. and Z. Chi, *Propagation and Imaging of Laser Beam in Atmosphere*, National Defense Industry Press, Beijing, 1997.
6. Zhang, J., H. Li, and Q. Zhang, "Present status and development tendency of laser stealth technology," *Journal of Material*, Vol. 21, 316–318, 2007.
7. Banchman, C. G., *Laser Radar Systems and Techniques*, Artech House, 1979.
8. Li, L., Z. Wu, and R. Deng, "Comparison of the back laser radar cross-section calculation of complex object with the measurement of scale-mod," *Chinese Journal of Lasers*, Vol. 32, 770–774, 2005.
9. Qu, W., X. Jia, and Y. Wu., "Space-ground bistatic (multi) radar based on communication satellite signal and its key technique," *Journal of Institute of Command and Technology*, Vol. 15, 68–71, 2004.
10. Yin, Y. and Z. Yuan, "Optimized disposition of radar net for detecting stealth airplane," *Journal of Airforce Radar College*, Vol. 13, 25–27, 1999.
11. Cai, C., "Abroad analysis on anti-stealth technology," *Land-based Air Defence Weapons*, Vol. 2, 40–45, 1999.
12. Wang, J., "Application of laser radar in army air-defense," *Fire Control Radar Technology*, Vol. 33, 48–50, 2004.
13. Li, L., Z. Wu, and Q. Xue, "A fast algorithm for LRCS of a complex objectwith a rough surface," *Journal of Xidian University*, Vol. 27, 577–580, 2000.
14. Zhang, X., D. Wang, and W. Chen, "An optimized method for detection probability of multi-static radar," *Journal of Radar Fire Controlling Technology*, Vol. 34, 26–28, 2005.
15. Chen, J. and L. Ding, "Optimum position finding algorithm for multi-static radars," *Journal of Xidian University*, Vol. 26, 397–400, 1999.

Enhancement of Microwave-assisted Organic Reactions Using Active Carbon

Zhibin Li, **Jianhua Chen**, **Haisheng Xu**, **Shan Hu**, **and Dong Shen**

Laboratory of Chemical Physics, East China University of Science and Technology
Shanghai 200237, China

Abstract— Active carbon was applied for the first time to microwave-assisted organic reactions, significant enhancement of the microwave reactions was observed in low polar and nonpolar media due to efficient energy transfer from active carbon to reaction mixtures.

1. INTRODUCTION

In 1986, Gedye and Giguere reported for the first time that organic reactions could be conducted very rapidly under microwave irradiation [1, 2]. Since then, microwave has been widely used in synthetic chemistry to reduce reaction time and increase product yield [3, 4]. In spite of its advantages, one of the drawbacks of microwave-assisted reaction is the reaction substrate and solvent shall be polar to absorb microwave efficiently, for the reactions with less polar substrates and solvents such as toluene, hexane, dioxane, p-xylene, et al., the microwave-assisted reactions are slow or even do not work because of the poor microwave absorbability of the less polar reaction mixtures. To solve this problem, it has been reported that polar additives such as ionic liquids were able to increase the microwave absorption level of low polar reaction mixtures and thus increase the rates and yields of the reactions [5]. Because of the fact that they have melting points near room temperature, negligible vapour pressure, ionic liquids attracted much attention in recent years [6–13]. But they are expensive, incompatible with some reactions [6], and their waste disposal is difficult after use. These disadvantages limit their application. Recently, cylinders of sintered silicon carbide were reported to be used in nonpolar microwave reactions [14].

Another method to improve the rate and yield of low polar microwave reaction is to use polar high boiling point solvent instead of nonpolar solvent [15], this method is convenient but the solvent with high boiling point is difficult to recover and separate from products when they have similar physical properties such as boiling point, polarity, and solubility.

In this paper we reported the use of active carbon to enhance the microwave-assisted organic reactions in low polar or nonpolar medium. Active carbon has strong absorption of microwave [16] and can be heated up very rapidly under microwave irradiation so can be used as energy-transfer medium to heat the reaction mixtures. Active carbon is inexpensive, commercial available. After reaction, it can be easily separated from product by filtration, column chromatography or distillation and can be also very easy and environment friendly disposaled after using. Cyanation of bromobenzene and Diels-Alder reaction of anthracene with diethyl maleate were chosen to study the effect of active carbon on microwave reactions in an open vessel with condenser. The results showed that active carbon enhanced effectively the microwave-assisted reactions with low polar and nonpolar reaction mixtures.

2. RESULTS AND DISCUSSION

2.1. Cyanation of Bromobenzene

The cyanation of bromobenzene under microwave irradiation was studied before in N-methyl-2-pyrrolidone (NMP) [17], which has medium microwave absorption ($\tan\delta$ 0.275) [4]. To study the effect of active carbon on this reaction in NMP, different quantities of active carbon were added to the reaction. The results were shown in Table 1. The yields with shorter reaction time were significantly improved by adding active carbon.

2.2. Diels-Alder Reaction of anthracene with *Cis*-diethyl Maleate

The Diels-Alder reaction of anthracene with *cis*-diethyl maleate took 72 h to get 87% yield in xylene or toluene by conventional method [3, 18]. In this reaction, both the reactant and solvent (xylene) have very low polarity. Under microwave irradiation the temperature of the reaction mixture rose very slowly (only 85°C after 40 min.) in the absence of active carbon due to the weak microwave absorption of xylene. Although there were reports that cycloaddition of anthracene with *cis*-diethyl

Table 1: The yields of adding different quantities of active carbon in different irradiation time.[a]

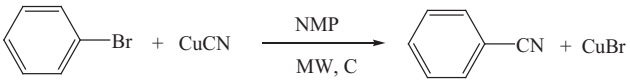

C (g)	Y (%)[b] (40 min.)[c]	Y (%) (60 min.)	Y (%) (80 min.)
0.0	11.49	51.04	95.19
0.2	45.74	93.25	96.62
0.3	47.58	96.77	97.67
0.4	48.15	96.86	97.64

[a] Reaction condition: 1.57 g (10.0 mmol) bromobenzene, 1.35 g (15.0 mmol) CuCN, 15 mL NMP.

[b] Conversion, determined by GC, average of two runs.

[c] Irradiation time, 300 W.

maleate could be conducted under microwave irradiation in a sealed vessel [19–20], the reaction did not work after 80 min. (300 W) irradiation under our reaction condition and no anthracene consumption was detected by NMR (Table 2). When 0.3 g active carbon was added, the mixture refluxed after 20 min. irradiation and 82.1% of anthracene consumed (determined by NMR) after 80 min.. The reaction proceeded cleanly without byproduct formation, so the consumptions of the anthracene corresponded to the product yields [20]. With stronger power (500 W) and more active carbon (0.4 g), the consumption of anthracene was increased to 89.8% after 76 min. irradiation (Employing high power could damage the reactor in the case of low microwave absorption!).

Table 2: The yields of adding different quantities of active carbon in different irradiation time.[a]

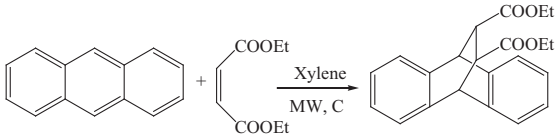

C (g)	Y (%)[c] (40 min.)[b]	Y (%) (80 min.)
0.0	0.0	0.0
0.3	37.5	82.1
0.4	39.4	84.1
0.4[d]		89.8

[a] Reaction condition: 10.50 g (61 mmol) cis-diethyl maleate, 1.09 g (6.1 mmol) anthracene, 20 mL xylene.

[b] Irradiation time, 300 W.

[c] Conversion, determined by NMR, average of two runs.

[d] 500 W power, 76 min. irradiation time were employed.

A test for investigating the effect of active carbon on nonpolar reaction was performed by the Diels-Alder reaction of anthracene with *trans*-dibutyl fumarate in p-xylene (Figure 1). 0.4 g active carbon and 400 W of power were employed, after irradiation for 80 min., 85.6% consumption of anthracene was reached, implied this method was also effective for nonpolar reaction.

It should be noted that all of the reactions in this paper were carried out without stirring, although it was ever before worried about its possibility of ignition by high temperature grad in the mixtures, it was however never happened with our experiments, even the irradiation time was prolonged to 80 min., indicates active carbon is stable enough and the energy transferring is efficient, so when the reactions are carried out with stirring, they are much safer and greater enhancement shall be observed. Active carbon was much lighter than the reaction mixtures, so it was just floated

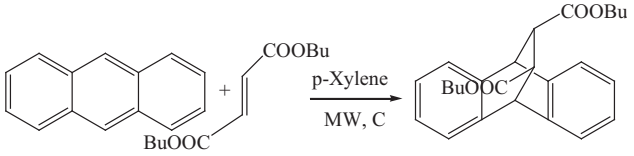

Figure 1: Diels-Alder reaction of anthracene with *trans*-dibutyl fumarate in p-xylene assisted with microwave and active carbon.

on the surface. Of course, this is not the most efficient way for energy transfer. Even so, adding active carbon still enhanced the reactions. Furthermore, active carbon has strong absorbance, a part of the products were absorbed by active carbon and could not be isolated, so the actual yields should be higher than the isolated one. This was proved by the reuse of active carbon, which was used again without any purification after the first use, the product yield was about 5% higher than the first time under the same reaction condition.

In conclusion, we found that active carbon significantly enhanced the microwave reactions with medium polarity from middle to low, especially for low polar or nonpolar reactions which were not working under microwave irradiation, active carbon helped finish the reaction within a short time. Active carbon is stable, easily available, convenient to use and their waste disposal is easy and environment friendly, so it is reasonable to expect this method to have great application in organic chemistry.

3. EXPERIMENTAL

All reactions were performed in a YW1600 multimode microwave reactor equipped with condenser, power controller. Reagents and solvents were obtained from commercial sources. ^{1}H NMR spectra were measured on a Brucker AM 500 (500 MHz) spectrometer using TMS as internal standard. GC analysis was performed using GC9790 (Wenling Analytical Instrument, Co., LTD).

General procedure of cyanation of bromobenzene: A mixture of 1.57 g (10.0 mmol) of bromobenzene, 1.35 g (15.0 mmol) CuCN, 15 mL NMP and appropriate active carbon was irradiated under microwave (300 W) for an appointed time and then was cooled down to room temperature. The mixture was poured into a solution of 5.0 g $FeCl_3$, 50 mL water and 2 mL concentrated hydrochloride (33%), stirred at 60°C for 30 min., after cooled down to room temperature, the solid was filtered off and washed with 50 mL petroleum ether, the organic phase was separated and the aqueous phase was extracted with ether tow times, the combined organic phase was washed with 5 mol/L hydrochloride, then neutralized with 10% $NaHCO_3$, washed with water, and dried with anhydrous $MgSO_4$, the solvent was removed and the sample was analyzed with GC.

General procedure of Diels-Alder reaction of anthracene with *cis*-diethyl maleate: A mixture of 10.5 g (61.0 mmol) of *cis*-diethyl maleate, 1.09 g (6.1 mmol) of anthracene, 20 mL xylene and appropriate active carbon was irradiated under microwave (300 W) for an appointed time, and was then cooled down to room temperature, 30 mL CH_2Cl_2 was added, and active carbon was then filtered off and washed with 10 mL CH_2Cl_2, a small sample of this solution was evaporated to dryness at room temperature on vacuum. The consumption of anthracene was then determined by ^{1}H NMR spectroscopy.

Diels-Alder reaction of anthracene with *trans*-dibutyl fumarate: A mixture of 13.9 g (61.0 mmol) *trans*-dibutyl fumarate, 1.09 g (6.1 mmol) of anthracene, 20 mL p-xylene and 0.4 g active carbon was irradiated under microwave (400 W) for 80 min., and was then cooled down to room temperature, 30 mL CH_2Cl_2 was added, and active carbon was then filtered off and washed with 10 mL CH_2Cl_2, a small sample of this solution was evaporated to dryness at room temperature on vacuum. The consumption of anthracene was then determined by ^{1}H NMR spectroscopy.

ACKNOWLEDGMENT

This work was financially supported by ECUST (Fund of Fundamental Theory).

REFERENCES

1. Gedye, R., F. Smith, K. Westaway, H. Ali, L. Baldisera, L. Laberge, and J. Rousell, "The use of microwave ovens for rapid organic synthesis," *Tetrahedron Lett.*, Vol. 27, No. 3, 279–282, 1986.

2. Giguere, R. J., T. L. Bray, S. M. Duncan, and G. Majetich, "Application of commercial microwave oven to organic synthesis," *Tetrahedron Lett.*, Vol. 27, No. 41, 4945–4948, 1986.
3. Jin, Q. H., *Microwave Chem.*, Science Press, Beijing, 1999.
4. Kappe, C. O., "Controlled microwave heating in modern organic synthesis," *Angew. Chem. Int. Ed.*, Vol. 43, 6250–6284, 2004.
5. Dubreuil, J. F. and J. P. Bazureau, "Rate accelerations of 1, 3-dipolar cycloaddition reactions in ionic liquids," *Tetrahedron Lett.*, Vol. 41, 7351–7355, 2000.
6. Leadbeater, N. E. and H. M. Torenius, "A study of the ionic liquid mediated microwave heating of organic solvents," *J. Org. Chem.*, Vol. 67, 3145–3148, 2002.
7. Van der Eycken, E., P. Appukkuttan, W. De Borggraeve, W. Dehaen, D. Dallinger, and C. O. Kappe, "High-speed microwave-promoted Hetero-Diels-Alder reactions of 2(1H)-pyrazinones in Ionic Liquid Doped Solvents," *J. Org. Chem.*, Vol. 67, 7904–7907, 2002.
8. Hoffmann, J., M. Nuechter, B. Ondruschka, and P. Wasserscheid, "Ionic liquids and their heating behaviour during microwave irradiation — A state of the art report and challenge to assessment," *Green Chem.*, Vol. 5, No. 3, 296–299, 2003.
9. Garbacia, S., B. Desai, O. Lavastre, and C. O. Kappe, "Microwave-assisted ring-closing metathesis revisited. On the question of the nonthermal microwave effect," *J. Org. Chem.*, Vol. 68, No. 23, 9136–9139, 2003.
10. Srinivasan, N. and A. Ganesan, "Highly efficient Lewis acid-catalysed Pictet-Spengler reactions discovered by parallel screening," *Chem. Commun.*, 916–917, 2003.
11. Shieh, W. C., M. Lozanov, and O. Repic, "Accelerated benzylation reaction utilizing dibenzyl carbonate as an alkylating reagent," *Tetrahedron Lett.*, Vol. 44, No. 36, 6943–6945, 2003.
12. Chen, I. H., J. N. Young, and S. J. Yu, "Recyclable organotungsten Lewis acid and microwave-assisted Diels-Alder reactions in water and in ionic liquids," *Tetrahedron*, Vol. 60, No. 51, 11903–11909, 2004.
13. Angrish, C., A. Kumar, and S. M. S. Chauhan, *Indian Journal of Chemistry, Section B: Organic Chemistry Including Medicinal Chemistry*, Vol. 44B, No. 7, 1515–1518, 2005.
14. Kremsner, J. M. and C. O. Kappe, "Silicon carbide passive heating elements in microwave-assisted organic synthesis," *J. Org. Chem.*, Vol. 71, 4651–4658, 2006.
15. Bose, A. K., M. S. M. Manhas, S. G. Mamta, V. S. Raju, A. S. Bari, S. N. Newaz, B. K. Banik, A. G. Chaudhary, and K. J. Barakat, "Microwave induced organic reaction enhancement chemistry. 2. Simplified techniques," *J. Org. Chem.*, Vol. 56, No. 25, 6968–6970, 1991.
16. Wang, L. and Q. Zhang, "Present research state and perspective of wave-absorbing agents," *Mater. Rev.*, Vol. 19, No. 9, 26–29, 2005.
17. Cai, L. Z., X. Liu, X. C. Tao, and D. Shen, "Efficient microwave-assisted cyanation of aryl bromide," *Synth. Commun.*, Vol. 34, No. 7, 1215–1221, 2004.
18. Huang, Z., "Application of microwave in organic synthesis," *Chemical Reagent*, Vol. 6, 349–352, 1996.
19. Berlan, J., P. Giboreau, S. Lefeuvre, and C. Marchand, "Organic synthesis with microwave. First example of specific activation in homogenous phase," *Tetrahedron Lett.*, Vol. 32, No. 21, 2363–2366, 1991.
20. Raner, K. D., C. R. Strauss, F. Vyskoc, and L. Mokbel, "A comparison of reaction kinetics observed under microwave irradiation and conventional heating," *J. Org. Chem.*, Vol. 58, No. 4, 950–953, 1993.

Passive Radar Imaging Based on Correlation Motion Compensation

Xiaoyan Fan, **She Shang**, **Wei Ma**, **Jie Li**, **and Xuan Li**
National Key Laboratory of Space Microwave Technology
Xi'an Institute of Space Radio Technology, Xi'an 710100, China

Abstract— A novel passive radar imaging method for moving target, which uses external illuminators as the transmitters, has become an interesting research. The current motion compensation of target does not take into account using the narrow-band continues broadcast or television signal. Since there exists a best correlation between the two adjacent echoes in short time, this paper presents a new motion compensation based on passive radar imaging. The algorithm uses the maximal value of the correlation function between the two adjacent echoes to estimate the compensation factor, to reconstruct target image with direct FFT algorithm. Simulation results demonstrate that the algorithm can achieve a better performance for an actual target moving model.

1. INTRODUCTION

There exist several external illuminator based on algorithms for passive radar imaging, such as a polar coordinate algorithm, convolution reverse projection algorithm and direct FFT algorithm. All the algorithms are accomplished by single/multiple illuminator and single/multiple receiver to analyze the relation between received signal and target scattering function in passive radar imaging system. These algorithms are based on a turntable model but a motion compensation is not considered. In fact, motion component can make image defocus in range and azimuth direction. There is a cross-correlation algorithm, minimum entropy and keystone transformation algorithm for the motion compensation algorithm of target imaging by using a wideband pulse signal. No attentions have been made on the narrow-band continues broadcast or television signal. This paper presents a new motion compensation algorithm based on passive radar imaging.

2. SIGNAL MODEL

The multiple illuminators/single receiver model is discussed, i.e., a passive radar system consisting of a properly positioned receiver and different multi-television station transmitting signal as illuminator of opportunity. In this mode, a coordinate system is built by assuming an imaged target center o to be the origin of coordinates, a positive semiaxis y to be zero degree and anticlockwise direction to be the positive direction. System structure is shown in Fig. 1. Where S is a television station and R is a receiver. Positions of n television stations are respectively represented by (r_1, θ_1), (r_2, θ_2), $\ldots (r_n, \theta_n)$. An initial position of the receiver is represented by (r_0, α) and a position in any scattering point P is represented by (r_P, ϕ). The signal frequencies of the television stations are respective $f_1, f_2, \ldots f_n$ (waves $\lambda_1 \sim \lambda_n$). The distance among n television stations and receiver P are respective $r_{11}, r_{22}, \ldots r_{nn}$ and r_{00}.

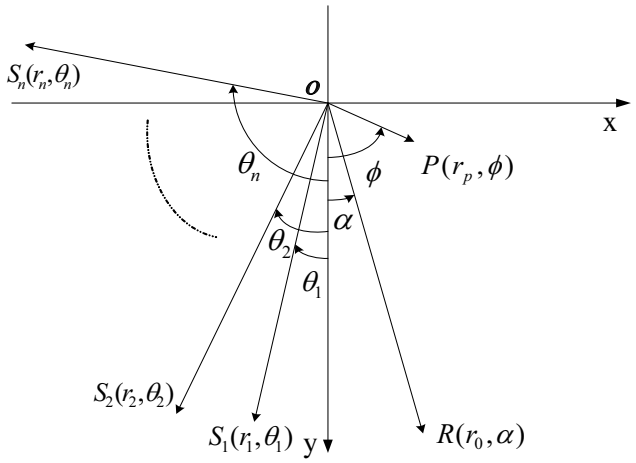

Figure 1: Multistatic passive radar simulation system.

Though the scattering function $g(r_p, \phi)$ is stochastic, its value is definitive in a specific sampling. Assuming $g(r_P, \phi) = 1$ in point P.

Given the carrier frequency of the transmission signal in the i-th television station,

$$s_i(t) = \exp(j2\pi f_i t + \varphi_i) \quad i = 1, 2, \ldots n \tag{1}$$

where f_i and φ_i are the frequency and the initial phase of the i-th television signal respectively.

When a target clockwise rotates $\Delta\beta$ around the origin, the echo signal can be represented by,

$$s_{ri}(t, \tau_i) = \exp(\varphi_i) \cdot \exp(j2\pi f_i(t - \tau_i)) \quad i = 1, 2, \ldots n \tag{2}$$

where τ_i is the time which it takes for the i-th television signal through the distance $r_{ii} + r_{00}$.

Assuming the initial phase φ_i of each signal is invariable during imagining. $\exp(\varphi_i)$ of multi-channel television signals in Equation (1) are constant and they are still synchronized, which does not have an impact on imaging. The echo signal is multi-channel sampled synchronously, then each path signal is respectively mixed. We have following echo data,

$$\mathbf{D}(\boldsymbol{\tau}) = \exp(-j2\pi(\mathbf{f} \cdot \boldsymbol{\tau})) \tag{3}$$

where $\mathbf{f} = [f_1, f_2, \ldots f_n]$, $\boldsymbol{\tau} = [\tau_1, \tau_2, \ldots \tau_n]$.

As $r_P \ll r_i$ $(i = 1, 2, \ldots n)$, assuming the distance r_{ii} $(i = 1, 2, \ldots n)$ between n television stations and point P approximately equals to the projection of r_{ii} on r_i and the distance r_{00} between the receiver and point P approximately equals to the projection of r_{00} on r_0. Substitute $\boldsymbol{\theta}$, $\boldsymbol{\lambda}$, $\boldsymbol{\beta}$ in parameter $\boldsymbol{\tau}$ of Equation (3) and we can obtain,

$$\mathbf{D}(\boldsymbol{\theta}, r, r_0, \boldsymbol{\beta}) = \exp\left\{-\frac{j2\pi}{\boldsymbol{\lambda}} \cdot \{(r_0 + \mathbf{r}) - [r_P \cos(\phi - \boldsymbol{\theta} - \boldsymbol{\beta}) + r_P \cos(\phi - \boldsymbol{\theta})]\right\} \tag{4}$$

where $\boldsymbol{\theta} = [\theta_1, \theta_2, \ldots \theta_n]$, $\mathbf{r} = [r_1, r_2, \ldots r_n]$, $\boldsymbol{\lambda} = [\lambda_1, \lambda_2, \ldots \lambda_n]$. The bistatic angle $\boldsymbol{\beta} = \alpha - \boldsymbol{\theta}$.

3. MOTION COMPENSATION ALGORITHM

It is known that the phase variation of echo signals received from flying target is determined by the relative moving shift between the received/emission station and the center point of the target, between the other scattering points and the center. In general, the distance r_0 between the receiving station and the target, the distance r_i $(i = 1, 2, \ldots n, n$ is the number of emission station) between the transmission station and the target is variable during imaging accumulation. A target can not be imaged because of its position moving in range and azimuth direction. We must overcome this problem. This is the purpose of the motion compensation.

Assuming the distance r_0 and r_i are invariable, it can be considered as a turntable imaging. Fig. 2 illustrates that, supposing the target with a constant velocity v with A degree along axis y, the referential center O moves to O' $(vt\sin A, vt\cos A)$ and the point $P(r_p, \phi)$ moves to $P'(r_p \sin\Phi +$

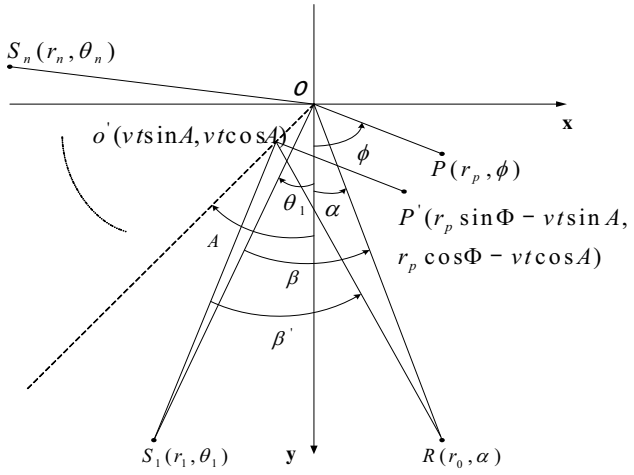

Figure 2: Multistatic passive radar simulation system scheme after t seconds.

$vt\sin A,\ r_p\cos\Phi + vt\cos A)$ after t seconds, Take television station 1 as an example, the bistatic angle becomes $\beta_1^{'}$ and the azimuth angle of the receiving station is $\alpha^{'}$. $\beta_1^{'}$ and $\alpha^{'}$ can be computed as follow:

$$\begin{aligned}\beta_1^{'} &= \arccos\left(\frac{S_1O'^2 + RO'^2 - S_1R^2}{2S_1O' * RO'}\right) \\ &= \arccos\left(\frac{(vt)^2 + r_1r_0\cos(\theta_1-\alpha) - r_0vt\cos(A-\alpha) - r_1vt\cos(A-\theta_1)}{\sqrt{r_0^2+(vt)^2-2r_0vt\cos(A-\alpha)}\sqrt{r_1^2+(vt)^2-2r_1vt\cos(A-\theta_1)}}\right) \quad (5)\end{aligned}$$

$$\alpha^{'} = \phi - \arccos\frac{O'P'^2 + O'R^2 - RP'^2}{2O'P' * O'R} = \phi - \arccos\left(\frac{r_1r_P\cos(\phi-\alpha) - r_Pvt\cos(\phi-A)}{r_p\sqrt{r_0^2+(vt)^2-2r_0vt\cos(A-\alpha)}}\right) \quad (6)$$

Owing to the signal variation only relates to the transmission time, namely to the distance of carrier wave transmission, the line segment $S_1O^{'}$, $RO^{'}$ and $P^{'}O^{'}$ motion along the flight path, Thus $P^{'}O^{'}$ coincides with PO, the coordinate $S_1(r_1,\ \theta_1)$ of transmission station 1 becomes $S_1^{'}(r_1^{'},\ \theta_1^{'})$ and coordinate $R(r_0,\ \alpha)$ of receiving station becomes $R^{'}(r_0^{'}, \alpha^{'})$. Changing form is shown in Fig. 3, which is equivalent to Fig. 2 in signal model. It is obvious that the receiving station turns $\Delta\alpha$ degrees and the transmission station turns $\Delta\theta$ degrees. Δr_0 and Δr_1 are the respective difference of $r_0^{'}$ and r_0, $r_1^{'}$ and r_1. Where $r_0^{'}$ is the distance between the receiving station and the target referential center and $r_1^{'}$ is the distance between the transmission station and the target reference center after t seconds. Namely $r_0^{'} = r_0 + \Delta r_0$, $r_1^{'} = r_1 + \Delta r_1$. According to Equation (4), the echo data can be written as follow:

$$\mathbf{D}(\boldsymbol{\theta}_1^{'},\ r^{'},\ r_0^{'},\ \boldsymbol{\beta}_1^{'}) = \exp\left\{-\frac{j2\pi}{\boldsymbol{\lambda}}\cdot\{(r_0^{'}+\mathbf{r}_1^{'}) - \left[r_P\cos(\phi-\boldsymbol{\theta}_1^{'}-\boldsymbol{\beta}_1^{'}) + r_P\cos(\phi-\boldsymbol{\theta})_1^{'}\right]\right\} \quad (7)$$

According to Fig. 3, the motion compensation means Δr_0 and Δr_1 only to be eliminated. It also implies that $S_1^{'}(r_1^{'},\ \theta_1^{'})$ becomes $S_1^{''}(r_1,\ \theta_1^{'})$ and $R^{'}(r_0^{'},\ \alpha^{'})$ becomes $R^{''}(r_0,\ \alpha^{'})$. Here it becomes a turntable model.

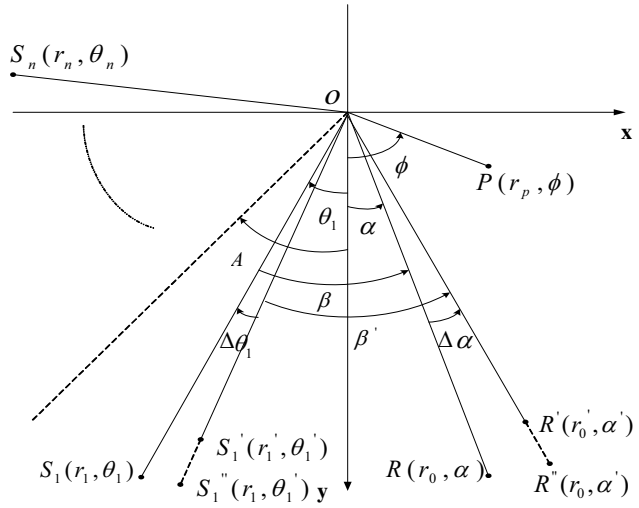

Figure 3: Multistatic passive radar simulation system equivalent scheme after t seconds.

The bistatic angle $\boldsymbol{\beta}$ becomes $\boldsymbol{\beta}^{'}$, let $\Delta\boldsymbol{\beta} = \boldsymbol{\beta}^{'} - \boldsymbol{\beta}$. Included angle $\boldsymbol{\theta}$ between the transmission station and axis y becomes $\boldsymbol{\theta}^{'}$, let $\Delta\boldsymbol{\theta} = \boldsymbol{\theta}^{'} - \boldsymbol{\theta}$. The correlation function between the echoes can be written as follow:

$$\begin{aligned}R(\Delta\mathbf{r}+\Delta r_0) &= \int D(\boldsymbol{\theta}^{'},\ r_0+\Delta r_0,\ \mathbf{r}+\Delta\mathbf{r},\ \boldsymbol{\beta}+\Delta\boldsymbol{\beta})D^*(\boldsymbol{\theta},\ r_0,\ \mathbf{r},\ \boldsymbol{\beta})d(\mathbf{r}^{'}+r_0^{'}) \\ &= \int \exp\left\{\frac{j2\pi}{\boldsymbol{\lambda}}\cdot\{(\Delta r_0+\Delta\mathbf{r}) - [r_P\cos(\phi-\boldsymbol{\theta}-\boldsymbol{\beta}) + r_P\cos(\phi-\boldsymbol{\theta}) \right. \\ &\quad \left. -r_P\cos(\phi-\boldsymbol{\theta}-\boldsymbol{\beta}-\Delta\boldsymbol{\theta}-\Delta\boldsymbol{\beta}) - r_P\cos(\phi-\boldsymbol{\theta}-\Delta\boldsymbol{\theta})]\right\} d(\mathbf{r}^{'}+r_0^{'}) \quad (8)\end{aligned}$$

where $\boldsymbol{\theta} = [\theta_1, \theta_2, \ldots \theta_n]$, $\mathbf{r} = [r_1, r_2, \ldots r_n]$, $\boldsymbol{\lambda} = [\lambda_1, \lambda_2, \ldots \lambda_n]$, $\mathbf{r}^{'} = [r_1^{'}, r_2^{'}, \ldots r_n^{'}]$, $r_i^{'}(i = 1, 2, \ldots, n)$ is the distance between n television stations and the target referential center after t seconds. The bistatic angle is $\boldsymbol{\beta} = \alpha - \boldsymbol{\theta}$.

When $\Delta\boldsymbol{\beta}$ is enough little, there are little difference and strong correlation between the echoes, we can obtain estimated value of the motion distance by evaluating the maximal value of Equation (8). Compute the derivation of Equation (8) on $\mathbf{r}^{'} + r_0^{'}$, let $\frac{\partial R(\Delta\mathbf{r}+\Delta r_0)}{\partial(\mathbf{r}^{'}+r_0^{'})} = 0$ and the value of $\Delta r_0 + \Delta\mathbf{r}$ can be estimated, through which the image in distance direction can be compensated, the corresponding phase compensation factor is $\Delta\varphi = 2\pi(\Delta r_0 + \Delta\mathbf{r})/\boldsymbol{\lambda}$. The compensated echo data is as follow:

$$\begin{aligned}\mathbf{D}^{'}(\boldsymbol{\theta}, r, r_0, \boldsymbol{\beta}) = &\exp\left\{-\frac{j2\pi}{\boldsymbol{\lambda}} \cdot \{(r_0 + \mathbf{r} + \Delta r_0 + \Delta\mathbf{r}) - [r_P \cos(\phi - \boldsymbol{\theta} - \boldsymbol{\beta} - \Delta\boldsymbol{\theta} - \Delta\boldsymbol{\beta})\right. \\ &\left. + r_P \cos(\phi - \boldsymbol{\theta} - \Delta\boldsymbol{\theta})]\} * (-\Delta\varphi)\} \\ = &\exp\left\{-\frac{j2\pi}{\boldsymbol{\lambda}} \cdot \{(r_0 + \mathbf{r}) - [r_P \cos(\phi - \boldsymbol{\theta} - \boldsymbol{\beta} - \Delta\boldsymbol{\theta} - \Delta\boldsymbol{\beta}) + r_P \cos(\phi - \boldsymbol{\theta} - \Delta\boldsymbol{\theta})]\}\right\} \quad (9)\end{aligned}$$

As $r_0 + \mathbf{r}$ is constant in Equation (9) and has no use to imagining, the echo data can be written as follow:

$$\begin{aligned}\mathbf{D}^{''}(\boldsymbol{\theta}, r, r_0, \boldsymbol{\beta}) &= \exp\left\{\frac{j2\pi}{\boldsymbol{\lambda}} \cdot [r_P \cos(\phi - \boldsymbol{\theta} - \boldsymbol{\beta} - \Delta\boldsymbol{\theta} - \Delta\boldsymbol{\beta}) + r_P \cos(\phi - \boldsymbol{\theta} - \Delta\boldsymbol{\theta})]\right\} \\ &= \exp\left\{\frac{j2\pi}{\boldsymbol{\lambda}} \cdot \{r_P \cos\phi[\cos(\boldsymbol{\theta} + \boldsymbol{\beta} + \Delta\boldsymbol{\theta} + \Delta\boldsymbol{\beta}) + \cos(\boldsymbol{\theta} + \Delta\boldsymbol{\theta})]\right. \\ &\quad \left. + r_P \sin\phi[\sin(\boldsymbol{\theta} + \boldsymbol{\beta} + \Delta\boldsymbol{\theta} + \Delta\beta) + \sin(\boldsymbol{\theta} + \Delta\boldsymbol{\theta})]\}\right\} \quad (10)\end{aligned}$$

As $\Delta\boldsymbol{\theta} = \Delta\alpha - \Delta\boldsymbol{\beta}$. Given the time sampling frequency, we can get $\Delta\boldsymbol{\theta}$, $\Delta\boldsymbol{\beta}$ and $\Delta\alpha$ according to Equations (5) and (6).

Let

$$u = (\cos(\boldsymbol{\theta} + \boldsymbol{\beta} + \Delta\boldsymbol{\theta} + \Delta\boldsymbol{\beta}) + \cos(\boldsymbol{\theta} + \Delta\boldsymbol{\theta}))/\boldsymbol{\lambda} v = (\sin(\boldsymbol{\theta} + \boldsymbol{\beta} + \Delta\boldsymbol{\theta} + \Delta\boldsymbol{\beta}) + \sin(\boldsymbol{\theta} + \Delta\boldsymbol{\theta}))/\boldsymbol{\lambda} \quad (11)$$

By Equation (11) and Equation (10), we can obtain

$$\mathbf{D}^{''}(\boldsymbol{\theta}, r, r_0, \boldsymbol{\beta}) = \exp[j2\pi(x * u + y * v)] \quad (12)$$

where $x = r_p \sin\phi$, $y = r_p \cos\phi$. The echo data of all the target scattering point can be written as follow,

$$\mathbf{G}_{\boldsymbol{\theta}, \boldsymbol{\lambda}, \boldsymbol{\beta}}(\mathbf{u}, \mathbf{v}) = \iint g(x, y) \exp[j2\pi(x * \mathbf{u} + y * \mathbf{v})] dxdy \quad (13)$$

Equation (13) shows that the echo data has the two-dimension fourier transformation form on the target scattering function. As the echo data in the different television stations is sparse and non-uniform in the fourier space, we choose the densely and relative uniform data for the two-dimension interpolation and reconstruction of uniform data. Then the target image is reconstructed by the direct two-dimension fourier transformation, that is as follow,

$$g(x, y) = \iint \mathbf{G}_{\boldsymbol{\theta}, \boldsymbol{\lambda}, \boldsymbol{\beta}}(\mathbf{u}, \mathbf{v}) \cdot \exp(-j2\pi(x \cdot \mathbf{u} + y \cdot \mathbf{v})) d\mathbf{u}d\mathbf{v} \quad (14)$$

4. PERFORMANCE ANALYSES

By Equation (13), the echo data of the target scattering point is the function of the position of television station, the frequency and the bistatic angle. The relative position of television station $\boldsymbol{\theta}$ and the bistatic angle $\boldsymbol{\beta}$ are variable during imaging, which shows the corresponding motion of the target scattering point to the target referential center. It is the key of imaging. Let $\Delta\boldsymbol{\theta} = \Delta\alpha - \Delta\boldsymbol{\beta}$ and $\Delta\alpha = -\Delta(\phi - \alpha)$, $\Delta\beta$ and $\Delta(\phi - \alpha)$ can be obtained by Equations (5) and (6). $\boldsymbol{\beta}$, $\Delta\boldsymbol{\beta}$ and $\Delta\boldsymbol{\theta}$ are of the function of the sampling time t. An Initial value $\boldsymbol{\theta}$ is invariable. When $\Delta\boldsymbol{\theta}$ is uniformly interpolated, $\boldsymbol{\theta}$ is linear variation with the time. Namely $\boldsymbol{\theta}$ is stationary variable. $\boldsymbol{\beta}$ is nonlinear variable. When $\boldsymbol{\theta}$ is uniformly interpolated, the effect on the imaging of the time sample mainly is in the bistatic angle $\boldsymbol{\beta}$. By analyse: (1) the total cumulate angle is too little to meet the request of

imaging owning to too short time t. (2) the bistatic angle $\boldsymbol{\beta}$ is nonlinear variation when the time t is too long. Take 10 television stations as an example, let the total cumulate time is 40 seconds and the variation of the bistatic angle $\boldsymbol{\beta}$ is shown as Fig. 5. $\boldsymbol{\beta}$ begins to decrease 20 seconds later. The changing amplitude of the bistatic angle $\boldsymbol{\beta}$ is different in every television station, which results in the different total cumulate angle of 10 television stations, even have an influence on the imaging effect. The variation of $\boldsymbol{\beta}$ is shown as in Fig. 6. Simulation results show that it is difficult to distinguish among the five strong scattering points of target. Namely too long time results in imaging obscurity. It is difficult to obtain a perfect imaging in too short and too long cumulative time and the relative perfect imaging is obtained in about 15 seconds.

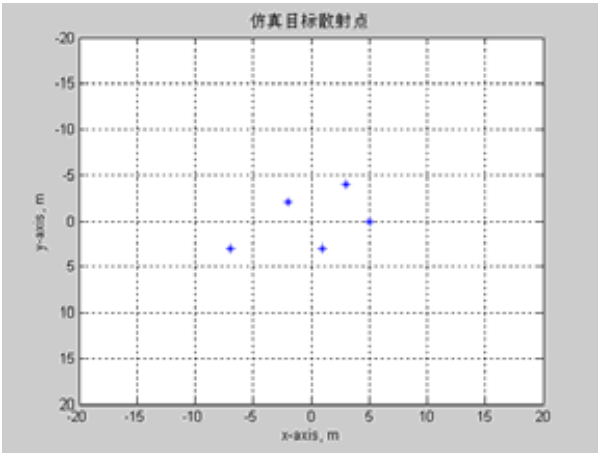

Figure 4: Five strong scattering point of target.

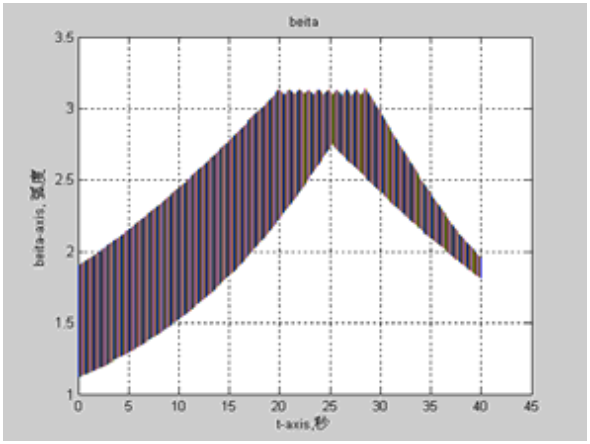

Figure 5: Variation of bistatic angle $\boldsymbol{\beta}$ with time.

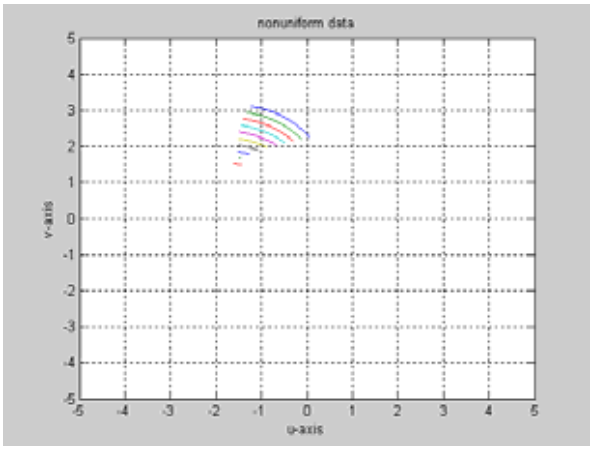

Figure 6: Total cumulative angle in 10 television stations.

5. CONCLUSION

Passive radar imaging based on external illuminators is considered in an ideal condition at present. For example, carrier frequency component is only taken into account while other factors are ignored such as the direct wave component, external noise and motion compensation. The influence of motion and the motion compensation are considered in imaging algorithm. When the motion factor is considered, a few factors such as the direction, velocity of target motion, television station position and receiving station position can affect the bistatic angle which is the main factor of imaging. A better image can be obtained by placing stations reasonably, which limit the action scope of system. That is, the target which flies in a certain scope of direction can only be imaged. Theoretically, the problem can be resolved by adding the amounts of receiving station. There are several other factors on passive radar imaging, such as the analyses of signal waveform, effect of direct wave, and low signal noise ratio, which demand further research.

ACKNOWLEDGMENT

This work was supported by the National Key Laboratory Foundation of China (No. 9140C53050206 0C53). The authors would like to acknowledge the valuable comment and suggestions of their associates in National Key Laboratory of Space Microwave Technology Xi'an Institute of Space Radio Technology. Special thanks are expressed to Doctor Wanzhao Cui for his interesting and rewarding comment.

REFERENCES

1. Griffiths, H. D. and N. R. W. Long, "Television based bistatic radar," *IEE Proceeding Part F.*, Vol. 133, No. 7, 1986.
2. Howland, P. E., "Target tracking using television based bistatic radar," *IEE Proceeding Part F.*, Vol. 146, No. 3, 1999.
3. Skolnik, M. I., *Radar Handbook*, National Defensive Industry Publisher, 1978.
4. Papoulis, A., *Probability, Random Variables, and Stochastic Process*, 2nd Edition, McGraw-Hill Book Company, NewYork, 1984.
5. Compton, R. T., "The bandwidth performance of a two-element adaptive array with tapped delay-line," *IEEE Trans. AP*, Vol. 36, No. 1, 1988.
6. Fante, R. L. and J. A. Torres, "Cancellation of diffuse jammer multipath by an airborne adaptive radar," *IEEE Trans. AES*, Vol. 31, No. 1, 1995.
7. Monzingo, R. A. and T. W. Miller, *Introduction to Adaptive Arrays*, J. Wiley and Sons, Inc, 1980.

Enhancement Gradient Pulse Waveforms in MR Tomography

E. Gescheidtova and R. Kubasek
Department of Theoretical and Experimental Engineering
Faculty of Electrical Engineering and Communication, Brno University of Technology
Kolejni 2906/4, 612 00 Brno, Czech Republic

Abstract— The magnetic resonance (MR) imaging techniques of tomography and spectroscopy are exploited in many applications. For the MR instruments to function properly it is necessary to maintain a high quality of homogeneity of the fundamental magnetic field. The pre-emphasis compensation of the generated gradient field increases the homogeneity of the generated magnetic field and reduces the minimum switching times of the gradients. This enables measuring the MR images of incisions in the human body, the relaxation properties of nuclei, self-diffusion processes, flows of liquids and movements of solids faster and more accurately.

1. INTRODUCTION

When defining the area being measured in localized spectroscopy and tomography, the gradient field is excited by very short pulses of sufficient magnitude. This gives rise to a fast changing magnetic field, which induces eddy currents in the conducting material near the gradient coils. These currents then cause retrospectively unfavourable deformation of the total magnetic field [1]. The basic idea of a method that compensates this effect consists in replacing the missing leading edge of the field waveform by an overshoot of excitation current as shown in Fig. 1. To have the best possible compensation it is necessary to find an optimum shape of excitation pulse. Basically, this consists in obtaining the spectrometer response pulse, inverting it and using this inversion to filter the excitation (usually square) pulse. The term pre-emphasis compensation method is based on the fact that the compensation filter is in the nature of a differentiating element (high-pass filter).

At the present time, pre-emphasis filters are implemented by digital means, most frequently digital signal processors. At the Institute of Scientific Instruments, Academy of Sciences of the Czech Republic in Brno, pre-emphasis filters are implemented on a Motorola 96002 DSP as a fifth-order IIR filter in the first canonical form.

The principle of measuring the waveform of gradient pulse consists in determining the changes in instantaneous frequency [2] of an MR signal produced by the resonance of nuclei excited in two thin layers positioned symmetrically about the gradient field centre. The instantaneous frequency of MR signal is directly proportional to the induction of magnetic field $B(\pm\alpha_n, t)$. The average inductions of magnetic field $B(\alpha_n, t)$ are measured in the excited layer in the $+\alpha_n$ and $B(-\alpha_n, t)$ positions in the $-\alpha_n$ layer; α is one of the (x, y, z) directions.

From the differences of the two inductions measured the magnitude of gradient can be calculated according to the relation

$$G_\alpha(t) = \frac{1}{2\alpha_n} \left[B(\alpha_n, t) - B(-\alpha_n, t) \right]. \tag{1}$$

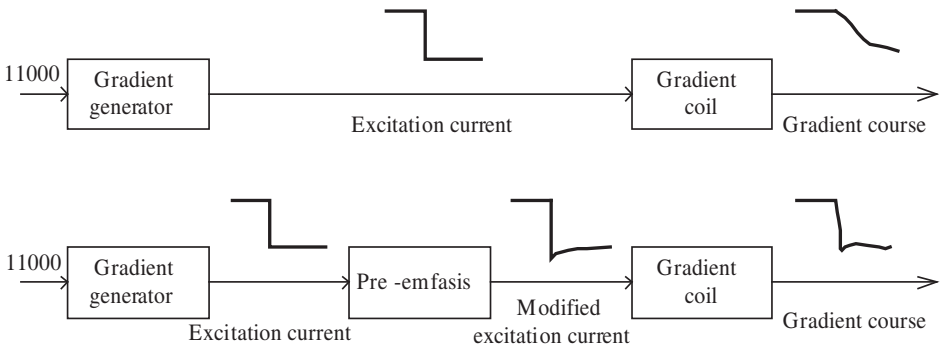

Figure 1: Principle of pre-emphasis compensation.

The measured waveform of magnetic inductions $B(\alpha_n, t)$ and $B(-\alpha_n, t)$ is much distorted due to noise. The gradient $G_r(t)$ calculated according to Equation (1) is even more distorted, due to the incorrelatibility of noise. To obtain an accurate and undistorted waveform of the gradient $G_\alpha(t)$, we must remove the noise.

2. DENOISING

The principle of sub-band denoising is shown in Fig. 2. Using an analysing filter bank the input signal is divided into a series of sub-band filters. Partial sub-band signals are thresholded appropriately in order to optimally suppress noise without influence on the useful signal. The magnitudes of thresholds p_i are calculated by within-block threshold estimation. In the block of synthesis filter bank the sub-band signals are again synthesized into the resultant signal.

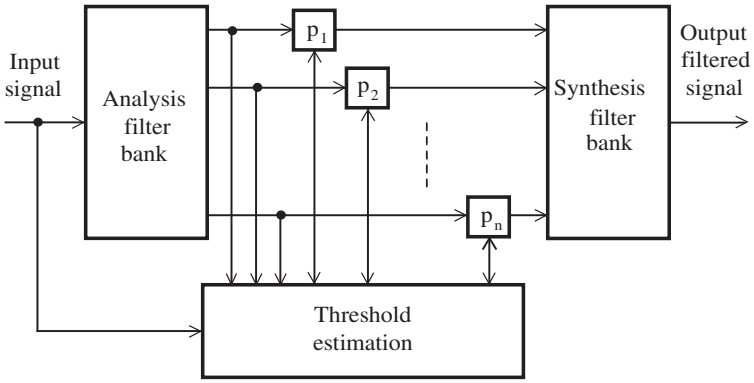

Figure 2: Block diagram of sub-band denoising.

The choice of the parameters of individual parts of blocks depends in the first place on the input signal properties. The filter bank base is chosen in dependence on the distribution of input signal spectral density. The length of pulse characteristics and the type of filter bank are chosen with a view to the required attenuation in the stop band, computation complexity, and the potential occurrence of transition phenomena. To suppress noise, filter banks without downsampling are usually used. Using a filter bank with downsampling will reduce the number of operations and the application demands on memory but at the cost of worse results. The threshold magnitudes calculated in block threshold estimation are usually calculated from the standard deviations of noise δ. Perhaps the best known relation derived for white additive noise is that with Gaussian distribution for global threshold $p = \delta\sqrt{2\ln(L)}$, where L is the input signal length. This value is usually very high, it is necessary to choose the threshold magnitude to be $p = \delta \cdot K$, where K is the empirically obtained constant. There are many types of thresholding [3], the most widely used thresholding is the soft or the hard type. By analysing the operation of calculating instantaneous frequency from the FID signal it is possible to obtain the noise parameters of instantaneous frequency signal necessary for automatic threshold adjustment [4]. The instantaneous phase of FID signal will be calculated using

$$\varphi = \arctan\left(\frac{\mathbf{Im}\,[\mathrm{FID}]}{\mathbf{Re}\,[\mathrm{FID}]}\right). \tag{2}$$

It is exactly $\Delta\varphi$ that represents the noise contained in the instantaneous frequency signal of FID signal. The magnitude of the change Δ in the real and the imaginary parts of the signal is directly linked with the magnitude of standard noise deviation, $\delta \approx \Delta$. Since the standard noise deviation of FID signal is constant, $\Delta\varphi$ changes in dependence on the magnitude of the FID signal and is thus non-linearly dependent also on SNR. Fig. 3 gives the waveforms of magnetic induction $B(\alpha_{n,t})$ before and subsequent to filtering. As can be seen, there has been considerable noise attenuation. The gradient $G_\alpha(t)$ is free from noise and, at the same time, measured with sufficient accuracy to be used in determining the coefficients of the pre-emphasis filter.

3. PREEMFASIS COMPENSATION

The lay-out of pre-emphasis filters is as shown in Fig. 4. Pre-emphasis filters are basically inverse filters to the model of tomographic scanner. The task is to generate a waveform of the gradient

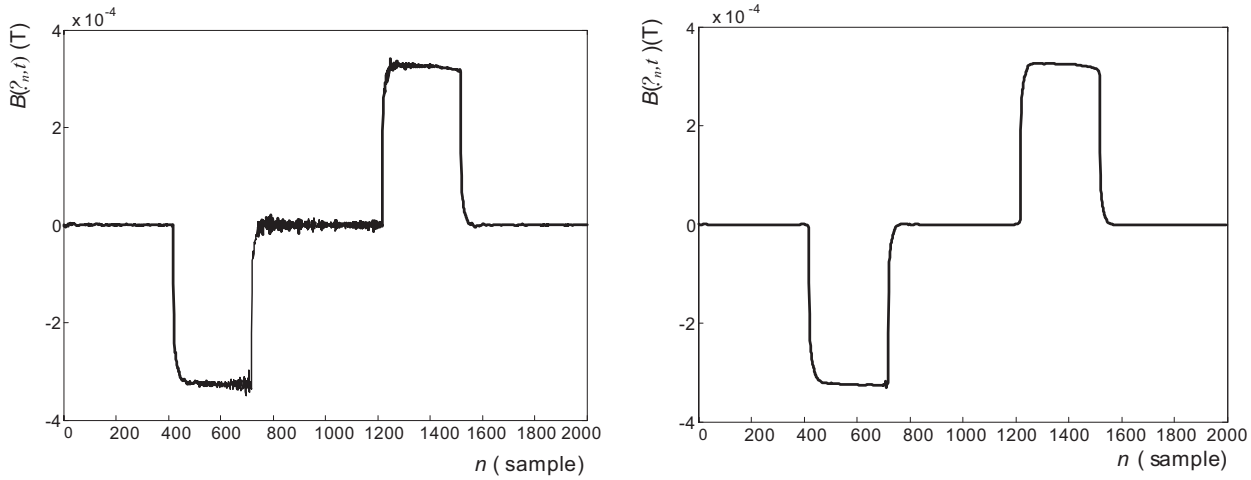

Figure 3: Waveforms of magnetic inductance $B(\alpha_n, t)$, (a) before filtering, (b) after denoising filtering.

$G'_\alpha(t)$ pre-distorted to such a degree that subsequent to the action of eddy currents the generated gradient $g_\alpha(t)$ is of the required waveform, i.e., $G_\alpha(t)$. The following equation must hold

$$g_\alpha(t) = G_\alpha(t), \tag{3}$$

and there must not be any change in the basic magnetic field $B_0(t)$. For a direct pre-emphasis filter $P_\alpha(z)$ it holds

$$G_\alpha(z)P_\alpha(z)M_\alpha(z) = g_\alpha(z). \tag{4}$$

$$P_\alpha(z) = M_\alpha^{-1}(z) = \frac{G_\alpha(z)}{g_\alpha(z)}. \tag{5}$$

The effect of eddy currents will be compensated under the conditions (5). The measurement itself must be performed for the setting $P_\alpha(z) = 1$, preferably for $P_{\tilde{\alpha}}(z) = 0$. The transfer of the coil $M(z)$, which compensates the basic magnetic field B_0 will be measured for quite the opposite setting, namely $P_\alpha(z) = 0$ and $P_{\tilde{\alpha}}(z) = 1$. The basic field B_0 is excited directly by the gradient in the respective direction, and for $M_0(z)$ it holds

$$G_\alpha(z)P_{\alpha 0}(z)M_0(z) = \Delta B_0(z). \tag{6}$$

The cross transfer of the gradient in the given direction $G_\alpha(z)$ to the basic field B_0 via $M_{\alpha 0}(z)$ is given

$$\Delta B_0(z) = G_\alpha(z)P_\alpha(z)M_{\alpha 0}(z). \tag{7}$$

The compensation of the basic field using the cross pre-emphasis filter $P_{\alpha 0}(z)$ will take place if a basic field of opposite polarity is generated,

$$G_\alpha(z)P_{\alpha 0}(z)M_0(z) = -\Delta B_0(z). \tag{8}$$

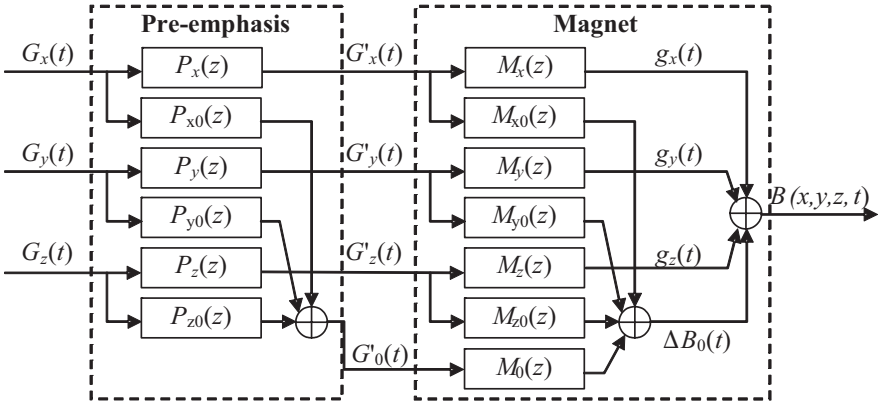

Figure 4: Pre-emphasis compensation and model of tomograph.

Thus it must hold

$$P_{\alpha 0}(z) = -\frac{\Delta B_0(z)}{G_\alpha(z) M_0(z)}. \tag{9}$$

Equation (9) says that the cross transfer of the gradient in the given direction $G_\alpha(z)$ to the basic field B_0 via $M_{\alpha 0}(z)$ must be measured for an already set direct pre-emphasis filter $P_\alpha(z)$. Its calculation must include an earlier determined transfer of the compensation coil $M_0(z)$. The sequence in which measurements are performed cannot be changed. The calculation of pre-emphasis filters by relations (4), (6) and (9) is always determined from two signals, one input signal and one output signal. The ratio of their Z-images gives the desired transfer characteristic of the pre-emphasis filter. The directly found characteristic is basically always unstable; none of its poles are inside the unit circle. We must find a stable IIR filter, which by its properties is the closest to the ideal inversion. There are several ways how to find this IIR filter. The best results have been obtained using the Matlab function *stmcb*, which employs the Steiglitz-McBride iteration process [5] used to calculate the approximation error by the LMS method.

4. EXPERIMENTAL RESULTS

Figure 5 gives the waveforms of positive gradient impulse G_x, G_y, and $G_z$with and without pre-emphasis compensation. The most essential change consists in the shortening of the leading and trailing edges of the gradient impulse $-G_x$ rise time from 250 µs to 70 µs. The leading edge has been shortened ca. three times. The lengths of the edges of the gradient impulses G_y and G_z were reduced from 350 µs to 60 µs.

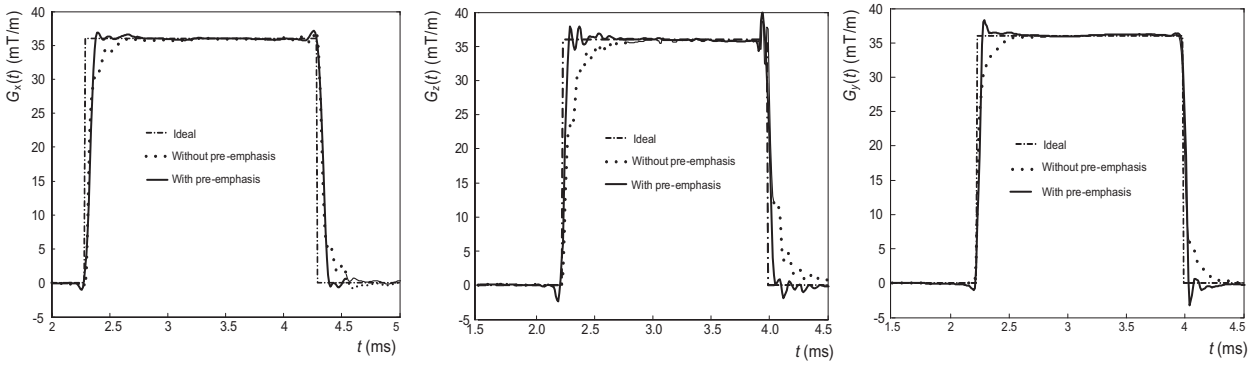

Figure 5: Comparison of positive gradient impulse G_x, G_y, and G_z with and without pre-emphasis compensation.

5. CONCLUSIONS

The application of pre-emphasis compensation of gradient magnetic field has led to a qualitative improvement in the parameters of the magnetic field generated in an MR tomograph. It can therefore be expected that better results will be obtained in all regions of MR tomography and spectroscopy where the generation of gradient fields of a defined waveform with minimum switching times is required. Today the minimum applicable switching time of gradients in MR tomography is a limiting factor in the application of fast imaging sequences in MRI. Shortening the gradient edges and improving the magnetic field homogeneity after a gradient impulse result in shortening the minimum applicable switching time of magnetic field gradients and the waiting time between gradient impulses, when the magnetic field is required to drop to the level of the homogeneity of the basic magnetic field B_0. In that case the images of incisions in the human body can be measured faster and more accurately.

ACKNOWLEDGMENT

This work was supported within the framework of the research plans MSM 0021630513 and project 102/07/0389 of the Grant Agency of the Czech Republic.

REFERENCES

1. Vlaardingerbroek, M., *Magnetic Resonance Imaging*, Springer-Verlag, 2000.

2. Kubasek, R., E. Gescheidtova, and K. Bartusek, "Measurements of time characteristics of the gradient magnetic field," *Proceedings of 27th Annual International Conference of the IEEE Engineering in Medicine and Biology Society*, 1–4, Shanghai, China, 2005.
3. Rajmic, P., "Statistical properties of wavelet spectrum thresholding rules," *Proceedings of 48th International Scientific Colloquium*, 87–88, Ilmenau, Germany, 2003.
4. Gescheidtova, E., R. Kubasek, Z. Smekal, and K. Bartusek, "Automatic adjustment of time-variant thresholds when filtering signals in MR tomography," *Lecture Notes in Computer Science*, No. 3421, 384–391, 2005.
5. Ljung, L., *System Identification: Theory for the User*, Prentice-Hall, Englewood Cliffs, 1987.

Three-scale Radar Backscattering Model of the Ocean Surface Based on Second-order Scattering

Ying Yu[1, 2], **Xiao-Qing Wang**[1], **Min-Hui Zhu**[1], **and Jiang Xiao**[1],

[1]National Key Laboratory of Microwave Imaging Technology
Institute of Electronics, Beijing 100080, China
[2]Graduate University of Chinese Academy of Sciences, Beijing 100049, China

Abstract— Based on the second-order composite surface and stochastic multi-scale models, an ocean surface backscattering model is proposed in this paper, including both the large-/intermediate-/small-scale scattering and the second-order Bragg scattering. Within this frame, we derive a second-order Bragg scattering expression, and develop an analytic solution of hydrodynamic modulation function according to weak hydrodynamic interaction theory. In addition, tilt modulation is simulated through the observation angle transform between nominal and local coordinate systems. The result shows that reasonable agreement between measured and simulated data is obtained, and this model is better than the two models mentioned above.

1. INTRODUCTION

In recent years, airborne and spaceborne imaging radars have received considerable attentions in the area of ocean observation. But it is expensive and difficult to obtain accurate data in the measurements due to complicated conditions on the ocean surface. Therefore, a number of radar backscattering models are given, which have been important approaches in the remote sensing of the ocean. Before 1990s, many physical models of microwave backscatter from the ocean surface have relied on Kirchhoff scattering, Bragg scattering, two-scale and composite surface theories [1–3]. After 1990s, more and more accurate models have been proposed based on the fruit of previous ones. One of them is the improved composite surface model proposed by Romeiser et al., [4], which considers second-order Bragg scattering. And another one is the stochastic multi-scale model proposed by Plant et al., [5], which divides ocean surface waves into large-/intermediate-/small-scale waves continuously.

In this paper, the model divides ocean surface into intermediate-small-scale and large-scale spectra. Within this frame, the second-order Bragg scattering expressions are derived and an analytic solution of hydrodynamic function is developed according to weak hydrodynamic interaction theory. In addition, tilt modulation is implemented through the observation angle transform between nominal and local coordinate systems. Finally, a comparison between simulated and measured data is made, which shows well performance of the model.

2. THREE-SCALE MODEL BASED ON SECOND-ORDER SCATTERING

2.1. Large-/Intermediate-small Scale Backscatter Cross Section

If only considering single scattering, backscatter cross section for large scale waves is computed by traditional Kirchhoff method [6]:

$$\sigma_l = \exp\left\{-4\varepsilon_{is}k_z^2\right\} \frac{k_e^2 \left|f_{pq}\right|^2 \left(4k_z^2 + k_x^2 + k_y^2\right)}{16k_z^4 (SS)^{1/2}} \cdot \exp\left\{ \frac{-\left(S_{yy}k_x^2 + S_{xx}k_y^2 - 2S_{xy}k_xk_y\right)}{8 \cdot SS \cdot k_z^2} \right\} \tag{1}$$

where k_e is transmitted wavenumber, θ_i is incidence angle, ε_{is} is mean square of intermediate-small scale wave height, SS is slope variance of large scale waves, S_{xx}, S_{yy} are mean square of large scale slopes in x and y directions, f_{pq} is polarization coefficient [6], $p = h_s$, v_s, $q = h_i$, v_i denote received and transmitted polarization modes respectively.

And backscatter cross section for intermediate-small scale waves is obtained from integral equation:

$$\sigma_{is} = \frac{k_e^2}{4\pi} \exp\left[-4k_z^2\right] \left|\Gamma_{pq}\right|^2 \cdot \int \exp\left[j\left(-\mathbf{k_B}\right) \cdot \mathbf{x}\right] \left\{\exp\left[4k_z^2 \varphi_{is}\left(\mathbf{x}\right)\right] - 1\right\} d\mathbf{x} \tag{2}$$

where $\varphi_{is}\left(\mathbf{x}\right)$ is correlation function of intermediate-small scale waves, $\mathbf{k_B}$ is Bragg wavenumber, $|\Gamma_{pq}|$ is polarization coefficient [6]. Because $\varphi_{is}\left(\mathbf{x}\right)$ includes intermediate and small scale waves, σ_{is} also includes traditional Bragg scattering besides intermediate scale waves scattering.

2.2. Second-order Bragg Backscatter Cross Section

For a small facet which is tilted with respect to a horizontal reference plane, one obtains:

$$\sigma_{pq0} = 4\pi k_e^4 \cos\theta_i^2 \left|\Gamma_{pq}\right|^2 \left[\psi\left(\mathbf{k_B}\right) + \psi\left(-\mathbf{k_B}\right)\right] = T\left(s_p, s_n\right)\left[\psi\left(\mathbf{k_B}\right) + \psi\left(-\mathbf{k_B}\right)\right] \tag{3}$$

where $\psi(\mathbf{k_B})$ denotes Bragg wave spectrum, s_p, s_n denote large scale waves slopes parallel and normal to the radar look direction respectively, $T\left(s_p,\, s_n\right)$ denote tilt modulation term.

The Taylor expansion of $T\left(s_p,\, s_n\right)$ with respect to slope $(s_p,\, s_n)$, which only keeps up to second order, reads as follow:

$$T\left(s_p,\, s_n\right) \approx T(0) + T_{1p} + T_{1n} + T_{2pp} + T_{2nn} + T_{2pn} \tag{4}$$

where $\left.\frac{\partial T}{\partial s_p}\right|_{s=0} s_p = T_{1p}$, $\frac{1}{2}\left.\frac{\partial^2 T}{\partial s_p^2}\right|_{s=0} s_p^2 = T_{2pp}$, $\left.\frac{\partial^2 T}{\partial s_p \partial s_n}\right|_{s=0} s_p s_n = T_{2pn}$.

When considering hydrodynamic modulation, wave spectrum turns as:

$$\psi = \psi_0\left(1 + \psi_h\right) \tag{5}$$

where $\psi_h = \Delta\psi/\psi_0$ denotes relatively change rate of spectrum.

Do the same thing to ψ as to $T\left(s_p,\, s_n\right)$, we obtain:

$$\psi \approx \psi\left(0\right) + \psi_{1p} + \psi_{1n} + \psi_{2pp} + \psi_{2nn} + \psi_{2pn} + \psi\left(0\right)\psi_h + \psi_{1p}\psi_h + \psi_{1n}\psi_h \tag{6}$$

where $\left.\frac{\partial \psi_0}{\partial s_p}\right|_{s=0} s_p = \psi_{1p}$, $\frac{1}{2}\left.\frac{\partial^2 \psi_0}{\partial s_p^2}\right|_{s=0} s_p^2 = \psi_{2pp}$, $\left.\frac{\partial^2 \psi_0}{\partial s_p \partial s_n}\right|_{s=0} s_p s_n = \psi_{2pn}$.

We insert Equation (4) and (6) into (3), and compute expectation values in a cell:

$$\begin{aligned}
\left\langle\sigma_{pq}\right\rangle &= \left\langle\sigma_{pq+}\right\rangle + \left\langle\sigma_{pq-}\right\rangle \approx \sigma_+^{(0)} + \sigma_-^{(0)} + \left\langle\sigma_+^{(2)}\right\rangle + \left\langle\sigma_-^{(2)}\right\rangle \\
\sigma_+^{(0)} &= \psi\left(\mathbf{k_B}\right)T\left(0\right) \qquad \left\langle\sigma_+^{(2)}\right\rangle = \left\langle\sigma_{tt+}^{pp}\right\rangle + \left\langle\sigma_{tt+}^{nn}\right\rangle + \left\langle\sigma_{tt+}^{pn}\right\rangle + \left\langle\sigma_{th+}^{pp}\right\rangle + \left\langle\sigma_{th+}^{nn}\right\rangle \\
\left\langle\sigma_{tt+}^{pp}\right\rangle &= \left\langle\psi\left(\mathbf{k_B}\right)T_{2pp}\right\rangle + \left\langle T_{1p}\psi_{1p}\right\rangle + \left\langle T\left(0\right)\psi_{2pp}\right\rangle \qquad \left\langle\sigma_{th+}^{pp}\right\rangle = \left\langle T\left(0\right)\psi_{1p}\psi_h\right\rangle + \left\langle\psi\left(0\right)\psi_h T_{1p}\right\rangle \\
\left\langle\sigma_{tt+}^{nn}\right\rangle &= \left\langle\psi\left(\mathbf{k_B}\right)T_{2nn}\right\rangle + \left\langle T_{1n}\psi_{1n}\right\rangle + \left\langle T\left(0\right)\psi_{2nn}\right\rangle \qquad \left\langle\sigma_{th+}^{nn}\right\rangle = \left\langle T\left(0\right)\psi_{1n}\psi_h\right\rangle + \left\langle\psi\left(0\right)\psi_h T_{1n}\right\rangle \\
\left\langle\sigma_{tt+}^{pn}\right\rangle &= \left\langle\psi\left(\mathbf{k_B}\right)T_{2pn}\right\rangle + \left\langle T_{1n}\psi_{1p}\right\rangle + \left\langle T_{1p}\psi_{1n}\right\rangle + \left\langle T\left(0\right)\psi_{2pn}\right\rangle
\end{aligned} \tag{7}$$

Here $\left\langle\sigma_{tt+}^{pp}\right\rangle$ represents second-order contributions associated with surface slopes parallel to the azimuthal radar look direction, symbol + represents Bragg waves traveling away from the antenna, the rest are named by analogy. The second-order hydrodynamic modulation terms are neglected in this paper the same as in literature [4].

Part of second-order scattering terms is derived as follow, the rest can be deduced by analogy:

$$\begin{aligned}
\left\langle\sigma_{tt+}^{pp}\right\rangle &= \left\{\frac{1}{2}\psi\left(\mathbf{k_B}\right)\left.\frac{\partial^2 T}{\partial s_p^2}\right|_{s=0} + \left.\frac{\partial T}{\partial s_p}\right|_{s=0} \cdot \left(\left.\frac{\partial \psi}{\partial k}\right|_{\mathbf{k}=\mathbf{k_B}}\left.\frac{\partial k_B}{\partial s_p}\right|_{s=0} + \left.\frac{\partial \psi}{\partial \phi}\right|_{\mathbf{k}=\mathbf{k_B}}\left.\frac{\partial \phi_B}{\partial s_p}\right|_{s=0}\right)\right. \\
&\quad + \frac{1}{2}T(0)\left[\left.\frac{\partial^2 \psi}{\partial k^2}\right|_{\mathbf{k}=\mathbf{k_B}}\left(\left.\frac{\partial k_B}{\partial s_p}\right|_{s=0}\right)^2 + \left.\frac{\partial^2 \psi}{\partial \phi^2}\right|_{\mathbf{k}=\mathbf{k_B}}\left(\left.\frac{\partial \phi_B}{\partial s_p}\right|_{s=0}\right)^2\right] + T(0)\left.\frac{\partial^2 \psi}{\partial k \partial \phi}\right|_{\mathbf{k}=\mathbf{k_B}}\left.\frac{\partial k_B}{\partial s_p}\right|_{s=0}\left.\frac{\partial \phi_B}{\partial s_p}\right|_{s=0} \\
&\quad \left. + \frac{1}{2}T(0)\left(\left.\frac{\partial \psi}{\partial k}\right|_{\mathbf{k}=\mathbf{k_B}}\left.\frac{\partial^2 k_B}{\partial s_p^2}\right|_{s=0} + \left.\frac{\partial \psi}{\partial \phi}\right|_{\mathbf{k}=\mathbf{k_B}}\left.\frac{\partial^2 \phi_B}{\partial s_p^2}\right|_{s=0}\right)\right\} \cdot \iint dk d\phi k^3 \cos^2\left(\phi - \phi_0\right)\psi\left(\mathbf{k}\right)
\end{aligned} \tag{8}$$

$$\begin{aligned}
\left\langle\sigma_{th+}^{pp}\right\rangle &= \left.\frac{\partial T}{\partial s_p}\right|_{s=0} \iint dk d\phi \psi_h(\mathbf{k_B}) \cdot \psi(\mathbf{k_B}) \cdot k^2 \cos\left(\phi - \phi_0\right)\psi(\mathbf{k}) \\
&\quad + T(0)\iint dk d\phi \left[\psi_h(\mathbf{k_B}) \cdot \left(\left.\frac{\partial \psi}{\partial k}\right|_{\mathbf{k}=\mathbf{k_B}}\left.\frac{\partial k_B}{\partial s_p}\right|_{s=0} + \left.\frac{\partial \psi}{\partial \phi}\right|_{\mathbf{k}=\mathbf{k_B}}\left.\frac{\partial \phi_B}{\partial s_p}\right|_{s=0}\right)\right] k^2 \cos\left(\phi - \phi_0\right)\psi(\mathbf{k})
\end{aligned} \tag{9}$$

where $\psi_h(\mathbf{k_B})$ denotes hydrodynamic modulation term of Bragg waves by intermediate scale waves. As we can see, expressions (8) and (9) are consistent with (7).

3. HYDRODYNAMIC AND TILT MODULATIONS

3.1. An Analytic Solution of Hydrodynamic Modulation

According to weak hydrodynamic interaction theory, the action balance equation reads:

$$\frac{dN}{dt} = \left(\frac{\partial}{\partial t} + \frac{d\mathbf{x}}{dt}\cdot\nabla_{\mathbf{x}} + \frac{d\mathbf{k}}{dt}\cdot\nabla_{\mathbf{k}}\right)N = S(\mathbf{x},\mathbf{k},t) \tag{10}$$

$$N(\mathbf{x},\mathbf{k},t) = \Psi(\mathbf{x},\mathbf{k},t)\frac{\rho\omega_0(k)}{k} \tag{11}$$

where N is the action spectral density of the wave packet, S is a source function. The source function in this model is a nonlinear form:

$$S(\mathbf{k},\mathbf{x},t) = \mu N\left(1 - \frac{N}{N_0}\right) \tag{12}$$

An analytic solution of the action balance equation is derived as follow:

$$\frac{\delta Q(x,\mathbf{k},t)}{Q_0} = \iint\left\{\frac{j\left[\mathbf{k}\cdot u(\mathbf{K},\omega_c)\right](\mathbf{K}\cdot\nabla_{\mathbf{k}}Q_0)}{-j\omega_c - \mu + j(c_g + \mathbf{U}_0)\cdot\mathbf{K}}\cdot\exp\left[j(\mathbf{K}\cdot\mathbf{x} - \omega_c t)\right] + c.c.\right\}d\mathbf{K}d\omega_c \tag{13}$$

where $Q(\mathbf{x},\mathbf{k},t) = 1/N(\mathbf{x},\mathbf{k},t)$, $Q_0 = 1/N_0$, μ is relaxation rate, c_g is group velocity of the wave packet.

3.2. Tilt Modulation

As in Figure 1, according to the transformation between nominal and local coordinate systems, local observation angles are obtained:

$$\begin{aligned}
\theta &= atg(-s_p) \qquad \delta = atg\left[-s_n\cos\theta\right]\\
\theta_i' &= a\cos\left[\cos(\theta+\theta_i)\cos\delta\right]\\
\varphi_i' &= atg\left(\frac{-\sin\theta_i\sin\delta\sin\theta + \cos\theta_i\sin\delta\cos\theta}{\sin\theta\cos\theta + \cos\theta_i\sin\theta}\right)
\end{aligned}$$

θ_i' represents local incidence angle, φ_i' is local azimuth angle.

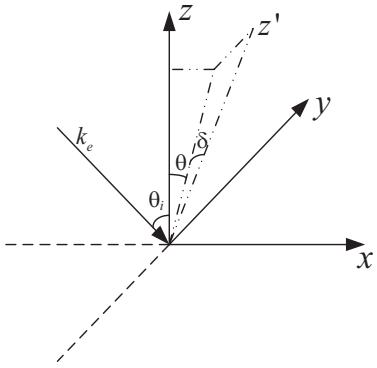

Figure 1: Nominal and local coordinate system.

4. MODEL RESULTS

In this section, we compute average cross sections of different parameter sets. And we compare them with the measured data in the literatures cited. The result shows well agreement with the measured data.

Figure 2 compares model results with data collected from an airship by Plant et al., [5] as a function of azimuth angle. It shows well agreement between them quantitatively, and suggests this model is not only fit for scattering of intermediate incidence angles but also small incidence angles. The reason lies in that the model considers not only traditional Bragg scattering but also intermediate and large scale scattering.

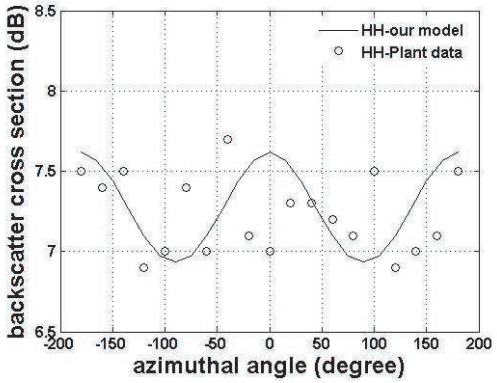

Figure 2: Average cross sections at various azimuthal angles. (Frequency: 14 GHz; incidence angle: 10 degree; wind speed: 8 m/s).

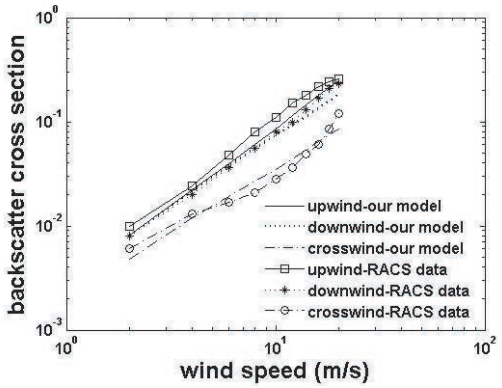

Figure 3: Average cross sections at various wind speeds. (Frequency: 5.3 GHz; VV polarization; incidence angle: 45 degree).

Figure 3 shows model predictions and data from Romeiser et al., [4] for cross sections versus wind speed in upwind, downwind and crosswind directions. The fit of all predictions to the data is rather good. As we can see, the magnitudes of backscatter cross sections from the bottom up are in crosswind, downwind and upwind directions.

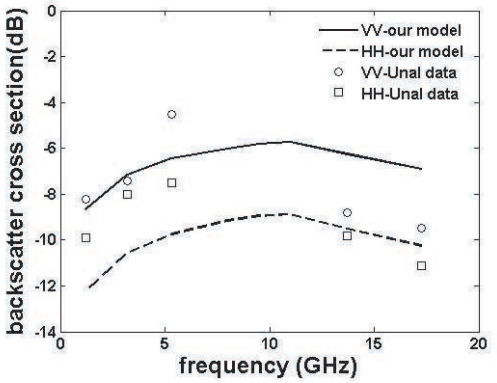

Figure 4: Azimuthally averaged cross sections at various frequencies. (Incidence angle: 30 degree; wind speed: 10 m/s).

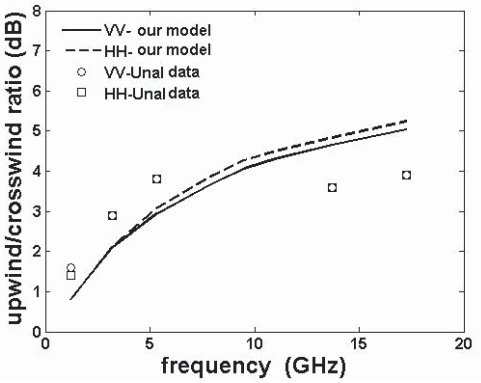

Figure 5: Upwind/crosswind ratio at various frequencies. (Parameters are the same as Figure 4).

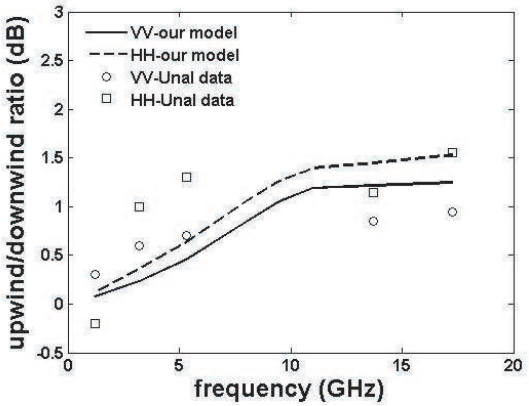

Figure 6: Upwind/downwind ratio at various frequencies. (Parameters are the same as Figure 4).

Figures 4, 5, 6 compare measured and modeled cross sections, upwind/crosswind ratio and upwind/downwind ratio for the two like-polarizations. The results show fits of the model to the data [7] are reasonably good. And the model predictions are better than those in literature [5]. It is because we consider second-order scattering here which is not included in [5].

5. CONCLUSIONS

The radar backscattering model in this paper is better than those mentioned in [4] and [5]. To explain it theoretically, our model considers not only traditional Bragg scattering but also second-order scattering. Besides Bragg scattering, intermediate and large scale waves scattering is considered as well. Therefore, this model can predict the backscatter characteristics for small to intermediate incidence angles, frequencies from L to Ku band, wind speeds up to 20 m/s.

REFERENCES

1. Wright, J. W., "A new model for sea clutter," *IEEE Trans. Antennas Propag.*, AP-16, 217–223, 1968.
2. Holliday, D., "Resolution Of a controversy surrounding the Kirchhoff approach and the small perturbation method in rough surface scattering theory," *IEEE Trans. Antennas Propag.*, AP-35, 120–122, 1987.
3. Plant, W. J., "A two-scale model of short wind generated waves scatterometry," *J. Geophys. Res.*, Vol. 91, 10,735–10,749, 1986.
4. Romeiser, R. and W. Alpers, "An improved composite surface model for the radar backscattering cross section of the ocean surface 1. Theory of the model and optimization/validation by scatterometer data," *Journal of Geophysical Research*, Vol. 102, No. C11, 25,237–25,250, 1997.
5. Plant, W. J., "A stochastic, multiscale model of microwave backscatter from the ocean," *Journal of Geophysical Research*, Vol. 107, No. C9, 3120, doi:10.1029/2001JC000909, 2002.
6. Fung, A. K., *Microwave Scattering and Emission Models and Their Applications*, Artech House, Boston London, 1994.
7. Unal, C. M. H., P. Snoeij, et al., "The polarization-dependent relation between radar backscatter from the ocean surface and surface wind vector at frequencies between 1 and 18 GHz," *IEEE Trans. Geosci. Remote Sens.*, Vol. 29, No. 4, 621–626, 1991.

Remote Sensing Image Compression Based on Classification and Detection

Minqi Li, **Quan Zhou**, **and Jun Wang**

National Key Laboratory of Space Microwave Technology, Xi'an Institute of Space Radio Technology
Xi'an, China

Abstract— The major bottleneck of remote sensing satellites is the transmission of the obtained images to the ground station. Traditional compression algorithms can not process the huge data volume captured by the high resolution sensors. In this paper, a novel compression scheme based on classification and detection algorithms is proposed. In the proposed scheme, based on the regions of interest, the image of high compression ratio is obtained which is compressed in different strategy. And also its computational complexity is low and tends to be realized. The novel scheme is appropriate for on-board processing.

1. INTRODUCTION

In many remote sensing satellites, a large amount of data is collected by the on-board sensors and must be transmitted to ground through a channel with limited capacity. In this case, it is often only a limited number of images can be down-load. To solve this problem, image compression is one of the key techniques for reducing the redundancy that exists in data. However, the next generation of remote sensing satellites will extremely exceed their downlink capability and conventional compression algorithms are not powerful enough to meet the demands. Therefore, it is essential to further develop include data compression, data reduction as well as other new technologies [2, 3].

Depending on the application for which these images are to be used, one may be interested only in a subset of the imaged regions [1]. For example, in weather forecast application, cloud is significant while it is useless for military observation. But, they are still cost numbers of bits to be encoded and transmitted. It is then desirable that intelligent processing the images, such as categorizing images, selection the data of interest and discarding the data those are with minor information. Therefore, once the regions of interest are extracted, a region-based approach seems to be a good solution to the problem. And the last task is to choose the coding methods that should be used for coding interest data or the background ones. JPEG2000 is a natural choice for its many advantages, such as allowing lossless and lossy compression, rate control and regions of interest coding [10].

In this paper, the algorithm of segmentation and identification of the interest regions with the help of the texture analysis and Hough transform is proposed. The proposed algorithm is useful to narrow gap between the volume of data collected by the instruments and the capacity of the data link to earth. The algorithms used in the scheme are simple and can be implemented in a low computation complexity, so that it is appropriate for on-board implementation [9].

The paper is organized as follows. In Section 2, the overall strategy and related methods are described. In Section 3, the details of our algorithms are presented. In Section 4, we give some experimental results. Section 5 concludes this paper.

2. OVERALL STRATEGY AND RELATED WORK

A brief compression scheme based on classification and target detection is shown in Fig. 1.

According to Fig. 1, the processing procedures of an image include steps as follows:

(1) The whole image is divided into square blocks. The size of each block is n by n, and categorized into two classes based on their application. The two classes are useful part and useless part. For example, cloud regions in a military application belong to useless part and man-made areas belong to the useful part.

(2) The two parts are processed in different strategy. As for the useless part, the blocks are discarded or compressed in a high ratio; but for the useful part, the blocks are detected and defined two segments "background" and "target", which are subjected to different compression algorithms. Here, "background" means the regions that are useful but not important and "target" is region-of-interest (ROI) that is important regions.

(3) The whole image is compressed in different ratio depends on the classification and detection results.

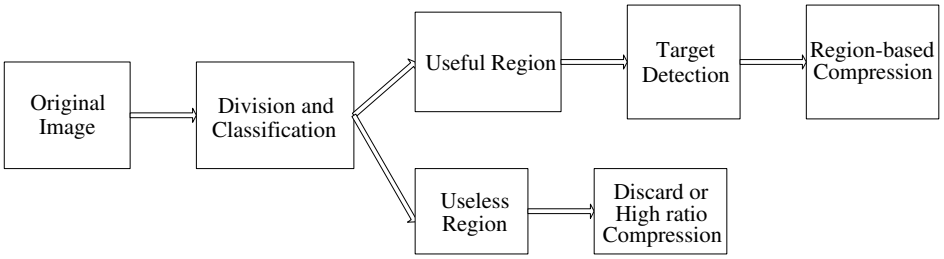

Figure 1: Proposed scheme: Image compression based on classification and detection.

From Fig. 1, we can see the scheme is a complex process which involves classification, target detection and compression algorithms. In order to ensure the maximum efficiency, a classification, detection algorithm and a compression should be devised. In this paper, we will choose the suitable algorithms for the system.

In the classification module, different methods have been proposed for remote sensing image segmentation and classification. Using textural information for image classification is an effective way [3, 5, 8, 11]. According to remote sensing image character, where different surfaces such as those of sea-water, vegetation, urban areas, man-made objects, etc. can be characterized by distinct textural features. The texture features proposed here are based on grey-level co-occurrence matrix (GLCM) and fractal dimension. The GLCM features and fractal features are respectively well used in image segmentation [6, 7]. Here, a method which combines the GLCM feature and the fractal dimension feature is used for the system to identify the man-made regions from the natural regions.

In the target detection module, we focus on linear target which is the main different character between natural target and man-made target. As the Hough transform is a standard technique for detecting features as lines in a given image, it is a natural and powerful choice.

However, the transform is computationally expensive and ineffective for real-time applications. As we have divided the image into blocks and classified, it is an efficient way for the Hough transform. More details will be described in Section 3.

Finally, a suitable compression algorithm is essential for the different kinds of regions processed. JPEG2000 is a general compression method for various kinds of images which has been recommended for image compression in space applications by The Consultative Committee for Space Data Systems (CCSDS) [10]. It has many advantages such as allowing lossless and lossy compression, progressive coding rate control and regions of interest coding which is very suitable for our compression strategy.

3. REGION CLASSIFICATION AND DETECTION

3.1. Classification

We utilize two methods to analysis texture: grey-level co-occurrence matrix (GLCM) and fractal dimension.

The grey-level co-occurrence matrix is the most widely used method in remote sensing to compute second order texture measure [5]. Various textural features have been defined based on the GLCM. The specific texture features used in this work are energy(E), contrast(CON), entropy(ENT), which are defined as follows:

$$E = \sum_{i}^{n}\sum_{j}^{n}\{P(i,\,j)\}^2 \tag{1}$$

$$CON = \sum_{i}^{n}\sum_{j}^{n}(i-j)^2 P(i,\,j) \tag{2}$$

$$ENT = \sum_{i}^{n}\sum_{j}^{n}P(i,\,j)\lg P(i,\,j) \tag{3}$$

In the GLCM method, we define the window size is same as the block size or smaller than it. Some approaches such as gray-level quantization can be used to reduce computational complexity.

On the other hand, since many natural surfaces are fractal in nature, it is possible to distinguish man-made areas from natural ones from their fractal signatures, and to differentiate between different natural regions.

The concept of self-similarity can be used to estimate the fractal dimension. A bounded set A in Euclidean n-space is self-similar if A is the union of N_r distinct (non-overlapping) copies of itself scaled up or down by a ratio r. The fractal dimension D of A is given by the relation:

$$D = \lim \frac{\log(N_r)}{\log(1/r)}. \tag{4}$$

In this paper, we will use the Differential Box Counting (DBC) methods to calculate the fractal dimension which is faster and more accurate than other box counting approaches [5].

In practice, as various regions have different average grey, we found that combining grey character with fractal dimension is superior than the only using fractal dimension in identifying the different regions. The grey-weighting fractal dimension can be defined as follows:

$$D1 = m \times D = m \times \lim \frac{\log(N_r)}{\log(1/r)}. \tag{5}$$

where, m is the average grey value of the selected region and can be represented as: $m = (g_{\max} + g_{\min})/2$ where, $g_{\max}$ and $g_{\min}$ denote the maximum and minimum of grey value in the selected block.

Once the texture features are extracted from the texture spectrum, most classification algorithms can be used to discriminate the texture patterns.

3.2. Hough Transform

The principal concept of Hough transform is to define a mapping between an image space and a parameter space. Typically points or edges are mapped into a Hough space as individual votes. The chosen cells are accumulated considering all the set of points in the image. The local maxima in the accumulator correspond then the parameters of the specified shape.

Nevertheless, the main drawbacks of the standard Hough transform are its high memory requirements and computational complexity, and these pose a limitation on the use of the transform for real-time application [12].

In the compression scheme, as the whole image has been segmented and classified, it is more effective for computing the Hough transform for it is only necessary to the selected blocks. The compute complexity can be explained:

Assume the image size is n by n. And it is divided into k blocks. When the parameters are in same discrete accuracy, the whole computation complexity will be $\mathrm{O}((n/k)^3 \times k)$ as it is divided. Comparing with computation complexity $\mathrm{O}(n^3)$ before it is divided, it will reduce the computation complexity.

4. SIMULATION RESULTS

In this section, the scheme proposed above is adopted to remote sensing image of 256 gray levels.

Figure 2 is the original source image, which includes water area, airport, and land background. We define the water area is useless part, and airport is ROI. The other regions are background.

In Fig. 3 the original source image is divided into some small regions (blocks), such as land area, the airport, water region and transition region.

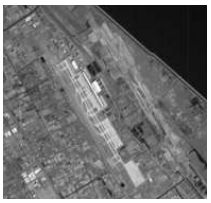

Figure 2: Original image.

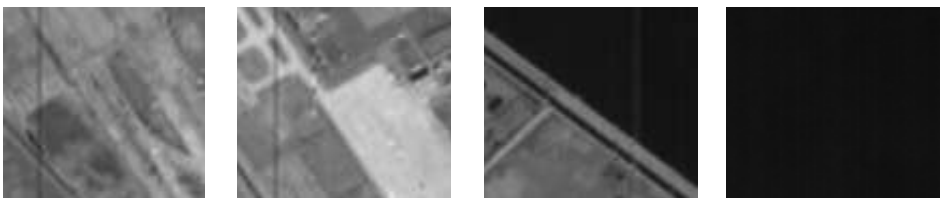

(a) land (b) airport (c) transition (d) water

Figure 3: Different class of regions.

Based on the results of simulation, we choose energy(E), contrast(CON) and grey-weighting fractal dimension as the division features.

From Table 1, $D1$ can be well used to identify water region and transition region, although it is not an accurate way to divide land and airport areas. At the same time, E and CON are selected for the division of land and airport areas.

Table 1: Texture analysis of different regions.

Texture feature / Regions	E	CON	$D1$
Land	0.057∼0.324	0.107∼0.453	12.5∼15.4
Airport	0.005∼0.027	0.423∼0.647	11.2∼19.6
Transition	0.111∼0.190	0.261∼0.347	5.5.∼11.1
Water	0.518∼0.534	0.031∼0.023	2.13∼2.18

The combined three features are well performed in the classification module. Once the texture features are extracted from the image, most classification algorithms can be used to categorize the regions. Here, the simple minimum-distance classification algorithm is used.

For the land and airport regions, Hough transform is used to detect linear targets. In Fig. 4, the ROI (runway of airport) is extracted.

Because the whole image has been segmented and classified, it is more effective for computing the Hough transform as it is only necessary to the selected blocks.

Finally, the image will be compressed based on the JPEG2000.

In Fig. 5, (a) is the original source image. The detected airport area is the ROI whose bits are placed in higher bitplanes. During the embedded coding process, those bits are placed in the bit-stream before the background regions of the image. So, at the same compression ratio, it is prior ensuring the quality of ROI. Figs. 5(b), (c), and (d) respectively shows the constructed image with ratio 32, 16, and 8. There is almost no change visually comparing the original image with the ratio 32, in the ROI. Despite significant changes occur in background regions.

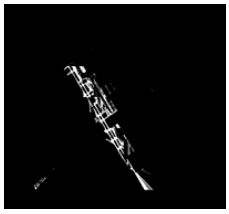

Figure 4: Airport detection by Hough transform.

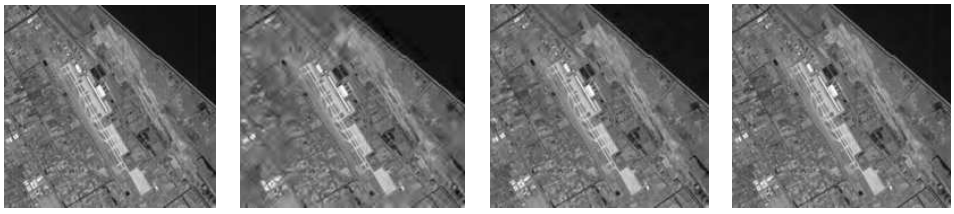

(a) Original Image (b) 0.25bpp (c) 0.5bpp (d) 1.0bpp

Figure 5: Original image and constructed images with different compression ratios.

5. CONCLUSIONS

In this paper, a novel image compression scheme based on classification and target detection is proposed. In order to reduce the overall computation complexity, some improved methods of classification and detection are used.

We have shown that the classification task can be accomplished with texture analysis. The texture features based on GLCM and gray-weighting fractal dimension show a good result in natural and man-made regions classification. In another hand, Hough transform is used for the detection of linear features to identify ROI. As the original image has been divided and classified, it achieves a notable complexity reduction at the expenses of computation and storage. Computer simulation results show that a good reconstructive image in ROI region when the whole image compressed in a high ratio.

REFERENCES

1. Murroni, M., M. Petrou, and D. D. Giusto, "Region-based image coding for remote sensing [C]," *International Conference on Image Processing and Its Applications*, 808–812, Cagliari Univ., Italy, 1999.
2. Magli, E. and G. Olmo, "Integrated compression and linear feature detection in the wavelet domain [A]," *International Conference on Image Processing [C]*, 889–892, Dipt. di Elettronica, Politecnico di Torino, Italy, 2000.
3. Guzman, A. and M. Beltran, "Satellite on-board image compression adviser [C]," *Proceedings of the Fourth IEEE International Symposium on Signal Processing and Information Technology*, 296–301, Madrid, Spain, 2004.
4. Chaudhuri, B. B. and N. Sarkar, "Texture segmentation using fractal dimension [J]," *IEEE Transactions on Pattern Analysis and Machine Intelligence*, Vol. 17, No. 1, 72–77, 1995.
5. Soo, C. L. and L. Hock, "Texture analysis of SAR images [C]," *Geosciences and Remote Sensing Symposium*, 1412–1414, Singapore, 1995.
6. Kandaswamy, U., D. A. Adjeroh, and M. C. Lee, "Efficient texture analysis of SAR imagery [J]," *IEEE Transactions on Geoscience and Remote Sensing*, Vol. 43, No. 9, 2075–2083, 2005.
7. De Martinao, M., F. Causa, and S. B. Serpico, "Classification of optical high resolution images in urban environment using spectral and textural information [C]," *Geoscience and Remote Sensing Symposium*, 467–469, Genova, Italy, 2003.
8. Ge, M., Q. Lin, and W. Lu, "Realizing the box-counting method for calculating fractal dimension of urban form based on remote sensing image [C]," *Geoscience and Remote Sensing Symposium*, 1423–1426, 2006.
9. Mayasandra, K., H. M. Ladak, and W. Wei, "A distributed arithmetic hardware architecture for real-time hough transform based segmentation [C]," *Canadian Conference on Electrical and Computer Engineering*, 1477–1480, 2005.
10. Zhai, L., T. Xinming, and L. Lin, "Effects of JPEG2000 compression on remote sensing image quality [C]," *IEEE International Conference on Geoscience and Remote Sensing Symposium*, 3297–3300, 2006.
11. Baraldi, A. and F. Parmiggiani, "An investigation of the textural characteristics associated with gray level cooccurrence matrix statistical parameters [J]," *IEEE Transactions on Geoscience and Remote Sensing*, Vol. 33, No. 1, 293–304, 1995.
12. Guil, N., J. Villalba, and E. L. Zapata, "A fast Hough transform for segment detection [J]," *IEEE Transactions on Image Processing*, Vol. 4, No. 11, 1057–7149, 1995.

Far-field Diffraction Characteristics of a Short Pulse from a Slit with Gaussian form of Transmittance

Pin Han
Institute of Precision Engineering, National Chung Hsing University
250, Kuo Kuang Road, Taichung 402, Taiwan, R.O.C.

Abstract— The spectrum changes of a Gaussian pulse in the far-field is studied with Fresnel diffraction integral when it is incident on a slit with Gaussian form transmittance. It is found that the side-lobes of the spectral intensity which exist in normal slit with unit transmittance will be eliminated under such a condition. This effect could be useful for optical engineering or optical communications.

1. INTRODUCTION

Recently there is increasing interests in so called "aperture dispersion", that is, the spectral changes of a short pulse resulting from the aperture diffraction. It also includes the red or blue shift of the spectrum maximum or the distortion of the incident pulse's spectrum [1–5]. In this work, we study the spectral characteristics of a time-dependent Gaussian pulse when it is incident on a slit with Gaussian form transmittance, which is not investigated before. It can be shown that the resultant diffracted intensity is free of the side-lobes which may not be wanted and exist in normal silt with unit transmittance.

2. THEORY

Consider an incoming wave with a spectral scalar field $U'(p', \omega)$ incident on a slit with Gaussian form transmittance, as show in Fig. 1. The diffraction field $U(p, \omega)$ on the observation plane can be obtained by using the Fresnel diffraction integral [6]:

$$U(p, \omega) = \frac{1}{j\lambda} \iint_{\Sigma'} U'(p', \omega) \frac{\exp(j\omega r/c)}{r} \chi(\theta) \mathrm{d}\sigma', \tag{1}$$

where $\chi(\theta)$ is the obliquity factor, λ is the wavelength, ω is the angular frequency, c is the velocity of the light wave, and r is the distance from point $p'(x', y', 0)$ on the aperture plane to point $p(x, y, z)$ on the observation (image) plane. Σ' is the aperture function and $\mathrm{d}\sigma'$ is the integration to it, as shown in Fig. 1. The factor $1/j\lambda$ in front of the integral of Eq. (1) is important because $1/\lambda (= \omega/2\pi c)$ includes the ω dependence and the diffraction spectrum analysis will not be correct if it is omitted [7, 8]. It is also noted that Eq. (1) is usually used for a monochromatic incident field, $U'(p', t) = U'(p', \omega)e^{-j\omega t}$, with a single frequency ω and the constant complex amplitude $U'(p', \omega)$, but it is also applicable for a broad-band incident pulse [1–5], which can be superposed by monochromatic fields via the Fourier integral [9].

The aperture function for the slit with Gaussian form transmittance can be written as:

$$g(x') = \exp\left[-\left(\frac{x'}{a}\right)\right]^2, \tag{2}$$

where a is the characteristics length and means that the transmission drops to e^{-1} at $x' = \pm a$. Let $u(p', t) = \exp\left[-1/2(t/\tau)^2 + j\omega_0 t\right]$ is the incident time-dependent Gaussian pulse where ω_0 is the pulse central frequency and τ is its duration time. Its spectral amplitude is $U'(p', \omega) = \tau \cdot \exp\{-1/2[(\omega - \omega_0)\tau]^2\}$. Substituting $U'(p', \omega)$ into Eq. (1) and using the far-field approximation, the diffraction field $U(p, \omega)$ is

$$U(p, \omega) = \frac{1}{j\lambda z} \exp\left[jk\left(z + \frac{x^2}{2z}\right)\right] \cdot U'(p', \omega) \cdot F(g(x')), \tag{3}$$

where z is the distance for $\overline{o'p}$, $k = \omega/c = 2\pi/\lambda$ and the last term $F(g(x')) = (a/\sqrt{2}) \cdot \exp\left[-(\pi a f_x)^2\right]$ is the Fourier transform of the aperture function $g(x')$ with the spatial frequency $f_x = x/\lambda z$. Using

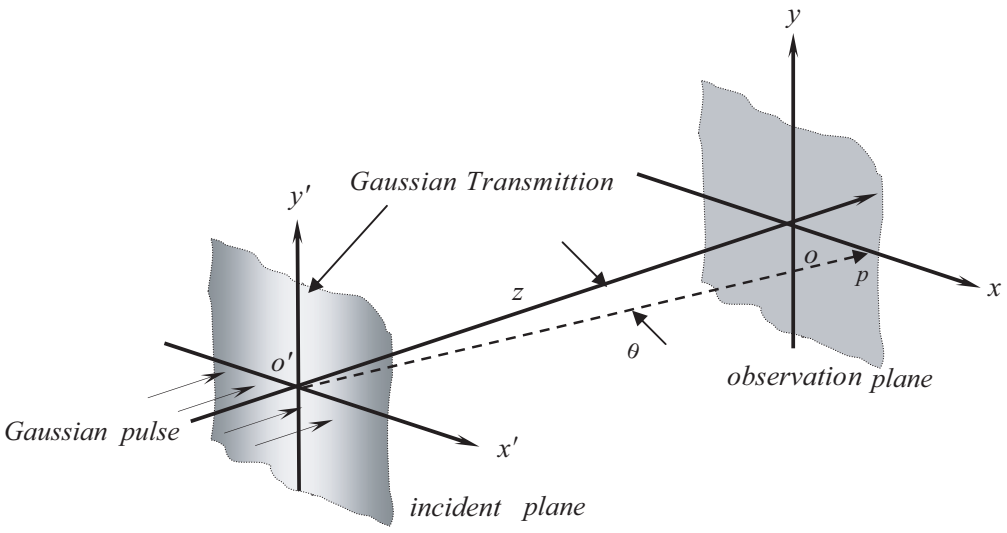

Figure 1: The geometry of the set up.

the relations $1/\lambda = \omega/2\pi c$, $f_x = \omega x/2\pi cz$, the diffraction field $U(p, \omega)$, can be rewritten as

$$U(\theta, \omega) = \frac{\tau}{jz}\left(\frac{\omega}{2\pi c}\right)\exp\left[jk\left(z + \frac{x^2}{2z}\right)\right] \cdot \cdot \exp\left\{-\frac{1}{2}[(\omega - \omega_0)\tau]^2\right\} \cdot \exp\left\{-\left[\frac{\omega a \sin\theta}{2c}\right]^2\right\}, \quad (4)$$

where $\sin\theta \approx x/z$ and θ is the angle between $\overline{o'o}$ and $\overline{o'p}$ as shown in Fig. 1.

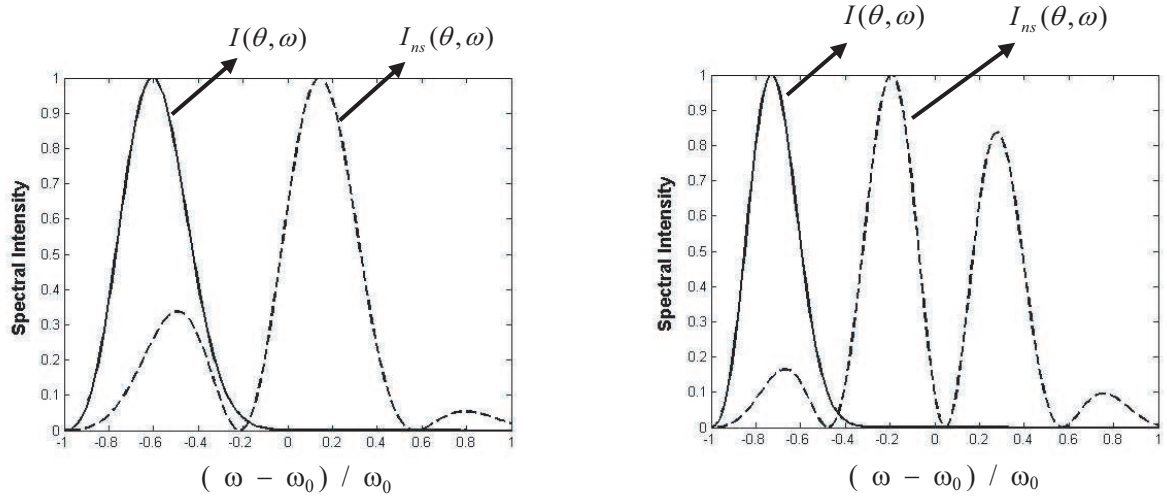

Figure 2: (a) The spectral intensity for $k = 4.0$. (b) The spectral intensity for $k = 6.0$.

With the formula $I(\theta, \omega) = |U(\theta, \omega)|^2 = U(\theta, \omega) \cdot U(\theta, \omega)^*$, the spectral intensity $I(\theta, \omega)$ of the diffraction field, can be obtained as:

$$I(\theta, \omega) = A \cdot \omega^2 \exp[-(\omega - \omega_0)\tau]^2 \cdot \exp\left\{-\frac{1}{2}\left[\frac{\omega a \sin\theta}{c}\right]^2\right\}, \quad (5)$$

where $A = \tau^2 a^2/8\pi^2 c^2 z^2$. As a comparison, a normal slit with unit transmittance and width $2a$, the resultant spectral intensity $I_{ns}(\theta, \omega)$ is [10]

$$I_{ns}(\theta, \omega) = A' \cdot \omega^2 \cdot \exp\left\{-[(\omega - \omega_0)\tau]^2\right\} \cdot \sin c^2\left(\frac{a \sin\theta}{c}\omega\right), \quad (6)$$

where $A' = \tau^2 a^2/2\pi^2 c^2 z^2$ and the subscript ns in $I_{ns}(\theta, \omega)$ indicates the normal slit.

3. NUMERICAL RESULTS

Figures 2(a) and (b) show the numerical results of $I(\theta, \omega)$ and $I_{ns}(\theta, \omega)$ according to Eqs. (5) and (6) for two different values of $k = a\omega_0 \sin\theta/c$ with $\gamma = 1/\omega_0\tau = 0.5$. It is noted that, there is no any side-lobes for $I(\theta, \omega)$; however, side-lobes are obvious for $I_{ns}(\theta, \omega)$ which is due to the oscillating behavior of the sinc function in Eq. (6) and the number of the side-lobes increases with the increasing of the values k. Therefore, we find that a slit with Gaussian from transmittance can lead to a diffracted spectral intensity without any side-lobes because the modulation functions have no any oscillation properties, as shown in Eq. (5).

4. CONCLUSIONS

In this work, the aperture dispersion of a short Gaussian pulse is studied when it is diffracted by a slit with Gaussian form transmittance. It is found that there is no any side-lobes for the diffracted spectral intensity under this type of aperture; whereas, there are many of side-lobes in the case of normal slit with unit transmittance. From our theoretical and numerical analysis, the main contributions of side-lobes come from the oscillating property of aperture function for a normal slit and there is no any oscillation behavior for a Gaussian transmittance slit. Thus, this important characteristic can be applied when the side-lobes want to be eliminated completely in such as optical communication field.

ACKNOWLEDGMENT

This study was supported by the National Chung Hsing University Taiwan, R.O.C. The authors also like to thank the colleagues for their thoughtful comments and useful suggestions. This work was also supported by the NSC of R.O.C. under the contract nos. NSC 96-2221-E-005 -061.

REFERENCES

1. Han, P., "Far-field spectral intensity characteristics of a time-dependent Gaussian pulse from two types of apodized slits," *Jpn. J. Appl. Phys.*, Vol. 43, 3386–3393, 2004.
2. Ponomarenko, S. A. and E. Wolf, "Spectral anomalies in a Fraunhofer diffraction pattern," *Opt. Let.*, Vol. 27, 1211–1213, 2002.
3. Han, P. and H. E. Hwang, "Far-field spectral intensity characteristics of a time-dependent Gaussian pulse from two types of apodized slits," *Optik*, Vol. 115, 499–506, 2004.
4. Han, P., G. H. Yang, and H. E. Hwang, "Far-field diffraction characteristics of a Gaussian pulse incident on a sinusoidal amplitude grating," *J. Opt. A: Pure Appl. Opt.*, Vol. 5, 442, 2003.
5. Hwang, H. E., G. H. Yang, and P. Han, "Near-field diffraction characteristics of a time dependent Gaussian-shaped pulsed beam from a circular aperture," *Opt. Eng.*, Vol. 42, 686–695, 2003.
6. Hecht, E., *Optics*, 511, Addison Wesley, New York, 4th ed., 2002.
7. Sereda, L., A. Ferrari, and M. Bertolotti, "Diffraction of a time Gaussian-shaped pulsed plane wave from a slit," *Pure Appl. Opt.*, Vol. 5, 349–353, 1996.
8. Liu, Z. Y. and D. Y. Fan, "Diffraction characteristics of an ultra-short pulsed beam in the far field," *Pure Appl. Opt.*, Vol. 6, L43–47, 1997.
9. Goodman, J. W., *Introduction to Fourier Optics*, 53, Mcgraw-Hill, New York, 2nd ed., 1996.
10. Hwang, H. E., G. H. Yang, and P. Han, "Far-field diffraction characteristics of a time dependent Gaussian-shaped pulsed beam from a rectangular aperture," *Jpn. J. Appl. Phys.*, Vol. 41, 3683–3687, 2002.

Differential Theory with Genetic Algorithms in Design Periodic Absorbers

N. Lassouaoui, H. Hafdallah Ouslimani, and A. Priou
University Paris X, Nanterre, Pole Scientifique and Technique, Ville d'Avray
Applied Electromagnetism Group (GEA) 50, rue de Sèvre 92410, Ville d'Avray, France

Abstract— A differential theory and a real-valued genetic algorithm are implemented to design the periodic gratings. The differential theory is well established to analyse the periodic structures and to compute its reflectivity. With genetic algorithms, we search the optimum geometry characteristics (thickness and period) and material composition (permittivity and permeability) which minimize the reflectivity on a wide frequency band. We apply our study to optimize a stuck structure constituted by a periodic grating and homogeneous layers. Numerical results of the frequency behaviour of the optimized structures are presented.

1. INTRODUCTION

Scattering of waves by rough surfaces has aroused the interest of physicists and engineers since these surfaces have large application in optics and microwave domains. In the electromagnetic applications, the problems are particularly complex, since there is no prior knowledge of the multidimensional research space topology which is determined by the complex interdependence of Maxwell' equations.

Considerable research has been focused on the use of evolutionary techniques in electromagnetic [1–4]. In [1], the NASA Ames Research Center (Evolvable Systems Group) conducts research on antenna designs. Their approach is to encode antenna structure into a genome and to use genetic algorithm to evolve the desired antenna performance as defined in a fitness function. In [2], a GA was designed to minimize the reflectivity of a number of layers positioned at either the center of an infinitely long rectangular waveguide, or adjacent to the perfectly conducting back plate of a semi-infinite shorted-out rectangular waveguide. The thicknesses of the layers are the input data. The optimization allows finding the electric properties. In [3], the authors adopted the binary GAs with the finite element boundary integral method to optimize the geometry parameters of the periodical absorber structures.

Here in, we are interested in designing a stack of absorber periodic gratings. Knowing that the dimensions and material composition of each layer define the performances; the hope in using the GAs is to obtain the configuration which minimizes the reflectivity on a wide frequency band. To compute the reflectivity, we need electromagnetic methods for analysis the absorber structures. A huge number of approaches and methods exist in area of wave diffraction by periodic wavy surfaces [3, 5–7], such as the moment method (MM), the finite-difference time-domain (FDTD) method, and the finite element method (FEM). The MM is not efficient for problems involving material inhomogeneities; the FDTD handles admirably material inhomogeneities, but is extremely difficult to implement for oblique incidence case (although many attempts have been made [3]); the FEM can model material inhomogeneities efficiently and can simulate periodic boundaries without any difficulty. There are also approaches based on using Green's formulae, partial domains ... In our work, we use the differential theory [5] which is adapted to various kinds of gratings (periodic 1D and 2D, dielectric, real metals, multilayer, anisotropic gratings, ...).

In Section 2, we present briefly how we use the GA to find the configuration for an optimal response of the absorber according to the minimization of its reflectivity. In Section 3, we give the differential theory. We present the numerical results of the studies in Section 4. Finally, we give the conclusions.

2. DEVELOPED METHODOLOGY FOR THE SYNTHESIS WITH GAS

In general, the GAs [8, 9] act on the population of chromosomes to cause an evolution toward an optimal solution according to an objective function that provides a measure of the fitness of a given chromosome. They begin by randomly creating a population of chromosomes, and evaluating their objective function. They work by iteratively applying three genetic operators (selection, crossover and mutation) to the population. The selection operator generates a new population of chromosomes from the existing population based on fitness values. It allows the variations in the

species arising from *mutation*, which produces new genes previously unseen in the population; and *crossover*, which is the random recombination of genetic material that occurs during reproduction. After, the chromosomes are revaluated; the process begins anew with selection. The algorithm is stopped when either a design goal is reached, or no progress is observed in the population for several generations. To adapt the GAs to our problem, we follow:

- To minimize the reflectivity over a wide frequency band, then for each chromosome in the population and a fixed incidence angle θ_i, we compute the reflectivity for several frequencies over the X-band, and the minimum reflectivity (in dB) is taken as the fitness of chromosome.
- The chromosomes are arrays composed by the real and imaginary parts of the dielectric and magnetic constants and the morphological characteristics (thickness T_j and period P_j) of all layers.
- To delimitate the research space, the user specify the variation limits of the genetic values of the chromosome. We note that after each generation, because the mutation effects, it is possible that the obtained values of genes lying outside the specified interval. So, the GA must examine each child for genetic defects, if one is found, the mutation is ignored.
- There are energy constraints to respect. Indeed, in the theory of complex Maxwell equations (when electromagnetic fields and material parameters are complex-valued vectors and scalars correspondingly), because of energy conservation law, the material parameters ε and μ of passive media must be situated in the first or second quadrant of complex plane, i.e., imaginary parts of the dielectric and magnetic constants must be positive [6].
- We chose an elitist selection [8, 9], so, the best chromosome is always passed and never retrogrades to the next generation. Also, the chromosomes with fitness lower than average fitness of all individuals are eliminated; others will be created from the survival by reproduction.
- Reproduction: With crossover and mutation, new individuals are created. The crossover can occur in possible ways [2, 8, 9], a universal operator able of the best performances for all the problems is not yet discovered, and it is probable that there does not exist. So, we use various crossover operators [2, 8, 9], and from generation to other, we chose one with equal probability.

  The mutation [8] insures the diversity in genetic population; it may alter the phenotype of the gene in chromosome, thereby giving it a greater or lesser advantage in the selection. So, to protect the fittest individuals from its damaging effects, it is applied only on the children obtained by preceding steps. We also take a mutation probability Pm exponentially decreased according the generations, which tends to suppress it potentially damaging effects along the generations.
- To avoid that the research became redundant or converge towards a local optimum, we check the diversity of the population. Then, if the fittest chromosomes of several successive generations are the same, we propose to eliminate the worst chromosomes (the half of the population), which are replaced by the new chromosomes randomly generated. This way allows to test another candidates which ensure the diversity and the research does-not stagnate.

In what follows, we give the various algorithms used for computing the reflectivity which is used in fitness to direct the research in GAs.

3. DEVELOPED ANALYSIS INTERFACE FOR PERIODIC GRATINGS

The differential theory DT of the gratings is now well established and is known to provide both simplicity and versatility [5]. Before given the DT in analyzing the gratings and the various algorithms used for computing the reflectivity, we describe the diffraction problem.

3.1. Diffraction Problem

The uniqueness of the solution of the diffraction problem is mathematical problem. However, the radiation condition guarantees the uniqueness of the solution. The diffraction problem can be formulated as the necessity to find out the scattered field which satisfies [5, 6]:

1. Helmholtz equation in each media;
2. Quasi-periodicity of the field;
3. The standard boundary (transform) condition on the boundary surface between two media is the continuity of the components of the total electromagnetic field U. These conditions can

be written in the following standard form [5, 6]:

$$U^{(+)}(p) = U^{(-)}(p) \quad \frac{\partial U^{(+)}(p)}{\partial n_p} = \gamma \frac{\partial U^{(-)}(p)}{\partial n_p} \quad p \in L \tag{1}$$

$\gamma = \mu_1/\mu_2$ in TE-mode and $\gamma = \varepsilon_1/\varepsilon_2$ in TM Mode, with $(\mu_m, \varepsilon_m)\, m = 1, 2$, correspond to the permittivity and permeability of the layer m.

Subscripts $(+)$ and $(-)$ denote the limits of functions $U(p)$ and $\partial U(p)/\partial n_p$ of arguments $p + sn_p$ and $p - sn_p$ respectively, when $s \to +0$, with n_p is the unit normal to the contour in a point p.

4. Radiation condition is that outside of contour L the scattered field must be presented in the form of the uniformly converging series of the outgoing and decaying plane waves:

$$U(x,y) = \begin{cases} \sum\limits_{n=-\infty}^{+\infty} A_n^{(1)} \exp\left(i\alpha_n x - i\beta_n^{(1)} y\right) + \sum\limits_{n=-\infty}^{+\infty} B_n^{(1)} \exp\left(i\alpha_n x + i\beta_n^{(1)} y\right) & for \quad y > a \\ \sum\limits_{n=-\infty}^{+\infty} A_n^{(2)} \exp\left(i\alpha_n x - i\beta_n^{(2)} y\right) + \sum\limits_{n=-\infty}^{+\infty} B_n^{(2)} \exp\left(i\alpha_n x + i\beta_n^{(2)} y\right) & for \quad y < 0 \end{cases} \tag{2}$$

with: $\alpha_n = \alpha_0 + n2\pi/d_x$, $\beta_n^{(1)} = \begin{cases} \sqrt{k_1^2 - \alpha_n^2} & for \quad k_1^2 - \alpha_n^2 \geq 0 \\ i\sqrt{\alpha_n^2 - k_1^2} & for \quad k_1^2 - \alpha_n^2 < 0, \end{cases}$ $\beta_n^{(2)} = \sqrt{k_2^2 - \alpha_n^2}$ and imaginary part of $\beta_n^{(2)} \geq 0$.

5. Energy finiteness (which is necessary only if contour is not smooth).

Now, we present the differential theory which allows the solving the diffracting problem.

3.2. Description of the Differential Method

We consider the most common problem in the classical one-dimensional grating, with the shape of the structure is given by: $y = g(x)$, with period d_x and the groove depth a. The grooves are parallel to the Oz axis. The grating surface separates the superstrate and the substrate. The incident angle θ_i is measured from the normal to the mean plane of the grating, the incident wave vector is $\vec{k_1} = \nu \frac{2\pi}{c \cdot f}(\sin\theta_i, -\cos\theta_i, 0)$, with f, c and ν are respectively the frequency, the speed of light on vacuum and the refractive index of the vacuum. The incident electric field vector is given $\vec{E}^{(i)} = \vec{A} \exp[ik_1(x\sin\theta_i - y\cos\theta_i)]$ with $k_1 = \left|\vec{k_1}\right|$ and $\vec{A}$ is the polarization vector.

The Maxwell equations are projected onto a Fourier basis and enable us to obtain a set of ordinary differential equations which can be integrated. Since $k^2(x, y)$ (k is wave vector) is a periodic function according to x, with period d_x, the Maxwell equations are expressed in Fourier basis by [5]:

$$\text{TE polarization} : \forall n \begin{cases} \frac{d\tilde{E}_{z,n}}{\partial y} = H_{x,n} \\ \frac{dH_{x,n}}{\partial y} = -\sum\limits_{m=-\infty}^{+\infty} k_{n-m}^2(y)\tilde{E}_{z,m}(y) - \alpha_n^2 \tilde{E}_{z,n}(y) \end{cases} \quad \text{with } \alpha_n = \alpha_0 + n2\pi/d_x \tag{3}$$

$$\text{TM polarization} : \begin{cases} \left[\frac{\partial H_z}{\partial y}\right] = -i\omega \left[\left[\frac{1}{\varepsilon}\right]\right]^{-1} [E_x] \\ \left[\frac{\partial E_x}{\partial y}\right] = \frac{i}{\varpi} \alpha \left[[\varepsilon]\right]^{-1} \alpha \left[H_z\right] - i\omega\mu \left[H_Z\right] \end{cases} \quad \text{with } \alpha \text{ is a diagonal matrix with elements } \alpha_n = k_1 \sin\theta_i + n2\pi/d_x \text{ and } [[\varepsilon]] \text{ is Toeplitz matrix.} \tag{4}$$

3.3. Numerical Solution of Differential Equations

The field components are unknown at interfaces (B_n? in (2), we have only the link between the functions and their derivatives. Then, we cannot use the numerical algorithms which solved differential equations with initial values of the function and its derivative are known.

The shooting method [5] is used for solving a boundary-value differential problem. For that, we construct $(2N + 1)$ particular linearly independent solutions $[\hat{U}(y)]_p$ $(p = -N, \ldots, +N)$. We take:

$$\hat{U}_{n,p}(0) = \delta_{n,p} \quad \text{where :} \quad \delta_{n,p} = \begin{cases} 1 & if \quad n = p \\ 0 & if \quad n \neq p \end{cases} \tag{5}$$

For TE (respectively TM) mode: $\hat{U}$ corresponds to E_z (respectively H_z), and by Maxwell Equations (3) (respectively (4)) with the expansion of Rayleigh (2), we deduce the initial value of H_x (respectively E_x). With these various initial values and set of Equations (3) for TE mode or (4) for TM mode, a process of $(2N+1)$ consecutive integrations is performing from 0 to a(depth of layer). By defining the vector F which contains the various components of the fields and the matrix Ω which is block-diagonal with 4×4 blocks, each one having $2N+1$ diagonal components [5]:

$$F(y_i) = \begin{pmatrix} [E_x(y_j)] \\ [E_z(y_j)] \\ [H_x(y_j)] \\ [H_z(y_j)] \end{pmatrix} \quad \Omega = \frac{1}{2} \begin{pmatrix} 0 & 1 & \frac{1}{q_h} & 0 \\ \frac{1}{q_e} & 0 & 0 & 1 \\ 0 & 1 & -\frac{1}{q_h} & 0 \\ -\frac{1}{q_e} & 0 & 0 & 1 \end{pmatrix} \quad q_{e,mn} = \delta_{mn} \frac{\omega \mu_0 \beta_n^{(1)}}{k_1^2} \quad q_{h,mn} = -\delta_{mn} \frac{\omega \varepsilon_0 \beta_n^{(1)}}{k_1^2} \quad (6)$$

The transmission matrix T for the jth layer is obtained by: $T^{(j)} = \Omega * \hat{F}_{\text{integrated}}(y_j)$.

For M horizontal layers (modulated and/or homogeneous), we compute the $T^{(j)}$ matrix for each one. Then, we apply the S-matrix propagation algorithm [5] which combines the various matrices $T^{(j)}$, and gives the reflectivity and transmission matrices.

4. APPLICATION AND RESULTS

We present numerical application results obtaining with a stack (Fig. 1) constituted by a homogeneous layer (ε_2, μ_2, T_2), lamellar periodic structure (ε_1, μ_1, T_1, P, DP) along x and layer of Teflon ($T = 0.5\,\text{mm}$). We take $\mu_1 = 1$, and with GAs, we search the other characteristics which ensure the minimization of the reflectivity over the X frequency band.

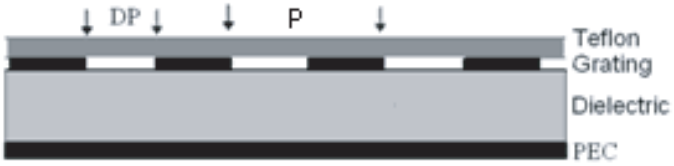

Figure 1: Schema of a stack of grating.

Numerical experiments [5] show that in many grating problems, stable converging results are obtained with a truncation index N between 5 and 15. Here in; we try to check the stability of the computes according the number $(2N+1)$ of the Fourier components of the fields. For that, we compute for various values of N the reflectivity of a given configuration for a frequency f and an incidence angle θ_i. Then, we analyze the relative error of the reflectivity. By Figs. 2(a) and 3(a), we present the obtained curves for TE and TM modes. We note that from $N = 17$ (Relative error is less than 5×10^{-3}), we have a stability of the compute in TE mode, which requires at least 35 components for each field. For TM mode, we have a stability from $N = 5$ which corresponds at least to 11 Fourier components.

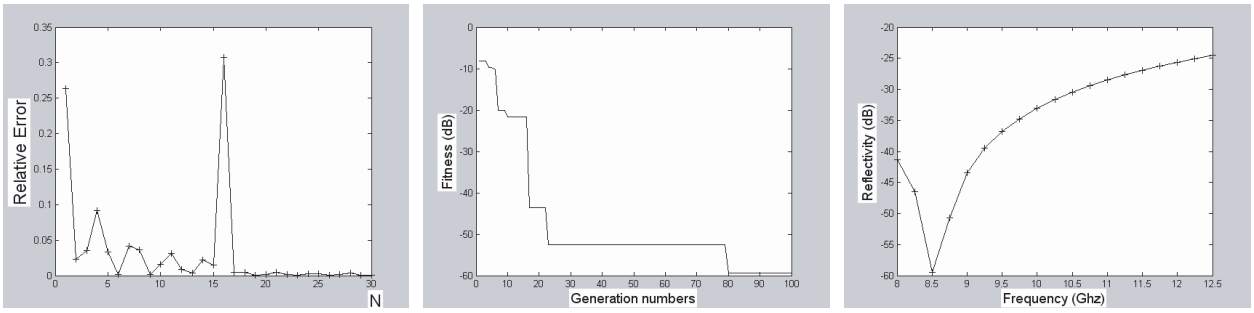

(a) (b) (c)

Figure 2: TE mode (a) Relative error in the reflectivity according the number of Fourier components, (b) Variations of the best fitness according the generations, (c) Response of solution at generation 100.

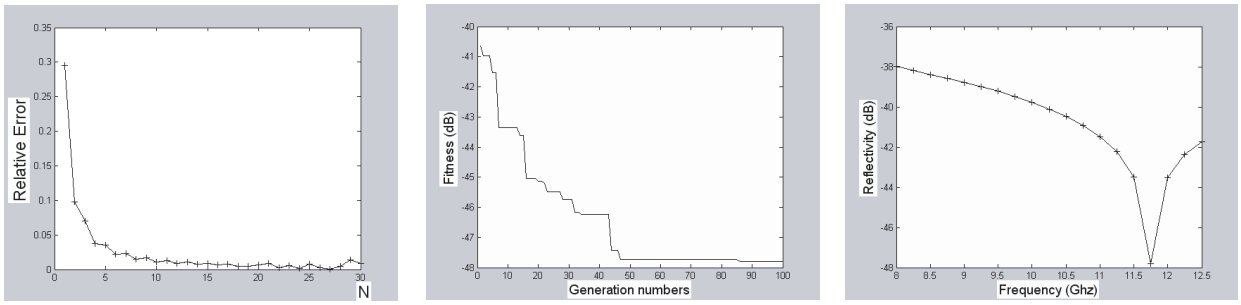

(a) (b) (c)

Figure 3: TM mode (a) Relative error in the reflectivity according the number of Fourier components, (b) Variations of the best fitness according the generations, (c) Response of obtained solution in generation 100.

By Fig. 2(b), (c) and 3(b), (c), we present the obtained results for TE and TM modes for a normal incidence. We reach at least (−25 dB) on the X-frequency band for TE mode and (−38 dB) for TM mode. We specify that all values of dielectric and magnetic constants falling between −4 and 4, the thicknesses T of layers between 0.6–10 mm, the period P between 5.1–10 mm, and the distance between lamellar DP 0.6–5.0 mm.

At 100 generations, the obtained characteristics for:

- TE mode: $\varepsilon_1 = 0.2000 + i0.8000$, $T_1 = 4.0350\,\text{mm}$, $P = 8.6573\,\text{mm}$, $DP = 1.4000\,\text{mm}$, $\varepsilon_2 = 1.4000 + i0.5433$, $\mu_2 = 0.4000 + i0.2000$, $T_2 = 5.8345\,\text{mm}$.
- TM mode: $\varepsilon_1 = -3.9189 + i1.1557$, $T_1 = 8.7685\,\text{mm}$, $P = 8.2975\,\text{mm}$, $DP = 3.9900\,\text{mm}$, $\varepsilon_2 = -3.9900 + i3.9900$, $\mu_2 = -3.9900 + i2.5938$, $T_2 = 6.6964\,\text{mm}$.

5. CONCLUSION

This paper demonstrates the use of the differential theory method and genetic algorithms to design the periodical gratings and a stack of gratings for both TE and TM polarizations with the requirement to ensure a minimal reflectivity over X-frequency band.

The differential theory methods allow the compute of the reflectivity, which is used in fitness function in genetic algorithms to search the material (μ_r and ε_r) and morphological (thicknesses and periods) characteristics of the stack which minimize the reflectivity over a frequency band.

In future works, we propose to use other theories in analysis, to allow a comparison between the obtained results with differential theory.

REFERENCES

1. Lohn, J., J. Crawford, A. Globus, G. Hornby, W. Kraus, G. Larchev, A. Pryor, and D. Srivastava, "Evolvable systems for space applications," *Proceeding of International Conference on Space Mission Challenges for Information Technology*, Pasadena, July 13–16, 2003.
2. Hall, J. M., "A novel, real-valued genetic algorithm for optimizing radar absorbing materials," NASA/CR-2004-212669, March 2004.
3. Cui, S. and D. S. Weile, "Robust design of absorbers using genetic algorithms and the finite element-boundary integral method," *IEEE Transactions on Antennas and Propagation*, Vol. 51, No. 12, 3249–3258, December 2003.
4. Donelli, M., S. Caorsi, F. De Natale, M. Pastorino, and A. Massa, "Linear antenna synthesis with a hybrid genetic algorithm," *Progress in Electromagnetics Research*, PIER 49, 1–22, 2004.
5. Neviere, M. and E. Popov, *Light Propagation in Periodic Media, Differential Theory and Design*, Marcel Dekker, 2003.
6. Poyedinchuk, A. Y., Y. A. Tuchkin, N. P. Yashina, J. Chandezon, and G. Granet, "C-method: Several aspects of spectral theory of gratings," *Progress in Electromagnetics Research*, PIER 59, 113–149, 2006.
7. Granet, G., K. Edee, and D. Felbacq, "Scattering of a plane wave by rough surfaces: A new curvilinear coordinate system based approach," *Progress in Electromagnetics Research*, PIER 37, 235–250, 2002.
8. Goldberg, D. E., *Genetic Algorithms in Search, Optimization and Machine Learning*, Addison-Wesley, 1989.
9. Mitchell, M., *Introduction to Genetic Algorithms*, MIT Press, 1996.

Optical Mode Parameters of the 2.3-μm Al(In)GaAsSb/GaSb Ridge-waveguide Laser Diodes and Laser Diode Arrays

Yimin Chen and Dmitry Donetsky
Department of Electrical and Computer Engineering, MS-2350
Stony Brook University, NY 11794, USA

Abstract— Optical field distribution, effective indices and optical losses of the ridge-waveguides and ridge-waveguide arrays of the 2.3 μm InGaAsSb/AlGaAsSb Type-I heterostructure laser diodes were simulated. The ridge waveguide depth and width were varied in the ranges from 0.5 to 1.45 μm and from 5 to 20 μm, respectively, in order to study effects of the ridge geometry on the optical mode parameters. Discrimination between groups of modes of the ridgewaveguide array with different optical field distributions was maximized by narrowing the array pumping region. The simulation was performed by Beam Propagation Method (BPM) with software BeamProp from Rsoft using experimental data on the material indices. Processing of the output data from the BeamProp were programmed in MathCAD favoring reduction of time in repetitive calculations and data analysis.

1. INTRODUCTION

Ridge-waveguide laser diodes for diffraction-limited performance and coupled arrays of ridgewaveguide laser diodes for high-power operation with near-diffraction-limited performance have been studied for over 25 years [1]. Reliable operation of short-wavelength arrays of ridge-waveguide laser diodes with focusable output power of Watt range was demonstrated [2]. For mid-infrared GaSb-based laser diodes achievement of high quality of the output beam still represents a challenge due to specifics of the material parameters, wavelength range, etc. The interest to development of high-power diffraction limited sources for the 2.3 μm wavelength region is motivated with applications for free-space optical communications, range-finding, infrared countermeasures in the range of atmospheric transparency. A WattClevel room-temperature operation of multi-mode broad-area InGaAsSb/AlGaAsSb/GaSb lasers for this wavelength has been demonstrated indicating high potential of the material system [3]. The major goal of this work was to perform necessary background work for support of the effort on design of the laser emitters based on the developed material with the diffraction-limited performance of the output power.

Among several basic types of laser diode arrays, evanescent-wave-coupled array is one of the most intensively studied types. Evanescent-wave-coupled devices use array modes whose field-intensity peaks reside in the high-index array region. Many classic works have been done on single-lobed operation of ridged waveguide for diode laser arrays [4, 5]. The ridge waveguide lasers are intensively studied up to present time [6–8] These days, leaky-type array modes, for which the fields are peaked in the low-index array regions, are considered as a more favored type, because of stable diffraction-limited beam operation at high pumping levels [9]. Although more effort has been put on development of the laser diode arrays based on leaky-type array modes, evanescent mode waveguides still hold its value due to several reasons to be discussed further. One of the reasons is that for few-element arrays, the leaky modes are less favored because of the high optical losses [1]. In addition, the modal gain is often higher in the high-index regions compared to that in the low-index regions favoring the evanescent type.

For evanescent-wave-coupled arrays, positive-index guides are used to provide a periodic modulation of refractive-index profiles along the lateral direction for the optical mode confinement. One easiest approach is to etch a series of ridges on the cladding layer, providing a lateral variation in the effective index [4, 5]. Modes of the array are said to be "in-phase" when the fields in each element are in the same phase and "out-of-phase" when fields in adjacent elements are a π phase-shift apart. Generally, out-of-phase evanescent mode have the optical field nulls in the lossy inter-element region and has better field overlap with the gainy element regions than does the in-phase mode. However, stability of such a beam is not satisfying; the beam patterns rapidly broadens from the near-diffraction-limited beam as the current pumping level increases above 1.5 times of the threshold value [1].

Based on the theory of in-phase and out-of-phase modes [10], evanescent array modes can be denoted with parameters [n, p], where n is the lateral mode number in the high-index region, and

p is the number of field intensity nulls in the low-index regions. In this work arrays of the ridge-waveguides with up to ten coupled ridges were simulated for the 2.3 µm GaSb-based laser diodes; parameters were found to suppress any modes with n value higher than 0, thus to maintain a fundamental mode in the high index region. For several modes with $n = 0$, other than in-phase coupling mode are allowed to exist simultaneously. However, with the goal of achieving of single-lobe far field some modes which peak on the two sides in the lateral direction are to be eliminated. One means of selecting modes is to preferably pump the region where the favored modes are peaking in intensity. In this paper, pumping region was narrowed toward the center in order to suppress the modes peaking at the sides. Because doing this is defeating the purpose of achieving high-power array operation possible with wide emitting area, a tradeoff exists between the emitting area width and quality of the mode selection. In this work it was shown that only a small change needs to be done to the pumping area in order to achieve large discrimination between the favored and less favored modes.

2. SIMULATION RESULTS AND DISCUSSION

For the simulation, the refractive indices and the absorption coefficients of the AlGaAsSb core layer and the cladding layers can be calculated according to the composition [11]. According to the Landolt- Börnstein Physical Chemistry Table, the imaginary part of the index of the Titanium cover layer was taken to be 5. Each element of the array of coupled ridges is an enhance version of a single ridge waveguide [4]. In the transverse (vertical) direction, the heterostructure provides similar confinements for single ridge waveguide and coupled ridges waveguide. In the lateral direction, the index modulation of the waveguided structure provides the required confinement. It's predictable that the optimized geometry for a single ridge can also be applied to the coupled ridges to suppress the modes which are not fundamental mode in the high-index region. Therefore, to study the array of coupled ridges waveguide, the single ridge structure was started with.

All possible modes below cut-off for a single ridge waveguide were simulated. As expected, the fundamental mode was found to be more confined with higher modal gain. Geometry of the ridged waveguide was changed in order to simulate and compare the losses and the confinement for different modes.

For the simulation of the single ridge waveguide, the core layer ($d = 0.8$ µm) refractive index 3.9 was taken based on the parameter obtained from the experimental emission spectrum of broad-area laser diodes with similar waveguide structure. The cladding layers the thickness was taken as 1.5 µm. The spacing width between the ridges was taken to be the same as the ridge width.

Simulation was performed for ridged waveguides with ridge widths of 5 µm, 10 µm and 20 µm. For each of the ridge widths, the ridge depth was varied from 0.5 µm to 1.45 µm. In Figures 1 and 2, the optical losses for the fundamental mode and TE1 mode are plotted against the ridge depth with different ridge widths. To compare the optical losses of different waveguide geometries, the ratios of optical losses for TE0 and TE1 modes, TE0 and TE2 modes are presented in Figures 3 and 4.

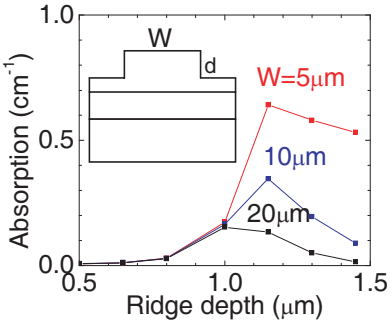

Figure 1: Relationship between absorption and ridge depth for single ridge waveguide TE0.

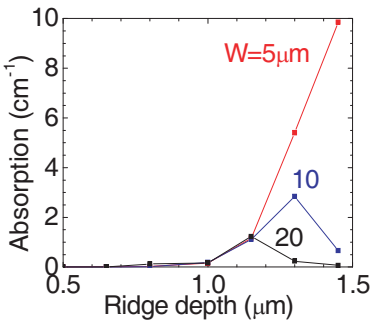

Figure 2: Relationship between absorption and ridge depth for single ridge waveguide TE1.

From Figures 3 and 4, one can see that when the geometry of 1.3 µm ridge depth and 5 µm ridge width is the only geometry in the plot that provides over 5 time difference in optical loss between both TE0 and TE1, TE0 and TE2. Therefore, for the following steps 1.3 µm ridge depth and 5 µm ridge width were adopted.

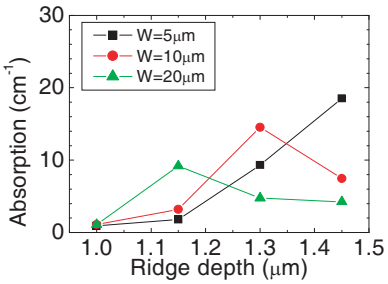

Figure 3: Ratio in optical loss between TE0 and TE1 modes of single ridge waveguide.

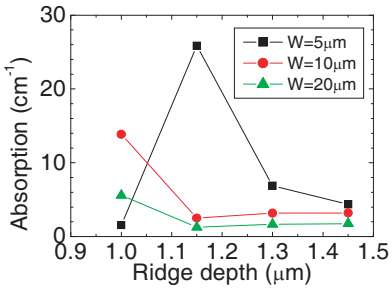

Figure 4: Ratio in optical loss between TE0 and TE2 modes of single ridge waveguide.

The array of coupled ridges waveguide was simulated in BeamProp CAD using the parameter obtained in the previous step. Ten coupled ridges on the top cladding layer were simulated. The schematic is shown in Figure 5 and the simulation results are presented in Figure 6. One can see that in the first eleven modes obtained by the simulation, 8 modes are with $n = 0$, which corresponds to the fundamental modes in the high-index region, and the other 3 modes are with $n = 1$ corresponding to the TE1 modes in the high index region. Comparing the waveguide with array of ridges with the single ridge waveguide, it was shown that the optical losses of the modes in one specific group discriminated by the n value are similar to the optical loss of the corresponding single ridge waveguide mode. Therefore, the optimal geometry of the single ridge waveguide found in the previous steps also provides the condition to suppress the $n = 1$ or higher order modes. For the $n = 0$ modes, it can be seen from the simulation results that some of modes are well confined in the lateral direction and have close values of effective index and optical loss to the fundamental mode. Actually, these modes are all expected to lase. However, there're some modes that consists of two peaks on both sides (Figure 8). These modes could be suppressed by narrowing of the pumping region.

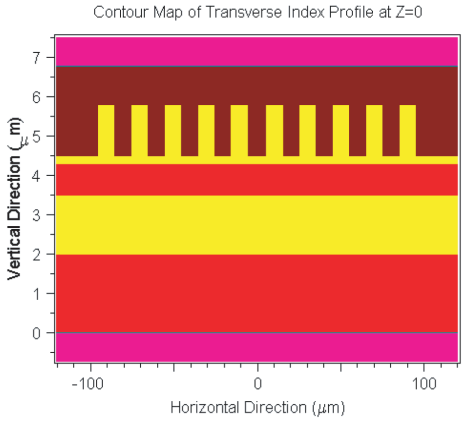

Figure 5: Schematic diagram of the array of coupled ridges waveguide cross-section.

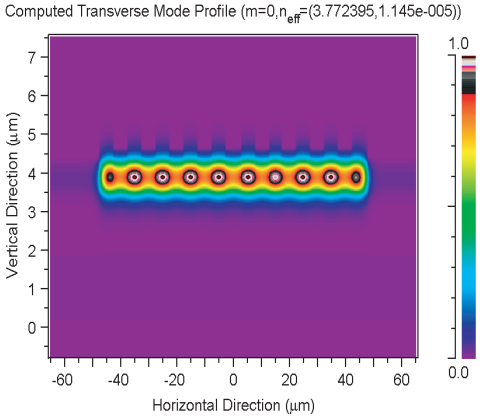

Figure 6: Contour map of the field distribution for coupled ridges waveguide, fundamental mode.

In Figures 7 and 8, the planar power distributions for the fundamental mode and one for the modes with less favored field distribution are shown at the cross-section level corresponding to location of the quantum well active region.

The fundamental mode and one of the $n = 0$ modes with two peaks on the sides can be compared as follows. The discrimination between two modes can be increased by altering the dimension of the active region. Integral of the power distribution over the distance along the lateral direction corresponding to the current pumping region was performed and divided by the total integral of the power. Thus the relative gain at the active region was obtained. The ratio between these gains for the fundamental mode and the less favored mode with peaks on the sides was plotted against the width of the current pumping region (Figure 10). One can see in Figure 10 that the mathematical maximum value happens at width of 17 μm; however in practice this would lead to much penalty in power due to significant narrowing of the pumping region. A more optimal will be the pumping

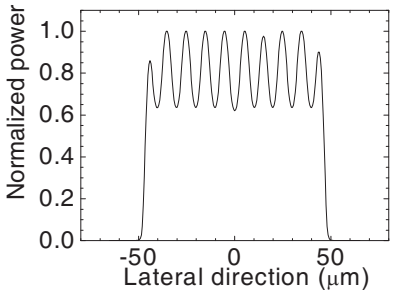

Figure 7: Normalized power distribution at QW for coupled ridges waveguide, fundamental mode.

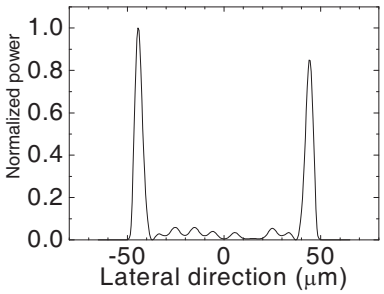

Figure 8: Normalized power distribution at QW for coupled ridges waveguide, one of the less favored modes.

region width of about 80 μm with the peak value of about 3, which means when current pumping region is decreased from the whole ridged region (100 μm) to 80 μm, a significant discrimination with the factor 3 in optical loss between the favored modes and the less favored modes can be achieved.

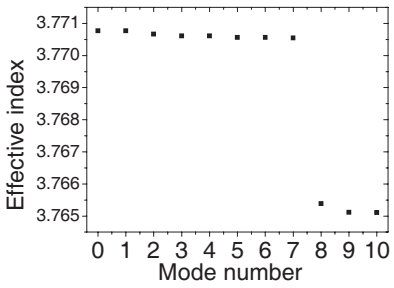

Figure 9: Dependence of effective index on mode numbers of the waveguide with array of ridges.

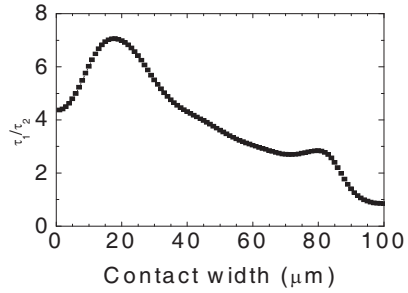

Figure 10: Ratio between the gains of the fundamental mode and the high order mode against the width of the active region.

3. CONCLUSION

The ridge and coupled ridge waveguides with the ranges of width and depth were simulated. It was found that for the ridge waveguide with 5 μm width and 1.3 μm depths, the waveguide geometry provides a three-fold difference in optical losses between the favored modes which peak at the center, and the less favored modes, which peak at the sides. This geometry can create more adequate conditions for generation of the output power with improved divergence of the laser output beam.

ACKNOWLEDGMENT

Y. Chen thanks Undergraduate Research & Creative Activities (URECA) at State University of New York at Stony Brook for support of the work in frames of the URECA Summer Research Program. D. Donetsky appreciates the support from NYSTAR, contract C020000.

REFERENCES

1. Botez, D. and D. R. Scifres, *Diode Laser Arrays*, ISBN 0-521-41975-1, 1994.
2. Endriz, J. G., M. Vakili, G. S. Browder, M. DeVito, J. M. Haden, G. L. Harnagel, W. E. Plano, M. Sakamoto, D. F. Welch, S. Willing, D. P. Worland, and H. C. Yao, "High power diode laser arrays," *IEEE Journal of Quantum Electronics*, Vol. 28, Issue 4, Apr. 1992.
3. Donetsky, D. V., G. Kipshidze, L. Shterengas, T. Hosoda, and G. Belenky, "'2.3-μm type-I quantum well GaInAsSb/AlGaAsSb/GaSb laser diodes with quasi-CW output power of 1.4 W," *Electron. Lett.*, Vol. 43, No. 15, 810–812, 2007.
4. Mukai, S., C. Lindsey, J. Katz, E. Kapon, Z. Rav-Noy, S. Margalit, and A. Yariv, "Fundamental mode oscillation of a buried ridge waveguide laser array," *Appl. Phys. Lett.*, Vol. 45, No. 8, Oct. 15, 1984.

5. Kapon, E., L. T. Lu, Z. Rav-Noy, M. Yi, S. Margalit, and A. Yariv, "Phased arrays of buried-ridge InP/InGaAsP diode lasers," *Appl. Phys. Lett.*, Vol. 46, 136, 1985.
6. Maiorov, M., J. Wang, D. Baer, H. Lee, G. Belenky, R. Hanson, J. Connolly, and D. Garbuzov, "New room temperature CW InGaAsSb/AlGaAsSb QW ridge diode lasers and their application to CO measurements near 2.3 µm," *SPIE*, Vol. 3855, 62–71, 1999.
7. Achtenhagen, M., A. Hardy, and C. S. Harder, "Lateral mode discrimination and self-stabilization in ridge waveguide laser diodes," *IEEE Photonics Technologies Letters*, Vol. 18, No. 3, Feb. 1, 2006.
8. Xu, M. L., G. L. Tan, R. Clayton, and J. M. Xu, "Increased threshold for the first-order lateral mode lasing in low-ridge waveguide high power QW lasers," *IEEE Photonics Technology Letters*, Vol. 8, No. 11, Nov. 1996.
9. Botez, D., L. J. Mawst, G. Peterson, and T. J. Roth, "High power antiguided semiconductor laser with interelement loss," *Appl. Phys. Lett.*, Vol. 53, 2183, 1989
10. Eliseev, P. G., R. F. Nabiev, and Y. M. Popov, "Laterally coupled periodic semiconductor laser structures: Blochfunction analysis," *J. Sov. Las. Res.*, Vol. 10, No. 6, 449, 1989.
11. Adachi, S., "Band gap and refractive indices of AlGaAsSb, GaInAsSb, InPAsSb: Key properties for a variety of 2–4 µm optoelectronic device applications," *J. Appl. Phys.*, Vol. 61, No. 10, May 15, 1987.

Wavefront Phase Modulation of Cylindrical Vector Beam in Optical Focusing System

X. Gao and J. Wang
Electronics and Information College, Hangzhou Dianzi University
Hangzhou 310018, China

Abstract— Wavefront phase modulation is employed in focusing system of cylindrical vector beams to from concentric piecewise wavefront, and focusing properties of the concentric piecewise cylindrical vector beams is investigated theoretically. Results show that the evolution of the focal shape is very considerable by changing the radius and polarization rotation angle of the vector beam, and some interesting focal spots may occur. For certain geometric parameters of the beam, the focal shift occurs and can be adjusted by phase shift. Some gradient force patterns are computed to show that the kind of beam can be used to construct controllable optical tweezers.

1. INTRODUCTION

Recently, there is an increasing interest in laser beams with cylindrical symmetry in polarization, which is called cylindrical vector beams. These beams can be generated by active or passive methods. Due to the symmetry of the polarization, the electric field at the focus of a cylindrical vector beam has unique polarization properties. For example, it has been shown that the longitudinal component of the focus from such a cylindrical beam is much stronger than the transversal component [1]. K. S. Youngworth and T. G. Brown calculate cylindrical-vector fields, near the focal region of an aplanatic lens [2]. It is showed that, in the particular case of a tightly focused radially polarized beam, the polarization shows large inhomogeneities in the focal region, while the azimuthally polarized beam is purely transverse even at very high numerical apertures. Applications of such beams include microscopy, lithography [3], frequency shifting [4], electron acceleration [5], optical trapping and manipulating [6], and material processing [7].

In the investigation of the focusing properties of optical beams, tracing the movement of the point of absolute maximum intensity along optical axis has attracted many researchers for several decades [8]. It was found that the point of absolute maximum intensity does not coincide with the geometrical focus but shifts along optical axis. This phenomenon is referred to as focal shift. More interesting, the focal shift may be incontinuous in certain optical focusing systems. In this paper, wavefront phase modulation is employed in focusing system of cylindrical vector beams to from concentric piecewise section, and focusing properties of the concentric piecewise cylindrical vector beams is investigated theoretically.

2. PRINCIPLE OF THE SYSTEM

The transverse section diagram of the concentric piecewise cylindrical vector beam is illustrated in Figure 1. It can be seen that the section diagram consists of three zones: center circular portion, inner annular portion, and outer annular portion. The electric field in focal region can be written as

$$\vec{E}\left(r,\varphi,z\right) = E_r\vec{e}_r + E_z\vec{e}_z + E_\varphi\vec{e}_\varphi \tag{1}$$

where $\vec{e}_r$, $\vec{e}_\varphi$, and $\vec{e}_z$ are the unit vectors in the radial, azimuthal, and propagating directions, respectively. E_r, E_z, and E_ϕ are amplitudes of the three orthogonal components and can be expressed as

$$E_r\left(r,z\right) = A\sum_{j=1}^{3}\cos\phi_j\exp\left(i\varphi_i\right)\int_{\theta_{j-1}}^{\theta_j}\cos^{1/2}\theta P(\theta)\sin\left(2\theta\right)\cdot J_1\left(kr\sin\theta\right)\exp\left(ikz\cos\theta\right)d\theta \tag{2a}$$

$$E_z\left(r,z\right) = 2iA\sum_{j=1}^{3}\cos\phi_j\exp\left(i\varphi_i\right)\int_{\theta_{j-1}}^{\theta_j}\cos^{1/2}\theta P(\theta)\sin^2(\theta)\cdot J_0\left(kr\sin\theta\right)\exp\left(ikz\cos\theta\right)d\theta \tag{2b}$$

$$E_\varphi\left(r,z\right) = 2A\sum_{j=1}^{3}\sin\phi_j\exp\left(i\varphi_i\right)\int_{\theta_{j-1}}^{\theta_j}\cos^{1/2}\theta P(\theta)\sin(\theta)\cdot J_1\left(kr\sin\theta\right)\exp\left(ikz\cos\theta\right)d\theta \tag{2c}$$

where r and z are the radial and z coordinates of observation point in focal region, respectively. k is wave number. ϕ_1, ϕ_2 and ϕ_3 are the polarization rotation angles from radial direction for center circular zone, inner annular zone, and outer annular zone, respectively. $P(\theta)$ is the pupil apodization function. ϕ_1, φ_2, and φ_3 denote the phase shifts for center circular zone, inner annular zone, and outer annular zone, respectively. θ_j $(j = 1, 2, 3)$ represents the polar angle corresponding to the jth zone, in this paper $\theta_0 = b$, $\theta_1 = a$, and $\theta_2 = \arcsin(NA)$, which practically indicate the radius corresponding to each section zone of the cylindrical vector beam. The gradient force on the particle is investigated numerically. Gradient force can be expressed as [1, 14]

$$F_{grad} = \frac{n_b^2 a^3}{2} \cdot \left(\frac{m^2 - 1}{m^2 + 2} \right) \nabla \left| E\left(r, \varphi, \theta\right) \right|^2 \tag{3}$$

where r is radius of the trapped particle, n_b is the refraction index of the surrounding medium. m, the relative index of refraction, equals to the ratio of the refraction index of the particle to the refraction index of the surrounding medium. The distributions of gradient force in focal region can be computed numerically by substituting Equation (1) into Equation (3). Without losing generality and validity, it is supposed that $P(\theta) = 1$, $A = 1$. It should be noted that in this paper $Vr = kr$, and $Vz = kz$, and the polarization rotation angle changes from 0 to $\pi/2$.

3. OTHER SECTIONS ...

The three-dimensional intensity distribution and the corresponding optical gradient force in focal region of the cylindrical beam can be calculated from Equation (1) and Equation (3), respectively. Firstly, intensity distribution in focal region with $\varphi_1 = \varphi_3 = \phi_1 = \phi_3 = 0$, $\varphi_2 = \pi$, $b = 30°$, $a = 60°$, $NA = \text{asin}(80°)$, and different ϕ_2 is chosen to investigate the focal shape evolution. Focal shapes are illustrated in Figure 1. It can be seen that when ϕ_2 is very small, there are two intensity peaks, which predicts two optical traps may occur. With increasing ϕ_2, the intensity of the two peaks decrease, and one ring shape intensity distribution comes into being, which results in one dark hollow focal spot at geometrical focus position, shown as Figure 1(b). In other words, the intensity at geometrical focus position is weaker than that around it. This kind of focus is sometimes called dark hollow focus, which can be used to construct stable optical trap for those particle whose diffractive index of particles is smaller than that of surrounding medium. Then increase the ϕ_2 continuously, dark hollow focus disappears, the former two intensity peaks shrink very rapidly so that become only small local peaks. Intensity maximum at geometrical focus position occurs with

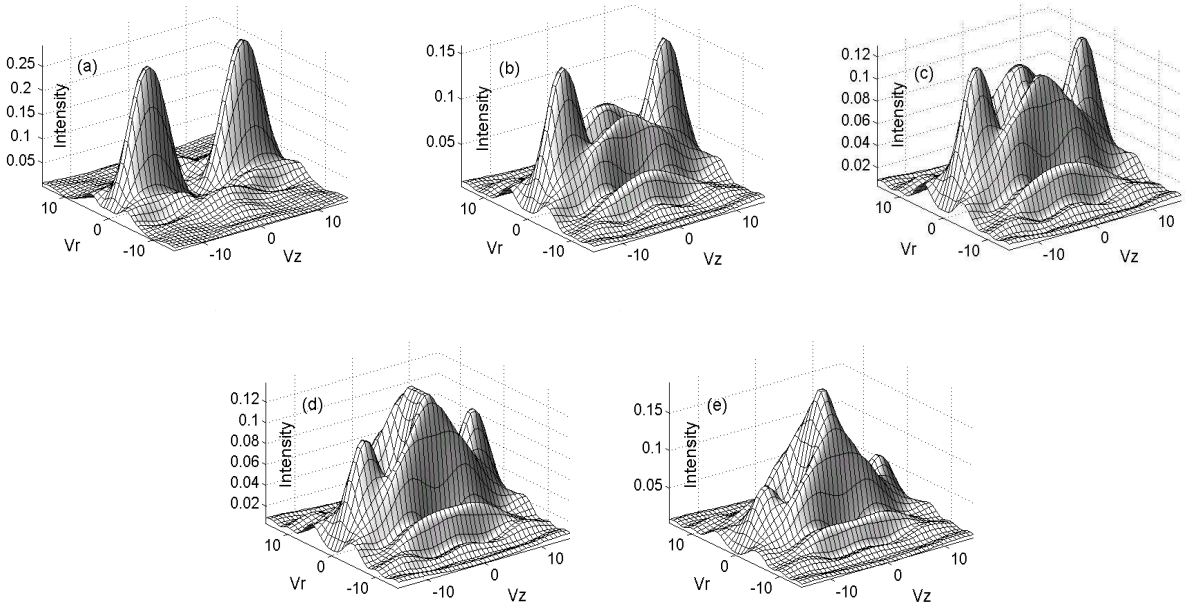

Figure 1: Intensity distribution in focal region for $\varphi_1 = \varphi_3 = \phi_1 = \phi_3 = 0$, $\varphi_2 = \pi$, $b = 30°$, $a = 60°$, $NA = \text{asin}(80°)$, and (a) $\phi_2 = \pi/20$, (b) $\phi_2 = 7\pi/20$, (c) $\phi_2 = 2\pi/5$, (d) $\phi_2 = 9\pi/20$, and (e) $\phi_2 = \pi/2$.

two local intensity minimums beside along propagating direction. The intensity maximum peak is wider considerably in radial direction than in propagating direction. With ϕ_2 approaching to $\pi/2$, the center intensity peak increases and sharpens in radial direction, with other local intensity peaks shrink.

In order to show that this focus evolution may be used to construct tunable optical tweezers, corresponding optical gradient force distribution in focal region is calculated. The evolution of optical gradient force patterns is shown in Figure 2. For $\phi_2 = \pi/20$, there are two optical traps along axis. With increasing ϕ_2, a cup shape shell force pattern occurs between the two optical traps, so one optical trap with all force pointing outside at geometrical focus, as shown in Figure 2(b). When ϕ_2 increases from $7\pi/20$ to $2\pi/5$, the outer two trap does not change considerably, however, gradient optical force at the inner cup shell force pattern changes very much. Firstly, the inside layer of cup shell force pattern breaks, then one rectangle optical trap come into being at geometrical focus, shown in Figure 2(d). Increase ϕ_2 continuously, Figure 2(e) illustrates that the outer two traps weaken, and the center trap shrinks sharply. From above process, we can see that optical gradient force in focal region can be adjusted by means of changing polarization rotation angles.

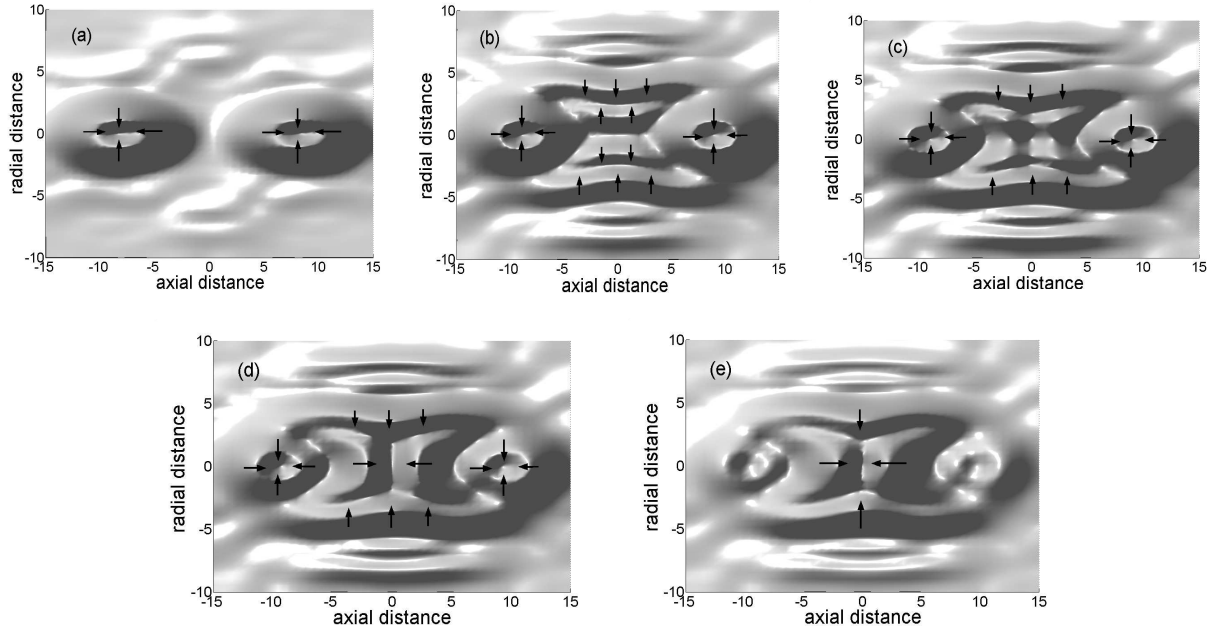

Figure 2: Optical gradient force pattern for $\varphi_1 = \varphi_3 = \phi_1 = \phi_3 = 0$, $\phi_2 = \pi$, $b = 30°$, $a = 60°$, $NA = \text{asin}(80°)$, and (a) $\phi_2 = \pi/20$, (b) $\phi_2 = 7\pi/20$, (c) $\phi_2 = 2\pi/5$, (d) $\phi_2 = 9\pi/20$, and (e) $\phi_2 = \pi/2$.

In order to understand focal spot shaping more generally, $b = 10°$ is chosen to investigate the f optical gradient force with increasing ϕ_2 as shown in Figure 3, other parameters are the same as those in Figure 1. For small value of ϕ_2, there are two traps along axis in this change process. Then increasing ϕ_2 continuously, interesting phenomenon happens, one force spherical shell pattern occurs between the two optical traps. So at geometrical focus, one spherical optical trap comes into being with all force pointing outside, as shown in Figure 3(b). a shell optical gradient force pattern occurs, tough the force is not uniform. Then increase ϕ_2 approaching to $\pi/2$, outer two optical traps weaken and then disappear. Simultaneously, center spherical optical trap turns into cup shell force pattern. The gradient force pattern for $\phi_2 = 9\pi/20$ is shown as Figure 3(c). This force pattern is very interesting, since particle in focal region can be collected and transport to ring optical trap. Collecting region is very big. By adjusting the geometrical parameter of the concentric cylindrical vector beam, the principle of the force pattern with polarization rotation angles changes considerably.

Now the focal shift is investigated in detail. It should be noted that the focal shift refers to the shift of those intensity peak whose intensity value is within 90% of the maximum intensity value below. Namely, the peak whose intensity is within 90% of the maximum intensity is called focal peak. The focal shift is shown in Figure 4 for $\phi_2 = 7\pi/20$, $\theta_0 = \pi/6$, $\theta_1 = \pi/3$, $\theta_2 = 4\pi/9$. The

dark line indicates the focal shift, and the dash line shows the shift of the local intensity minimum. It can be seen that all focal shifts are in the same move direction towards optical aperture, and the shift velocity with increasing phase φ_2 is nearly same. There are only one focal peak that shifts for small phase φ_2. And when value of phase φ_2 belongs to the range of about 0.72 to 0.77, there are three focal intensity peaks. And when phase φ_2 is bigger than 0.77, three focal peaks evolve into two focal peaks. The local intensity minimum shifts towards optical aperture in all changing process.

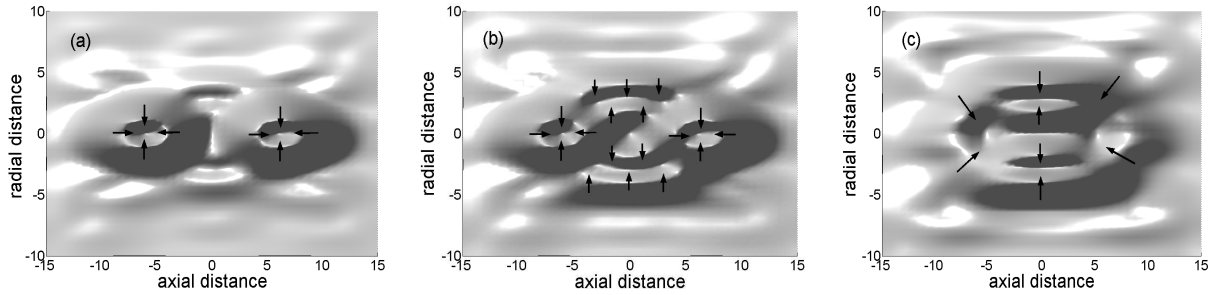

Figure 3: Optical gradient force pattern for $\varphi_1 = \varphi_3 = \phi_1 = \phi_3 = 0$, $\varphi_2 = \pi$, $b = 10°$, $a = 60°$, $NA = \text{asin}(80°)$, and (a) $\phi_2 = \pi/20$, (b) $\phi_2 = \pi/4$, (c) $\phi_2 = 9\pi/20$.

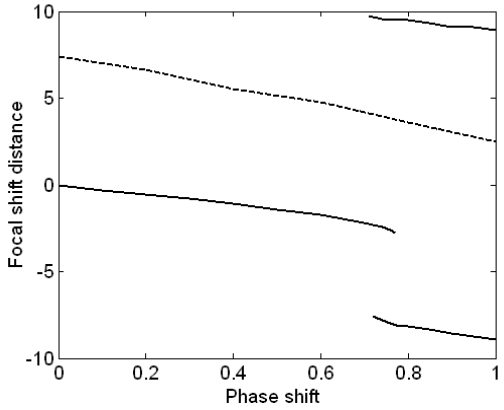

Figure 4: Focal shifts with increasing φ_2 for $\phi_2 = 7\pi/20$, $\theta_0 = \pi/6$, $\theta_1 = \pi/3$, $\theta_2 = 4\pi/9$.

4. CONCLUSIONS

Wavefront phase modulation is employed in focusing system of cylindrical vector beams to from concentric piecewise wavefront section, and focusing properties of the cylindrical vector beams is investigated theoretically. Results show that the evolution of the focal shape is very considerable by changing the radius and polarization rotation angle, and some interesting focal spots may occur. Focal shift occurs and can be adjusted by phase shift and polarized direction of inner annular portion. Some gradient force patterns are also computed to show that the concentric piecewise cylindrical vector beam can be used to construct controllable optical tweezers.

ACKNOWLEDGMENT

This work was supported by Science Research Project of Hangzhou Dianzi University (KYS051506021), National Natural Science Foundation of China (60708002, 50574035).

REFERENCES

1. Quabis, S., R. Dorn, M. Eberler, O. Glöckl, and G. Leuchs, "The focus of light-theoretical calculation and experimental tomographic reconstruction," *Appl. Phys. B*, Vol. 72, 109–113, 2001.
2. Youngworth, K. S. and T. G. Brown, "Focusing of high numerical aperture cylindrical-vector beams," *Optics Express*, Vol. 7, 77–87, 2000.

3. Helseth, L. E., "Roles of polarization, phase and amplitude in solid immersion lens systems," *Opt. Commun.*, Vol. 191, 161–172, 2001.
4. Courtial, J., D. A. Robertson, K. Dholakia, L. Allen, and M. J. Padgett, "Rotation frequency shift of a light beam," *Phys. Rev. Lett.*, Vol. 81, 4828–4830, 1998.
5. Hafizi, B., E. Esarey, and P. Sprangle, "Laser-driven acceleration with Bessel beams," *Phys. Rev. E*, Vol. 55, 3539–3545, 1997.
6. Kuga, T., Y. Torii, N. Shiokawa, T. Hirano, Y. Shimizu, and H. Sasada, "Novel optical trap of atoms with a doughnut beam," *Phys. Rev. Lett.*, Vol. 78, 4713–4716, 1997.
7. Niziev, V. G. and A. V. Nesterov, "Influence of beam polarization on laser cutting efficiency," *J. Phys. D*, Vol. 32, 1455–1461, 1999.
8. Li, Y. and E. Wolf, "Focal shifts in diffracted converging spherical waves," *Opt. Commun.*, Vol. 39, 211–215, 1981.

All-optical Switching Structure Using Nonlinear Photonic Crystal Directional Coupler

A. Eshaghi, M. M. Mirsalehi, A. R. Attari, and S. A. Malekabadi
Department of Electrical Engineering, Ferdowsi University of Mashhad, Iran

Abstract— In this paper, a new all-optical switching structure is proposed and analyzed. Switching is accomplished by embedded Kerr nonlinear rods in the coupling region of a photonic crystal directional coupler. We show that by modifying the supermodes dispersion curves, the switch length can be reduced 22% with respect to similar structures. Finite-Difference Time-Domain and Plane Wave Expansion methods are used to analyze the device characteristics. The results show that the transmission efficiency of the proposed structure has been significantly improved.

1. INTRODUCTION

Photonic crystals are of great importance because of their unique properties in integrating all-optical data-processing chips [1, 2]. Nonlinear photonic crystals are promising structures to realize optical devices such as: optical diodes, nonlinear bends [3], transistors [4], and switches [5]. Due to their important role in optical networks, all-optical switches were investigated during the past decade, in order to decrease the switching length, power and time [6, 7].

Directional couplers can be used to implement all-optical switches [8, 9]. Attempts were made to design couplers with shorter coupling length [10]. However, realizing switches with short lengths and high extinction ratio is still under research. In this paper, a photonic crystal all-optical switching structure with short length and low crosstalk is introduced. A modified 60° bend structure is used to improve the transmission from input to the outputs of the switch.

2. SWITCHING OPERATION IN DIRECTIONAL COUPLERS

In a directional coupler consisting of two parallel waveguides (Fig. 1), the wave confined to one of the waveguides consists of even and odd supermodes with a phase difference. If the phase difference is equal to an odd product of π, the wave will transfer to the other waveguide. This means

$$(k_{even} - k_{odd})L_c = (2n+1)\pi \tag{1}$$

where k_{even} and k_{odd} are the wavenumbers of even and odd supermodes, respectively, and L_c is the coupling length. When photonic crystal fabrication is finalized, L_c will be fixed. Through the use of nonlinearity, one can change the effective index of refraction in different input intensities and as a result, the wavenumbers of the supermodes will change and switching operation can be obtained. It can be shown that switch length is proportional to $(\Delta k_{even} - \Delta k_{odd})^{-1}$, where Δk_{even} and Δk_{odd} are the difference between the wavenumbers of even and odd supermodes in the two

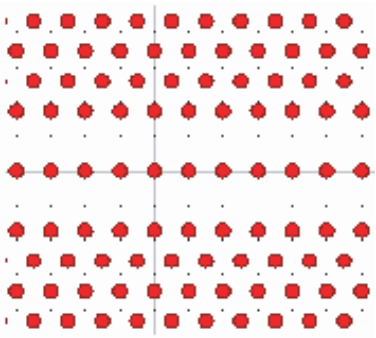

Figure 1: A photonic crystal directional coupler.

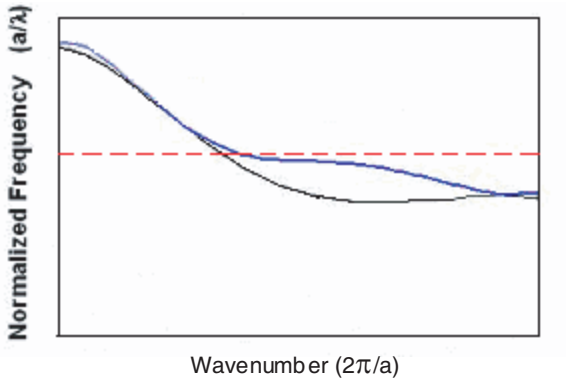

Figure 2: Desired dispersion curves of even (blue) and odd (black) supermodes. Red line shows the fixed-frequency region in the even supermode.

states of switch operation, respectively. Increasing the difference between Δk_{even} and Δk_{odd} will result in reduction of the switch length.

Different structures were proposed to reduce the switch length. The main idea is to modify the supermodes dispersion relation to enlarge the difference between the wavenumbers of linear and nonlinear regimes. Introducing a fixed-frequency region in the dispersion curve of one of the supermodes increases the wavenumber difference drastically. The related band diagram is depicted is Fig. 2. In this structure, the odd mode has a decreasing dispersion curve, while the even mode dispersion curve consists of two decreasing parts and a fixed-frequency region. If the operating frequency is set between the fixed frequencies before and after switching, by changing the input intensity and performing switching operation, Δk_{even} will be larger than Δk_{odd}, and as a result the switch length will decrease. Another advantage of such a structure is that in the fixed-frequency region, the small group velocity leads to reinforce the nonlinear interaction and hence, reduces the power consumption in comparison with optoelectronic devices.

Huang et al. proposed a structure that has a fixed-frequency region [11]. In this structure which consists of air holes in a dielectric substrate, index of refraction in the coupling region has been reduced and the desired dispersion curve was obtained. This directional coupler can be used in an all-optical switch. However, the amount of crosstalk between the output ports in photonic crystal switches with dielectric rods structure is more desirable [9].

3. PROPOSED SWITCH STRUCTURE

Figure 3(a) shows a schematic view of the proposed structure. The PC is formed by a triangular lattice of rods in air. The radius of the rods is $r = 0.2a$, where a is the lattice constant. Two parallel waveguides are obtained by removing two rows of rods. The coupling region is made of rods with Kerr nonlinearity. The Kerr coefficient is assumed $n_2 = 1.5 \times 10^{-17}\,\mathrm{m}^2/\mathrm{W}$. Introducing

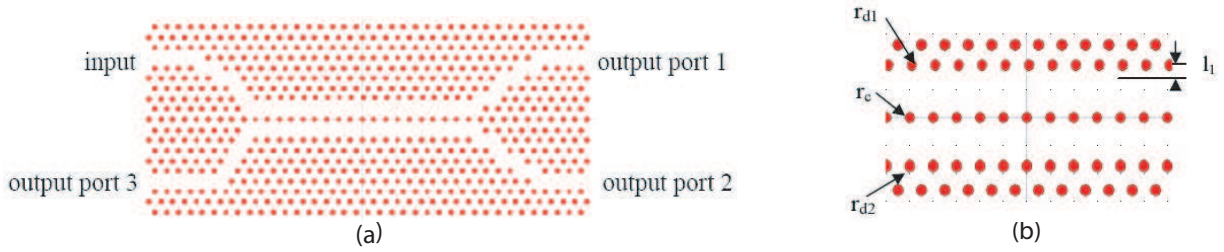

Figure 3: (a) Schematic view of the proposed switch structure (b) Coupling region of directional coupler, used in the switch structure.

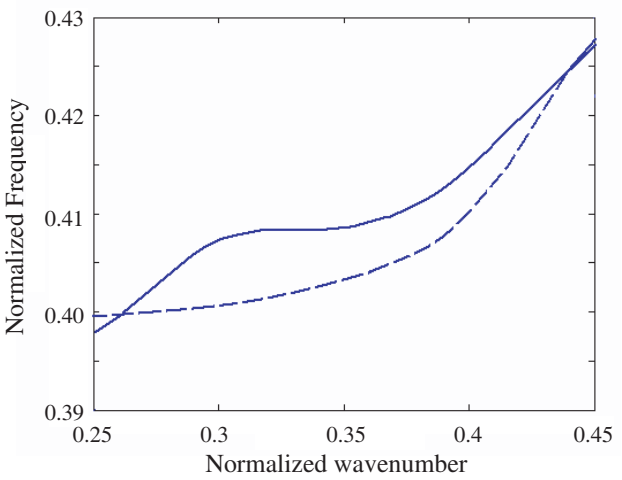

Figure 4: Band diagram of even (solid line) and odd (dashed line) supermodes of the proposed structure. The fixed-frequency region occurs at a normalized frequency of 0.407.

a new coupling region structure, as shown in Fig. 3(b), the difference between the wavenumbers of linear and nonlinear regimes has increased, so the coupling length is reduced to $18a$. This is

equivalent to a reduction of 22% in comparison with similar structures [9, 12]. The radius of central rods (r_c) and those in the two rows adjacent to the waveguides (r_{d1}, r_{d2}) and the amount of shift of rods from their regular positions in the above mentioned rows (l_1 and l_2) were used as the design parameters. By adjusting these five parameters to the following values, the band diagram, shown in Fig. 4 was obtained by PWE simulations

$$r_c = 0.18a,\ r_{d1} = 0.19a,\ r_{d2} = 0.2a,\ l_1 = 0.18a,\ l_2 = 0.$$

The operating frequency is $\frac{a}{\lambda} = 0.405$ (in the fixed-frequency region). The operating wavelength is chosen $\lambda = 1.55\,\mu\text{m}$, therefore $a = 627.75\,\text{nm}$.

Switching operation is accomplished by tuning the input intensity. In the linear regime, where the input intensity is so low that the nonlinear effects are negligible, the switch output is port 2. By intensifying the input wave, the index of refraction of coupling region increases due to the Kerr effect. This results in transferring the input signal to port 1.

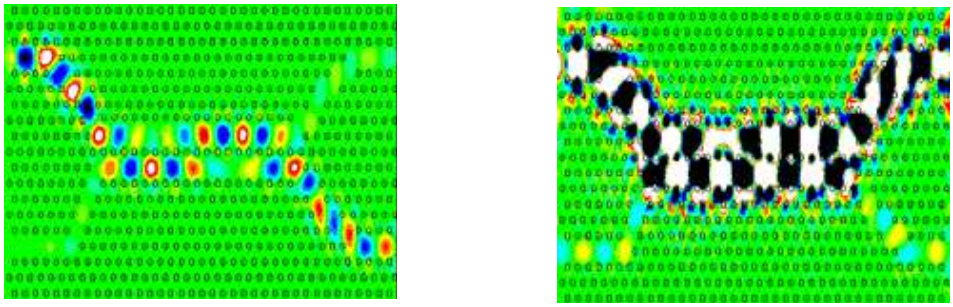

(a) (b)

Figure 5: Different states of the proposed switch (a) In the linear regime, where the input intensity is low (b) In the nonlinear regime, where the input intensity is high.

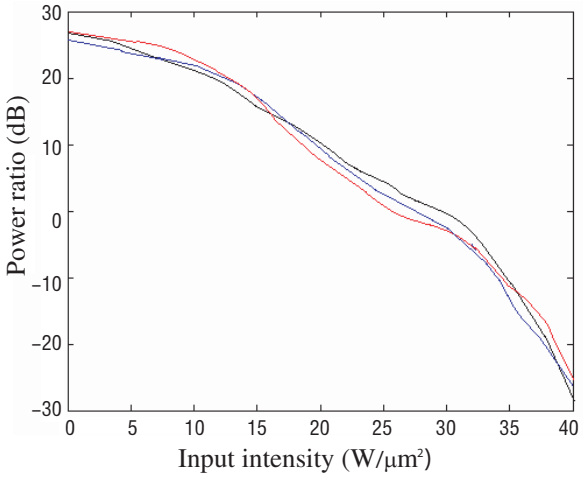

Figure 6: Power ratio of output port 2 to 1 versus input intensity in wavelengths; 1550 nm (black line), 1542 nm (blue line), and 1555 nm (red line).

The FDTD simulations show two states of the device in Fig. 5. The power ratio of output port 2 to 1, versus the input intensity is depicted in Fig. 6. The simulations demonstrate that the device can be considered an optically-controlled switch with a power ratio more than 25 dB in a wide range of wavelengths.

4. IMPROVEMENT OF TRANSMISSION SPECTRA

In order to reduce the crosstalk between output ports, waveguide bends is used in most of the optical switches. Although these bends increase the power ratio in the switch outputs, they decrease the transmission efficiency from the input to the outputs. Attempts were made to improve the

efficiency of the waveguide bends [13, 14]. In this work, modified bends, presented in reference [14], are applied. To decrease the crosstalk and at the same time increase the transmission efficiency, different bend types are used in this structure. Bends, placed at the end of the coupling region have the one-rod-moved structure (Fig. 7(a)) while the bends placed near the input and outputs have the three-rods-moved structure (Fig. 7(b)). In order to prevent signal leakage to the output port 3, bends at the beginning of the coupling region are remained unchanged. Other combinations of bends were analyzed. Although those structures improve transmission spectra in some cases, they were not used, due to the crosstalk increase. Fig. 8 shows the transmission spectra from the input to the outputs in the case of modified and usual 60° bends. Transmission efficiency in the proposed switch is improved in comparison with the case of usual bends.

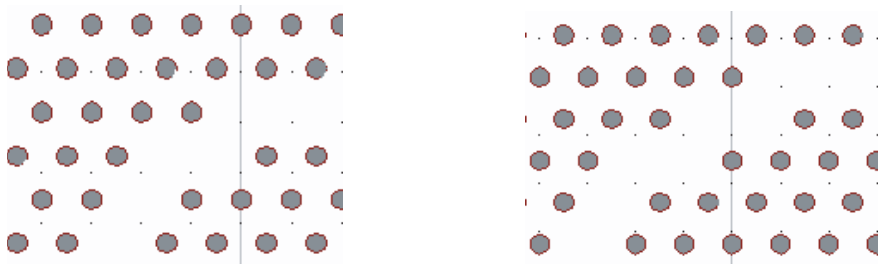

Figure 7: Modified 60° bends, applied in the proposed switch (a) one-rod-moved structure (b) three-rods-moved structure.

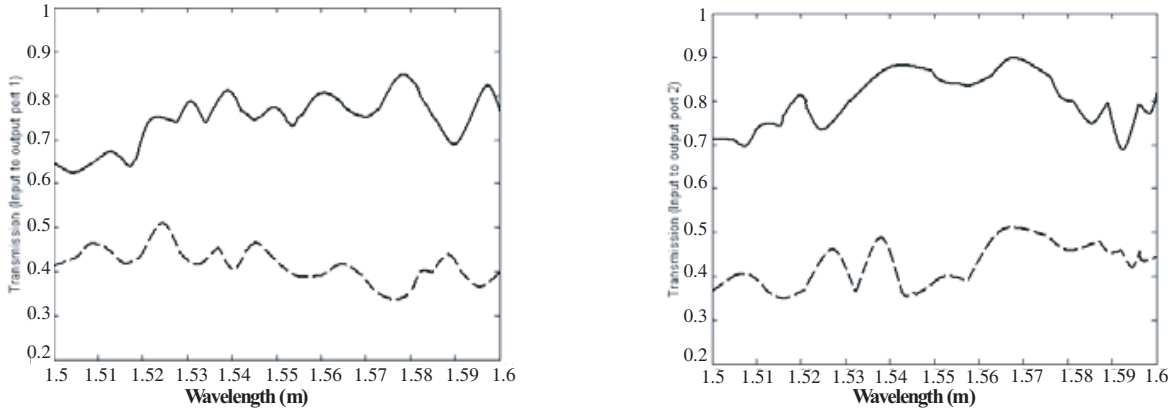

Figure 8: Transmission spectra from the input to (a) output 1 (b) output 2; solid line (proposed structure), dashed line (usual bends).

5. CONCLUSION

In this research, an all-optical switch based on photonic crystal directional coupler was proposed and analyzed. By introducing a new coupling region structure the difference between wavenumbers of linear and nonlinear regimes has been enlarged, so the coupling length is reduced to $18a$. The crosstalk between output ports is decreased in comparison with similar devices. Taking into consideration the effect of waveguide bends on the extinction ratio in the switch outputs and the amount of signal leakage to the output port 3, modified 60° bends were applied in this structure. As a result, the transmission spectrum of the proposed switch is improved in comparison with usual bends.

REFERENCES

1. Joannopoulos, J. D., R. D. Meade, and J. N. Winn, *Photonic Crystal; Molding the Flow of Light*, Princeton University Press, 1995.
2. Slusher, R. E. and B. J. Eggleton, *Nonlinear Photonic Crystals*, Springer, 2003.

3. Mingaleev, S. F. and Y. S. Kivshar, "Nonlinear transmission and light localization in photonic-crystal waveguides," *J. Opt. Soc. Am. B*, Vol. 19, 2241–2249, 2002.
4. Yanik, M. F., S. Fan, M. Soljacic, and J. D. Joannopoulos, "All-optical transistor action with bistable switching in a photonic crystal cross-waveguide geometry," *Opt. Lett.*, Vol. 28, No. 24, 218–219, 2003.
5. Soljacic, M., M. Ibanescu, C. Luo, S. G. Johnson, S. Fan, Y. Fink, and J. D. Joannopoulos, "All-optical switching structure using optical bistability in non-linear photonic crystals," *J. SPIE*, Vol. 5000, 200–214, 2003.
6. Cuesta-Soto, F., A. Martinez, J. Garcia, F. Ramos, P. Sanchiz, J. Blasco, and J. Marti, "All-optical switching structure based on a photonic crystal directional coupler," *Opt. Express*, Vol. 12, No. 1, 161–167, 2003.
7. Li, Z., Y. Zhang, and B. Li, "Terahertz photonic crystal switch in silicon based on self-imaging principle," *Opt. Express*, Vol. 14, No. 9, 3887–3892, 2006.
8. Cuseta-Soto, F., A. Martinez, B. Garcia-Banos, and J. Marti, "Numerical analysis of all-optical switching based on a 2-D nonlinear photonic crystal directional coupler," *IEEE J. of Quantum Elec.*, Vol. 10, No. 5, 1101–1106, 2004.
9. Locatelli, A., D. Modotto, D. Paloschi, and C. D. Angelis, "All optical switching in ultrashort photonic crystal couplers," *Opt. Comm.*, Vol. 237, 97–102, 2004.
10. Martinez, A., F. Cuesta, and J. Marti, "Ultrashort 2-D photonic crystal directional couplers," *IEEE Photonics Technol. Lett.*, Vol. 15, 694–696, 2005.
11. Huang, S. C., M. Kato, E. Kuramochi, C. P. Lee, and M. Notomi, "Time-domain and spectral-domain investigation of inflection-point slow-light modes in photonic crystal coupled waveguides," *Opt. Express*, Vol. 15, No. 6, 3546–3549, 2007.
12. Zhou, H., X. Jiang, T. Yu, J. Yang, and M. Wang, "Two-mode interference switching in photonic crystal waveguide," *Proceedings of International Symposium on Biophotonics, Nanophotonics and Metamaterials*, 332–334, 2006.
13. Rauscher, K., D. Erni, J. Smajic, and C. Hafner, "Improved transmission for 60° photonic crystal waveguide bends," *Proceedings of Progress In Electromagnetics Research Symposium*, 2004.
14. Talneau, A., L. Gouezigou, N. Bouadma, M. Kafesaki, C. M. Soukoulis, and M. Agio, "Photonic-crystal ultrashort bends with improved transmission and low reflection at 1.55 μm," *Appl. Phys. Lett.*, Vol. 80, No. 4, 547–549, 2002.

Studying of the Dipole Characteristic of THz from Photoconductors

Hong Liu, **Weili Ji**, **and Wei Shi**
School of Automation and Information Engineering, Xi'an University of Technology, China

Abstract— Under the different experimental conditions, THz waveform which was generated by the different GaAs photoconductive switch provided with diverse carrier lifetimes triggered by femo-second laser pulse are calculated. The results indicate the main course of the dipole characteristic of THz waveforms emitting from low-temperature grown GaAs is the lifetime of optical-generated carriers less than the generation time; To SI-GaAs photoconductive semiconductor switches with the lifetime of optical-generated carriers more than 100 ps, the dipole characteristic of THz waveforms is mainly because of intra-valley scatter and the space charge field screening on different experimental conditions (different biased electric field and different optical pulse energy).

1. INTRODUCTION

With the development of the ultra-short laser pulse technology, the range applications of photoconductive semiconductor switches (PCSS) become very wide [1–4]. Photoconductive semiconductor switches, holding dc voltage, triggered by femo-second laser pulse are calculated has been used to generate high power THz electromagnetic waves [5–8]. Because of the widespread application of THz electromagnetic waves, the people try to understand the physical mechanism of PCSS generating THz by large numbers of experiment and theoretical analysis to improve the power of THz wave. There have been several groups that investigated into the phenomenon of saturation limiting the power of THz wave generated by single pulse triggering PCSS. To avoid saturation, Liu et al. and Siders et al. demonstrated the generation of THz wave by multi-pulse triggering PCSS. Rodriguez et al. studied the physical mechanism of saturation as a result of the screening effect of radiation field by numerical simulation. To penetrate the physical mechanism of PCSS emitting THz, there is very profound to study THz waveform and the dynamic characteristic of optical-generated carriers which usually rely on strangely the biased electric field and the optical pulse.

In this paper, the dipole characteristic of THz waveforms which was emitted from low-temperature grown GaAs and SI-GaAs photoconductive semiconductor switches on the different experimental conditions are calculated. The results indicate the dipole characteristic of THz waveforms emitted from low-temperature grown GaAs is due to the influence of the lifetime of optical-generated carriers, and we have observed that symmetry of the dipole THz waveforms is more well if the life time is more smaller. To SI-GaAs photoconductive semiconductor switches, the dipole characteristic of THz waveforms is mainly because of different experimental conditions (different biased electric field and different optical pulse energy), the dipole THz waveforms was both happened on the condition that high optical power with low biased voltage or high biased voltage with low optical power triggering PCSS, but in the physical mechanism of the dipole characteristic of THz waveforms, the former differs entirely from the latter on this two different conditions.

2. THEORETICAL CONSIDERATIONS

On the base of Maxwell's electromagnetic theory, people have qualitatively and quantitatively described the theory of THz radiation produced by optically emitting the photoconductor. The theory accepted in general is the model of current surge [17]. This model persist in THz wave radiated by the photoconductor is formed from the transient surface current which flow in the photoconductor. From the Ohm's law, we can deduce the equation of surface current:

$$\vec{J}_s(t) = \sigma_s(t)(\vec{E}_b + \vec{E}_s(t)) \tag{1}$$

where $\sigma_s(t)$ is time surface electric conductance, $\vec{E}_b$ is electric field biased the photoconductor. Using the boundary condition of Maxwell equation, the relation of $\vec{J}_s(t)$ to $\vec{E}_s(t)$ can be given:

$$\vec{E}_s(t) = -\frac{\eta_0}{1+\sqrt{\varepsilon}}\vec{J}_s(t) \tag{2}$$

where η_0 is the magnetic conductivity the free-space, it's the numerical value is 337, ε is relative inductivity. Further more, we can get the relation between surface radiation field and the biased electrical field:

$$\vec{E}_s(t) = -\frac{\eta_0\sigma_s(t)}{\eta_0\sigma_s(t) + (1+\sqrt{\varepsilon})}\vec{E}_b \tag{3}$$

From the Equations (3) and (1), we can get the direct relation of surface and the biased electrical field:

$$\vec{J}_s(t) = -\frac{(1+\sqrt{\varepsilon})\sigma_s(t)}{\eta_0\sigma_s(t) + (1+\sqrt{\varepsilon})}\vec{E}_b \tag{4}$$

In far field, detect THz radiation field according the axis of the photoconductor, at now THz radiation field can be expressed [18]:

$$\vec{E}_{r-far}(t) \approx -\frac{1}{4\pi\varepsilon_0 c^2}\frac{A}{z}\frac{d}{dt}\vec{J}_s(t) \tag{5}$$

where A is the area of the gap between the electrodes, z is the distance from the radiation center to the observational point. By the means of time domain differential method to the expression (4), the relation of the biased electrical field to the radiation far field of the photoconductor be denoted as:

$$\vec{E}_{r-far}(t) = -\frac{1}{4\pi\varepsilon_0 c^2}\frac{A}{z}\frac{\frac{d\sigma_s(t)}{dt}}{\left(1+\frac{\sigma_s(t)\eta_0}{1+\sqrt{\varepsilon}}\right)^2}\vec{E}_b \tag{6}$$

Supposing the time domain surface conductance is given by

$$\sigma_s(t) = \frac{q(1-R)}{h\upsilon}\frac{F_{opt}}{\sqrt{\pi}t_{las}} \times \int_{-\infty}^{t}\mu(t,t')\exp\left(-\frac{t-t'}{\tau_c}\right)\exp(-t^2/t_{las}^2)dt' \tag{7}$$

where, q is quantity of electricity of electron, R is the optical reflectance of the PCSS material, $h\upsilon$ is the energy of a single photon, F_{opt} is the energy of a single laser pulse, τ_c is lifetime of the carriers, t_{las} is FWHM of optical pulses, $\mu(t,t')$ is transient mobility. If the biased voltage is lower, the photogenerated carriers can not scatter from the central valley to the satellite valleys, the transient mobility can be given by the following:

$$\mu(t) = \frac{q\tau_s}{m^*}\left[1-\exp\left(-\frac{t}{\tau_s}\right)\right] \tag{8}$$

where m^* is the valid mass of the electron, τ_s is relaxation time.

We can drew a conclusion from these equations: the intension of THz far field radiation is directly affected by the lifetime of carriers in device material, the bias electronic field and activating laser pulse.

3. CALCULATION AND DISCUSSION

3.1. The Relation Between the Lifetime of Carriers and the Dipole Characteristic of THz Waveforms

From the formula (4), (5), (6), (7) and (8), we can calculate the THz waveform radiated by photoconductors with different carrier lifetime. In Figure 1, it shows the different THz waveforms generated by triggering PCSS which semiconductors have four kinds of current carrier lifetime, the PCSS biased at 2 KV/cm electronic field and excited with 800 nm wavelength of light. The typical parameters used in the calculation are: the size of optical spot $A = 1.0 \times 10^{-6}\,\mathrm{m}^2$; the distance between radiation center and observation point $z = 1.0 \times 10^{-2}\,\mathrm{m}$; the energy of a single pulse $F = 8.0 \times 10^{-6}\,\mathrm{J}$, the FWHM of the laser pulse $t_{las} = 100\,\mathrm{fs}$; the photoconductive switches which have different carrier lifetime are three kinds of LT-GaAs (300 fs, 500 fs, 1000 fs) and 100 ps of SI-GaAs. Figure 1(a) shows the THz waveform that radiated by the LT-GaAs whose current carrier lifetime is 300 fs. On the same experimental condition, the amplitude of wave's positive is minimum, the amplitude of negative is maximal and the waveform is the narrowest, the symmetrical characteristic of dipole is the best; Figure 1(b) is the THz waveform that radiated by LT-GaAs semiconductor with carrier lifetime of 500 fs, the amplitude of positive has increased, at

the same time, the amplitude of negative has decreased, and the waveform is wider, the symmetry is weaker; Figure 1(c) is the THz waveform that radiated by the LT-GaAs semiconductor whose current carrier lifetime is 1000 fs, the amplitude of positive is the highest among the three emitter sources of LT-GaAs, the amplitude of negative is the lowest and the waveform is becoming wider, the symmetry become further weaker; Figure 1(d) is THz waveform that radiated by the LT-GaAs whose current carrier lifetime is 1000 fs, the amplitude of waveform is the highest, the wave has became complete single-pole. From Figure 1, we can draw a conclusion that the current carrier lifetime have important factor on the dipole characteristic and amplitude of the wave, thus the PCSS with shorter lifetime of the current carriers will generate THz wave with better symmetry and smaller amplitude of positive part of dipole THz waveform.

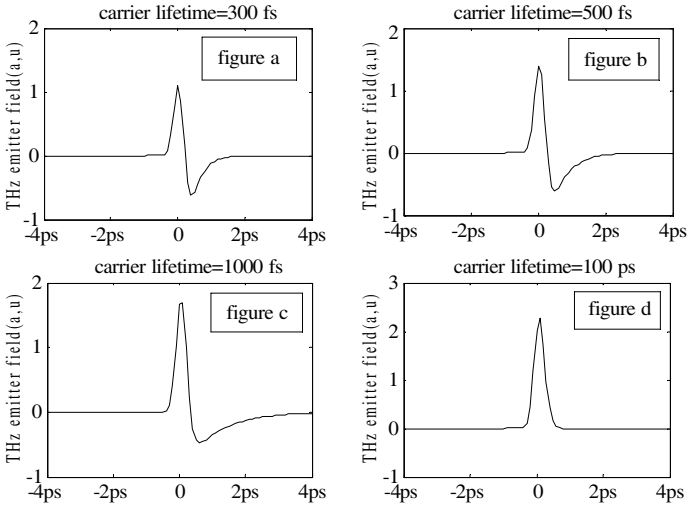

Figure 1: THz waveforms for different photoconductors with different lifetime of carriers and the same experimental.

When laser pulse illuminate on GaAs PCSS surface, a large number of the optical-generated carriers generate rapidly within the period of the laser pulse because of the width of laser pulse less than the lifetime of carriers; at the same time, transient current densities increase rapidly also due to the biased electrical field. This process comes into being the positive part of dipole THz waveform. Subsequently, the processes come into the negative part of dipole THz waveform with the quantity decreasing quickly of the optical-generated carriers. In this process, the carriers nevertheless accelerated continually with the biased electrical field, because the ratio of the decreasing number of optical-generated carriers with time is greater than the ratio of the increasing of current density from accelerating by the bias field, the current densities still present obviously the performance of degradation.

3.2. Influence of Different Experimental Conditions on the Dipole Characteristic of THz Waveforms

The relation of the carriers' lifetime to the dipole characteristic of THz waveforms was numerically simulated. From the former formulations, we can get the generation of THz pulse by exciting the PCSS which material has longer lifetime carriers such as GaAs et al. has no dipole characteristic. But, the experimental results showed the THz pulse emitted by SI-GaAs has observable characteristic of dipole, even has characteristic of symmetry. In this paper, we present the results of Monte Carlo simulations of the dipole characteristic of THz waveforms generated by simi-insulting GaAs photoconductive switches on different experimental conditions.

3.2.1. The Relation of the Biased Electric Field to the Dipole Characteristic of THz Wave

Figure 2 shows THz waveforms generated at 100 kV/cm biased electric field has oscillation at some degree, while THz waveforms generated at 30 kV/cm, 10 kV/cm biased electric field both have negative part, but at 2 kV/cm, THz waveform entirely demonstrate single-pole characteristic.

Using the single laser pulse wavelength is 800 nm, so it's energy is 1.55 eV, only 0.12 eV wider than energy gap of SI-GaAs, therefore initial distribution of the carriers is in the central valley. The biased electric field accelerates the optical-generated carriers' average velocity. Consider higher effective mass and slower drift velocity of the optical-generated holes, so the effect of the optical-

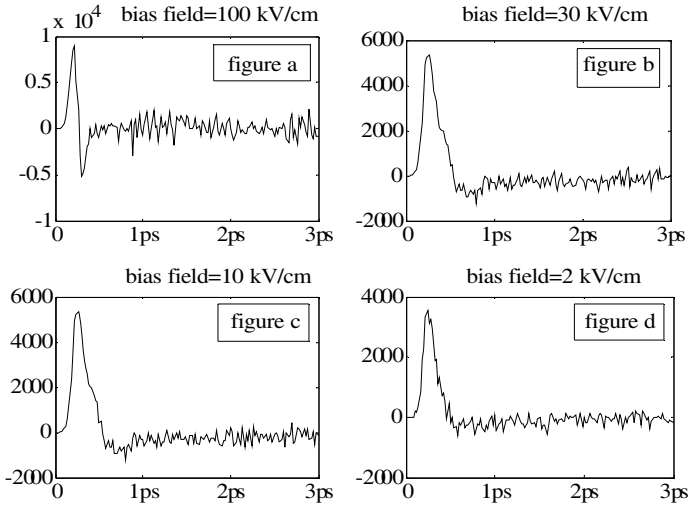

Figure 2: THz waveforms generated by SI-GaAs PCSS with a 30 μm gap activated by 100 fs, 8 nJ optical pulse at different biased electric field.

generated holes to THz radiation can be ignored. In PCSS, the photo-generated electrons move to the electrode and happen to various scatterings. So, the energy of carriers increases from the electric field and loses energy from scattering. Thereby its energy and momentum present a relaxation. When the dc bias electric field greater than 4.0 kV/cm (Gunn electric field), a photo-generated hot electron gain enough energy to transfer from the central valley to two satellite valleys, this process was defined as non-equivalence inter-valley scattering. Subsequently the electrons in the satellite valley decrease mobility and velocity rapidly due to its high-effective-mass. The velocity of a photo-generated hot electron at first increases and secondly decreases at end drive to stable stage. In the reference paper [19], the alteration process of acceleration of the electrons has been described. While the dc bias electric field is equal to or greater than 100 kV/cm, the electron's velocity increasing and decreasing take on periodic oscillation process. Its periodicity is up to oscillating central frequency (115 fs) of LO Phonon. This process will cause the oscillating of far-field THz radiation. The dc bias electric field is higher, the force of it in the electrons is greater, and consequently, the acceleration is greater also, thus the time current density grows more rapidly. This case presents that the higher electric field leads to the rise time of THz waveform is shorter and the peak power of THz waveform is higher. While the electric field is smaller, the energy get from the electric field is not enough to inter-valley transfer for the electrons. The photo-generated hot electrons obtain energy from the electric field, meanwhile lose energy under the influence of polar optical scattering; thereby its energy and momentum present a relaxation phenomena and drive to stable stage.

The electrons increase continuously in quantity and velocity during the period of the electrons' acceleration. These appear the rise of THz pulseform. When the rate of increase in quantity reduces, thus the change rate of current density decrease, this appears the fall of THz pulseform. As the quantity and velocity of carries is constant, a THz pulse is end.

3.2.2. The Relation of the Light Energy to the Dipole Characteristic of THz Wave

Figure 3 shows far-field THz radiation waveform generated by exciting SI-GaAs semiconductor with a 30 μm gap and biased at 2 kV/cm electric field. Activating light is laser pulse with 8 μJ energy, 800 nm wavelength, 100 fs FWHM. Comparing with Figure 2(d), the experimental condition is totally similar except for laser energy is 10^3 greater.

At actual, the difference of laser energy cause the great difference of THz waveform radiated from the semiconductor surface. In Figure 3, the positive THz radiation has same peak value with the negative THz radiation, while in Figure 2(d), obviously, THz radiation only has positive radiation. In a word, only illuminated by high-power laser pulse, far field THz radiation has the characteristic of dipole.

Actually, not only the switch semiconductor and the bias electric field have influence on THz wave but also the activating light (its wavelength, width and energy). With respect to SI-GaAs with the lifetime greater than 100 ps, we analyzed the reason for the dipole characteristic of THz wave

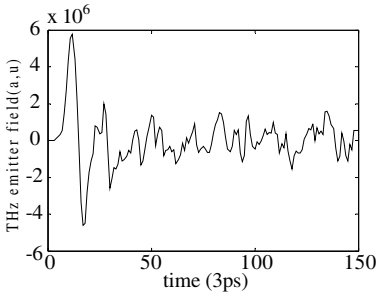

Figure 3: THz waveform radiated by activating a 30 μm gap PCSS excited with 8 μJ laser pulse.

produced by high-power laser pulse triggering SI-GaAs PCSS at low bias electric field and found that the important reason is space charge field screening. In the area of SI-GaAs semiconductor irradiated by optical spot, there are a large number of electron-hole pairs producing in very short time, these electron-hole pairs drift with various velocity towards two electrodes, this case cause the separation of electron and hole, thus form the space charge field contrary to the bias electric field. Therefore, the space charge field acts as a function of screening for the bias electric field. At low electric field, because the space charge field generating from high density carriers can far greater than the bias electric field in some cases, the effect of screening can not be ignored. We can draw a conclusion that it is the space charge field that affects the variation of local carriers' acceleration. Time-changed current density is reverse, due to the space charge field contrary to the bias electric field, this case forms the negative part of THz wave.

4. CONCLUSIONS

In summary, the conclusion we can drawn that various semiconductor material of PCSS and different experimental condition all affect directly the characteristics of THz wave. The reasons for the dipole characteristic of THz pulse produced by LT-GaAs semiconductor with short lifetime is the carriers' rapid decrease in very short time, the carriers generate in fs range and recombining in fs level time. While to SI-GaAs semiconductor with long lifetime, the experimental mostly affect the dipole characteristic of THz pulse. When biased at high electric field (to SI-GaAs, greater than Gunn electric field 4.0 kV/cm), inter-valley scattering can happen to the carriers whin the switch semiconductor of III-V group, and its process of acceleration and deceleration finish in fs level time, this case leads to the dipole characteristic of THz wave; When biased at low electric field, the space charge field formed by the high density of carriers can cause the effect of electric field screening, and thus result in the dipole characteristic of THz wave.

ACKNOWLEDGMENT

This research is supported by the National Natural Science Foundation of China (50477011) and the National Basic Research Program of China (2007CB310406).

REFERENCES

1. Shi, W., D. M. Ma, and W. Zhao, *Acta Physica Sinica*, Vol. 53, 1716, 2004.
2. Shi, W., W. L. Jia, and W. L. Ji, *Chinese Journal of Semiconductors*, Vol. 26, 11, 2005.
3. Shi, W., W. L. Ji, and W. Zhao, *Acta Electronic Sinica*, Vol. 32, 1891, 2005.
4. Shi, W., X. B. Zhang, W. L. Jia, et al., *Chinese Journal of Semiconductors*, Vol. 25, 1735, 2004.
5. Budiarto, E., J. Margolies, S. Jeong, J. Son, and J. Bokor, *IEEE J. Quantum Electron.*, Vol. 32, 1839, 1996.
6. Zhao, G., R. N. Schouten, N. van der Valk, and W. T. Wenckebach, *Rev. Sci. Instrum*, Vol. 73, 1715, 2002.
7. Darrow, J. T., X.-C. Zhang, D. H. Auston, and J. D. Morse, *IEEE J. Quantum Electron.*, Vol. 28, 1607, 1992.
8. You, D., R. R. Jones, P. H. Bucksbaum, and D. R. Dykaar, *Opt. Lett.*, Vol. 18, 290, 1993.
9. Jones, R. R., D. You, and P. H. Bucksbaum, *Phys. Rev. Lett.*, Vol. 70, 1236, 1993.
10. Cook, D. J., J. X. Chen, E. A. Morlino, and R. M. Hochstrasser, *Chem. Phys. Lett.*, Vol. 309, 221, 1999.

Influence of External-cavity Length on the Route-to-chaos of Semiconductor Lasers under Optical Feedback

Moustafa Ahmed[1] **and Minoru Yamada**[2]

[1]Department of Physics, Faculty of Science, Minia University, 61519 El-Minia, Egypt
[2]Division of Electrical Engineering and Computer Science
Graduate School on Natural Science and Technology, Kanazawa University
Kakuma-machi, Kanazawa 920-1192, Japan

Abstract— This paper investigates influence of the external-cavity length on the route-to-chaos of semiconductor lasers operating under optical feedback. The study is based on numerical solution of a time-delay model of rate equations. The route is period doubling when the ratio of the relaxation frequency to the external-cavity resonance frequency is less than unity. The route is sub-harmonic when the ratio is near above unity, and is quasi-periodic characterized by the compound-cavity frequency and the relaxation frequency as well as their difference when the ratio is far above unity.

1. INTRODUCTION

In most of their applications, semiconductor lasers are unavoidably subjected to an amount of optical feedback (OFB) due to reflection of laser radiation by an external reflector. OFB may cause dramatic changes in the laser dynamics, ranging from regular oscillation with improved coherency to chaos with coherency collapse [1, 2]. Therefore OFB is one of the most studied problems in laser dynamics, but yet it has not been fully understood because of its complexity, nonlinearity and the large number of included parameters. The route to chaos is one of the interesting nonlinear phenomena associated with OFB; it may include dynamics with period-doubling (PD), sub-harmonics (SH), or quasi-periodicity [3–6]. PD is observed in the limit of short-external cavity [4–6]; it follows a region of periodic oscillation (PO) and is characterized by the PO frequency and its half harmonic. Kao et al. [4] predicted that this frequency should correspond to Hopf-bifurcation point (the onset of PO). The quasi-periodic route (QP) to chaos dominates the long-external cavity dynamics and is a manifest of competition between resonances of the laser cavity and the external cavity [1, 3–6]. Kao et al. [4] reported that QP is characterized by the Hopf-bifurcation frequency with a beaten component of nearly the external-cavity resonance frequency. SH transitions were predicted as an intermediate state from PD to QP associated with increasing the external cavity length [4]. It is characterized by the Hopf-bifurcation frequency and one of its rational sub-harmonics, and is followed by mode locking with these frequencies [4]. Determination of the ranges of the external-cavity length that correspond to each of these routes is necessary for understanding and controlling the dynamics of lasers under OFB.

In this paper, we survey dynamics of semiconductor lasers along the route-to-chaos as a function of the external-cavity length. The study is based on numerical simulation of laser dynamics by solving the time-delay rate equations. The route dynamics are classified in terms of the bifurcation diagram of the photon number and the fast-Fourier transform (FFT) power spectrum at each OFB level. The ratio of the relaxation frequency of the solitary laser to the resonance frequency of the external cavity is used to quantify influence of the external-cavity length. The study is applied to Fabry-Perot (FP) AlGaAs lasers. The results show that the route-to-chaos is PD when the frequency ratio is less than unity. When this frequency ratio exceeds unity, the route becomes SH and then changes to QP. The obtained results are compared with those reported by Kao et al. [4].

In the next section, the simulation model of laser dynamics under OFB is given. The results of classifying the rout to chaos and the typical power spectra are given in Section 3. The conclusions appear in Section 4.

2. THEORETICAL MODEL OF LASER MODULATION DYNAMICS

Dynamics of semiconductor lasers operating under OFB are described by the following time-delay rate equations of the photon number $S(t)$, optical phase $\theta(t)$ and injected electron number $N(t)$ [7]

$$\frac{dS}{dt} = \left(A - BS - G_{th0} + \frac{c}{n_D L_D}\ln|U|\right)\ S + \frac{a\xi}{V}N \tag{1}$$

$$\frac{d\theta}{dt} = \frac{1}{2}\ \left[\frac{\alpha a\xi}{V}\left(N - \overline{N}\right) - \frac{c}{n_D L_D}\varphi\right] \tag{2}$$

$$\frac{dN}{dt} = -A\ S - \frac{N}{\tau_e} + \frac{I}{e} \tag{3}$$

where A and B are linear and nonlinear coefficients of optical gain, respectively, and are defined as,

$$A = \frac{a\xi}{V}\left(N - N_g\right) \tag{4}$$

$$B = B_c\left(N - N_s\right) \tag{5}$$

G_{th0} is the threshold gain of the solitary laser. The function U and its argument φ describe inclusion of OFB due to a roundtrip of laser radiation between the front facet of reflectivity R_f and the external reflector of reflectivity R_{ex}. The function U is given in terms of the roundtrip time $\tau = 2n_{ex}L_{ex}/c$, with L_{ex} and n_{ex} being the length and refractive index of the external cavity, respectively, as [1]

$$U = 1 - K_{ex}\frac{S(t-\tau)}{S(t)}\ e^{-j\psi} = |U|\ e^{-j\varphi} \tag{6}$$

where ψ is an arbitrary phase term. K_{ex} is a coefficient measuring strength of OFB and is given by

$$K_{ex} = (1 - R_f)\sqrt{\eta R_{ex}/R_f} \tag{7}$$

where η is the coupling ratio of the externally reflected light into the laser cavity.

Definitions of the other parameters appeared in the above equations follow. a is the tangential gain coefficient, N_g is the electron number at transparency, N_s is an electron number characterizing B, B_c is a parameter measuring nonlinear gain, ξ is the field confinement factor in the active layer whose volume is V, length is L_D and refractive index is n_D, α is the linewidth enhancement factor, and τ_e is the electron lifetime.

3. NUMERICAL RESULTS AND DISCUSSION

Rate Equations (1)–(3) are solved numerically by the fourth-order Runge-Kutta method. The time step of integration is set as short as $\Delta t = 5\,\text{ps}$ to guarantee fine resolution of the dynamics. The integration is first solved without OFB (solitary laser) between $t = 0$ and τ. The calculated values of $S\,(t = 0 \to \tau)$ and $\theta\,(t = 0 \to \tau)$ are then stored for use as time delayed values $S\,(t-\tau)$ and $\theta\,(t-\tau)$ for integration over a long period of time $T = 3 \sim 4\,\mu\text{s}$ during which the operation is stabilized [8]. The phase ψ is set to zero. In the calculations, we considered 780 nm-FP-AlGaAs lasers whose parameters have the following typical values. $a = 2.75 \times 10^{-12}\,\text{m}^3\text{s}^{-1}$, $\xi = 0.2$, $\alpha = 2$, $R_f = 0.3$, $V = 150\,\mu\text{m}^3$, $L_D = 300\,\mu\text{m}$, $n_D = 3.59$, $N_g = 3.15 \times 10^8$, $N_s = 2.55 \times 10^8$, $\tau_e = 2.79\,\text{ns}$, and $B_c = 6.2 \times 10^{-5}\,\text{s}^{-1}$. The calculated threshold gain and current of the solitary laser are $G_{th0} = 7.817 \times 10^{10}\,\text{s}^{-1}$ and $I_{th0} = 22.5\,\text{mA}$. The injection current is set to $2I_{th0}$, which corresponds to relaxation frequency $f_{r0} = 3.5\,\text{GHz}$. The external-cavity length is assumed to vary from $L_{ex} = 1$ to 20 cm with $n_{ex} = 1$, which correspond to $f_{r0}/f_{ex} = 214\,\text{MHz}$ to 4.29 GHz. The laser dynamics are classified in terms of the time variation of $S(t)$ and the corresponding FFT power spectrum.

3.1. Bifurcation Diagram Analysis

The bifurcation diagram is constructed by plotting the peak(s) of the temporal trajectory of $S(t)$ at each level of OFB (K_{ex}). Figs. 1(a)–(c) shows such diagrams under weak OFB when $f_{r0}/f_{ex} = 0.7\,(L_{ex} = 3\,\text{cm})$, $f_{r0}/f_{ex} = 1.67\,(L_{ex} = 5\,\text{cm})$ and $f_{r0}/f_{ex} = 3.5\,(L_{ex} = 15\,\text{cm})$, respectively. General features of these diagrams are as follows. Under very weak OFB, the solution of rate equations is still stationary and the laser operates in continuous wave (CW). With the increase

of OFB, this stationary solution bifurcates first into a stable limiting cycle characterizing PO (undamped relaxation oscillation), which is represented by a single point in the diagram. The solution then bifurcates into a torus (multiple bifurcation points) followed by a chaotic state. With further increase of OFB, the laser is attracted again to CW operation. The frequency f_{po} of PO is not necessary equal to f_{r0}; it changes around it with the increase of f_{r0}/f_{ex}. Moreover over the range of PO, the frequency f_{po} decreases from $f_{po(H)}$ at the Hopf-bifurcation point with the increase of OFB. In Fig. 1(a), the torus is PD in which PO bifurcates first into two branches. With the increase of K_{ex}, the oscillation period is increased to more than twice attracted to the chaos region. In Figs. 1(b) and (c), PO is no longer followed by PD; it is followed by multiple bifurcation points referring to noisier routes-to-chaos. Such a route is SH in Fig. 1(b) and QP in Fig. 1(c). The range of OFB of the induced chaos cycle decreases with the increase of f_{r0}/f_{ex}. In the following subsection, we characterize the three types of route-to-chaos in terms of the power spectrum.

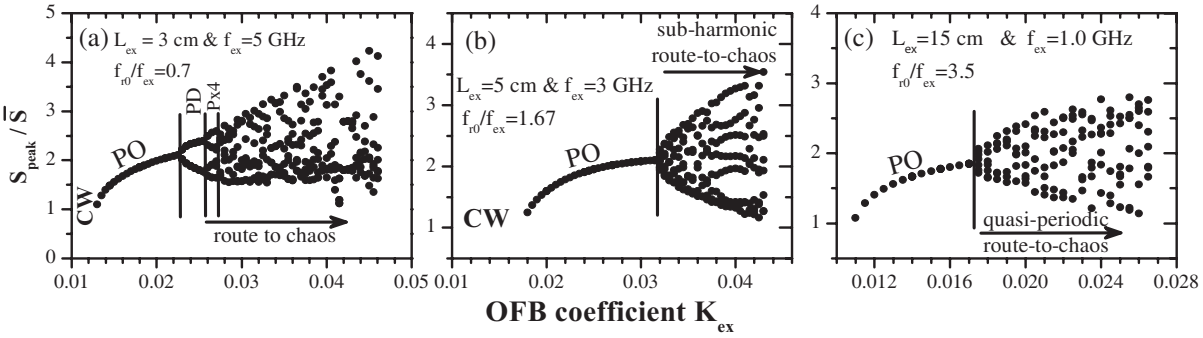

Figure 1: Bifurcation diagram showing the relevant route-to-chaos when (a) $f_{ex} = 0.7$ (PD), (b) $f_{ex} = 1.67$ (SH), and (c) $f_{ex} = 3.5$ (QP).

3.2. Period-doubling Route-to-chaos when $f_{r0}/f_{ex} < 1$

Figure 2 plots typical examples of the power spectra characterizing the PD route of Fig. 1(a). Fig. 2(a) corresponds to PO at the Hopf-bifurcation point ($K_{ex} = 0.013$). The spectrum is characterized by frequency $f_{po(H)} = 3.31\,\text{GHz}$. Fig. 2(b) shows the case that the nonlinearity of the laser under this short-delay OFB induces PD when $K_{ex} = 0.025$. The spectrum shows two peaks at $f_{op} = 3.26\,\text{GHz}$ and its half-harmonic $f_{po}/2$, which correspond to two different peaks of $S(t)$ separated with period of $1/f_{po}$. Contrary to results of Kao et al. [4], $f_{po} \neq f_{po(H)}$; it is the frequency of the end point of the PO region. Fig. 2(c) shows the case that the system nonlinearity increases irregularities of $S(t)$ and attracts the PD into period multiplication (PM) by 4 when OFB is increased to $K_{ex} = 0.026$. The power spectrum shows four peaks at f_{po} and its sub-harmonics $f_{po}/4$, $f_{po}/2$, $3f_{po}/4$. Finally the chaos spectrum is seen in Fig. 2(d) when $K_{ex} = 0.039$.

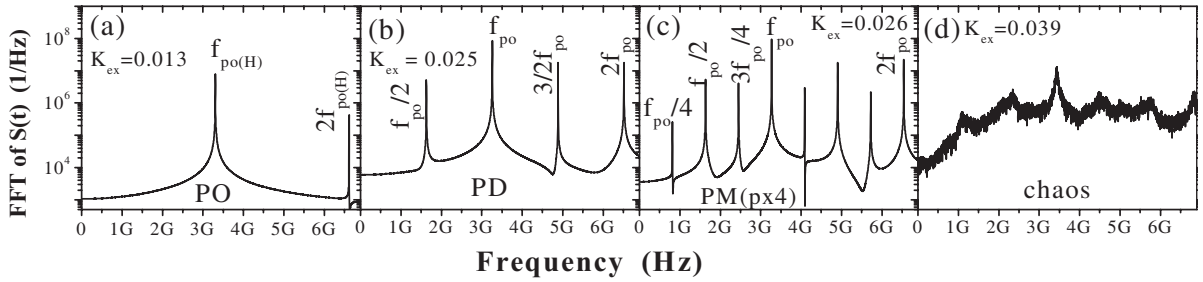

Figure 2: Power spectra when (a) $K_{ex} = 0.015$ (PO), (b) $K_{ex} = 0.025$ (PD), (c) $K_{ex} = 0.026$ (PM), and (d) $K_{ex} = 0.039$ (chaos).

3.3. Sub-harmonic (SH) Route-to-chaos when f_{r0}/f_{ex} is Slightly Higher than Unity

The laser dynamics characterizing the SH route-to-chaos in Fig. 1(b) are illustrated in Fig. 3. Fig. 3(a) plots the case of PO when $K_{ex} = 0.018$; the spectrum is characterized by frequency $f_{po} = 3.95\,\text{GHz} > f_{r0}$. Figs. 3(b) and (c) plot typical spectra of the relevant torus when $K_{ex} = 0.032$ and 0.041, respectively. The spectra are characterized by two locked frequencies. The first frequency

f_{po} corresponds to the end point of the PO region, and the second is its 5/8 sub-harmonic frequency. This frequency locking results in the beaten component $f_{po}/8$ of the spectrum. The beating sub-harmonics of these locked frequencies are more pronounced with the increase of OFB as found in Fig. 3(c). These results indicate that the transition to chaos becomes more irregular with the increase of the frequency ratio. Fig. 3(d) shows the chaos spectrum characterizing this length of external cavity. It corresponds to $K_{ex} = 0.043$. Spectral peaks can be seen at frequencies nearly equal to the locked frequencies.

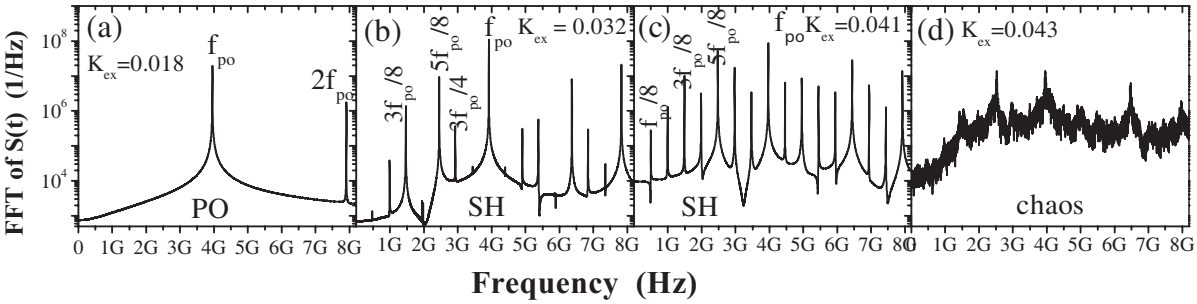

Figure 3: Power spectra when (a) $K_{ex} = 0.018$ (PO), (b) $K_{ex} = 0.041$ (SH), and (d) $K_{ex} = 0.043$ (chaos).

3.4. Quasi-periodic (QP) Route-to-chaos when $f_{r0}/f_{ex} > 1$

When $f_{r0}/f_{ex} \gg 1$, the route becomes QP with more than two frequencies. Typical power spectra of this type represented by Fig. 1(c) are illustrated in Figs. 4(a)–(c) when $K_{ex} = 0.011$, 0.0175 and 0.0264, respectively. Fig. 4(a) shows the spectrum of PO; it is characterized by frequency $f_{po} = 3.55\,\text{GHz}$, which is close to f_{r0}. Fig. 4(b) plots a typical spectrum of the relevant QP transition; it shows QP dynamics characterized by three frequencies. The first frequency is PO frequency $f_1 \approx f_{po}$, the second is $f_2 = 823\,\text{MHz}$, which is slightly lower than the compound-cavity frequency $f_c = 2(n_D L_D + n_{ex} L_{ex})/2 = 930\,\text{MHz}$, and the third is their frequency difference $f_1 - f_2$. Spectral peaks of frequency locking at $f_1 - f_2$ and $f_1 - 2f_2$ are clearly shown in the figure. Kao et al. [4] predicted QP transition, however the route is characterized only by f_{r0} and f_{ex} and is found when $f_{r0}/f_{ex} > 0.9$. This noisy transition originates from competition between resonances of the laser cavity and the compound cavity. Fig. 4(c) shows the corresponding chaos spectrum. Broad peaks are seen at frequencies nearly equal to f_1, f_2, and $f_1 - f_2$.

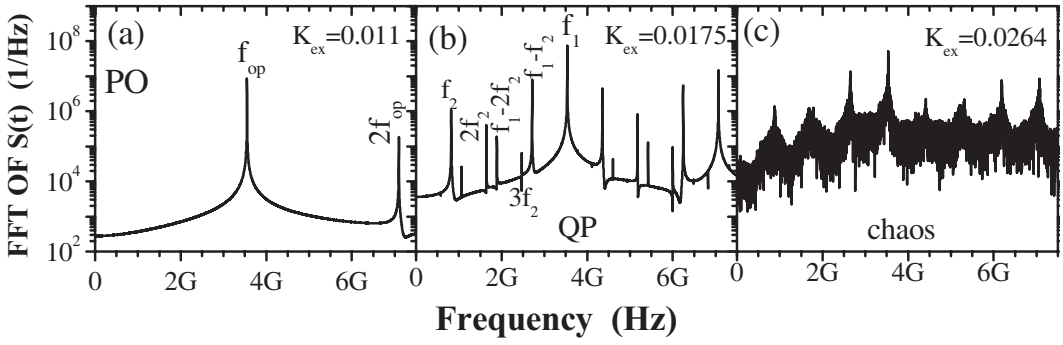

Figure 4: Power spectra when (a) $K_{ex} = 0.011$ (PO), (b) $K_{ex} = 0.0175$ (QP), and (d) $K_{ex} = 0.0264$ (chaos).

4. CONCLUSIONS

We characterized influence of the external-cavity length on the route-to-chaos of semiconductor lasers operating under OFB. The influence of length was included as the ratio of the relaxation frequency to the external-cavity resonance frequency. The route is PD when the ratio is less than unity. The route becomes SH with the PO frequency when the ratio is slightly higher than unity. When the ratio is far above unity, the route is QP characterized by the compound-cavity frequency, the relaxation frequency and their frequency difference.

REFERENCES

1. Ahmed, M. and M. Yamada, "Field fluctuations and spectral lineshape in semiconductor lasers subjected to optical feedback," *J. Appl. Phys.*, Vol. 95, No. 12, 7573–7583, 2004.
2. Tkach, R. W. and A. R. Chraplyvy, "Regimes of feedback effects in 1.5-µm distributed feedback lasers," *IEEE J. Lightwave Technol.*, Vol. 4, No. 11, 1655–1961, 1986.
3. Mork, J., B. Tromborg, and J. Mork, "Chaos in semiconductor lasers with optical feedback: Theory and experiment," *IEEE J. Quantum Electron.*, Vol. 28, No. 1, 93–108, 1992.
4. Kao, Y. H., N. M. Wang, and H. M. Chen, "Mode description of routes to chaos in external-cavity coupled semiconductor lasers," *IEEE J. Quantum Electron.*, Vol. 30, No. 8, 1732–1739, 1994.
5. Ryan, A. T., G. P. Agrawal, G. R. Gray, and E. C. Gage, "Optical-feedback-induced chaos and its control in multimode semiconductor lasers," *IEEE J. Quantum Electron.*, Vol. 30, No. 3, 668–678, 1994.
6. Ahmed, M., M. Yamada, and S. W. Z. Mahmoud, "Numerical analysis of optical feedback phenomenon and intensity noise of fibre-grating semiconductor lasers," *Int. J. Numer. Model.*, Vol. 20, 117–132, 2007.
7. Ahmed, M. and M. Yamada, "An infinite-order approach to gain calculation in injection semiconductor lasers," *J. Appl. Phys.*, Vol. 84, No. 6, 3004–3015, 1998.
8. Abdulrhmann, S., M. Ahmed, and M. Yamada, "New model of analysis of semiconductor laser dynamics under strong optical feedback in fiber communication systems," *SPIE*, Vol. 4986, 490–501, 2003.

Longitudinal Relaxation Time Measurement in MR with Transient-state Magnetization

E. Gescheidtova[1] and K. Bartusek[2]

[1]Department of Theoretical and Experimental Engineering
Faculty of Electrical Engineering and Communication, Brno University of Technology
Kolejni 2906/4, 612 00 Brno, Czech Republic
[2]Academy of Sciences of the Czech Republic, Institute of Scientific Instruments
Kralovopolska 147, 612 64 Brno, Czech Republic

Abstract— To measure the relaxation times T_1 of polarized gases an unusual method has been proposed that makes use of the transient state of the magnetization of the nuclei being measured. The transient state is the result of multiple excitations by RF pulses with a small flip angle and an appropriate repetition time T_R. The method was designed and experimentally tested for measuring the relaxation times T_1 of polarized gases with transient-state magnetization, based on measuring the MR signal levels after the termination of RF pulses. For a higher precision of determining T_1 two measurements with different repetition times were performed. The relaxation time was calculated from one or two measurements, using an optimization method. In the method described no precise calibration of the flip angle of RF pulses is necessary. The measuring precision achieved was better than 1%, and it depends on a precise determination of the magnitude of MR signal. The technique described will be used when measuring the properties of polarized gases or even liquids in porous materials.

1. INTRODUCTION

Inert gases, in particular polarized xenon (^{129}Xe), have recently been frequently used in diagnostic MR methods of examining the lungs, brain, blood vessels and other tissues. This is because xenon enables measuring MR images with high sensitivity. The period for which hyperpolarized ^{129}Xe remains polarized is a critical parameter and it must be shorter than the time in which the gas reaches the area being measured in the tissue and when the picture can be taken. Since the hyperpolarized magnetization decays with the longitudinal relaxation constant T_1, the knowledge of this parameter for ^{129}Xe in the tissue is very important. T_1 for xenon has been measured in conventional thermal equilibrium ^{129}Xe MR experiments, *in vitro* [1, 2] and recently using hyperpolarized ^{129}Xe, and *in vivo* [3–5].

An interesting mechanism for the loss of hyperpolarization is the so-called $\cos\alpha$ loss, where α is the magnetization flip angle introduced by the RF pulse. In conventional ^{1}H magnetic resonance, we are generally not concerned about this loss, because the magnetization is recovered to its thermal equilibrium value after the pulse. In new magnetic resonance experiments, however, each radiofrequency (RF) pulse causes a permanent loss of hyperpolarized magnetization; for example, after a 90° pulse, all the hyperpolarized magnetization is gone. The losses mentioned above are the reason why relaxation time T_1 is measured in one excitation or with a minimum number of new measurements.

2. METHOD

For our proposed method to be measured with sufficient accuracy it is necessary to fulfill two prerequisites. The nuclei of the sample being measured must be excited by a series of regularly repeated RF pulses with identical flip angles α and with identical repetition time T_R. The other important prerequisite of the method is a short spin-spin relaxation time T_2 of the medium being measured; the condition $T_2 << T_R$ must be fulfilled. The pulse sequence of the proposed method for a simple series of RF pulses is illustrated in Fig. 1.

In order to cancel the transversal component of magnetization, a short gradient pulse is applied prior to each new RF pulse. On the above assumptions, the longitudinal magnetization component $M_z(n)$ can at time τ after excitation by the n-th RF pulse ($n > 0$) be expressed by the relation [1]

$$M_{z(n)}(\tau) = M_{z(n)}(0) \cdot \mathrm{e}^{-\tau/T_1} + M_{\mathrm{eq}} \left(1 - \mathrm{e}^{-\tau/T_1}\right), \tag{1}$$

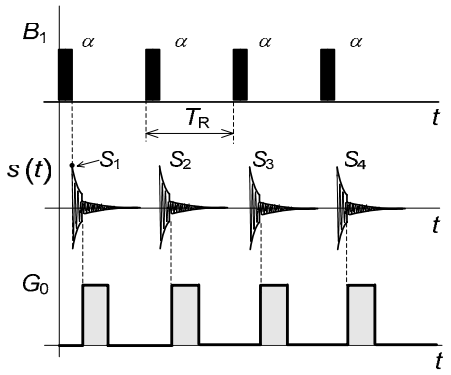

Figure 1: The pulse sequence of the proposed method.

where M_{eq} is the magnetization of nuclei in thermal equilibrium. For zero transversal magnetization and a negligible RF pulse length the RF pulse with flip angle α will excite transversal magnetization

$$M_{xy(n)}(0) = M_{z(n-1)}\left(T_R\right) \sin\alpha, \tag{2}$$

and change the longitudinal magnetization to

$$M_{z(n)}(0) = M_{z(n-1)}\left(T_R\right) \cos\alpha. \tag{3}$$

Prior to each n-th RF pulse the initial longitudinal magnetization $M_{z(n-1)}(T_R)$ is, subsequent to the termination of RF pulse, determined by relation (3). Longitudinal magnetization before the $(n+1)$-th RF pulse is for $\tau = T_R$ expressed by relation (1). The n-th NMR signal being detected is equal to the magnitude of longitudinal magnetization flipped into transversal plane according to relation (2). Using iterative substitution in relations (1) to (3) the magnitude of detected MR signal after each RF pulse can be calculated:

$$M_{xy(n)}(0) = \left[M_0 \cdot \left(E_{1T_R} \cdot \cos\alpha\right)^{n-1} + M_{\text{eq}}\left(1 - E_{1T_R}\right) \frac{1 - \left(E_{1T_R} \cdot \cos\alpha\right)^{n-1}}{1 - \left(E_{1T_R} \cdot \cos\alpha\right)}\right] \cdot \sin\alpha, \tag{4}$$

where $E_{1T_R} = \mathrm{e}^{-T_R/T_1}$ and M_0 is the equilibrium component of magnetization in the z axis. Using Equation (4) the flip angle α and the relaxation time T_1 can be calculated. It is necessary to know the first three levels of MR signal at the end of RF pulses, and the repetition time T_R. Rewriting Equation (4) for these conditions we obtain relations for expressing the flip angle α and the relaxation time T_1

$$\alpha = \arccos \frac{M_{xy(3)}(0) - M_{xy(2)}(0)}{M_{xy(3)}(0) - M_{xy(2)}(0) - \left[M_{xy(2)}(0) - M_{xy(1)}(0)\right]^2 / M_{xy(1)}(0)}, \tag{5}$$

$$T_1 = \frac{-T_R}{\ln \dfrac{M_{xy(3)}(0) \cdot M_{xy(1)}(0) - M_{xy(2)}(0) \cdot M_{xy(1)}(0) - \left[M_{xy(2)}(0) - M_{xy(1)}(0)\right]^2}{M_{xy(1)}(0) \cdot \left[M_{xy(2)}(0) - M_{xy(1)}(0)\right]}}. \tag{6}$$

In a real MR experiment it is something of a problem to ensure a high precision of determining the levels of MR signals after the end of RF pulses. To increase the precision of determining α and T_1 it is of advantage to measure the magnitude of MR signal after the end of n RF pulses (n is $3 \div 5$) and to repeat the measurement for m different values of repetition time TR (m is $3 \div 5$). The measurement will yield a matrix of the magnitudes of MR signal. Matrix equation with three unknown variables (M_0, α, and T_R) is solved using an optimization method, and the minimum difference between the measured and the theoretically calculated values is sought.

3. EXPERIMENTAL VERIFICATION

The proposed method was experimentally verified on a 4.7 T/120 mm MR scanner and an actively shielded gradient system in the Institute of Scientific Instruments AS CR by measuring the longitudinal relaxation time T_1. The sample to be measured was a glass flask of 38 mm in diameter,

filled with deionized water with nickel sulphate. Using the Inversion Recovery (IR) method the relaxation time $T_{\mathrm{IV}} = 331\,\mathrm{ms}$ was established for a temperature of 20.1°C; we consider this value the true value of time T_1. The relaxation time T_2 was measured using the Spin-Echo (SE) method and it is $T_2 = 150\,\mathrm{ms}$.

Applying the pulse sequence shown in Fig. 1 with gradient pulses of 20 mT/m level and 1 ms length the maximum values of MR signals S_1 to S_4 were measured after the first four RF pulses. The measurement was performed with different repetition times T_R set to 50, 100, 150 and 250 ms. A large set of measured data was used to calculate α and T_1 using relations (5) and (6) and the optimization method. Only a small number of measurements (one to two) can be used in an actual case. The length of the 90° flip pulse was determined from the dependence of the maximum magnitude of MR signal after the first RF pulse S_1 on the RF pulse duration, and it is $t_{90} = 165\,\mu\mathrm{s}$. The actual values of flip angle α_{A} in have been calculated from the RF pulse duration. By calculating from relations (5) and (6) for the maximum values of MR signal after the first three RF pulses S_1, S_2, and S_3 of length t_{RF} the relaxation time T_1 and its relative error with respect to the value $T_{\mathrm{IV}} = 331\,\mathrm{ms}$ can be determined for a chosen value of time T_R. It follows from obtained resuts that the error of T_1 determination will be less than 5% for flip angles ranging from 80° to 104° and for repetition time $T_1 > T_R > (T_1/2)$.

To determine time T_1 with a higher precision it is necessary to use several values measured and to approximate them or to find, using a suitable optimization algorithm, their minimum deviation from the theoretical value. The dependence of the magnitude of amplitudes S_n detected after RF pulses on times T_R (50, 100, 150, and 250 ms) and on the number of RF pulses n forms an area illustrated in Fig. 2(b). A similar area is formed by the theoretical values calculated according to relation (4) for chosen parameters α and T_1 (Fig. 2(a)). The aim of the optimization process is to seek such parameters α and T_1 for which the difference in the two areas is minimal. The waveform or relative error for $\alpha = 56.8°$, $T_1 = 331\,\mathrm{ms}$ and $M_0 = 5271$ is given in Fig. 2(c). The flip angles α_{A} are considered reference angles while the angles α_{M} are angles calculated from the values measured.

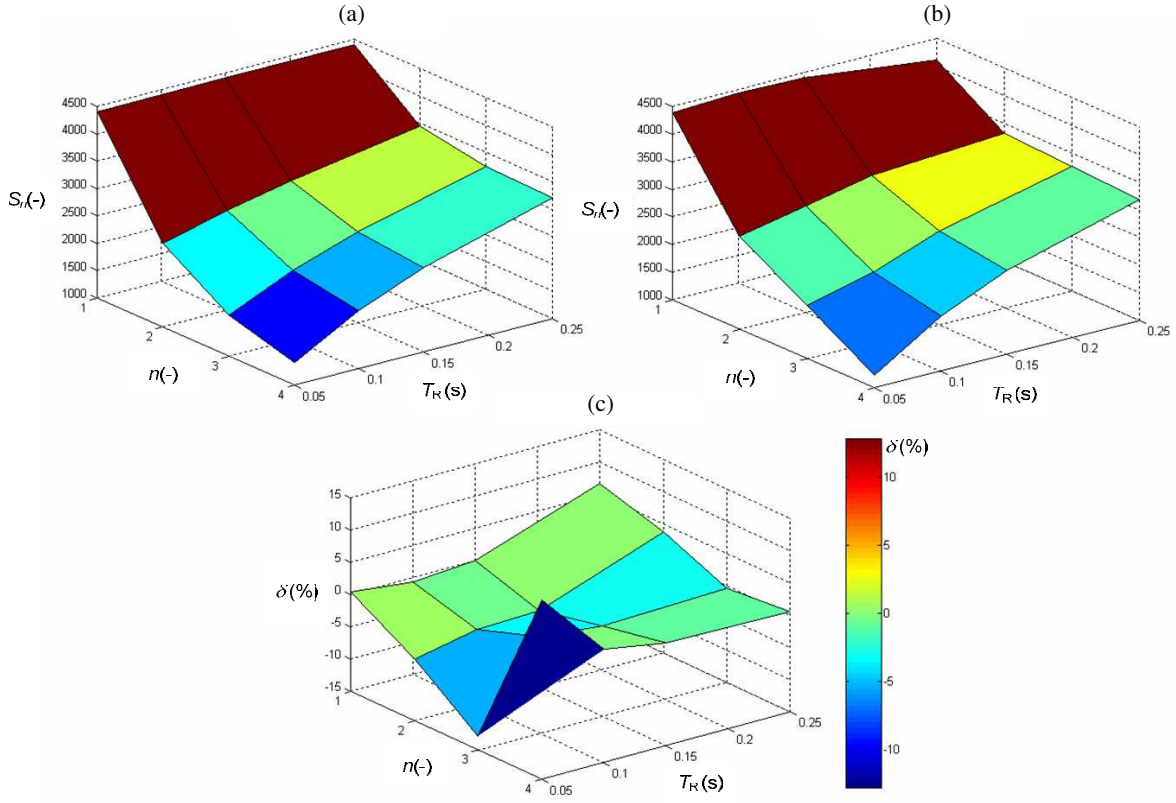

Figure 2: Dependence of magnitudes of amplitudes S_n detected after RF pulses on time T_R and on the number of RF pulses n for $\alpha = 56.8°$, $T_1 = 331\,\mathrm{ms}$, and $M_0 = 5271$, (a) theoretical values, (b) values measured, (c) relative errors.

Errors in calculating relaxation time T_1 from a greater number of values measured exhibit lower values for flip angles from 50° to 100°. Fig. 3 gives the dependence of the established relaxation time T_1 on flip angle α. The optimum range of flip angles is shown in grey color. When measuring the relaxation times of polarized gases it is of advantage to measure with one series of n RF pulses with a chosen flip angle α and with the same repetition time T_R. The reason is the loss of polarization subsequent to each RF pulse. After one experiment, i.e., after the application of n RF pulses, the polarization drops to zero, and it is necessary to polarize the gas again before the next experiment. For this reason the relaxation time T_1 and its relative errors (with respect to $T_{1V} = 331\,\text{ms}$) were calculated from the measured values $S_n (n = 1, \ldots, 4)$ using the optimization algorithm. To achieve a higher degree of accuracy of determining T_1 it is necessary to use two experiments with flip angles α in the range from 80° to 115° and repetition time $T_1 > T_R > (T_1/2)$. The relative error of measurement (with respect to $T_{1V} = 331\,\text{ms}$) will then be less than 1%.

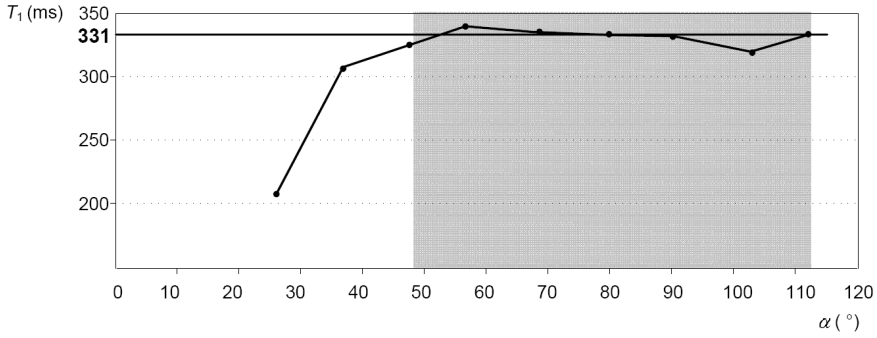

Figure 3: Dependence of relaxation time T_1 on flip angle α.

4. CONCLUSIONS

An interesting method was proposed for measuring relaxation times T_1 with transient-state magnetization. The method is appropriate for the measurement of polarized gases. The method consists in measuring the magnitude of RF signal after the end of a train of RF pulses with repetition time T_R. To make the measurement more accurate it is good to carry out two measurements and by processing the data with the aid of the optimization method to determine the relaxation time. The method described does not require a precise calibration of the employed flip angle of RF pulses. In the case of long spin-spin relaxation times T_2 gradient pulses are used to shorten the MR signal. The measurement error is less than 1% and it depends on a precise determination of the magnitude of MR signal. The technique described will be used in the measurement of the properties of polarized gases or also liquids in porous materials.

ACKNOWLEDGMENT

This work was supported within the framework of project No. 102/07/0389 of the Grant Agency of the Czech Republic and research plan MSM 0021630516.

REFERENCES

1. Albert, M. S., C. S. Springer, and A. Wishnia, *Abstracts of the Society of Magnetic Resonance in Medicine*, *11th Annual Meeting*, 2104, New York, USA, 1992.
2. Albert, M. S., C. S. Springer, and A. Wishnia, *Abstracts of the Society of Magnetic Resonance in Medicine*, *11th Annual Meeting*, 4710, New York, USA, 1992.
3. Wagshul, M. E., T. M. Button, H. F. Li, Z. Liang, C. S. Springer, K. Zhong, and A. Whishnia, *Magn. Reson. Med.*, Vol. 36, 183–191, 1996.
4. Albert, M. S., C. H. Tseng, D. Williamson, E. R. Oteiza, R. L. Walsworth, B. Kraft, D. Kacher, B. L. Holman, and F. A. Jolesez, *J. Magn. Reson.*, Vol. 111, 300–304, 1996.
5. Sakai, K., A. M. Bilek, E. R. Oteiza, R. L. Walsworth, D. Balamore, F. A. Jolesez, and M. S. Albert, *J. Magn. Reson.*, Vol. 111, 300–304, 1996.

Anti-interference Design of Quasi-resonant Tank for Magnetic Induction Heating System

Cheng-Chi Tai and Ming-Kun Cheng

Department of Electrical Engineering, National Cheng Kung University, Tainan 70101, Taiwan

Abstract— In the paper, we present the design of a quasi-resonant tank for magnetic induction heating system, also discuss some anti-interference applications using a half-bridge inverter with optimal construction of the filter circuits and the decoupling capacitance. The paper also presents a method for the design of filter and the insertion of decoupling capacitor. By using this method, the problems of high-frequency voltage interference can be significantly reduced. Experiments indicated that the magnetic induction heating system can satisfy well the heating requirement of the magnetic nanoparticle (MNP) with a resonant frequency of approximately 220 kHz.

1. INTRODUCTION

The electromagnetic inducing of heat has been extensively studied for the treatment of hyperthermia, wherein case deposited magnetic particles are used to locally heat human tissues. Application of magnetic materials for hyperthermia of biological tissue has been known, in principle, for more than four decades [1]. Many empirical works were done in order to confirm a therapeutic effect on several types of tumors by performing experiments with animals [2] or using cancerous cell cultures [3], and poor AC magnetic field parameters [3]. At least two full-sized human prototypes have been built by magnetic fluid hyperthermia (MFH) and will be used shortly for the first clinical trials of hyperthermia [3]. But, these systems are too bulky and with poor heating efficiency. Therefore, we want to develop a more compact, stable and efficient heating applicator.

Electromagnetic interference (EMI) is a relevant problem in the electronic system [4–8]. In fact, devices have to meet industry standards concerned with conducted interference. To avoid disturbing the half-bridge series-resonated (HBSR) inverter, the oscillation circuit and the digital signal for MNP heating system, which make electromagnetic compatibility (EMC) design for the MNP very challenge. Most of the current EMI designs use experimental trial-and-error methods, which are time consuming and difficult for system stability. In order to optimize EMC performance, the EMI characteristics of power lines need to be analyzed at an early design stage for a system-stable and time-efficient design approach. Common-mode (CM) and differential-mode (DM) conducted EMI noises are related to the circuit and circuit layout, the high dv/dt and di/dt slew rates in the power rails [9]. Therefore, for successful EMI prediction and stable system, the correctness-insertion of the power line filter and the decoupling capacitance circuit is necessary.

2. BASIC MAGNETIC NANOPARTICLE HEATING SYSTEM

The essential elements of the MNP heating system using power-MOSFET is depicted in Fig. 1, where the dashed-line block is the place where a proper conducted EMI filter will be inserted. The EMI filter with the capacitance (C_1 and C_2) and the inductance (L_3) reduces conducted EMI to input source. The full-wave diode bridge rectifies the AC commercial power and produces a DC voltage of HBRS power supply, which is then smoothed by the capacitance (C_3 and C_4) and the inductance (L_2). Because of the variable switching frequency control of CD40106, IC gate driver and the power-MOSFET, the conducted EMI problem in this MNP heating system is serious, and it is a challenge to design a proper filter to reduce the conducted EMI noise to a required low level. The main specifications of this MNP heating system are: input voltage 110 V, the operating frequency 220 kHz, and output DC voltage 154 V.

In Fig. 1, HBRS tank of power-MOSFETs (Q_1, Q_2) and capacitance (C_{S1}, C_{S2}) are connected in a full bridge configuration and switched at 220 kHz to convert the DC to high frequency AC. The main source of the EMI noise in the MNP heating system is the inductance of the switch Q_1 and Q_2 (IRFP 460) interconnections shown in Fig. 1 [10]. When these power-MOS FET are operating as a switch in the HBRS tank, the high frequency drain and source voltage swing in power-MOS FET causes charging and discharging of the FET parasitic inductance, resulting in EMI noise currents flowing out through power wire and returning via the ground wire. Those parts of the HBRS tank which are mounted on its chassis via parasitic inductance and have an AC wave form flowing through them also contribute EMI noise.

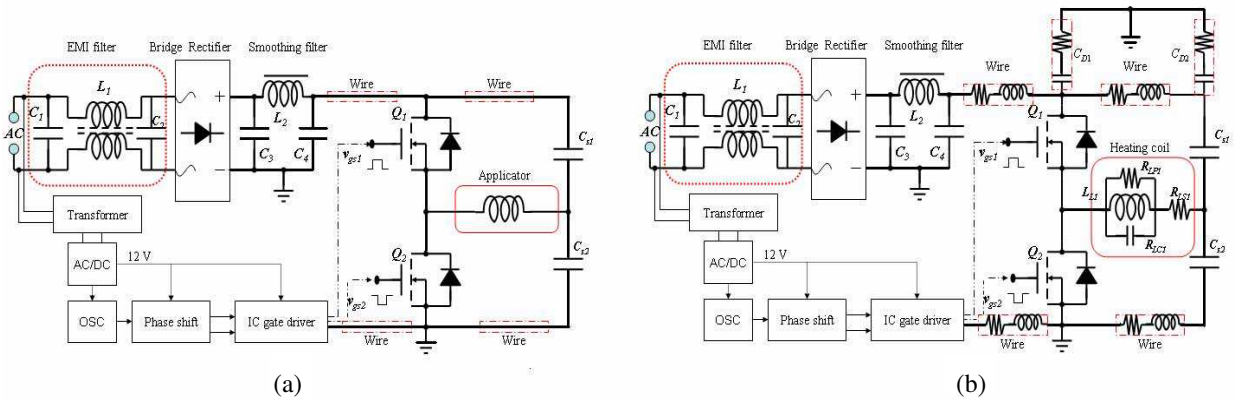

Figure 1: Circuit diagram of the MNP heating system used power-MOSFET. (a) The dashed-line block is the place the EMI filter and the wire, (b) the parasitic inductance in the real-case of HBRS tank, the wire model and the decoupling capacitance.

In order to maintain a stable voltage supply during the fast transients of HBRS tank, the power lines with the high frequency and the external decoupling capacitors are required. Fig. 1(b) shows a power distribution model for the power supply and the HBRS tank. The decoupling capacitors (C_{d1}, C_{d2}) are used to minimize ringing, and the decoupling capacitors are spread evenly across the circuit to maintain stable power distribution.

3. NOISE REDUCTION

Because of the high-voltage HBSR inverter, most designs use high-speed power MOSFETs as the inverter switch to ensure cost effectiveness and efficient operation. However, these fast switching inverters generate high voltage slew rates (dv/dt), high current peak rates (di/dt), and high common-mode voltage at HBSR, causing some serious EMI problems [6, 7]. The main path of the conducted EMI is the high-frequency switching noise produced by the HBSR tank feeding back through the power inverter circuit, and back to the AC source. One of the most popular solutions of the EMI filter is shown in Fig. 2(a), where L_1 is the common mode choke which provides both the common mode filtering by its leakage inductance and the differential mode filtering by its primary inductance. L_1, C_1, and C_2 form the differential filtering network that would filter out noise between the supply lines. The EMI filter operates according to a principle whereby inductance connected directly in series with the line has virtually no affect on the noise current at low frequencies. But at high frequencies, it demonstrates a high interruptive effect with respect to the noise current. The two capacitors (C_1, and C_2) connected in parallel with the line are used as a side path to return high frequency back to the power line. The result is that normal mode noise passes through the capacitor and is shunted back to the other line.

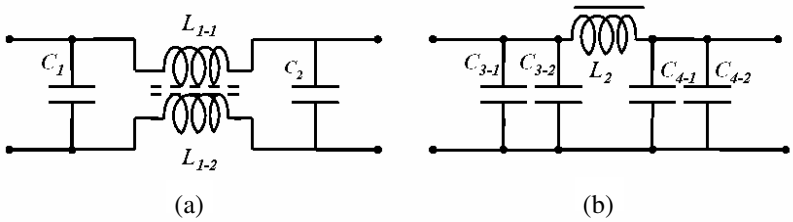

Figure 2: (a) EMI filter and (b) smoothing filter.

In the power supply circuit, the capacitor acts as a charge storage reservoir. The smoothing filter is performed by a large value electrolytic capacitor connected across the DC supply to act as a reservoir, and supplying current to the output when the varying DC voltage from the rectifier is falling. In Fig. 2(b) shows the unsmoothed varying DC and the smoothed DC. The capacitor charged quickly approach the peak of the varying DC, and then discharged when it supplies current to the output. The smoothing filter that consists of L_2, C_{3-1}, C_{3-2}, C_{4-1}, and C_{4-2} is to filter

out noise between the supply lines. The smoothing filter operates according to a principle whereby inductance connected directly in series with the line has virtually no affect on the noise current at low frequencies, but at high frequencies it demonstrates a high interruptive effect with respect to the noise current. The four capacitors (C_{3-1}, C_{3-2}, C_{4-1}, and C_{4-2}) connected in parallel with the line is used as a side path to return high-frequency components back to the power line. The bigger value of C_{3-1} and C_{4-1} reduce the switching frequency voltage ripple of MHz range. The smaller value of C_{3-2} and C_{4-2} reduce the switching frequency voltage ripple of MHz range. The result is that the normal mode noise passes through the capacitor and is shunted back to the other line.

The decoupling of a high-frequency HBRS tank is paramount to power delivery and minimization of emission. In Fig. 1(b), the decoupling capacitances amount to creating low AC impedance between power line and ground line. The control strategy employs a current loop of decoupling capacitance (C_{C1} and C_{C2}) with a switching noise of HBRS tank.

In the power distribution model shown in Fig. 1(b), C_{C1} and C_{C2} represents decoupling capacitors for the power supply. The decoupling capacitors supply current to the HBRS tank during sudden excessive current demands that cannot be supplied by the smoothing filter. The required C_{C1} or C_{C2} can be calculated by the following equation:

$$C \geq \frac{\Delta I}{\Delta V}\Delta t \tag{1}$$

where ΔI is the maximum processor current transient, ΔV is the tolerance times the nominal processor voltage, and Δt is the voltage regulator response time.

The decoupling capacitors (C_{C1} and C_{C2}) should be located as close to the resonant tank power and ground pins as possible, which to minimize resistance and inductance in the lead length. When possible, use wires to connect capacitors directly to the resonant tanks power and ground pins. In most cases, the decoupling capacitors can be placed in the MOSFET on the same side of the resonant tank (top side) or the opposite side (bottom side).

4. RESULTS AND DISCUSSION

The hard-switching HBSR tank is designed for MNP heating system applications. The circuit parameters for both HBSR tanks are: input AC voltage V_{AC} = 110 V, output DC voltage of bridge rectifier V_{DC} = 154 V, duty cycle = 50%, switching frequency = 220 kHz, inductance of applicator 56.2 µH. Fig. 3 shows the diagram of the implemented MNP heating system, which shows a suggested component placement for the decoupling capacitors. The wires connected to the capacitor should be short and wide. The measured results for the driver circuit and applicator waveform are presented in Fig. 4. It is shown that magnetic induction heating system can satisfy well with the heating requirement of the MNP with a resonant frequency of approximately 220 kHz.

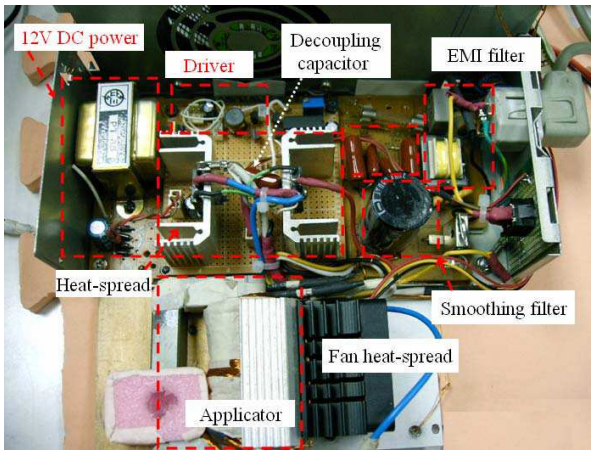

Figure 3: The diagram of the implemented prototype.

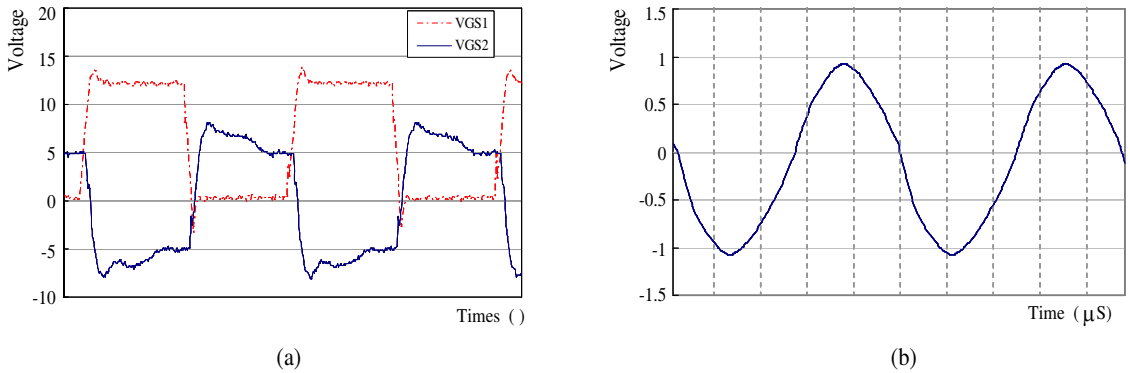

Figure 4: Measured results of the driver circuit and the applicator waveform.

5. CONCLUSIONS

The conducted EMI filter and decoupling capacitance can be integrated into a MNP heating system. The aim of this research is to implement the MNP heating system and improve its conducted emission. The power line filter and decoupling capacitance are used to reduce the conducted emission of MNP heating system.

ACKNOWLEDGMENT

This research was supported by the grant from National Science Council, Taiwan (NSC 95-2221-E-006-016). Also, this work made use of Shared Facilities supported by the Program of Top 100 Universities Advancement, Ministry of Education, Taiwan.

REFERENCES

1. Shang, Y. H., W. Finlay, and W. Moussa, "Thermally induced fiber deformation using high frequency magnetic field," *Proc. of the 2004 Int'l Conference on MEMS, NANO and Smart Systems*, 1–3, 2005.
2. Lisa, B. P. and J. O. Blanchette, "Nanoparticle and targeted systems for cancer therapy," *Advanced Drug Delivery Reviews*, Vol. 56, 1649–1659, 2004.
3. Jordan, A., R. Scholz, P. Wust, H. Fahling, and F. Roland, "Magnetic fluid hyperthermia (MFH): Cancer treatment with AC magnetic field induced excitation of biocompatible superparamagnetic nanoparticles," *J. of Magnetism and Magnetic Materials*, Vol. 201, No. 1–3, 413–419, 1999.
4. Azaro, R., L. Ioratti, M. Martinelli, and A. Massa, "Automatic design and optimisation of EMI filter using commercially-available components," *Electronic Letters*, Vol. 43, No. 6, 2007.
5. Shih, F. Y., D. Y. Chen, Y. P. Wu, and Y. T. Chen, "A procedure for designing EMI filters for AC line applications," *IEEE Trans. on Power Electronics*, Vol. 11, 170–181, 1996.
6. Lofti, A. W. and F. C. Lee, "A high frequency model for litz wire for switch-mode magnetics," *IEEE Industry Applications Conference Twenty-8th IAS Annual Meeting*, 1169–1175, Toronto, Ont., Canada, Oct. 1993.
7. Ferreira, J. A., "Analytical computation of ac resistance of round and rectangular litz wire windings," *IEE Proc.-B Electric Power Applications*, Vol. 139, No. 1, 21–25, 1992.
8. Kazimiercruk, M. K. and D. Czarkowski, *Resonant Power Converters*, Wiley, New York, 1995.
9. Guo, T., D. Y. Chen, and F. C. Lee, "Separation of common-mode and differential-mode conducted EMI noise," *IEEE Trans. on Power Electronics*, Vol. 1, No. 3, 480–488, 1996.
10. Tai, C.-C. and M.-K. Chen, "A Compact half-bridge induction heating system for magnetic nanoparticle thermotherapy applications," *Biomedical Engineering: Applications, Basis and Communications (BME)*, Vol. 19, No. 1, 27–35, 2007.

The Design of a Half-bridge Series-resonant Type Heating System for Magnetic Nanoparticle Thermotherapy

Cheng-Chi Tai and Chien-Chang Chen

Department of Electrical Engineering, National Cheng Kung University, Tainan, Taiwan

Abstract— Application of magnetic materials for hyperthermia of biological tissue has been known, in principle, for more than four decades. Many empirical works were done in order to confirm a therapeutic effect on several types of tumors by performing experiments with animals or using cancerous cell cultures. The main idea of magnetic nanoparticle (MNP) thermotherapy is to utilize 7- to 50-nm diameter of ferric oxide (Fe_3O_4) particles which are heated up to 42°C under AC magnetic field for cancer therapy applications. In order to achieve the goal of killing cancer cells using the AC magnetic field, we designed a heating system to generate magnetic field which can be focused and frequency adjustable. This study adopts the half-bridge series-resonant type circuit as the core scheme of the heating system, and utilizes the frequency-adjustable design to conduct the heating experiment. The experiment results show that the designed coil and the heating system can warm up the magnetic nanoparticle 6°C in 32 minutes.

1. INTRODUCTION

Electromagnetic inducing of heat has been extensively studied for the treatment of hyperthermia, wherein case deposited magnetic particles are used to locally heat human tissues. The basic idea of hyperthermia is raising the tissue temperature up to between 41.5 and 46°C to kill malignant cells while preserving normal cells [1]. Many empirical works were done in order to confirm the therapeutic effect on several types of tumors by performing experiments with animals [2] or using cancerous cell cultures, and poor AC magnetic field parameters [3]. At least two full-sized human prototypes have been built based on magnetic fluid hyperthermia (MFH) and used shortly for the first clinical trials of hyperthermia [3]. But, these systems are too bulky and with poor heating efficiency. Therefore, we want to develop a more compact, stable and efficient heating applicator. Our research is focused on heating system design and the improvement of applicator [4, 5].

2. SYSTEMATIC CIRCUIT STRUCTURE

The circuit diagram of the heating system is shown in Fig. 1, which includes a rectification circuit, a converter circuit, gates driver, a half-bridge MOSFET inverter and an applicator. The halfCbridge series-resonance circuit [6] basically has two bi-directional switches of power MOSFET (Q_1 and Q_2) and a resonant circuit. Each power switch (S_1 or S_2) is composed of a switch of MOSFET (Q_1 or Q_2), as shown in Fig. 2. According to the combined form of the MOSFETs and the resonant circuit, it can commonly be classified into the series resonant topology, parallel resonant topology, and a combination series-parallel resonant topology. The power MOSFET is focused on turn-on resistance, reducing conduction losses, operating junction temperatures, and switching speeds. This proposed circuit is adopted to avoid introducing any DC voltage upon the applicator during operation. The power MOSFET switches, Q_1 and Q_2, of the HBSR inverter are gated by two complementary signals, v_{gs1} and v_{gs2}, respectively. Each switch (S_1 or S_2) is composed of a switch of power MOSFET Q_1 (Q_2) and its intrinsic anti-parallel diode D_1 (D_2). To prevent cross condition, the waveforms of v_{gs1} and v_{gs2} should be non-overlapping and have a short dead time. AC voltage supply is given in input voltage 110 V_{rms} and output voltage. By symmetrically driving two power MOSFET switches, the output of the HBSR inverter is a sine-wave voltage with a DC term of $V_{dc}/2$ on the applicator circuit. Thus, a DC-blocking capacitor (C_{S1} and C_{S2}) must be used for blocking the DC term of the square-wave. On the other hand, the HBSR inverter outputs a square-wave voltage without any DC term on the applicator circuit. Hence, there is no DC component across the applicator to increase the current during resonant [7, 8].

3. COIL MODELING AND HEATING SYSTEM

The applicator consisted of two parts, wire coil and ferrite core. Although the structure of the electromagnetic coil seems quite simple, its high frequency and high current mechanism are very complicated. Fortunately, when the applicator operated in high frequency, it has been demonstrated

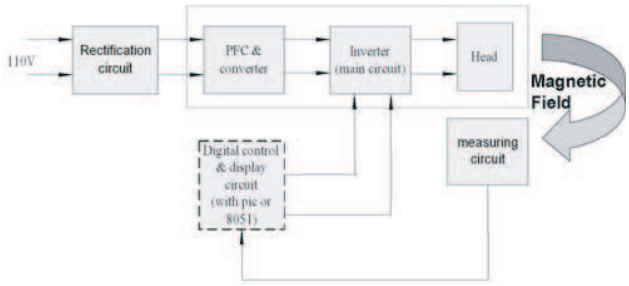

Figure 1: System structure.

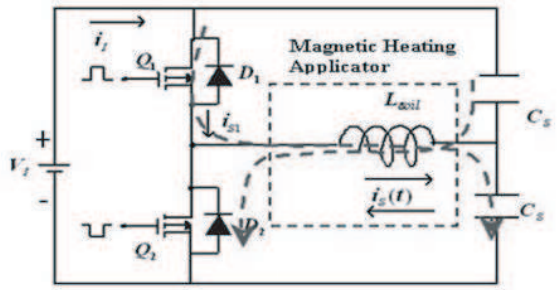

Figure 2: Half-bridge series-resonant type circuit.

to be approximately an open circuit, and the coil characteristic is not sensitive as verified from the impedance analyzer (Agilent 4294 A). Fig. 3 shows the comparison of coil models from measurement and simulation (impedance and phase). The operation characteristics of the high-frequency heating system can be calculated by using the applicator model shown in Fig. 4. The measured parameter values of the coil model are listed in Table 1. The E-type geometry structure of the applicator and the simulated distribution of magnetic field are shown in Figs. 5 and 6. The MNP heating system is shown in Fig. 7.

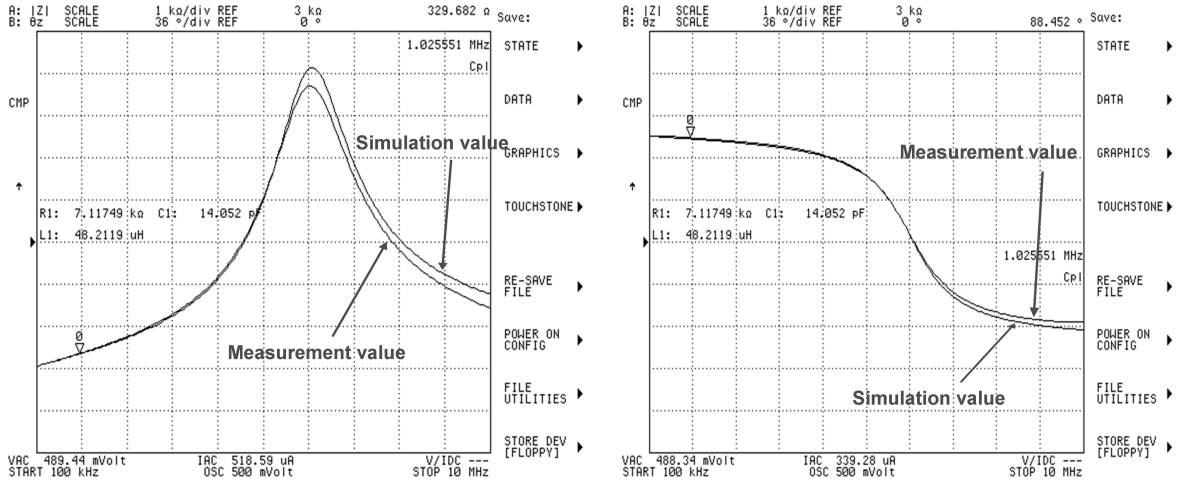

Figure 3: Comparison of coil models from measurement and simulation: (a) impedance and (b) phase.

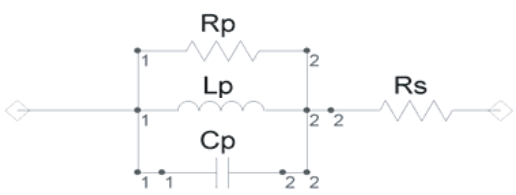

Figure 4: Coil model.

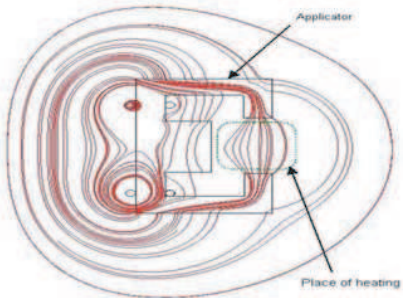

Figure 5: The geometry structure of the applicator and the simulated distribution of magnetic field.

4. EXPERIMENT RESULTS AND DISCUSSION

The induced electromagnetic heating effect in magnetic materials is mainly attributed to three physical phenomena, namely, hysteresis, eddy current, and Néel or Brownian relaxation losses.

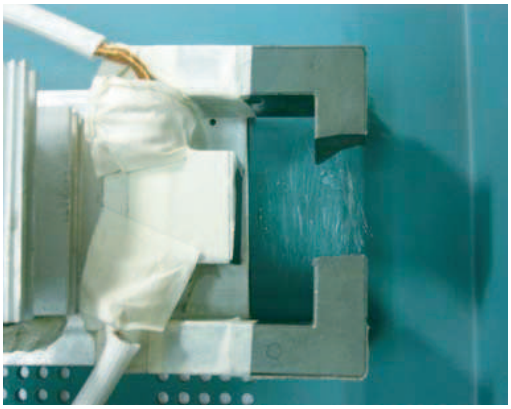

Figure 6: The magnetic coil of the applicator.

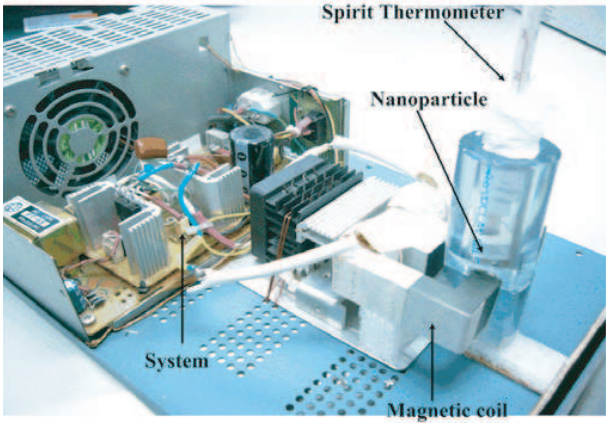

Figure 7: The MNP heating system.

Table 1: Parameters of the coil model.

Parameter Name	Measurement Value
Lp	$48.3804\,\mu H$
Cp	14.1527 pF
Rp	7.08915 kΩ
Rs	0.02 Ω

The total power loss in a conductor media is [9]:

$$P_{total} = \left(\beta_h \mu + \beta_e \frac{\mu^2 f}{\rho} + \beta_{nb} \frac{2\pi f \tau}{1 + (2\pi f \tau)^2}\right) f H^2, \tag{1}$$

where β_h, β_2 and β_{nb} are the geometry constant coefficients of hysteresis, eddy current, and Néel or Brownian relaxation, μ is the permeability of the magnetic material, H is the amplitude of the applied AC magnetic field, ρ is electrical resistivity, τ is relaxation time and is exponentially size dependent. However, heating of MNP is inherently due to hysteresis losses and Brownian relaxation losses [10, 11]. In fact, the experiment results of many studies revealed that the heating power loss is affected by the strength of magnetic field and the characters of the material, such as particle

Table 2: SAR experiment results.

Experiment	Concentration (Fe/mL)	Amount (mL)	Temperature Difference ($\Delta T/\Delta t$)	SAR values (W/g)
A	0.02887	Fe_3O_4 (2.0 mL)	4.9E-3	0.653
B	0.0144	Fe_3O_4 (1.0 mL) + Water(1.0 mL)	2.6E-3	0.694
C	0.02887	Fe_3O_4 (1.5 mL)	5.2E-3	0.693
D	0.02887	Fe_3O_4 (1.5 mL)	5.1E-3	0.679
E	0.02887	Fe_3O_4 (1.5 mL)	4.4E-3	0.586

size, size variation, and magnetization saturation [12]:

$$SAR = C\frac{\Delta T}{\Delta t}\frac{1}{m_{Fe}}, \tag{2}$$

where C is the specific heat of sample, $\Delta T/\Delta t$ is temperature gradient. The experimental values of SARs for five different cases are shown in Table 2.

In experiments A and B (Fig. 8), the results show absolute heating temperature for different Fe_3O_4 concentration. Furthermore, the heating effects on nanoparticle (Fe_3O_4) are mainly attributed to three physical phenomena, as indicated in (1). The heating curves, C, D, and E, for different initial temperatures are shown in Fig. 9. The results show similar curves which agree with the expected physical characteristics.

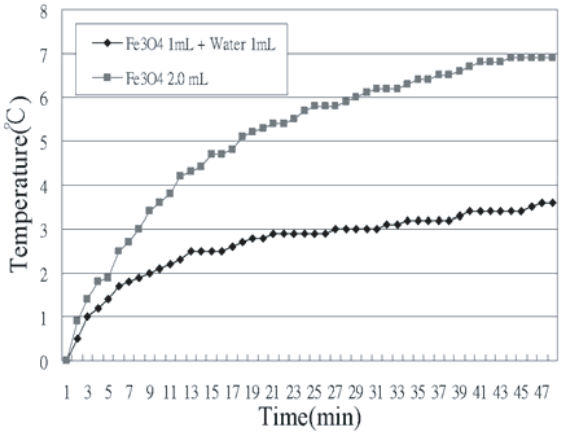

Figure 8: Experimental results for absolute heating temperature at different concentration.

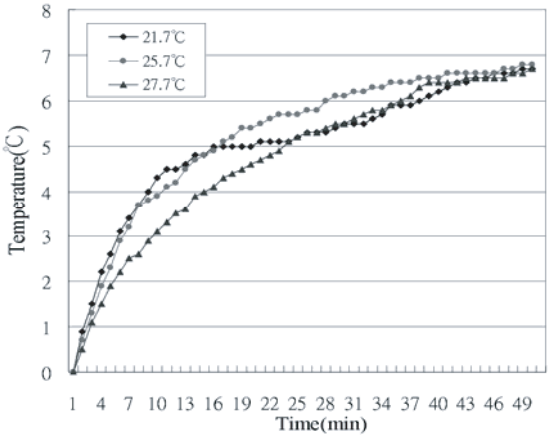

Figure 9: Experimental results for absolute heating temperature at different initial temperature.

5. CONCLUSION

In this study, we have succeeded in using the half-bridge resonant methods with coil design using Litz wire to heat iron powder and magnetic nanoparticle. The results show that under different background temperature all the samples can be heated up to 42°C in AC magnetic field. There is an absolute temperature increased about 6°C in 32 minutes. We have achieved a substantial step to the final goal of killing cancer cells using the AC magnetic field and have attained the expected heating effect for the study.

ACKNOWLEDGMENT

This research was supported by the grant from National Science Council, Taiwan (NSC 95-2221-E-006-016). Also, this work made use of Shared Facilities supported by the Program of Top 100 Universities Advancement, Ministry of Education, Taiwan.

REFERENCES

1. Ferguson, S. D., J. A. Paulus, R. D. Tucker, S. A. Loening, J. B. Park, *J. of Applied Biomaterials*, 55–60, April, 1993.
2. Lisa, B. P. and J. O. Blanchette, "Nanoparticle and targeted systems for cancer therapy," *Advanced Drug Delivery Reviews*, Vol. 56, 1649–1659, 2004.
3. Jordan, A., R. Scholz, P. Wust, H. Fahling, and F. Roland, "Magnetic fluid hyperthermia (MFH): Cancer treatment with AC magnetic field induced excitation of biocompatible superparamagnetic nanoparticles," *J. of Magnetism and Magnetic Materials*, Vol. 201, Nos. 1–3, 413–419, 1999.
4. Tai, C.-C. and M.-K. Chen, "A compact half-bridge induction heating system for magnetic nanoparticle thermotherapy applications," *Biomedical Engineering — Applications, Basis, and Communication*, Vol. 19, No. 1., 27–35, 2007.

5. Chen, C.-C., C.-L. Chen, M.-K. Chen, and C.-C. Tai, "Experimental study on the heating characteristics of magnetic nanoparticles by an AC magnetic field for local hyperthermia," *International Symposium on Nano Science and Technology (2006-ISNST)*, Southern Taiwan University of Technology, Tainan, Taiwan.
6. Kazimierczuk, M. K. and D. Czarkowski, *Resonant Power Converter*, John Wiley & Sons, Inc, 1995.
7. Steigerwald, R. L., "A comparison of half-bridge resonant converter topologies," *IEEE Transactions on Power Electronic*, Vol. 3, No. 2, 174–182, April 1988.
8. Mohan, N., T. M. Undeland, and W. P. Robbins, *Power Electronics, Applications and Design*, John Wiley & Sons, Inc, 2nd Ed., 1995.
9. Hergt, R., "Physical limits of hyperthermia using magnetite fine particles," *IEEE Transactions on Magnetics*, Vol. 34, No. 5, 3745–3754, Sept. 1998.
10. Rosensweig, R. E., *Journal of Magnetism and Magnetic Materials*, Vol. 252, 370–374, 2002.
11. Mornet, S., S. Vasseur, F. Grasset, and E. Duguet, *Journal of Materials Chemistry*, Vol. 14, 2161–2175, 2004.
12. Ma, M., "Size dependence of specific power absorption of Fe_3O_4 particles in AC magnetic field," *Journal of Magnetism and Magnetic Material*, Vol. 268, No. 1, 33–39, Jan. 2004.

Fiber Grating Designing Method Based on Multi-subpopulation Competition Evolutionary Algorithm

Zhaoniu Huang[1, 2], **Songfen Liu**[3], **and Guiling Huang**[4]

[1]Guangxi Shipping School, Guangxi 530007, China
[2]Guilin University of Electronic Technology, Master's Degree of Engineering
[3]Department of Physics, Nankai University, Tianjin 300071, China
[4]Institute of Modern Optics, Nankai University, Tianjin 300071, China

Abstract— This paper presented a powerful method to synthesize the physical parameters of fiber Bragg grating numerically from chirp FBG reflection spectrum. The method is based on a Multi-subgroup competition evolutionary algorithm. The analysis curve of the gratings designed here shows the multi-subpopulation competition evolutionary algorithm is better than the single population evolutionary algorithm in the aspects of global optimization and convergence.

1. INTRODUCTION

With recent advances in fiber Bragg grating technology, it has become possible to fabricate complex gratings with different physical parameters such as index modulation profile, length of grating. Such gratings are useful for dispersion compensation, wavelength-division multiplexing, fiber lasers, and fiber sensors. The inverse problem is a classical problem in applied physics and engineering fields. An example of such a problem is to synthesize or reconstruct the physical parameters (such as length of grating L, grating period Λ, and difference in refractive indices Δn) of a fiber Bragg grating (FBG) structure from its reflectivity. Such research is most important for device design. Many synthesis methods have been proposed and achieved various degrees of success in recent years [1–6], such as the Fourier transform technique [1], the GLM method [2], time-frequency signal representations [3] and layer peeling techniques [3, 4], which have been shown to be effective in the design of some special FBG devices. But all these methods require information on both the amplitude and the phase of the FBG reflection coefficient. Other powerful synthesis methods are the optimization methods based on some global optimization techniques. Main school of evolutionary algorithms, Genetic algorithms (GA) [5] is the most widely used optimization methods. Although very powerful, for the solution of real-world applications it is often difficult to decide which of the available Evolutionary Algorithms are best suited and how the operators and parameters should be combined. In this paper, by using the Genetic and Evolutionary Algorithm Toolbox for Matlab (GEATbx) developed by Hartmut Pohlheim [7] and combining transfer matrix methods [8], We reconstruct the physical parameters of a FBG structure from its reflectivity based on a classical single population evolutionary algorithm and a multi-subpopulation competition evolutionary algorithm. The analysis curve of the gratings designed here shows a good agreement with the expected curve and the multi-subpopulation competition evolutionary algorithm is better than the single population evolutionary algorithm in the aspects of global optimization and convergence.

2. BASIC PRINCIPLE OF EVOLUTIONARY ALGORITHM

Evolutionary algorithms are stochastic search methods that mimic the metaphor of natural biological evolution. In the literature there have been various types of EA algorithms that differ in the procedures of initialization, selection, mutation, and recombination. Among them, the evolutionary programming (EP) and the genetic algorithms (GA) are the two important branches. Evolutionary algorithms operate on a population of potential solutions applying the principle of survival of the fittest to produce better and better approximations to a solution. At each generation, a new set of approximations is created by the process of selecting individuals according to their level of fitness in the problem domain and breeding them together using operators borrowed from natural genetics. This process leads to the evolution of populations of individuals that are better suited to their environment than the individuals that they were created from, just as in natural adaptation. Fig. 1 shows the structure of a simple evolutionary algorithm and Fig. 2 shows the structure of an multipopulation evolutionary algorithm [7].

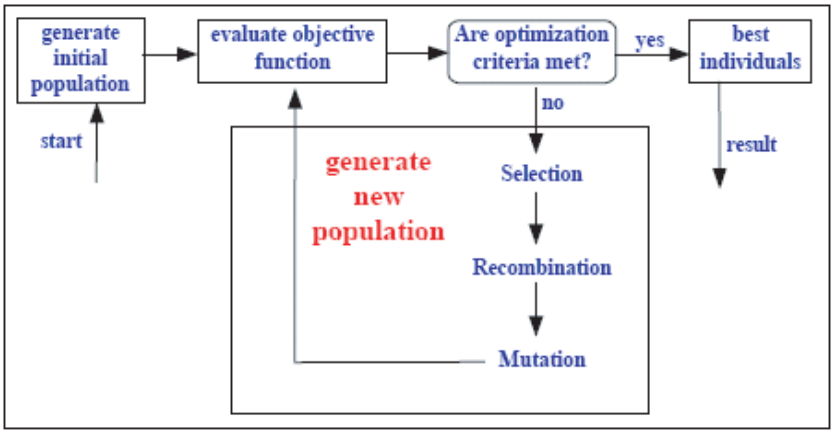

Figure 1: Structure of a single population evolutionary algorithm.

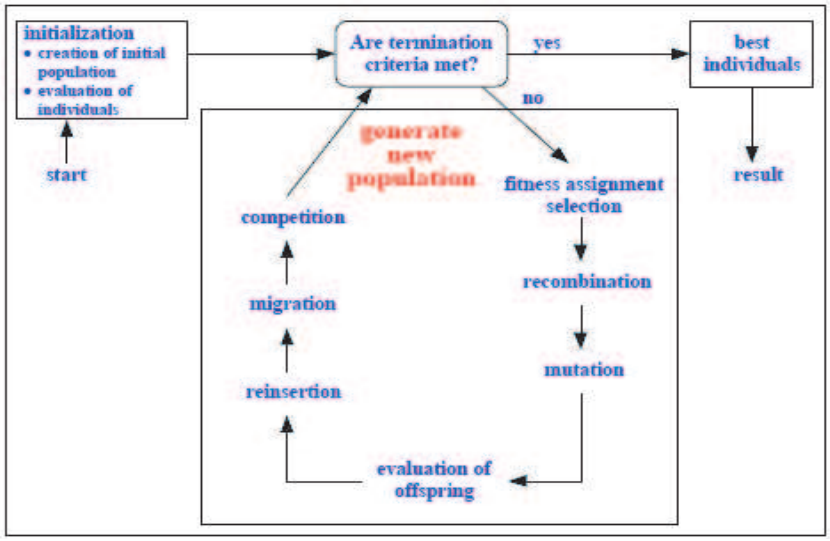

Figure 2: Structure of a multipopulation competition evolutionary algorithm.

3. IMPLEMENITATION AND NUMERICAL SIMULATION

To begin with, the objective function E is defined by Eq. (1), which provides a measurement of the deviation between the target reflection spectrum (measured reflectivity) $R_{target}(\lambda)$ and the calculated reflectivity $R_{cal}(\lambda)$:

$$E = \sum_{j=1}^{N} \left(R_{target}(\lambda_j) - R_{cal}(\lambda_j)\right)^2 \quad j = 1, 2, \ldots, N \tag{1}$$

where $\{\lambda j\}$ is the discrete set of wavelengths where the reflection spectra are evaluated.

We apply the multi-subpopulation competition evolutionary algorithm and the single population evolutionary to synthesize a numerically simulated chirped FBG, which are similar to those synthesized in Ref. [9]. The target reflection spectra are numerically calculated from the grating physical parameters by using transfer matrix method. In this way, we know the exact values of the target parameters to be reconstructed and we can obtain a better reference on the accuracy. In this case, four parameter values must be reconstructed. We choose $L = 10.2\,\text{mm}$, $\Lambda = 534.3\,\text{nm}$, $\Delta n = 1.1 \times 10^{-4}$ and the grating period chirp, $C = 0.8805\,\text{nm/cm}$, the corresponding $R_{target}(\lambda)$ is represented in Fig. 3 (solid curve). The search space (discrete set of possible values for each parameter) is fixed using usual fabrication values and covering a wide range. Typically, the search space covers from 1 nm to 4 centimeters for the grating length L, a band of 50 nm for the grating

period Λ, from 10-5 to 10-3 for the peak index modulation Δn and from 10-8 to 10-7 for the grating period chirp C.

The parameters of the single population evolutionary algorithm are: subpopulations = 1; individuals = 20 (at start per subpopulation); termination 1: max. generations = 500; 2: max. comp. time = 60; 3: diff to optimum = 1e-006 (Min: 1e-005); variable format = real values; selection: function = selsus, pressure = 1.7, gen. gap = 0.9; reinsertion: rate = 1; method = recombination; name = recdis, rate = 1; mutation: name = mutreal, rate = 1, range = 0.1; precision =12. And the parameters of the multipopulation competition evolutionary algorithm are: subpopulations = 3; individuals = 30 (at start per subpopulation); termination 1: max. generations = 1000; 2: max. comp. time = 60; 3: diff to optimum = 1e-006 (Min: 1e-005); variable format = real values; selection: function = selsus., pressure=1.7, gen. gap=0.9; reinsertion: rate = 1, method = 2, recombination: name = recdis recdis recline; rate = 1; mutation: name = mutreal, rate = 1; range = 0.1, 0.03, 0.01; precision = 12; migration: rate = 0.1, interval = 20, topology = 0; selection = 1; competition: rate = 0.4, interval= 4; subpop minimum= 5; div. pressure = 2.

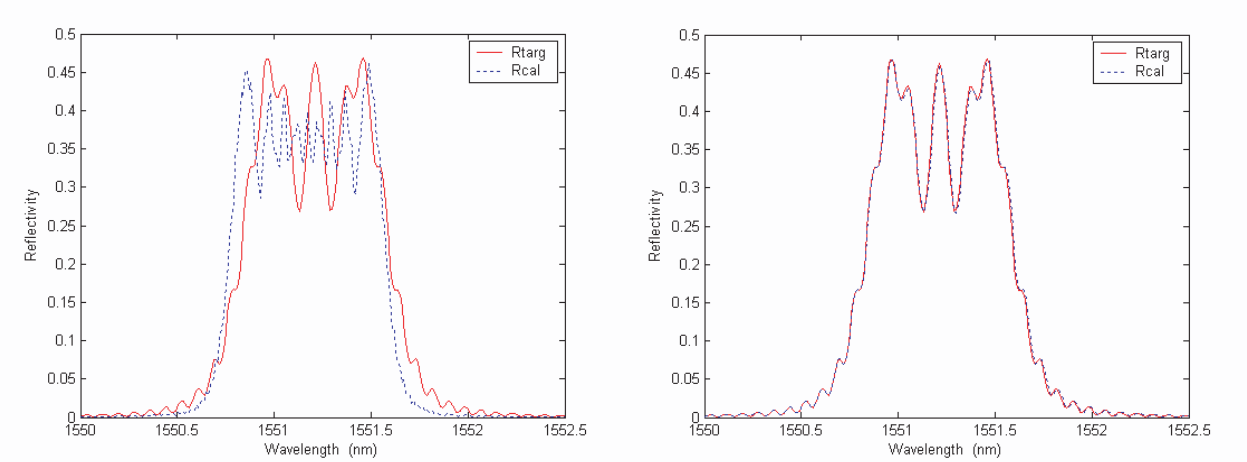

Figure 3: Results from the synthesis of numerically simulated chirp FBG from reflectivity: target (solid curve) and reconstructed (dashed curve) spectra: (a) constructed with a single population evolutionary algorithm; (b) constructed with a multipopulation competition evolutionary algorithm.

In this case, two evolutionary algorithms are both end of optimization maximum compute time. The best reconstructed parameters with the single population evolutionary algorithm are: $L = 34.079\,\text{mm}$, Λ=586.15 nm and $\Delta n = 5.3431 \times 10^{-4}$, $C = 0.5519$; the reflectivity corresponding to the reconstructed parameters is showed in Fig. 3(a) (dashed curve). And the best reconstructed parameters with the single population evolutionary algorithm are: $L = 10.144\,\text{mm}$, $\Lambda = 534.3\,\text{nm}$ and $\Delta n = 1.1033 \times 10^{-4}$, $C = 0.89206$; the reflectivity corresponding to the reconstructed parameters is showed in Fig. 3(b) (dashed curve).

4. CONCLUSIONS

In this paper, we reconstruct the physical parameters of a chirp FBG structure from its reflectivity based on a classical single population evolutionary algorithm and a multi-subpopulation competition evolutionary algorithm. The analysis curve of the gratings designed here shows the multi-subpopulation competition evolutionary algorithm is better than the single population evolutionary algorithm in the aspects of global optimization and convergence.

ACKNOWLEDGMENT

The authors would like to thank Hartmut Pohlheim for the generous help with using the GEATbx.

REFERENCES

1. Winick, K. A., J. E. Roman, *IEEE J. Quantum Electron.*, 26 1918, 1990.
2. Peral, E., J. Capmany, J. Marti, *IEEE J. Quantum Electron.*, 32 2078C, Jones (private communication), 1996.

3. Muriel, M. A., J. Aza∼na, A. Carballar, *Opt. Lett.*, 23 1526, 1998.
4. Skaar, J., L. Wang, and T. Erdogan, *IEEE J. Quantum Electron.*, 37 165, 2001.
5. Cornier, G., R. Boudreau, S. Theriault, *J. Opt. Soc. Am. B*, 18 1771, 2001.
6. Dong, P., J. Azana, and A. G. Kirk, *Opt. Commun.*, 228.303, 2003.
7. Pohlheim, H., http://www.geatbx.com.
8. Erdogan, T., *J. Lightwave Technol.*, 15 (1997) 1277, 1997.
9. Lhommé, F., C. Caucheteur, K. Chah, et al., *Applied Optics.*, 44 49, 2005.

A Compact Filter with Good Performance Based on Super-compact Multilayered Left-handed Transmission Line

Hao Hu, **Anxue Zhang**, **Yansheng Jiang**, **and Zhuo Xu**
School of Information and Electronics Engineering, Xi'an Jiaotong University, China

Abstract— In this paper, an improved structure for the design of bandpass filters with obviously size reduction and good performance at high frequency is proposed. This structure is based on super-compact multilayered (ML) composite-right/left-handed (CRLH) transmission line, firstly proposed by the authors Y. Horii, C. Caloz and T. Itoh. However the frequency of this structure is low (about 0.4 GHz) and the performance in the passband is not desired. To improve this, some research has been done on the architecture properties, and an improved filter has been proposed, not only exhibiting particularly small dimensions, less than 5 by 4 mm on a very high frequency (e.g., 9.5 GHz), but also have the distinct advantage of less than 0.7 dB in-band loss, −30 dB transmission coefficients at 8 GHz, and 1 GHz bandwidth.

1. INTRODUCTION

Recently, the left-handed (LH) materials have gained growing interest in the development of the compact microwave applications and devices [3]. Compared with the traditional method in designing these applications, structure based on the LH materials could exhibit particularly small dimensions. In [1], a multilayered (ML) composite-right/left-handed (CRLH) transmission line (TL) with vertically stacked LH unit cells was proposed in order to design compact microwave components. However its passband center frequency was low and it had undesired pass bands. An improved filter with compact structure, high frequency and good performance is designed and verified by simulations.

2. NOVEL COMPACT FILTER DESING

An improved compact filter is desired to have good performance with passband center frequency 9.5 GHz: passband extends from 9.2 to 10 GHz, less than 1 dB in-band loss, and more than −20 dB transmission coefficient (S_{21}) at 8 GHz. As the filter with the ML CRLH TL structure proposed in [1] (see Fig. 1) has low frequency and not desirable performance (see Fig. 2), further research and improvements will be done on two sections, increasing the frequency and improving the performance.

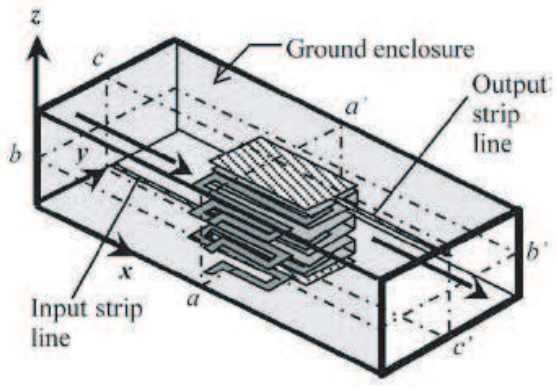

Figure 1: The primal ML CRLH TL structure proposed in [1].

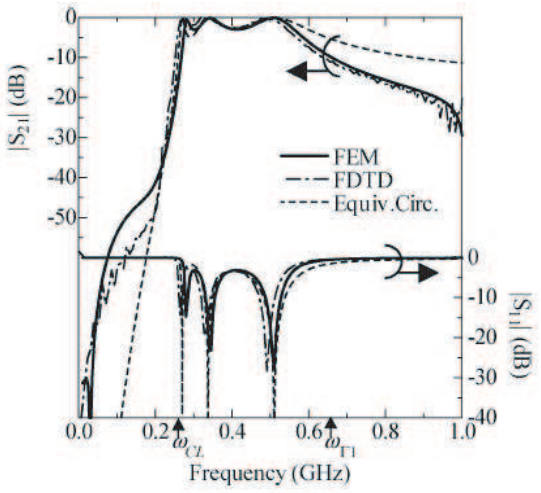

Figure 2: Simulated S-parameters for the ML CRLH TL of Fig. 1 in [1].

In the ML CRLH TL structure, the lower frequency branch exhibits antiparallel phase and group velocities (LH branch) and the higher frequency branch exhibits parallel phase and group velocities (RH branch) [1]. Several frequencies are given by the following expressions [1, 2]:

The higher edge of the LH branch

$$w_{\Gamma 1} = \min\left(\frac{1}{\sqrt{L_R C_L}}, \frac{1}{\sqrt{L_L C_R}}\right) \tag{1}$$

The lower edge of the RH branch

$$w_{\Gamma 2} = \max\left(\frac{1}{\sqrt{L_R C_L}}, \frac{1}{\sqrt{L_L C_R}}\right) \tag{2}$$

The lower edge of the LH branch

$$w_{CL} = \frac{1}{2\sqrt{C_L L_L}} \tag{3}$$

where C_L and L_L are the series capacitance and shunt inductance in the LH structure, C_R and L_R are the shunt capacitance and series inductance in the RH structure.

Apparently decreasing the value of the C_L, L_L, C_R and L_R can shift the band towards higher frequency. Based on these, we choose the material which has small permittivity (ε) to obtain small C_L, using metal rectangle line in the LH unit cell instead of metal meander lines to get less value of L_L. The wider and shorter the metal rectangle line is, the smaller the L_L is. What's more, decreasing the size of the whole structure by the same proportion also contributes to the increased frequency. After these changes, the frequency of this improved filter can be increased easily to 9.5 GHz.

When frequency increases, we find an undesired resonance appears. In order to eliminate it, lots of research have been done and we find using much narrower rectangle line in the middle layer of the periodic architecture can improve this effectively. Moreover, based on much experimental work, we give out the conclusion: performance is much better when each distance satisfied the following expression:

$$\mathrm{d1} : \mathrm{d2} : \mathrm{d3} : \mathrm{d4} = 1 : 1 : 1 : 2 \tag{4}$$

where d1 is the distance between the ground enclosure and top plate; d2 is the distance between the top plate and the U-shaped metallization; d3 is the gap from the upper plate of the U-shaped metallization to the metal rectangle line and d4 is the gap between two U-shaped metallization. (see Fig. 3).

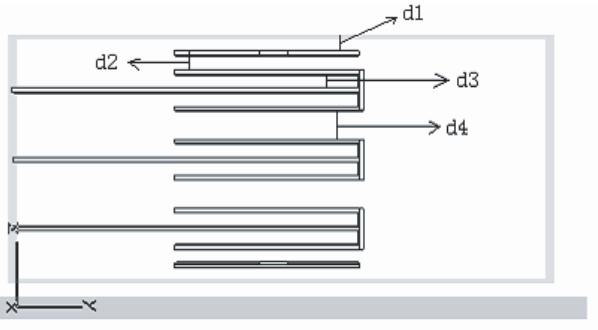

Figure 3: The description of the d1, d2, d3 and d4.

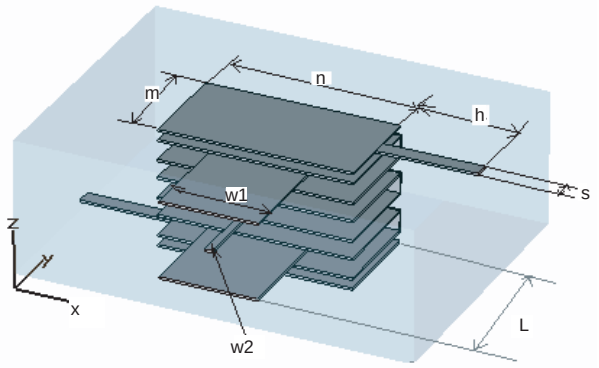

Figure 4: The structure of the filter with desired performance (w1 = 1.62 mm, w2 = 0.1 mm, L = 1.6 mm, m = 1.3 mm, n = 2.5 mm, h = 1.3 mm, s = 0.2 mm).

Finally, based on these improvements, a compact filter with small dimension (5.1 × 3.8 × 1.4 mm) is proposed to achieve the desired filter characteristics. To get better performance, proportion of d1 : d2 : d3 : d4 = 1 : 1 : 1 : 2 is also preferred. Take d1 = 0.1 mm for simple. Choose $\varepsilon = 2.65$ and adjust the width and length of the metal rectangle line to reach the center frequency at 9.5 GHz. Other specific dimensions can be found in Fig. 4.

3. SIMULATED RESULTS

With the commercial 3D electromagnetic stimulation tool-CST, the simulated S-parameters are shown in Fig. 5. It has been found that the simulated frequency response fits the targeted specifications to a good agreement: Only 0.7 dB in-band loss, greater than 15 dB return loss in the passband, 1 GHz bandwidth with center frequency 9.5 GHz, and Transmission coefficients (S_{21}) is -30 dB at 8 GHz.

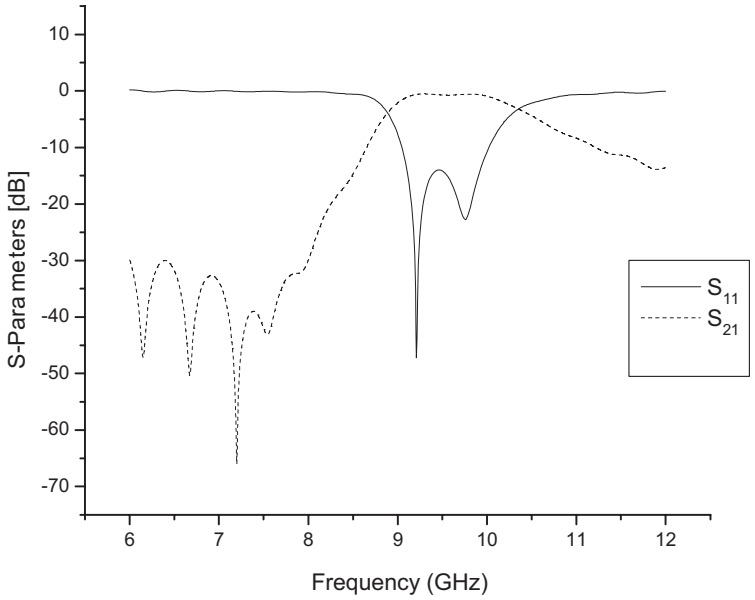

Figure 5: Simulated S-parameters of filter in Fig. 6.

4. CONCLUSIONS

Compared to the conventional structure used to design the filter, the improved filter in this paper based on ML CRLH TL in [1] makes it possible to simultaneously achieve small dimensions, high frequency and good performance. Simulated results confirm the efficient analysis and design procedure. Using modern low-temperature co-fired ceramic (LTCC) processes, this structure can be implemented. It is believed that this improved structure can be of practical interest for the compact filter design with good performance at microwave frequencies.

ACKNOWLEDGMENT

The work is sponsored by the National Nature Science Foundation of China (No. 50632030).

REFERENCES

1. Horii, Y., C. Caloz, and T. Itoh, "Super-compact multilayered left-handed transmission line and diplexer application," *IEEE Trans. Microw. Theory Tech.*, Vol. 53, No. 4, 1527–1533, Apr. 2005.
2. Pozar, D. M., *Microwave Engineering*, Third Edition, Publishing House of Electronics Industry, Beijing, 2006.
3. Lai, A., C. Caloz, and T. Itoh, "Composite right/left-handed transmission line metamaterials," *IEEE Microwave Magazine*, 2004.
4. Sanada, A., C. Caloz, and T. Itoh, "Characteristics of the composite right/left-handed transmission lines," *IEEE Microw. Wireless Compon. Lett.*, Vol. 14, No. 2, 68–70, Feb. 2004.
5. Hunter, I. C., *Theory and Design of Microwave Filters*, 2001.

The Research on Application of Composite Meta-material in Rectangular Waveguide

Man-na Han[1], **Chao Li**[2], **and Qiang Sui**[1]

[1]Communication University of China, Beijing, China
[2]Institute of Electronics, Chinese Academy of Sciences, Beijing, China

Abstract— In this paper, the application of meta-material on the design of rectangular waveguide filters is presented and discussed. Split-ring resonators (SRRs) are applied in rectangular waveguide, the propagation property of electromagnetic wave in rectangular waveguide loaded with SRR has been investigated. A narrow-band bandpass filter which based on the combination of rectangular waveguide irises and split-ring resonators (SRRs) were designed and fabricated. The agreement between the simulation and measurement results is overall good.

1. INTRODUCTION

In the last few years, the research of composite meta-material has become a new hotpot of electromagnetic study because of the first experimental demonstration of a negative refraction effect, which confirmed the predictions of a very early theoretical paper already published in 1968 [1]. As early as in 2002, the application of the structures likes split-ring resonators (SRRs) which were proposed by J. B. Pendry et al. [2, 3] has been researched by Espanol scholar R. Marqués et al. [4], the transmission of electromagnetic wave in metallic waveguide which loaded with SRRs are studied.

It's found that the structures which are constituted by SRRs exhibit negative effective permeability in certain frequency range, when the direction of the magnetic filed is parallel to the axis of the rings in the periodic arranged SRRs. If loading the SRRs into rectangular waveguides, a clearly passband will be clearly observed when the resonant frequency of SRRs is below the cutoff frequency of the dominant mode of the waveguide [4, 5], and a stopband will be seen when above the cutoff frequency of the dominant mode [5]. Experiment by B. Jitha et al., proved that the rejection band can be made very narrow by placing the SRR array at the electric-field minimum, and the stopband attenuation depends on the number of unit cells in the array [6].

When the direction of the electric field is parallel to the periodically arranged wires, the effective permittivity will be negative in certain frequency range. Hence, if iris similar with wires and SRRs are both loaded in a rectangular waveguide, a left-handed passband can be obtained when the dominant mode transmits in this rectangular waveguide, and the out-of-band rejection is dependent on the number of cells which are combined of iris and SRR [7].

In this paper, the transmission characteristics of electromagnetic wave in rectangular waveguide which loaded with the combination of irises and SRRs has been investigated, the results of the simulation and measured are presented and discussed.

2. DESIGN AND FABRICATION

The SRR which shows a negative permeability in a certain frequency has been used in this study, this property in a R32 waveguide (72.14 mm × 34.04 mm) is simulated and validated. It is centered in the waveguide, as the H-filed reaches maximum values in the center of the waveguide, it can give maximum excitation of the SRR in this location. Meanwhile, the axial direction of the ring is parallel to the magnetic filed to obtain negative permeability, the cut of SRR is parallel to the electric filed. The symmetrical SRRs are fabricated on a double-sided substrate with dielectric constant $\varepsilon_r \approx 2.65$ and thickness $h = 1$ mm. The dimension of a SRR with a resonance in the S-band is shown in Figure 1, single ring was selected. The other SRR is on the symmetrical side of the substrate, which is the same with one shown in Figure 1.

The inductive iris is also used in this study, and then an inductive window is composed of two irises. An inductive window produces a one-dimensional evanescent medium, which can be characterized by an equivalent negative effective permittivity [7]. The thickness of iris is 0.5 mm, the height which along with the short side of the waveguide is 34.04 mm, and the other side is 24.2 mm. Furthermore, the SRR is located in the center of the cavity formed by two inductive windows, this structure is defined as a cell. The analyzed structure is shown in Figure 2, is a cell of combination of irises and SRR in a R32 waveguide designed to operate in the S-band.

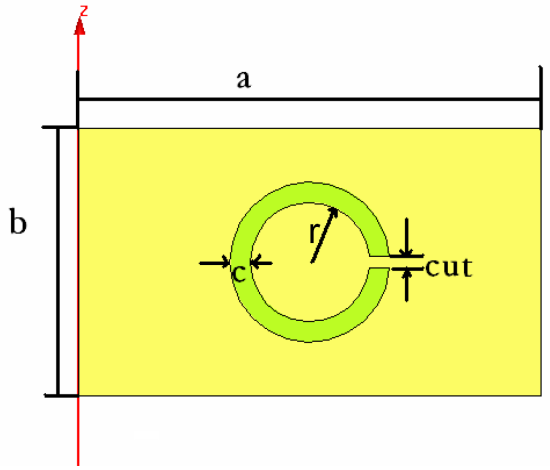

Figure 1: The dimension of the SRR which is fabricated on a double-sided substrate ($r = 4.9\,\text{mm}$, $c = 1.6\,\text{mm}$, $cut = 1.5\,\text{mm}$, $a = 72.14\,\text{mm}$, $b = 17.5\,\text{mm}$).

The whole structure is in Figure 2, the total length of the waveguide is 90 mm, and the length of the body loaded with iris and SRR is 16.5 mm, as the iris thickness is 0.5 mm which is pasted on the body. A cell of iris combining with SRR is fabricated which is shown in Figure 3, and so the whole structure.

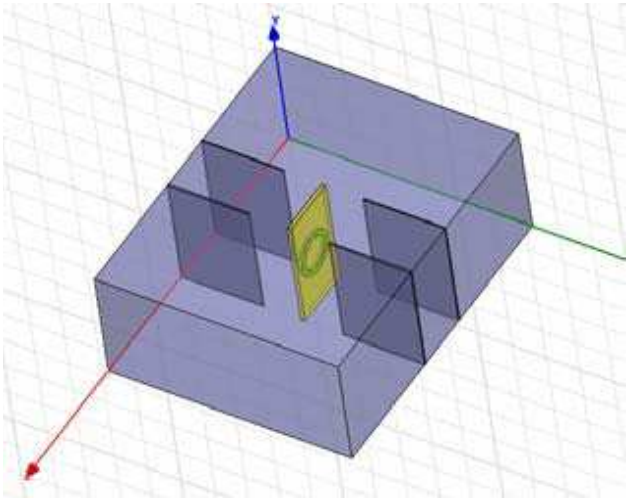

Figure 2: The rectangular waveguide bandpass filter which loaded with iris and SRR.

3. EXPERIMENTAL RESULTS AND ANALYSIS

As we all known, the electromagnetic wave will transfer through the rectangular waveguide which with nothing loaded completely. However, when SRRs are loaded in a waveguide, the axial direction of the ring is parallel to the magnetic field, the magnitude of the transmission coefficient S_{21} shows a stopband in a certain frequency range, this indicates the effective permeability with SRR device in the waveguide is negative in this frequency range.

An experiment of SRRs loaded in rectangular waveguide is carried out, the fabricated prototypes have been measured by HP8753E Network Analyzer in a certain frequency range (2.9–3.5 GHz), which is in the range of the dominant TE_{10} mode of the waveguide. The comparison between simulated and experimental results are shown in Figure 4, the agreement is good with the frequency shift probably due to the tolerances in the fabrication and the results are better than the device of Jorge Carbonell's [7].

Figure 5 shows the measured and simulated results for the transmission coefficient S_{21} of the rectangular waveguide bandpass filter, a passband is clearly show in the result. As the analysis above, there is a stopband when a single SRR loaded in the waveguide which offered a negative

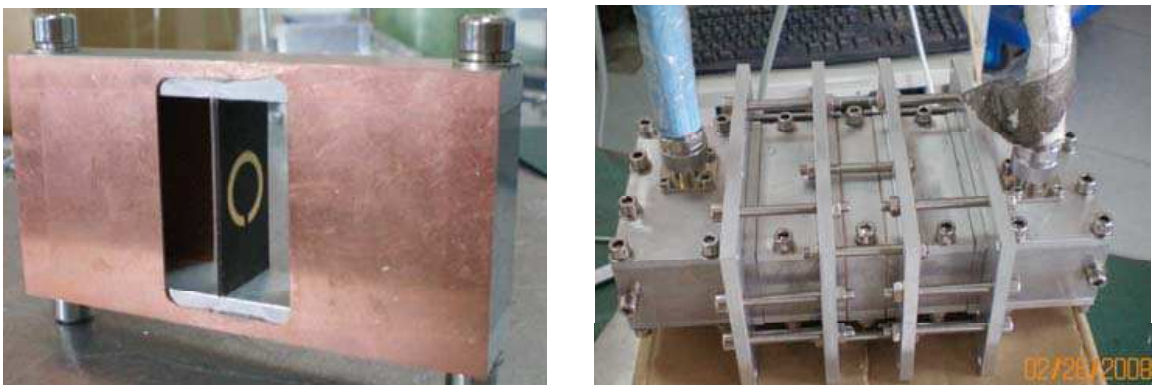

Figure 3: The cell of iris combining with SRR (left) and the whole structure (right).

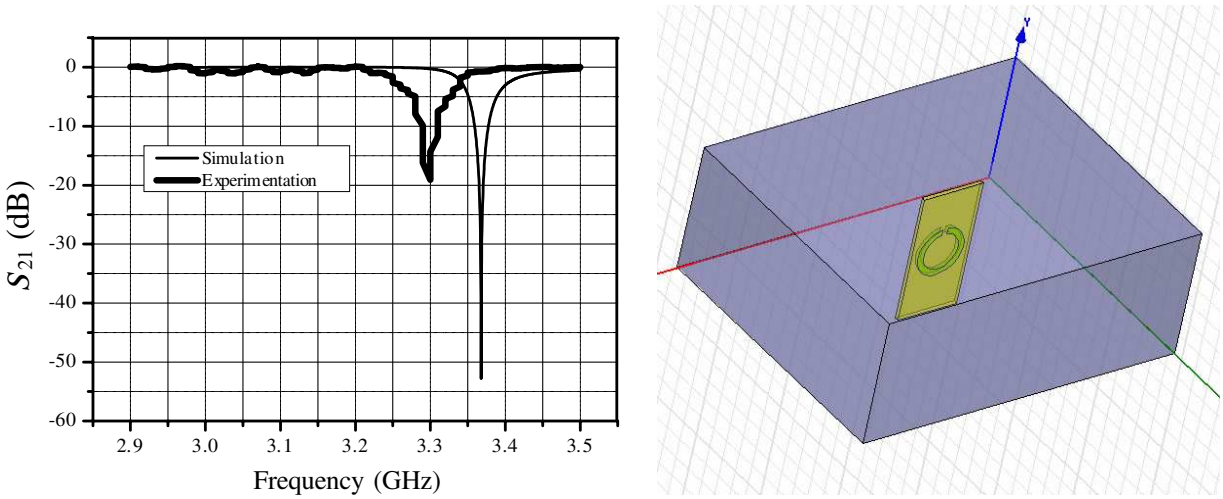

Figure 4: The magnitude of the transmission coefficient S_{21} for structure of single SRR loaded waveguide (left).

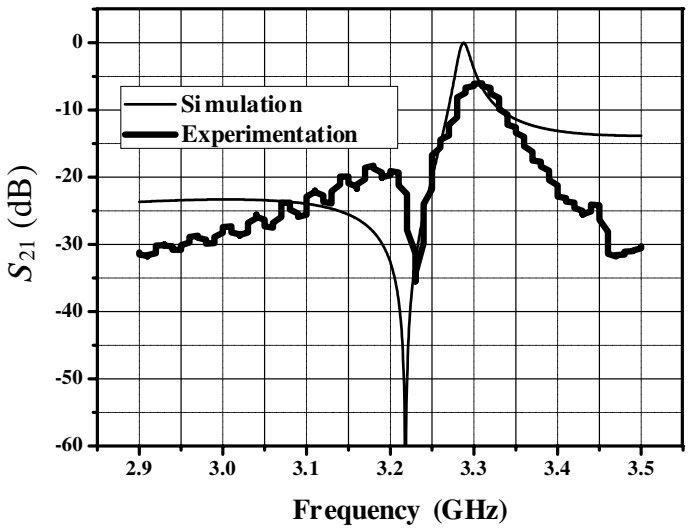

Figure 5: The magnitude of the transmission coefficient S_{21} for rectangular waveguide bandpass filter.

permeability, then we can obtained that the inductive windows in the filter offered a negative permittivity, because the electromagnetic wave can transfer when the permittivity and permeability of the structure are both negative. The agreement is good with frequency shift and the magnitude

loss probably due to the tolerances in the manufacturing process and the allowance of the coaxial-waveguide adapter.

4. CONCLUSION

In this study, an experimental verification of electromagnetic wave propagation behavior through a rectangular waveguide which loaded with SRR and irises has been carried out. When the electromagnetic wave transfers through a rectangular waveguide loading with SRRs, there is a stopband in a frequency range, as the permeability of this structure is negative in this frequency range. When the waveguide loaded with both SRRs and inductive windows, the structure is shown as a property of bandpass filter, there will be a passband in a frequency range.

REFERENCES

1. Veselago, V. G., "The electrodynamics of substances with simultaneously negative values of ε and μ," *Sov. Phys.-Usp.*, Vol. 10, No. 4, 509–514, 1968.
2. Pendry, J. B., A. J. Holden, W. J. Stewart, et al., "Extremely low frequency plasmons in metallic mesostructures," *Phys. Rev. Lett.*, Vol. 76, 4773–4776, 1996.
3. Pendry, J. B., A. J. Holden, D. J. Robbins, and W. J. Stewart, "Magnetism from conductors and enhanced nonlinear phenomena," *IEEE Transactions on Microwave Theory and Techniques*, Vol. 47, No. 11, 2075–2084, 1999.
4. Marqués, R., J. Martel, F. Mesa, and F. Medina, "Left-handed-media simulation and transmission of EM waves in subwavelength slit-ring-resonator-lodaed metallic waveguides," *Phys. Rev. Lett.*, Vol. 89, 183901-1–183901-4, 2002.
5. Hrabar, S., J. Bartolic, and Z. Sipus, "Waveguide miniaturization using uniaxial negative permeability metamaterial," *IEEE Transactions on Antennas and Propagation*, Vol. 53, No. 1, 110–119, 2005.
6. Jitha, B., C. S. Nimisha, C. K. Anaandan, P. Mohanan, and K. Vasudevan, "SRR loaded waveguide band rejection filter with adjustable bandwidth," *Microwave and Optical Technology Letters*, Vol. 48, No. 7, 1427–1429, July 2006.
7. Carbonell, J., L. J. Roglá, V. E. Boria, and D. Lippens, "Design and experimental verification of backward-wave propagation in periodic waveguide structures," *IEEE Transactions on Microwave Theory and Techniques*, Vol. 54, No. 4, 1527–1533, 2006.

The Negative Parameters of Left-handed Materials Consisting of Granular Composite

X. Gao
Electronics and Information College, Hangzhou Dianzi University
Hangzhou 310018, China

Abstract— The effective refractive index of a kind of granular composite, which consists of granular metallic and magnetic granular inclusions with different radius embedded in a host medium, is theoretically investigated. Simulation results show that for certain volume fractions of these two inclusions, the negative permittivity peak shifts to low frequency and the peak value increases with increasing radius ratio of the magnetic granulae to that of metallic granulae. Peak value of permeability decreases with the radius ratio, and value peak shifts to high frequency with increasing volume fraction of magnetic inclusion. In addition, the possibility of constructing tunable granular composite LHM by using electrorheological and Magetorheological effect also investigated.

1. INTRODUCTION

A medium, for which both dielectric constant and magnetic permeability are negative values, will have peculiar properties, including reverse Doppler shift, reverse Cerenkov radiation, reverse circular Bragg phenomenon, and negative Goos-Hänchen shift [1, 2]. In such medium, the electric field, the magnetic field and the wave vector of an electromagnetic wave obey the left-handed rule, thus it is usually called the left-handed materials (LHM) [1]. Recently, left-handed media have received much attention for potential applications and their interesting properties [2–5]. J. B. Pentry proposed that the refractive index should be negative when both permittivity and permeability are negative3, which is also proved by A. L. Pokrovsky and A. L. Efros [4]. D. R. Smith and co-workers reported experimentally a medium, consisting of array of conducting nonmagnetic split ring resonators and continuous thin wires, would have effective negative permittivity and permeability at microwave frequencies [5].

Aim at constituting LHM, some approaches have been proposed. There are some investigations in the possibility of preparing LHM with metallic magnetic granular composites [6, 7]. Based on the effective medium approximation, it was shown that by incorporating insulating matrix and controlling the directions of magnetization of metallic magnetic component, it is possible to prepare a composite medium with negative effective refractive index. Y. Huang and L. Gao also investigated the effective index of a granular composite, with metallic magnetic inclusions having dispersive permittivity and permeability embedded in a host medium. In this letter, the effective refractive index of a kind of three-component granular composite, which consists of metallic and magnetic granular inclusions with different radius embedded in a host medium, is theoretically investigated by means of Claisius-Mossotti approximation. In addition, the possibility of constructing tunable granular composite LHM by using electrorheological and Magetorheological effect also investigated.

2. PRINCIPLE AND FORMULAE

The three-component composite we investigated is a composite with metallic and magnetic granulae embedded in a host medium. The radii of the two inclusions are different and the radius ratio (represented by the symbol C) is defined as the ratio of the radius of the magnetic granulae to that of the metallic granulae. The volume fraction of metallic component is p_1, and the volume fraction of the magnetic component is p_2. Both components are assumed to be spherical and the radii are R_1 and R_2 for metallic and magnetic granulae, respectively. The metallic component granulae have the permittivity $\varepsilon_1(\omega)$ and the permeability μ_1, with wave number $k_1 = \omega/\mathrm{c}\sqrt{\varepsilon_1\mu_1}$, while the magnetic granulae have the dispersive permittivity ε_2 and the permeability $\mu_2(\omega)$, with wave number $k_2 = \omega/\mathrm{c}\sqrt{\varepsilon_2\mu_2}$. The permittivity of metallic component and the permeability of the magnetic component have the following forms [7]

$$\varepsilon_1(\omega) = 1 - \frac{\omega_p^2}{\omega(\omega + i\gamma)} \qquad \mu_2(\omega) = 1 - \frac{F\omega^2}{\omega^2 - \omega_0^2 + i\omega\Gamma} \tag{1}$$

where ω_p is the plasma frequency of the metal, γ is the damping parameter. F is the fill factor, Γ is the resonance width, and ω_0 is resonant frequency. In order to obtain the effective permittivity ε_e and effective permeability μ_e, we calculate the effective permittivity based on the Clausius-Mossotti relation [8],

$$\frac{\varepsilon_e - \varepsilon_h}{\varepsilon_e + 2\varepsilon_h} = \frac{p_1}{R_1^3}\alpha_1 + \frac{p_2}{R_2^3}\alpha_2 \tag{2}$$

where α_i is the dipole polarizability. In the terms of the Mie coefficient, α_i is given by,

$$\alpha_1 = i\frac{3R_1^3}{2\sigma_h^3}b_1, \qquad \alpha_2 = i\frac{3R_2^3}{2\sigma_{hh}^3}b_2 \tag{3}$$

where $\sigma_h = k_h R_1$, $\sigma_{hh} = k_h R_2$, so $\sigma_{hh}/\sigma_h = C$. k_h is the wave number of the host medium, and $k_h = \omega/c\sqrt{\varepsilon_h\mu_h}$, where ε_h and μ_h are the permttivity and permeability of the host medium, respectively. Substitute Eq. (3) into Eq. (2), the effective permttivity can be rewritten as

$$\varepsilon_e = \frac{1 + 2i\dfrac{3}{2k_n^3}\left(\dfrac{p_1}{R_1^3}b_1 + \dfrac{p_2}{R_2^3}b_2\right)}{1 - i\dfrac{3}{2k_n^3}\left(\dfrac{p_1}{R_1^3}b_1 + \dfrac{p_2}{R_2^3}b_2\right)}\varepsilon_h \tag{4}$$

On the other hand, the effective permeability is given by

$$\mu_e = \frac{1 + 2i\dfrac{3}{2k_n^3}\left(\dfrac{p_1}{R_1^3}a_1 + \dfrac{p_2}{R_2^3}a_2\right)}{1 - i\dfrac{3}{2k_n^3}\left(\dfrac{p_1}{R_1^3}a_1 + \dfrac{p_2}{R_2^3}a_2\right)}\mu_h \tag{5}$$

In this letter, the a_i, b_i $(i = 1, 2)$ are dipolar coefficients. Without loss of generality, it is assumed that $\mu_1 = 1$, $\varepsilon_2 = 1$, $\mu_h = 1$, and $\varepsilon_h = 1$. Then we choose the second approximation of field coefficients in this letter to investigate the composite, so

$$a_1 = -\frac{2}{3}i\sigma_h^3\frac{\mu_1 - \mu_h}{\mu_1 + 2\mu_h} - 2i\sigma_h^5\frac{\varepsilon_1\mu_1^2 + \mu_1^2\varepsilon_h - 6\mu_1\mu_h\varepsilon_h + 4\mu_h^2\varepsilon_h}{10\varepsilon_h\left(\mu_1 + 2\mu_h\right)^2} \tag{6a}$$

$$b_1 = -\frac{2}{3}i\sigma_h^3\frac{\varepsilon_1 - \varepsilon_h}{\varepsilon_1 + 2\varepsilon_h} - 2i\sigma_h^5\frac{\mu_1\varepsilon_1^2 + \varepsilon_1^2\mu_h - 6\varepsilon_1\varepsilon_h\mu_h + 4\varepsilon_h^2\mu_h}{10\mu_h\left(\varepsilon_1 + 2\varepsilon_h\right)^2} \tag{6b}$$

$$a_2 = -\frac{2}{3}i\sigma_{hh}^3\frac{\mu_2 - \mu_h}{\mu_2 + 2\mu_h} - 2i\sigma_{hh}^5\frac{\varepsilon_2\mu_2^2 + \mu_2^2\varepsilon_h - 6\mu_2\mu_h\varepsilon_h + 4\mu_h^2\varepsilon_h}{10\varepsilon_h\left(\mu_2 + 2\mu_h\right)^2} \tag{6c}$$

$$b_2 = -\frac{2}{3}i\sigma_{hh}^3\frac{\varepsilon_2 - \varepsilon_h}{\varepsilon_2 + 2\varepsilon_h} - 2i\sigma_{hh}^5\frac{\mu_2\varepsilon_2^2 + \varepsilon_2^2\mu_h - 6\varepsilon_2\varepsilon_h\mu_h + 4\varepsilon_h^2\mu_h}{10\mu_h\left(\varepsilon_2 + 2\varepsilon_h\right)^2} \tag{6d}$$

And due to $\varepsilon_h = \mu_h = 1$ and $\varepsilon_2 = \mu_1 = 1$, we can get the effective permittivity and permeability as,

$$\varepsilon_e = \frac{1 + \left(p_1\left(2\dfrac{\varepsilon_1 - 1}{\varepsilon_1 + 2} + 6C^2\sigma_{hh}^2\dfrac{\varepsilon_1^2 - 3\varepsilon_1 + 2}{5\left(\varepsilon_1 + 2\right)^2}\right) + p_2\sigma_{hh}^2\dfrac{\mu_2 - 1}{15}\right)}{1 - \left(p_1\left(\dfrac{\varepsilon_1 - 1}{\varepsilon_1 + 2} + 3C^2\sigma_{hh}^2\dfrac{\varepsilon_1^2 - 3\varepsilon_1 + 2}{5\left(\varepsilon_1 + 2\right)^2}\right) + p_2\sigma_{hh}^2\dfrac{\mu_2 - 1}{30}\right)} \tag{7}$$

$$\mu_e = \frac{1 + \left(p_2\left(2\dfrac{\mu_2 - 1}{\mu_2 + 2} + 6\sigma_{hh}^2\dfrac{\mu_2^2 - 3\mu_2 + 2}{5\left(\mu_2 + 2\right)^2}\right) + p_1\left(C^2\sigma_{hh}^2\dfrac{\varepsilon_1 - 1}{15}\right)\right)}{1 - \left(p_2\left(\dfrac{\mu_2 - 1}{\mu_2 + 2} + 3\sigma_{hh}^2\dfrac{\mu_2^2 - 3\mu_2 + 2}{5\left(\mu_2 + 2\right)^2}\right) + p_1\left(C^2\sigma_{hh}^2\dfrac{\varepsilon_1 - 1}{30}\right)\right)} \tag{8}$$

Without loss of generality, it is assumed that $\omega_p = 10\,\mathrm{GHz}$, $\omega_0 = 4\,\mathrm{GHz}$, $\gamma = \omega_p/300$, $\Gamma = 0.03\omega_0$, $F = 0.56$ in simulation [1, 7].

3. OTHER SECTIONS

First, we investigate the effect of the radius ratio C on the effective permittivity of the composite with the assumption $p_2 = 0.38$ according to Eq. (7). Fig. 1 shows the effective permittivity versus frequency for different radius ratio C. For certain volume fractions of the metallic and magnetic inclusions, there is a frequency range within which the effective permittivity is negative and one negative value peak occurs. When the radius ratio C increases from 0 to 4, the negative permittivity peak firstly does not shift considerably, then shift to high frequency quickly. Simultaneously, the peak value increases wholly with the increasing radius ratio C. From the figure, it can be seen that for certain volume fraction of the magnetic inclusion p_2 and the radius ratio C, the negative permittivity peak shifts to low frequency with increasing volume fraction of metallic.

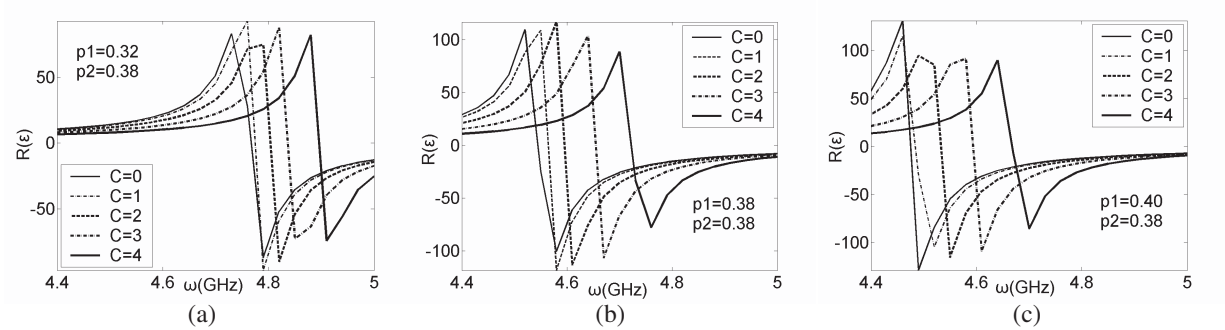

Figure 1: Effective permittivity of the composite versus frequency for different radius ratio and (a) $p_1 = 0.324$, (b) $p_1 = 0.38$, and (c) $p_1 = 0.40$.

Now, the effect of the radius ratio C on the effective permeability of the composite is investigated for p_1=0.38 basing on Eq. (8). Fig. 2 illustrates the permeability distribution versus frequency for different radius ratio C. It can be seen that there is a frequency range within which the effective permeability is negative. For certain volume fractions of the two inclusions, the permeability peak shifts toward high frequency with increasing radius ratio C weakly. And the peak value decreases with radius ratio. Under certain volume faction of metallic inclusion p_1 and radius ratio C, the smallest value of effective permeability decreases with increasing volume fraction of magnetic inclusion p_2. Therefore, the effective permeability may be negative when the volume fraction of magnetic inclusion p_2 exceeds a threshold for certain volume fraction of metallic inclusion p_1 and radius ratio C, and the negative value range of effective permeability extends with radius ratio C.

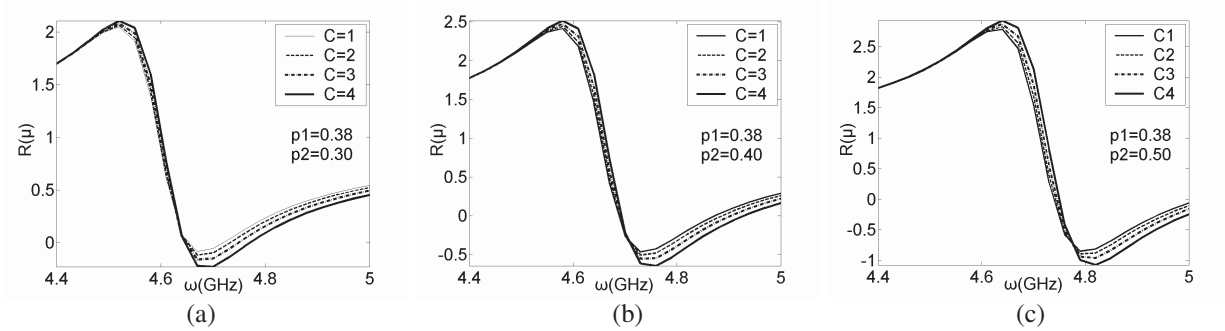

Figure 2: Effective permeability of the composite versus frequency for different radius ratio and (a) $p_2 = 0.30$, (b) $p_2 = 0.40$, and (c) $p_2 = 0.50$.

Electrorheological fluid, a kind of typical soft matter, is usually a suspension of particles dispersed in insulating oil of low dielectric constant. Its mechanical properties (viscosity, shear stress), optical properties (diffraction, optical rotation) and the microwave behavior (scattering, attenuation) can be adjusted under external electric field. Magetorheological fluid is similar to electrorheological fluid, the difference is external field is magnetic field. There is possibility of constructing tunable granular composite LHM by using electrorheological and Magetorheological effect. By altering the external electric and magnetic fields, the magnetic granulae and metallic granulae can

be arrayed and clustered, which maybe lead to certain concentration of the two kinds of particles, in turn forms tunable granular composite LHM.

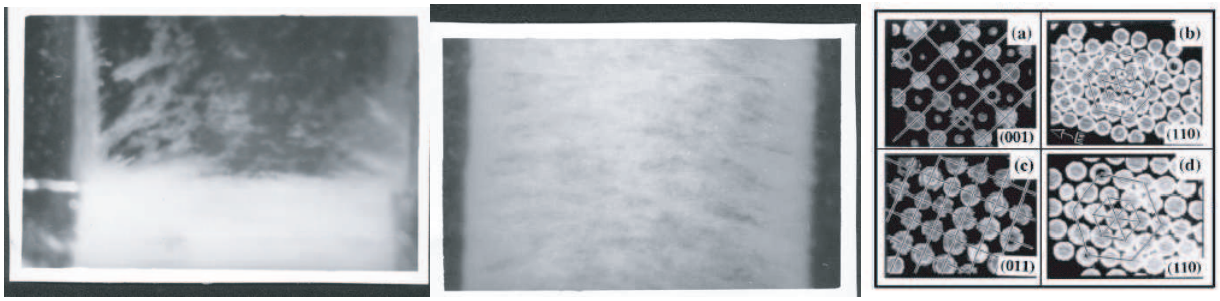

(a) (b) (c)

Figure 3: The granular cluster by external field on (a) lower half part, and (b) whole region, and (c)granular cluster under external electric and magnetic fields.

4. CONCLUSIONS

The effective refractive index of a kind of granular composite, which consists of granular metallic and magnetic granular inclusions with different radius embedded in a host medium, is theoretically investigated. Simulation results show that for certain volume fractions of these two inclusions, the negative permittivity peak shifts to low frequency and the peak value increases with increasing radius ratio of the magnetic granulae to that of metallic granulae. Peak value of permeability decreases with the radius ratio, and value peak shifts to high frequency with increasing volume fraction of magnetic inclusion. In addition, the possibility of constructing tunable granular composite LHM by using electrorheological and Magetorheological effect also investigated.

ACKNOWLEDGMENT

This work was supported by Science Research Project of Hangzhou Dianzi University (KYS051506021), National Natural Science Foundation of China (60708002, 50574035).

REFERENCES

1. Ruppin, R., "Evaluation of extended Maxwell-Garnett theories," *Solid State Communications*, Vol. 166, 411–415, 2000.
2. Lakhtakia, A., "Reversal of circular Bragg phenomenon in ferrocholesteric materials with negative real permittivities and permeabilities," *Adv. Mater.*, Vol. 14, 447–449, 2002.
3. Pentry, J. B., "Negative refraction makes a perfect lens," *Phys. Rev. Lett.*, Vol. 85, 3966–3969, 2000.
4. Pokrovsky, A. L. and A. L. Efros, "Sign of refractive index and group velocity in left-handed media," *Solid State Commun.*, Vol. 124, 283–287, 2002.
5. Shelby, R. A., D. R. Smith, and S. Schults, "Experimental verification of a negative index of refraction," *Science*, Vol. 292, 77–79, 2001.
6. Chui, S. T. and L. B. Hu, "Left-handed materials in metallic magnetic granular composites," *Phys. Lett. A*, Vol. 319, 85–88, 2003.
7. Huang, Y. and L. Gao, "Negative refractive index in composite medium with metallic magnetic inclusions," *Phys. Lett. A*, Vol. 318, 592–599, 2003.
8. Koschny, T. and M. Kafesaki, "Effective medium theory of left-handed materials," *Phys. Rev. Lett.*, Vol. 93, 107402–4, 2004.

An Inverse Model for Localization of Low-diffusivity Regions in the Heart Using Ecg/Mcg Sensor Arrays

Ashraf Atalla and Aleksandar Jeremic
Department of Electrical and Computer Engineering, McMaster University, Hamilton, Ontario, Canada

Abstract— Cardiac activation and consequently performance of the heart can be severely affected by certain electrophysiological anomalies such as irregular patterns in the activation of the heart. Since the wavefront propagation occurs through the diffusion of ions (Na^+, K^+, etc.) the reduced mobility of ions can be equivalently represented as a reduction of ionic diffusivity causing irregularities in heartbeats. In this paper we propose models for the cardiac activation using inhomogeneous reaction-diffusion equations in the presence of diffusivity disorders. We also derive corresponding statistical signal processing algorithms for estimating (localizing) parameters describing these anomalies. We illustrate applicability of our techniques and demonstrate the identifiability of the parameters through numerical examples using a realistic geometry.

1. INTRODUCTION

The phases of myocardial action potentials and processes of myocardial depolarization and repolarization are well studied and described in most handbooks of electrophysiology and electrocardiography (Gulrajani, Malmivuo). The underlying processes controlling the (re)polarization in the cardiac activation can be described, on a molecular level, as diffusion of ions through various channels (Na, K, etc.) giving a rise to ionic current which in turn creates electromagnetic field on the torso surface which can be externally measured.

Modeling the cardiac activation on a cellular level (Gulrajani) has been a subject of considerable research interest resulting in numerous models related to membrane potential (e.g., Hodgkin-Huxley model). However, these models are mainly suitable for forward modeling in which the cardiac activation is simulated using *a priori* knowledge of various parameters. Complimentary to this approach is inverse modeling in which information on cardiac activation (and some physiological parameters) is deduced from ECG/MCG measurements.

One of the most important parameters controlling the activation wavefront propagation is the diffusivity (i.e., mobility of ions). Namely, significant loss of ionic mobility can cause occurrence of irregular activation patterns and lead to various pathological conditions such as arrhythmia, early after-depolarization, etc. From a physiological point of view, these changes usually occur due to ion depletion from a particular region of the heart. As a result, the diffusivity in this region becomes very small preventing the propagation of the activation wavefront and causing the aforementioned irregular patterns. Therefore, any algorithm capable of detecting these anomalies can potentially be useful to predict the onset of these cardiac physiopathologies.

In this paper we propose a new activation model based on the diffusion equation. Although the FitzHugh- Nagumo model is based on the diffusion equation its applicability to inverse approach and real data is limited because of its isotropic and homogeneous nature. In Section 2 we develop cardiac activation model based on the reaction-diffusion equation with nonhomogeneous and anisotropic diffusion tensor. Such a model can be used for detecting different physiological conditions such as conductivity anomalies, which can predate onset of various pathological conditions such as cardiac arrhythmia, early after-depolarization, etc. In Section 3 we derive the statistical and measurements model using Geselowitz equations corresponding to our diffusion based source. Using these models we derive the generalized least squares (GLS) estimator for localizing conductivity anomalies/disorders. In Section 5 we demonstrate the applicability of our results using numerical simulations and in Section 6 we present conclusions.

2. PHYSICAL MODEL

During the spread of activation in the heart, the most significant bioelectric source is the large potential difference that exists across the moving wavefront that divides active (depolarized) from resting tissue. It has been proposed that the cardiac excitation can be modeled using reaction diffusion systems i.e., a set of nonlinear partial differential equations (Panfilov and Holden, 1997)

$$\frac{\partial u_i}{\partial t} = f_i(u) + \nabla \cdot (D_i \nabla u_i) \quad i = 1, \ldots, n \tag{1}$$

where $u = [u_1, \ldots, u_n]^T$ is the state variable vector, f_i are excitations, and D_i diffusion tensors. Although the above models can be used to model the propagation even down to a cellular level, in order to develop an inverse model a simplified approach similar to (FitzHugh, 1961), (Rogers and McCulloch, 1994) is needed. Therefore, we propose a reaction diffusion model consisting of two state variables but with spatially dependent diffusivity tensor

$$\begin{aligned}
\frac{\partial u_1(r,\, t)}{\partial t} &= \nabla \cdot (D(r)\nabla u_1(r,\, t)) + g^T(u(r,\, t))A_1 g(u(r,\, t)) \\
\frac{\partial u_2(r,\, t)}{\partial t} &= u^T(r,\, t)A_2 u(r,\, t) \\
g(u(r,\, t)) &= \left[u_1^2(r,\, t),\, u_1(r,\, t),\, u_2(r,\, t),\, 1\right]^T
\end{aligned}$$

where u_1 is the activation potential and u_2 is the resting potential.

The above model is the generalization of the existing models from at least two standpoints: a) by allowing the diffusivity matrix to be spatially dependent we can test for the presence of arbitrarily shaped anomalies, and b) by adding higher-order polynomial components we allow for wider range of dynamic behavior in the cardiac excitation. Note that in order to apply the above model to the realistic geometry we need to define boundary conditions. In our case we impose $\partial u_1/\partial n$ on the epicardial surface of the heart. As for initial conditions, we define the active potential at time $t = 0$ as $u_1(r,\, 0) = u_0\delta(r - r_0)$ where $\delta()$ is a Dirac delta function and r_0 is the activation point in the myocardium. The initial condition for the inhibition (u_2) is set to zero.

To compute the electro-magnetic field on the torso surface we utilize the Geselowitz (Geselowtiz, 1970) equations that compute the potential $\phi(r,\, t)$ and magnetic field $B(r,\, t)$ at a location r on the torso surface at a time t from a given primary current distribution $J(r',\, t) = \nabla u_1(r,\, t)$ within the heart. We use a piecewise homogeneous torso model consisting of the following surfaces: the outer torso, the inner torso, and the heart. Therefore, we model the heart as a volume G of $M = 3$ homogeneous layers separated by closed surfaces S_i, $i = 1, \ldots, M$. Let σ_i^- and σ_i^+ be the conductivities of the layers inside and outside S_i respectively. We will denote by G_i the regions of different conductivities, and by G_{M+1} the region outside the torso, which behaves as an insulator i.e., $\sigma_{M+1}^- = \sigma_M^+ = 0$.

It has been shown that in the case of a piecewise homogeneous torso model and using quasi-static assumption the magnetic field at a location r and time t is given by (Gulrajani, 1998) and (Malmivuo and Plonsey, 1995)

$$B(r,\, t) = B_0(r,\, t) + \frac{\mu_0}{4\pi}\sum_{i=1}^{M}(\sigma_i^- - \sigma_i^+) \cdot \int_{S_i} \phi(r',\, t)\frac{r - r'}{\|r - r'\|^3} \times \mathrm{d}S(r')$$

$$B_0(r,\, t) = \frac{\mu_0}{4\pi}\int_G \frac{J(r',\, t) \times (r - r')}{\|r - r'\|^3}\mathrm{d}^3 r', \tag{2}$$

where μ_0 is the magnetic permeability of the vacuum. Similarly, the potential $\phi(r,\, t)$ is given by (Geselowitz)

$$\frac{\sigma_k^- + \sigma_k^+}{2}\phi(r,\, t) = \phi_0(r)(\sigma_i^- - \sigma_i^+) + \frac{1}{4\pi}\sum_{i=1}^{M}(\sigma_i^- - \sigma_i^+)\int_{S_i} \phi(r',\, t)\frac{(r - r')}{\|r - r'\|^3} \cdot \mathrm{d}S(r'),$$

$$\phi_0(r,\, t) = \frac{1}{4\pi}\int_G \frac{J(r',\, t) \cdot (r - r')}{\|r - r'\|^3}\mathrm{d}^3 r', \tag{3}$$

where we k is chosen so that $r \in G_k$.

3. MEASUREMENT MODEL AND STATISTICAL MODEL

In this section we introduce our parametric description of the diffusion anomaly and measurement noise signals. To simplify the approach we assume that the anomaly region can be modeled with an ellipsoid i.e., the region $\mathcal{R}$ of anomaly is given by

$$\mathcal{R} = \left\{r : (r - r_a)^T F(a,\, b,\, c,\, \psi, \phi)^{-1}(r - r_a) \leq 1\right\}$$

where

$$F = T(\phi,\, \psi) \begin{bmatrix} a^2 & 0 & 0 \\ 0 & b^2 & 0 \\ 0 & 0 & c^2 \end{bmatrix} T^T(\phi,\, \psi)$$

where a, b, c are the axes of anomaly ellipsoid, r_a is the center, and ψ and ϕ are the orientation parameters (in 3D). The matrix $T(\phi,\, \psi)$ is the rotation matrix given by

$$T(\phi,\, \psi) = \begin{bmatrix} \cos\phi & \sin\phi & 0 \\ -\sin\phi & \cos\phi & 0 \\ 0 & 0 & 1 \end{bmatrix} \cdot \begin{bmatrix} \cos\psi & 0 & \sin\psi \\ 0 & 1 & 0 \\ -\sin\psi & 0 & \cos\psi \end{bmatrix} \tag{4}$$

The diffusion tensor is then

$$D(r) = \begin{cases} 0 & \mathrm{r} \in \mathcal{R} \\ D & \text{otherwise.} \end{cases} \tag{5}$$

In the remainder of the myocardium tissue we assume homogeneous but possibly anisotropic diffusion tensor D.

Next, we assume that a bimodal array of n_{B} MCG and n_{E} ECG sensors is used for the measurements. Let $n = n_{\mathrm{B}} + n_{\mathrm{E}}$. We assume that the sensors are located at ρ_j, $j = 1, \cdots, n$, and that time samples are taken at uniformly spaced time points t_k, $k = 1, \ldots, n_s$. In addition, we assume that data acquisition is repeated n_c times during several heart cycles in order to improve the signal-to-noise (SNR) ratio. Then, the n_s-dimensional measurement vector of this array obtained at time t_k in the lth cycle is

$$y_{lk} = f(\theta,\, t_k) + e_l(t_k), \tag{6}$$

where $y_{lk} = [y_{\mathrm{B}}^{\mathrm{T}}(t_k),\, y_{\mathrm{E}}^{\mathrm{T}}(t_k)]^{\mathrm{T}}$, θ is the collection of all the parameters (a, b, c, r_0, ψ, ϕ, u_0, D, A_1, A_2), $f(\theta,\, t_k)$ is the vector solution computed using finite elements, and $e_l(t_k) = [e_{\mathrm{B}}^{\mathrm{T}}(t_k),\, e_{\mathrm{E}}^{\mathrm{T}}(t_k)]^{\mathrm{T}}$ is additive noise. In the remainder of the paper we omit the subscript l whenever it is obvious that the samples belong to the same heart cycle. The subscripts $_{\mathrm{B}}$ and $_{\mathrm{E}}$ correspond to magnetic and electric components of the measurement vector (noise), respectively. We further assume that both magnetic and electric components of the noise are zero-mean Gaussian, uncorrelated in space and time with variances, σ_{B}^2 and σ_{E}^2, respectively.

4. PARAMETER ESTIMATION

We first start by splitting the unknown parameters θ into three groups: a) the unknown activation parameters $\theta_0 = [u_0,\, r_a]^T$, and b) the unknown anomaly parameters $\theta_{\mathrm{a}} = [a,\, b,\, c,\, r_0,\, \phi,\, \psi]^T$. For simplicity in the remainder of the paper we assume that the heart parameters

$$\theta_{\mathrm{h}} = [\mathrm{vec}(D),\, \mathrm{vec}(A_1 1),\, \mathrm{vec}(A_2)]^T \tag{7}$$

where vec is the vector operator, are known. Note that some *in vitro* studies (Sachse, 2004) suggest that these parameters do not vary significantly between different subjects and thus can be easily estimated using data gathered from human subjects without any anomalies. Complicating the matter is the fact that the diffusion tensor in general is inhomogeneous. Namely, the ionic diffusion process is much larger along the myocardium fiber than across different fibers. Since the fiber orientations change in space the diffusion tensor should be spatially dependent. However, these changes are smooth in nature and can be easily modeled using a set of *a priori* known basis functions. Furthermore, information about fiber orientation can be easily obtained using cardiac diffusion MRI (et al., 2003).

To compute estimates $\hat{\theta}_0$ and $\hat{\theta}_a$ we use the generalized least squares (GLS) estimator which minimizes the following cost function (Vonesh and Chinchilli, 1997)

$$\begin{aligned} c\left(\theta_0,\, \theta_a,\, \hat{\sigma}_{\mathrm{E}}^2,\, \hat{\sigma}_{\mathrm{B}}^2\right) &= \sum_{k=1}^{n_s} \sum_{l=1}^{q} \frac{1}{\hat{\sigma}_{\mathrm{E}}^2} \|y_{kl}^{\mathrm{E}} - f^{\mathrm{E}}(\theta_0,\, \theta_{\mathrm{a}},\, t_k)\|^2 + \frac{1}{\hat{\sigma}_{\mathrm{B}}^2} \|y_{kl}^{\mathrm{B}} - f^{\mathrm{B}}(\theta_0,\, \theta_{\mathrm{a}},\, t_k)\|^2 \\ \hat{\sigma}_{\mathrm{E}}^2 &= \frac{1}{n_{\mathrm{E}} n_s q} \sum_{k=1}^{n_s} \sum_{l=1}^{q} \|y_{kl}^{\mathrm{E}} - f^{\mathrm{E}}(\theta_0,\, \theta_{\mathrm{a}},\, t_k)\|^2 \\ \hat{\sigma}_{\mathrm{B}}^2 &= \frac{1}{n_{\mathrm{B}} n_s q} \sum_{k=1}^{n_s} \sum_{l=1}^{q} \|y_{kl}^{\mathrm{B}} - f^{\mathrm{B}}(\theta_0,\, \theta_{\mathrm{a}},\, t_k)\|^2 \end{aligned}$$

where we use superscripts $_{\mathrm{E}}$ and $_{\mathrm{B}}$ to denote electrical and magnetic, components of the measured field and solution vector.

The above GLS estimator is more efficient than the ordinary least squares estimator due to each contribution to the objective function is being normalized to the same unit variance (i.e., those measurements with less variation are given greater weight). The actual optimization can be done using any of the well known algorithms such as Davidson-Fletcher-Powell or Broyden-Fletcher-Goldfarb-Shanno. To further simplify the computational complexity, we propose to estimate θ_0 assuming that $a = b = c = 0$, i.e., the diffusivity of the heart is homogeneous and using ordinary least squares. Then we can use this estimate as the initial guess for GLS estimation alghorithm.

5. NUMERICAL EXAMPLES

We now describe numerical study that demonstrates the applicability of the proposed algorithms. We used an anatomically correct mesh of the human torso that was kindly provided to us by Prof. McLeod, Utah University. In our model the Purkinje network was approximated by a set of nodes near the apex. To achieve higher precision we remeshed the original data into a new mesh (see Figure 1). The volumetric mesh was created using 15902 elements with 20830 degrees of freedom for the torso (electromagnetic) model and 1856 elements and 6190 degrees of freedom for the heart (diffusion) model. The computational model was developed using a general partial differential (PDE) toolbox in COMSOL software.

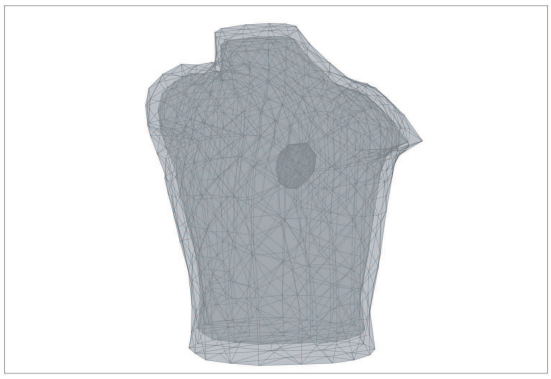

Figure 1: Mesh geometry used for numerical study.

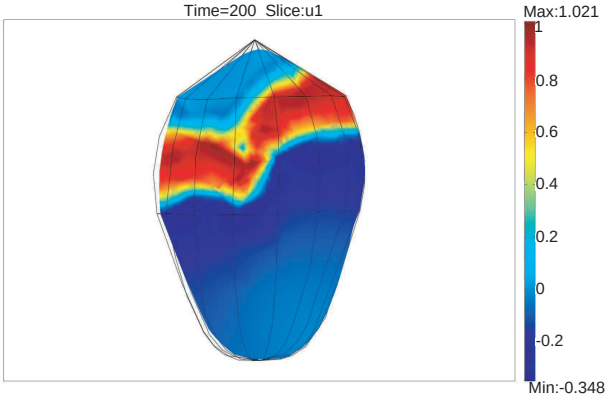

Figure 2: Activation wavefront, at $t = 2T/3$.

The torso conductivity was set to 5 µS respectively as in (Malmivuo). To simplify the complexity of the numerical study we simulated the anomaly using $a = b = 2\,\mathrm{cm}$, $c = 0.5\,\mathrm{cm}$, and $\psi = \phi = 0$. The diffusion tensor was set to be isotropic with diagonal elements equal to $40\,\mathrm{cm}^3/\mathrm{s}$. The diffusivity

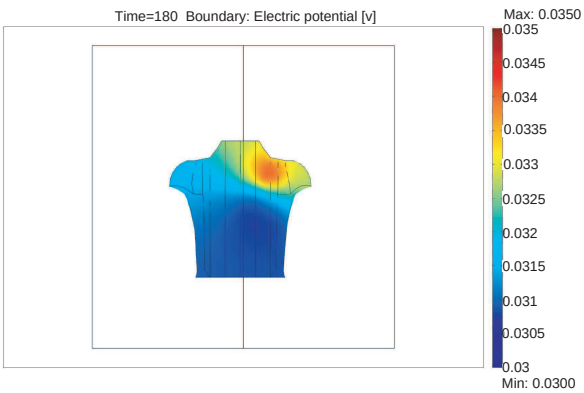

Figure 3: Body surface map of electric field at $t = 2T/3$.

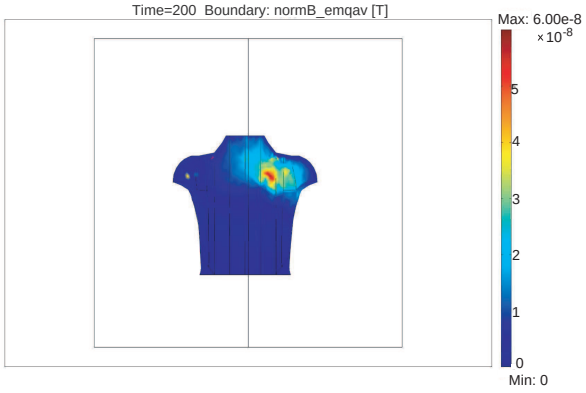

Figure 4: Body surface map of magnetic field at $t = 2T/3$.

was chosen according to (Gulrajani) so that the activation wavefront propagates the whole heart in 0.2 s. The control matrices A_1 and A_2 were chosen following the approach of (Rogers and Culloch). The heart rate was set to 72 beats per minute. We assume that the measurements are obtained using 64-channel ECG/MCG sensor array with sensors locations uniformly distributed on the chest. To evaluate the localization accuracy we use $\mathrm{MSE}r_0 = \|r_0 - \hat{r}_0\|^2/\|r_0\|^2$, $\mathrm{MSE}_a = \|a - \hat{a}\|^2/\|a\|^2$, and $\mathrm{MSE}_c = \|c - \hat{c}\|^2/\|c\|^2$.

Figure 2 illustrates the activation wavefront in myocardium at approximately $t = 2T/3$ after the activation where T is the time length of the heart cycle. In Figure 3 we illustrate the body surface map of the electric field (voltage) on the torso surface. Similarly, Figure 4 illustrates the magnetic field map at the same time. In Figure 5 we illustrate the mean square error of the axis parameters with $c = a/10$ and $b = a$. The location of an anomaly was arbitrarily set to $r_0 = (0, 0.5, 0.75)$. As expected, due to the wavefront orientation as well as difference in size, the estimation accuracy of the cross-sectional axis parameters is much smaller. In Figure 6 we illustrate the localization accuracy i.e., MSE of r_0 as a function of noise. The SNR was defined as $\mathrm{SNR} = 10\log(\sum \|y_{lk}\|^2/\sigma_{\mathrm{E}}^2 + \sigma_{\mathrm{B}}^2)$.

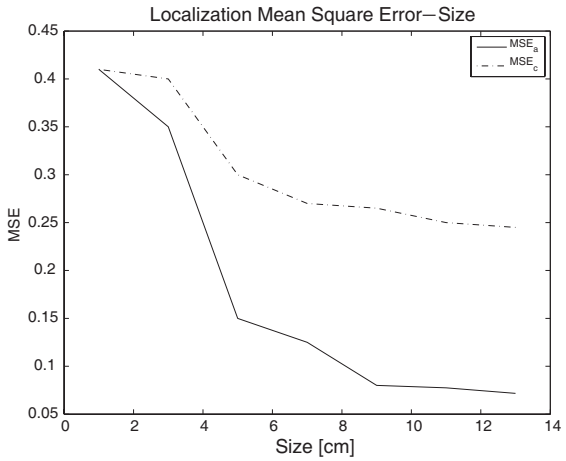

Figure 5: Mean square error for estimating the size of the anomaly.

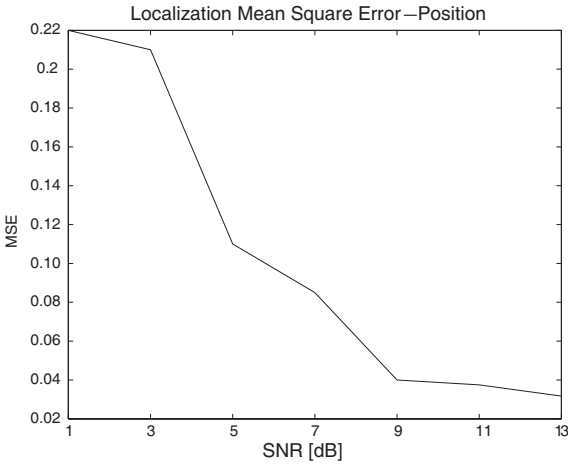

Figure 6: Mean square error for estimating the location of the anomaly.

6. CONCLUSIONS

We addressed the problem of localizing the diffusivity disorder in the myocardium using ECG/MCG sensor arrays. To model the cardiac activation we considered an inhomogeneous reaction-diffusion model in a real human torso. To model a the loss we used a parametric model for an oblate spheroid and set its conductivity to zero. We assumed that the remainder of the myocardium tissue was homogeneous. The proposed algorithm can be easily extended to account for an arbitrary spatial variation in the diffusivity tensor using a set of *a priori* known basis functions. In addition the parametric shape of the anomaly can be extended to model an arbitrary region using a three-dimensional spatial Fourier transform. An effort should be made to examine the sensitivity of the proposed algorithms to the size of diffusivity difference between "regular" tissue and anomaly as well as the number of the unknown parameters needed to model arbitrary shapes.

REFERENCES

1. Zhukov, L., et al.,"Heart-muscle fiber reconstruction from diffusion tensor MRI.," *Proc. 14th IEEE Visualization Conference*, IEEE, 2003.
2. FitzHugh, R. A., "Impulses and physiological states in theoretical models of nerve membrane," *Biophys. J.*, 1961.
3. Geselowtiz, D., "On the magnetic field generated outside an inhomogeneous volume conductor by internal current sources," *IEEE Trans. Magn.*, Vol. 6, 346–347, 1970.
4. Gulrajani, R. M., *Bioelectricity and Biomagnetism*, John Wiley & Sons, New York, 1998.
5. Malmivuo, J. and R. Plonsey, *Bioelectromagnetism*, Oxford University Press, New York, 1995.
6. Panfilov, A. and A. V. Holden, *Computational Biology of the Heart*, John Wiley & Sons, Chichester, 1st edition, 1997.

7. Rogers, J. M. and A. D. McCulloch, "A collocation-galerkin finite element model of cardiac action potential propagation," *IEEE Transactions on Biomedical Engineering*, Vol. 41, 743–757, 1994.
8. Sachse, F. B., *Computational Cardiology*, Springer, Berlin, 2004.
9. Vonesh, F. and V. M. Chinchilli, *Linear and Nonlinear Models for the Analysis of Repeated Measurements*, Marcel Dekker, New York, 1997.

Cloaking of Metallic Cube by Plasmonic Shell in Quasistatic Limit

Adnan Noor and Zhirun Hu
The University of Manchester, Manchester, UK

Abstract— In this paper cloaking of a cubic metallic object by plasmonic cover is investigated and numerically analyzed. Cloaking of PEC objects by plasmonic covers, especially plasmonic shells, has been recently investigated [1], and promising results have been produced. Most of these work concern with cloaking of sub-wavelength PEC spheres. Cloaking using plasmonic material was first theoretically investigated in reference [2] and [3]. Cloaking of electrically large objects has also been reported [4].

1. INTRODUCTION

Cloaking of objects using artificial electromagnetic materials, also known as matamaterials, has been investigated by several authors over last few years.

There are basically three ways of cloaking an object; first to absorb the radar signal, second to cancel out the radar signature of the object, and third one is to guide the radar waves around the object.

Cancelation of field generated by the target can be achieved by two means; first having a cloak with polarizability equal and opposite to the target; second to a permittivity and permeability profile which will result in anomalous resonance (when field approaches infinity in presence of finite polarization of target) in either the cloak or its vicinity, in such a case, the only possible electromagnetic solution is having the target polarization equal to zero, cloaking by anomalous resonance require spacialy varying non isotropic constitutive parameters.

Cloaking by cancellation of target polarization using plasmonic metamaterials has been investigated theoretically by Engheta [2] and Sihvola [3]. In the above mentioned paper, Engheta presented a mathematical model of such a cloak. Later the same author extended the concept to collection of partials [4].

Extension of these studies on plasmonic cloaks is subject of this paper. Cloaking by simply having a cloaking shell with polarizablity equal and opposite to the target is easy, however this can only achieved for subwavelength object.

The idea is, that field generated by an object can be decomposed into spherical harmonics, when one solves Maxwell's equation using spherical coordinates. Lowest order spherical harmonic represent electric and magnetic dipole terms, whereas higher order terms represent multipole terms. For subwavelength objects, multipole terms are negligible, and scattered field primarily consists of electric and magnetic dipole terms, with electric dipole being dominant. This means that subwavelength metallic object behave in similar way independent of their exact geometry. The only important parameters are their dimensions and material properties. For a given material, this means that a cloak can be designed which will cloak a verity of geometrical shapes, as long as the dimensions are roughly the same. In the discussion below cloaking a metallic cube is investigated.

The object investigated here is an aluminium cube, while the cloak is spherical plasmonic shell. Monostatic and Bistatic RCS are calculated using Ansoft HFSS, and compared to that of uncloaked cube. The reduction of RCS is also compared to the case of metallic sphere, the structure investigated in [1] .The operating frequency is selected to be 1.2 GHz.

Simulation results as good as that for cloaked metallic sphere investigated by Engheta [1], are obtained for the metallic cube, implying that for monostatic case the object geometry is not very critical. The cloaked structure is also investigated in presence of losses in the plasmonic shell. In case of losses the performance degrades slightly, however the reduction in RCS is still sufficient for potential practical applications.

2. SIMULATIONS AND RESULTS

In our study, an aluminium cube is enclosed in a plasmonic shell (relative permittivity 0.1, relative permeability 5.1) with outer radius of 57.5 mm and inner radius of 50 mm. Dimensions of the cube are chosen such that it would fit in the shell. The structure is simulated using Ansoft HFSS.

For shell plasmonic material, simulation was performed using two different parameters for losses. In first case dielectric loss tangent was 0.015 and magnetic loss tangent was nil, in second case a

magnetic loss tangent of 0.01 was added to the model. Results, with structures and detail of constitutive parameters of shell are given below.

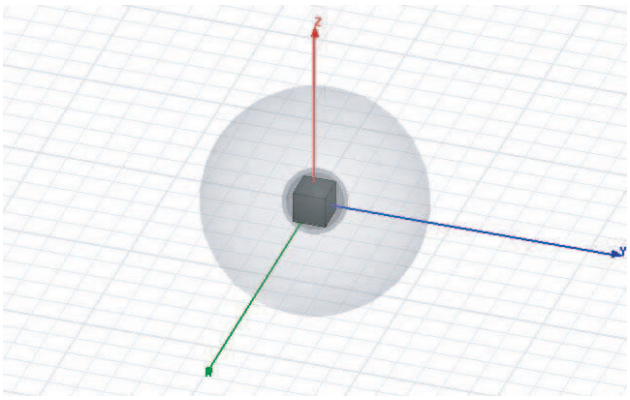

Figure 1: Structure with radiation boundries, R-rad=200 mm, $r_{\text{out}} = 1.15r_{\text{in}} = 57.5\,\text{mm}$, $r_{\text{in}} = 0.2\lambda = 50\,\text{mm}$, $\varepsilon_r = 0.1$, $\delta_e = 0.015$, $\mu_r = 5.1$.

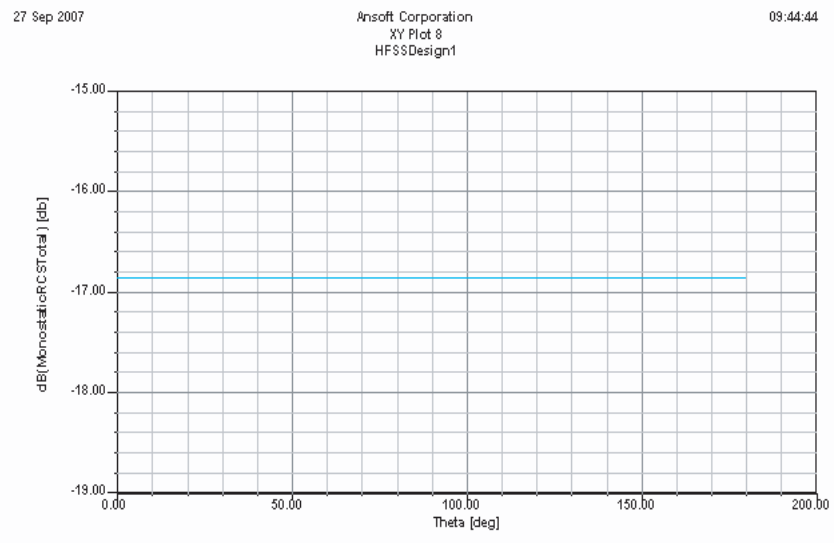

Figure 2: Monostatic RCS of cube shown in Fig. 1, without cloaking.

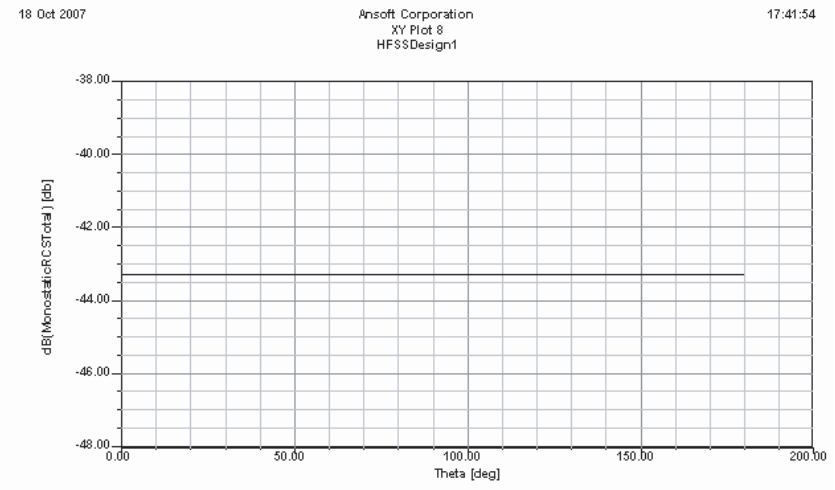

Figure 3: Monostatic RCS for structure shown in Fig. 1.

The simulation was then repeated with vector k having theta and phi of 45 whereas E having theta of 45 and phi -45. The purpose was to simulate the structure for oblique incidence. The results are shown below.

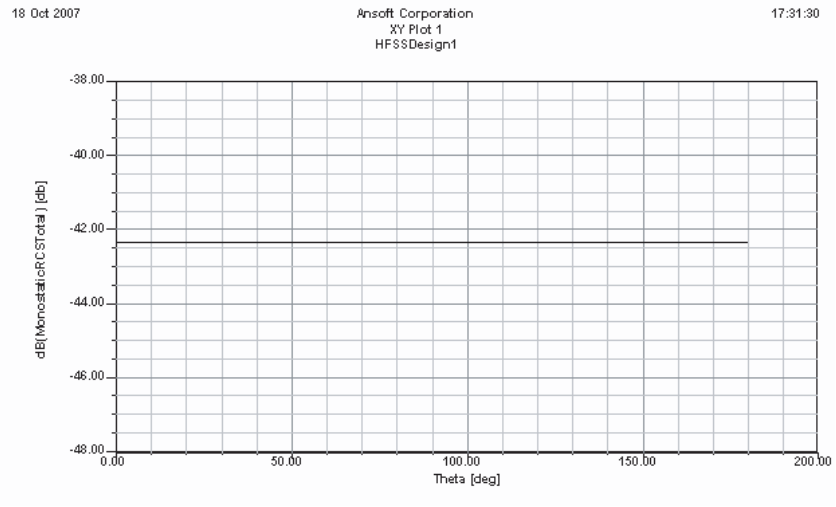

Figure 4: Monostatic RCS with $\delta m = 0.01$.

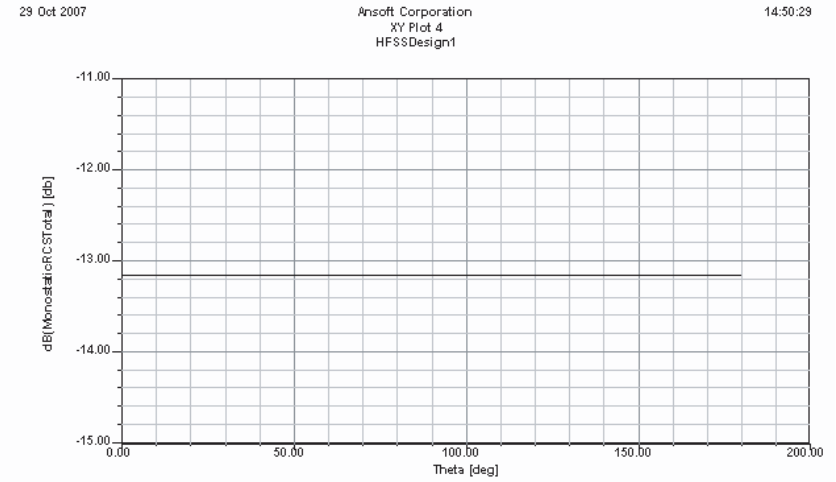

Figure 5: Monostatic RCS for oblique incidence without cloaking, for structure shown in Fig. 1, theta = 45, phi = 45 for k vector; theta = 45, phi = -45 for E vector.

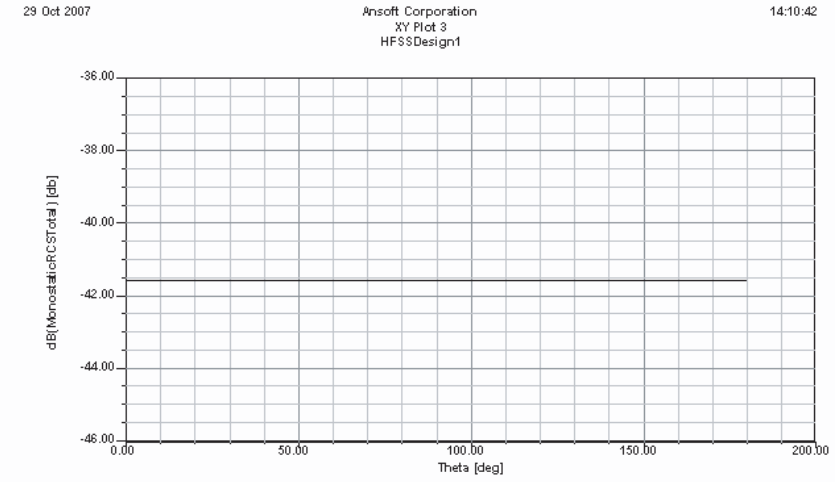

Figure 6: Monostatic RCS with cloaking , other parameters same as that for Fig. 5.

Now it can be seen from Fig. 5 and Fig. 6 that even in case of oblique incidence, reduction in Monostatic RCS is 99.8%. Furthermore, a dielectric loss tangent of 0.015 and magnetic loss tangent of 0.01 is also included in the model.

However repeating the experiment with cubical cloaking shell didn't given any reduction in RCS.

3. CONCLUSION

From the results above, it can be seen that for objects which are small compared to the operating wavelength, and hence can be modelled as superposition of electrical and magnetic dipole good cloaking can be achieved using hallow shell of magnetic plasmonic material. It is further evident that the geometry of the cloaked object is of little consequence, as long as the dimensions remain roughly the same, the reason being that in case of these small objects the only important parameters are electrical and magnetic dipole moment, which only depends on the dominant dimension in case of conducting objects.

REFERENCES

1. Engheta, N. and A. Alù, "Plasmonic materials in transparency and cloaking problems: mechanism, robustness, and physical insights," *Optics Express*, Vol. 15, No. 6, March 19, 2007.
2. Alù, A. and N. Engheta, "Achieving transparency with plasmonic and metamaterial coatings," *Phys. Rev. E*, Vol. 72, 016623, 2005.
3. Sihvola, A., "Peculiarities in the dielectric response of negative-permittivity scatterers," *Progress In Electromagnetics Research*, PIER 66, 191–198, 2006.
4. Alù, A. and N. Engheta, "Cloaking and transparency for collections of particles with metamaterial and plasmonic covers," *Optics Express*, Vol. 15, No. 12, June 11, 2007.

Resonance as a Tool to Transfer Informations to Living Systems

Antonella Lisi[1], **Deleana Pozzi**[2], **Mario Ledda**[1], **Flavia de Carlo**[1]
Roberto Gaetani[2], **Enrico D'Emilia**[3], **Livio Giuliani**[3], **Francesca Bertani**[2]
Isotta Chimenti[2], **Lucio Barile**[2], **Alberto Foletti**[4], **and Settimio Grimaldi**[1]

[1]Istituto di Neurobiologia e Medicina Molecolare, C.N.R., Rome, Italy
[2]Dipartimento di Medicina Sperimentale, Università "La Sapienza", Rome, Italy
[3]ISPESL DIPIA, Italy
[4]Bititalia, Milano, Italy

Abstract— Studies for the identification of suitable stem cells culture and differentiating conditions that are devoid of xenogenic growth supplements is actually considered an important issue for the clinical applicability of cell therapy for heart failure and bone remodeling, growth and repair.

About the first one we have recently demonstrated the possibility to obtain Cardiac Stem Cells (CSCs), from human endomyocardial biopsy specimens. CSCs self-assemble into multicellular clusters known as cardiospheres (CSps) that engraft and partially regenerate infarcted myocardium.

CSps and Cardiospheres-derived-Cells CDCs were exposed for five days in an incubator inside a solenoid system with temperature and humidity and CO_2 regulated. This exposure system were placed in an amagnetic shielded room in the simultaneous presence of a static MF and a low-alternating-frequency-MF, close to the cyclotron frequency corresponding to the charge/mass ratio of Ca^{++} ion. In this exposure conditions CSps and CDCs modulate their differentiation turning on cardiogenesis and turning off vasculogenesis. Cardiac markers such as Troponin I (TnI) or Myosin Heavy Chain (MHC) were up-regulated, conversely angiogenic markers such as Vascular Endothelial Growth Factor (VEGF) or Kinase Domain Receptor (KDR) were down-rugulated as evidenced by immunocytochemistry. The improvement in the cardiogenic differentiation was confirmed by Real-Time PCR and Western Blotting. Interestingly, an increase in the proliferation (particularly of the CDCs) was observed and evidenced by Brd-U incorporation (ELISA) and cell counting kit-8 (WST-8) analysis.

Exposure to Calcium ion ICR can modulates the cardiogenic *versus* angiogenic differentiation process of *ex vivo* expanded CSCs.This may pave the way for novel approaches in tissue engineering and cell therapy.

Concerning bone remodelling our study shows that exposure of human MSC to ELF-MF enhanced expression of osteoblast marker differentiation such as Alkaline phosphatase, (AP), Osteocalcin (OCL), and osteopontin (OPN), analyzed by real-time quantitative PCR, without affecting cell proliferation. As expected, while the markers differentiation factors where up regulated, electromagnetic field down regulate osteoprotegerin (OPG) gene expression, a critical regulator of postnatal skeletal development and homeostasis in humans as well as mice. The exposure of hMSC for 5 days to the field resulted in a change in shape and in plasma membrane morphology and this modification were also accompanied by a rearrangement in actin filaments, as showed by confocal miscroscopy analysis after cells labelling with FITC-phalloidin.

1. INTRODUCTION

The middle of the eighties was marked with the discovery by Blackman [2] and Liboff [6] of a surprising phenomenon: a low frequency alternating (AC) magnetic field (MF) changed free calcium concentration in nervous tissue only in the presence of a simultaneously acting static (DC) MF. The most prominent effect was observed at the AC field frequency close to the cyclotron frequency of a calcium ion. The cyclotron frequency is defined [6] as

$$f_C = \frac{q}{2\pi m} B_o,$$

where q and m are the charge and mass of the ion, and B_o is the DC field. These works opened a new line of research in Bioelectromagnetics.

There were three unexpected qualities in this phenomenon: 1) the necessity simultaneous action of DC and AC MFs, 2) the resonance effect on cyclotron frequency, and 3) very small values of acting

MFs, measured with tens of μT, and extremely low frequencies of AC MFs, measured with several tens of Hz. Therefore, these results evoked a suspicion in the scientific community. Afterwards, many confirmations for these data were obtained in works performed on different objects and in different experimental situations [7, 5, 3, 11] which convinced the scientific community of the real existence of the above effects.

Exposure porotocols: Calcium ICR exposure protocols, were generated in a properly alimented large solenoid (3 meter long 30 cm width) in a μ metal shielded room. A thermostatic equipment within a large solenoid and proper probes have been developed to provide both static and alternating magnetic fields suitable to expose cells, in strictly controlled microclimatic and electromagnetic environment.

The large solenoid were properly powered in order to continuously generate low magnetic field frequencies from 0 to 10 Hz. The alternating magnetic field was combined with the appropriate static magnetic field. In such way the parallelism of the two combined magnetic fields is ensured and the intensity of the static field is fixed, in order to provide the appropriate cyclotronic frequency of the concerned ions or aminoacids.

2. RESULTS

2.1. Cardiac Stem Cells

We have recently demonstrated the possibility to obtain Cardiac Stem Cells (CSCs), from human endomyocardial biopsy specimens. CSCs self-assemble into multi-cellular clusters known as cardiospheres (CSps) that engraft and partially regenerate infarcted myocardium.

CSps and Cardiospheres-derived-Cells CDCs were exposed for five days in an incubator inside a solenoid system with temperature and humidity and CO_2 regulated. This exposure system were placed in an amagnetic shielded room in the simultaneous presence of a static MF and a low-alternating-frequency-MF, close to the cyclotron frequency corresponding to the charge/mass ratio of Ca^{++} ion. In this exposure conditions CSps and CDCs modulate their differentiation turning on cardiogenesis and turning off vasculogenesis. Cardiac markers such as Troponin I (TnI) or Myosin Heavy Chain (MHC) were up-regulated (Fig. 1) , conversely angiogenic markers such as Vascular Endothelial Growth Factor (VEGF) or Kinase Domain Receptor (KDR) (Fig. 2) were down-rugulated as evidenced by immunocytochemistry. The improvement in the cardiogenic differentiation was confirmed by Real-Time PCR and Western Blotting. Interestingly, an increase in the proliferation (particularly of the CDCs) was observed and evidenced by Brd-U incorporation (ELISA) and cell counting kit-8 (WST-8) analysis.

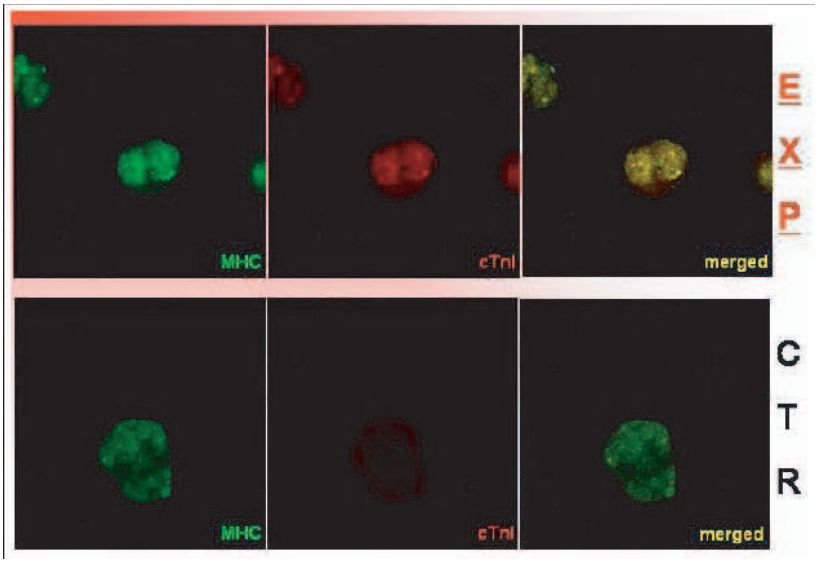

Figure 1: Indirect immunofluorescence of cardiac differentiation markers Troponin I (TnI) and Myosin Heavy Chain (MHC) were up-regulated in ICR exposed cells.

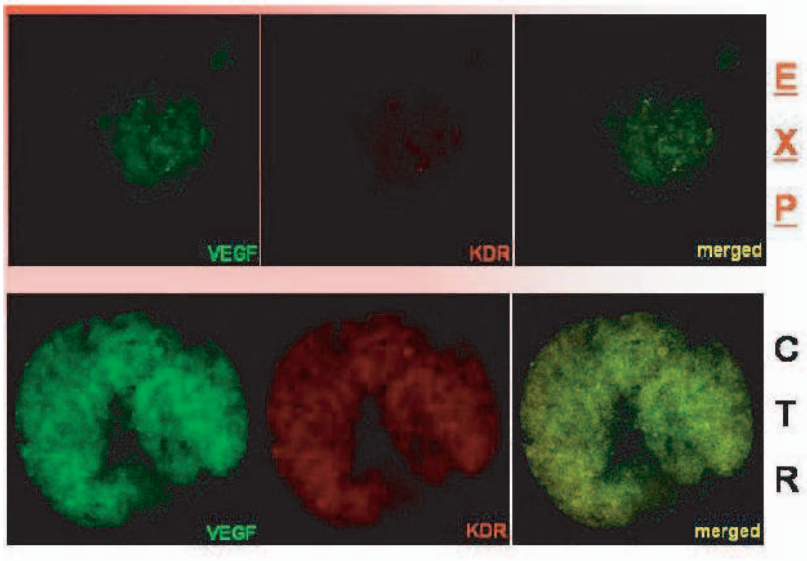

Figure 2: Indirect immunofluorescence of the angiogenic markers Vascular Endothelial Growth Factor (VEGF) and Kinase Domain Receptor (KDR) in ICR exposed cells.

2.2. Mesenchimal Stem Cells

Exposure to low frequency electromagnetic field for 5 days resulted in a change in plasma membrane morphology and this modification were also accompanied by a rearrangement in actin filaments as showed by confocal miscroscopy analysis after cells labeling with FITC-phalloidin.

In particular, mesenchimal cells exposed to the field showed a different actin organization in cells after field treatement. The same effect were found in cell treated with the differentiating drugs dexamethasone.

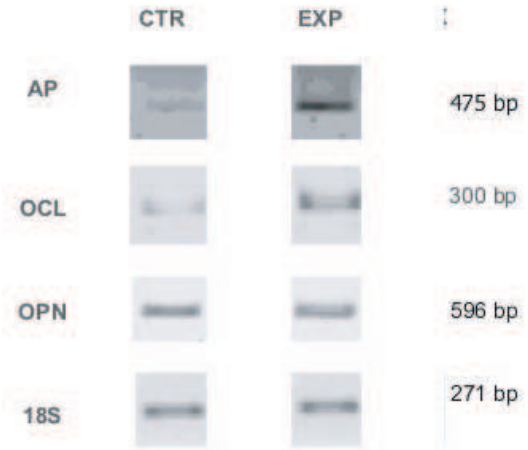

Figure 3: RT-PCR analysis. Total mRNA was extracted from Control (CTR), and Exposed (EXP) stem cells. RT-PCR analysis was used for osteoblast differentiation markers detection with specific primers: Alkaline Phosfatase (AP), Osteocalcin (OCL) and Osteopontin (OPN). The amount of template and the number of amplification cycles were preliminarily optimized for each PCR reaction to avoid conditions of saturation.

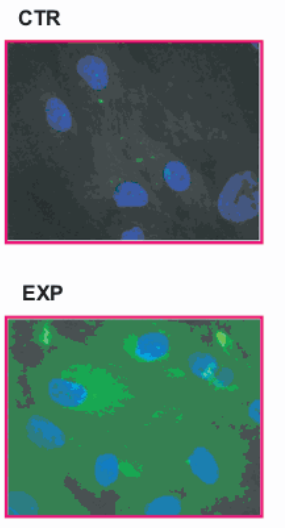

Figure 4: ELF-MF modulation Osteopontin differentiation marker expression see by indirect immunofluorescence microscopy. Images show modulation of Osteopontin expression in control (CTR), Exposed (EX) stem cells. Figures were executed with 100x objective.

After 5 days of exposure, the mRNA expression for osteoblast markers differentiation such as Alkaline Phosfatase (AP), Osteocalcin (OCL) and Osteopontin (OPN) increase (Fig. 3) this result were further confirmed by indirect immunofluorescence assay for osteopontin Osteopontin showed an increase in exposed cells with respect to control (Fig. 4).

In conclusion our finding demonstrated that exposure to ELF can act as a differentiating agent on mesenchymal human cells outlining the relevance of low frequency electro-magnetic field as a terapeutical agent suggesting a possible use of ELF as support in medicine for different pathologies therapy.

3. DISCUSSION

Earlier there were attempts to understand the physical mechanisms of resonance action of combined MFs. Prof A. Liboff [6], considering the motion of free ions under action of these MFs, supposed a mechanism similar to the one working in a living system like a cyclotron. But at room temperature this idea could be realized only in very large systems capable to include the long radius of ion rotation measured by meters. The idea [4]; on participation of parametric resonance in such sort of effects was not very fruitful for lack of a necessary low frequency harmonic oscillator in living systems. The Larmor precession could not help in this situation, not being such an oscillator because of lack of restoring force with proper parameters. The problem solving had come from Quantum Electrodynamics of Condensed Matter. According to the quantum electro-dynamical theory by Preparata (1995), the liquid water consists of two components: coherent and incoherent ones. The coherent component is contained within spherical so called "coherence domains" (CDs) where all molecules synchronously oscillate with the same phase. CDs are surrounded by the incoherent component where molecules oscillate with casual phases regarding each other. Diameters of CDs are measured by tenths of a micron, and at room temperature the total volume of domains is about 40% of the whole water media. At resonance action of the calcium ion cyclotron frequency the ion is accelerated by the MFs, increasing its kinetic energy till its escape from CD jumping into the incoherent component of the water molecule where the ion became biologically available.

4. CONCLUSION

Exposure to Calcium ion ICR can modulates the cardiogenic versus angiogenic differentiation process of ex vivo expanded CSCs; as well as mesenchimal versus osteocytes differention. This may pave the way for novel approaches in tissue engineering and cell therapy.

ACKNOWLEDGMENT

This work has been supported by ISPESL grant number: B1/4/DIPIA/2005.

REFERENCES

1. Adair, R. K., "Biophysical limits on athermal effects of RF and microwave radiation," *Bioelectromagnetics*, Vol. 24, 39–48, 2003.
2. Blackman, C. F., S. G. Benane, D. E. House, and W. T. Joines, "Effects of ELF (1–120 Hz) and modulated (50 Hz) RF fields on the efflux of calcium ions from brain tissue in vitro," *Bioelectromagnetics*, Vol. 6, 1–11, 1985.
3. Blackman, C. F., J. P. Blanchard, S. G. Benane, and D. E. House, "Empirical test of an ion parametric resonance model for magnetic field interactions with PC-12 cells," *Bioelectromagnetics*, Vol. 15, 239–260, 1994.
4. Lednev, V. V., "Possible mechanism for the influence of weak magnetic fields on biological systems," *Bioelectromagnetics*, Vol. 12, 71–75, 1991.
5. Lerchi, A., R. J. Reiter, K. A. Howes, K. O. Nonaka, and K. A. Stokkan, "Evidence that extremely low frequency Ca-cyclotron resonance depresses pineal melatonin synthesis in vitro," *Neurosci Lett.*, Vol. 124, 213–215, 1991.
6. Liboff, A. R., "Cyclotron resonance in membrane transport," Chiabrera, A., C. Nicolini, H. P. Schwan (eds): *Interaction between Electromagnetic Fields and Cells*, 281–296, Plenum Press, London, 1985.
7. Liboff, A. R., S. D. Smith, and B. R. McLeod, "Experimental evidence for ion cyclotron resonance mediation of membrane transport," Blank, M., E. Findl (eds): *Mechanistic Approaches to Interaction of Electric and Electromagnetic Fields with Living Systems*, 109–132, Plenum Press, New York, 1987.

8. Zhadin, M. N., "Effect of magnetic fields on the motion of an ion in a macromolecule: Theoretical analysis," *Biophysics*, Vol. 41, 843–860, 1996.
9. Zhadin, M. N., "Combined action of static and alternating magnetic fields on ion motion in a macromolecule: Theoretical aspects," *Bioelectromagnetics*, Vol. 19, 279–292, 1998.
10. Zhadin, M. N., V. V. Novikov, F. S. Barnes, and N. F. Pergola, "Combined action of static and alternating magnetic fields on ionic current in aqueous glutamic acid solution," *Bioelectromagnetics*, Vol. 19, 41–45, 1998.
11. Zhadin, M. N., O. N. Deryugina, and T. M. Pisachenko, "Influence of combined DC and AC magnetic fields on rat behavior," *Bioelectromagnetics*, Vol. 20, 378–386, 1999.
12. Zhadin, M. and L. Giuliani, "Some problems in modern bioelectromagnetics," *Electromagnetic Biology and Medicine*, Vol. 25, 227–243, 2006.

Dual-beam Interferometric Laser Trapping of Rayleigh and Mesoscopic Particles

V. L. Y. Loke, T. A. Nieminen, N. R. Heckenberg, and H. Rubinsztein-Dunlop
The University of Queensland, Australia

Abstract— There has been a significant amount of experimental work with counter-propagating, crossed-beam, and other interferometric laser trapping of neutral dielectric particles. Apart from the benefits of these configurations, such as the compensation or neutralization of scattering forces, there are a number of interesting applications. For example, the optical lattice resulting from interference can be used to sort particles of different refractive indices or sizes. The system can also be used to study thermal hopping between potential wells or to investigate Brownian motion subject to a quasi-periodic external potential.

Most theoretical work on dual-beam systems has been focused on Rayleigh particles. For mesoscopic particles, where Rayleigh scattering is not applicable, we employ the generalized Lorenz–Mie theory (GLMT) which is synonymous with the T-Matrix method when considering spherical particles. GLMT is an exact method which is applicable in both the Rayleigh and mesoscopic regimes.

We calculate the fields and optical forces on the particles in the vicinity of the trapping region for several dual beam configurations such as counter-propagating, axially offset, and crossed beams, and with different particle sizes. We present the intensity profiles which demonstrate the interference fringes and the force vectors to predict the positions where a given particle can be localized. Surprisingly, our results show that sub-wavelength localization by interference fringes of particles that are much larger than the wavelength (or fringes) of the trapping beams is possible. The competition between such localization by interference fringes and attraction to the focus can be controlled by the beam convergence angle, or, equivalently, the numerical aperture of the focussing system.

1. INTRODUCTION

Single tweezers — the single beam gradient trap — were first demonstrated by Ashkin et al. in 1986 [1]. However, even before that, Ashkin [2] achieved trapping by means of the dual counter-propagating beam configuration, taking advantage of the neutralization of scattering forces along the axial direction. Dual beam trapping and manipulation continues to be of interest in more recent times, ranging from steerable dual beams [5], cross beam configurations [3] to biological application applications [7]. Optical forces have been calculated theoretically, often by approximate methods, such as Rayleigh scattering [4] by nanoparticles in evanescent interference fields.

Since many experiments are performed using mesoscopic particles, we use the generalized Lorenz-Mie theory [6] (GLMT) which is also valid in the Rayleigh regime. The GLMT is synonymously known as the T-matrix method [8–11] when the scatterer (particle) is homogeneous isotropic sphere. Our calculations are performed using an optical tweezers computational toolbox for MATLAB [12]. The toolbox is available for download at [13].

We present the intensity profiles of the trapping beams and the forces experienced by the particles particularly in the region around the foci and along the beam axes. We investigate the co-focused counter propagating beam and cross beam configurations. In this paper, we do not place any emphasis on radial trapping forces because in general, the radial equilibrium position is on the beam axis and is easily attained.

2. COUNTER-PROPAGATING BEAMS

Two counter-propagating, otherwise identical mutually-coherent beams, produce interference fringes. This provides an intensity profile that has a rapid spatial variation along the beam axis, which is of interest for optical trapping. The simple case where the beams share the same focal point in shown in Figure 1, along with a single beam for comparison. The beams are linearly polarized. The force vectors acting on a Rayleigh particle are shown in Figure 1(c); these point towards regions with high intensity, and demonstrate the localization of small particles within individual interference fringes. For the beam convergence angle shown, 20°, the curvature of the wavefronts is small, and effects should be qualitatively understandable in terms of a simple model based on a plane-wave interference pattern with radial and axial variation of intensity.

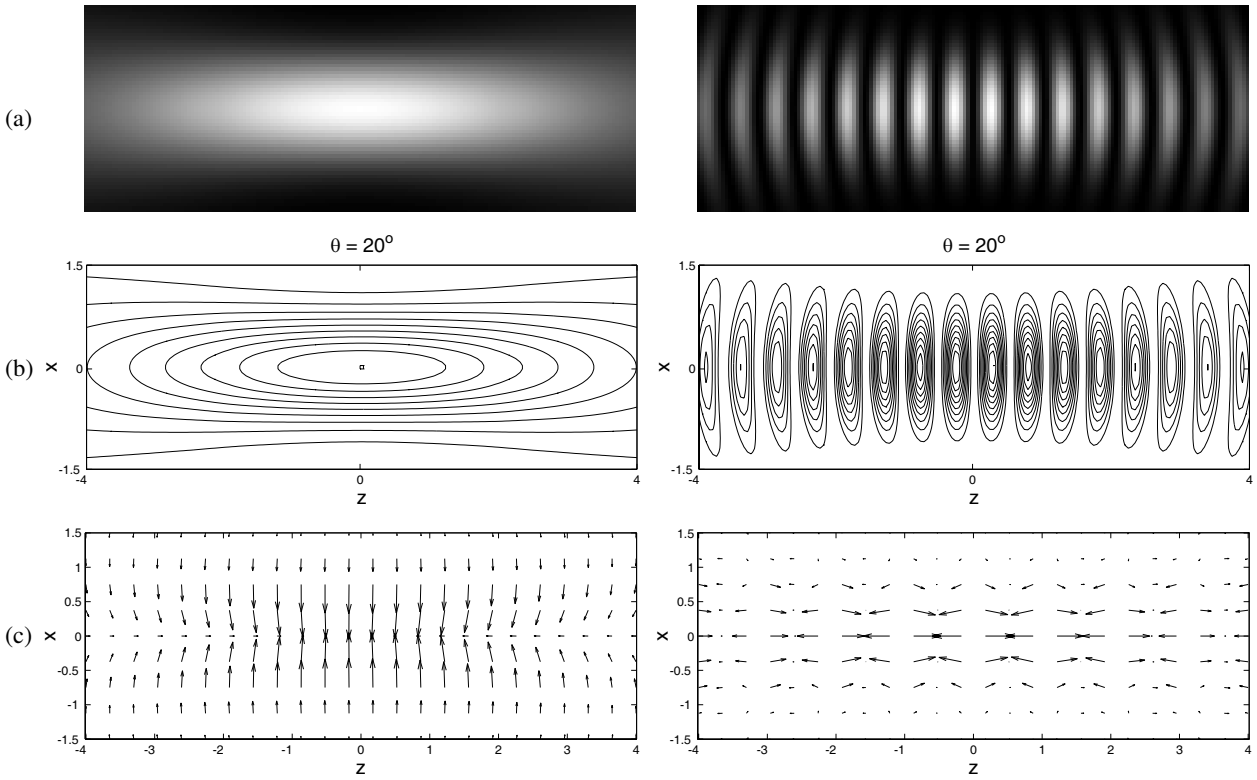

Figure 1: Single beam (left column) and dual counterpropagating beams (right column). (a) Intensity profiles, (b) intensity contours and (c) force vectors for a 0.1λ sized particle.

We calculate the axial forces (Figures 2 & 3) experienced by particles of various sizes and beam convergence angles in counter propagating beams. As expected, Rayleigh particles are clearly localized in the fringes. Mesoscopic particles (radii of 0.5λ and 5λ) also experience a force attracting them to the focus. This force is combined with a gradient force acting to localize the particles within individual fringes, and consequently appears as a trend modifying the interference fringe force. For the 10° beam (Figure 2, right), this force is small as the overall axial intensity change is small. Surprisingly, it appears that even the large particles, with diameters spanning many intereference fringes, are still localized by individual fringes. This occurs even for a highly convergent beam, although in this case, the number of fringes available to the particle in which it can be trapped is small. For the less convergent beams, large particles can be localized by individual fringes as long as the brightest fringes lie within the particle.

This suggests that interference fringe trapping of large particles, which are much easier to see under the microscope than nanoparticles, could provide an interesting probe of Brownian motion in a 1D series of potential wells.

3. CROSSED BEAMS

Interferometric trapping with multiple beams [3] has been performed on nanoparticles. Here we demonstrate that it is also possible to similarly trap mesoscopic particles. We set the beams at right angles but maintain the foci at the same point. Figure 4 shows that for low beam convergence angles, the interference fringes are clearly visible, and as the beam convergence angle is increase the fringes merge to form one bright spot.

There is an important physical distinction between this crossed-beam case and the counter-propagating beam case, clearly visible for the 10° beam convergence angle case — in the counter-propagating case, the scattering forces from the two beams are in opposite directions, and cancel. In the crossed beam case, on the other hand, the two individual scattering forces are at right angles, and the resultant force is about 1.4 times greater than either individually. As a result, we no longer see localization within individual interference fringes. What does occur is that the combined scattering force pushes the particle to the far corner of the region where the two beams overlap, at which point the gradient force — effectively, the combined radial gradient forces of the two beams

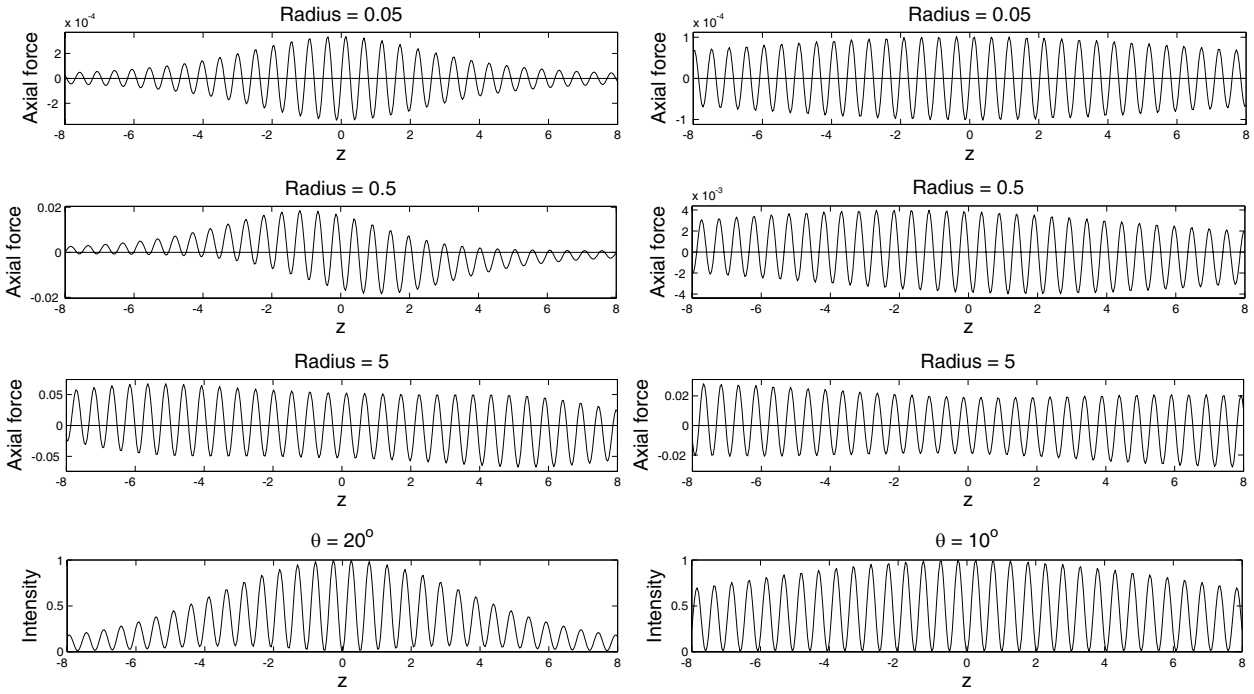

Figure 2: Axial forces on particles with a range of sizes and for beam convergence angles of 20° (left) and 10° (right) in dual counter propagating beams.

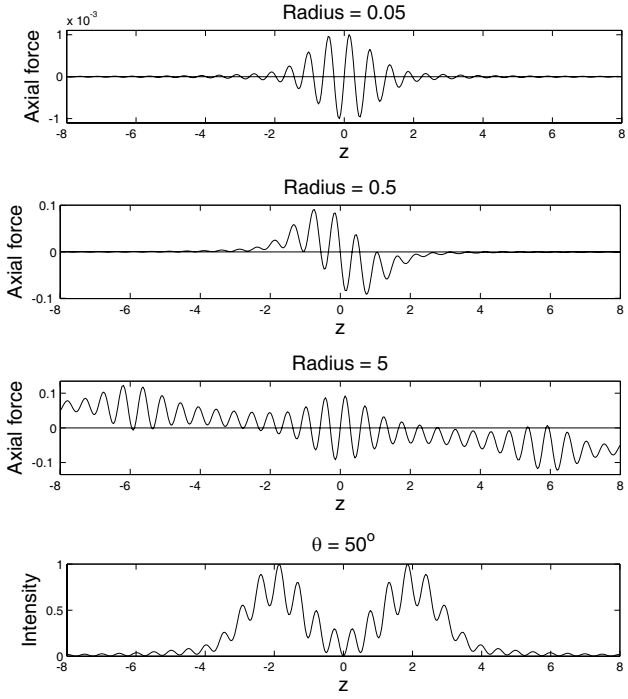

Figure 3: Axial forces on particles with a range of sizes and for the beam convergence angle of 50° in dual counter propagating beams.

— overcomes the scattering force, and no further motion in this direction is possible. However, the particle is not trapped, as the intensity gradient along the beams is smaller than the intensity gradient in the diagonal direction, and the gradient force is not large enough to stably trap the particles. The force vectors (Figure 4, left) show that only an unstable equilibrium position exists.

One possible application of this trap geometry is guiding and sorting of particles. Particles could be introduced along one beam, and sorted into the two output beams. Control could be achieved

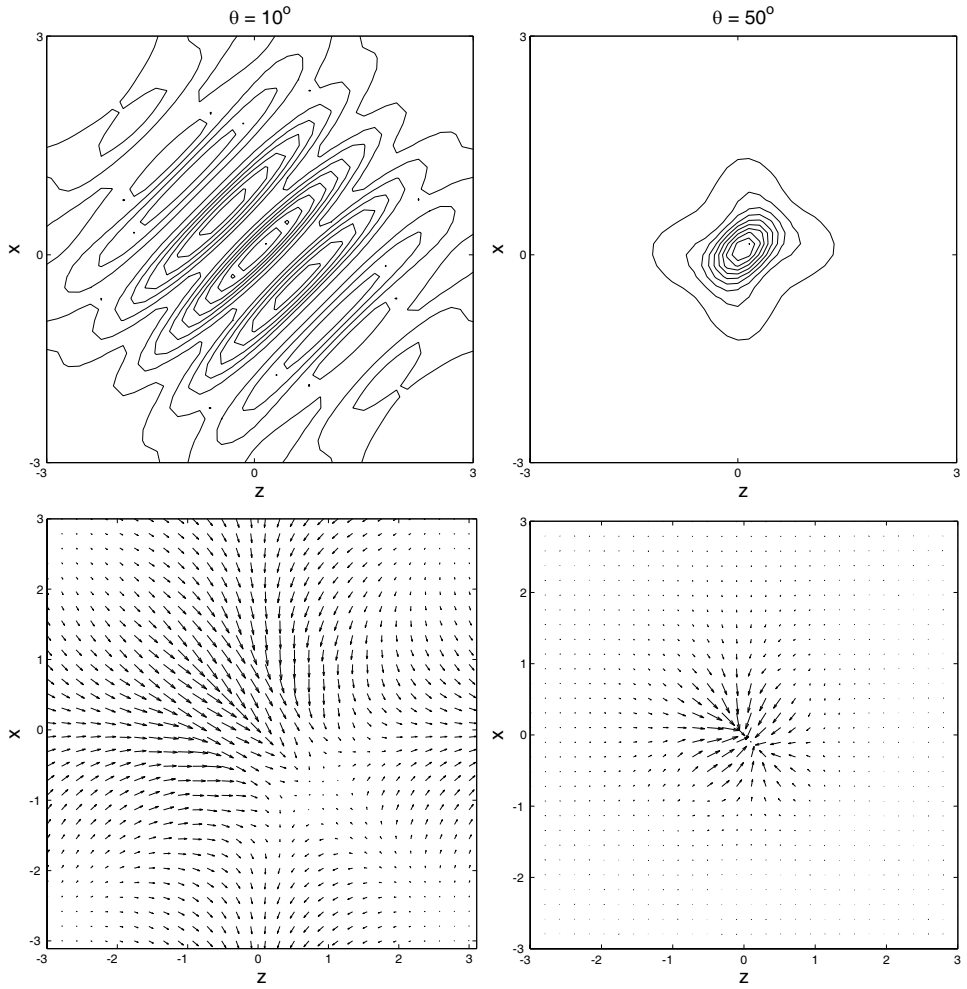

Figure 4: Contour of beam intensity of cross beams and force vectors for 1λ sized particle for beam convergence angles of 10° and 50°.

by varying the intensity of one of the second beam.

Rayleigh particles, with a greatly reduced scattering force, will still be localized in the fringes.

Stable trapping of mesoscopic particles can be achieved with a more convergent beam (Figure 4, left), but in this case, there is no localization within individual fringes. In practice, this geometry with highly convergent beams will be difficult to achieve but, depending on the particles in question, it may be possible to achieve 3D trapping. An interesting application would be a 3D trap with a built-in particle ejection system — one would have both beams switched on for 3D trapping, and turn one off to eject a particle using the scattering force.

4. CONCLUSION

We have demonstrated the capability to calculate optical forces on spherical particles with radii on the order of the trapping wavelength, using a Matlab optical tweezers computational toolbox [12]. While we have only investigated the simplest geometries, any number and combination of beams is theoretically possible, with computational requirements being dominated by characteristic size of the multiple-beam combination, typically the larger of the sum of the beam width and the maximum distance between two focal points, and the particle radius. This allows for any combination of number of beams, convergence angles, orientations and axial and transverse offsets of focal points to simulate interferometric trapping of particles ranging from Rayleigh sized to mesoscopic. Our simulations show that high gradient fringes can be exploited to localize even macroscopic particles.

For low beam convergence angles, this localization by individual fringes can allow even large particles to be used for the investigation of 1D Brownian motion — for instance, the evolution of the position of the particle in the optical lattice.

As the beam convergence angle increases, a counter-propagating trap behaves similarly to a

convential optical tweezers trap with no scattering force, although some localization by individual fringes remains. This lack of scattering force indicates the possiblity of the strong confinement of particles normally considered untrappable due to high relative refractive index or absorptivity. This type of technique predates optical tweezers [2], as mentioned earlier, but it could still be a useful complement to conventional optical tweezers.

Further investigation is warranted for crossed-beam traps, with the potential for confinement through the radial gradient force of one beam overcoming the axial scattering force of another, or simply as regions where a particle being pushed along one beam can be switched to another beam. In this way, a number of beams that cross at different points could provide useful sorting and guided of particles in a microfluidic device.

REFERENCES

1. Ashkin, A., J. M. Dziedzic, J. E. Bjorkholm, and S. Chu, "Observation of a single-beam gradient force optical trap for dielectric particles," *Optics Letters*, Vol. 11, 288–290, 1986.
2. Ashkin, A. and J. M. Dziedzic, "Observation of radiation-pressure trapping of particles by alternating light-beams," *Physical Review Letters*, Vol. 54, 1245–1248, 1985.
3. Casaburi, A., G. Pesce, P. Zemanek, and A. Sasso, "Two- and three-beam interferometric optical tweezers," *Optics Communications*, Vol. 251, 393–404, 2005.
4. Siler, M. and P. Zemanek, "Optical forces acting on a nanoparticle placed into an interference evanescent field," *Optics Communications*, Vol. 275, 409–420, 2007.
5. Fallman, E. and O. Axner, "Design for fully steerable dual-trap optical tweezers," *Applied Optics*, Vol. 36, 2107–2113, 1997.
6. Gouesbet, G., "Generalized Lorenz-Mie theory and application," *Particle and Particle Systems Characterization*, Vol. 11, 22–34,, 1994.
7. Lincoln, B., S. Schinkinger, K. Travis, F. Wottawah, S. Ebert, F. Sauer, and J. Guck, "Reconfigurable microfluidic integration of a dual-beam laser trap with biomedical applications," *Biomedical Microdevices*, Vol. 9, 703–710, 2007.
8. Waterman, P. C., "Matrix formulation of electromagnetic scattering," *Proceedings of IEEE*, Vol. 53, 805–812,, 1965.
9. Mischenko, M. I., J. W. Hovenier, and L. D. Travis, *Light Scattering by Nonspherical Particles: Theory, Measurements and Applications*, Academic Press, San Diego, 2000.
10. Nieminen, T. A., N. R. Heckenberg, and H. Rubinsztein-Dunlop, "Multipole expansion of strongly focussed laser beams," *Journal of Quantitative Spectroscopy and Radiative Transfer*, Vol. 79–80, 1005–1017, 2003.
11. Nieminen, T. A., N. R. Heckenberg, and H. Rubinsztein-Dunlop, "Computational modelling of optical tweezers," *Proceedings of SPIE*, Vol. 5514, 514–523, 2004.
12. Nieminen, T. A., V. L. Y. Loke, A. B. Stilgoe, G. Knöner, A. M. Brańzyk, N. R. Heckenberg, and H. Rubinsztein-Dunlop, "Optical tweezers computational toolbox," *Journal of Optics A*, Vol. 9, S196–S203, 2007.
13. http://www.physics.uq.edu.au/people/nieminen/software.html

Development of Thin Soft Magnetic Amorphous Microwires for High Frequency Magnetic Sensors Applications

A. Zhukov[1], **M. Ipatov**[1], **C. García**[1], **J. Gonzalez**[1]
L. Panina[1,2], **J. M. Blanco**[3], **and V. Zhukova**[3]

[1]Dpto. de Física de Materiales, Fac. Químicas
Universidad del Pais Vasco, San Sebastián 20009, Spain
[2]School of Computing, Communications and Electronics
University of Plymouth, Pl4 8AA, UK
[3]Dpto. de Física Aplicada, EUPDS
Universidad del Pais Vasco, San Sebastián 20009, Spain

Abstract— In this paper we report novel results on hysteretic properties and GMI effect (diagonal and off-diagonal components) at high frequency region (between 10 MHz and 500 MHz) in thin amorphous microwires (Fe-rich, Co-rich and Co-Fe-rich with nearly-zero magnetostriction constant) with metallic diameter between 5 and 15 μm. Control of the samples composition and geometry allows to tailor their magnetoelastic anisotropy and respectively magnetic softness and GMI. On the other hand special thermal treatment allows inducing the magnetic anisotropy by stress and/or magnetic field annealing. Such induced anisotropy allows achieving better magnetic softness, stress and temperature sensitivity. Development of novel soft magnetic microwires compositions with low Curie temperature allows obtaining temperature sensitive GMI effect.

1. INTRODUCTION

Amorphous glass-coated wires obtained by the Tailor- Ulitovski method (with total diameter between 10–50 μm, consisting of metallic nucleus of 1–30 μm in diameter and glass-coating with thickness between 0.5–10 μm) gained special attention within last few years because of their interesting magnetic and transport properties (spontaneous magnetic bistability, GMI effect, enhanced magnetic softness, etc.) [1, 2].

Main possible applications are related with the detection of the magnetic fields, small weights and vibrations [3]. Additionally new types of stress- tuneable composite materials consisting of short pieces of conductive ferromagnetic wires embedded into a dielectric matrix with the effective microwave permittivity depending on an external dc magnetic field, temperature or tensile stress recently have been introduced [4]. The advantage of these composite materials is that the electric contact problems can be avoided because of the wireless signals detection. Therefore thin wires with enhanced stress sensitivity of the GMI effect and with Stress impedance (SI) effect are quite desirable for designing of such stress- tuneable composite materials.

Hysteretic magnetic properties of glass-coated microwires are affected by strong magnetoelastic energy related with strong internal stresses induced during simultaneous and rapid solidification of the thin metallic nucleus surrounded by the glass coating having quite different thermal expansion coefficients and the value and sign of the magnetostriction constant, λ_s. Consequently the magnetoealstic anisotropy of glass-coated microwires is generally larger because of such additional source of internal stresses [2]. This magnetoelastic anisotropy depends on the geometric parameters (thickness of glass coating) and conditions of annealing allowing to enhance soft magnetic properties and GMI effect (up to 600%) even in the same chemical composition of the metallic nucleus. Therefore the compositional range of alloys with enhanced magnetic softness can be also slightly extended by using special heat treatment allowing induction of magnetic anisotropy and/or compensation of existing magnetoelastic anisotropy [5, 6]. Another possible application of such thin microwires is based on the ferromagnetic-paramagnetic transition at Curie temperature, when the magnetization and magnetic permeability drops down. Usually the Curie temperature of Fe and Co-rich amorphous microwires is about 300–400°C [7]. On the other hand it is known that the addition of Cr and Ni results in drastic decrease of the Curie temperature. In this way a wide variety of microwires with the Curie temperatures ranging between room temperature and 400°C can be obtained. This can give the possibility to use the ferromagneticparamagnetic transition at around Curie temperature to detect the temperature. Such changes can be detected through the change of the magnetization, magnetic permeability or even GMI effect closely related with the ferromagnetic origin of magnetic conductor.

Consequently the aim of this paper is to present results on tailoring of soft magnetic properties of Co and Fe-rich glass-coated microwires sensitive to applied stress an/or temperature by designing their composition and/or by induction of weak transverse magnetic anisotropy by the heat treatment.

2. EXPERIMENTAL METHOD AND SAMPLES

Thin magnetic glass-coated microwires based on Co, Fe and Ni (with additions of Cr to decrease the Curie temperature) have been fabricated by the Taylor-Ulitovsky method. The method itself is described elsewhere [2]. The modern Taylor-Ulitovsky process [2] is based on direct casting from the melt.

The longitudinal M-H hysteresis loop of the samples was measured at room temperature by means of an induction method at 50 Hz, such as described elsewhere [2, 5, 6]. The *AC* magnetic field, H, with a maximum field of 5 kA/m has been applied by a pair Helmholtz coils.

Furnace annealing without applied stress (CA) and under applied tensile stress (SA) at annealing temperatures, T_{ann}, below crystallization temperature and/or Joule heating have been employed to induce magnetic anisotropy and/or reduce the residual stresses. It is worth mentioning that the SA annealing has been performed with the sample previously loaded by the stress, then placed in the furnace already heated till desirable temperature and finally slowly cooled under applied stress with the furnace.

The impedance, Z, of the microwire was evaluated by means of the four-point technique at *AC* current frequency, f, 10 MHz for the driving current amplitude, I, ranging between 1–2 mA.

The magneto-impedance ratio, $\Delta Z/Z_H$, has been defined as:

$$\Delta Z/Z_H = [Z(H) - Z(H_{\max})]/Z(H_{\max}) \tag{1}$$

A maximum *DC* longitudinal magnetic field, $H_{\max}$, up to 8 kA/m has been supplied by a pair of Helmholtz coils.

The off-diagonal surface tensor component $\int_{z\varphi}$ with the pulse excitation, as described in ref. [8] is measured.

3. RESULTS AND DISCUSSION

3.1. Development of Magnetically Soft Microwires (Nearly-zero Magnetostriction Co-rich Microwires)

Hysteresis loops of $Co_{67}Fe_{3.85}Ni_{1.45}B_{11.5}Si_{14.5}Mo_{1.7}$ microwires with vanishing magnetostriction constant ($\lambda_s \approx -3 \cdot 10^{-7}$) [2] and with the metallic nucleus diameter around 10 μm are shown in Fig. 1. Microwires were obtained under different fabrication conditions allowing to change the glass coated thickness. It is worth mentioning that excellent magnetic softness has been achieved in both samples with coercivity, $H_c \approx 10$ A/m.

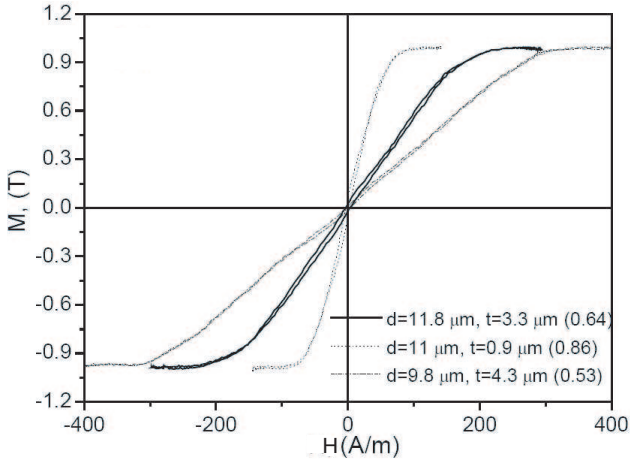

Figure 1: Effect of the sample geometry on the hysteresis loops of $Co_{67}Fe_{3.85}Ni_{1.45}Mo_{1.7}Si_{14.5}B_{11.5}$ microwires.

The geometric ratio of measured microwires, $\rho = d/D$, where d is the metallic nucleus diameter and D is the total microwire diameter, significantly affects the hysteresis loops. Such effect should

be attributed to the magnetoelastic energy given by

$$K_{me} \approx 3/2\lambda_s\sigma_i, \tag{2}$$

where λ_s is the saturation magnetostriction and σ_i is the internal stress. The magnetostriction constant depends on the chemical composition and nearly vanishes in amorphous Fe-Co based alloys with Co/Fe $\approx$ 70/5 [2]. On the other hand, the strength of the internal stresses in these amorphous microwires arising from the difference in the thermal expansion coefficients of metallic nucleus and glass coating depends on the thickness of glass coating and metallic core diameter [2]. Such dependence of the internal stresses on sample geometry give rise to a drastic change of the magnetoelastic energy, K_{me}. Additionally, such a change of the ρ-ratio should be related to the change of the magnetostriction constant with applied stress [2]:

$$\lambda_s = (\mu_o M_s/3)\,(dH_k/d\sigma)\,, \tag{3}$$

where $\mu_o M_s$ is the saturation magnetization.

Therefore can assume that there are a few factors that can affect the GMI behavior of the glass coated microwires such as

a) Metallic nucleus chemical composition,
b) Samples geometry, and
c) Thermal treatments.

Magnetic field dependences of real, R, and imaginary, X, components of GMI measured in the $Co_{67}Fe_{3.85}Ni_{1.45}B_{11.5}Si_{14.5}Mo_{1.7}$ microwires with $d = 6\,\mu m$ and $D = 10.2\,\mu m$ at frequencies 100–500 MHz are presented in Figs. 2(a) and 2(b), respectively.

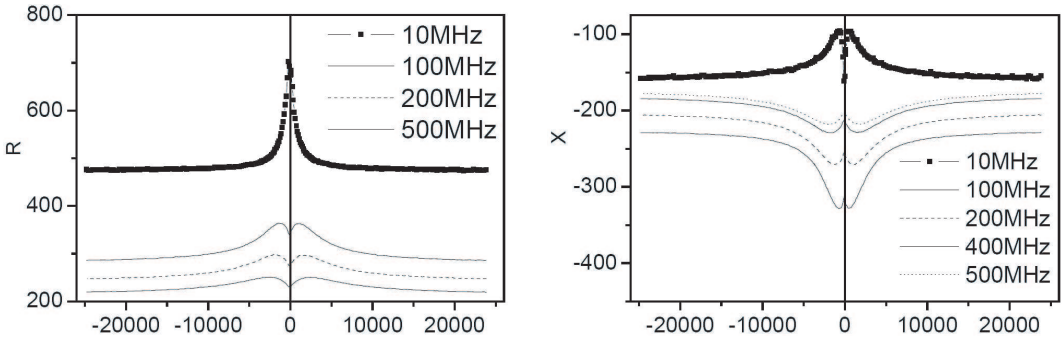

Figure 2: Real (R) and imaginary (X) parts of magneto-impedance of $Co_{67}Fe_{3.85}Ni_{1.45}B_{11.5}Si_{14.5}Mo_{1.7}$ microwires with metallic nucleus diameter and total diameter with glass coating of 6.0/10.2 μm.

Figure 3(a) shows field dependence of the off-diagonal voltage response of nearly zero magnetostriction ($\lambda_s \approx 3 \cdot 10^{-7}$) $Co_{67.1}Fe_{3.8}Ni_{1.4}Si_{14.5}B_{11.5}Mo_{1.7}$ microwire with diameters 9.4/17.0 μm. The $V_{out}(H_{ex})$ curves have antisymmetrical shape exhibiting almost linear growth within the field range from $-H_m$ to H_m

The effect of the Joule heating at 50 mA on off-diagonal field characteristic of $Co_{67.1}Fe_{3.8}Ni_{1.4}Si_{14.5}B_{11.5}Mo_{1.7}$ microwire. One can see that the thermal annealing reduces the H_m from 480 A/m in as-cast state to 400 A/m after 1 min annealing and to 230 A/m after 5 min annealing. After the Joule heating treatment the $V_{out}(H_{ex})$ curve becomes sharper giving the higher magnetic field sensitivity. The increase of V_{out} can be related with enhancement of magnetic softness after heat treatment.

3.2. Development of Stress Sensitive Microwires

As-prepared $Fe_{74}B_{13}Si_{11}C_2$ microwires exhibit rectangular hysteresis typical for the microwires with positive magnetostriction constant (see Fig. 1(a)). Conventional annealing without applied stress does not affect significantly the hysteresis loop of studied sample: some decrease of coercivity, H_c, observed after annealing should be attributed to the stress relaxation. Alternatively, SA treatment performed at the same annealing temperature with applied stress results in drastic changes of the hysteresis loop (see Fig. 4(b)): hysteresis loop becomes inclined with a high enough axial magnetic anisotropy field (about 1000 A/m).

A number of heat treatments with annealing temperatures between 100 and 400°C have been performed (see Figs. 4(b)). As can be deduced from Fig. 4(b) the transverse magnetic anisotropy

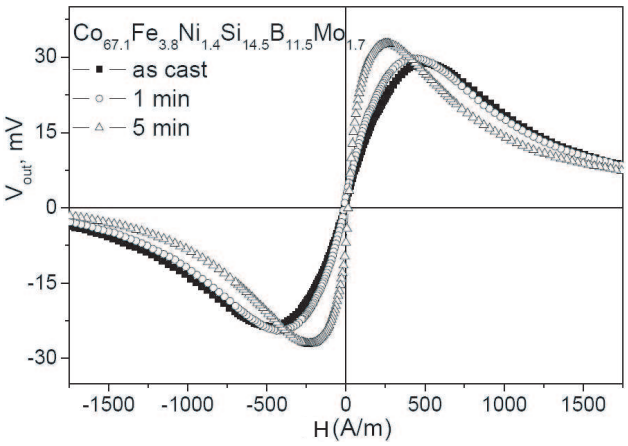

Figure 3: Field dependence of the off-diagonal voltage response of nearly zero magnetostriction $Co_{67}Fe_{3.85}Ni_{1.45}B_{11.5}Si_{14.5}Mo_{1.7}$ Joule-heated microwire annealed with 50 mA currents for different time.

depends on both annealing temperature and time. Strong dependence of the transverse magnetic anisotropy is reflected in the shape of axial hysteresis loop, which depends on both annealing time and temperature. As it is shown in Fig. 4(b), the hysteresis loop becomes more and more inclined increasing the annealing time and annealing temperature. Another important result is that the application of tensile stresses to the samples subjected to the SA treatment results in the recovery of the rectangular hysteresis loop typical for the as-prepared state (see Fig. 4(c)). This gives the way to tailor quite stress-sensitive thin wires able to detect small stresses.

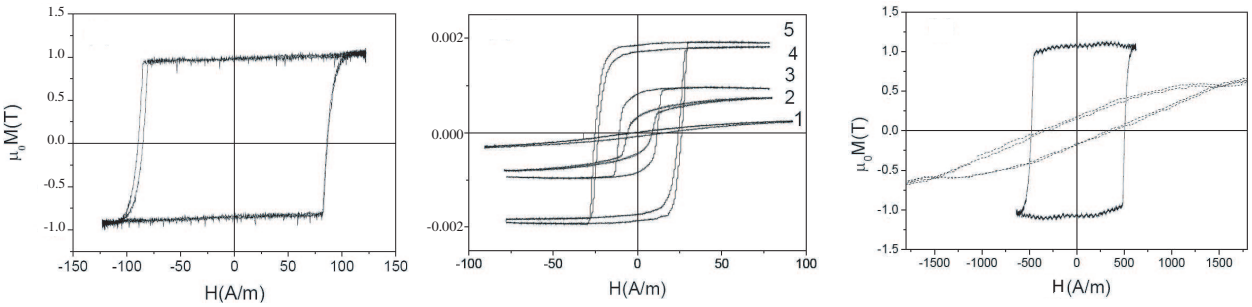

(a) (b) (c)

Figure 4: Hysteresis loop of stress annealed $Fe_{74}B_{13}Si_{11}C_2$ glass-coated microwire treated under applied stress of 500 MPA at (1) −300°C 3 hours, (2) −280°C 40 min, (3) −265°C 40 min, (4) 235°C 40 min and (5) −215°C 40 min.

Observed induction of transverse magnetic anisotropy after SA annealing (see Fig. 5) allows us to predict the existence of the magneto-impedance effect in such samples. Indeed, if as-prepared samples do not present any detectable GMI effect at $f = 10$ MHz, the samples subjected to SA exhibit significant magneto-impedance (see Fig. 5). As shown in Fig. 5, significant GMI effect (up to 60% at $f = 10$ MHz) is observed in stress-annealed microwires. GMI ratio, $\Delta Z/Z_H$, has non-monotonic dependence on the annealing temperature increasing with the annealing temperature until 275°C and then decreasing when the transverse anisotropy becomes too large (see Fig. 5).

Application of applied stresses gives rise to the stress impedance effect, SI, in the sample subjected to SA treatment. Such SI effect [2] consists of a change of the electrical impedance, $\Delta Z/Z$, under applied stress, σ (see Fig. 5(b)) without application of magnetic field.

The origin of this creep annealing induced anisotropy can be attributed to both: i) redistribution of the residual stresses during the stress annealing and consequent slow cooling or ii) induced magnetic anisotropy related to the atomic ordering.

The peculiarity of studied materials is that apart of conventional thermal stresses related with the rapid quenching of the wire from the surface they have additional source of the internal stresses related with the difference in the thermal expansion coefficients of metallic nucleus and glass coating [6, 8, 10]. The peculiarity of proposed SA treatment is that the applied stress is maintained during all the time, i.e. during the annealing and consequent cooling of the sample with the furnace. In this

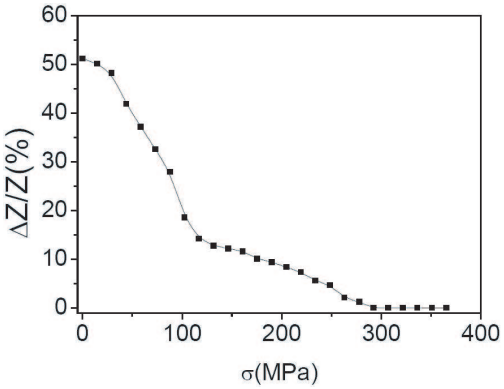

Figure 5: Effect of applied stress on GMI ratio of SA sample treated at 280°C.

way, one can assume that slow cooling and consequent removal of the mechanical load after stress annealing affect mostly the longitudinal stresses and results in drastic decrease of the longitudinal stress component and even in the appearance of the compressive longitudinal stresses (so-called "back stresses"). It is worth mentioning that the stress annealing and slow cooling under stress probably results in a stress relaxation in the stressed state and consequent applied stress removal gives rise to the compressive axial stresses.

Observed change of the hysteresis loop of the sample subjected to SA treatment when measured under applied tensile stress (Fig. 4) confirms such assumption. This effect should be attributed to the increasing of the longitudinal stress component under application of the tensile stress and consequently to the alignment of the easy magnetization axis along the highest stress component due to the positive magnetostriction constant of the studied sample. There is a competition between the magnetoelastic anisotropy induced by the applied stress (with a longitudinal easy axis) and the transverse anisotropy induced by the stress annealing. Upon overcoming the transverse anisotropy related to the creep induced anisotropy the longitudinal axis becomes easy magnetization axis again and magnetic bistability recovers. Such microwires can be quite useful for stress sensitive magnetoelastic sensors as well as for non-destructive remote control using tuneable composite stress sensitive meta-materials [9].

3.3. Development of Temperature Sensitive Microwires

The hysteresis loop of 3 typical compositions: Co-rich compositions with Ni and Fe (samples $Co_{50.69}Fe_{8.13}Ni_{17.55}B_{13.29}Si_{10.34}$ and $Co_{23.67}Fe_{7.14}Ni_{43.08}B_{13.85}Si_{12.26}$), Co-rich compositions with Cr

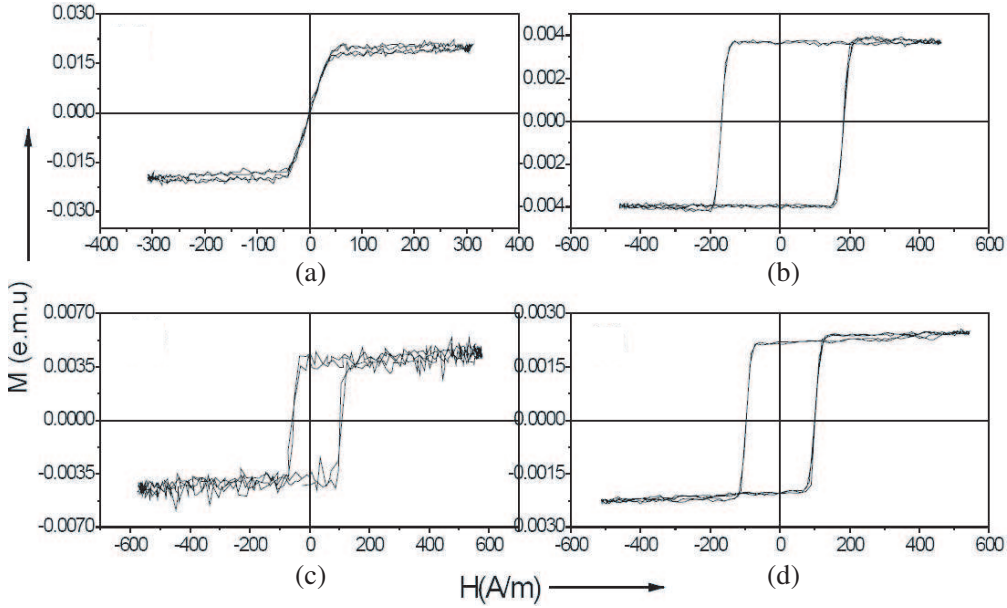

Figure 6: (a) Hysteresis loops of the samples $Co_{50.69}Fe_{8.13}Ni_{17.55}B_{13.29}Si_{10.34}$, (b) $Fe_{15.16}Ni_{59.26}B_{15.04}Si_{10.54}$, (c) $Co_{23.67}Fe_{7.14}Ni_{43.08}B_{13.85}Si_{12.26}$, and (d) $Co_{58.64}Fe_{4.67}Cr_{12.36}B_{13.05}Si_{11.28}$.

($Co_{58.64}Fe_{4.67}Cr_{12.36}B_{13.05}Si_{11.28}$) and Ni-rich compositions ($Fe_{15.16}Ni_{59.26}B_{15.04}Si_{10.54}$) are shown in Fig. 6. As can be observed, the chemical composition of glass-coated microwires drastically affects their magnetization curves: the hysteresis loop changes from almost rectangular shape for Fe-Ni-rich compositions without Co (Fig. 6(b)) to almost unhysteretic in Co-Ni-rich compositions (Fig. 6(a)).

The shape of the μ (Ha) depends on the magnetic anisotropy and gives us the possibility to study the magnetization reversal process in our material. The magnetic amplitude dependence of magnetic permeability, μ (Ha), for $Co_{53.99}Fe_{9.02}Ni_{11.88}B_{14.11}Si_{11}$ microwire is shown in Fig. 7. These dependencies give us the information on the remagenization process [10]:

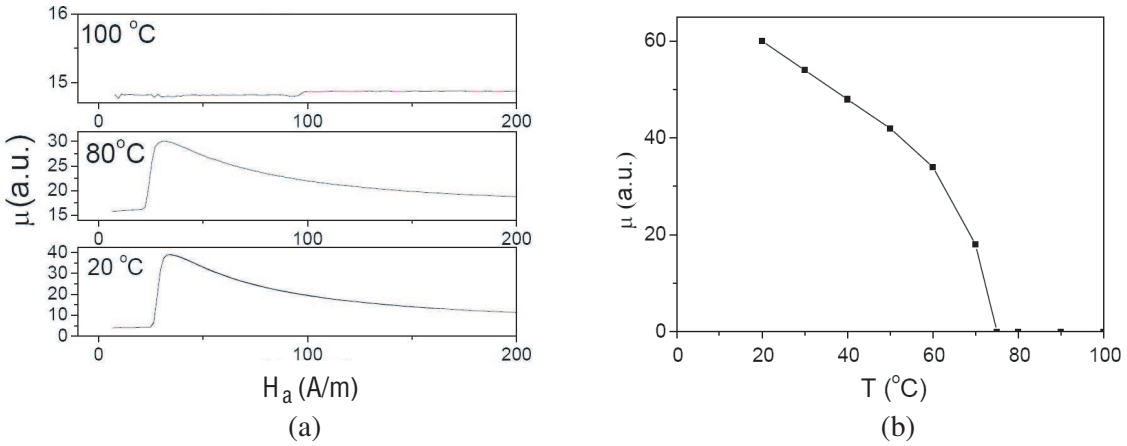

Figure 7: (a) Magnetic amplitude dependence of magnetic permeability, μ (Ha) measured in $Co_{23.67}Fe_{7.14}Ni_{43.08}B_{13.85}Si_{12.26}$ at different temperatures and (b) temperature dependence of magnetic permeability, μ (Ha) measured in $Co_{60.51}Fe_{3.99}Cr_{12.13}B_{13.53}Si_{9.84}$ microwire.

Typical μ (Ha) curve has a shape with maximum at certain field, $H_{\max}$, and consists of 3 regions:

1. Low fields: reversible movements of domain walls (DW).
2. Above same critical field, $H > H_{cr}$, irreversible DW movements.
3. Above the field corresponding to the maximum, $H > H_{\max}$, magnetization rotation.

As expected, μ (Ha) dependence drastically changes with the temperature because of the ferromagnetic-paramagnetic transition at around Curie temperature (see Fig. 7(a) where μ (Ha) dependence measured in $Co_{23.67}Fe_{7.14}Ni_{43.08}B_{13.85}Si_{12.26}$ microwire at different temperatures is shown). Fig. 7(b) shows the dependence of the magnetic permeability maximum on temperature

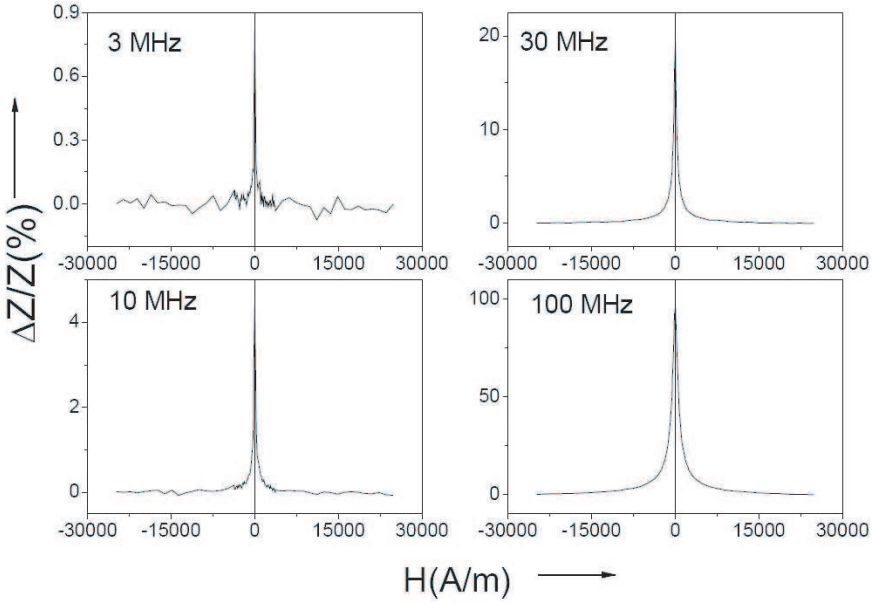

Figure 8: $\Delta Z/Z(H)$ dependences of the $Co_{60.51}Fe_{3.99}Cr_{12.13}B_{13.53}Si_{9.84}$ measured at different frequencies.

for $Co_{60.51}Fe_{3.99}Cr_{12.13}B_{13.53}Si_{9.84}$ microwire. Such dependence allows us to estimate the Curie temperature, T_C. For example, for $Co_{60.51}Fe_{3.99}Cr_{12.13}B_{13.53}Si_{9.84}$ microwire $T_C \approx 75°C$.

Figure 8 shows $\Delta Z/Z(H)$ dependences $Co_{60.51}Fe_{3.99}Cr_{12.13}B_{13.53}Si_{9.84}$ microwire with T_C of about 50°C. As can be appreciated from Fig. 8, $Co_{60.51}Fe_{3.99}Cr_{12.13}B_{13.53}Si_{9.84}$ microwire exhibits high enough GMI effect, especially at high enough frequency.

Glass coating microwires are generally very attractive materials for the sensors application mostly because their reduced exhibiting low Curie temperatures, achieved in a number of studied samples allow us to design few magnetic sensors of temperature based on this drastic change of the GMI effect or on the magnetic permeability change with temperature.

Particularly, the functioning of the temperature sensors based on disappearance of the ferromagnetic ordering above Curie temperature, T_c. It is clear that both GMI effect and magnetization disappear when heating above T_c. Thus, a sensor based on GMI effect is based on drastic drop of the GMI effect after achieving of the Curie temperature (see Fig. 8). In this case the GMI effect of microwire disappears above Curie temperature, which is detected by the proposed circuitry consisting on the AC generator applying the AC current of high frequency (HF) to the sample, DC power supply producing the magnetic DC field and the detecting voltmeter, measuring AC voltage, V, between the sample ends.

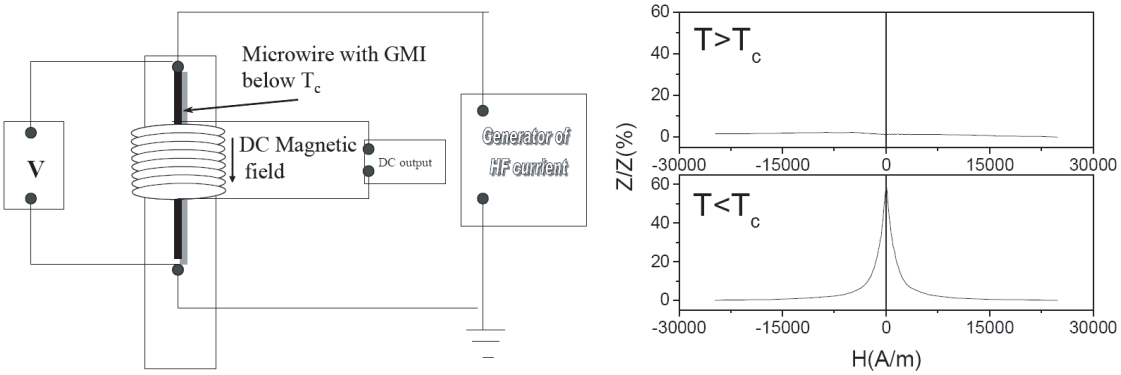

Figure 9: Schematic picture showing the working of the temperature sensor based on GMI effect in microwires with low T_C.

4. CONCLUSIONS

Thin amorphous wires (with metallic nucleus below 15 μm) with excellent magnetic softness and large GMI effect have been developed. It is demonstrated that the magnetic properties can be tailored by an appropriate selection of the metallic nucleus diameter, glass-coating thickness and chemical composition of the metallic nucleus and even by the heat treatment. The investigation of off-diagonal MI tensor component with pulse excitation in 6–10 μm amorphous glass-coated microwires has shown the great potential of these materials for microminiaturized magnetic field sensor application. Their main advantages are high sensitive non-hysteresis field dependence, low power consumption, and quite simple sensor scheme.

Microwires with nearly zero magnetostriction exhibit asymmetrical shape of the off-diagonal voltage response on magnetic field with almost linear behavior within the working range. The off-diagonal MI of negative magnetostriction microwire after annealing becomes similar to the microwire with vanishing magnetostriction. Thermal treatment is an additional effective method of tuning of MI dependence together with alloy composition and geometric parameters.

Stress annealing of $Fe_{74}B_{13}Si_{11}C_2$ glass-coated microwire allows to tailor the hysteresis loop of glass-coated microwires: varying the time and the temperature of such stress annealing we are able to change both magnetic properties and GMI of Fe-rich microwires. Enhanced stress-sensitive GMI effect and magnetic softness are achieved in such stress annealed samples, allowing application of such samples for various magneto-elastic sensor applications. Thus application of tensile stresses in the samples subjected to the SA treatment results in the reappearance of the rectangular hysteresis loop typical for the as-prepared state, stress impedance. Such enhanced stress sensitivity of the obtained magnetic properties and GMI effect allows use of these thin wires for designing of the tuneable composite materials based on thin ferromagnetic wires and in magnetoelastic sensors.

The appearance of such hysteresis loop is explained by the re-distribution of the internal stresses arising from the difference of the thermal expansion coefficients of the metal and glass during SA during such stress annealing.

We also report novel results on the fabrication and characterization of glass-coated microwires with compositions Co_{100-x}-Fe-Ni_x-Si-B and Co-Fe-Cr-Si-B fabricated by the Taylor-Ulitovsky method and divided into 3 main groups: Co-rich compositions with Ni and Fe, Co-rich compositions with Cr and Ni-rich compositions. Additions of Ni or Cr resulted in decreasing of the Curie temperature. Few samples possessing low T_C also present high GMI effect. Applications of such microwires in magnetic sensors such as the temperature sensors applications based on drastic change of the magnetic properties in the vicinity of Curie temperature have been described.

ACKNOWLEDGMENT

Authors acknowledge a technological support of Tamag Ltd and AmoTec Ltd. This work was supported in part by the Spanish Ministry of Science and Technology under Grant MAT2004-05348-C04-04

REFERENCES

1. Giles, D. C., "Recent advances and future directions in magnetic materials," *Acta Materialia*, Vol. 51, 5907–5939, 2003.
2. Zhukov, A. and J. González, "Processing of advanced magnetic materials," *Advanced Magnetic Materials*, Vol. 3, Cap. 5, 115–181, (Eds. David J. Sellmyer, Yi Liu and Daisuke Shindo), Kluwer Academic Publishers, Norwell, 2004.
3. Kanno, T., K. Mohri, T. Yagi, T. Uchiyama, and L. P. Shen, "Amorphous wire MI microsensor using C-MOS IC multivibrator," *IEEE Trans. Magn.*, Vol. Mag-22, 3358–3360, 1997.
4. Panina, L. V., S. I. Sandacci, and D. P. Makhnovskiy, "Stress effect on magnetoimpedance (MI) in amorphous wires at GHz frequencies and application to stress-tunable microwave composite materials," *J. Appl. Phys.*, Vol. 97, 13701, 2005.
5. Zhukova, V., V. S. Larin, and A. Zhukov, "Stress induced magnetic anisotropy and giant magnetoimpedance in Fe-rich glass-coated magnetic microwires," *J. Appl. Phys.*, Vol. 94/2 1115–1118, 2003.
6. Zhukova, V., A. Chizhik, A. Zhukov, A. Torcunov, V. Larin, and J. Gonzalez, "Optimization of giant magnetoimpedance in Co-rich amorphous microwires," *IEEE Trans. Magn.*, Vol. 38/5, 3090–3092, 2002.
7. Zhukova, V., S. Kaloshkin, A. Zhukov, and J. Gonzalez, "DSC studies of finemet-type glass-coated microwires," *J. Magn. Magn. Mat.*, Vol. 249, 108–112, 2002.
8. Makhnovskiy, D. P., L. V. Panina, and D. Mapps, "Field-dependent surface impedance tensor in amorphous wires with two types of magnetic anisotropy: Helical and circumferential," *Phys. Rev. B.*, Vol. 63/14, 144424–41, 2001.
9. Ouslimani, H. H., R. Abdeddaim, and A. C. Priou, "Free-space electromagnetic characterization of materials for microwave and radar applications," *PIERS Online*, Vol. 1, No. 2, 128–132, 2005.
10. Varga, R., P. Vojtanik, and R. Andrejco, "Pinning field distribution in the amorphous CoFeSiB wire," *Phys. Stat. Sol.*, Vol. 193, 103–116, 2002.

Design of Metamaterial Based-on Ferromagnetic Substrate

Boren Zheng[1,2], **Guangjun Wen**[1], **Zhenghai Shao**[1], **Yunjian Cao**[1], **and Kang Xie**[1]

[1]Key Laboratory of Broadband Optical Fiber Transmission & Communication Networks
University of Electronic Science and Technology of China, Chengdu 610054, China
[2]School of Computer and Information, Chongqing Jiaotong University, Chongqing 400074, China

Abstract— In this paper, a broad-band metamaterial operating in x-band has been designed by using of a ferromagnetic substrate embedded with an array of metal wire or strip. The transmission and reflection characteristics of EM wave in the designed metamaterial and at the interface between metamaterial and positive refraction index material was simulated by HFSS simulator, the effective permittivity, effective permeability and refraction index of the composite substance were extracted out by the transfer matrix method. The simulation results show that the effective refraction index of the composite substance is negative in the broad-band from 8.5 GHz to 10.7 GHz. The refraction feature of EM wave passing through a prism which is made of the designed metamaterial has been simulated, and negative refraction phenomena at the interface between metamaterial and positive refraction index material were observed in the preceding frequency range. The focusing of a line source thru flat lens which is made of the designed metamaterial has got by the simulator too. The results demonstrated the method to synthesis metamaterial based on ferromagnetic substrate embedded with an array of metal wire or strip is viable.

1. INTRODUCTION

Substances with simultaneously negative permittivity and permeability predicted by Veselago [4] in 1960s has attracted increasingly attention recently. The material support backward waves and their most striking feature is that they are characterized by a negative index of refraction which gives rise to unique phenomena and possibilities. The motivation of these studies was to determine a particular configuration which may lead to electromagnetic properties not generally found in nature. In 2000, based upon suggestion of Pendry et al. [2, 3], Smith et al. [1] found a composite (metamaterials) made of thin wire trips and split ring resonators to synthesize negative permittivity and permeability. Further, shelby et al. [5], observed negative refraction in the composite. V. Eleftheriades et al. [6] got a new planar negative refractive index material by periodically L-C loaded transmission lines. Subsequently, many modification composite means, such as O resonators and double S resonators, arose. However, most metamaterial constructed by SSRs typically display fixed narrow operation frequency bandwidths, and the means of periodically L-C loaded transmission lines produce a planar metamaterial only.

In this paper, a broad-band metametarial has been designed using ferromagnetic substrate to replace the SSR to produce negative μ and the array of metal wire or strip embedded in the ferromagnetic substrate to produce negative ε. We have simulated the properties of the EM wave through the designed metamaterial by HFSS simulator, and extracted the effective permittivity, effective permeability and refraction index. The results show that the effective permittivity, and effective permeability and refraction index are negative simultaneously in the broad-band frequency range from 8.5 GHz to 10.7 GHz. The negative refraction phenomena and focusing using flat lens made of the designed metamaterial were verified. The results demonstrated that such a structure is vastly more practical in frequency band and sharp than the wire-SRR structure and the composite method of metamaterial using ferromagnetic substrate embedded with an array of metal wire or strip is viable.

2. THE DESIGN OF METAMATERIAL

A ferromagnetic substrate with in-plane anisotropy provides a low loss $\mu < 0$ and embedded wire array achieve an $\varepsilon < 0$. The combining of the ferromagnetic and wire array produces effective $\mu < 0$ and $\varepsilon < 0$ simultaneously to yield $n < 0$ similar to that previously demonstrated in SSRs or wire structures.

In this design, the wire array spacing and wire diameter was chosen to tune a high pass cut off frequency ω_p slightly above the ferromagnetic substrate anti-resonance as the Eq. (1) described [2]. When the $\omega < \omega_p$, the wire array can produce $\varepsilon_{eff} < 0$, where $\omega_p^2 = 2\pi c_0^2/(a^2 \ln(a/r))$, ω_p is the

plasmas frequency, a is the array spacing, r the wire diameters, δ the conductivity of the metal, and ω is the operating frequency.

$$\varepsilon_{eff} = 1 - \frac{\omega_p^2}{\omega(\omega + i\varepsilon_0 a^2 \omega_p^2 / \pi r^2 \sigma)} \tag{1}$$

The effective permeability μ of a slab substrate of ferromagnetic material magnetized in the plane can be calculated by Eq. (2), where μ_0 is the free space permeability, H_0 is the externally applied magnetic field, M_s is the magnetization of ferromagnet, ω is the angular frequency of the electromagnetic radiation, γ is the gyromagnetic ratio, and Λ is a phenomenological damping parameter describing losses intrinsic of the magnetic material. The resonance frequency of the ferromagnetic is 8.4 GHz, and in 8.4–11 GHz frequency range the slab substrate produce effective $\mu < 0$, when $H_0 = 2500$ Oe, $\gamma = 1.759 \times 1011$ C/Kg, $Ms = 2000$ Gs, $\Delta H = 301.6$ Oe,

$$\begin{aligned} \mu &= \left(\frac{(\tilde{H}_0 + M_S)^2 - \left(\frac{\omega}{\mu_0 \gamma}\right)^2}{\tilde{H}_0(\tilde{H}_0 + M_S) - \left(\frac{\omega}{\mu_0 \gamma}\right)^2} \right) \mu_0 \\ \tilde{H}_0 &= H_0 - j \left(\frac{\omega}{\mu_0 \gamma}\right) \left(\frac{4\pi\Lambda}{\mu_0 \gamma M_s}\right) \end{aligned} \tag{2}$$

As the preceding analysis, the designed composite structures are indicated in Fig. 1. The wire array is constructed by 11 wires along y direction and 16 wires along x direction. The wire diameter d is 0.3 mm and the height along z direction is 10 mm. The dimensions of the structure are optimized by the HFSS simulator. Each simulation model consists of two-port waveguide which formed by both perfect electric conductor (PEC) and perfect magnetic conductor (PMC) walls. The input wave is launched from free space onto the slab at normal incidence from each port. All inclusions are located in the slab. This model allows the effective simulation of a semi-infinite slab illuminated by a normally incident plane wave. The incidence wave has a polarization with electric field normal to the plane of incidence, which is similar with the perfect matched layer (PML) boundary conditions.

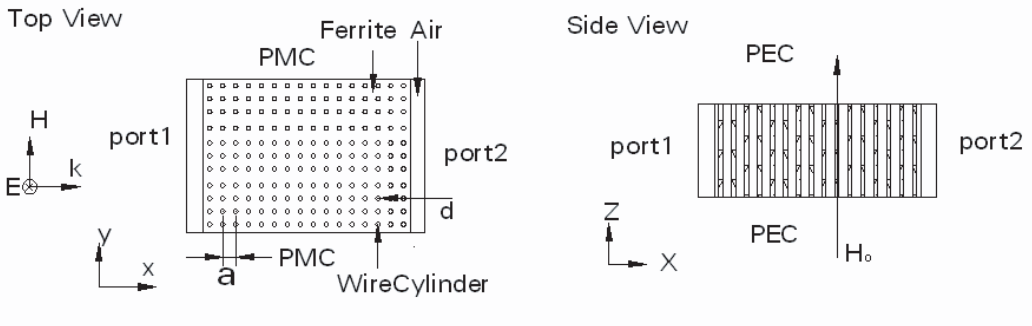

Figure 1: The model of designed metamaterial.

3. NUMERICAL ANALYSIS AND RESULTS

The HFSS simulated magnitudes of S_{11} and S_{21} de-embedded to the front face of the ferromagnetic region for full designed structure are shown in Fig. 3. Only the wire array inclusions and only ferromagnetic slab inclusion have the same boundary conditions, and the corresponding magnitudes of S_{11} and S_{21} are given in Fig. 2(a) and Fig. 2(b), respectively. From Fig. 2(a), we can see the only ferromagnetic slab displays a stop band extending form 8.4–11.5 GH as Eq. (2). Fig. 2(b) shows that the only wire array has a plasma frequency at about 18 GHz as Eq. (1). In Fig. 3, the composite metamaterial has three pass bands, one is from 8.5 to 10.7 GHz, a little differs with the stop band of the ferromagnetic slab only, the other two which are the near 7 GHz and 14 GHz were produced by the alignment of the wire array and the ferromagnetic slab.

To extract effective medium parameters from the normal incidence scattering parameter data, the Nicolson-Rose-Weir (NRW) [7] approach was implemented. The real parts of permeability

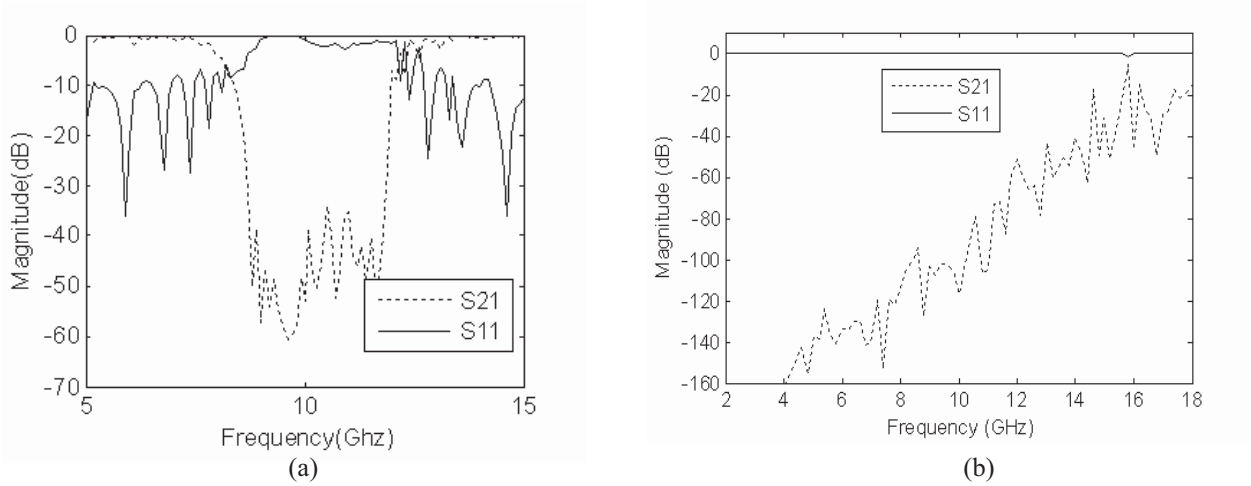

Figure 2: Magnitude of HFSS predicted S parameter for restricted the designed matematerial cases corresponding Fig. 3, (a) the ferromagnetic slab only, (b) the wire array only.

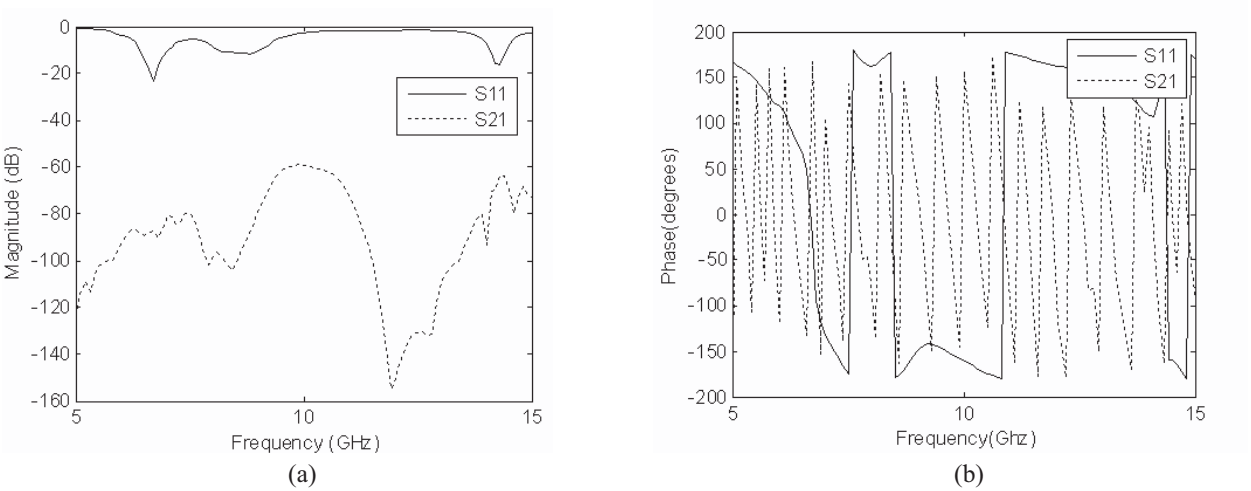

Figure 3: HFSS predicted S parameter for the designed metamaterial, (a) magnitude of S_{11} and S_{21}, (b) phase of S_{11} and S_{21}.

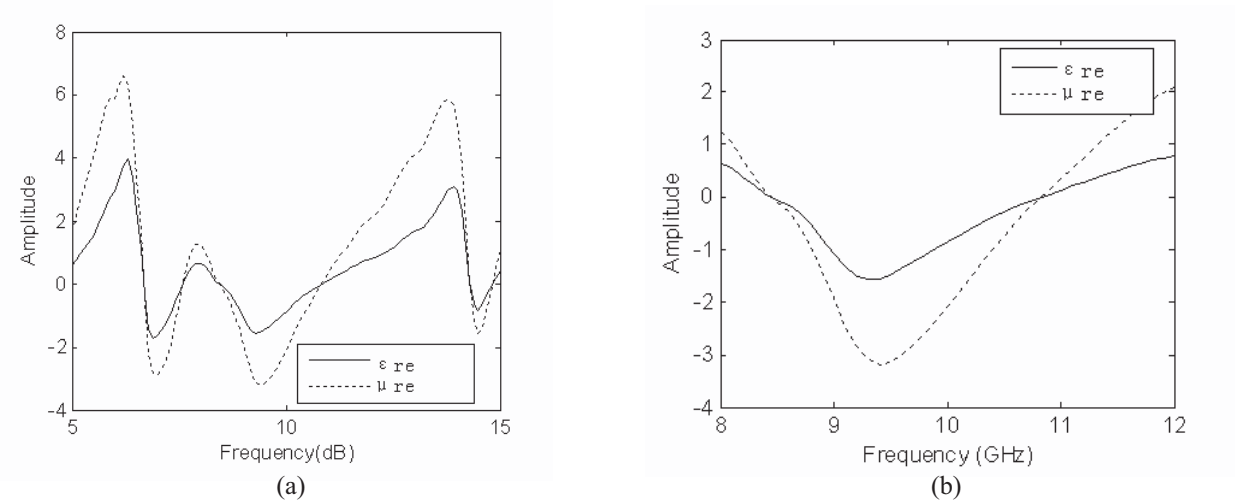

Figure 4: Extracted the permeability and permittivity for the designed matematerial, (a) the real part of the permeability and permittivity, (b) zoom.

and permittivity obtained by NRW approach was given in Fig. 4(a). As shown in Fig. 4(a), the permittivity and permeability have three bands go through a resonance where S_{21} has a peak and its nontrivial negative value is near 7 GHz, 14 GHz and the 8.5–10.7 GHz. We are interested in the 8–12 GHz only as shown in Fig. 4(b). The index of refraction is computed corresponded with the band in Fig. 4(b).The real parts of the index of refraction is negative in the 8.5–10.7 GHz shown in Fig. 5. The results show the designed metamaterial has a broad-band of negative index of refraction.

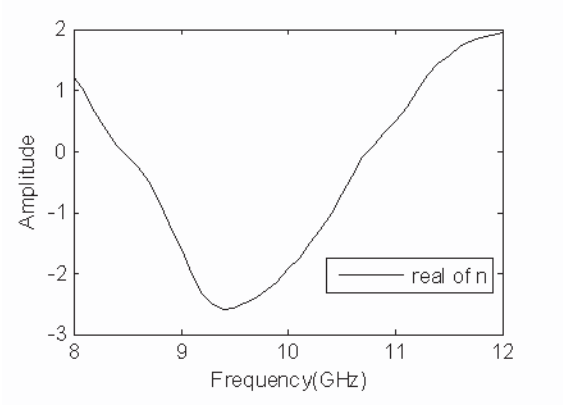

Figure 5: Extracted the real parts of the index of refraction for the designed matematerial.

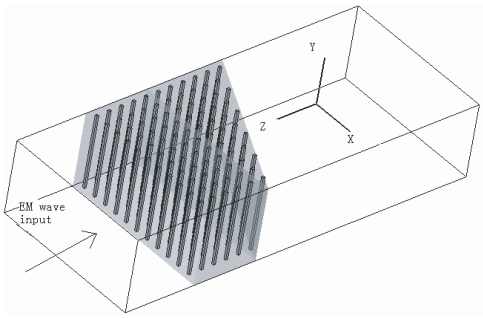

Figure 6: The model of refraction using a prism.

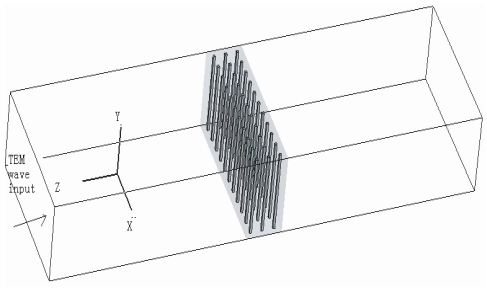

Figure 7: The model of imaging by flat lens.

For more detail of negative refractive index, the refraction of EM wave through a prism which is made of the designed metamaterial was investigated as shown in Fig. 6. The EM wave incidenced from one port, and the other port condition are PML which cannot reflect the EM wave. The equivalent electric field surface is located in the prism parallel $x\,z$ plane is shown in Fig. 8, Fig. 8(a) demonstrates EM wave thru the prism frequency at 9 GHz, and Fig. 8(b) at 10 GHz. The results show that the refracted EM wave lies on the same side of the interface normal, and this inversion

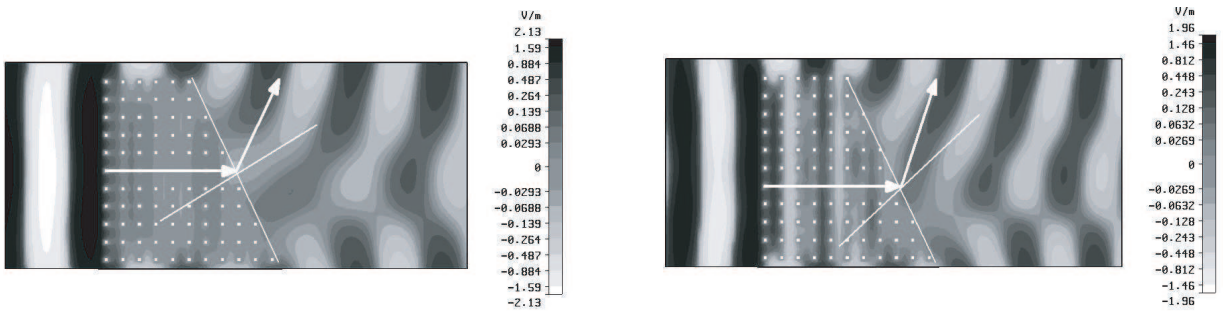

(a) (b)

Figure 8: The refraction of the EM wave through the prism, (a) incident wave frequency at 9 GHz, (b) incident wave frequency at 10 GHz.

Snell's phenomenon is just a representative feature of the metamaterial. The prism is replaced with the flat lens made of designed metamaterial as Fig. 7, using a line source frequency at 9.5 GHz positioned far away incidenced the flat lens. Fig. 9(a) sculpted the focusing of the line source back the flat lens. For the comparing, the flat lens is replaced by normal material with the positive index of refraction in Fig. 7. It can not focus the line source as Fig. 9(b) shown. The focusing using flat lens proved that the index of refraction of the designed metamaterial is negative again.

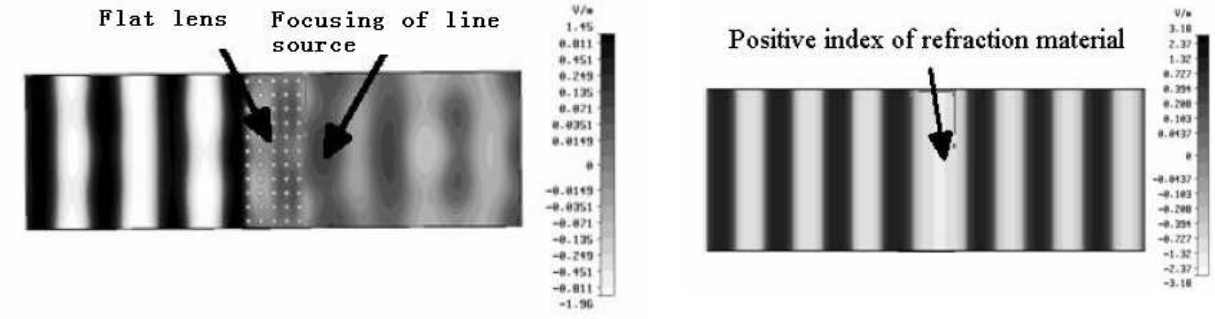

(a) (b)

Figure 9: The focusing of flat lens, (a) the flat lens made by designed metamaterial, (b)the flat lens made by normal material.

4. CONCLUSIONS

In this paper, a metamaterial which constructed by ferromagnetic substrate embedded with an array of metal wire is designed, and the refraction feature of EM wave passing through a prism which is made of the designed metamaterial has been simulated. Negative refraction phenomena, the refracted EM wave lies on the same side of the interface normal, at the interface between metamaterial and positive refraction index material were got. The focusing property using flat lens made of designed metamaterial is investigated. The results shown the designed metamaterial has a negative index of refraction in a broad band from 8.5 GHz to 10.7 GHz. Such a wire array embedding in a ferromagnetic substrate method should provide a means to fabricate a broad-band tunable metamaterial.

ACKNOWLEDGMENT

This work was supported by National Natural Science Foundation of China (Projects 60571024, 60771046 and 60588502).

REFERENCES

1. Smith, D. R., W. J. Padilla, D. C. Vier, et al., "Composite medium with simultaneously negative permeability and permittivity," *Phys. Rev. Lett.*, Vol. 84, No. 18, 4184–4187, 2000.
2. Pendryy, J. B., A. J. Holdenz, D. J. Robbinsz, and W. J. Stewartz, "Low frequency plasmons in thin-wire structures," *J. Phys.*, Vol. 10, 4785–4809, 1998.
3. Pendry, J. B., A. J. Holden, D. J. Robbins, et al., "Magnetism from conductors and enhanced nonlinear phenomena," *IEEE Trans. on MTT*, Vol. 47, No. 11, 2075–2084, 1999.
4. Veselago, V. G., "The electrodynamics of substances with simultaneously negative values of ε and μ, *Sov. Phys. USPEKHI*, Vol. 10, 509, 1968.
5. Shelby, A., D. R. Smith, and S. Schultz, "Experimental verification of a negative index of refraction," *Science*, Vol. 292, No. 6, 77–79, 2001.
6. Eleftheriades, G. V., O. Siddiqui, and A. K. Iyer, "Transmission line models for negative refractive index media and associated implementations without excess resonators," *IEEE Micr. and Wire. Comp. Lett.*, Vol. 13, No. 2, 51–53, 2003.
7. Ziolkowski, R. W., "Design, fabrication, and testing of double negative metamaterials," *IEEE Trans. on Antennas and Propagat.*, Vol. 51, No. 7, 1516–1528, 2003.

Lossless DNG-DPS Bilayer Structures for Tunneling and Zero Reflection

Homayoon Oraizi and Majid Afsahi
Iran University of Science and Technology, Narmak, Tehran 16846-13114, Iran

Abstract— Distributions of the electromagnetic field and power flux inside and outside of a lossless DNG-DPS bilayer structure are investigated by the Transmission Line Transfer Matrix Method (TLTMM) and appropriate conditions are determined that under which complete wave tunneling occurs with no reflection at any angle of incidence and at all frequencies. This structure may have applications in antenna radomes.

1. INTRODUCTION

Double negative (DNG) media are made of small metallic rods and split ring resonators in the microwave frequency bands [1–3]. It is shown that the DNG-DPS bilayer structures exhibit unusual and interesting wave propagation [4]. By an iterative method [5] and by a full wave analysis method [6], it just mentioned without details that under appropriate conditions the reflection from a lossless DNG-DPS bilayer structure becomes zero. Also, field and power flux distribution is determined inside and outside of a lossless MNG-ENG bilayer by a full wave method [6].

In this paper, which is complementary to [5, 6], field and power flux distribution is determined inside and outside of a DNG-DPS bilayer under TM plane wave incidence by the TLTMM method [7, 8]. The dependence of reflection coefficient on angle of incidence and wave frequency is investigated. Furthermore, the necessary and sufficient conditions for zero reflection of loosless DNG-DPS bilayer structure are obtained.

2. PROBLEM FORMULATION

Consider a lossless DNG-DPS bilayer, with thicknesses d_1 and d_2. A TM plane wave is incident on it at an arbitrary angle of incidence in the y-z plane with the following electric and magnetic incident field:

$$\begin{aligned}\overrightarrow{H}_i &= \hat{x}H_0 e^{-(\gamma_{oy}y+\gamma_{0z}z)}\\ \overrightarrow{E}_i &= (\hat{y}\frac{\gamma_{0z}}{j\omega\varepsilon_0} - \hat{z}\frac{\gamma_{0y}}{j\omega\varepsilon_0})H_0 e^{-(\gamma_{oy}y+\gamma_{0z}z)}\end{aligned} \tag{1}$$

as shown in Fig. 1.

The transmission line transfer matrix method (TLTMM) is introduced in [7, 8] for the numerical analysis of multilayered structures with arbitrary number of layers at any angle of incidence and any frequency with an arbitrary wave polarization. In TLTMM the original problem shown in Fig. 1 is treated by the equivalent transmission line model shown in Fig. 2, characterized by the characteristic impedance (Z_n) and propagation constant (γ_{nz}) in the z -direction, which are functions of the angle of incidence, frequency and wave polarization, namely

$$\begin{aligned}Z_n &= \begin{cases}\sqrt{\mu_n/\varepsilon_n}\cos\theta_n & for \quad TM\\ \sqrt{\mu_n/\varepsilon_n}\sec\theta_n & for \quad TE\end{cases}\\ \gamma_{nz} &= j\omega\sqrt{\mu_n\varepsilon_n}\cos\theta_n\end{aligned} \tag{2}$$

which θ_n is the angle of incidence in the n'th medium. The Snell's law at the boundary between two consecutive layers in terms of incidence angles θ_i are:

$$\gamma_n \sin\theta_n = \gamma_{n+1}\sin\theta_{n+1}, \quad n = 0, 1, 2 \tag{3}$$

It is necessary to select the correct sign for the characteristic impedances ($Z = \sqrt{\mu/\varepsilon}$) and propagation constants ($\gamma_z = j\omega\sqrt{\mu\varepsilon}\cos\theta$) in metamaterials [9]. The necessary and sufficient conditions for tunneling may be obtained from the equivalent transmission lines as

$$\begin{aligned}Z_1 &= Z_2,\\ \beta_1 d_1 &= -\beta_2 d_2\end{aligned} \tag{4}$$

where β_n and Z_n (n =1, 2) indicate the characteristic impedance and propagation constant of the equivalent transmission lines for the first and second layers.

Consequently, if for a known angle of incidence θ_i, the parameters of layer 1 namely ε_1, μ_1 and d_1 and those of layer 2 namely ε_2, μ_2 and d_2 characterizing DNG and DPS media, are selected so that relations (4) are satisfied, the total transmission occurs through the lossless DNG-DPS bilayer. This phenomenon is called matched pair. The designed DNG-DPS layer is called matched pair. The lossless bilayer with $\varepsilon_2 = -\varepsilon_1$, $\mu_2 = -\mu_1$ and $d_2 = d_1$ called the conjugate matched pair is of particular interest. In this case, the transmission coefficient is equal to one and reflection coefficient is zero for any type of polarization and at complete tunneling occurs.

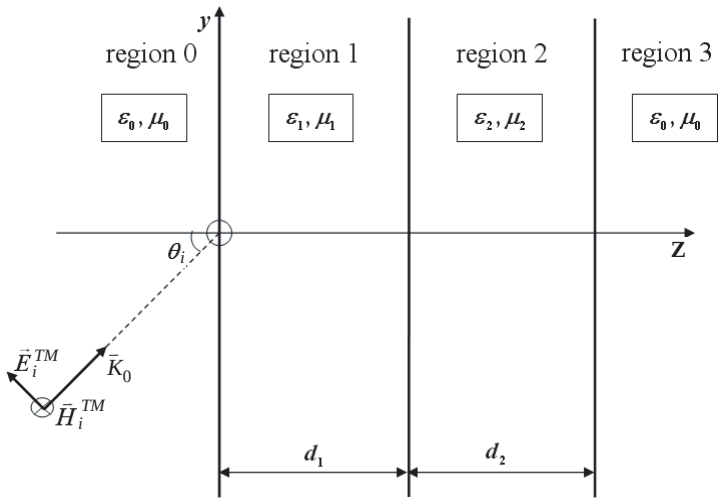

Figure 1: A DNG-DPS bilayer under oblique incidence of a TM plane wave.

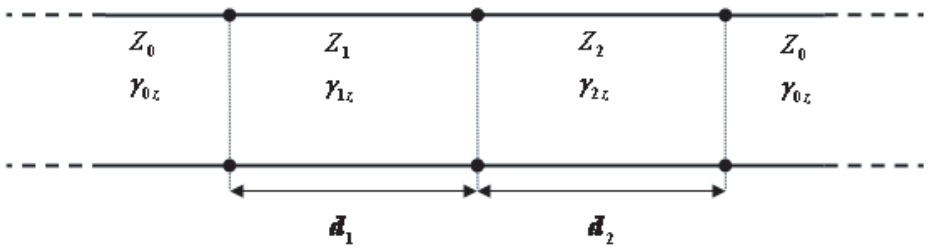

Figure 2: The equivalent transmission line model for Fig. 1.

3. DEPENDENCE ON MATERIAL PROPERTIES AND STRUCTURE GEOMETRY

The following conclusions may be derived by the conditions of zero reflection in (4).

(a) It is expected that the reflectionless property of the DNG-DPS bilayer is bidirectional. However, the field distribution and the real part of Poynting's vector depend on the direction of wave incidence.

(b) The condition in (4) were obtained for the lossless cases of DNG-DPS and DPS-DNG bilayers. However, for other bilayer combinations of DPS, DNG, ENG and MNG, reflectionless conditions are not realized.

(c) The no reflection conditions in (4) do not depend on the material properties of the similar half spaces on both sides of the bilayer. The only depend on the parameters of the DPS and DNG layers.

(d) The reflectionless conditions in (4) indicate that zero reflection is not depend on the total thickness of the bilayer namely $(d_1 + d_2)$. Therefore, the DNG and DPS layers may be thick or thin leading to total transmission.

(e) The zero reflection conditions in (4) depend on the angle of incidence θ_i. The Brewster angle of no reflection of the bilayer under TM wave incidence may be determined by $Z_1 = Z_2$ and Eqs. (2) and (3).

$$\theta_{r=0} = \arcsin\sqrt{\frac{\varepsilon_1\varepsilon_2(\varepsilon_2\mu_1 - \varepsilon_1\mu_2)}{\mu_0\varepsilon_0(\varepsilon_2^2 - \varepsilon_1^2)}} \tag{5}$$

(f) Assuming nondispersive metamaterials, the no reflection conditions (4) with Eq. (2) are seen to be independent of frequency.

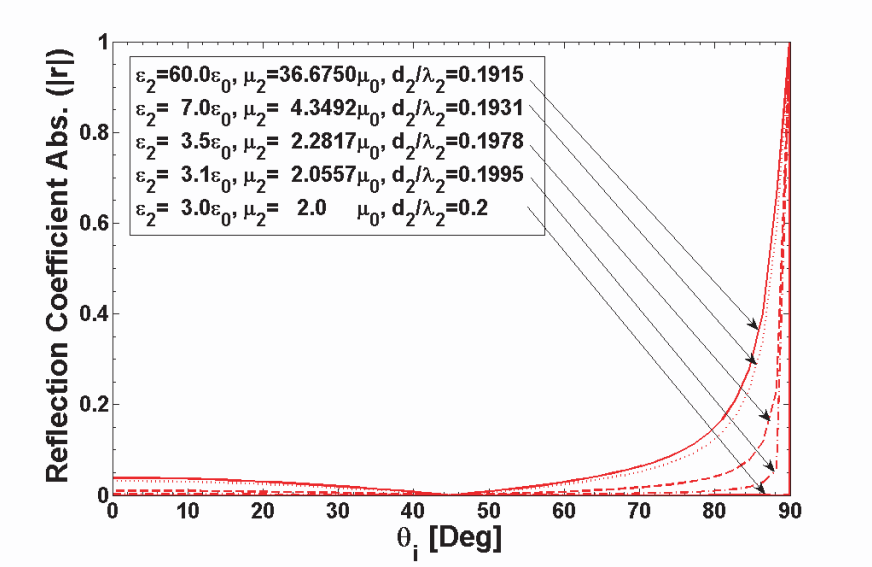

Figure 3: Variation of reflection coefficient versus incidence angle of a TM plane wave. The design is for brewster angle of 45° at frequency f_0. The DNG parameters are $\varepsilon_1 = -3\varepsilon_0$, $\mu_1 = -2\mu_0$, $d_1/\lambda_1 = 0.2$ and those of DPS are shown in the caption.

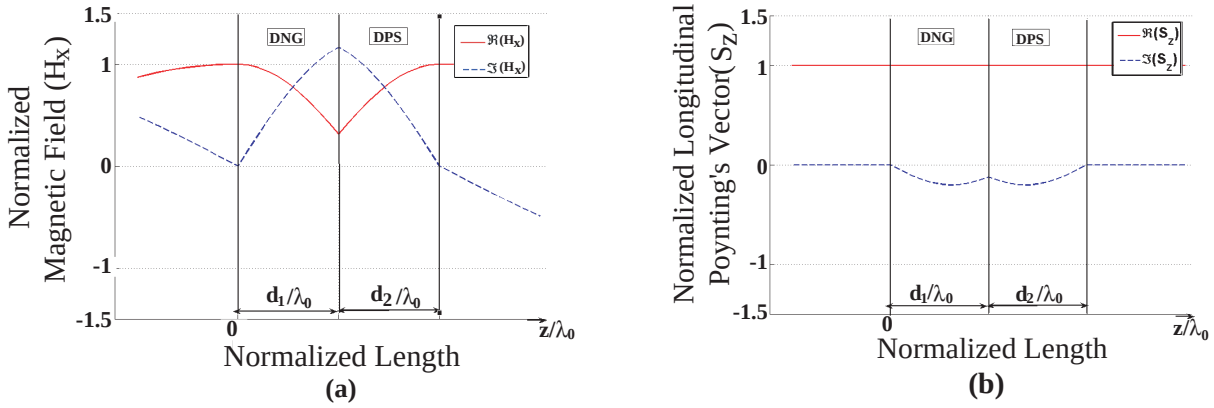

Figure 4: Field and power flux variation versus distance in the layers. The angle of incidence of TM plane wave is 45° and the parameters are $\varepsilon_2 = -\varepsilon_1 = 3\varepsilon_0$, $\mu_2 = -\mu_1 = 2\mu_0$, $d_2/\lambda_2 = d_1/\lambda_1 = 0.2$, $r = 0$, $t = 1$. (a) Normalized magnetic field; (b) Normalized Poynting's vector.

4. EXAMPLE

As an example, the reflection coefficient of a DNG-DPS layer is drawn in Fig. 3 for the Brewster angle of $\theta_{r=0} = 45°$ and the set of parameters shown in the figure. It is seen that the reflection coefficient becomes zero at any angle of incidence for the case $\varepsilon_2 = -\varepsilon_1$, $\mu_2 = -\mu_1$, $d_2 = d_1$. The field and power flux of this structure are drawn versus distance in Fig. 4 for the TM incident wave at the angle of incidence $\theta_{r=0} = 45°$.

5. CONCLUSION

In this paper, the conditions for zero reflection of a planar DNG-DPS bilayer under TM wave incidence are determined for all angles of incidence. The distribution of electromagnetic fields and Poynting's vector inside and outside the bilayer under no reflection conditions are determined. By the application of the transmission line transfer matrix method (TLTMM) the necessary and sufficient conditions for zero reflection and complete transmission are obtained. The effects of parameters of bilayer materials and thicknesses on its reflection properties are determined. The application of TLTMM for the analysis of DNG-DPS bilayer may be equally as well carried out for the TE wave polarization.

ACKNOWLEDGMENT

This research was in part supported by Iran Telecommunication Research Center under contract number 500/1911 dated 2007/5/8.

REFERENCES

1. Shelby, R. A., D. R. Smith, and S. Schultz, "Experimental verification of a negative index of refraction," *Science*, Vol. 292, No. 5514, 77–79, 2001.
2. Smith, D. R., W. J. Padilla, D. C. Vier, S. C. Nemat-Nasser, and S. Schultz, "Composite medium with simultaneously negative permeability and permittivity," *Phys. Rev. Lett.*, Vol. 84, No. 18, 4184–4187, 2000.
3. Shelby, R. A., D. R. Smith, S. C. Nemat-Nasser, and S. Schultz, "Microwave transmission through a two-dimensional, isotropic, left-handed metamaterial," *Appl. Phys. Lett.*, Vol. 78, No. 4, 489–491, 2001.
4. Engheta, N., "Ideas for potential applications of metamaterials with negative permittivity and permeability," *Advances in Electromagnetics of Complex Media and Metamaterials*, 19–37, S. Zouhdi, A. H. Sihvola, and M. Arsalane, Eds., *NATO Science Series*, Kluwer, Norwell, MA, 2003.
5. Cory, H. and C. Zach, "Wave propagation in metamaterial multi-layered structures," *Microwave and Optical Technology Letters*, Vol. 40, No. 6, 460–465, 2004.
6. Alù, A. and N. Engheta, "Pairing an epsilon-negative slab with a mu-negative slab: Resonance, tunneling and transparency," *IEEE Trans. on Antennas and Propagation*, Vol. 51, No. 10, 2558–2571, 2003.
7. Oraizi, H. and M. Afsahi, "Analysis of planar dielectric multilayers as FSS by transmission line transfer matrix method (TLTMM)," *Progress in Electromagnetics Research*, PIER 74, 217–240, 2007.
8. Oraizi, H. and M. Afsahi, "Application of transmission line transfer matrix method (TLTMM) for the analysis of wave propagation in metamaterial multilayer mtructures as FSS," under submission.
9. Oraizi, H. and M. Afsahi, "Determination of correct values for propagation constant, intrinsic impedance and refraction index of metamaterials," *IEEE Applied Electromagnetic Conference, AEMC*, Calcutta, India, December 2007.

On the Study of Left-handed Coplanar Waveguide Coupler on Ferrite Substrate

M. A. Abdalla and Z. Hu
MACS Group, School of EEE, University of Manchester
P. O. Box 88, Manchester M60 1QD, UK

Abstract— This paper introduces a 3 dB tunable symmetric left handed coupled line coupler implemented on ferrite substrate. The proposed coupler is realized in LH coplanar waveguide configuration constructed using interdigital capacitors and meandered line inductors. The analytical analysis and the numerical verification of the proposed couple line coupler are presented. The full wave numerical simulation results for different DC magnetic bias indicate that a tunable left handed coupled line coupler propagation with transmission coefficient up to 3 dB and isolation level more than 25 dB over a wide bandwidth can be achieved.

1. INTRODUCTION

In the past few years, there has been a great interest in left handed materials (LHMs) i.e., materials whose both permittivity and permeability are negative, due to their unique properties that make them attractive to be used in many applications. The LHMs have been realized in different configurations either as a volume version or a planar version [1–4] Recently the use of left-handed (LH) coplanar waveguides (CPW) in RF/microwave applications have been proposed and demonstrated experimentally, where different types of loading series capacitors and parallel inductors have been illustrated in realizing the left handed nature [5].

Ferrite medium substrate has tunable dispersive properties depending on the direction and value of the applied magnetic bias to the ferrite substrate [6]. Therefore, a tunable LH transmission line (TL) is expected on ferrite substrates which has been recently demonstrated in different planar configurations [7–10].

The different types of conventional microwave coupled line couplers have a trade off between bandwidth, coupling level, and structure implementation constraints. The novel properties of the LH TL can lead to novel performance of LH coupled line coupler [11]. Unlike to the conventional quarter wave coupled line coupler, the LH coupler can provide arbitrary high coupling level, even 0 dB, with relatively wide lines separation over a broad bandwidth. Also, it has high forward coupling at lower frequency without the need to increase the physical length which is the case in conventional one. The left handed coupled line couplers were introduced in microstrip configuration [12, 13] and using CPW configuration [14].

In this paper we will present a uniplanar and symmetric LH CPW coupled line coupler (CLC) on ferrite substrate. The individual LH CPW TLs were designed using planar meandered line segment wires as shunt meandered line inductors and series interdigital capacitors. The proposed coupler has the advantages of its compact size and high coupling level. Also, it has the capability of being tunable due to the effect of the ferrite substrate. Moreover, in comparison with ferrite microstrip configuration, the ferrite CPW one requires lower dc magnetic bias since it has much smaller demagnetization factor. The performance of the proposed coupler is explained analytically and verified numerically structure is presented.

2. THEORY

The layout diagram of the proposed LH CPW coupled line coupler over ferrite substrate is shown in Figure 1(a). The CPW coupled line coupler is designed using two identical LH transmission lines separated by a distance s_o. Each individual LH transmission line is designed using a CPW transmission line loaded periodically using a shunt meandered line inductor and series interdigital capacitor in two unit cell configurations.

The series load interdigital capacitor has six fingers. Two identical interdigital capacitors used at both the input and the output of the coupler are identical whereas the one between the two periodic cells has double length, ta, and double air gap between the capacitor fingers and the periodic cell end, tac, compared to the dimensions of the two capacitors at both ends. Otherwise, all interdigital capacitors have the same finger width, Wc and separation, Sc. The shunt inductive load is formed

by a meandered line inductor has only two meandered arms. The detailed dimensions of the loading elements are shown in Figures 1(b) and (c).

Extension legs of the two coupled line are added at each line at each port for the proper simulation of the real case of fabricated circuit. The dimensions of the CPW TL at each port of the proposed coupler are identical such that they represent a 50 ohm transmission line.

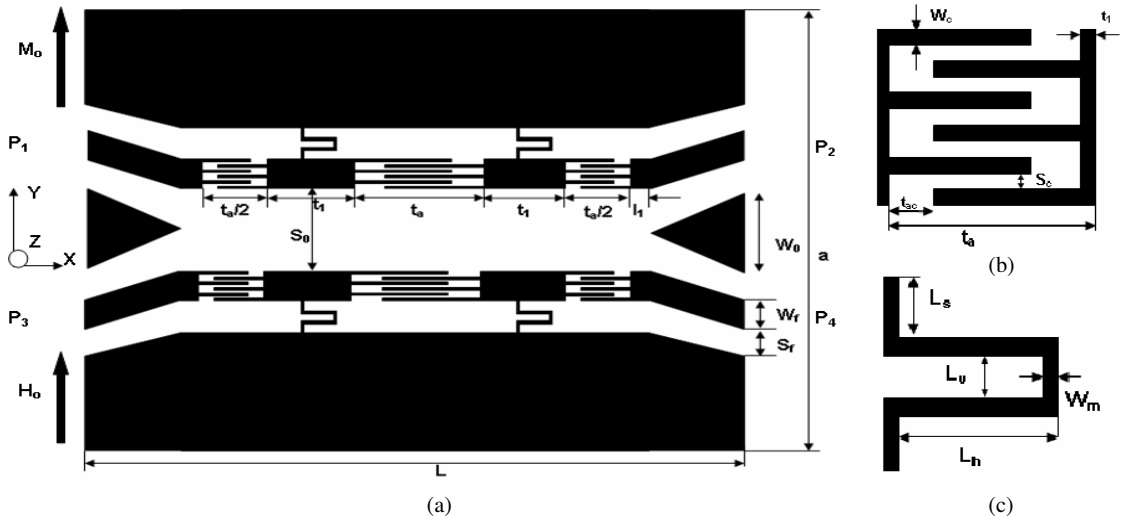

Figure 1: (a) The layout geometry of the ferrite LH CPW CLC, $a = 19.8\,\text{mm}$, $L = 10.32\,\text{mm}$, $W_0 = 6\,\text{mm}$, $t_a = 2.06\,\text{mm}$, $t_1 = 1.5\,\text{mm}$, $l_1 = 0.25\,\text{mm}$, $S_o = 2.5\,\text{mm}$, $S_f = 0.8\,\text{mm}$, $W_f = 1.3\,\text{mm}$, (b) the inter digital capacitor geometry $S_c = W_c = 0.1\,\text{mm}$, $t_{ac} = 0.4\,\text{mm}$, (c) the meandered line inductor geometry $W_m = 0.25\,\text{mm}$, $L_s = 0.25\,\text{mm}$, $L_v = 0.25\,\text{mm}$, $L_h = 0.5\,\text{mm}$.

The ferrite substrate has a relative permittivity of 15, height of $h = 1\,\text{mm}$. The magnetic properties of the ferrite substrate are a magnetic saturation, $M_o = 1780\,\text{Gauss}$ and a magnetic loss, $\Delta H_0 = 30\,\text{Gauss}$. An external DC magnetic field (H_o) is applied to the ferrite substrate in the shown direction in Figure 1(a) inducing an internal magnetic field which causes the ferrite substrate to have the saturation magnetization in the same direction.

The performance of the LH coupler can be explained using the coupled mode approach [11]. The coupled mode equations for the forward and backward modes along the two coupled lines can be given as

$$\frac{\partial a_1^+}{\partial z} = -j\beta a_1^+ + jC_{BW}a_1^- \tag{1}$$

$$\frac{\partial a_1^-}{\partial z} = +j\beta a_1^- - jC_{BW}a_1^+ \tag{2}$$

where β is the propagation constant of the individuals LH lines and can be obtained from [8]

$$\cos(\beta d) = 1 - \frac{1}{2}\omega^2 d^2 \left(\mu_0\mu_f - \frac{1}{\omega^2 Cd}\right)\left(\varepsilon_0\varepsilon_f - \frac{1}{\omega^2 Ld}\right) \tag{3}$$

where C_{BW} is the backward coupling coefficient that can be described as

$$C_{BW} = \omega\sqrt{\frac{\varepsilon_0\varepsilon_f}{\mu_0\mu_f}}L_m \tag{4}$$

and L is the shunt inductance, C is the series capacitance, L_m is the mutual inductance between the two coupled lines, ε_f is the ferrite relative permittivity, and μ_f is the ferrite equivalent relative permeability. Through this analysis, the propagation constant along the coupled lines can be obtained as

$$\beta_{I,II} = \sqrt{\beta^2 - C_{BW}^2} \tag{5}$$

From the above equations, it is clear that both the propagation constant of the forward and backward waves along the coupler and the coupling factor have a dispersive nature due the dispersive

nature of the ferrite permeability. Therefore, it is expected to have a tunable LH coupler by varying the applied DC magnetic bias.

The optimum performance of the proposed CPW LH coupler is obtained through the parametric studies of the different circuit geometry parameters and the coupling performance for the different values of DC magnetic bias.

3. NUMERICAL REULTS

The performance of the proposed CLC has been analyzed numerically using full wave simulation. The commercial software ANSOFT-HFSS is employed. For simplicity the applied DC magnetic field is assumed to be uniform in all studied cases. The numerical transmission characteristics of the proposed CPW ferrite LH coupler are simulated for different dc bias values of 1000, 1250, and 2000 Oe.

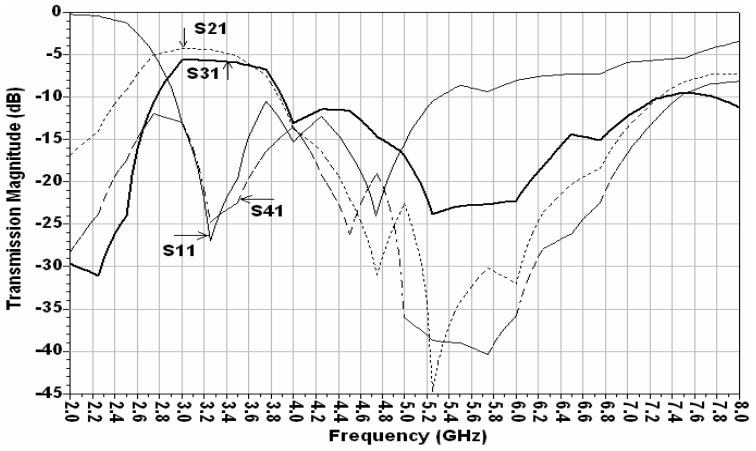

Figure 2: The full wave simulated magnitude of scattering parameters of the proposed coupler for H_o = 1000 Oe.

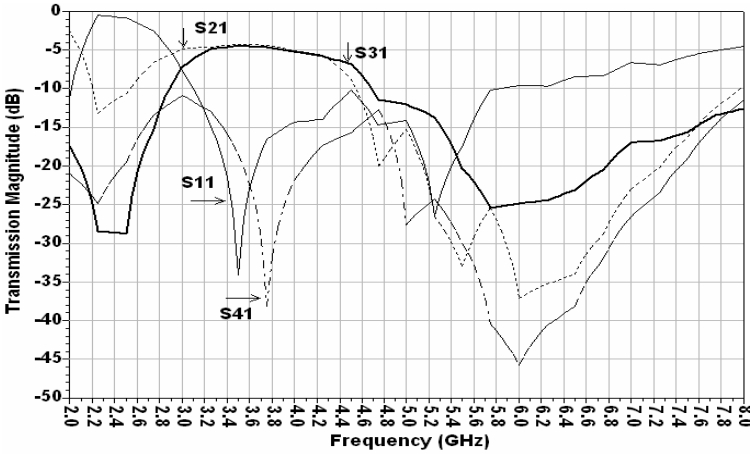

Figure 3: The full wave simulated magnitude of scattering parameters of the proposed coupler for H_o = 1250 Oe.

For the case of 1000 Oe, the resultant scattering parameters shown in Figure 2 show a backward coupler with an equal through and coupling level approximately equal to 5 dB and an isolation level up to 27 dB.. The center frequency at which the reflection and the isolation level is minimum is 3.2 GHz with a bandwidth at which both the through and the coupled level changes by 2 dB is approximately 25%.

For the case of 1250 Oe, the simulated scattering parameters which are shown in Figure 3 shows also a backward coupler with approximately 4 dB coupling and through level with an isolation level up to 40 dB. The centre frequency is observed to be shifted to 3.6 GHz while the coupler has a bandwidth equals 29%.

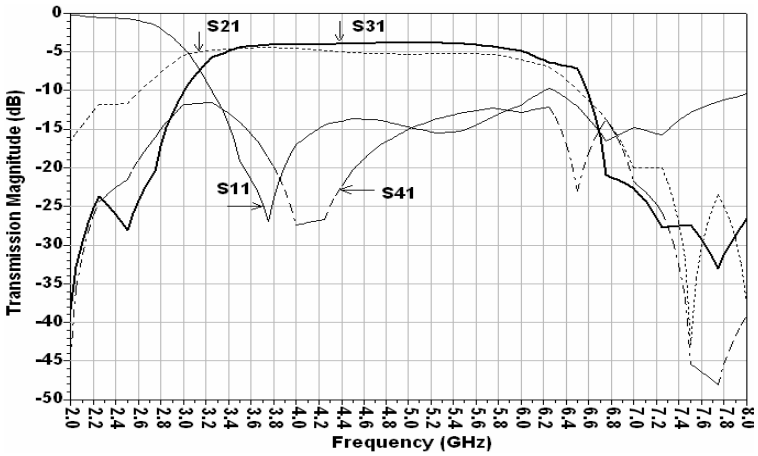

Figure 4: The full wave simulated magnitude of scattering parameters of the proposed coupler for H_o = 2000 Oe.

Finally, the last case of 2000 Oe dc bias, the simulated scattering parameters which are shown in Figure 4 shows a 3 dB backward coupler with isolation up to 27 dB. The centre frequency in this case is shifted again to 3.9 GHz where the bandwidth is 61%.

From the above results it is clear that the proposed LH coupler has tuning capability for both the centre frequency and the bandwidth.

4. CONCLUSIONS

A tunable LH CPW coupled line coupler over a ferrite substrate has been studied. The coupler was designed only using two identical LH TLs. The performance of the proposed coupler has been studied numerically through its scattering parameters. The results show tunable transmission characteristics by varying the DC magnetic bias with coupling level up to a 3 dB coupling factor and isolation level more than 25 dB over a wide bandwidth. The proposed ferrite CPW coupler has the advantage of its small size and its small demagnetization factor and hence it does not require high applied DC magnetic field compared to the microstrip configuration.

REFERENCES

1. Smith, D. R., W. J. Padilla, D. C. Vier, S. C. Nemat-Nasser, and S. Schultz, "Composite medium with simultaneously negative permeability and permittivity," *Phys. Rev. Lett.*, Vol. 84, No. 18, 4184–4187, 2000.
2. Falcone, F., T. Lopetegi, J. D. Baena, R. Marques, F. Martin, and M. Sorolla, "Effective negative-ε stopband microstrip lines based on complementary split ring resonators," *IEEE Microwave and Wireless Components Lett.*, Vol. 14, No. 6, 280–282, 2004.
3. Elefteriades, G. V., A. K. Iyer, and P. C. Kremer, "Planar negative refractive index media using planar L-C loaded transmission line," *IEEE Trans. Microwave Theory & Tech.*, Vol. 50, No. 12, 2702–2712, 2002.
4. Caloz, C. and T. Itoh, "Transmission line approach of left handed (LH) materials and microstrip implementation of an artificial LH transmission line," *Proceedings of IEEE AP-S Int. Symp.*, 412–415, USA, June 2002.
5. Gao, J. and L. Zhu, "Guided-wave characteristics of CPW transmission line metamaterials, effective per-unit-length parameters," *Proceedings of IEEE International Workshop on Antenna Technology: Small Antennas and Novel Metamaterials*, 175–178, Singapore, March 7–9, 2005.
6. Lax, B. and K. Button, *J. Microwave Ferrites and Ferrimagnetics*, McGraw Hill, 1962.
7. Tsutsumi, M. and T. Ueda, "Nonreciprocal left-handed microstrip lines using ferrite substrate," *Proceedings of IEEE MTT-S Int. Microwave Symposium*, 249–252, USA, June 2004.
8. Abdalla, M. and Z. Hu, "On the study of cwp dual band left handed propagation with reciprocal and nonreciprocal characteristics over ferrite substrates," *Proceedings of IEEE AP-S Int. Symp.*, 2578–2581, USA, June 2007.
9. Tsutsumi, M. and T. Ueda, "Left handed transmission characteristics of ferrite microstrip lines without series capacitive load," *IEICE Trans. Electron.*, Vol. E89, No. 9, 1318–1323, 2006.

10. Abdalla, M. and Z. Hu, "On the study of nonreciprocal left handed coplanar waveguide over ferrite substrate with only shunt inductive load," *IEEE Microwave and Optical Technology Lett.*, Vol. 49, No. 11, 2810–2814, 2007.
11. Nguyen, H. V. and C. Caloz, "Generalized coupled mode approach of metamaterial coupled line couplers: coupling theory, phenomenological explanation, and experimental demonstration," *IEEE Trans. Microwave Theory & Tech.*, Vol. 55, No. 5, 1029–1039, May 2007.
12. Caloz, C., A. Sanada, and T. Itoh, "A broadband left handed (LH) coupled line backward coupler with arbitrary coupling level," *Proceedings of IEEE MTT-S Int. Microwave Symposium*, 317–320, USA, June 2003.
13. Islam, R. and G. Eleftheriades, "A planar metamaterial co-directional coupler that couples power backwards," *Proceedings of IEEE MTT-S Int. Microwave Symposium*, 321–324, Philadelphia, USA, June 8–13, 2003.
14. Shau, G. M. and M. S. Mu, "A novel 3-dB directional coupler with broad bandwidths and compact size using composite right/left handed coplanar waveguide," *IEEE Microwave and Wireless Components Lett.*, Vol. 17, No. 5, 331–333, May 2007.

The Effect of Cooling Systems on HTS Microstrip Antennas

S. F. Liu[1] and S. D. Liu[2]

[1]Xidian University, Xi'an 710071, China
[2]Xi'an Institute of Space Radio Technology, Xi'an 710000, China

Abstract— High-temperature superconducting (HTS) antennas must work at a temperature below the critical temperature of the HTS material, so a cooling system is needed and the antenna should be placed inside it. Would the cooling system influence the properties of the HTS antenna? And if any, how does it? To answer these questions, a cryocooler is simulated with a 3-D model and its effect on HTS microstrip antennas is studied. It is found that when the vacuum chamber of the cryocooler has a suitable dimension, the gain of the antenna inside it can be improved greatly.

1. INTRODUCTION

Since the surface resistance of high-temperature superconductor (HTS) is much lower than that of the normal conductors [1], HTS has found wide applications in various fields [2–6]. These HTS devices should work at temperatures below the critical temperature of HTS materials, which is usually over the boiling point of liquid nitrogen. A cryocooler is often used to cool these devices because of its easy handing and convenience compared with liquid N_2. In a cooling system, the HTS antenna to be cooled is packaged in a vacuum chamber for thermal isolation. However, a vacuum chamber is generally made of metallic or dielectric materials. If the distance between an antenna and a chamber is within a wavelength, interference of the chamber on the antenna properties strongly appears. Therefore, it is important to investigate the effect of cooling systems on the HTS antenna.

K. Ehata and his fellows [7] have first presented an experimental radiation property of a HTS antenna in a cryocooler. In their experiment, the gain of the Cu antenna in the cryocooler is 11.2 dB higher than that in free space, while a HTS microstrip antenna at the temperature of 60 K can obtain a gain of 2.6 dB higher than that of its Cu counterpart. That is, the gain of a HTS antenna at 60 K is 13.8 dB higher than that of the same Cu antenna in free space. In a paper in 2001 [8], they gave a rough theoretical explain to this phenomena, but no thorough analysis was made.

In this work, a 3-dimensional structure is constructed to model the vacuum chamber of the cryocooler and the radiation characteristics of a HTS microstrip antenna inside it is studied in detail.

2. THE COOLING SYSTEM FOR HTS ANTENNAS

The cooling system consists of a compressor, a cold head, a vacuum chamber and other related parts. Among these, the vacuum chamber is the part which influences the properties of HTS antenna most. Figure 1 shows a schematic diagram of the vacuum chamber [7, 8]. The vacuum chamber consists of a cylindrical stainless jacket, a stainless flange with a cold head, and a dielectric window. The dielectric window is employed for microwave propagation between the vacuum environment and the atmosphere. The antenna to be cooled is mounted on the sample stage and a Cu-Ni coaxial cable is used to feed it. Since the thermal conductivity of Cu-Ni is 1/20 comparing with that of Cu, heat coming from room temperature to the cooled environment can be reduced.

3. PROPERTIES OF HTS ANTENNAS IN A COOLING SYSTEM

For comparison, the same antenna as in [8] is analyzed. It was cooled in a vacuum chamber with a quartz glass window which had a permittivity of 3.8 and thickness of 8.0 mm. The antenna was placed 11 mm apart from the window as shown in Figure 1.

According to the structure shown in Figure 1, a cylindrical cavity of perfect conductor is used to model the cylindrical stainless jacket of the vacuum chamber as well as the stainless flange at the bottom. The dielectric window of vacuum chamber is assumed as a circle dielectric plate of thickness t, which has the same radius as that of the cylinder and serves as a cover of the cylindrical cavity (shown in Figure 2). The height and radius of the cylinder is denoted as H and R respectively, and the distance between the antenna and the underside of the dielectric plate is denoted as d.

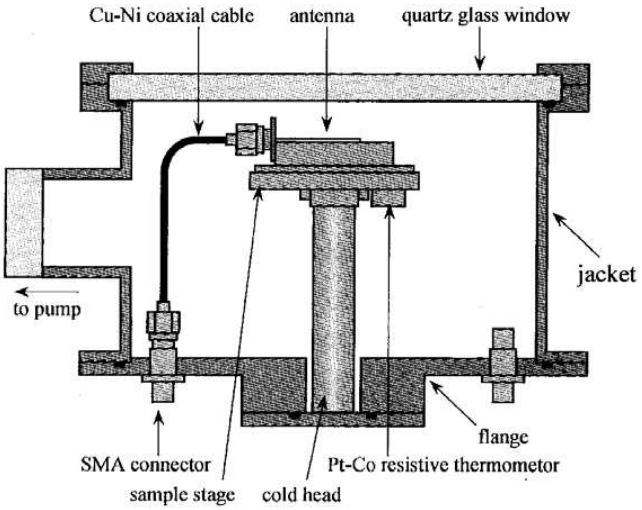

Figure 1: Schematic diagram of the vacuum chamber.

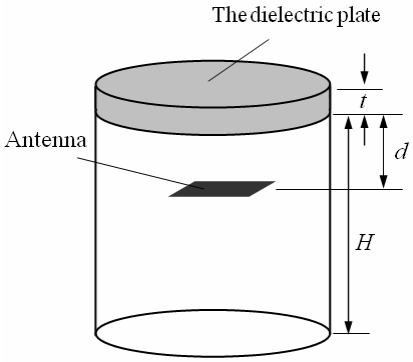

Figure 2: Schematic diagram of the 3-D model.

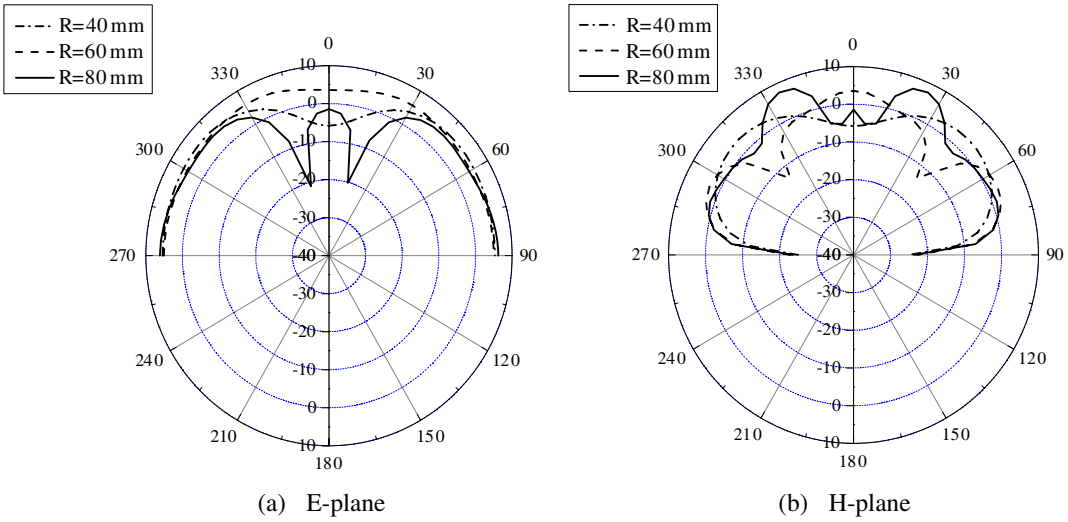

Figure 3: The gain patterns for various radius of the dielectric plate.

First, we studied the variation of the antenna's radiation performance with the vacuum chamber's radius. Figure 3 shows the simulated gain patterns when $R = 40$, 60 and 80 mm with $t = 8.0$ mm and $d = 11.0$ mm. It can be seen from the two figures that when $R = 60$ mm the gain in the forward direction is the highest.

To demonstrate whether the thickness of the dielectric plate affects the antenna gain, the gain patterns with $t = 7$, 8, 9 mm and $R = 60$ mm is calculated and shown in Figure 4. It shows that

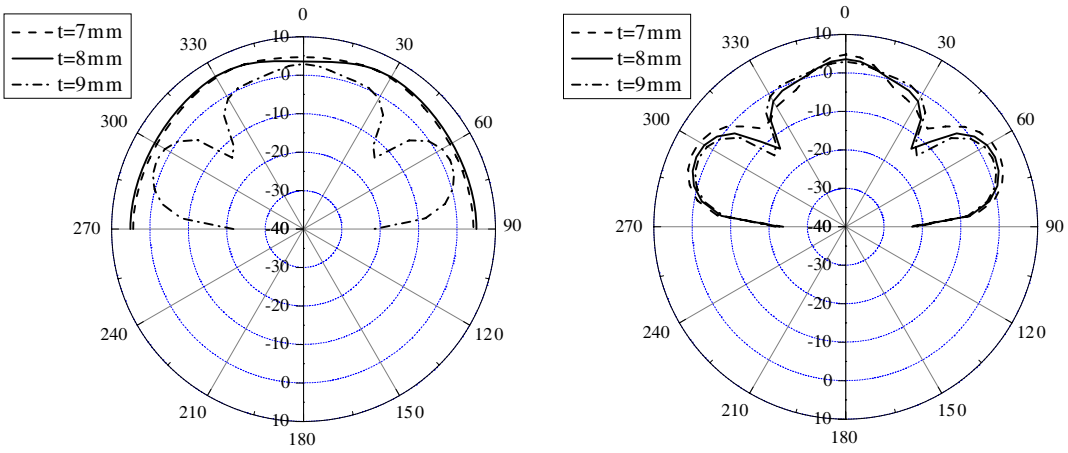

(a) E-plane (b) H-plane

Figure 4: The gain patterns for various thickness of the dielectric plate.

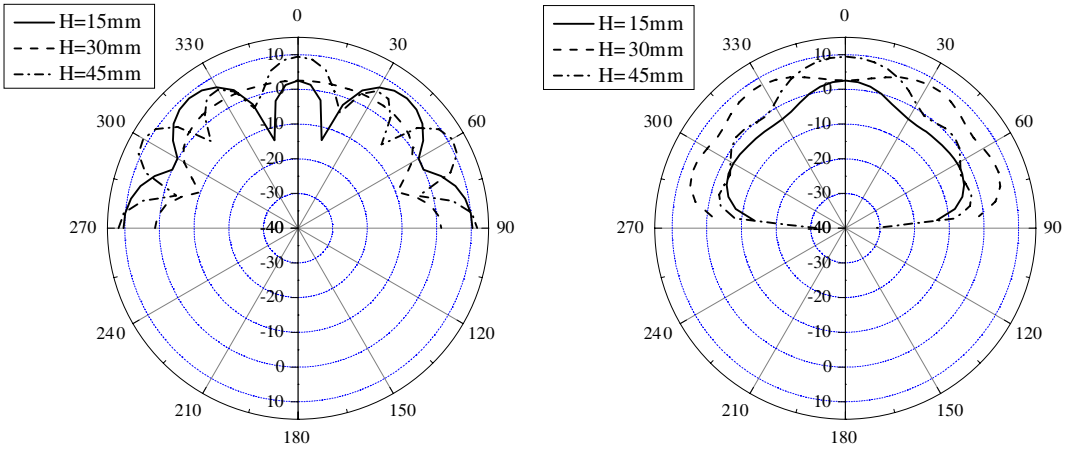

(a) E-plane (b) H-plane

Figure 5: The gain patterns for various height of the cylinder ($R = 40\,\text{mm}$).

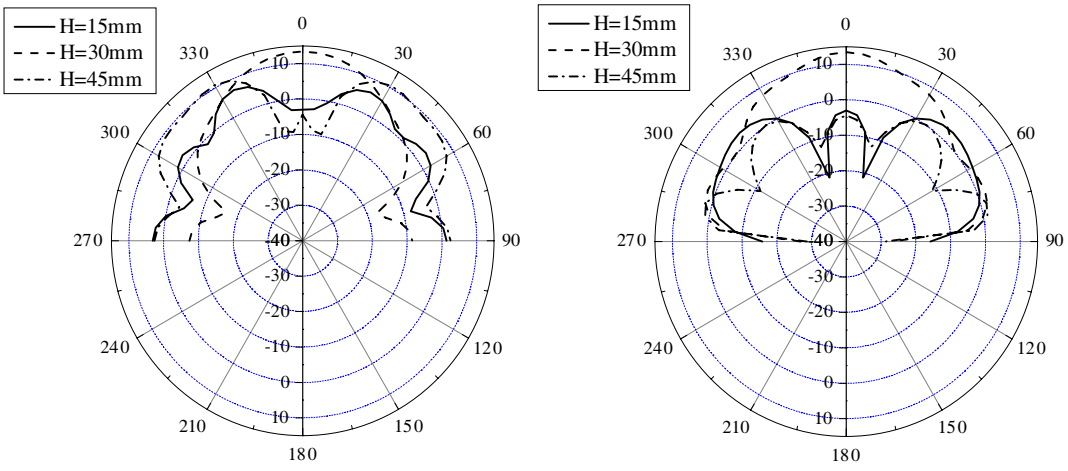

(a) E-plane (b) H-plane

Figure 6: The gain patterns for various height of the cylinder ($R = 60\,\text{mm}$).

the gain is highest when $t = 7$ mm, but no remarkable enhancement is observed compared with the other cases.

According to the above analysis, we suppose that the rather high gain enhancement in [8] is due to the whole structure of the vacuum chamber. So the antenna is simulated for various structure parameters of the chamber. The patterns for various H when $R = 40$, 60, and 80 mm are shown in Figures 5, 6 and 7, respectively. From these figures we can see that the cooling system will severely affect the radiation characteristics of HTS antennas inside it, which leads to a large distortion of the radiation patterns. But it can be found from Figure 6 that when $R = 60$ mm and $H = 30$ mm a remarkably enhanced gain of 13.45 dB can be obtained. And Figure 7 shows that the antenna can even achieve a gain of 14.15 dB when $R = 80$ mm and $H = 30$ mm.

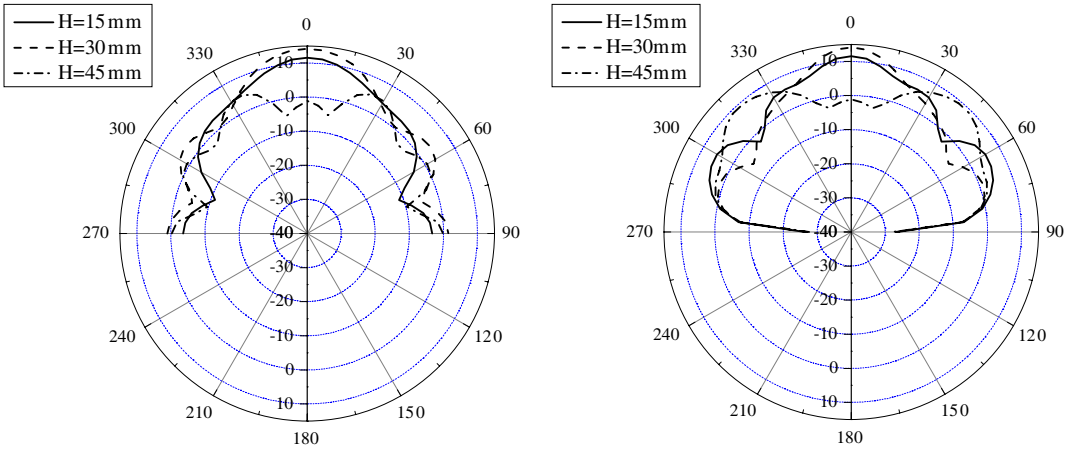

(a) E-plane (b) H-plane

Figure 7: The gain patterns for various height of the cylinder ($R = 80$ mm).

4. CONCLUSIONS

To study the effect of the cooling system on HTS antennas, a cylindrical structure is constructed to model the vacuum chamber of the cooling system. Analysis of the antenna's properties is made for various structure parameters of the 3-D model, which shows that the existence of the cooling system will cause a great distortion of the antenna's radiation patterns, but when the vacuum chamber has an appropriate dimension the gain of the antenna can achieve a remarkable enhancement.

REFERENCES

1. Wu, C. J., C. M. Fu, and T. J. Yang, "Microwave surface impedance of a nearly ferroelectric superconductor," *Progress In Electromagnetics Research*, PIER 73, 39–47, 2007.
2. Bourne, L. C., R. B. Hammond, et al., "Low-loss microstrip delay line in $Tl_2Ba_2CaCu_2O_8$," *Appl. Phys. Lett.*, Vol. 56, No. 23, 2333–2335, 1990.
3. Bonetti, R. R. and A. E. Williams, "Preliminary design steps for thin-film superconducting filters," *IEEE MTT-S Int. Microwave Symp. Digest*, Vol. 1, 273–275, 1990.
4. Awan, S. A. and S. Sali, "Self-field ac power dissipation in high-Tc superconducting tapes and a prototype cable," *Progress In Electromagnetics Research*, PIER 36, 81–100, 2002.
5. Tchernyi, V. V. and E. V. Chensky, "Electromagnetic background for possible magnetic levitation of the superconducting rings of saturn," *Journal of Electromagnetic Waves and Applications*, Vol. 19, No. 7, 987–995, 2005.
6. Liu, S. F., S. D. Liu, and B. R. Guan, "A novel wideband high-temperature superconducting microstrip antenna," *Journal of Electromagnetic Waves and Applications*, Vol. 19, No. 15, 2073–2079, 2005.
7. Ohshima, S., K. Ehata, and T. Tomiyama, "High-temperature superconducting microwave passive devices, filter and antenna," *IEICE Trans. Electron.*, Vol. E83-C, No. 1, 2–6, 2000.
8. Ehata, K., K. Sato, M. Kusunoki, et al., "Miniaturized cooling systems for HTS antennas," *IEEE Trans. on Applied Superconductivity*, Vol. 11, No. 1, 111–114, 2001.

GL Time Domain Modeling for EM Acoustic and Elastic Wave Field with Dispersion in Crystal and Porous Material

Jianhua Li, **Ganquan Xie**, **Lee Xie**, **and Feng Xie**
GL Geophysical Laboratory, USA

Abstract— In the last few years, we have proposed electromagnetic (EM), mechanical, acoustic and flow GL modeling and applications in the frequency domain. In this paper, we propose GL modeling for EM, acoustic, and elastic field in aperiodic space time domain and their dispersion field in periodic space time domain, respectively. The GL modeling in this paper is based on integral equation. We, first, derive EM and acoustic integral equation in time domain. Based on these time domain integral equations, we construct GL modeling for EM, acoustic, and elastic field in aperiodic space time domain and their dispersion field in periodic lattice space time domain. The GL modeling method can fast and accurate to calculate EM, acoustic, and elastic in space time domain, in particular, can simulate the field dispersion in the periodic lattice space time domain. Similar with GL method in the frequency domain, the time domain GL method does not need to solve any large matrix, only needs to solve 6×6 and 9×9 small matrices. Moreover, the artificial boundary and absorption condition are unnecessary in the time domain GL method. The time domain GL EM, acoustic, and elastic modeling method have wide applications which are described in this paper.

1. INTRODUCTION

Global and Local field (GL) modeling in frequency domain for solving EM, elastic, acoustic, flow, and quantum field have been proposed by authors [1–3] since 2002. In meantime, we proposed GL inversion in frequency domain to recover the EM and other above wave field velocity and parameters in various applications [4–5]. These GL modeling methods in frequency domain are based on EM, elastic, acoustic frequency domain integral equations, respectively [1–3, 6–9].

In this paper, we propose GL field modeling method for EM, acoustic, and elastic field propagation in time domain. These GL time domain modeling methods in this paper are based on EM, acoustic, and elastic field integral equation in time domain, respectively. Our other GL time domain modeling is based on differential integral equation [10]. We derive EM, acoustic, and elastic integral equation in time domain. Based on these time domain integral equations, we construct GL EM, acoustic and elastic modeling in time domain. Similar with our GL method in the frequency domain, the time domain GL method does not need to solve any large matrix, only 6×6 and 9×9 matrices are needed to solve in the time domain GL EM, acoustic and elastic modeling respectively. Moreover, the artificial boundary and absorption condition are unnecessary in the time domain GL modeling method. The time domain EM, acoustic, and elastic GL modeling method have wide application. Many applications are described in this paper. GL modeling method has advantages to challenge to FEM and FDTD methods.

In contrast with FEM and FD method, instead of FEM process to build matrix and then solve large matrix, GL method process to build inverse matrix and update solution sub domain by sub domain successively. There is no any large matrix needs to be solved in GL method. In FEM and FD EM and seismic modeling, artificial boundary and absorption condition on it is necessary for truncating infinite domain. To challenge to the FEM and FD method, GL method does not need any artificial boundary and no absorption on it for infinite domain. The analytic method and numerical method in GL method are consistent combined.

Dispersion is an important physical phenomenon in the EM, elastic, acoustic wave field, quantum field, and flow field. Because these wave field are superposition of the sub waves with different phase velocities, they produce the dispersion in the dispersion materials and waveguide. The dispersion has desirable benefit and undesirable harms. Therefore, to enhance the benefit the dispersion and avoid its harm is interesting research target in the sciences and engineering. Recent years, the high frequency EM wave or light dispersion in the optical materials and periodic crystals, and flow dispersion in the porous mediums become an attract research project. In paper [10, 12], authors developed AGILD EM, mechanical, and quantum field modeling and inversion to simulate these wave field in the macro and micro nanometer materials. The field dispersion in the nanometer is displayed. The band cap of simulation in the figure of [3] and is similar with thephysical band cap in figure of [3].

Several simulations of 2D and 1D EM wave field propagation in the photonic crystals are presented. The FDTD is used to simulate the dispersion engineering of photonic crystals in Pustai and Chen'paper [13]. In paper [14], Song et al. presented a numerical simulation and analysis on mode property of photonic crystal fiber with high birefringence by fast multipole method.

The fast and accurate computational method for wave dispersion in the periodic crystals is necessary. The GL and AGILD modeling is suitable for wave dispersion propagation in the periodic and aperiodic materials, photonic crystal, and waveguide. We develop various GL and AGILD EM, acoustic, and elastic field modeling for global periodic and local periodic, global aperiodic and local periodic, global periodic and local aperiodic, and global aperiodic and local aperiodic space time modeling multiple scale algorithms and software [15, 18]. In this paper, EM, acoustic, and elastic integral equation and GL modeling for these wave field in aperiodic and periodic space time domain are original and new equations and methods.

The presenting plan of this paper is as follows. The introduction has been presented in Section 1. We derive EM time domain integral equation in Section 2. In Section 3, we propose 3D GL EM time domain modeling. Acoustic wave time domain integral equation is presented in Section 4. In Section 5, we propose 3D GL acoustic wave time domain modeling. In Section 6, we propose 3D GL elastic wave field time domain modeling. In Section 7, we propose 3d GL modeling for EM dispersion in periodic space time domain. The advantages of the GL time domain modeling. are described in Section 8. The 1D wave time domain GL modeling is proposed in Section 9. We describe several applications and simulations in Section 10. The conclusion of this paper is concluded in Section 11.

2. EM INTEGRAL EQUATION IN TIME DOMAIN

2.1. An EM Integral Equation in Time Domain

In this section, we propose the EM integral equation in time domain as follows

$$\begin{bmatrix} E(r,\,t) \\ H(r,\,t) \end{bmatrix} = \begin{bmatrix} E_b\,(r,\,t) \\ H_b\,(r,\,t) \end{bmatrix} - \int\limits_{\Omega} G_{E,\,H}^{J,\,M}\left(r',\,r,\,t\right) *_t \left[D_b - D\right] \begin{bmatrix} E_b\,(r',\,t) \\ H_b\,(r',\,t) \end{bmatrix} \mathrm{d}r', \tag{1}$$

where

$$G_{E,\,H}^{J,\,M}\left(r',\,r,\,t\right) = \begin{bmatrix} E^J\,(r',\,r,\,t) & H^J\,(r',\,r,\,t) \\ E^M\,(r',\,r,\,t) & H^M\,(r',\,r,\,t) \end{bmatrix}, \tag{2}$$

$$D_b = \begin{bmatrix} \sigma_b + \varepsilon_b \dfrac{\partial}{\partial t} & \\ & -\mu_b \dfrac{\partial}{\partial t} \end{bmatrix},\ D = \begin{bmatrix} \sigma + \varepsilon \dfrac{\partial}{\partial t} & \\ & -\mu \dfrac{\partial}{\partial t} \end{bmatrix}, \tag{3}$$

$E\,(r,\,t)$ is the electric field, $H\,(r,\,t)$ is the magnetic field, $E^J\,(r',\,r,\,t)$ is the electric Green's field function excited by the impulse current, $H^J\,(r',\,r,\,t)$ is the magnetic Green's field function excited by the impulse current, $E^M(r',\,r,\,t)$ is the electric Green's field function exited by the impulse magnetic moment, $H^M(r',\,r,\,t)$ is the magnetic Green's field function excited by the impulse magnetic moment, $E^J\,(r',\,r,\,t)$, $H^J(r',\,r,\,t)$, $E^M\,(r',\,r,\,t)$, and $H^M\,(r',\,r,\,t)$ are EM Green's function field in the electric conductivity σ, dielectric ε, and magnetic permeability μ media, $E_b\,(r,\,t)$ and $H_b\,(r,\,t)$ are EM wave field in the background σ_b, ε_b, and μ_b media, $*_t$ is convolution with respect to time t.

2.2. Dual EM Integral Equation in Time Domain

We propose the dual EM integral equation in time domain as follows

$$\begin{bmatrix} E\,(r,\,t) \\ H\,(r,\,t) \end{bmatrix} = \begin{bmatrix} E_b\,(r,\,t) \\ H_b\,(r,\,t) \end{bmatrix} - \int\limits_{\Omega} G_{E,\,H,\,b}^{J,\,M}\left(r',\,r,\,t\right) *_t \left[D_b - D\right] \begin{bmatrix} E\,(r',\,t) \\ H\,(r',\,t) \end{bmatrix} \mathrm{d}r', \tag{4}$$

where

$$G_{E,\,H,\,b}^{J,\,M}\left(r',\,r,\,t\right) = \begin{bmatrix} E_b^J\,(r',\,r,\,t) & H_b^J\,(r',\,r,\,t) \\ E_b^M\,(r',\,r,\,t) & H_b^M\,(r',\,r,\,t) \end{bmatrix}, \tag{5}$$

the D_b and D are denoted by (3).

3. 3D GL EM MODELING IN TIME DOMAIN

In this section, we propose the 3D GL EM modeling time domain as follows,

(**3.1**) The domain Ω is divided into set of the N sub domains $\{\Omega_k\}$, such that. $\Omega = \bigcup_{k=1}^{N} \Omega_k$, where the division can be mesh or meshless.

(**3.2**) suppose that, when $k = 0$,

$$[E_0(r,\, t) \quad H_0(r,\, t)] = [E_b(r,\, t) \quad H_b(r,\, t)]\,,$$

and

$$G^{J,\,M}_{E,\,H,\,0}\left(r',\, r,\, t\right) = G^{J,\,M}_{E,\,H,\,b}\left(r',\, r,\, t\right) = \left[\begin{array}{cc} E^J_b\left(r',\, r,\, t\right) & H^J_b\left(r',\, r\right) \\ E^M_b\left(r',\, r\right) & H^M_b\left(r',\, r\right) \end{array}\right],$$

is the global analytical EM field and EM Green's tensor in time domain and in the global background medium with constant EM parameter, or half space medium, or waveguide medium, or multiple layered medium. By induction, suppose that the time domain EM field $[E_{k-1}(r,\, t) \quad H_{k-1}(r,\, t)]$, and the EM Green's tensor $G^{J,\,M}_{E,\,H,\,k-1}\left(r',\, r,\, t\right)$ have been calculated in the $(k-1)^{\text{th}}$ step.

(**3.3**) In Ω_k, we solve the EM Green tensor integral equation system in time domain which is based on the Equations (1) and (4). By dual operation, the equation system is reduced into a 6×6 matrix equations. By solving the 6×6 equations, we obtain Green tensor field $G^{J,\,M}_{E,\,H,\,k}\left(r',\, r,\, t\right)$, i.e., $E^J_k\left(r',\, r,\, t\right), \ldots,$ and $H^M_k\left(r',\, r,\, t\right)$ in time domain.

(**3.4**) We improve the Global EM field $[E_k\left(r,\, t\right) \quad H_k\left(r,\, t\right)]$ by the Local time domain scattering filed as follows,

$$\left[\begin{array}{c} E_k\left(r,\, t\right) \\ H_k\left(r,\, t\right) \end{array}\right] = \left[\begin{array}{c} E_{k-1}\left(r,\, t\right) \\ H_{k-1}\left(r,\, t\right) \end{array}\right] - \int\limits_{\Omega_k} G^{J,\,M}_{E,\,H,\,k}\left(r',\, r,\, t\right) *_t \left[D_b - D\right] \left[\begin{array}{c} E_{k-1}\left(r',\, t\right) \\ H_{k-1}\left(r',\, t\right) \end{array}\right] \mathrm{d}r' \qquad (6)$$

$k = 1,\, 2,\, \ldots,\, N$, successively. The $[E_N\left(r,\, t\right) \quad H_N\left(r,\, t\right)]$ is GL EM field solution of the EM integral Equations (1) and (4) and EM Maxwell equation in time domain.

4. ACOUSTIC WAVE FIELD INTEGRAL EQUATION IN TIME DOMAIN

4.1. An Acoustic Wave Field Integral Equation in Time Domain

In this section, we propose the acoustic wave field integral equation in time domain as follows,

$$u\left(r,\, t\right) = u_b\left(r,\, t\right) - \int\limits_{\Omega} \left(\frac{1}{c_b^2\left(r\right)} - \frac{1}{c^2\left(r\right)}\right) G\left(r',\, r,\, t\right) *_t \frac{\partial^2}{\partial t^2} u_b\left(r',\, t\right) \mathrm{d}r', \qquad (7)$$

where r is space variable $r = (x,\, y,\, z)$, $r \in R^3$, $c\left(r\right)$ is the coefficient, so called wave velocity, which is inhomogeneous media function in a finite bounded domain $\Omega \subset R^3$, $c\left(r\right) = c_b$ in $r \in R^3 \backslash \Omega$, c_b is a constant, t is time, $u\left(r,\, t\right)$ is the unknown wave field, If the $c\left(r\right) = c_b$ in whole space R^3, the solution $u_b(r,\, t)$ of the wave equation is called incident wave in the background media, $u_b\left(r,\, t\right) = \delta\left(t - \frac{|r - r_s|}{c_b}\right) / \left|r - r_s\right| / \left(4\pi\right)$, The solution of the wave equation satisfies the following radiation condition,

$$\lim_{r \to \infty} r\left(\frac{\partial u}{\partial n} - \frac{\partial}{c \partial t} u\right) = 0,$$

and *ru(r, t)* is bounded in infinite, $G\left(r',\, r,\, t\right)$ is Green's function of the wave equation, $*_t$ is convolution with respect to time t.

4.2. Dual Acoustic Wave Field Integral Equation in Time Domain

In this section, we propose the dual acoustic wave field integral equation in time domain as follows,

$$u\left(r,\, t\right) = u_b\left(r,\, t\right) - \int\limits_{\Omega} \left(\frac{1}{c_b^2\left(r\right)} - \frac{1}{c^2\left(r\right)}\right) G_b\left(r',\, r,\, t\right) *_t \frac{\partial^2}{\partial t^2} u\left(r',\, t\right) \mathrm{d}r', \qquad (8)$$

where $G_b\left(r',\, r,\, t\right)$ is the Green's function of the wave equation in the background media, $*_t$ is convolution with respect to time t.

5. 3D GL ACOUSTIC WAVE MODELING IN TIME DOMAIN

In this section, we propose the 3D GL acoustic wave modeling in time domain as follows

(**5.1**) The domain Ω is divided into set of the N sub domains $\{\Omega_k\}$, such t.hat $\Omega = \bigcup_{k=1}^{N} \Omega_k$, where the division can be mesh or meshless.

(**5.2**) Suppose that, when $k = 0$, $u_0(x, t) = u_b(r, t) = \delta\left(t - \frac{|r-r_s|}{c_b}\right) / |r - r_s| / (4\pi)$, is the global analytical time domain acoustic wave field and $G_0(r', r, t) = G_b(r', r, t)$ is the wave Green's function in the global background medium with constant wave velocity $c(r) = c_b$, or half space medium, or waveguide medium, or multiple layered medium. By induction, suppose that the time domain EM field $u_{k-1}(x, t)$, and the acoustic wave Green's function $G_{k-1}(r', r, t)$ have been calculated in the $(k-1)^{\text{th}}$ step.

(**5.3**) In Ω_k, we solve the acoustic wave Green's function integral equation system in time domain which is based on the Equations (7) and (8). By dual operation, the integral equation are reduced into an algebra equations. By solving the algebral equations, We obtain time domain Green tensor field $G_k(r', r, t)$.

(**5.4**) We improved the Global acoustic wave field $u_k(x, t)$ by the Local time domain scattering filed in the Ω_k,

$$u_k(r, t) = u_{k-1}(r, t) - \int_{\Omega_k} \left(\frac{1}{c_b^2(r)} - \frac{1}{c^2(r)}\right) G_k(r', r, t) *_t \frac{\partial^2}{\partial t^2} u_{k-1}(r', t)\, \mathrm{d}r' \tag{9}$$

$k = 1, 2, \ldots, N$, successively. The $u_N(x, t)$ is GL acoustic wave field solution of the acoustic wave time domain integral Equations (7) and (8). We can prove that $u_N(x, t)$ is the solution of the wave equation.

6. 3D ELASTIC WAVE FIELD GL MODELING IN TIME DOMAIN

In this section, we propose the 3D GL elastic wave field modeling in time domain as follows

(**6.1**) It is same as (5.1)

(**6.2**) suppose that, when $k = 0$, the elastic displacement and stress,

$$[u_0(r, t) \quad \sigma_0(r, t)] = [u_b(r, t) \quad \sigma_b(r, t)],$$

and

$$G^{D,S}_{u,\sigma,0}(r', r, t) = G^{D,S}_{u,\sigma,b}(r', r, t)$$

are the global analytical elastic field and elastic Green's tensor in the global background medium with constant elastic mechanical parameter, or half space medium, or waveguide medium, or multiple layered medium. By induction, suppose that elastic wave field $[u_{k-1}(r, t) \quad \sigma_{k-1}(r, t)]$, and the elastic wave field Green's tensor $G^{D,S}_{u,\sigma,k-1}(r', r, t)$ in the time domain have been calculated in the $(k-1)^{\text{th}}$ step.

(**6.3**) In Ω_k. by solving the 9×9 matrix equations, we obtain elastic wave field Green tensor field $G^{D,S}_{u,\sigma,k}(r', r, t)$, i.e., $u^D_k(r', r, t), \sigma^D_k(r', r, t)$, $u^S_k(r', r, t)$ and $\sigma^S_k(r', r, t)$ in time domain.

(**6.4**) We improve the global elastic mechanical wave field $[u_k(r, t) \quad \sigma_k(r, t)]$ by the local time domain elastic scattering filed in Ω_k,

$$\begin{bmatrix} u_k(r, t) \\ \sigma_k(r, t) \end{bmatrix} = \begin{bmatrix} u_{k-1}(r, t) \\ \sigma_{k-1}(r, t) \end{bmatrix} - \int_{\Omega_k} G^{D,S}_{u,\sigma,k}(r', r, t) *_t [D_b - D] \begin{bmatrix} u_{k-1}(r', t) \\ \sigma_{k-1}(r', t) \end{bmatrix} \mathrm{d}r' \tag{10}$$

$k = 1, 2, \ldots, N$, successively. The $[u_N(r, t) \quad \sigma_N(r, t)]$ is GL elastic mechanical wave field solution of the elastic wave equation.

7. 3D GL MODELING FOR EM DISPERSION IN PEIODIC SPACE TIME DOMAIN

In this section, we propose the 3D GL EM modeling for 3D EM field dispersion time domain as follows

(**7.1**) The lattice unit cell domain Ω_{UC} is divided into set of the N sub domains $\{\Omega_{UCk}\}$, such that $\Omega_{UC} = \bigcup_{k=1}^{N} \Omega_{UCk}$, where the division can be mesh or meshless.

(**7.2**) suppose that, when $k = 0$,

$$\lfloor E_{\beta,0}(r) \quad H_{\beta,0}(r) \rfloor = \lfloor E_{\beta,b}(r) \quad H_{\beta,b}(r) \rfloor,$$

and

$$G^{J,M}_{E,H,\pm\beta,0}(r',\, r) = G^{J,M}_{E,H,\pm\beta,b}(r',\, r) = \begin{bmatrix} E^{J}_{\pm\beta,b}(r',\, r) & H^{J}_{\pm\beta,b}(r',\, r) \\ E^{M}_{\pm\beta,b}(r',\, r) & H^{M}_{\pm\beta,b}(r',\, r) \end{bmatrix},$$

is the global analytical Bloch periodic EM field and bi periodic EM Green's tensor in unit cell and in the background medium with constant EM parameter, or periodic waveguide medium. By induction, suppose that the EM field $\lfloor E_{\beta,k-1}(r) \quad H_{\beta,k-1}(r) \rfloor$, and the EM Green's tensor $G^{J,M}_{E,H,\pm\beta,k-1}(r',\, r)$ have been calculated in the $(k-1)^{\text{th}}$ step.

(**7.3**) In Ω_k, we solve the EM Green tensor integral equation system By dual operation, the equation system is reduced into a 6×6 matrix equations. By solving the 6×6 equations, We obtain Green tensor field $G^{J,M}_{E,H,\pm\beta,k}(r',\, r)$.

(**7.4**) We improve the Global EM field $\lfloor E_{\beta,k}(r) \quad H_{\beta,k}(r) \rfloor$ by the Local scattering filed

$$\begin{bmatrix} E_{\beta,k}(r) \\ H_{\beta,k}(r) \end{bmatrix} = \begin{bmatrix} E_{-\beta,k-1}(r) \\ H_{-\beta,k-1}(r) \end{bmatrix} - \int_{\Omega_k} G^{J,M}_{E,H,-\beta,k}(r',\, r)\,[D_b - D] \begin{bmatrix} E_{\beta,k-1}(r') \\ H_{\beta,k-1}(r') \end{bmatrix} \mathrm{d}r' \tag{11}$$

$k = 1, 2, \ldots, N$, successively. The $\lfloor E_{\beta,N}(r) \quad H_{\beta,N}(r) \rfloor$ is GL periodic EM field solution of the EM Bloch field equation with crystal moment β in irreducible Brillouin zone. Finally, we obtain the EM dispersion field in the periodic lattice space time domain

$$\begin{bmatrix} E(r) \\ H(r) \end{bmatrix} = \int_{-\infty}^{\infty}\int_{-\infty}^{\infty} \begin{bmatrix} E_{\beta,N}(r) \\ H_{\beta,N}(r) \end{bmatrix} e^{i\beta r}\mathrm{d}\beta e^{-i\omega t}\mathrm{d}\omega. \tag{12}$$

8. THE ADVANTAGES OF THE GL MODELING IN TIME DOMAIN

8.1. GL Method Assembles to Build Inverse Matrix and Does Not Need to Solve Any Big Matrix

The Finite Element Method (FEM) and implicit Finite Difference (FD) method is to build matrix and then to solve matrix, For large scale scientific and engineering problem, the large FEM matrix solving is massive storage and run time cost. In contrast of FEM and FD method, our GL time domain and frequency domain modeling assemble to build inverse matrix and does not need to save big matrix. Therefore, the GL modeling overcome the difficulty of FEM and FD method for solving big matrix. The GL method is more fast than FEM and implicit FD method. The Green's function is inverse operator of the differential equation. Its discretization is more accurate than the inversion of FEM or FD matrix. The GL modeling for EM, elastic, and acoustic is more accurate than FEM and FD method.

8.2. The Artificial Boundary to Truncate Infinite Domain is Unnecessary in the GL Modeling

When the FEM and FD etc numerical method is used to solve PDE in the infinite domain, the artificial boundary and on which the absorption boundary condition are necessary to truncate the infinite domain. From Sommerfeld's radiation condition, the research for constructing the absorption condition on the artificial boundary has been 80 years. There are many papers and books to report the construction of the absorption condition on the artificial boundary. In interntional mathematical congress, there are 45 minute speaker for the absorption boundary condition. However, there is refelection in all absorption condition from the corner of the artificial boundary. The

error refelection degrade the accuracy of the modeling solution, in particular, the error reflections of the absorption condition from the artificial boundary prapagate into the internal domain in inverse iteration that will be a unremoveable noise to damage the inversion. In contrast of all effort for studying absorption condition, the GL method removed the artificial bounday for infinite domain. Because the Sommerfeld's radiation condition in the far field in the infinite domain, we derive the EM, elastic, and acoustic field equation are equivalent to their corresponding integral equation, respectively, the volumical integral equation does not include any boundary condition term, therefore, The GL method based on these integral equation does not need any artificial boundary and absorption condition for the infinite domain. The GL method overcome the FEM and FD's difficulty of the reflction errors from their artificial boundary and absorption condition for the infinite domain.

8.3. The Analytical Method and Numerical Method is Consistently Combining in the GL Method

The Analytical and numerical methods are two main methods for solving the differential equation. They have been developing separately in the history. The analytical method is suitable for the whole space, half space, multiple layered media, spherical, cylindrical and regular geometry domain, but it is not available for solving differential equation in the irregular and complex geometry and inhomogeneous media domain. The FEM and FD etc. numerical method is available for solving differential equation in the irregular and complex geometry and inhomogeneous media, but it is not suitable for the whole space, half space, multiple layered media infinite domain. In the numerical method, the artificial boundary and the absorption condition on it is necessary that produces reflection errors to degrade the accuracy of forward solution and damage inversion. The GL method combines the analytical method and numerical method consistently together. The GL method is either available for whole space, half space, multiple layered media, spherical, cylindrical and regular geometry domain, also is suitable to solve the differential equation in the irregular and complex geometry and inhomogeneous media domain without artificial boundary.

8.4. The GL Method is Natural Parallel Algorithm and Multiple Scale Parallel Algorithm in Periodic Space Time Domain

The GL modeling method is natural parallel algorithm. The GL EM. acoustic, and elastic wave field dispersion modeling are useful to construct global periodic to local periodic, global periodic to local aperiodic, global aperiodic to local periodic multiple scale parallel algorithms.

8.5. The GL Method Overcome the Coordinate Singularity Difficulty in FEM and FD Method

There exist the coordinate singularity in the pole of the differential equation in cylindrical coordinate pole, south pole and north pole of the spherical coordinate system. The cylindrical pole singularity and spherical poles' singularity are difficulties of FEM and FD method. The GL method overcomes the coordinate singularity difficulty.

8.6. The Accurate GL Method Vs. Inaccurate Born Approximation

The Born approximation is sample iteration but it is inaccurate method and only suitable for low frequency and low contrast. The GL method can available for all frequency from low to high and high contrast medium anomalous.

8.7. There is No Complexity for High Order Differential Term in the GL Method, if the Inhomogeneous Medium is Located in the Low Order Term

8.8. GL Method Displays Methodology From Inversion to Forward Modeling

8.9. The Solution of GL Time Domain Converges to Exact Solution and Has Superconvergence

We prove that the solution of GL time domain modeling converges to exact wave field. Provided the middle point and trapezoid integral is used in the integrals in GL method, the convergent rate is $O(h^2)$. If the high accurate 20 nodes curve isoparameter element [19] and Gaussion integral is used in the integrals in GL method, then GL method has super convergent rate $O(h^4)$ [17, 18]. In paper [19], the author use a novel method to construct the 20 nodes curve isoparameter element and develop 3D elastic FEM and its software first in China, also author used the 3D isoparameter FEM software to calculate all dams and underground structures displacement and stress of China. In particular, author Xie and Li discovered superconvergence of the isoparameter element first of the world that the discover has been recognized by Brandts, J. and M. Krizek's paper "History and Future of Superconvergence in Three Dimensional Finite Element Methods" [20] and Michael Krizek' paper "Superconvergence Phenomena on Three Dimenional Meshes" [21]. By using the

20 nodes curve isoparameter element [19] and Gaussion integral, GL method products pointwise superconvergence $O(h^4)$.

9. APPLICATIONS AND SIMULATIONS

The 3D and 2D GL modeling for EM field dispersion in periodic space time domain is useful to simulate EM dispersion in the macro and nanometer materials, optical materials, and dispersion engineering of photonic crystals. In paper [3], we present coupled GL EM and quantum mechanical modeling for studying nanometer material properties. The nanometer material is mixed periodic photonic crystal and other aperiodic structure. The GL modeling to simulate coupled EM dispersion in periodic domain and for EM field in aperiodic domain and obtained very reasonable imaging.

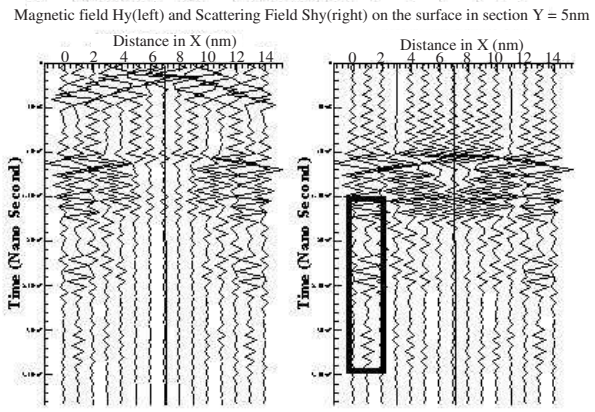

Figure 1: Hy in the transverse section $Y = 5\,\text{nm}$ and on surface, Hy is in left, scattering field SHy is in right. A quanta is shown in rectangle frame.

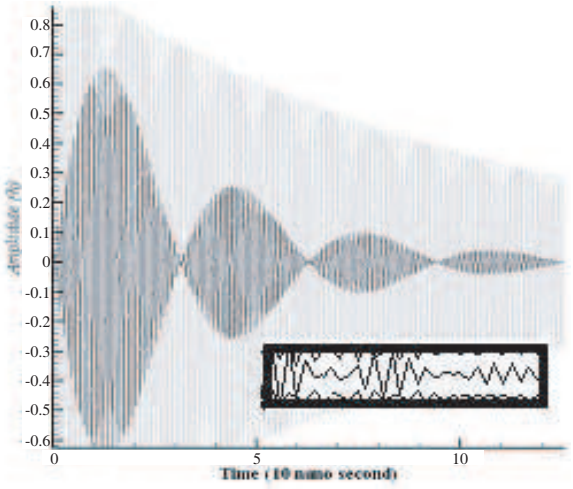

Figure 2: GLEMQUAN quanta in the rear of the scattering magnetic field Hy which is shown in black rectangle frame In Figure 1.

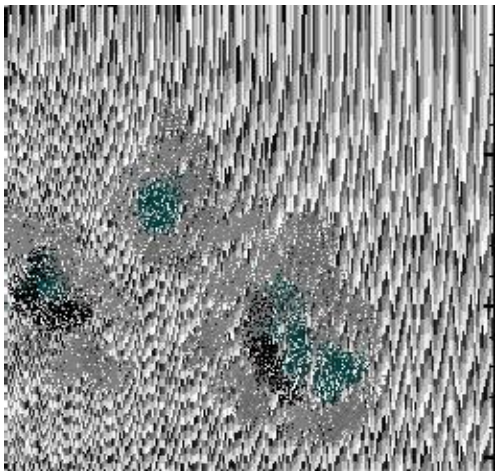

Figure 3: The deformation of the nanometer material crystal due to the quantum fiber strain.

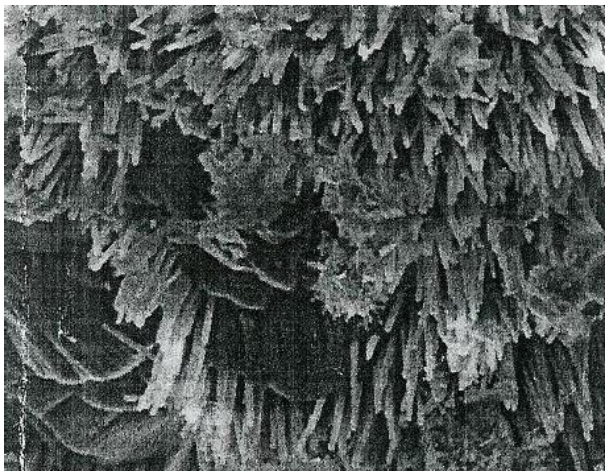

Figure 4: The scan electric microscope SEM image of the deformation of the nanometer material crystal.

The $20\,\text{nm}\times20\,\text{nm}\times20\,\text{nm}$ Bragg crystal optical sensor material is embedded into the metal bulk cheap with $5\,\mu\text{m}\times5\,\mu\text{m}\times5\,\mu\text{m}$. The X ray propagate through the periodic and aperiodic composite material. The optical material is divided 4096 unit cell lattices. The outside gasket metal bulk is divided into 1024 domains. The initial quantum field is ψ_0 which satisfies Schrödinger equation with Hamiltonian H_0. We use the GLEMQUAN EM and Quantum field global aperiodic to local periodic modeling to calculate the EM field and quantum wave field function. The Hy in the transverse section $Y = 5\,\text{nm}$ and on surface of the bulk is shown in Figure 1, Hy is shown in left

graphic, scattering field SHy is shown in right graphic which includes dispersion wave packets. A quanta dispersion wave package is obviously shown in rectangle frame in rear of the scattering wave. The quanta dispersion wave package is an EM-quantum coupled effect which is match to the X ray observation. The GLEMQUAN quanta dispersion wave package is shown in the Figure 2, it is different from the rear part of macro EM field in which the scattering wave vanished to zero from peak. From the GLEMQUAN EM field and quantum wave field, the quantum fiber strain is calculated. The deformation of the nanometer material crystal due to the quantum fiber strain is shown in the Figure 3. The electric microscope image of the deformation of the nanometer material is shown in Figure 4. The similarity between images in Figure 3 and Figure 4 shows that the GLEMQUAN modeling can obtain high resolution image of the nanometer fiber deformation. Figure 5 and Figure 6 show other crystal deformation. The simulations show that the GLEMQUAN modeling is fast and accurate [3].

10. CONCLUSION

Simulations show and validate that the GL EM, acoustic, and elastic aperiodic and periodic space time domain modeling are fast, accurate, stable high resolution and have the advantages over FEM and FDTD method. These advantages are described in the context of the paper. GL time domain modeling for EM, acoustic and elastic wave field with dispersion have wide applications in nanometer materials, optical materials, dispersion engineering of photonic crystals, porous material, nondestructive testing, desctructive mechanics, and geophysical exploration. The GL EM, acoustic, elastic quantum periodic lattice and aperiodic space time domain modeling algorithms and software are developed and patented by authors in GL Geophysical laboratory and all rights are reserved by authors in GLGEO.

REFERENCES

1. Xie, G., F. Xie, L. Xie, and J. Li, "New GL method and its advantages for resolving historical diffculties," *Progress In Electromagnetics Research*, PIER 63, 141–152, 2006.
2. Xie, G., J. Li, L. Xie, F. Xie, and J. Li, "The 3D GL EM-flow-heat-stress coupled modeling," *PIERS Online*, Vol. 3, No. 4, 411–417, 2007.
3. Xie, G., J. Li, F. Xie, and L. Xie, "3D GL EM and quantum mechanical coupled modeling for the nanometer materials," *PIERS Online*, Vol. 3, No. 4, 418–422, 2007.
4. Xie, G., J. Li, L. Xie, and F. Xie, "GL metro carlo EM inversion," *Journal of Electromagnetic Waves and Applications*, Vol. 20, No. 14, 1991–2000, 2006.
5. Li, J., G. Xie, L. Xie, and F. Xie, "A 3D GL EM modeling and inversion for forest exploration and felling," *PIERS Online*, Vol. 3, No. 4, 402–410, 2007.
6. Xie, G. and Y. M. Chen, "A modified pulse spectrum technique for solving inverse problem of two-dimensional elastic wave equation," *Appl. Numer. Math.*, Vol. 1, No. 3, 217–237, 1985.
7. Xie, G. and J. Li, "New parallel SGILD modeling and inversion," *Physics D*, Vol. 133, 477–487, 1999.
8. Xie, G., J. Li, E. Majer, D Zuo, and M. Oristaglio, "3-D electromagnetic modeling and non-linear inversion," *Geophysics*, Vol. 65, No. 3, 804–822, 2000.
9. Xie, G. and J. Li, "New parallel GILD-SOR modeling and inversion for E-O-A strategic simulation," *IMACS Series Book in Computational and Applied Math*, Vol. 5, 123–138, 1999.
10. Xie, G., J. Li, L. Xie, and F. Xie, "GL EM mechanical and acoustic field time domain modeling for materials and exploration with dispersion," to be appear to *PIERS 2008 in Hangzhou*.
11. Xie, G., J. Li, and C.-C. Lin, "New SGILD EM modeling and inversion in geophysics and nano-physics," *Three Dimensional Electromagnetics*, Vol. 2, 193–213, (SCI), 2002.
12. Xie, G., C.-C. Lin, J. Li, "GILD EM modeling in geophysics and nanometer materials using a magnetic field integral equation," *Three Dimensional Elctromagnetics III*, Vol. 3, 11–12, 2003.
13. Pustai, D. M., C. Chen, A. Sharkawy, S. Shi, J. Murakowski, and D. W. Prather, "Dispersion engineering of photonic crystal devices," *Mat. Res. Soc. Symp. Proc.*, Vol. 797, W. 6.8.1–6.8.6, 2004.
14. Song, W., Y. Zhao, Y. Bao, S. Li, Z. Zhang, and T. Xu, "Numerical simulation and analysis on mode property of photonic crystal fiber with high birefringence by fast multipole method," *PIERS Online*, Vol. 3, No. 6, 386–841, 2007.

15. Lin, C.-C., G. Xie, J. Li, and B.-J. Lin, "Deformation analysis for materials using GILD mechanical modeling," *The Chinese Journal of Mechanics-series A*, A special issue dedicated to Prof. T. C. T. Ting in celebration of his seventieth birthday, Invited paper, Vol. 19, No. l, 207–221 (SCI&EI), 2003.
16. Xie, G., C.-C. Lin, and J. Li, "New 3D gild mechanical modeling and inversion," *Mathematica Applicata*, 16 (2), 149–156, 2003.
17. Li, J., G. Xie, and L. Xie, "3D and 2D GL modeling for EM mechanical and heat field with dispersion in mixed aperiodic and periodic space time domain for material sciences and exploration," GL Geophysical Laboratory technological patent report, GL2007-1, 2007.
18. Xie, G., J. Li, and F. Xie, "GL time domain modeling based integral equation for EM acoustic and elastic wave field with dispersion in crystal and porous material," GL Geophysical Laboratory technological patent report, GL2007-2, 2007.
19. Xie, G., "Three dimensional finite element method in the elastic problem," *Mathematical Practice and Knowledge*, Vol. 1, 28–41, Chinese, 1975.
20. Brandts, J. and M. Krizek, "History and future of superconvergence in three dimensional finite element methods," *Mathematical Sciences and Applications*, Vol. 15, 24–35, 2001.
21. Krizek, M., "Superconvergence phenomena on three dimenional meshes," *International Journal of Numerical Analysis and Modeling*, Vol. 2, No. 1, 43–56, 2005.

Multi-temporal Backscattering Behavior of Rice Crop Canopies Based on Dense Medium Model Simulations

J. Y. Koay, **H. T. Ewe**, **and H. T. Chuah**
Multimedia University, Malaysia

Abstract— In recent years, efforts to study the backscattering behavior of rice crop canopies have resulted in the measurement of the multi-temporal backscattering coefficient of rice crops over various incident angles, frequencies and polarizations through the use of space-borne radars and ground-based scatterometers. With the availability of all these data, different scattering models have been developed for rice crop canopies in an attempt to further analyze the results obtained. One such model is based on the radiative transfer equations, and incorporates the Dense Medium Phase and Amplitude Correction Theory (DM-PACT) as well as the amplitude and Fresnel phase corrections to take into account coherent effects and Fresnel field effects of closely spaces scatterers, respectively. Hence, the canopy is modeled as a dense medium. An early variation of the dense medium model for rice crops employs needle-shaped scatterers to simulate the leaves of the rice plants. In this study, the phase matrix of the rice crop canopy is obtained using the scattered field of elliptic disk-shaped scatterers (with the inclusion of the Fresnel field effects) to model the leaves. This model is then used in the simulation of the backscattering coefficient of rice crop canopies at different stages of growth, through which the contribution of the different scatterers in the canopy and the backscattering mechanisms involved are then analyzed. This enables a better understanding of the multi-temporal backscattering behavior of rice crop canopies, particularly that of the sensitivity of the rice crop backscattering coefficient to the different scatterers in the medium and the input parameters of the model.

1. INTRODUCTION

There is currently a growing interest in employing microwave remote sensing technologies for the remote sensing of rice crops. Research in this field has been focused on image classification [1–3] and yield prediction [4] methods in the hope that more reliable and efficient methods of monitoring these crops will be available in the near future. To ensure that satellite images are interpreted correctly, various microwave scattering models have been developed to enable a better understanding of microwave interactions with rice crop canopies. One model employs Monte-carlo simulations [5] based on analytical wave theory to calculate the backscattering coefficients of rice crops. Another rice crop model is developed based on the radiative transfer equations [6], of which the iterative solutions provide valuable insight into the physical interactions involved. As in [6], the microwave scattering model for rice crops in this study is developed based on the second order iterative solutions of the radiative transfer equations, with consideration given to the coherent effects through the Dense Medium Phase and Amplitude Correction Theory (DM-PACT) [7]. The Fresnel field effects [8] of closely spaced scatterers are also included. While the phase matrix of the leaves in [6] is represented by needle-shaped scatterers, elliptic disks [9] are used in the development of the phase matrix in this study for a better geometrical representation of rice leaves, as has been done in [10]. This paper presents more results and further explores the backscattering behavior of rice crop canopies over various frequencies and incident angles obtained based on this model.

2. DEVELOPMENT OF MODEL

Depending on its growth stage, the rice crop canopy in this study is modeled as either a single-layer or multi-layer dense discrete random medium over a slightly rough underlying water surface to account for the effects of wind and surface tension (as opposed to the smooth surface employed in [10]). In the development of the phase matrix of the paddy canopy, elliptic disks are used to model the paddy leaves while cylinders are used to model the stems (also called tillers) and the rice grains. The various model configurations used for the various stages of rice growth is shown in Figure 1.

3. THEORETICAL ANALYSIS

Ground truth parameters from rice fields in Sungai Burung, Selangor, Malaysia are used as input parameters for the theoretical model. Through computer simulations of the backscattering coefficients, detailed theoretical analysis of the backscattering behaviour of rice crop canopies at various

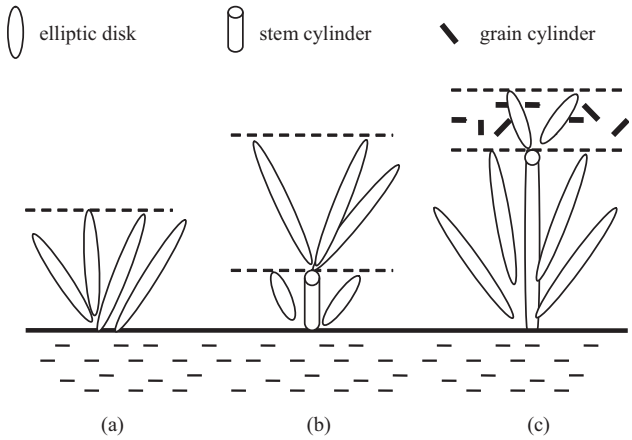

Figure 1: Variations in the model used for the computation of backscattering coefficients of rice fields in the (a) early vegetative stage, (b) late vegetative stage and (c) reproductive stage.

incident angles and frequencies can be studied. Figure 2(a) shows the plots of the HH backscattering coefficients for rice crop canopies at 21 days old over various incident angles. The frequency chosen for the simulations was at 5.3 GHz. Since the canopy is relatively sparse at this stage of growth, surface backscattering dominates at the lower incident angles, but then drops off quickly so that surface-volume backscattering becomes the dominant component at incident angles above 25°. In Figure 2(b), when the backscattering coefficients are calculated for canopies at 45 days old, single volume backscattering is the dominant contributor to the total backscattering coefficient whereas surface backscattering and surface-volume backscattering have become negligible. This is due to the increase in the density of the rice crop canopy, canopy height and the leaf sizes. To further analyze the backscattering trends, the plot of the single volume backscattering component is shown in Figure 3 together with the contribution of each class of scatterers to the total volume backscattering for HH polarization. It can be seen clearly that the dominant contributor to single volume backscatter are the stems in the canopy. When the rice crops are at about 69 days old, the backscattering trends are similar to that of rice crops at 45 days old, hence will not be shown here.

By letting the incident angle be 40°, the backscattering behaviour of rice crop canopies is analyzed over various frequencies, the results of which are shown in Figure 4. It can be observed that the total HH backscattering coefficient increases with the increase in frequency of the microwaves. This is true also for all the backscattering components involved. Generally, at low frequencies, the penetration level of the microwaves are very high, so that most of the energy is transmitted

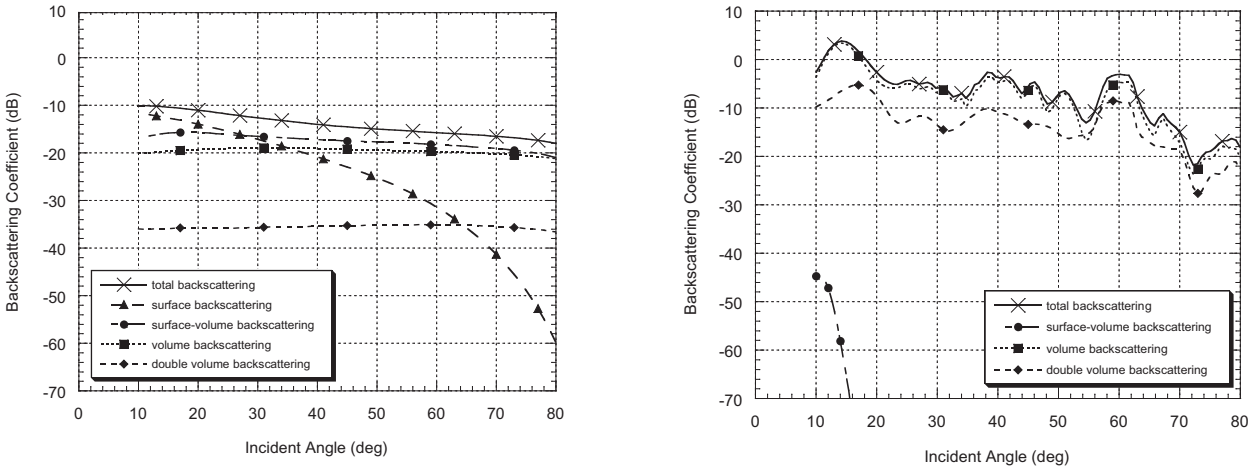

Figure 2: Plot showing the scattering mechanisms contributing to the total HH backscattering coefficients at a frequency of 5.3 GHz for a rice crop canopy at (a) 21 days of age (b) 45 days of age over various incident angles.

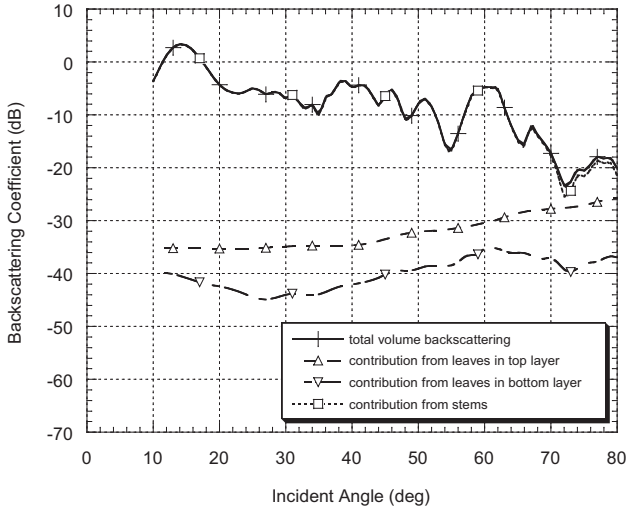

Figure 3: Plot showing the contribution of the different types of scatterers to the total HH volume backscattering coefficients for a rice crop canopy 45 days of age at a frequency of 5.3 GHz over various incident angles.

into the bottom surface instead of being scattered backwards. As the frequency increases, more and more of the energy is scattered backwards. This trend is seen clearly in Figure 4(a) for rice crop canopies at 21 days old. Surface-volume backscattering dominates due to the relatively sparse nature of the rice crop canopy at this stage of growth. As the rice crop canopy grows denser at age 45, a change is observed in the frequency trends. As shown in Figure 4(b), the surface and surface-volume backscattering components are no longer dominant over the range of frequencies. Volume backscattering has taken over as the dominant component. As the frequency increases, attenuation in the canopy increases as well to reduce the penetration level of the microwaves. Therefore, it is observed that while surface-volume backscattering is still significant at lower frequencies, it becomes negligible at larger frequencies when the microwaves are no longer able to reach the bottom surface.

The frequency trends of the rice crop canopy at 69 days old is generally similar to that at 45 days old, hence is not shown. However, further analysis of the impact of the different classes of scatterers to the total HH volume backscattering coefficient of the rice crops at 69 days old (with the addition of grains in the top layer of the medium) are shown in Figure 5. Backscattering from the stems is the main contributor to the total volume backscattering coefficient, though contribution from the leaves become more significant at larger frequencies.

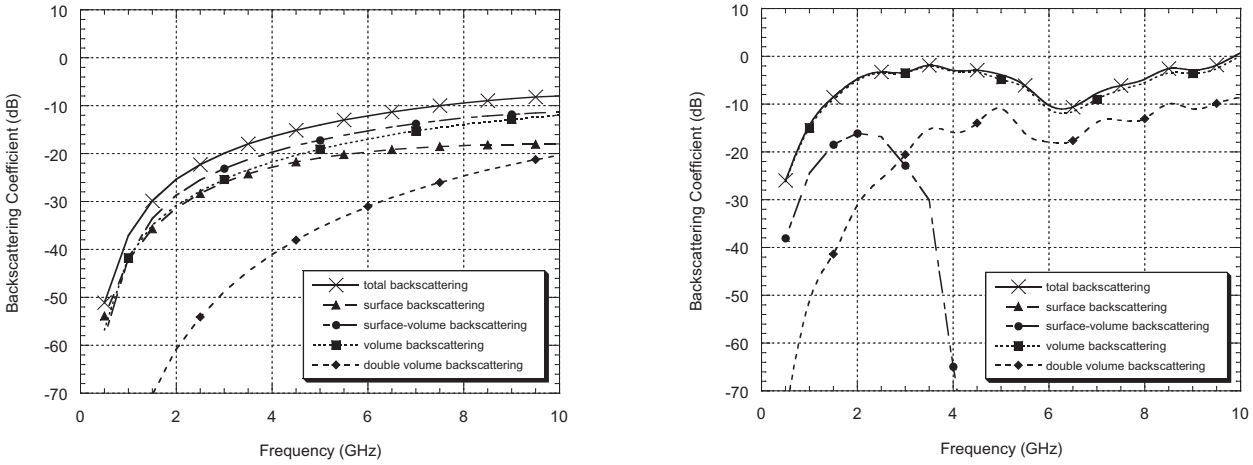

Figure 4: Plot showing the scattering mechanisms contributing to the total HH backscattering coefficients at an incident angle of 40° for a rice crop canopy at (a) 21 days of age (b) 45 days of age over various frequencies.

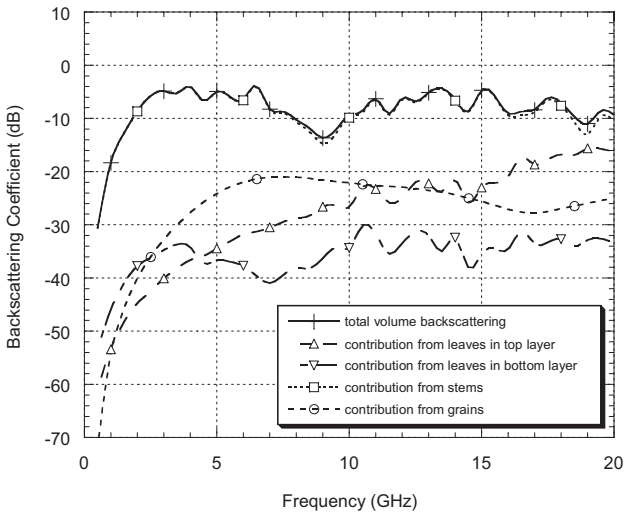

Figure 5: Plot showing the contribution of the different types of scatterers to the total HH volume backscattering coefficients for a rice crop canopy 45 days of age at an incident angle of 40° over various frequencies.

4. CONCLUSIONS

In this study, a dense medium model, developed based on the iterative solutions of the radiative transfer equations and using elliptic disks to represent the leaves in the canopy, is used to simulate the backscattering coefficient of rice crop canopies over various stages of growth. Analyses of the multi-temporal, angular and multi-spectral backscattering coefficients yield the following conclusions:

- When the rice crops are at a young age and the canopy is sparse, the surface and surface volume backscattering components are dominant. When the rice crops grow older and the canopy becomes denser, the volume backscattering components dominate.
- Except at very high frequencies, the dominant scatterer class in the calculation of surface-volume, single volume and double volume backscattering are the stems (for the latter stages of growth). Therefore, based on this model, the backscattering of the stems plays a very important role in this scattering model for rice crops.
- As frequency increases, the penetration level of the microwaves into the rice crop canopy decreases.

REFERENCES

1. Le Toan, T., F. Ribbes, L. F. Wang, N. Floury, K. H. Ding, J. A. Kong, M. Fujita, and T. Kurosu, "Rice crop mapping and monitoring using ERS-1 data based on experiment and modeling results," *IEEE Transactions on Geoscience and Remote Sensing*, Vol. 35, 41–56, 1997.
2. Ribbes, F. and T. Le Toan, "Rice field mapping and monitoring with RADARSAT data," *International Journal of Remote Sensing*, Vol. 20, No. 4, 745–765, 1999.
3. Tan, C. P., J. Y. Koay, K. S. Lim, H. T. Ewe, and H. T. Chuah, "Classification of multi-temporal SAR images for rice crops using combined entropy decomposition and support vector machine technique," *Progress in Electromagnetics Research*, PIER 71, 19–39, 2007.
4. Saiful Bahari, A. B., "Monitoring of wetland paddy fields using microwave remote sensing data," MEngSc Thesis, Multimedia University, 1999.
5. Wang, L., J. A. Kong, K. H. Ding, T. Le Toan, F. Ribbes-Baillarin, and N. Floury, "Electromagnetic scattering model for rice canopy based on Monte Carlo simulation," *Progress in Electromagnetics Research*, PIER 52, 153–171, 2005.
6. Koay, J. Y., C. P. Tan, K. S. Lim, Saiful Bahari, H. T. Ewe, H. T. Chuah, and J. A. Kong, "Paddy fields as electrically dense media: Theoretical modeling and measurement comparisons," *IEEE Transactions on Geoscience and Remote Sensing*, Vol. 45, No. 9, 2837–2849, 2007.

7. Chuah, H. T., S. Tjuatja, A. K. Fung, and J. W. Bredow, "A phase matrix for a dense discrete random medium: Evaluation of volume scattering coefficient," *IEEE Transactions on Geoscience and Remote Sensing*, Vol. 34, No. 5, 1137–1143, 1996.
8. Ewe, H. T. and H. T. Chuah, "A study of fresnel scattered field for non-spherical discrete scatterers," *Progress In Electromagnetics Research*, PIER 25, 189–222, 2000.
9. Koay, J. Y., H. T. Ewe, and H. T. Chuah, "A study of fresnel scattered fields for ellipsoidal and elliptic disk-shaped scatterers," *IEEE Transactions on Geoscience and Remote Sensing* (accepted for publication).
10. Koay, J. Y., C. P. Tan, H. T. Ewe, and H. T. Chuah, "Theoretical modeling and analysis of temporal microwave backscatter from paddy fields," *Proceedings of the 4th National Microwave Remote Sensing Seminar*, MACRES, Kuala Lumpur, 28 November 2006.

A Study of Optimized Observation Configuration in Determining Sea Ice Thickness Using Multilayer Backscattering Model in Antarctica

M. D. Albert[1], **H. T. Ewe**[2], **and H. T. Chuah**[1]

[1]Faculty of Engineering, Multimedia University, Malaysia
[2]Faculty of Information Technology, Multimedia University, Malaysia

Abstract— Global warming has been a topic highly interested by the research community. Researchers have been relating global warming to the condition in Antarctica and the increase in global temperature may speed up the melting of ice in the southern continent. This vast volume of ice has significant effects on climate, ocean salinity, current as well as its biological ecosystem. It is our interest to monitor physical changes in Antarctica, especially the sea ice condition, for global warming study using remote sensing technique.

Since Antarctica is a huge continent, monitoring the physical changes could be challenging. Therefore, remotely sensing the continent using satellite would be a perfect choice but the retrieval of physical parameters of sea ice from the satellite images needs a thorough understanding of interaction between microwave and sea ice.

In this paper, a multilayer model based on radiative transfer theory is developed to represent sea ice terrain in Antarctica. Unlike some single layer models in the literature, the multilayer model can represent the snow and sea ice layers more accurately. In this model, the snow and sea ice layers are considered electrically dense and therefore the Dense Medium Phase and Amplitude Correction Theory (DMPACT) is incorporated to consider the close spacing effect among the scatterers. The air-snow interface, snow-sea ice interface and sea ice-ocean interface are modeled using the Integral Equation Method (IEM). In order to better understand the interaction between microwave and snow and sea ice media, it is important to choose good observation configurations, such as frequency, incident angle and polarization of the wave. In this study, the optimization of observation configuration will be carried out and how various scattering mechanisms and also the physical parameters of sea ice and snow media can affect the backscattering coefficient with different observation configuration will be presented. This serves as practical guideline for future ground truth measurement in Antarctica and satellite monitoring in Antarctica.

1. INTRODUCTION

Remote sensing is the best option in monitoring and estimating sea ice thickness in Antarctica. In order to better estimate the sea ice thickness, proper observation configuration is needed. In this paper a multilayer model based on Radiative Transfer theory is developed to represent sea ice terrain accurately. The snow and sea ice layers are considered electrically dense and therefore Dense Medium Phase and Amplitude Correction Theory (DMPACT) is incorporated [1, 2]. This is to account the close spacing effect among the scatterers. The air-snow, snow-sea ice and sea ice-ocean interfaces are modeled using the Integral Equation Method (IEM) [3].

In this paper, simulations are done using the multilayer model and from the results, optimized observation configuration in determining the sea ice thickness is suggested. The proper configuration that can be used for sea ice thickness estimation for first year sea ice and multiyear sea ice also included. The new suggested optimized observation configuration in determining sea ice thickness would serve as a practical guideline for future ground truth measurement and satellite monitoring in Antarctica.

2. MODEL CONFIGURATION AND FORMULATION

The sea ice is modeled in three layers. Figure 1 shows cross section of sea ice layers. Snow layer is modeled as a layer with ice particles (as scatterers) embedded inside air (host medium). Meanwhile, sea ice is modeled as a layer with bubbles or brine inclusions (as scatterers) embedded inside ice medium (host medium). In first year sea ice it is safe for us to assume the majority of the scatterers are brine. On the other hand, multi-year sea ice scatterers are combination of bubbles and brine inclusions [4].

In this paper, using radiative transfer equation [5], propagation and scattering of microwave specific intensity in a medium can be written in the form of Equation 1 where, $\bar{\mathbf{I}}$, $\overline{\overline{\mathbf{K}}}_{\mathrm{e}}$ and $\overline{\overline{\mathbf{P}}}$ are

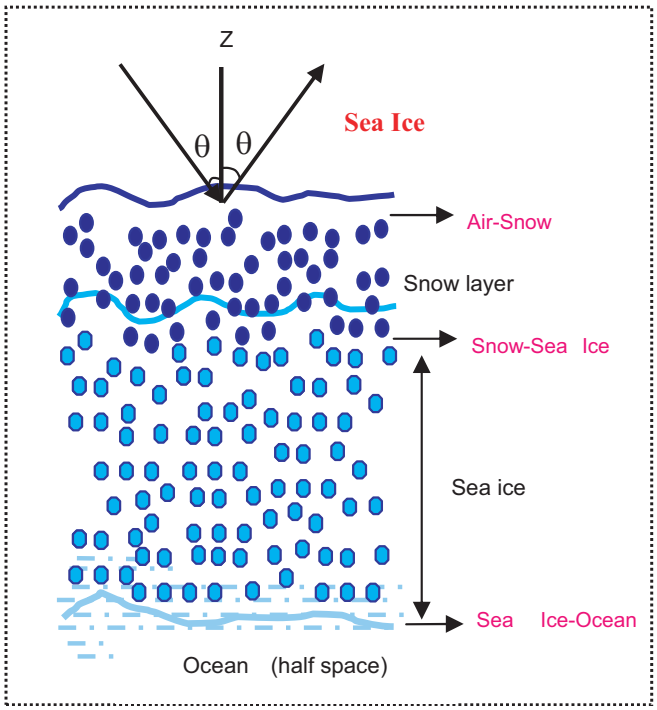

Figure 1.

the Stokes vector, extinction matrix and phase matrix of the medium, respectively. Meanwhile $\mathbf{d\Omega}$ and z are the solid angle and vertical direction respectively. The scattering and absorption losses of the Stokes vector along the propagation direction are taken into account by extinction matrix.

$$\cos\theta \frac{\mathbf{d\bar{I}}}{dz} = -\overline{\overline{\mathbf{K}}}_{\mathrm{e}}\bar{\mathbf{I}} + \int \overline{\overline{\mathbf{P}}}\bar{\mathbf{I}}\mathbf{d\Omega} \tag{1}$$

Equation (1) is firstly converted from differential radiative transfer equation to integral equation. Then the equation is solved iteratively by including boundary conditions. The solution consists of coherent and incoherent components including surface scattering, volume scattering and surface-volume scattering for different polarization. Detailed solution can be found in [6] and [7].

In general, volume scattering and rough surface scattering affects radar backscattering coefficient. Volume scattering happens due to inhomogeneities in the medium. Rough surface scattering happens due to difference in dielectric constant at the boundaries of a medium.

The phase matrix $\overline{\overline{\mathbf{P}}}$ mentioned earlier in Equation (1) is associated with the first two Stokes' parameters of the scatterers and given in Equation (2), where $\langle|\psi|^2\rangle_{\mathrm{n}}$ is the Dense Medium Phase Correction Factor [2] and $\overline{\overline{\mathbf{S}}}$ is the Stokes' matrix for Mie scatterers with close spacing amplitude correction [8]. For an electrically dense medium, such as snow, $\langle|\psi|^2\rangle_{\mathrm{n}}$ is the correction factor that needs to be incorporated into the phase matrix to take into account the coherent effect of the scattering of the closely spaced scatterers. The details of the formulation can be found in [2].

$$\overline{\overline{\mathbf{P}}}(\theta, \phi; \theta', \phi') = \langle|\psi|^2\rangle_{\mathrm{n}} \cdot \overline{\overline{\mathbf{S}}} = \begin{bmatrix} \mathbf{P}_{\mathrm{vv}} & \mathbf{P}_{\mathrm{vh}} \\ \mathbf{P}_{\mathrm{hv}} & \mathbf{P}_{\mathrm{hh}} \end{bmatrix} \tag{2}$$

Rough surfaces at the interfaces, air-snow interface, snow-sea ice interface, sea ice-ocean interface are modeled using IEM (Integral Equation Method). The terms included in the multi-layer model for backscattering coefficient computation are shown in Figure 2.

3. RESULTS AND DISCUSSIONS

The simulations are done for different incident angles and for frequencies of 0.1, 1 and 10 GHz. The thickness of the snow is set to 10 cm and the sea ice thicknesses are set to 1, 5 and 10 meters, respectively. These sea ice thickness are chosen as usually first year sea ice is 1 meter thick,

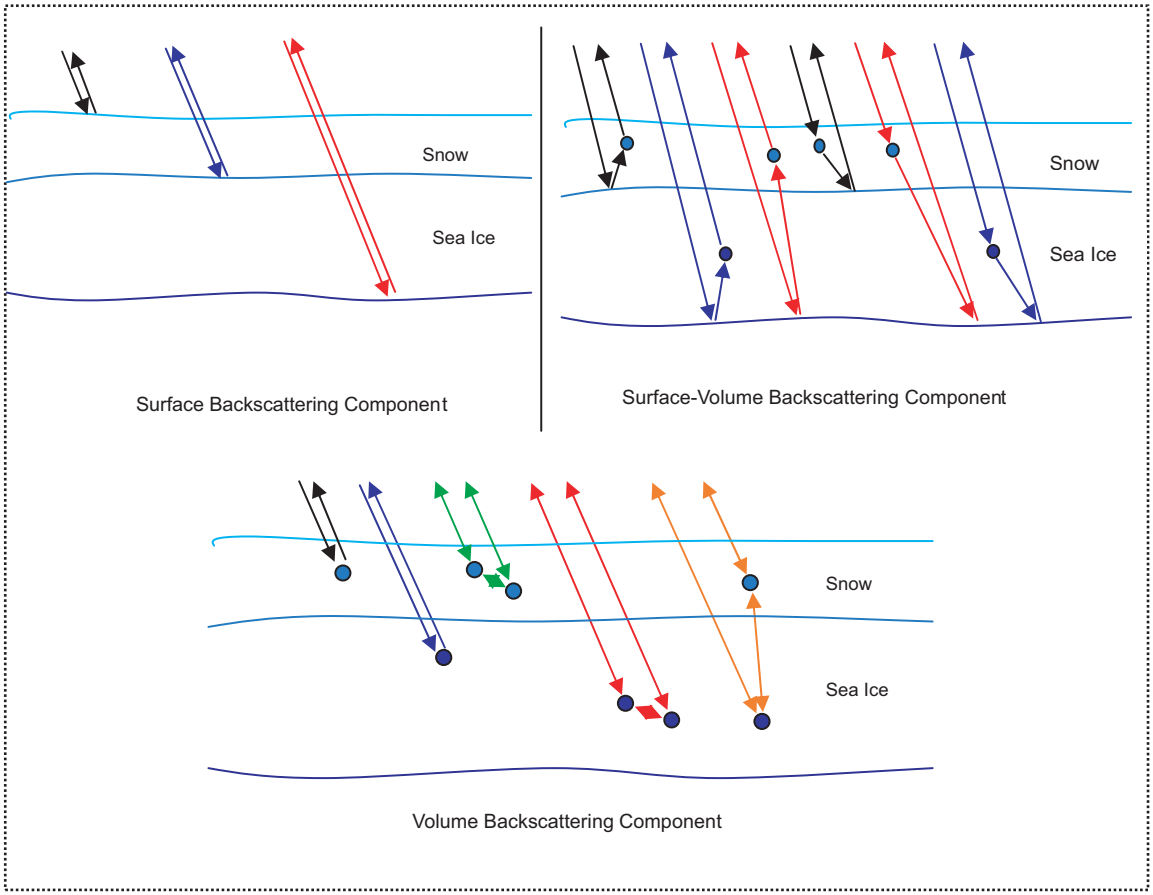

Figure 2.

Table 1: Measured and calculated parameters used in the multi-layer model (* denotes estimated).

	Layer 1 (Snow)		**Layer 2 (Sea Ice)**	
Layer Thickness (m)	0.1		Shown in graph	
Volume Fraction (%)	32%		2%	
Scatterer Radius (mm)	1.1 mm*		0.56 mm*	
Effective relative permittivity of top layer	1.00	0.00	Effective relative permittivity of layer 1	
Scatterer relative permittivity	1.61	8.42E-05	1.00 40.08	0.00 (Bubble) 42.57 (Brine)
Background relative permittivity	1.00	0.00	3.16	0.06
Effective relative permittivity of bottom layer	Effective relative permittivity of layer 2		59.66	44.15
Top Surface RMS height and correlation length (cm)	0.23E-02	5.50E-02	2.80E-04	2.10E-02
Bottom Surface RMS height and correlation length (cm)	2.80E-04	2.10E-02	2.80E-03*	2.10E-01*

multiyear sea ice is several meters thick and sea ice in general are less than 10 meters in thickness. Table 1 shows the parameters that are used in the model for simulation.

Figures 3 and 4 show the co-polarized wave with the frequency of 0.1 GHz. The trend for the VV and HH polarized are similar. The surface backscattering is seen to be dominating the total backscattering for 0.1 GHz. Meanwhile, the volume and surface-volume components are very small.

The penetration of the wave of 0.1 GHz into the sea ice is high. The amount of backscattering coefficient is different for different thicknesses of sea ice. This indicates that the wave penetrates the sea ice up to the sea ice-ocean interface. The difference in relative permittivity between sea ice and ocean is large, and therefore the amount of wave backscattered in this interface is high. As the thickness of the sea ice increases the wave has to travel further inside the sea ice medium to reach this interface, thus the backscattering is lower for sea ice with large thickness. The backscattering coefficient (VV polarized) for all sea ice thicknesses seem to be constant from the steep incident angle up to almost 50 degrees. This indicates that steeper angles are good to be used to reveal the thickness information of the sea ice.

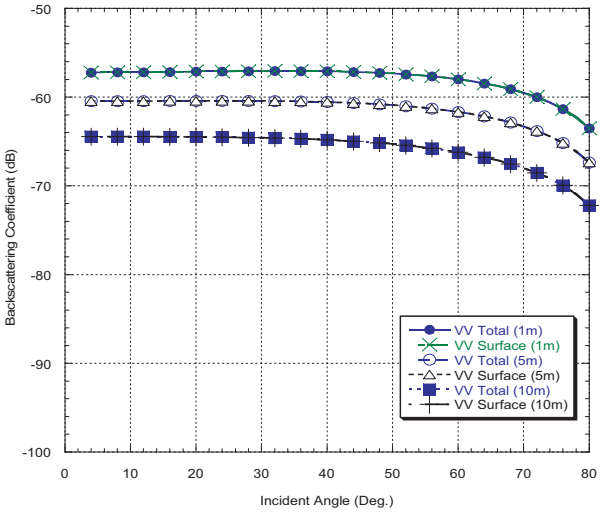

Figure 3: Backscattering coefficient against incident angle for VV polarization at 0.1 GHz.

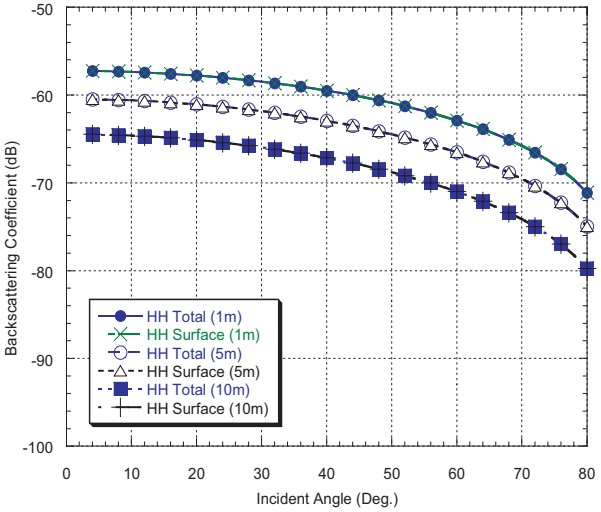

Figure 4: Backscattering coefficient against incident angle for HH polarization at 0.1 GHz.

Figures 5 and 6 show the co-polarized wave with the frequency of 1 GHz. For both VV and HH polarized wave, the highest backscattering coefficient comes from the sea ice with the thickness of 1 meter. This is because, at this thickness, the wave of 1GHz could still penetrate up to the bottom layer of sea ice and large amount of wave is backscattered at this interface. Meanwhile, for the thicknesses of 5 and 10 meters, the backscattering coefficients are the same. The changes in the thickness does not influence the change in backscattering coefficient and this indicates that sea ice-ocean interface backscattering is not the dominating component. At this frequency it can be seen that, to determine the different thickness of sea ice, especially the thickness which is bigger than 5 meters is difficult. The volume backscattering also can be seen as higher compared to volume

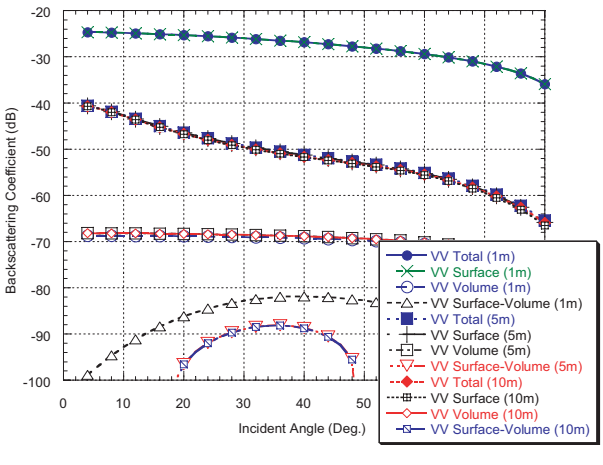

Figure 5: Backscattering coefficient against incident angle for VV polarization at 1 GHz.

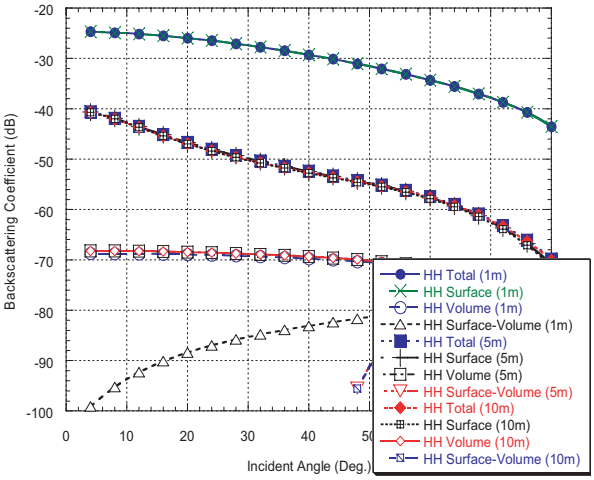

Figure 6: Backscattering coefficient against incident angle for HH polarization at 1 GHz.

backscattering for the frequency of 0.1 GHz. This is because as the frequency increases (1 GHz) the wavelength of the wave is small and interacts with the scatteres in the media.

Figures 7 and 8 show the co-polarized wave with frequency of 10 GHz. The surface backscattering component is dominant at the steep angles. At angles beyond 8 degrees, the volume backscattering component is dominant. It can be seen that the volume backscattering is almost constant for wide range of incident angles and for all the thicknesses of sea ice. This actually indicates that the penetration of the wave at this frequency is very limited. At this frequency, the wave interacts more with the scatterers in the snow. As a result, even the sea ice thickness change, the backscattering coefficient does not reflect the change in its value.

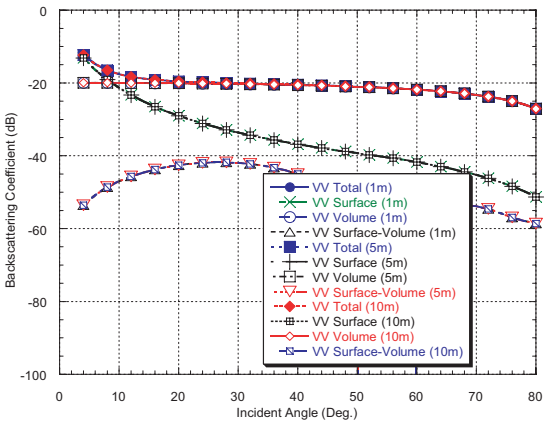

Figure 7: Backscattering coefficient against incident angle for VV polarization at 10 GHz.

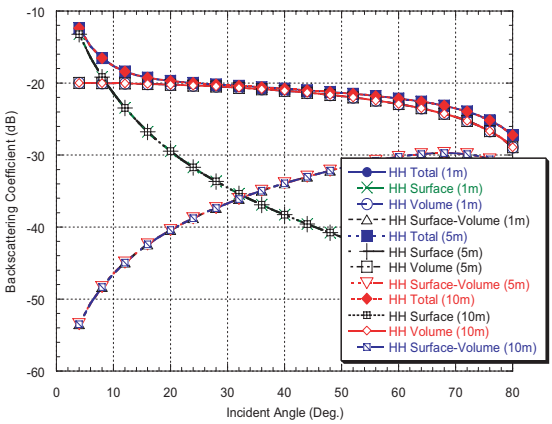

Figure 8: Backscattering coefficient against incident angle for HH polarization at 10 GHz.

Figure 9 shows the cross polarized wave at 10 GHz frequency. The contribution of cross polarized backscattering coefficient is frequently dominated by volume scattering. Volume scattering on the other hand, is important at high frequency, as the wave interacts with the scatterers (smaller wavelength). For the frequencies of 0.1 and 1 GHz, the volume contribution is small and therefore the total backscattering of the cross polarization is low as well (not shown in graph). Figure 9 shows that for different thicknesses of sea ice the total backscattering coefficient remains the same. This indicates again that the backscattering is dominated by the volume component from the snow layer.

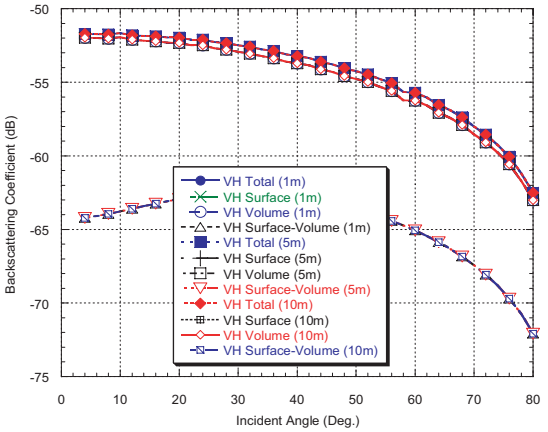

Figure 9: Backscattering coefficient against incident angle for VH polarization at 1 GHz.

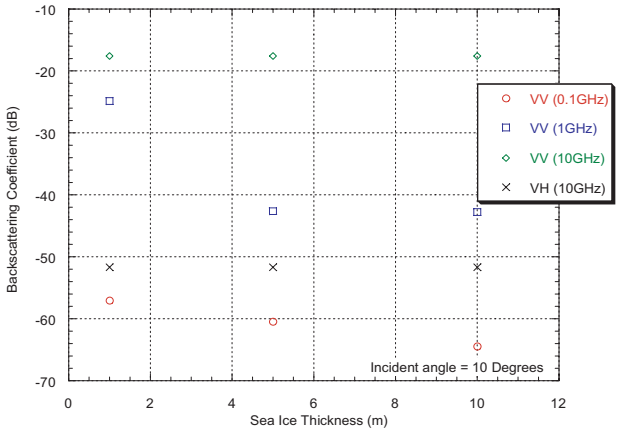

Figure 10: Backscattering coefficient against sea ice thickness for VV and VH polarization.

Figure 10 shows the backscattering coefficient against the sea ice thickness for VV and VH (only for the 10 GHz, as the other frequencies backscattering coefficient are low) polarization. It can be seen from the plot that the backscattering coefficient is sensitive to the sea ice thickness variation for the co-polarized wave at 0.1 GHz. Meanwhile for the cross-polarization, the backscattering coefficient seem constant for the range of sea ice thickness.

4. FURTHER DISCUSSION

Our ground truth measurement in Ross Island reveals that generally first year sea ice is less than 1.5 meter with very less snow accumulation. Meanwhile multiyear sea ice extends up to 4.5 meters.

The first year sea ice thickness estimation 1 GHz frequency is a good option. The co-polarization configuration also preferred as the backscattering coefficient is inversely proportional to the thickness of sea ice. The majority of the wave is backscattered from the sea ice-ocean interface for this type of sea ice. For estimation of thicker sea ice such as multiyear sea ice, low frequency (0.1 GHz) and co-polarization wave is a good option. This is because low frequency will have better penetration ability and reveals the thickness information from the thicker sea ice better.

The snow thickness estimation is also possible using proper observation configuration. Simulations show that high frequency (10 GHz) wave is best used for this purpose. Majority of the wave at this frequency is backscattered from the volume scattering inside the snow medium. The cross-polarization wave is preferred as volume scattering is clearly reflected in cross-polarization. Backscattering coefficient for this case is proportional to the snow thickness and this enables us to estimate the snow thickness.

5. CONCLUSIONS

As a summary it can be said that in low frequency (0.1 GHz), the dominating scattering component is surface scattering. At this frequency co-polarized wave is important and can be used for thickness retrieval. Meanwhile for high frequency (10 GHz) volume backscattering dominates and cross-polarization is the highest for this case. At high frequency, sea ice thickness estimation is difficult as the penetration of the wave is limited. As in for incident angle, steeper angles are preferred as the backscattering coefficient at these angles is large.

REFERENCES

1. Chuah, H. T., S. Tjuatja, A. K. Fung, and J. W. Bredow, "A phase matrix for a dense discrete random medium: Evaluation of volume scattering coefficient," *IEEE Transactions on Geoscience and Remote Sensing*, Vol. 34, No. 5, 1137–1143, 1996.
2. Chuah, H. T., S. Tjuatja, A. K. Fung, and J. W. Bredow, "The volume scattering coefficient of a dense discrete random medium," *IEEE Transaction of Geoscience Remote Sensing*, Vol. 34, No. 4, 1137–1143, 1996.
3. Fung, A. K., Z. Li, and K. S. Chen, "Backscattering from a randomly rough dielectric surface," *IEEE Transactions on Geoscience and Remote Sensing*, Vol. 30, 356–369, 1992.
4. National Snow and Ice Data center — All about Sea Ice: http://nsidc.org/seaice/characteristics/multiyear.html.
5. Chandrasekhar, S., *Radiative Transfer*, Dover, New York, 1960.
6. Ulaby, F. T., R. K. Moore, and A. K. Fung, *Microwave Remote Sensing, Active and Passive*, Vol. 3, Artech House Inc., 1986.
7. Fung, A. K., *Microwave Scattering and Emission Models and their Applications*, Artech House, Boston, 1994.
8. Fung, A. K. and H. J. Eom, "A study of backscattering and emission from closely packed inhomogeneous media," *IEEE Transactions on Geoscience and Remote Sensing*, Vol. 30, No. 4, 761–767, 1985.

Design and Optimization of Microstrip Interdigital Bandpass Filters with Impedance Matching

Homayoon Oraizi, **Nima Azadi-Tinat**, **and Shahrokh Saeedi**

Iran University of Science and Technology, Narmak, Tehran 16846-13114, Iran

Abstract— A least square based method is developed for the design and optimization of microstrip interdigital bandpass filters. The N coupled transmission line theory is employed to take into account the couplings among adjacent and nonadjacent conducting strips. The algorithm also incorporates the load and source impedance matching. The minimization of error function determines the length, width and spacing of strips. The performance of the optimized filter design perfectly agrees with the microwave simulation softwares.

1. INTRODUCTION

Interdigital filters were fabricated by inserting metallic round rods in rectangular cavities [1, 2], and were fabricated to obtain better than 10 percent bandwidth [3, 4]. Since that time, different types of interdigital filters have been devised and used in microwave circuits. Microstrip interdigital filters have also been developed, but their design procedures have usually ignored the significant nonadjacent resonant strip couplings. As reference [5] indicated that the coupling among consecutive strips on nonhomogeneous microstrip structures decreases gradually rather than abruptly, the nonadjacent strip couplings need to be considered in the design. Furthermore, the N different phase velocities on the N coupled strips need to be included in the design procedure.

Accordingly, in this paper a numerical procedure based on the method of least squares is proposed for the design of the interdigital bandpass filters, which utilizes the theory of N coupled transmission lines. The adjacent and nonadjacent couplings among strip lines, their distinct phase velocities, and dispersion relations are readily incorporated in the design method. Furthermore, impedance matching of load and source impedances over a frequency bandwidth is also incorporated into the design algorithm. In this paper two interdigital filter configurations with coupled feeds for narrow and wide band applications are considered as illustrations for the optimum design algorithm. The same general development has been applied for the optimum design of microstrip combline filters [6–8].

2. NUMERICAL PROCEDURE

Consider the general circuit configuration of the narrow and wide band microstrip interdigital bandpass filters, as shown in Fig. 1 and Fig. 2, respectively.

The common length of strips are L, the width of the ith strip is w_i, the gap spacings between adjacent strips is s_i, the source admittance is Y_S and the load admittance is Y_1, as shown in Figs. 1 and 2.

The transmission line equations of the N coupled lines are [9]:

$$\begin{aligned} \frac{d}{dz}[V] &= -(j\omega[L]+[R])[I] \\ \frac{d}{dz}[I] &= -(j\omega[C]+[G])[V] \end{aligned} \tag{1}$$

where $[C]$, $[L]$, $[R]$ and $[G]$ are the capacitance, inductance, resistance and conductance matrices, respectively [10–12]. The dispersion effects may be incorporated into the models, by considering C, L, R and G to be functions of frequency [13]. Now equations may be combined to obtain [14, 15]

$$(j\omega_k[L]+[R])(j\omega_k[C]+[G])-\gamma^2[U] = 0 \tag{2}$$

$$(j\omega_k[L]+[R])(j\omega_k[C]+[G])[M_v]_{i,k} = \gamma_{i,k}^2[M_v]_{i,k} \tag{3}$$

where $[M_v]$ and $[\gamma]$ are the matrix of eigenvectors and the vector of eigenvalues of $(j\omega[L]+[R])(j\omega[C]+[G])$. We may then calculate the N propagation constants due to the N conducting strips in the nonhomogeneous medium like microstrips. Consequently, we may determine the

voltages and currents on the N strips as functions of z

$$[V_i]_k = \left[M_{v_{ij}}\right]_k \left[a_j e^{-\gamma_{j,k}z} + a'_j e^{\gamma_{j,k}z}\right] \quad (4)$$

$$[I_i]_k = \left([Y_a]_k \cdot \left[M_{v_{ij}}\right]_k\right) \left[a_j e^{-\gamma_{j,k}z} - a'_j e^{\gamma_{j,k}z}\right] \quad (5)$$

where $[a_j]$ and $[a'_j]$ are the amplitudes of forward and backward traveling waves on the lines, k is the subscript indicating the frequency in the band, and $[Y_a]$ is the characteristic admittance of the lines corresponding to the propagation constants. Here Y_{ij} as the entry of $[Y_a]$ is the characteristic admittance of the ith line for the jth propagation constant.

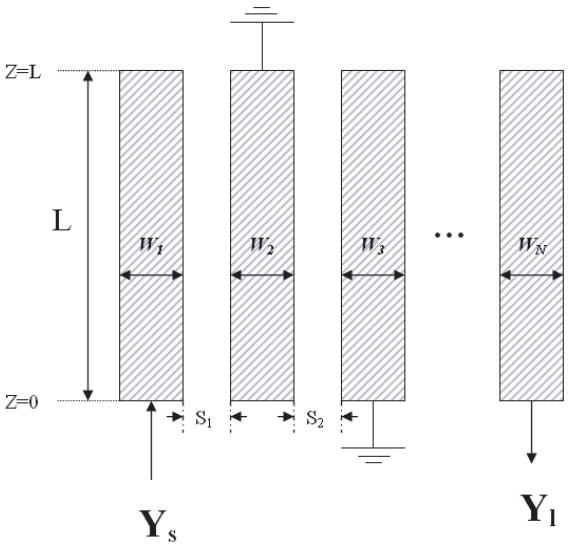

Figure 1: Circuit model of the wide band microstrip interdigital filter.

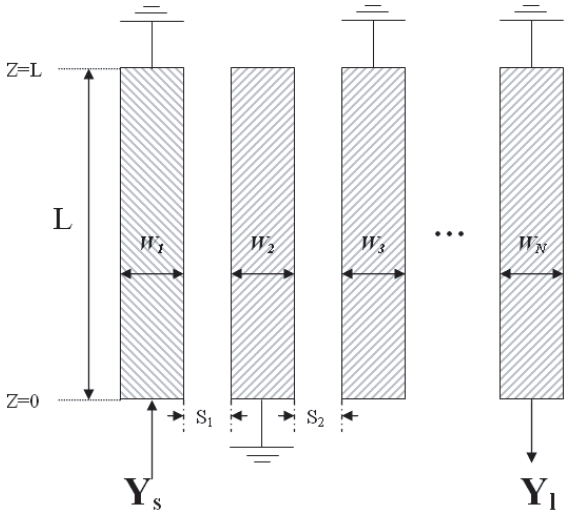

Figure 2: Circuit model of the narrow band microstrip interdigital filter.

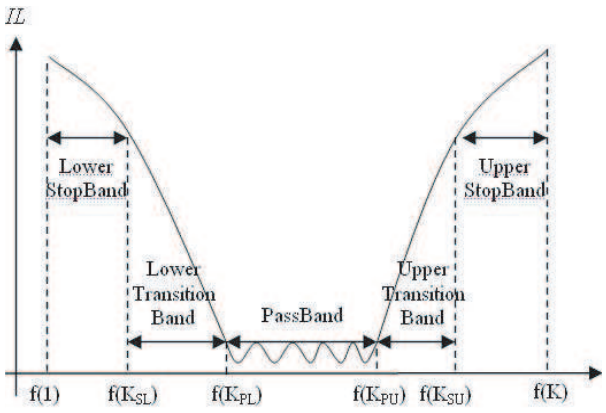

Figure 3: Frequency response of a bandpass filter showing stop.

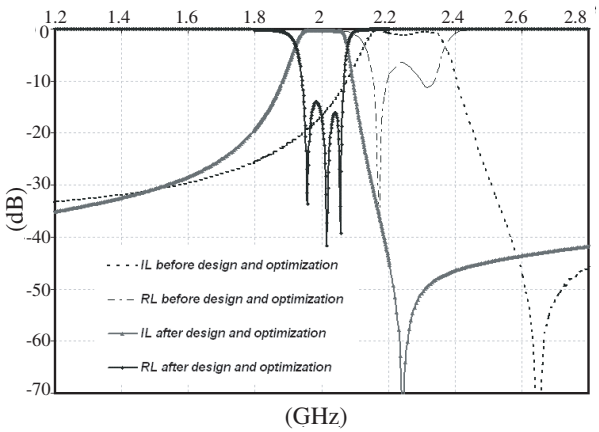

Figure 4: Frequency response of a narrowband interdigital filter before and after optimization.

Now the voltages and currents of the two terminals of the strips (at $z = 0$ and $z = L$) may be obtained from Eqs. (4) and (5), in terms of the unknown amplitudes a_j and a'_j. By eliminating these amplitudes among the equations, we may obtain the terminal currents of strips as a function of their voltages. Then the boundary conditions at the strip terminals are invoked. They are the short circuits to ground and open circuits at the end of strips. However, the open end of lines may be modeled as a capacitor and the shorting vias may be modeled as an inductor [16]. Then, inclusion of the boundary conditions at the strip terminals may lead to the admittance matrix of

the input/output two port network relating the source and load terminals.

$$\begin{bmatrix} I_1 \\ I_s \end{bmatrix} = \begin{bmatrix} Y_{11} & Y_{12} \\ Y_{21} & Y_{22} \end{bmatrix} \begin{bmatrix} V_1 \\ V_s \end{bmatrix} \tag{6}$$

where I_1 and I_s are the load and source currents and V_1 and V_s are the load and source voltages, respectively. We may then obtain the scattering matrix from the admittance matrix. The scattering parameter s_{21} as the transfer function is

$$s_{21} = -\frac{2Y_sY_{21}}{(Y_s + Y_{11})(Y_1 + Y_{22}) - Y_{12}Y_{21}} \tag{7}$$

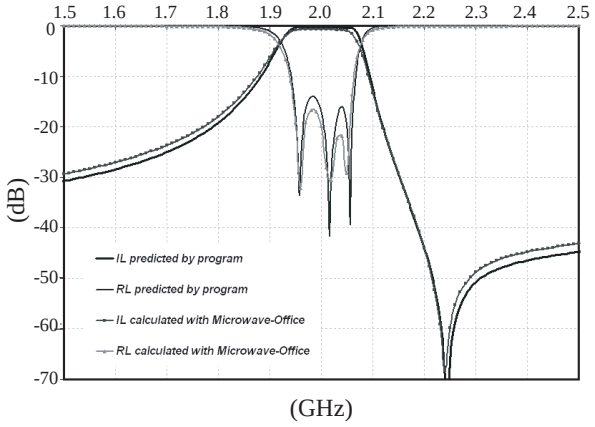

Figure 5: Comparison of the performance of MLS filter design with that of Microwave Office for Fig. 4.

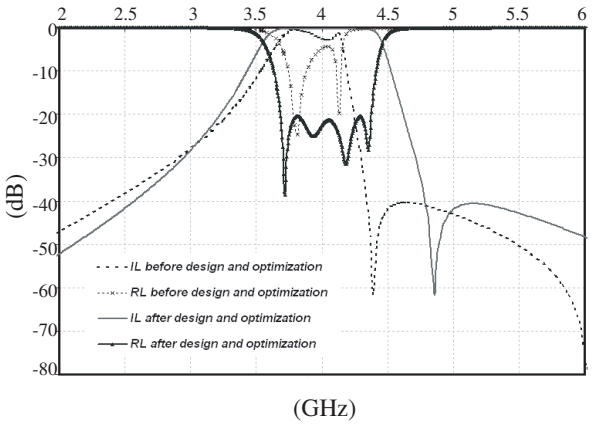

Figure 6: Frequency response of a wideband interdigital filter before and after optimization.

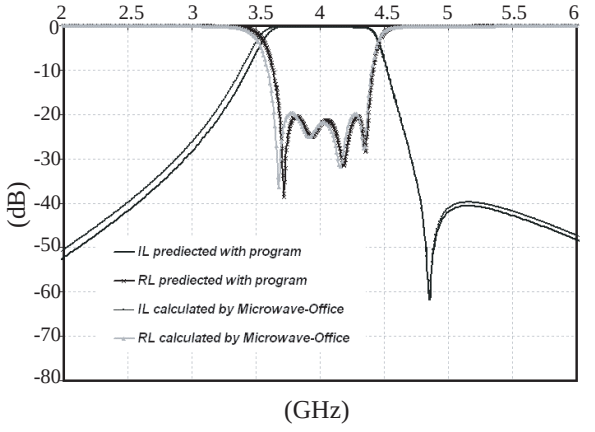

Figure 7: Comparison of the performance of MLS filter design with that of Microwave Office for Fig. 6.

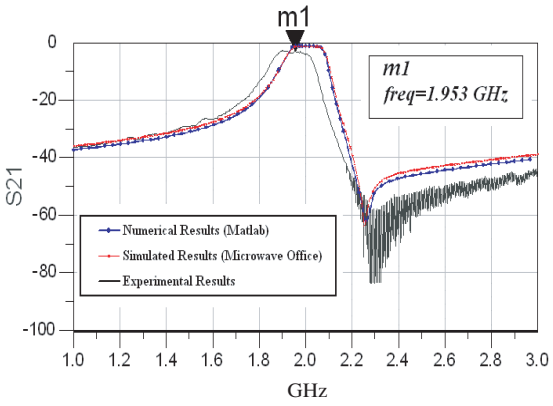

Figure 8: Comparison of the performance of interdigital filter designed by MLS with those obtained by Microwave-Office and fabrication and measurement.

The insertion loss is

$$IL_k = -20\log|s_{21}|_k \tag{8}$$

Finally, an error function is constructed for the specified insertion and return losses in the lower

and upper stopbands, transition bands and the passband, as shown in Fig. 3.

$$\begin{aligned} e \;=\; & \sum_{k=1}^{K_{SL}} \left((IL_k - ILSB_k)^2 + (RL_k - RLSB_k)^2 \right) \\ & + \sum_{k=K_{PL}}^{K_{PU}} \left((IL_k - ILPB_k)^2 + (RL_k - RLPB_k)^2 \right) \\ & + \sum_{k=K_{SU}}^{K} \left((IL_k - ILSB_k)^2 + (RL_k - RLSB_k)^2 \right) \end{aligned} \tag{9}$$

where IL_k and RL_k are the insertion and return losses calculated at the kth frequency and $ILSB$ and $RLSB$ are their specified values in the stopband and $ILPB$ and $RLPB$ are their values in the passband. The frequency band is divided into K discrete frequencies. wt_i are the weighting functions which may emphasize any of the terms in the error function, by adjusting their values.

The error function is minimized with respect to the values of w_i, s_i and L. However, some initial values are required for them to start the minimization of the error function. On the other hand, input values of the filter structure including the frequency band and the load and source admittances should be provided for the incorporated impedance matching.

3. NUMERICAL RESULTS

The design and optimization of the interdigital filter shown in Figs. 1 and 2 are performed as an illustration for the proposed MLS algorithm. The initial values are selected as follows:

$L = \lambda/4$ (center frequency), $w_i = h$ (thickness of substrate), $s_i = 2h$ (or as a function of strip width), $s_1 = s_n = h/4$ (the gap between the first two strips and the last two strips). Then the minimization of the error function is performed with respect to L, w_i and s_i to obtain the optimum design of the interdigital filter.

Two examples of filter designs are given for the narrow band and wide band versions. Their performances are also obtained by commercial softwares, namely Microwave-Office.

Table 1: Data for the narrow band filter design.

$\varepsilon_r = 3.38$, $Loss\,tangent = 0.0027$, $h = 20\,\text{mil}$, $Z_s = 50$, $Z_l = 50$, $f_0 = 2\,\text{GHz}$, $BW = 6\%$, $degree\,of\,filter = 3$	
Initial values	After Design and Optimization
$w1 = 0.508\,(\text{mm})$, $s1 = 0.152\,(\text{mm})$	$w1 = 1.038\,(\text{mm})$, $s1 = 0.219\,(\text{mm})$
$w2 = 0.508\,(\text{mm})$, $s2 = 1.016\,(\text{mm})$	$w2 = 1.032\,(\text{mm})$, $s2 = 1.342\,(\text{mm})$
$w3 = 0.508\,(\text{mm})$, $s3 = 1.016\,(\text{mm})$	$w3 = 0.621\,(\text{mm})$, $s3 = 1.381\,(\text{mm})$
$w4 = 0.508\,(\text{mm})$, $s4 = 0.152\,(\text{mm})$	$w4 = 0.993\,(\text{mm})$, $s4 = 0.254\,(\text{mm})$
$w5 = 0.508(mm)$	$w5 = 1.583(mm)$
$L = 21(mm)$	$L = 23.23(mm)$

In Table 1, the input voltages for the narrow band also the initial values of L, w and s are given for the filter degree $N = 3$. Their values for the optimum design of the filter are also given. In Fig. 3, the frequency response of the filter is given for its optimum design. In Fig. 4, its performance obtained by the proposed method and that obtained by the Microwave Office are compared which indicate an excellent agreement. The optimum design of the microstrip interdigital band pass filter for the wideband version is given in Table 2, Figs. 5 and 6.

4. IMPLEMENTATION

A sample filter is designed and optimized by the proposed method. The filter is fabricated and its performance is measured by HP 8563E and compared with that of Microwave Office simulation software and that computed by the proposed method in Fig. 8. The characteristics of the interdigital bandpass filter are:

Table 2: Data for the wide band filter design.

$\varepsilon_r = 4.2$, *Loss tangent* $= 0.0027$, $h = 20\,\text{mil}$, $Z_s = 50$, $Z_l = 50$, $f_0 = 4\,\text{GHz}$, $BW = 17.5\%$, *degree of filter* $= 4$	
Initial values	After Design and Optimization
$w1 = 0.508\,(\text{mm})$, $s1 = 0.152\,(\text{mm})$	$w1 = 0.287\,(\text{mm})$, $s1 = 0.152\,(\text{mm})$
$w2 = 0.508\,(\text{mm})$, $s2 = 1.016\,(\text{mm})$	$w2 = 1.151\,(\text{mm})$, $s2 = 0.484\,(\text{mm})$
$w3 = 0.508\,(\text{mm})$, $s3 = 1.016\,(\text{mm})$	$w3 = 1.598\,(\text{mm})$, $s3 = 0.557\,(\text{mm})$
$w4 = 0.508\,(\text{mm})$, $s4 = 1.016\,(\text{mm})$	$w4 = 1.505\,(\text{mm})$, $s4 = 0.496\,(\text{mm})$
$w5 = 0.508\,(\text{mm})$, $s5 = 0.152\,(\text{mm})$	$w5 = 0.967\,(\text{mm})$, $s5 = 0.146\,(\text{mm})$
$w6 = 0.508\,(\text{mm})$	$w6 = 0.282\,(\text{mm})$
$L = 10.78\,(\text{mm})$	$L = 10.01\,(\text{mm})$

Filter degree is three or five microstrip lines, center frequency 2 GHz in the range 1 to 3 GHz, $K = 300$ for 300 discrete frequencies for the error function, frequency bandwidth in the passband is 120 MHz (or 6%), $w_k = 1$, input and output impedances equal to $50\,\Omega$.

5. CONCLUSION

In this paper a design and optimization procedure for the inhomogeneous microstrip interdigital bandpass filter is developed based on the method of least squares which employs the N coupled transmission line theory. The proposed method incorporates impedance matching of the load and source impedances, which leads to shorter and simpler circuit configurations.

The performance of the proposed filter design method agrees very well with that of the commercial softwares for microwave circuits.

REFERENCES

1. Matthaei, G., L. Young, and E. M. T. Jones, *Microwave Filters, Impedance-Matching Networks, and Coupling Structures.*, Artech House, Boston, 614–647, Nov. 1985.
2. Pozar, D., *Microwave Engineering*, Third Edition, John Wiley and Sons, 416–438, 2005.
3. Dishal, M., "A simple design procedure for small percentage bandwidth round rod interdigital filters," *IEEE Trans. Microwave Theory Tech.*, Vol. 13, No. 5, 696–698, Sept. 1965.
4. Martin, P., "Design equations for tapped round rod combline and interdigital bandpass filters," Available: http://www.rfshop.com.au/C&IDES.DOC. Nov. 2002.
5. Milligan, T. A., "Dimensions of microstrip coupled lines and interdigital structure," *IEEE Trans. Microwave Theory Tech.*, Vol. 25, No. 5, 405–410, May 1977.
6. Oraizi, H. and N. Azadi, "A novel method for the design and optimization of microstrip combline filters with tapped-line input," *Mediterranean Microwave Symposium*, Genova, Italy, Sept. 2006.
7. Oraizi, H. and N. Azadi, "A novel method for the design and optimization of microstrip multisection bandpass Combline filters," *36th European Microwave Conference*, Manchester, UK, 1217–1220, Sept. 2006.
8. Oraizi, H. and N. Azadi, "Realization of transmission zeros for the improvement of the transition bands of combline filters by lumped capacitors," *Mediterranean Microwave Symposium*, Genova, Italy, Sept. 2006.
9. Gentili, G. and M. Salazar-Palma, "The definition and computation of modal characteristic impedance in quasi-TEM coupled transmission lines," *IEEE Trans. Microwave Theory Tech.*, Vol. 43, No. 2, 338–343, Feb. 1995.
10. Amirhossenini, M. K., "Determination of capacitances and conductonce matrices of lossy shilded coupled microstrip transmission lines," *Progress in Electromagnethics Research*, PIER 50, 267–278, 2005.
11. Harrington, R. F. and C. Wei, "Losses on multiconductor transmission lines in multilayered dielectric media," *IEEE Trans. Microwave Theory Tech.*, Vol. 32, No. 7, 705–710, July 1984.
12. Wei, C., R. F. Harrington, J. R. Mautz, and T. K. Sarkar, "Multiconductor transmission lines in multilayered dielectric media," *IEEE Trans. Microwave Theory Tech.*, Vol. 32, No. 2, 439–450, Feb. 1995.

13. Tripathi, V. K., "A dispersion model for coupled microstrips," *IEEE Trans. Microwave Theory Tech.*, Vol. 34, No. 1, 66–71, Jan. 1986.
14. Tripathi, V. K., "Asymmetric coupled transmission lines in an inhomogeneous medium," *IEEE Trans. Microwave Theory Tech.*, Vol. 23, No. 9, Sept. 1975.
15. Tripathi, V. K., "On the analysis of symmetrical three-line microstrip circuits," *IEEE Trans. Microwave Theory Tech.*, Vol. 23, No. 9, Sept. 1975.
16. Edwards, T. C. and M. B. Steer, *Foundations for Microstrip Circuits*, 3rd Edition, John Wiley & Sons, New York, 2000.